DOE/EV-0085
VOL. 2 OF 3

Liquefied Gaseous Fuels Safety and Environmental Control Assessment Program: Second Status Report

October 1980

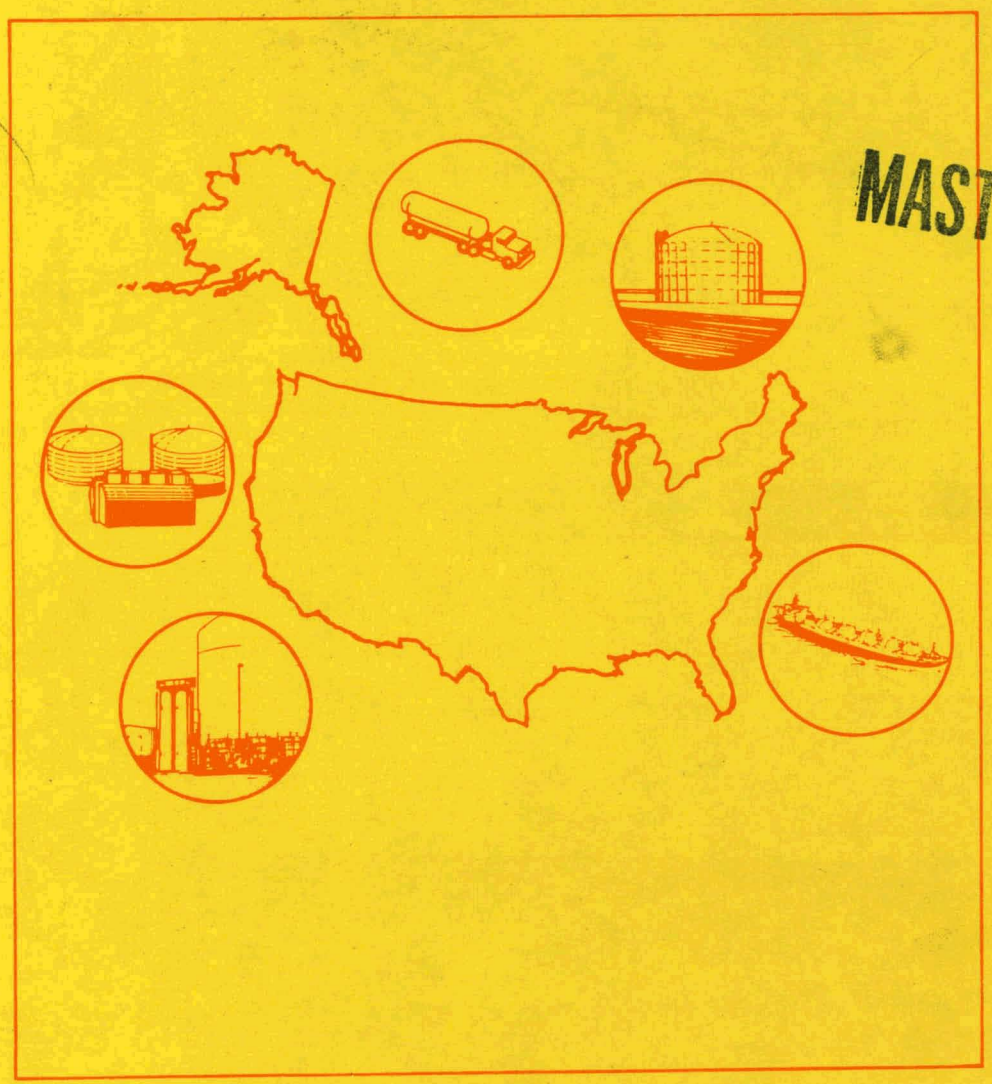

U.S. DEPARTMENT OF ENERGY
Assistant Secretary for Environment
Environmental and Safety Engineering Division

DISCLAIMER

Printed in the United States of America

Available from

National Technical Information Service
U.S. Department of Commerce
5285 Port Royal Road
Springfield, VA 22161

NTIS price codes

Printed Copy: $[illegible] A 24
Microfiche Copy: $ [illegible] A01

Master

DOE/EV-0085
VOL. 2 OF 3
UC-11

Liquefied Gaseous Fuels Safety and Environmental Control Assessment Program: Second Status Report

October 1980

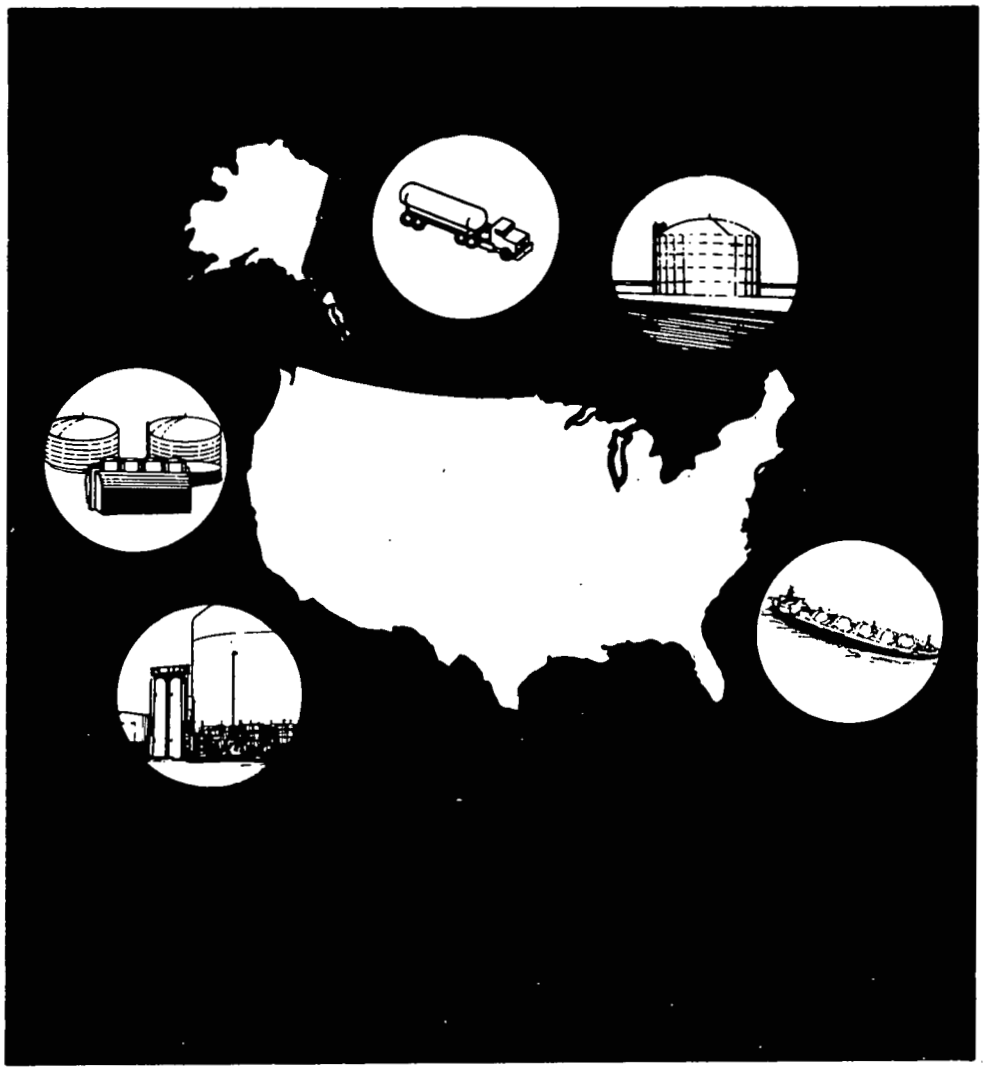

U.S. DEPARTMENT OF ENERGY
Assistant Secretary for Environment
Environmental and Safety Engineering Division
Washington, D.C. 20545

The Reports contained in this document were prepared for the government under a variety of contracts:

Aeroject Energy Conversion Company	DE-AC-03-78EV02057
Applied Technology Corporation	DE-AC-05-78EV06020
Arthur D. Little, Inc.	DE-AC-02-78EV04734
Jet Propulsion Laboratory	NAS-7-100
Lawrence Livermore Laboratory	W-7405-ENG-48
Los Alamos Scientific Laboratory	W-7405-ENG-36
Massachusetts Institute of Technology	DE-AC-02-77EV04204
	DE-AC-02-79EV04548
Naval Weapons Center	DE-AI-01-79EV10072
	MIPR Z-70099-8-816817A
Pacific Northwest Laboratory	DE-AC-06-76RLO 1830

This document is available under catalogue number DOE/EV-0085 from

National Technical Information Service
U.S. Department of Commerce
5285 Port Royal Road
Springfield, VA 22161

Printed copy: $21.50
Microfiche: $3.00

ACKNOWLEDGMENT

The Liquefied Gaseous Fuels Safety and Environmental Control Assessment Program originated in the Environmental and Safety Engineering Division, Office of the Assistant Secretary for Environment, U.S. Department of Energy. The Program is coordinated among the following:

U.S. Department of Commerce
Maritime Administration
National Bureau of Standards

U.S. Department of Transportation
Coast Guard
Federal Railroad Administration
Office of Pipeline Safety Regulations

National Aeronautics and Space Administration

National Science Foundation

The Fertilizer Institute

The Gas Research Institute

This document was compiled by Pacific Northwest Laboratory, operated by Battelle Memorial Institute, who is assisting the Environmental and Safety Engineering Division in the development and planning of this program.

THIS PAGE

WAS INTENTIONALLY

LEFT BLANK

FOREWORD

The Assistant Secretary for Environment has responsibility for identifying, characterizing, and ameliorating the environmental, health, and safety issues and public concerns associated with commercial operation of specific energy systems. The need for developing a safety and environmental control assessment for liquefied gaseous fuels was identified by the Environmental and Safety Engineering Division[(a)] as a result of discussions with various governmental, industry, and academic persons having expertise with respect to the particular materials involved: liquefied natural gas, liquefied petroleum gas, hydrogen, and anhydrous ammonia.

This document is arranged in three volumes and reports on progress in the Liquefied Gaseous Fuels (LGF) Safety and Environmental Control Assessment Program made in Fiscal Year (FY)-1979 and early FY-1980. Volume 1 (Executive Summary) describes the background, purpose and organization of the LGF Program and contains summaries of the 25 reports presented in Volumes 2 and 3. Annotated bibliographies on Liquefied Natural Gas (LNG) Safety and Environmental Control Research and on Fire Safety and Hazards of Liquefied Petroleum Gas (LPG) are included in Volume 1.

Volume 2 consists of 19 reports describing technical effort performed by Government Contractors in the area of LNG Safety and Environmental Control. Volume 3 is a similar compilation and contains 6 contractor reports on LPG, anhydrous ammonia and hydrogen energy systems.

(a) Effective June 1980, the Environmental Control Technology Division was augmented by acquiring additional functions: the new name of the organization is the Environmental and Safety Engineering Division. Throughout the text, where the old name is used, is should now refer, in all cases, to the Environmental and Safety Engineering Division, Office of the Assistant Secretary for Environment. Future publications will reflect this change completely.

THIS PAGE

WAS INTENTIONALLY

LEFT BLANK

TABLE OF CONTENTS

LIQUEFIED GASEOUS FUELS SAFETY AND ENVIRONMENTAL CONTROL ASSESSMENT PROGRAM: SECOND STATUS REPORT

VOLUME 2 - LNG REPORTS

VOLUME 2

LNG REPORTS

REPORT A

Simulation of LNG Vapor Spread and Dispersion by Finite Element Methods

S. T. Chan
P. M. Gresho
R. L. Lee

Prepared for the
Environmental and Safety Engineering
Division
U.S. Department of Energy
under Contract W-7405-ENG-48

Lawrence Livermore Laboratory
Livermore, California 94550

THIS PAGE

WAS INTENTIONALLY

LEFT BLANK

REPORT A

TABLE OF CONTENTS

FIGURES

TABLES

SUMMARY

Two finite element models - one based on solving the time-dependent, two-dimensional conservation equations of mass, momentum, and energy, with buoyancy effects included via the Boussinesq approximation; the other based on solving the otherwise identical set of equations except using the hydrostatic assumption - are described herein and applied to predict some aspects of the vapor dispersion phenomena associated with LNG spills. A number of controlled numerical experiments, representing a reasonable expected range of LNG spill scenarios and atmospheric conditions, have been carried out. Based on comparing the results obtained with these finite element models, some data regarding the applicability and limitations of the hydrostatic assumption for predicting LNG vapor spread and dispersion are established.

INTRODUCTION

Accurate and verified numerical models for the prediction of LNG (Liquefied Natural Gas) vapor dispersion in the atmosphere are a requirement for predicting possible hazards involved in LNG facilities and for developing and evaluating potential methods to minimize these hazards. Although a number of numerical models have been developed by various authors to simulate the vapor dispersion process associated with an LNG spill, unfortunately the predictive capabilities of the existing models are still far from being satisfactory. Recently Havens[1] has done a systematic evaluation of a number of models widely cited in the literature and reported very large (order of magnitude) differences in the predicted downwind distance to the lower flammability limit (LFL) of the dispersed vapor cloud resulting from a large LNG spill onto water. Havens concludes that the relatively simple Gaussian dispersion model by Germeles and Drake[2] and the most complex model developed by Science Applications, Inc. (SAI)[3] represent the most rational approaches, among all models considered, to estimate the downwind dispersion of the vapor cloud. However, he also cautions that further improvements to the Germeles and Drake model are necessary and a thorough evaluation and verification of the SAI model should be performed before results from these models can be accepted with confidence to predict the consequences of large LNG spills.

The Germeles and Drake model is basically a Gaussian plume model. With further improvements and adequate verification data, the model could probably be (cautiously) used as an alternative to a more complex numerical model, particularly for routine usage where time and cost constraints are important; nevertheless, due to its inherent simplifying approximations, such a model is probably inappropriate for predicting the vapor dispersion associated with large LNG spills. On the other hand, the SAI model, which solves, via the finite difference method, the transient, three-dimensional conservation equations of mass, momentum, energy, and species, represents a more viable approach. The SAI model has removed many of the simplifying approximations inherent in the Germeles and Drake model; however, in order to make the computations more tractable and less costly, the model assumes that the hydrostatic approximation (which states that the vertical pressure gradient is balanced completely by the buoyancy force) is valid for the LNG vapor dispersion process. The validity of such an approximation, however, remains to be thoroughly assessed and verified.[4]

It is well recognized that a general solution of the LNG dispersion problem must include, as a minimum, the following: three-dimensional velocity field, time-dependent terms, nonlinear mathematics, coupled energy, species, and momentum equations with buoyancy terms, an adequate turbulence model, and accounting for the nearby surroundings such as terrain, dikes, and buildings, if present. As can be imagined, any numerical model which takes all of the above phenomena into account is bound to be very complex and costly. Therefore the selection of appropriate numerical schemes and justifiable simplifying assumptions becomes very crucial.

With these in mind, we investigate, in the present study, the feasibility of using the finite element method (FEM) to simulate the LNG vapor spread and dispersion. At the same time, the numerical experiments are designed to attempt to shed some light on the level of accuracy attainable with a hydrostatic model, as compared to a more complete, nonhydrostatic model for some typical spill scenarios. Our two models solve the time-dependent, two-dimensional conservation equations of mass, momentum, and energy (temperature) by employing the FEM. In order to facilitate the study, the Boussinesq approximation has been invoked in both models but will be removed in our future LNG vapor dispersion model since the density variation is quite large. In addition, the fluid is assumed to be Newtonian, with constant properties except for density in the buoyancy force (our future model will consider variable properties). The concentration equation for the LNG vapor cloud has not yet been implemented in either code but its inclusion is straightforward. In fact, besides possible differences in certain coefficients and boundary conditions, the concentration equation (in the absence of chemical reactions) is the same as the temperature equation and thus the temperature field can be considered to represent, to a first approximation, the concentration of LNG vapor as well.

In the following sections, we describe briefly the mathematical formulation and numerical implementation of the two models, summarize and compare results on a number of test cases for LNG vapor dispersion from the models, and finally draw conclusions from these controlled numerical experiments to guide our future work toward developing a cost-effective, time-dependent, three-dimensional numerical model for predicting the vapor dispersion resulting from large LNG spills.

DESCRIPTION OF THE NUMERICAL MODELS

The Nonhydrostatic Model

The detailed formulation of the nonhydrostatic model for isothermal flows can be found in Refs. 5 and 6. The present model is a straightforward extension of the isothermal problem to include also the temperature equation, with the buoyancy force considered via the Boussinesq approximation. Here we summarize only the essential features of the present model.

- Governing Equations

The equations of motion and continuity for a constant property (except for density in the buoyancy force), incompressible Newtonian fluid are the Boussinesq approximation to the Navier-Stokes equations,

$$\rho\left(\frac{\partial \underline{u}}{\partial t} + \underline{u} \cdot \nabla \underline{u}\right) = \nabla \cdot \underline{\underline{\tau}} - \rho\gamma \underline{g} \top \tag{1}$$

$$\nabla \cdot \underline{u} = 0 \tag{2}$$

where $\underline{u} = (u,v)$ is the velocity, ρ is the (constant) density at the reference temperature, γ is the (constant) volumetric coefficient of thermal expansion, T is the temperature deviation from the reference temperature, $\underline{g}$ is the acceleration due to gravity, and

$$\tau_{ij} = - p \delta_{ij} + \mu\left(\frac{\partial u_i}{\partial x_j} + \frac{\partial u_j}{\partial x_i}\right) \tag{3}$$

is the stress tensor in which is the (constant) eddy viscosity, and p is the pressure deviation from hydrostatic. Finally, the energy equation for a constant property fluid (neglecting viscous dissipation) is

$$\frac{\partial T}{\partial t} + \underline{u} \cdot \nabla T = k \nabla^2 T \tag{4}$$

where k is the thermal diffusivity (eddy diffusion coefficient). The above set of equations can be used, given appropriate initial and boundary conditions, to solve for the velocity components u and v, the temperature T, and the pressure p.

The appropriate initial condition for the above equations is any solenoidal velocity field (i.e., one which satisfies the discretized version of $\nabla \cdot \underline{u}_o = 0$), plus any initial temperature field. Regarding boundary conditions: for the velocity field, one can either specify the velocity components or the corresponding tractions; for the temperature field, one can specify either the temperature itself, or a general heat transfer condition.

- Spatial Discretization

The finite element discretization of the above equations is performed via the Galerkin method:

$$u = \sum_{j=1}^{n} \phi_j(x,y)\ u_j(t)$$

with a similar expansion for v and T, and

$$p = \sum_{j=1}^{m} \psi_j(x,y)\ p_j(t)$$

where, in the discretized domain, there are n nodes for velocity and temperature and m nodes for the pressure. The resulting system of algebraic equations, written in a compact matrix form is

$$M\,\dot{u} + [K + N(u)]\,u + Cp + M'T = f,$$

$$C^T u = 0,$$

and (5)

$$M'\dot{T} + [K_T + N'(u)]\,T = f',$$

where now u is a global vector containing all nodal values of horizontal and vertical velocity components, $\dot{u}$ is the time derivative of u, p is a global vector of the pressure values, T is a global vector of the temperature values, and f, f' are global vectors which incorporate the appropriate boundary conditions. M is a 2n x 2n "mass" matrix. M' is an n x n subset of the mass matrix, K is the 2n x 2n viscous matrix, K_T is the n x n thermal diffusion matrix, C is the 2n x m pressure gradient matrix and its transpose, C^T, is the m x 2n divergence matrix, N(u) is the 2n x 2n nonlinear advection matrix, and finally N'(u) is an n x n subset of the advection matrix. Equation (5) describes a nonlinear system of ordinary differential equations (ODE's) in time with algebraic constraints, the solution of which yields the vectors of nodal values of u, v, p, and T. The nonlinear algebraic equations engendered by the application of the trapezoid rule for integrating the ODE's in time are currently being solved via a one-step Newton method (Ref. 6) in conjunction with the frontal technique (Gaussian elimination). Our element library contains three types of isoparametric elements: (1) 4-node bilinear approximation for velocity and temperature with piecewise constant pressure, (2) 8-node quadratic approximation (serendipity) for velocity and temperature with 4-node bilinear approximation for pressure, and (3) 9-node biquadratic approximation for velocity and temperature with 4-node bilinear approximation for pressure.

- Time Integration Method

The technique employed for integrating Eqn. (5) is an implicit, second-order accurate algorithm which automatically and dynamically selects an appropriate time step based solely on accuracy requirements. This is accomplished through an appropriate combination of two common time integration techniques, namely, the (implicit) trapezoid rule (TR) and an (explicit) Adams-Bashforth formula (AB). The algorithm basically consists of the following three steps: (1) Use the AB formula as a predictor equation for velocity and temperature, (2) Use the TR algorithm to solve for the corrected (final) velocity and temperature and for the pressure, (3) combine the predictor results with the corrector results for velocity and temperature to estimate the local time truncation error and, from this, the size of the next time step. This procedure thus provides a cost-effective integration scheme in that the time step size is increased whenever permissible and decreased only when necessary. More detailed information on this time integration scheme can be found in Refs. 5 and 6.

The Hydrostatic Model

As mentioned earlier, with the assumption that the convective motion, inertia, and shear forces in the vertical direction are all negligible, the equation for vertical motion is greatly simplified, implying that the vertical pressure gradient is balanced entirely by the buoyancy force. Thus the pressure field is no longer an implicit variable which instantaneously "adjusts itself" in such a way that the incompressibility constraint (continuity equation) remains satisfied. Rather, the pressure field can now be more easily obtained through integration of the buoyancy force. This (hydrostatic) assumption renders the flow field much easier to compute; however, as will be seen in the numerical results, its range of applicability is also greatly reduced. In the following, we describe the equations being solved, together with the numerical aspects of the hydrostatic model.

- Governing Equations

Applying the hydrostatic assumption to Eqn. (1) and rearranging, we obtain the following equations

$$\rho\left(\frac{\partial u}{\partial t} + u\,\frac{\partial u}{\partial x} + v\,\frac{\partial u}{\partial y}\right) = -\,\frac{\partial p}{\partial x} + \mu\nabla^2 u \qquad (6)$$

$$\frac{\partial p}{\partial y} = \rho\,\gamma g T \qquad \text{(the hydrostatic equation for pressure)}, \qquad (7)$$

$$\frac{\partial u}{\partial x} + \frac{\partial v}{\partial y} = 0, \qquad (8)$$

and

$$\frac{\partial T}{\partial t} + u\,\frac{\partial T}{\partial x} + v\,\frac{\partial T}{\partial y} = k\nabla^2 T, \qquad (9)$$

with the acceleration of gravity aligned in the negative y-direction.

The appropriate initial condition for the above set of equations is an initial horizontal velocity field (u_o), plus an initial temperature field (T_o), from which Equations (7) and (8) are then used to compute the corresponding initial pressure field (p_o) and the vertical velocity field (v_o). Regarding boundary conditions: for the horizontal velocity component u, one can specify u itself or a natural boundary condition ($\partial u/\partial n$ or $\mu\,\partial u/\partial n - p\,n_x$). For the vertical velocity component v, however, one is allowed only to specify v itself along either the top or bottom boundary, but generally along the bottom boundary (with a mass flux condition). For the pressure field, one is allowed to specify p itself along either the top or the bottom boundary, but it is generally more convenient and natural to specify p as a function of x along the top boundary. For the temperature field, again, one can either specify the temperature itself, or a general heat transfer condition.

- Spatial Discretization

Briefly, the discretized algebraic equations are again obtained using the concept of finite elements but, now, with two methods of weighted residuals; the Galerkin method is applied to equations (6) and (9) and the least squares method to equations (7) and (8). (Note. The latter method can be considered as a Galerkin method applied to the equivalent higher order equations.) Galerkin's method could have been applied to equations (7) and (8) as well; however, the least squares method is preferred for the following reasons:

(1) The Galerkin method, when applied to equation (7) or (8), generates unsymmetric matrices with some zero diagonal elements and would, in general, require pivoting to solve the system of equations. On the other hand, with the least squares method, the resulting matrices on the left hand side are symmetric and positive definite, which is more desirable computationally.

(2) The general shortcomings associated with the least squares method, such as the requirement of higher order approximations, difficulty with applying natural boundary conditions, and more computational effort, do not arise for the equations in the present form (Equations (7) and (8)).

Having selected the 'proper' methods of weighted residuals, we again assume the approximate solution to be in the following form

$$u = \sum_{j=1}^{m} \phi_j(x,y)\ u_j(t),$$

with a similar expression for v and T, and

$$p = \sum_{j=1}^{m} \psi_j(x,y)\ p_j(t)$$

In the above we assume the same order of approximations for u, v, and T, and for the pressure field, unlike the nonhydrostatic formulation, it is no longer a necessity that the approximating functions for p be one order less than those for u and v. Our element library contains three types of isoparametric elements: (1) 4-node bilinear element, (2) 8-node serendipity element; and (3) 9-node biquadratic element. Any of these element types can be used, in principle, to approximate any one of the unknowns u, v, p, or T and therefore many combinations of approximating the solution are possible.

After applying the selected methods of weighted residuals to the appropriate equations (i.e., the Galerkin method to Eqns. (6) and (9), and the least squares method to Eqns. (7) and (8)), we obtain the following matrix equations:

$$M\dot{u} + \left[K + N(u,v)\right]u = f(p) \quad , \tag{10}$$

$$Av = h(u) \quad , \tag{11}$$

$$A'p = h'(T) \quad , \tag{12}$$

and

$$M\dot{T} + \left[K' + N(u,v)\right]T = f' \tag{13}$$

where u, v, p and T are the global vectors containing nodal values of the horizontal velocity component, the vertical velocity component, the pressure, and the temperature, respectively. The other matrices are defined as follows

$$M_{ij} = \iint \phi_i \, \phi_j \; dA$$

$$K_{ij} = \frac{\mu}{\rho} \iint (\phi_{i,x} \, \phi_{j,x} + \phi_{i,y} \, \phi_{j,y}) \; dA$$

$$N_{ij} = \iint \phi_i \, (u\phi_{j,x} + v\phi_{j,y}) \; dA$$

$$f_i = \begin{cases} \frac{\mu}{\rho} \int_{\partial\Omega_1} \phi_i \, u_{,n} \, d\ell - \frac{1}{\rho} \iint \phi_i \, p_{,x} \, dA & \text{if } u_{,n} \text{ is specified on } \partial\Omega_1 \\ \frac{1}{\rho} \iint \phi_{i,x} \, p dA + \frac{1}{\rho} \int_{\partial\Omega_1} \phi_i \, (\mu u_{,n} - p n_x) \, d\ell & \text{if } (\mu u_{,n} - p n_x) \text{ is specified on } \partial\Omega_1 \end{cases}$$

$$A_{ij} = \iint \phi_{i,y} \, \phi_{j,y} \; dA$$

$$h_i = -\iint \phi_{i,y} \, u_{,x} \; dA$$

$$A'_{ij} = \iint \psi_{i,y} \, \psi_{j,y} \; dA$$

$$h'_i = \rho\gamma g \iint \psi_{i,y} \, T \; dA$$

$$K'_{ij} = k \iint (\phi_{i,x} \, \phi_{j,x} + \phi_{i,y} \phi_{j,y}) \; dA,$$

and

$$f'_i = k \int_{\partial\Omega_2} \phi_i \, T_{,n} \, d\ell \quad \text{if } T_{,n} \text{ is specified on } \partial\Omega_2.$$

The special arrangement of the terms in Eqns. (10)-(13) is related to the sequential solution procedure employed, which is described next.

- Solution of the Resulting Systems of Equations

Obviously, one possible way to obtain the solution to the above systems of equations is to solve all the equations simultaneously, using procedures similar to those employed for the nonhydrostatic model. However, core and auxiliary storage requirements will be enormous and become almost prohibitive for large scale problems. Additionally, because two of the four systems of algebraic equations are linear, the coupling between the field variables is now less intensive and therefore it is probably more efficient to solve them separately. Furthermore, as noted earlier, since the matrices for v and p are symmetric and depend on geometry only, a symmetric equation solver can be utilized to further increase the computational speed provided the system equations are solved separately. For these reasons, we chose to solve the four resulting systems of equations separately and loop through them successively until convergence is obtained at each time step. Currently the "profile method"[7] is being used to solve each of the linear systems of algebraic equations, which are obtained after applying the time marching scheme described in the next subsection.

The optimal order in which the equations for u, v, p, and T are solved may, in general, be problem dependent. However, as a general rule, the unknown (u or T) varying the fastest with respect to time should probably be solved first, p solved after T, and v after u. A logical order for most LNG problems appears to be: $T \rightarrow p \rightarrow u \rightarrow v$, which has been observed in our numerical experiments to yield a faster rate of convergence than some other possible combinations.

- Time Marching Scheme

Currently only a relatively simple time marching scheme has been implemented in the computer code to integrate the resulting system of equations in time. This scheme uses a direct iteration strategy and consists of essentially two steps to obtain the solution at time $t=t^{n+1}$, knowing the solution at $t=t^n$. The two steps are: (1) The Backward Euler Method (BE) is applied to equations (10) and (13) for half a time step (from $t=t^n$ to $t^a=t^n + \frac{t^{n+1}-t^n}{2}$) to obtain solutions for u and T at $t=t^a$, after which the solution for v and p at $t=t^a$ are computed immediately (i.e., p from T and v from u). The process of looping through all four systems of equations is repeated until the solution has converged at $t=t^a$. (2) The trapezoid rule (TR) algorithm is then applied to obtain solutions at $t=t^{n+1}$ for all field variables using the converged results at $t=t^a$ and those from $t=t^n$. The above steps, and iteration sequence, are then repeated for the next time step. Unlike the nonhydrostatic code, the time-step sizes in the present program are predetermined and controlled by input data. The time integration scheme used in the nonhydrostatic code could, of course, be employed here also but remains to be implemented.

To derive the recurrence relationship for the BE step and to clarify the scheme, let us consider equation (10). With superscripts "n" and "a" denoting variables at t^n and t^a respectively, we thus have

$$\frac{2}{\Delta t} M (u^a - u^n) + (K + N^a) u^a = f^a$$

or

$$\left[\frac{2}{\Delta t} M + K + N^a\right] u^a = f^a + \frac{2}{\Delta t} M u^n, \tag{14}$$

where $\Delta t = t^{n+1} - t^n$ is a full time step. The solution to Eqn. (14) is a first order accurate result for u^a from time t^n to time $t^n + \Delta t/2$ and is stable for any Δt. Similar results can be obtained for equation (13). Currently the nonlinear system of equations, Eqn. (14), is being solved by direct iterations, using results from the most recent iterate in forming the matrix N^a. To obtain the solutions at time $t=t^{n+1}$, we apply the 'trapezoid rule' in the form

$$u^{n+1} = 2u^a - u^n. \tag{15}$$

The above procedure can be considered as a modified TR (or, perhaps more precisely, as a nonlinear, implicit mid-point rule), since it can be shown that, for a linear system of ODE's, the combined result of the above steps is identical with that of TR, even though the first step (BE step) apparently is only first order accurate in time. Hence the final result would be second-order accurate in time from t^n to t^{n+1}. The attractive feature of the above procedure appears to be that somewhat fewer matrix multiplications are required than with the conventional TR in formulating the RHS vector. However, the accuracy, stability, and rate of convergence, as compared with the conventional TR applied to the nonlinear system, remains to be investigated.

- Convergence Criterion

The root mean square (RMS) error is used as the convergence criterion to determine whether the solution has converged adequately between two successive iterations m and m+1. This criterion is applied to both the temperature field and the horizontal velocity field. Mathematically, we require

$$|\delta T| = \frac{\sqrt{\frac{1}{N_T}\sum_{i=1}^{N_T}(T_i^{m+1} - T_i^m)^2}}{T_{max}} < \varepsilon$$

$$|\delta u| = \frac{\sqrt{\frac{1}{N_u}\sum_{i=1}^{N_u}(u_i^{m+1} - u_i^m)^2}}{u_{max}} < \varepsilon \tag{16}$$

where N_T and N_u are the total number of nodal values being computed (specified values excluded) for temperature and horizontal velocity components, respectively, T_{max} and u_{max} represent the expected maximum values for T and u within the domain, and ε is a (small) input parameter. Our numerical results indicate that a value of ε equal to 10^{-3} is generally sufficient, and that the typical number of iterations required for each time step varies from 2 to 6, depending mainly on the time step size and the "difficulty" of the simulated flow.

NUMERICAL RESULTS

In order to study the applicability of the present models for LNG vapor dispersion predictions, we have used both models to generate solutions to a series of test cases, with the diffusivity parameters varied and subject to a pre-existing wind or a no wind condition. In these test cases, two of the parameters were set to be constant (γ = 0.003 $^{o}C^{-1}$ g = 9.8 m/sec^2). The diffusivity parameters ($\nu \equiv \mu/\rho$ and k) were set equal to 0.1, 1, or 10 m^2/sec to approximate the turbulent eddy diffusivity. These values are crude estimates of what we believe might correspond to the minimum, nominal, and maximum expected average values of the turbulent diffusivity. We used consistent (but not identical) initial and boundary conditions whenever possible in the two models. For the results presented herein, 4-node bilinear approximations for u, v, T and piecewise constant for p have been used with the nonhydrostatic model, but 4-node bilinear approximations for all variables, u, v, T and p, have been used with the hydrostatic model. Because we intend to use only the 8-node trilinear elements in our future three-dimensional LNG dispersion model, for simplicity, and some other reasons (to be discussed in a future paper, Ref. 8), we conducted the two-dimensional calculations using, almost exclusively, the 4-node bilinear elements. In the following sections we present and discuss some key results from these test cases (velocity is in m/sec, temperature is in ^{o}C, and pressure is in nt/m^2).

For the cases without wind, we consider a domain of 240m x 24m, represented by a nonuniform mesh consisting of 552 bilinear elements and 611 nodal points. Due to symmetry, only half of the physical domain was used in our computations. The initial LNG vapor cloud is idealized as a thin slab, sitting on the ground, with temperature T=-180^{o}C (relative to the ambient air) within the slab but equal to a Gaussian distribution function along the top and edges of the slab (for numerical reasons) which rapidly brings the temperature from -180^{o}C to 0^{o}C. More specifically, the initial temperature is described by

$$T_o(x,y) = \begin{cases} -180 & \text{for } 0 \le x \le 100,\ 0 \le y \le 4 \\ -180e^{-(y-4)^2/2} & \text{for } 0 \le x \le 100,\ 4 < y \le 24 \\ -180e^{-(x-100)^2/2\cdot(5)^2} & \text{for } 100 < x \le 240,\ 0 \le y \le 4 \\ -180e^{-[(x-100)^2/(5)^2 + (y-4)^2]/2} & \text{for } 100 < x \le 240,\ 4 < y \le 24; \end{cases}$$

wherein it is seen that the vertical standard deviation (σ in $e^{-(y-y_o)^2/2\sigma^2}$) is one meter and the horizontal standard deviation is five meters. The remaining initial conditions together with boundary conditions used in our calculations are shown in Fig. 1. Besides the requirements of compatibility with the partial differential equations (PDE's) being solved, these boundary conditions have been selected to provide consistency between the two models and also to be as flexible as possible (rather than being too 'stiff' for the relatively small domain considered). The no-flux condition at the ground was invoked for two reasons: (1) simplicity, and (2) it permits an alternate interpretation of isotherms as concentration contours since the no-flux condition is appropriate for the species concentration equation and the eddy diffusivities for heat and mass transfer are essentially equal. This is only a very crude boundary condition for the temperature equation, however. Also, a boundary condition such as $\partial u/\partial n = 0$ (instead of $f_n = 0$) at the outlet for the nonhydrostatic model is probably more reasonable, considering the fact that the steady state solution (T being a constant, p linear in y, and both u and v being zero) will not be recoverable under the present condition. This is so because the above condition implies that the value of $\partial u/\partial n$ at the outlet must be nonzero and in balance with the resulting (hydrostatic) pressure in order to approximate the condition $f_n = 0$. Although the hydrostatic pressure field can, in theory, be removed and the above difficulty circumvented, it does not seem to be an easy task for transient calculations. Since the above natural boundary condition ($\partial u/\partial n = 0$) has not been implemented in the nonhydrostatic code yet, we use the condition $f_n = 0$ temporarily. As long as the outlet temperature is nearly zero (hence $p \simeq 0$), the use of such a boundary condition is not expected to contaminate the solution significantly.

In Figures 2 through 5, we plot and compare the temperature field, the pressure field, the streamlines, and the velocity field at various times for the nominal case ($\nu = k = 1\ m^2/sec$), as predicted by the hydrostatic and nonhydrostatic models. As is seen in Figs. 2 and 3, both the temperature field and pressure field predicted by the two models compare in general very well except in the vicinity of the vapor cloud front where the hydrostatic assumption is apparently not well satisfied. As expected, the difference is more noticeable in the pressure field than in the temperature field, with the hydrostatic predictions indicating a consistent phase lag for the lowest pressure contour line. In Fig. 2, if the temperature is alternately "interpreted" as species concentration, then the two lowest contour lines for temperature represent approximately the upper flammability limit (UFL) and the lower flammability limit (LFL) (i.e., 15% and 5% methane concentrations by volume) of the LNG vapor concentration, respectively. Obviously the predicted UFL and LFL for the present case by the two models agree quite well in spite of some noticeable differences in pressures. However, the flow fields as predicted by the two models are seen to be significantly different near the front of the density current, as shown in Figs. 4 and 5. The hydrostatic model, although capable of representing the general flow pattern for late times, is unable to accurately produce the proper recirculation region in the vicinity of the vapor cloud front, which is present in the nonhydrostatic model. Also, the hydrostatic model is seen to have produced some unreasonably large vertical velocities near the top boundary, obviously attributable to the presence of a rather strong eddy in the flow field.

The ratio of predicted maximum magnitude of velocity (at different locations, however) between the two models ranges from approximately 2.5 at t=10.5 sec to approximately 2 for later times (Note. The velocity vector plots in Figs. 5, 7 and 9 have been exaggerated by a factor of 2 in the vertical direction, therefore the real situation is not as bad as it looks).

Shown in Figs. 6 and 7 are the results of temperature and velocity fields corresponding to a case with large diffusion (ν=k=10 m^2/sec) as predicted by the two models. The results compare remarkably well, especially for the temperature field. The worst comparison appears to be in the predicted maximum velocity at rather early time (t=10 sec in Fig. 7a), in which the hydrostatic model predicts a value approximately 14% higher than that of the nonhydrostatic model. The discrepancy, nevertheless, diminishes quickly as the vapor continues to disperse, as indicated by the results in Fig. 7b.

In another test case, we reduced the diffusion parameters from the nominal case by an order of magnitude, i.e., ν=k=0.1 m^2/sec (or equivalently make the Reynolds and Peclet numbers an order of magnitude larger) and the results are shown in Figs. 8 and 9 for temperature and velocity, respectively. As suggested by the temperature contour plots in Fig. 8, this case, unlike the previous cases, is dominated by gravitational spread. For the present case, the nonhydrostatic model seems to run successfully, although smaller times steps than those used in the nominal case are required and some wiggles in the velocity field, due to coarse space resolution, are present. The predicted maximum velocity at t=10 sec is equal to 3.8 m/sec (see Fig. 9a), which is reasonably close to the velocity of a density intrusion ($v = \sqrt{2gh\,\Delta\rho/\rho} = 5.6$ m/sec) in a two fluid system, using the simple Bernoulli equation. (The above density intrusion speed is expected to be larger than that predicted by the nonhydrostatic model because viscous effects and the decrease in height of the dense fluid are not considered in the Bernoulli equation.) On the other hand, results obtained from the hydrostatic model are unacceptable. As seen in Fig. 8, the isotherms display significant spatial oscillations, and the velocity vectors, as shown in Fig. 9, are totally unreasonable. After time t=28.3 sec, difficulties were encountered in obtaining convergence, even when smaller time steps were used. The severe numerical difficulties encountered by the hydrostatic model in this case are believed to be caused primarily by the presence of a strong recirculation zone in the flow field, which obviously cannot be handled properly by a hydrostatic model. Additionally the mesh used in the present calculations is probably too coarse for the flow under consideration (The grid Reynolds number is several hundred for this case). Use of a finer mesh could have probably relieved the numerical difficulties to a certain extent but is not considered to be the solution to the above numerical problem. This point will become clearer after we analyze numerically the relative importance of various terms in the vertical momentum equation, thus either confirming or invalidating the hydrostatic approximation in various regions of the flow field.

Toward this end, we have evaluated, via simple finite difference formulae, the numerical values of all the terms in the vertical momentum equation for some typical nodal points for the cases with nominal and low diffusivities, and the results are tabulated in Tables 1 through 3. In these tables columns (1) and (2) are the two terms retained in the equation with the hydrostatic approximation, columns (3) through (6) are the terms neglected in the hydrostatic model, column (7) represents the sum of the neglected terms when put on the "right hand side" of the equation, and column (8) is the sum of all the terms in the equation except the vertical pressure gradient. Obviously, by definition, in order for the hydrostatic approximation to be valid, the values in columns (1) and (2) must be approximately equal and each individual term in columns (3) through (6) must be small (Note. The sum of these terms being small is necessary, but not sufficient), compared with the pressure gradient and the buoyancy terms. In theory, for the vertical momentum equation to be satisfied, values in column (8) must equal those in column (1). However, with the Galerkin finite element method, the equation can only be expected to be satisfied in an averaged sense over an area (over all the elements which are directly connected with the nodal point under consideration) instead of at that particular nodal point. Additionally, the time and space derivatives in the equation have been evaluated using rather simple (unsophisticated) central finite difference formulae and hence the truncation errors are likely to be significant, especially with the unequal time step sizes and nonuniform mesh presently used. For these reasons, the values under columns (1) and (8) are only closely agreeable.

Tabulated in Table 1 are the values of all the terms for two of the nodal points at time $t \tilde{=} 30$ sec for the case of nominal diffusivities. Node 329 is close to the ground and approximately 30m behind the vortex center and node 454 is nearly at the vortex center (see Figs. 4b and 5b). As seen in the table, the hydrostatic approximation is apparently valid at node 329 but is definitely invalid at node 454. At this location, although values of the convection and diffusion terms are small, the local acceleration term is large and is, in fact, the largest term in the equation. The large acceleration is caused principally by hydrostatic imbalance. Similar results are presented in Table 2 for the case of low diffusivities at approximately the same time. For this case, however, the vortex center is farther downstream and is closer to the ground, located approximately at node 503 (x = 167m, y = 8.65m, see Fig. 9b). Again, hydrostatic balance is seen to be present at node 329 (far from the density front) but is definitely not present at node 503, with the acceleration term playing an important role. By comparing the values in Tables 1 and 2 for node 329, we note also that the terms in columns (3) through (6) have changed from being negligibly small in the case of nominal diffusivities to being somewhat more important in the case of low diffusivities, even though the recirculation zone for the latter case is farther away from the point under consideration. These numerical values show clearly the importance of the local acceleration in the recirculation region and also help explain why the hydrostatic model encounters greater numerical difficulties when the diffusivities are reduced because, for such cases, the inertial terms are becoming more important

and should not be neglected. In Table 3, we tabulated, for the case of low diffusivities, the numerical values of all the terms in the vertical momentum equation for node 329 (the vortex center is approximately at x = 114m, y = 4.5m when t = 5.47 sec as the vortex moves past this point). As seen in the table, for such a location, the acceleration and the convective terms (in particular, the horizontal component) as well are apparently not negligible and should not be neglected, even though they tend to cancel each other. The values in columns (3) and (4), as expected, reach their maxima at t = 5.47 sec, the time when the vortex is passing by from above, and then decrease afterward.

In order to compare results predicted by the two models under a pre-existing wind, we computed also the above test cases with a nonzero initial flow field, using an extended mesh and more grid points. The presence of a pre-existing wind field, as expected, does not cause any additional computational difficulties except that smaller time steps are generally required, using the same accuracy requirement set forth for the no wind cases, because the advective terms are more important now. Compared to the nonhydrostatic model, the hydrostatic model, again, performs quite well for the case of high diffusivities ($\nu = k = 10$ m^2/sec), reasonably well for the case of nominal diffusivities ($\nu = k = 1$ m^2/sec) but totally unsatisfactorily for the case of low diffusivities ($\nu = k = 0.1$ m^2/sec). Due to space limitations, the results from these cases are not presented here but are available in Ref. 9.

SUMMARY AND CONCLUSIONS

We have described two finite element models: one based on solving the time-dependent, two-dimensional conservation equations of mass, momentum, and energy, with buoyancy effects included via the Boussinesq approximation; the other based on solving the otherwise identical set of equations except using the hydrostatic assumption, and applied these models to predict some aspects of the vapor dispersion phenomena associated with LNG spills. A number of controlled numerical experiments, representing a reasonable expected range of LNG spill scenarios and atmospheric conditions, have been carried out. The results of these test cases demonstrate clearly the applicability and versatility of the finite element method as a numerical tool in predicting the vapor dispersion phenomena of LNG spills and have established for the first time, some data regarding the applicability of the hydrostatic assumption for LNG vapor spread and dispersion.

Since the primary objective of the present study was to assess the feasibility of finite element methods and the validity of the hydrostatic assumption, as applied to modeling LNG vapor dispersion problems, less emphasis has been placed on optimizing the computational speeds of the computer codes and thus the timing information (computation costs) has not been closely monitored. Nevertheless, some approximate timing information is given here to indicate the level of computational efficiency one can expect to gain using a hydrostatic model. The computational speed of the nonhydrostatic code is approximately 4 time steps/minute which implies a total computation time ranging from approximately 10 to

20 minutes CPU time on a CDC 7600 computer for the cases studied. The hydrostatic code, as it stands now, runs about 2.5 times faster and, if optimized, would be expected to run 4 to 5 times faster than the nonhydrostatic code.

Although the models presented herein still need refinements and improvements, we believe that enough of the important physics involved in the LNG vapor dispersion process has been modeled, vis-a-vis our limited preliminary objectives, to permit the following conclusions:

1. Based on the controlled numerical experiments conducted in this study, the hydrostatic model and the nonhydrostatic model appear to agree remarkably well in all field variables (temperature, pressure, and velocity) for cases of high diffusivities ($\nu = k = 10\ m^2/sec$), with and without a pre-existing wind. For the cases of nominal diffusivities ($\nu = k = 1\ m^2/sec$), with and without wind, the hydrostatic model has yielded results for temperature and pressure fields quite agreeable with those from the nonhydrostatic model; however, for the velocity field, the hydrostatic model fails to produce the correct recirculatory flow which is generated near the front of the LNG vapor cloud and as a result, the flow field in that region is significantly in error, with unreasonably large vertical velocity components near the top boundary. For the most difficult cases of low diffusivities ($\nu = k = 0.1\ m^2/sec$), with and without wind, the hydrostatic model does not appear to be applicable. For flow regions where the hydrostatic approximation does not apply (such as a strong recirculation region), it has been found that the inertial terms are generally too important to be neglected. The viscous term, on the other hand, has been found to be relatively unimportant, at least for the cases studied.

2. Although a hydrostatic model appears to generate good solutions when applied to cases where the hydrostatic assumption is valid, its range of applicability, as has been demonstrated, is rather limited. Apparently, a hydrostatic model cannot be applied to the worst cases of LNG spills, where the atmospheric condition is calm and stable and the resulting diffusion coefficients are small. Also, when the constant eddy viscosity assumption is refined and improved, say by a K-model, the diffusivities near the vapor cloud and the ground might (for some time period) be expected to be even lower, which would create even more difficulty for a hydrostatic model. Furthermore, in the presence of complex terrain, dikes, and buildings, etc., the hydrostatic model is definitely inappropriate. For these reasons, we conclude that the final LNG vapor dispersion model should use the nonhydrostatic formulation.

3. Several refinements and improvements should be applied to our current version of the nonhydrostatic model to make it more realistic in simulating the LNG vapor dispersion phenomena as well as becoming computationally efficient. These include the removal of the constant property assumption for density and diffusivities, the implementation of more sophisticated and more realistic boundary conditions, incorporation of the vapor concentration equation, the elimination of the Boussinesq approximation and, finally, the use of more efficient algorithms for solving the discretized system of equations. All these will be implemented in our future two-dimensional, and three-dimensional LNG vapor dispersion models.

ACKNOWLEDGMENTS

We are grateful to Prof. R. L. Sani and J. M. Leone, Jr., who assisted us in both the conceptual modeling formulation and in the interpretation of some of the results. Thanks are also due to T. W. Stullich for consultation and assistance with programming.

REFERENCES

1. Havens, J. A., "Predictability of LNG Vapor Dispersion from Catastrophic Spills onto Water: An Assessment," DOT document CG-M-09-77, April 1977.

2. Germeles, A. E. and E. M. Drake, "Gravity Spreading and Atmospheric Dispersion of LNG Vapor Clouds," Fourth International Symposium on Transport of Hazardous Cargoes by Sea and Inland Waterways, Jacksonville, Florida, October 26-30, 1975.

3. "LNG Terminal Risk Assessment Study for Oxnard, California," Science Applications, Incorporated, 1200 Prospect Street, La Jolla, Calif. 92037, prepared for Western LNG Terminal Company, 720 West Eighth Street, Los Angeles, California 90017, December 1975.

4. Havens, J. A., "A Description and Assessment of the SIGMET LNG Vapor Dispersion Model," DOT document CG-M-3-79, February 1979.

5. Gresho, P. M., R. L. Lee, T. W. Stullich, and R. L. Sani, "Solution of the time-dependent Navier-Stokes equations via F.E.M.," Second International Conference on Finite Elements in Water Resources, July 10-14, 1978, London, England.

6. Gresho, P. M., R. L. Lee, R. L. Sani and T. W. Stullich, "On the Time-Dependent FEM Solution of the Incompressible Navier-Stokes Equation in Two and Three-Dimensions," Lawrence Livermore Laboratory, UCRL-81323, July 7, 1978; see also, Recent Advances in Numerical Methods in Fluids, Pineridge Press, Ltd., Swansea, U.K. 1980.

7. Zienkiewicz, O. C., The Finite Element Method, Chapter 24. Computer Procedures for Finite Element Analysis, McGraw-Hill, 1977.

8. Gresho, P. M., R. L. Lee, S. T. Chan and J. M. Leone, Jr., "A New Finite Element for Incompressible or Boussinesq Fluids," submitted to the Third International Conference on Finite Elements in Flow Problems, to be held at the Banff Centre, Banff, Alberta, Canada, June 10-13, 1980.

9. Chan, S. T. and P. M. Gresho, "A Comparison of Hydrostatic and Nonhydrostatic Models as Applied to the Prediction of LNG Vapor Spread and Dispersion," Lawrence Livermore Laboratory Report, UCID-18097, March 1979.

Table 1. Numerical Values of Various Terms in the Vertical Momentum Equation for the Case of Nominal Diffusivities (ν=k=1.0 m^2/sec, t=30.39 sec)

Terms / Nodes	(1) $\frac{\partial p}{\partial y}$	(2) $\rho\gamma gT$	(3) $\rho\frac{\partial v}{\partial t}$	(4) $\rho u\frac{\partial v}{\partial x}$	(5) $\rho v\frac{\partial v}{\partial y}$	(6) $\mu\nabla^2 v$	(7) (6)-(3)-(4)-(5)	(8) (2)+(7)
#329 (x=115, y=3)	-1.654	-1.657	0.00	0.00	0.00	-0.002	-0.002	-1.659
#454 (x=145, y=18.07)	0.065	-0.057	-0.128	-0.008	0.003	0.00	0.133	0.076

Table 2. Numerical Values of Various Terms in the Vertical Momentum Equation for the Case of Low Diffusivities (ν=k=0.1 m^2/sec, t=30.45 sec)

Terms / Nodes	(1) $\frac{\partial p}{\partial y}$	(2) $\rho\gamma gT$	(3) $\rho\frac{\partial v}{\partial t}$	(4) $\rho u\frac{\partial v}{\partial x}$	(5) $\rho v\frac{\partial v}{\partial y}$	(6) $\mu\nabla^2 v$	(7) (6)-(3)-(4)-(5)	(8) (2)+(7)
#329 (x=115, y=3)	-2.585	-2.525	0.069	-0.009	-0.006	0.019	-0.035	-2.560
#503 (x=167, y=8.65)	-0.037	-0.924	-0.891	-0.008	-0.009	0.003	0.911	-0.013

Table 3. Numerical Values of Various Terms in the Vertical Momentum Equation at Node 329 (x=115, y=3, ν=k=0.1)

Terms / Times	(1) $\frac{\partial p}{\partial y}$	(2) $\rho\gamma gT$	(3) $\rho\frac{\partial v}{\partial t}$	(4) $\rho u\frac{\partial v}{\partial x}$	(5) $\rho v\frac{\partial v}{\partial y}$	(6) $\mu\nabla^2 v$	(7) (6)-(3)-(4)-(5)	(8) (2)+(7)
4.92	-2.165	-2.587	-0.952	0.624	0.042	-0.017	0.269	-2.318
5.47	-2.440	-3.066	-1.126	0.775	-0.005	0.019	0.375	-2.691
6.03	-2.406	-2.581	-0.570	0.545	0.044	0.037	0.018	-2.563

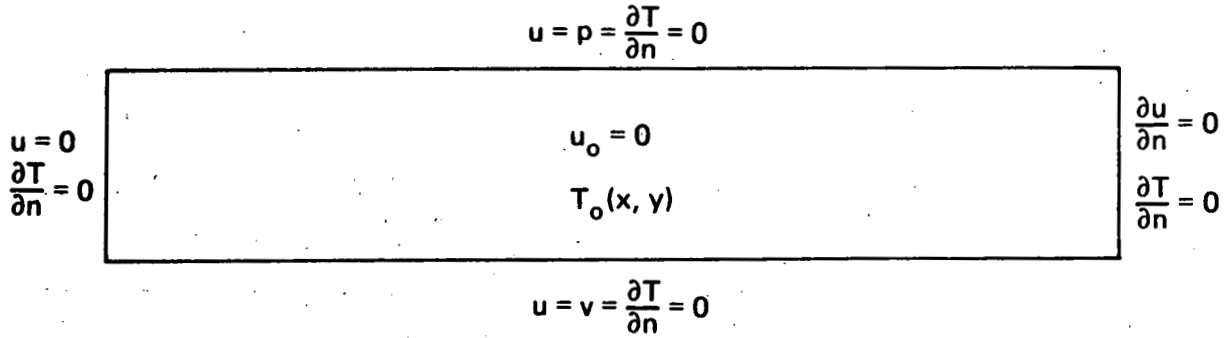

(a) Hydrostatic model

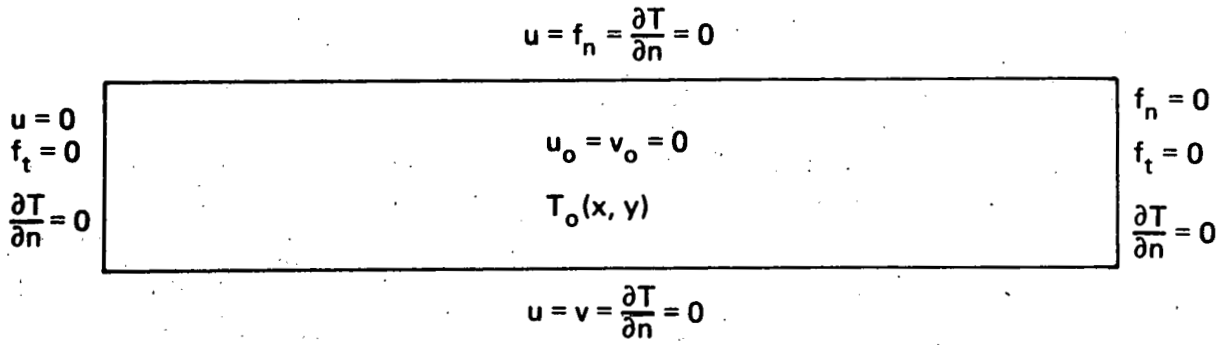

(b) Nonhydrostatic model

Fig. 1 — Initial and Boundary Conditions for Cases Without Wind

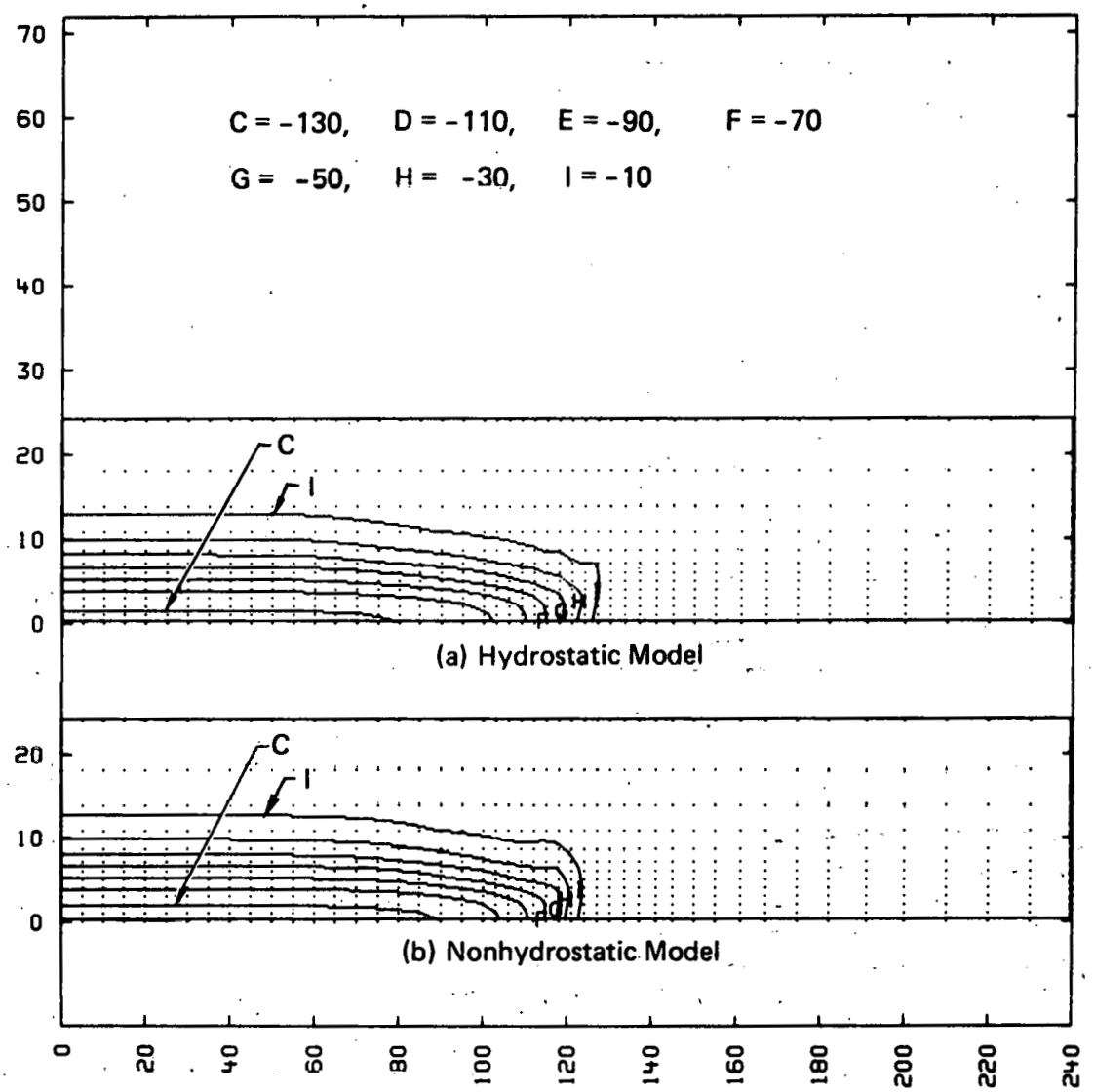

Fig. 2a — Temperature Field at t = 10.5 (ν = k = 1)

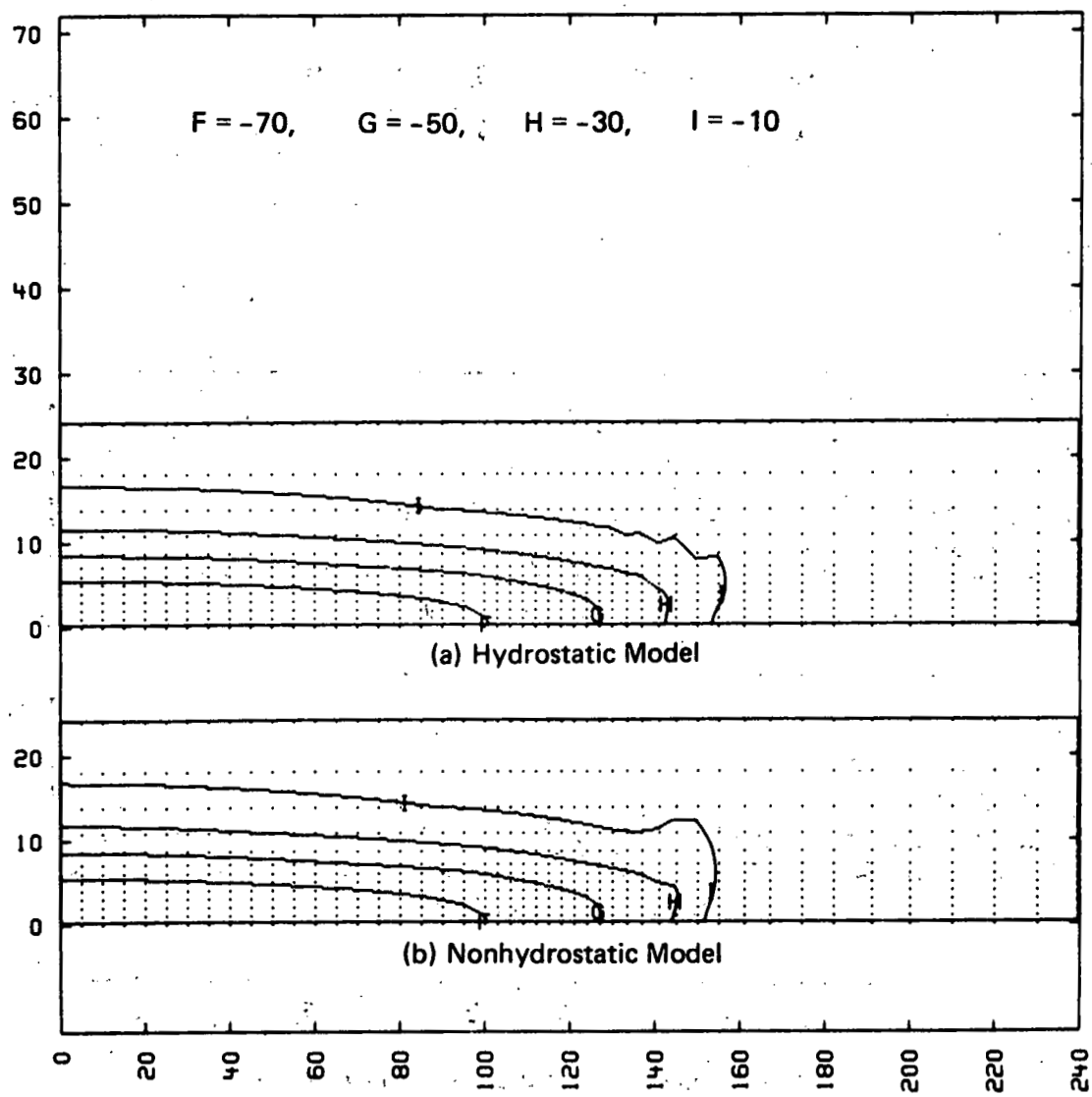

Fig. 2b — Temperature Field at t = 30 (ν = k = 1)

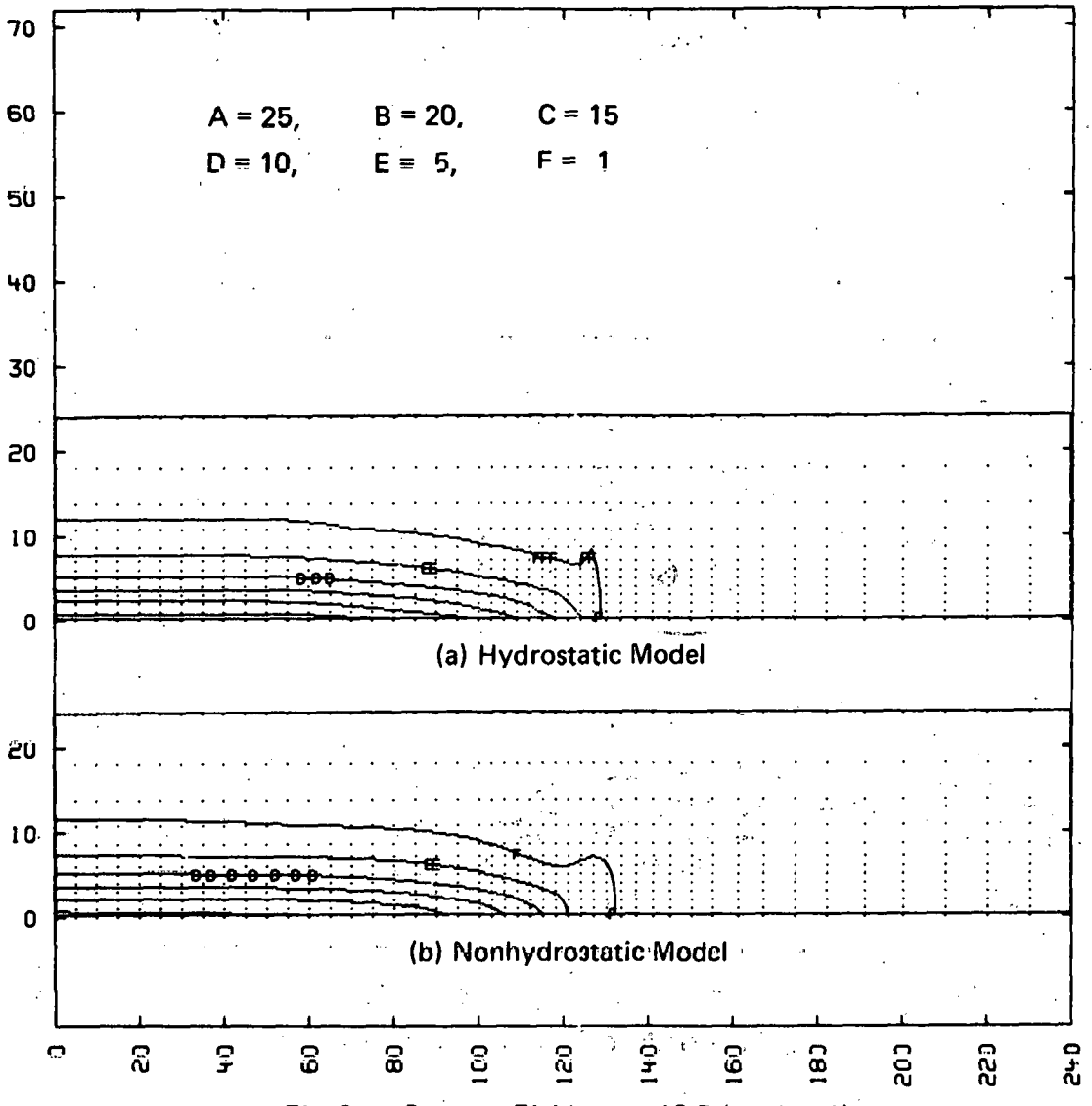

Fig. 3a — Pressure Field at t = 10.5 (ν = k = 1)

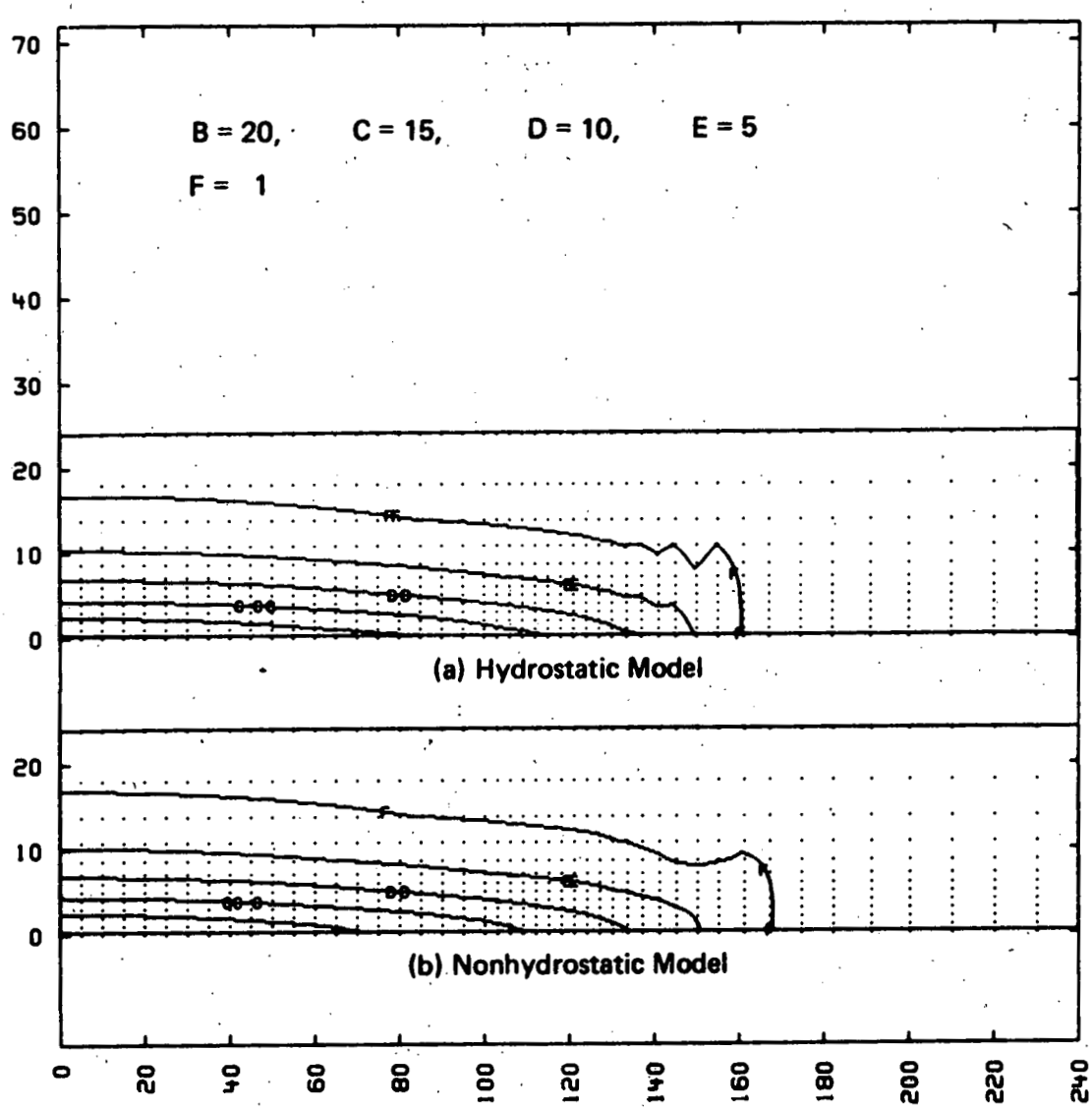

Fig. 3b — Pressure Field at t = 30 (ν = k = 1)

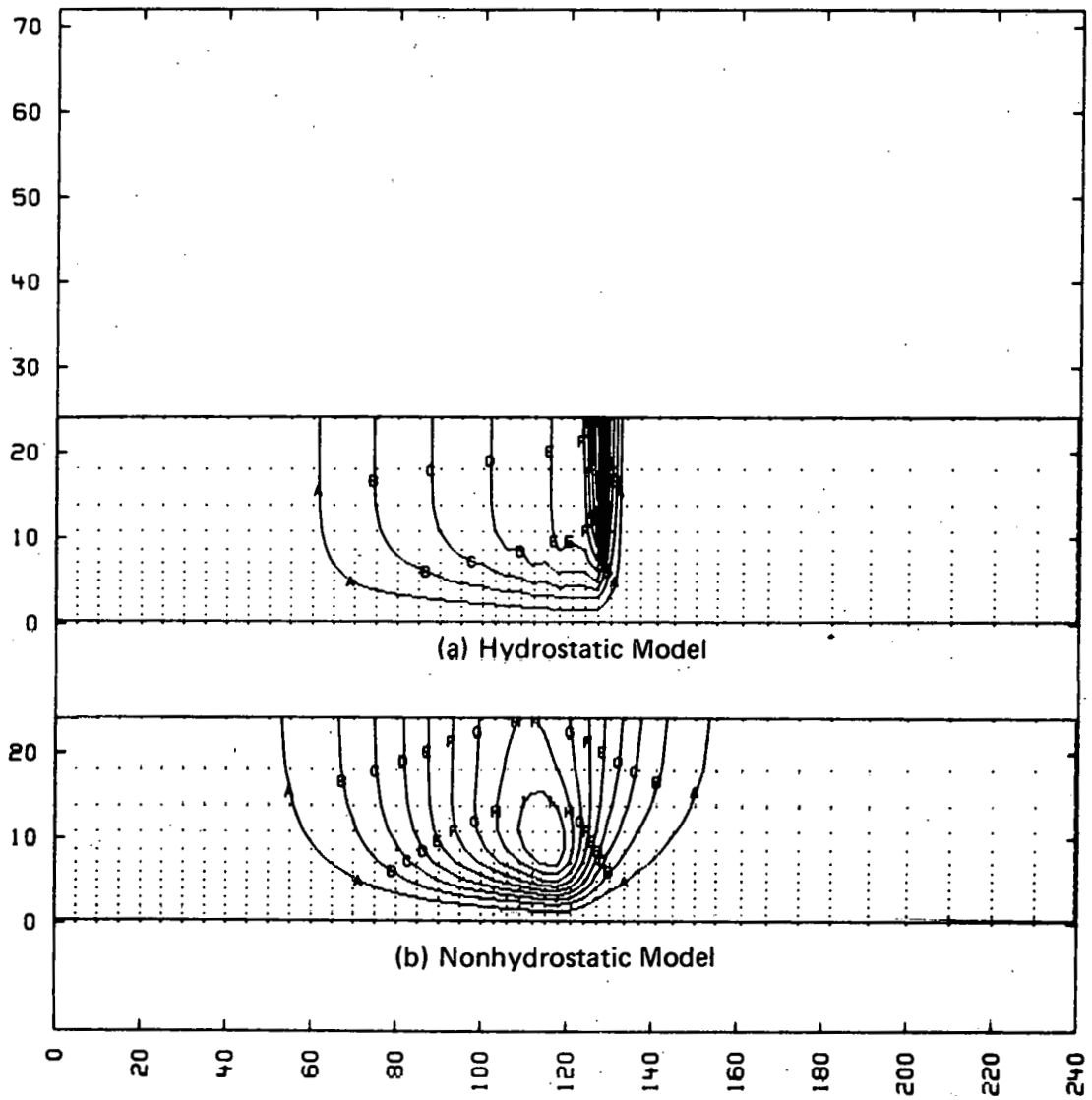

Fig. 4a – Streamlines at t = 10.5 (ν = k = 1).

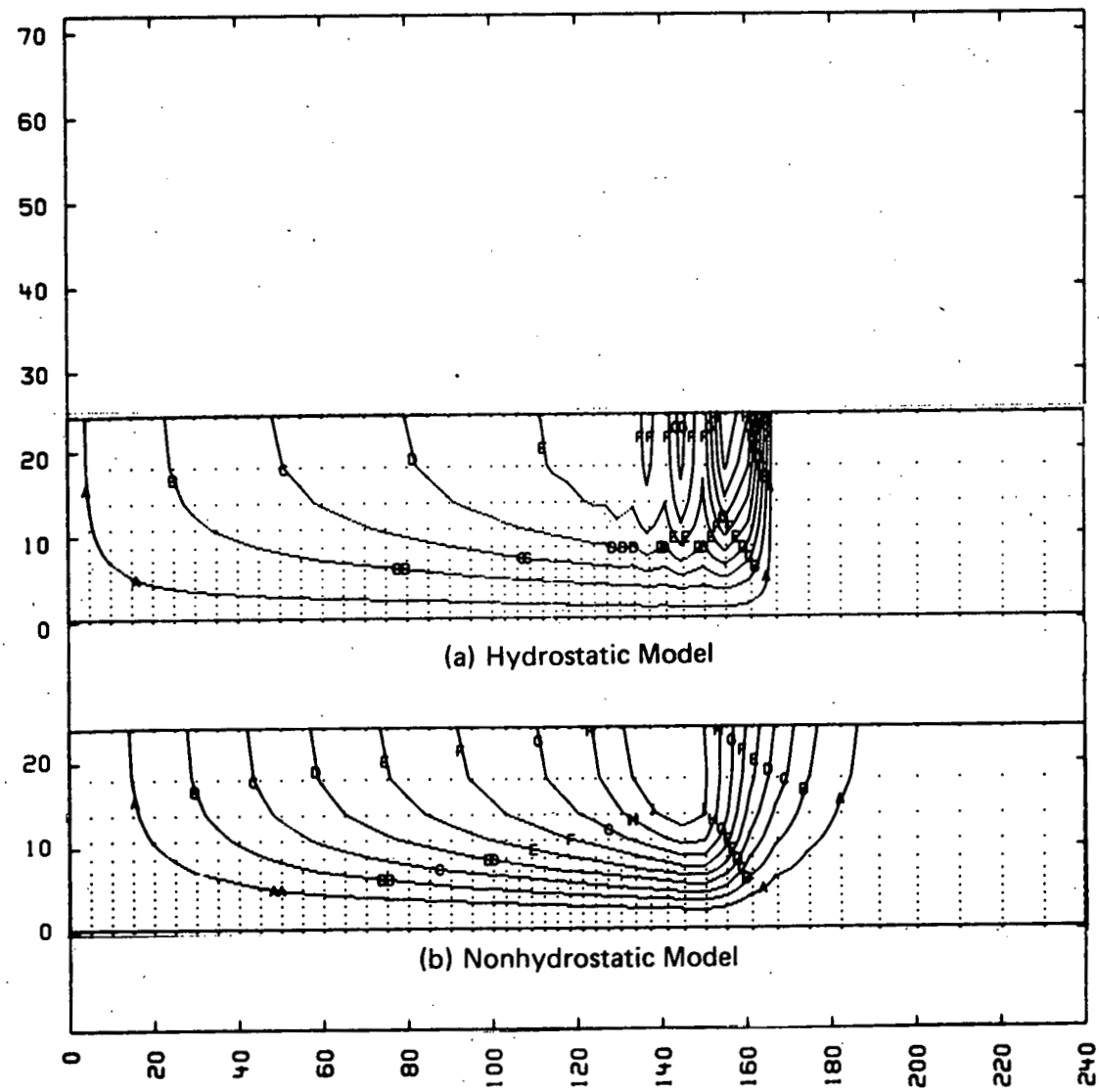

Fig. 4b — Streamlines at t = 30 (ν = k = 1)

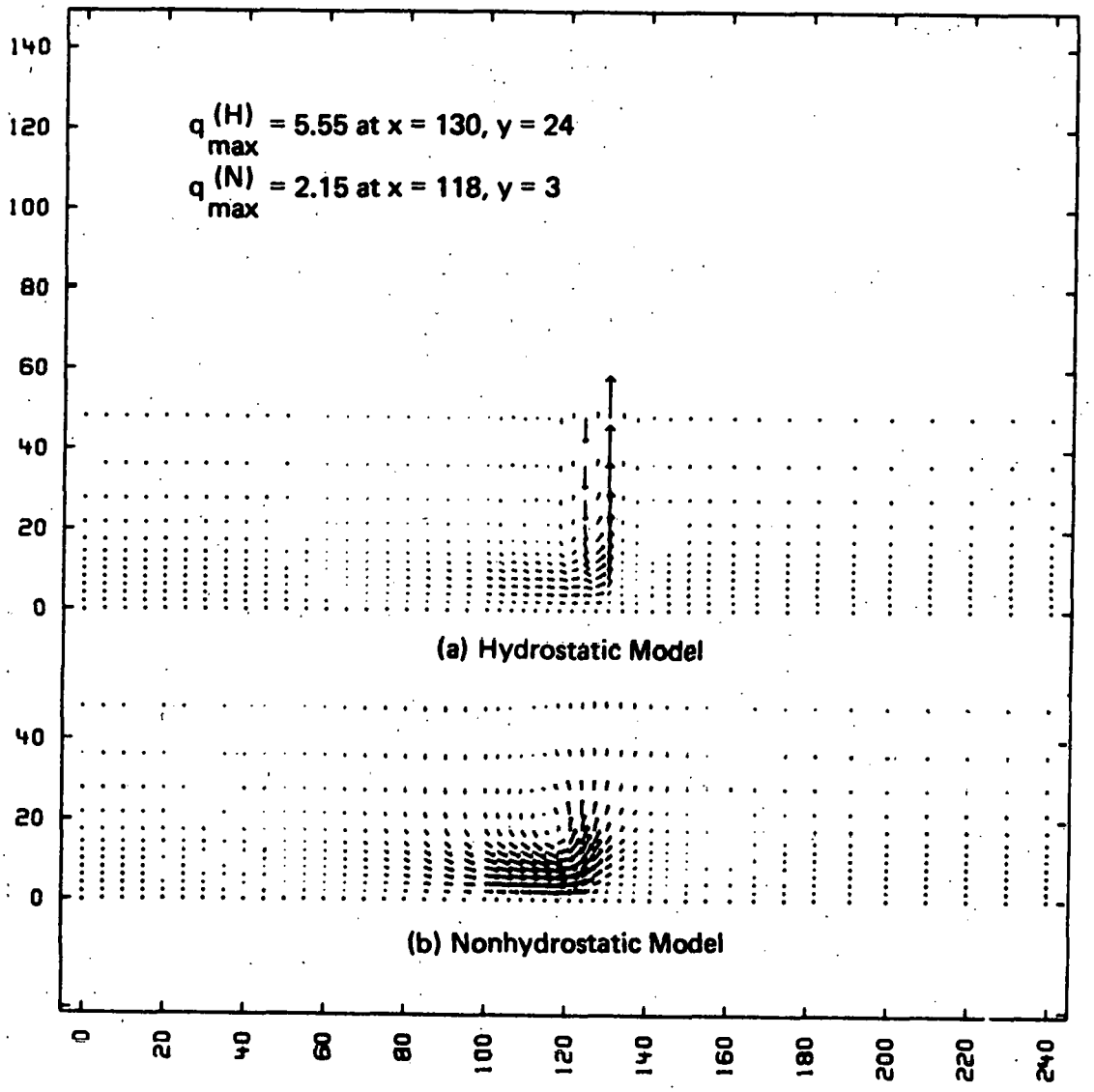

Fig. 5a — Velocity Field at t = 10.5 (ν = k = 1)

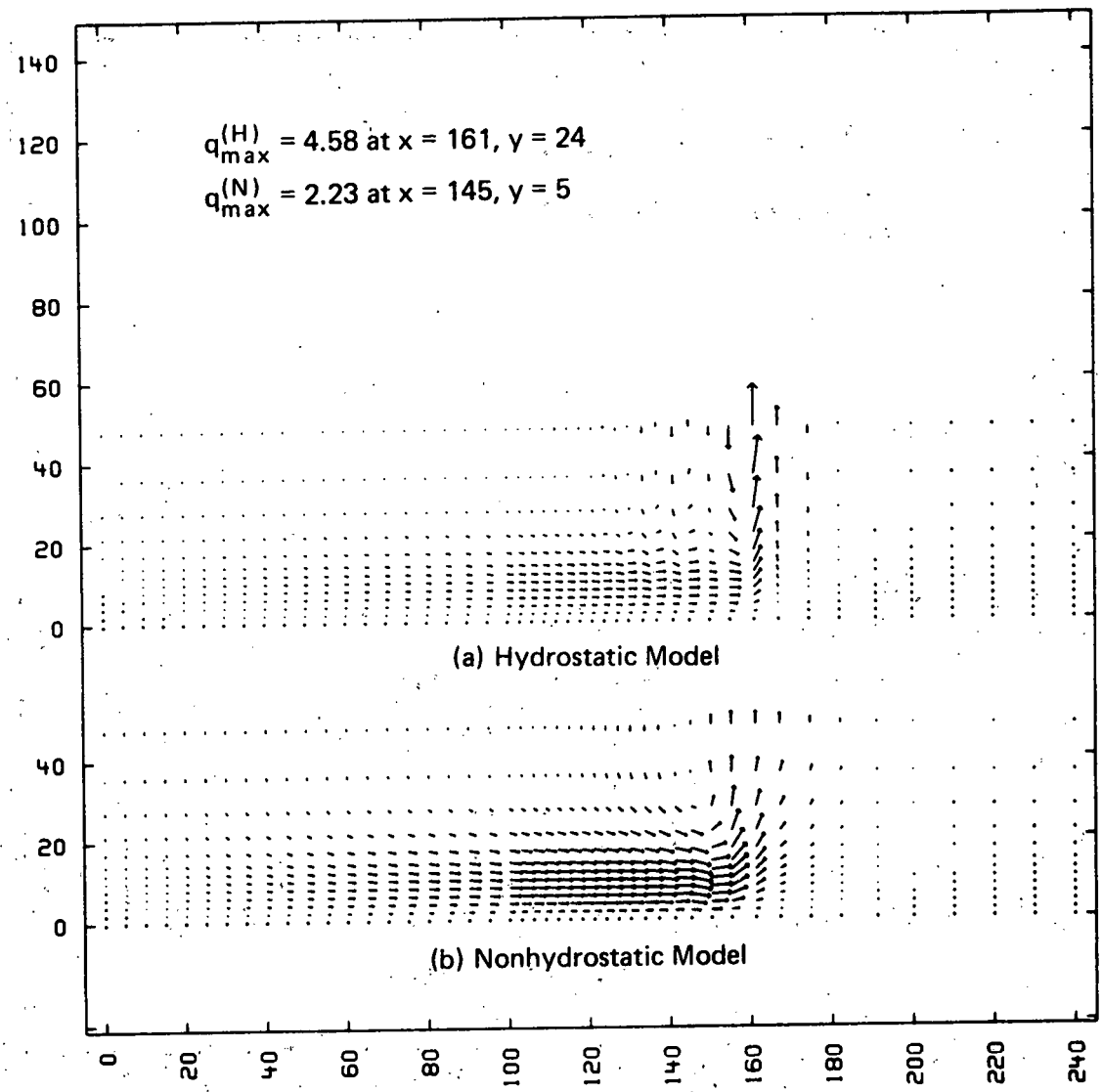

Fig. 5b – Velocity Field at t = 30 (ν = k = 1)

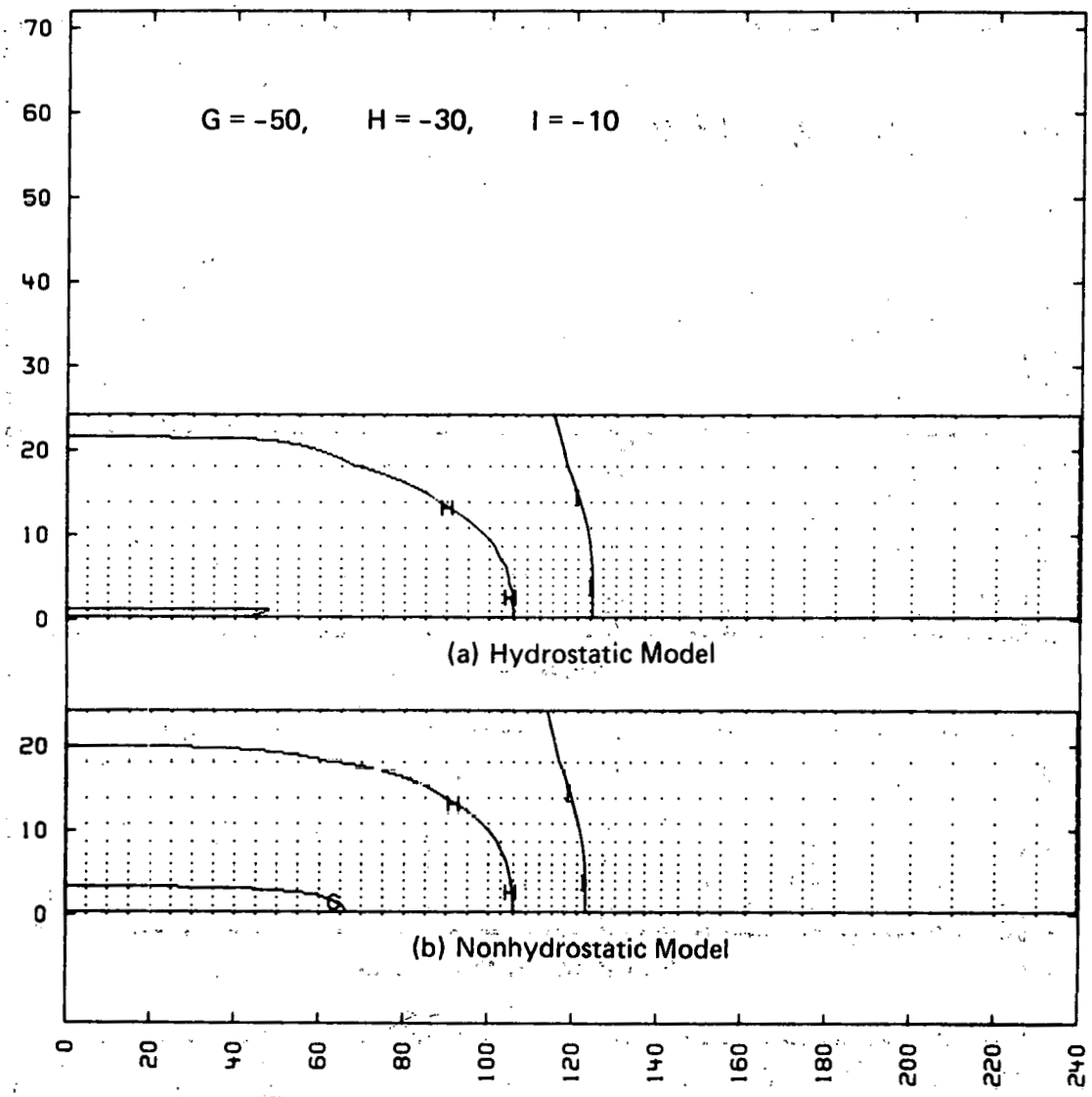

Fig. 6a — Temperature Field at t = 10 (ν = k = 10)

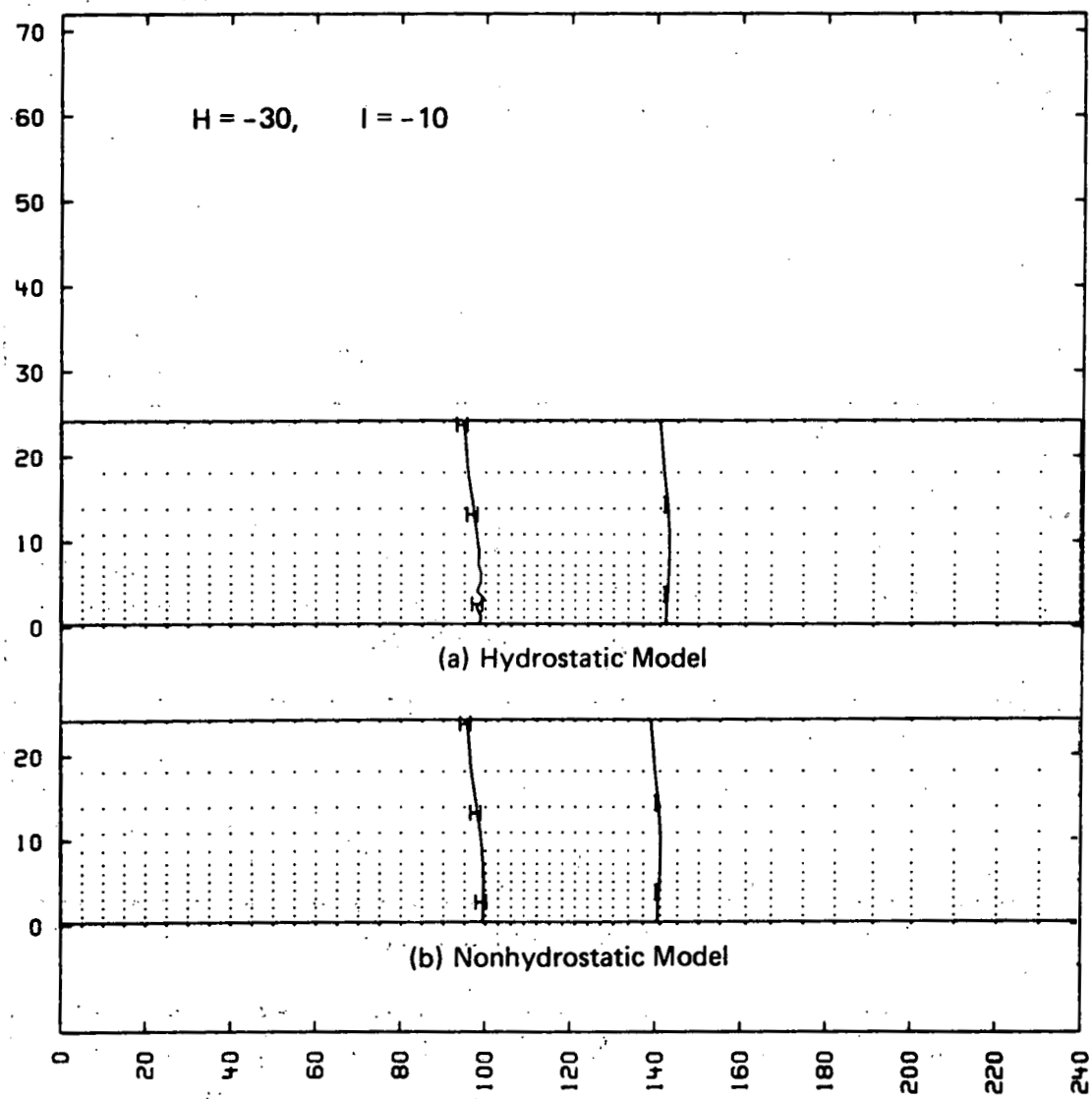

Fig. 6b – Temperature Field at t = 31 (ν = k = 10)

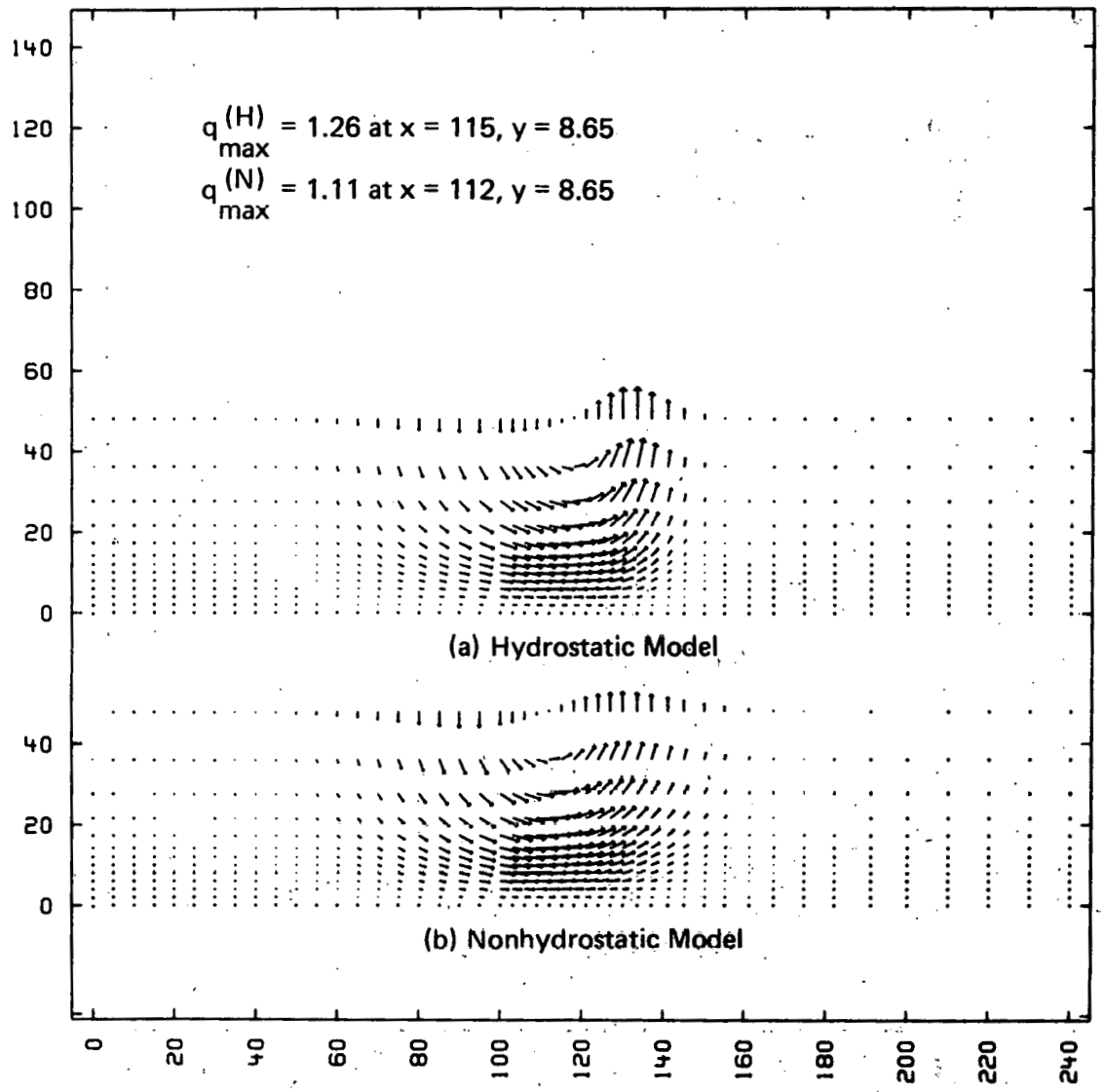

Fig. 7a — Velocity Field at t = 10 (ν = k = 10)

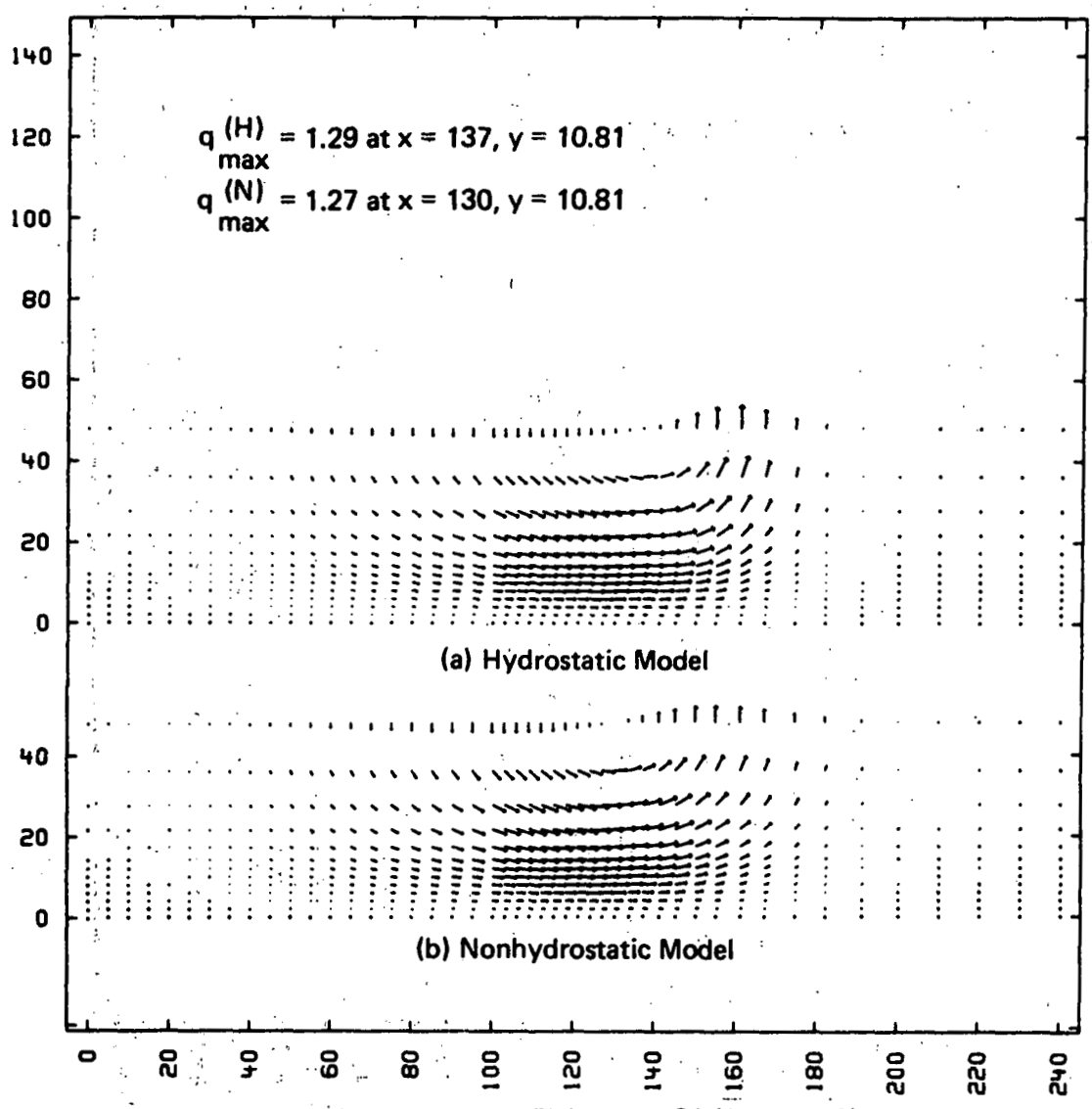

Fig. 7b – Velocity Field at t = 31 (ν = k = 10)

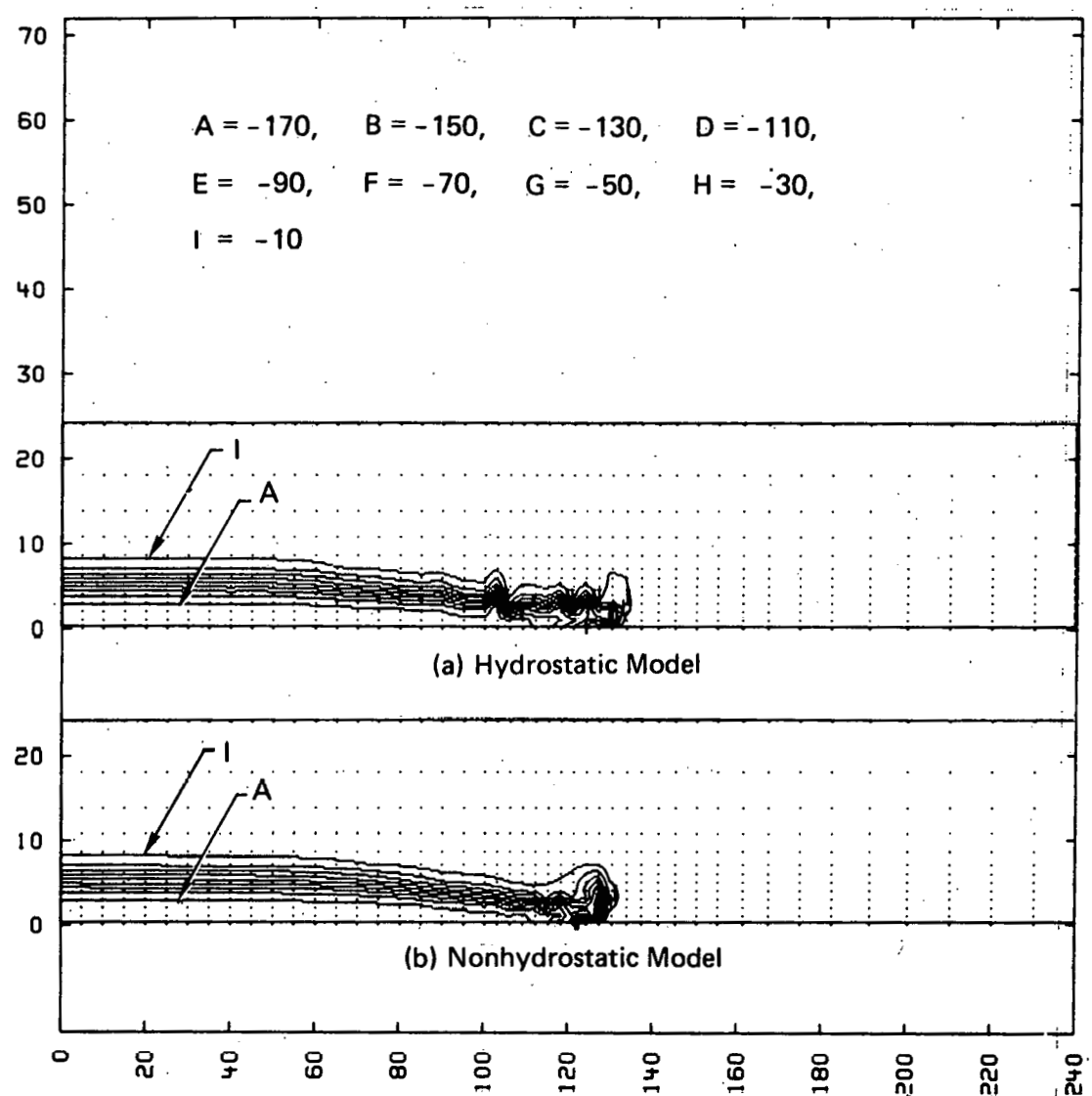

Fig. 8a – Temperature Field at t = 10 (ν = k = 0.1)

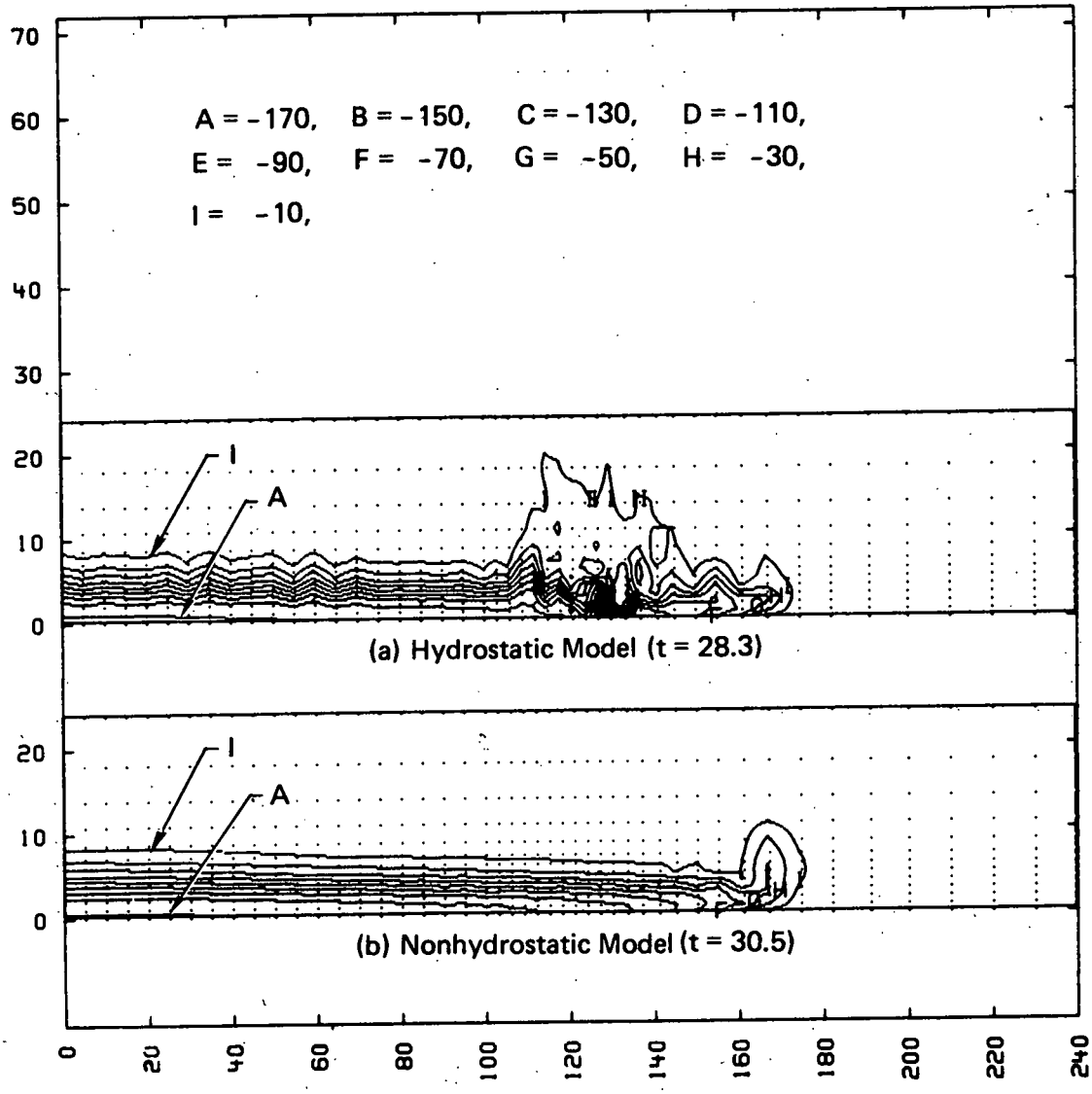

Fig. 8b – Temperature Field at $t \cong 30$ ($\nu = k = 0.1$)

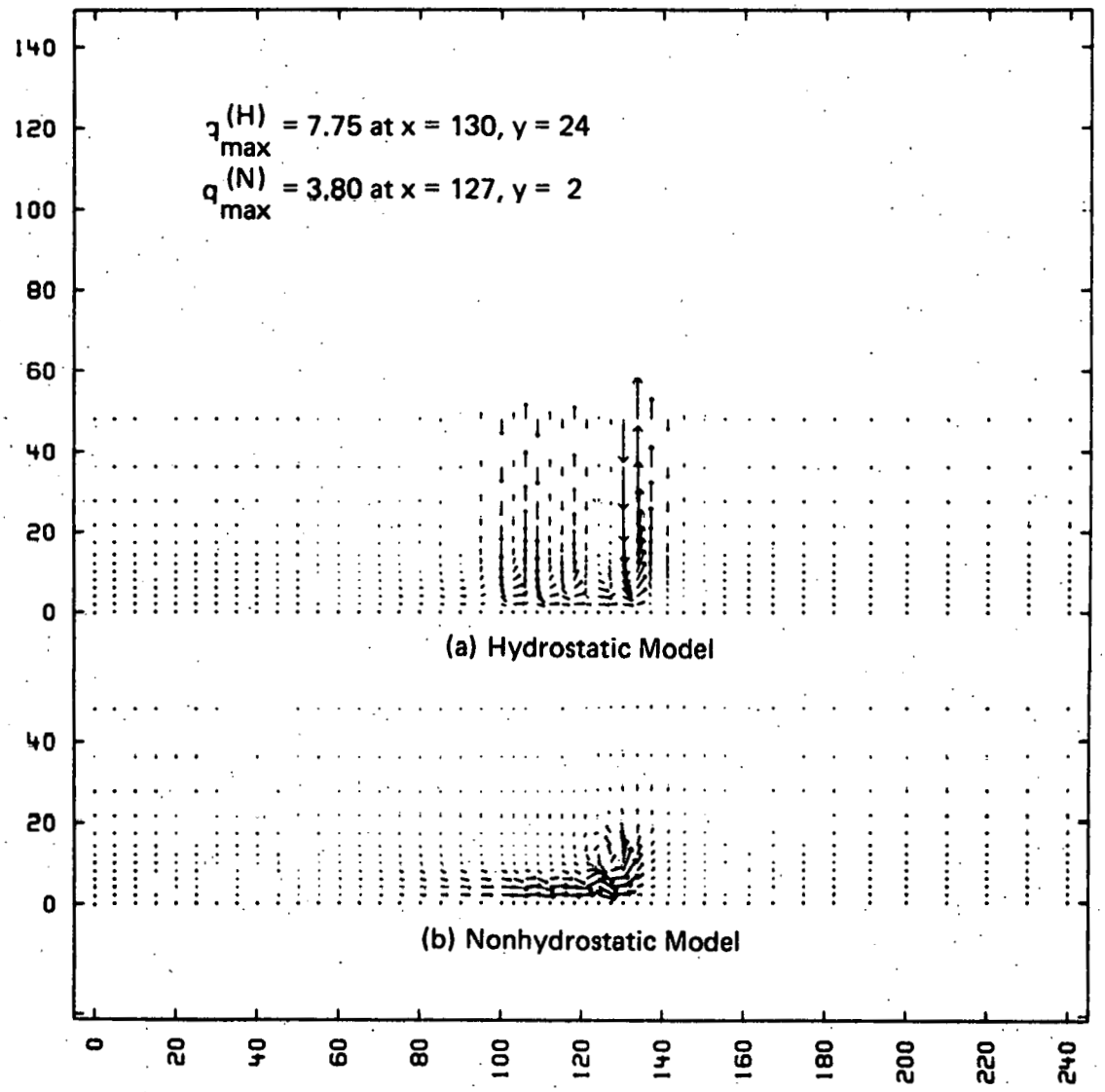

Fig. 9a — Velocity Field at t = 10 (ν = k = 0.1)

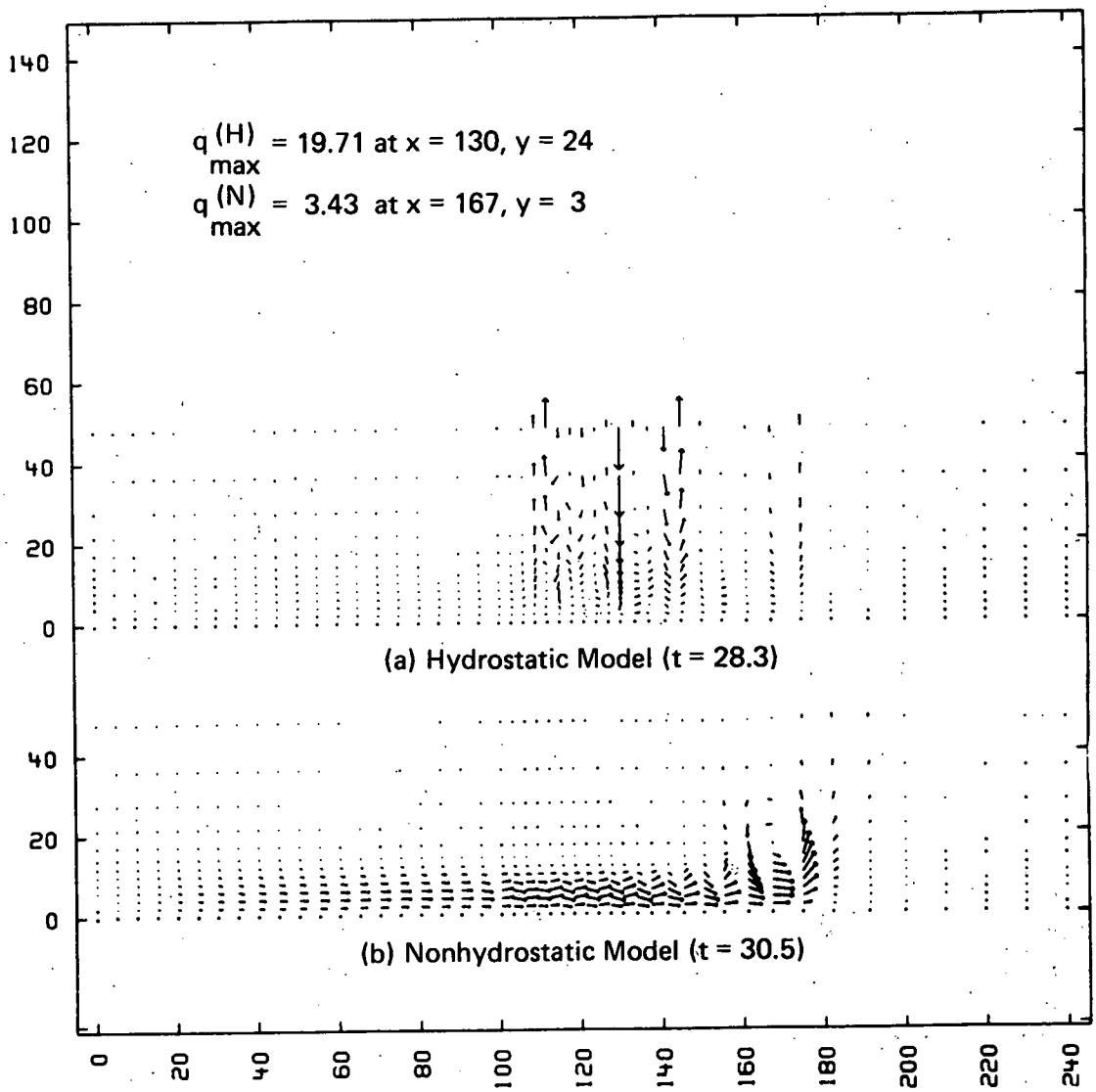

Fig. 9b — Velocity Field at t ≅ 30 (ν = k = 0.1)

REPORT B

Modeling of Negatively Buoyant Vapor Cloud Dispersion

J. A. Fay
Y. C. Doo
J. J. Rosenzweig

Prepared for the
Environmental and Safety Engineering
Division
U.S. Department of Energy
under Contract DE-AC-02-77EV04204

Massachusetts Institute of Technology
Cambridge, Massachusetts 02139

THIS PAGE

WAS INTENTIONALLY

LEFT BLANK

REPORT B

TABLE OF CONTENTS

FIGURES

SUMMARY

This report summarizes progress on a project to develop new analytical methods for correlating and comparing theoretical and experimental studies on the motion and dispersion of negatively buoyant vapor clouds. It describes the assumptions and simplifications used in constructing a new model analogous to boundary layer integral models and then identifies some quasi one-and two-dimensional steady and unsteady flows for which solutions were sought. A major finding of the studies to date is analytic asymptotic solutions which are practically applicable at long times when substantial dilution has occurred. These solutions will also help in future attempts to correlate both numerical and experimental results.

INTRODUCTION

This predominantly theoretical research is concerned with the development of a fluid mechanical model of the gravity spread and dispersion of negatively buoyant vapor clouds. This new model is of intermediate complexity, falling between the SAI SIGMET three-dimensional, unsteady flow model and the modified classical models of Fay and Lewis (1975) and Germeles and Drake (1975). A principal purpose of this development is to provide a common basis for the comparison of the numerical results from these earlier models, which are widely disparate (Havens 1977), and to attempt to delineate whether the differences are due to different assumptions regarding physical effects or to the nature of the mathematical analysis. As will be seen below, there is also evidence that the intermediate-level model will permit correlations of existing theoretical calculations and experimental measurements of vapor cloud dispersion.

There are two major physical effects which dominate the motion of negatively buoyant vapor clouds. The first is the lateral spreading caused by gravity and the second is dilution resulting from turbulent mixing with the atmosphere. For the cases of interest, which involve accidental releases of vaporizing liquid, the subsequent cloud motion will be an unsteady, turbulent, three-dimensional flow. There is no complete understanding of such complex flows, so that simplifying assumptions are necessary in constructing any flow model. It is thus the purpose of this research to construct a model which includes all the important physical effects, albeit in somewhat simplified form, but which retains the unsteady, multi-dimensional character of the flow. The model includes a level of complexity which matches our limited understanding of the basic physical processes at work.

A major goal in developing an understanding of vapor cloud dispersion is the determination of the conditions for which dilution with ambient air is sufficiently great that no further hazard (toxicity or inflammability) exists. Ordinarily, this involves dilution of the original vapor by a factor of ten to a hundred. In any turbulent mixing process which produces such substantial amount of mixing the early stages of mixing or initial conditions have very little effect upon the final state which is of interest. It may not therefore be essential, from this point of view, to develop models which accurately describe this early stage provided they properly treat the flow under conditions of considerable dilution. For this reason our research has emphasized the asymptotic behavior of the flow model, where justifiable simplifications can lead even to analytical solutions which may prove to be quite accurate for the practical conditions where great dilution exists.

MODELINC ASSUMPTIONS AND SIMPLIFICATIONS

Observations of LNG vapor cloud motion clearly show the dominant effect of lateral spread caused by gravity. This provides a starting point for constructing a simplified model; namely, the mixing processes in the vertical direction are much more significant than in the lateral directions because of the much greater vertical gradients. (In this respect the flow inside the cloud or plume resembles that in a turbulent boundary layer.) Because the vapor cloud height is small compared to its lateral width, the wind-driven flow of air above or beside the cloud will scarcely be affected by cloud growth - again, closely analogous to the flow external to a viscous boundary layer. However, there is one region of the flow in which these approximations do not hold; namely, the edge of the spreading cloud. Here a locally quasi-steady flow will prevail, with conditions the same as those at the head of an intrusive front where the front speed can be related to the negative buoyancy in the intrusive flow behind the front.

These considerations thus suggest a model which treats the flow within the vapor cloud in much the same manner as the flow within a viscous boundary layer. The external, wind-driven flow and the ground provide boundary conditions at the upper and lower surfaces of the cloud, while the lateral edges of the cloud move into the external flow field as does an intrusive front, thereby defining mixed boundary conditions along these edges.

An additional assumption and a simplification can now be made. Because the flow within the cloud is primarily in the horizontal direction, a hydrostatic pressure distribution is assumed. It is then convenient to integrate the fluid flow equations in the vertical direction (reducing the independent dimensions of the problem by one) thereby expressing all the

dependent variables as integrals, as has been found useful in some boundary layer flows.

At this stage the integro-differential equations expressing the physical conservation laws are not complete because the rate of vertical mixing has not been specified. To close the system, an entrainment relation similar to those used in simple free shear flows (Turner 1973) is proposed in which the rate of entrainment consists of two independently additive terms, the first due to horizontal shear and the second due to free-stream (atmospheric) turbulence. The entrainment proportionality constants are considered to depend upon local dimensionless parameters such as Richardson number and atmospheric stability class.

The resulting system of equations (conservation of mass, lateral components of momentum and energy, entrainment relation and caloric equation of state) is hyberbolic in character because the relatively thin layer of negatively buoyant fluid can propagate gravity waves. While numerical finite difference techniques can be used in their solution, we have concentrated on the development of asymptotic analytical solutions to these equations, but have also investigated numerical solutions for some simple cases.

When investigating asymptotic solutions, i.e., flow conditions far enough downstream that considerable dilution has taken place, the classical Boussinesq approximation is then used, simplifying the evaluation of the integral variables. Also, a uniform vertical distribution of the dependent variable quantities within the cloud is assumed as a simplification (more realistic profiles are easily treated).

To illustrate the net consequences of these assumptions and simplifications, we write here the differential equations for a quasi one-dimensional

isothermal flow of a negatively buoyant plume far downstream of the source:

Entrainment: $$\frac{d}{dx}[(u+1)\delta] = \alpha|u|+\gamma$$

Mass conservation: $$\frac{d}{dx}[\Delta(u+1)\delta] = 0$$

Momentum: $$\frac{d}{dx}[(u+1)^2\delta+F\Delta\delta^2] = \alpha|u|+\gamma-fu$$

where all quantities have been made dimensionless through use of the source length scale ℓ and wind speed u_∞. In these equations $1+u$ is the mean plume speed, δ the plume thickness, Δ the fractional density excess, α and γ are entrainment coefficients, f is a net drag coefficient acting on the plume and $F \equiv g\ell/2u_\infty^2$ is a dimensionless parameter. These equations thus describe the asymptotic behavior of a negatively buoyant plume originating from an infinite line or strip source and subjected to a crosswind normal to the source direction.

For more general flows, such as unsteady, two-dimensional flow and/or nonisothermal flow, additional terms and equations are required which are not reproduced here.

QUASI ONE-DIMENSIONAL STEADY FLOW

An extensive investigation of the application of this model to the case of a steady negatively buoyant plume emitted from a strip source oriented normal to a crosswind has been given by Doo (1979). This example illustrates the use of the model for a case which is easiest to analyze. At the same time, it could reasonably represent the vapor plume formed from a liquid spill into a road gutter or transfer pipe containment trench. We here quote the major conclusions from this study:

(i) A steady flow solution is possible only if the source strength is small compared with the wind speed (buoyancy flux per unit length/$u_\infty^3 \leq 8/27$).

(ii) Contrary to intuition, the vapor speed is always less than the wind speed at great distances downstream.

(iii) Two solutions exist for any source strength satisfying (i), either supercritical or subcritical, depending upon whether the plume speed u+1 is greater or less than the local gravity wave speed $(2F\delta\Delta)^{\frac{1}{2}}$. These solutions are also distinguished by the initial conditions of the plume at the source.

Numerical solutions for the flow close to the source have been carried out and are illustrated in Doo (1979).

QUASI ONE-DIMENSIONAL UNSTEADY FLOW

Two types of flow have been considered for this case. The first is the initiating phase of a plume, namely, a steady strip source turned on at time zero. The second is the line puff, i.e., a strip of pure vapor volume released at time zero which subsequently spreads laterally and drifts downwind. Some solutions of both types have been obtained by numerical integration using the method of characteristics (the equations are hyperbolic). For these cases only isothermal flows were considered and the Boussinesq approximation was used (although it is probably not accurate at small times). The results of these studies may be summarized as follows:

(i) For very strong sources, an upwind moving front as well as a downwind front was formed. The flow (as expected) did not approach a steady state.

(ii) For weaker sources, the solution was not followed in time sufficiently long to determine when a steady flow would be reached.

(iii) A line puff will accelerate to the wind speed, even in the absence of entrainment or friction. The physical mechanism for this acceler-

ation is simple to explain. Initially, a stationary puff would spread laterally with equal speed both upwind and downwind. But the relative speed upwind is greater, hence the puff thickness δ must be greater according to the intrusion front boundary condition. For the cloud as a whole, then, a hydrostatic horizontal pressure gradient is induced which accelerates the cloud in the downwind direction. Ultimately, the line puff drifts with the wind speed, spreading symmetrically about its center.

(iv) Once the acceleration mechanism is recognized, asymptotic solutions for the line puff can be found which express the motion with respect to the drifting cloud. These solutions have a form expressible in similarity variables whenever one of the two entrainment mechanisms is dominant. At early times (but not so early that the puff has not accelerated) shear entrainment will dominate whereas at long enough times entrainment will be caused by atmospheric turbulence. Analytic asymptotic solutions for both regimes have been found.

(v) Numerical solutions for the line puff have been followed out to times where the asymptotic analytic solution is reached to within acceptable accuracy.

These studies have proceeded as far as seems warranted at this time, considering the limited usefulness of the flow geometry and the practical difficulties of the numerical integration technique. The physical effects revealed in these solutions are the most significant result.

QUASI TWO-DIMENSIONAL UNSTEADY FLOW

The study of the line puff, which led to the conclusion that the asymptotic behavior could be determined by assuming the puff would ultimately drift with the wind speed, suggested that a similar approach would be possible for an axisymmetric vapor cloud released at time zero. Again assuming that the cloud would accelerate to wind speed, axisymmetric asymptotic solutions ex-

pressed in similarity form were found for the two entrainment limits. These solutions were not tested against a numerical integration scheme, which would require considerable effort. However, the form of the solution suggested the definition of useful dimensionless variables which might be used to correlate other numerical solutions or empirical observations, as described further below.

QUASI TWO-DIMENSIONAL STEADY FLOW

The plume formed from a steady point or area source in a crosswind is the two-dimensional analog of the one-dimensional plume described above. Because the flow is not constrained in the lateral dimension normal to the wind, however, we would expect to find a solution for any source strength. Although the plume might extend upwind of the source some distance, the fluid will ultimately be swept downwind and a steady flow should persist.

In this case an asymptotic solution is sought for which the plume flow speed approaches that of the oncoming wind. Again, the solutions found are expressible in similarity variables. As might be expected, the development of the transverse flow field as a function of downwind distance is closely analogous to the time dependence of the quasi one-dimensional line puff discussed above.

These solutions are expected to be useful in correlating steady plume model calculations and experimental observations of plumes from confined spills.

CORRELATION OF MODEL CALCULATIONS

The asymptotic solutions which have been for the proposed model equations and which are described above are all expressed in terms of dimensionless variables. Thus the dimensional parameters of the problem, such as vapor

source strength or initial mass, wind speed, wind turbulence level, etc. are grouped into dimensionless parameters. By examining the form of these solutions, it becomes apparent that there are appropriate ways to non-dimensionalize the variables which are of most direct interest. For a vapor cloud formed from the very rapid evaporation of a liquid spill, or instantaneous release, we have found it suitable to select the maximum ground level concentration $\dot{C}_m$ and the time t since the cloud was formed as the dependent/independent variable pair to be correlated. The corresponding dimensionless forms of these variables, denoted by a superscript asterisk, are:

$$C_m^* \equiv C_m (g^3 M/\rho_\infty)^{\frac{1}{2}}/u_\infty^3$$

$$t^* \equiv u_\infty^2 t/(gM/\rho_\infty)^{\frac{1}{2}}$$

where M is the mass of vapor in the cloud and ρ_∞ is the atmospheric density.

To illustrate the usefulness of these variables, we show on the attached Figure 1 a correlation of several calculations made using the SAI SIGMET model as reported by Havens (1979). These calculations cover a range of wind speed and spill size, but otherwise invariant atmospheric turbulent transport properties. The solid lines show the coresponding asymptotic solution as described above, using entrainment coefficients which best correlate these data.

CONCLUDING REMARKS

The model described above has proven to be very useful in revealing the relative importance of the different physical phenomena which affect the motion of negatively buoyant vapor clouds. The development of asymptotic solutions in an analytic form is especially convenient. Because much practical interest attaches to the later stages of the flow after great dilution has taken place, which is generally the regime of the asymptotic solution, precise

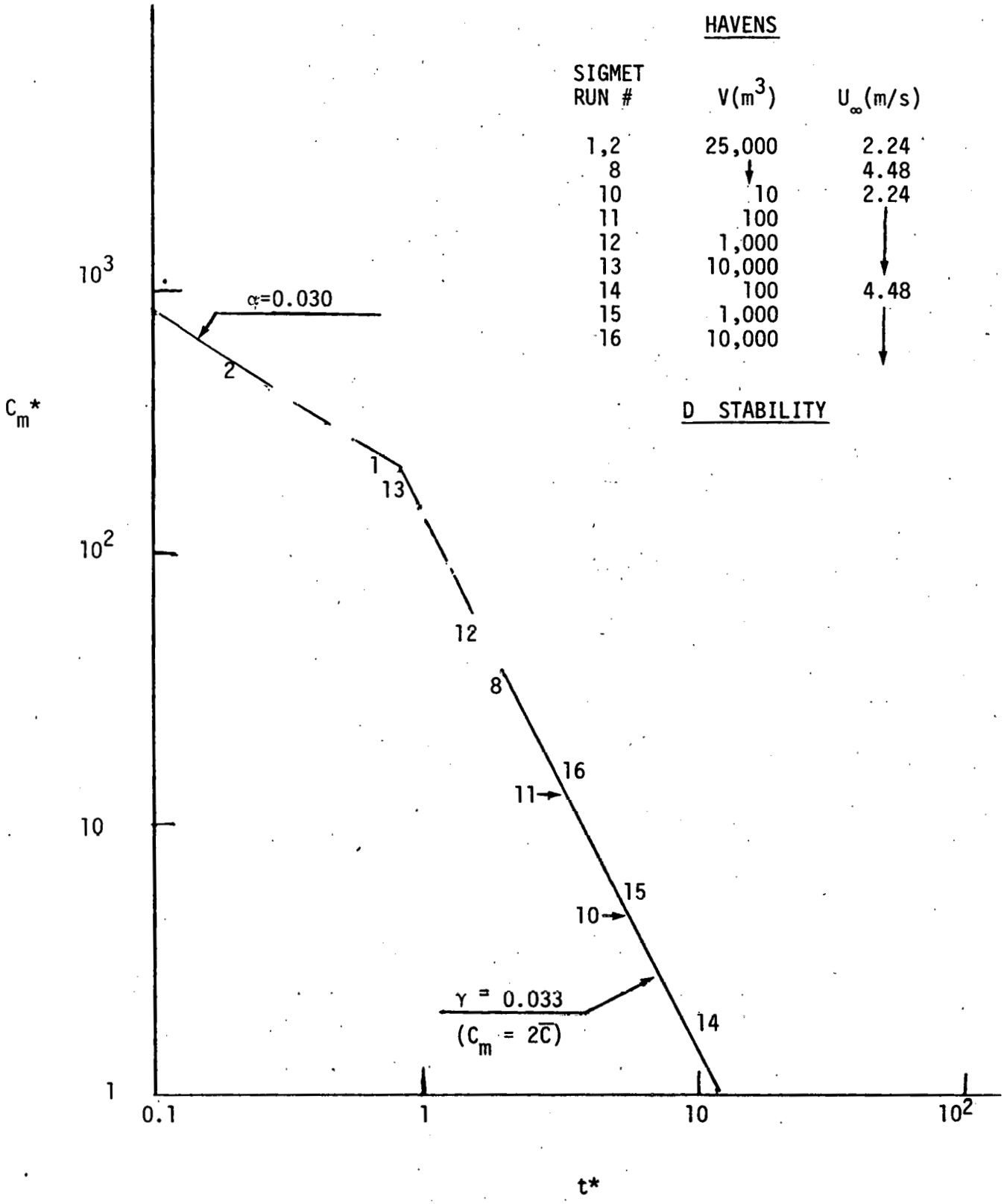

Figure 1. Correlation of several SIGMET calculations of maximum ground level concentration of LNG vapor as a function of time from beginning of a spill of LNG on water. All calculations were made for fixed stability class and turbulent transport properties but variable spill volume and wind speed. Straight lines are analytic asympt tic solutions for axisymmetric vapor cloud.

description of the early flow field may not be necessary as a practical matter.

Some current effort is devoted to the use of such solutions as a framework for correlating various calculations and measurements, especially from the point of view of distinguishing scale effects. While this is a promising approach, further analytical work may be needed to achieve this objective.

REFERENCES

Doo, Y-C. 1979. A two-dimensional model of negatively buoyant vapor cloud dispersion. M.S. Thesis, Massachusetts Institute of Technology, Cambridge, MA.

Fay, J.A., Lewis, Jr., D.H. 1975. The inflammability and dispersion of LNG vapor clouds. Proc. Fourth Int. Symposium on Transport of Hazardous Cargoes by Sea and Inland Waterway, Jacksonville, pp. 489-98.

Germeles, A.E., Drake E.M. 1975. Gravity spreading and atmospheric dispersion of LNG vapor clouds. Proc. Fourth International Symposium on Transport of Harzardous Cargoes by Sea and Inland Waterway, Jacksonville, pp. 519-39.

Havens, J.A. 1979. A description and assessment of the SIGMET LNG vapor dispersion model. CG-M-3-79, Office of Merchant Marine Safety, U.S. Coast Guard, Washington, D.C.

Havens, J.A. 1977. Predictability of LNG vapor dispersion from catastrophic spills on water: an assessment. Office of Merchant Marine Safety, U.S. Coast Guard, Washington, D.C.

Turner, J.S. 1973. Buoyancy effects in fluids. Cambridge University Press, Cambridge.

REPORT C

Effect of Humidity on the Energy Budget of a Liquefied Natural Gas (LNG) Vapor Cloud

L. C. Haselman

Prepared for the
Environmental and Safety Engineering
Division
U.S. Department of Energy
under Contract W-7405-ENG-48

Lawrence Livermore Laboratory
Livermore, California 94550

THIS PAGE

WAS INTENTIONALLY

LEFT BLANK

REPORT C

TABLE OF CONTENTS

FIGURES

TABLES

SUMMARY

The effect of the humidity of the air on the dispersion of the vapor rising from a liquefied natural gas (LNG) spill is studied. We developed a theory relating the temperature of a mixture of air and methane to the percent of methane in the mixture. The theoretical results are compared with experimental measurements. In general we found that the experimental temperature was higher than expected, suggesting that additional heat was added to the plume. Several mechanisms for this addition are evaluated.

INTRODUCTION

In the event of a liquefied natural gas (LNG) spill the liquid forms a pool that boils rapidly, producing a heavier-than-air vapor that is dispersed by the wind; or, with low wind velocities, spreads due to gravitational forces. If we assume that LNG is compared solely to its principal component, methane, then the density of the vapor is the density of methane at the normal boiling point temperature (112 K).[1] At this temperature methane gas is 1.45 times the density of air at 293 K. If, however, the methane gas is heated to 293 K, it has a density that is 0.55 that of air at this temperature. Thus, the buoyancy of an LNG/air mixture depends on the heat added to the cloud by external sources.

There are several sources of heat addition to the cloud. During the day, solar radiation warms the cloud. Heat may also be transferred from the surface over which the cloud is dispersing by three mechanisms--convective heat transfer, radiation from the surface, and heat transfer due to evaporation of water from the surface and then condensation in the cloud. Finally, the condensation of the water vapor in the air adds heat to the cloud due to the heat of vaporization/sublimation. If sufficient heat is added to the cloud from these sources, then it becomes positively buoyant and disperses much more rapidly. Estimating the amount of heat added to the dispersing vapor cloud from solar radiation and surface sources is difficult because the heat is

added to the cloud continually and thus presents a dynamic problem. The effect of the water vapor in the air is relatively easily determined since it is, for the most part, a function only of the temperature of the air and the relative humidity. In this report we address the effect of humidity on the buoyancy of the cloud and compare the theoretical expectations to experimental results.

THEORETICAL DEVELOPMENT

In developing the relationship between temperature, density, and methane concentration for mixtures of air, methane, and water vapor, we make the following assumptions:

- All gases conform to the ideal gas law and are in thermodynamic equilibrium.
- Mixing between methane and humid air is adiabatic.
- The temperature of condensed and frozen water is the same as the gas phase temperature.
- The heat necessary to cool or heat the condensed phase is negligible compared to the latent heat of sublimation.
- The condensed water vapor is assumed to be in the solid phase.

The last two assumptions introduce some error into the calculations; however, the effect is small and does not significantly affect the results. Since the water vapor mass fraction is of the order of 0.01, it is ignored in the computation of the thermodynamic variables for the methane-air mixtures.

The temperature of mixtures of methane and dry air can be found from

$$\bar{T} = \frac{C_{pm} T_m f_m + C_{pa} T_a f_a}{\bar{C}_p} , \qquad (1)$$

where C_p is the specific heat at constant pressure, T is the temperature, and f is the mass fraction. The m subscript refers to methane, and the a subscript to air. The expression $\bar{C}_p$ is the average specific heat calculated from

$$\bar{C}_p = C_{pm} f_m + C_{pa} f_a \quad . \qquad (2)$$

The saturation vapor pressure of water is found from an approximate solution to the Clausius-Claperon equation

$$P_s = P_r \, e^{(-A/T + B)} \quad , \tag{3}$$

where P_s is the vapor pressure, and P_r is a reference pressure taken as 1 bar. A and B are constants taken as 5514 K and 15.08, respectively. This provides a fit to the psychometric tables for water that is at least 2% accurate over the range of 0 to 50°C.

For air at a temperature T_a and a relative humidity RH, the mass fraction of water vapor f_i can be found from

$$f_i = \frac{W_v \, P_r \, RH}{W_a \, P_o \, 100} \, e^{(-A/T_a + B)} \quad , \tag{4}$$

where W is the molecular weight, the v subscript denotes water vapor, and P_o is the pressure of the air and water vapor. For a mixture of methane, air, and water vapor, the vapor pressure of water P_v is given by the equation

$$P_v = f_v \, P_o \, \frac{\bar{W}}{W_v} \quad , \tag{5}$$

where $\bar{W}$ is the molar average molecular weight.

At the same time the saturation vapor pressure P_s is obtained from Eq. (3) using T, the temperature of the mixture. If P_s is greater than P_v, then there is no condensation, and the temperature T is equal to $\bar{T}$ given by Eq. (1). If P_s is less than P_v, then there is condensation such that $P_v = P_s$. This requires that the fraction of water vapor not condensed has a mass fraction f_v determined by

$$f_v = \frac{P_s \, W_v}{P_o \, \bar{W}} \quad , \tag{6}$$

and the mass fraction of water vapor condensed f_c is

$$f_c = f_i \, f_a - f_v \quad . \tag{7}$$

The temperature of the mixture is obtained from

$$T = \bar{T} + \frac{f_c H_s}{C_p} \quad , \tag{8}$$

where H_s is the heat of sublimation of water. Combining Eqs. (3), (6), (7), and (8), we have

$$T = \bar{T} + \frac{H_s}{\bar{C}_p} \left(f_i f_a - \frac{W_v}{\bar{W}} \frac{P_r}{P_o} e^{(-A/T+B)} \right) . \tag{9}$$

Equation 9 gives the temperature of a mixture of methane, air, and water when P_s is less than P_v. It should be noted that the equation is implicit since the saturation vapor pressure depends on the temperature of the mixture.

Figure 1 shows the temperature vs the mole % methane for mixtures of methane and air at various humidities for an air temperature of 20°C and a methane temperature of -162°C, which is the boiling temperature of liquid methane at atmospheric pressure.[1] The effect of humidity at this air temperature is quite pronounced with a change in temperature as much as 26°C.

Figure 2 shows the ratio of the density of the mixture to the density of air vs the mole % methane where the density ratio is given by $\rho/\rho_o = (\bar{W} \cdot T_a)/(W_a \cdot T)$. These curves show that for high humidities the methane/air mixtures can become buoyant. Note that using the gradient of the temperature in a cloud of LNG vapor to estimate the buoyant stability of the cloud, as is done for example in the SIGMET model,[2] is not valid since an increase in temperature with height corresponding to decreasing concentration gradient of methane can have a density gradient that is either positive or negative, depending upon the humidity and the concentration of methane. Also note that this effect is most pronounced in the concentration regions where the methane/air mixture is flammable, e.g., the 5 to 15% methane range.

EXPERIMENT COMPARISONS

To test the assumption of adiabatic isothermal mixing, the preceding theory was compared with data from experiments performed at the Naval Weapons Center, China Lake, California.[3,4] In these experiments LNG was spilled at the center of a square pond 50 m on a side. Simultaneous measurements were made of methane concentration using a variety of sensors and temperature using thermocouples. Since a variety of instruments with various time responses was

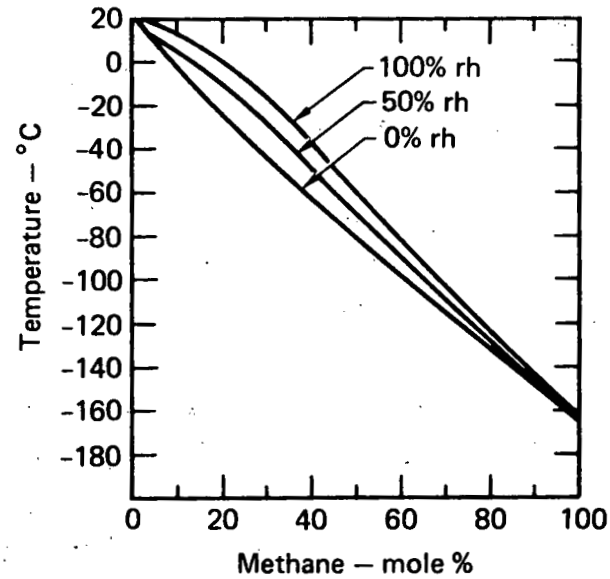

FIG. 1. The temperature of mixtures of methane and air with various humidities. The air temperature is 20°C, methane temperature -161.6°C.

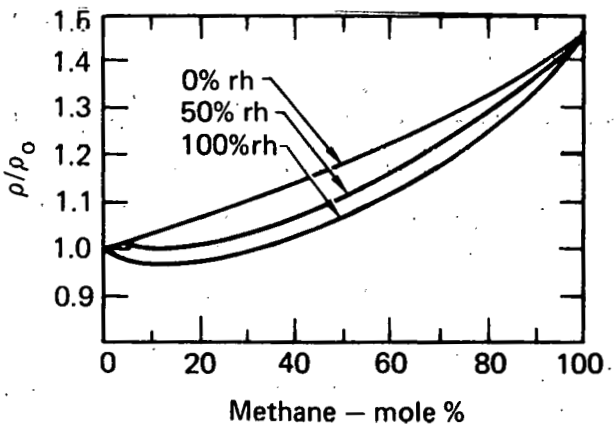

FIG. 2. The density of methane and air mixtures divided by the density of air with various humidities. The air temperature is 20°C, methane temperature -161.6°C.

used in these experiments, it is difficult to correlate temperature and concentration directly, particularly since large fluctuations in temperature and concentration were observed. Therefore, for this comparison, points were chosen at times when the fluctuations were small and when the concentration remained at an average value for a time period longer than the response time of the instrument.

It was observed that the methane in these experiments boiled off preferentially to the ethane and propane. Therefore, data from later times in the experiments were not used since the amounts of ethane and propane relative to methane could be large. For the data presented, the amounts of ethane and propane present are small and do not significantly affect the conclusions of this study.

Table 1 shows the conditions under which the four dispersion tests were done. For all tests the humidity was low, the heating effect was small, and the temperature vs concentration curve is close to that of dry air mixing with methane. Figures 3-6 show the comparison between the theoretical change of temperature vs methane concentration and the measured results. The measured results, in general, give a higher temperature than expected, and the low wind cases give poorer agreement than the high wind case. In addition, the magnitude of the disagreement does not appear to depend on the distance downwind from the spill point.

Several explanations are possible for this disagreement. As the wind blows across the spill pond, it evaporates water from the pond and forms a boundary layer of humid air close to the pond. Thus, the humidity over the pond, which was not measured, could be higher than the humidity measured at the weather tower upwind of the pond. The variation of humidity with height in the boundary layer varies with the distance from the upwind edge of the

TABLE 1. Parameters of four dispersion tests.

Test	Temperature, °C	Relative humidity, %	Wind velocity, m/s
LNG 18	36	16	6.2
LNG 19	27	29	5.1
LNG 20	27	15	11.3
LNG 21	20	21	4.6

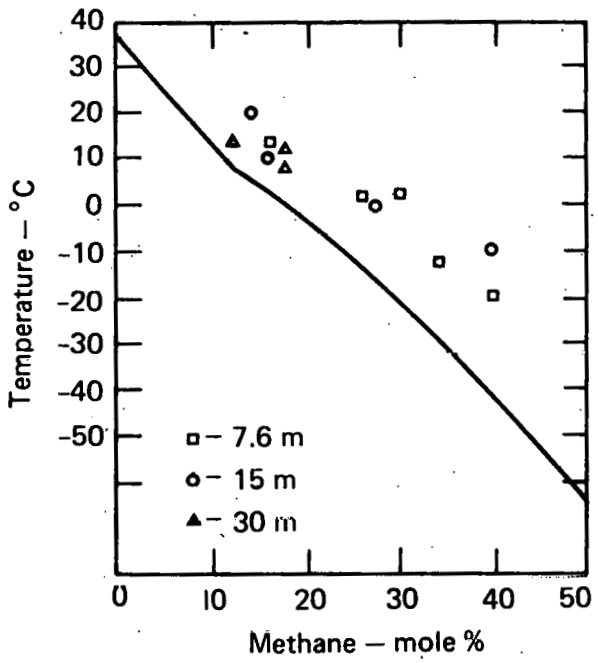

FIG. 3. The expected temperature vs methane concentration (solid curve) and measured data for LNG 18 at various distances from the spill point.

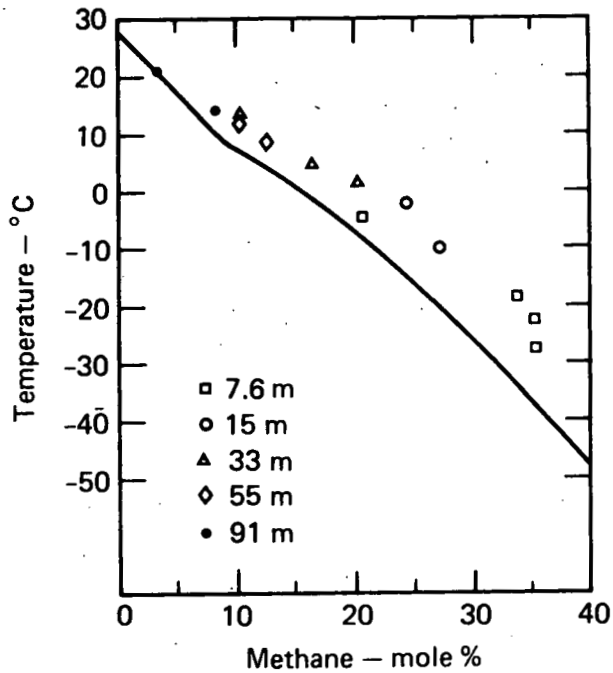

FIG. 4. The expected temperature vs methane concentration (solid curve) and measured data for LNG 19 at various distances from the spill point.

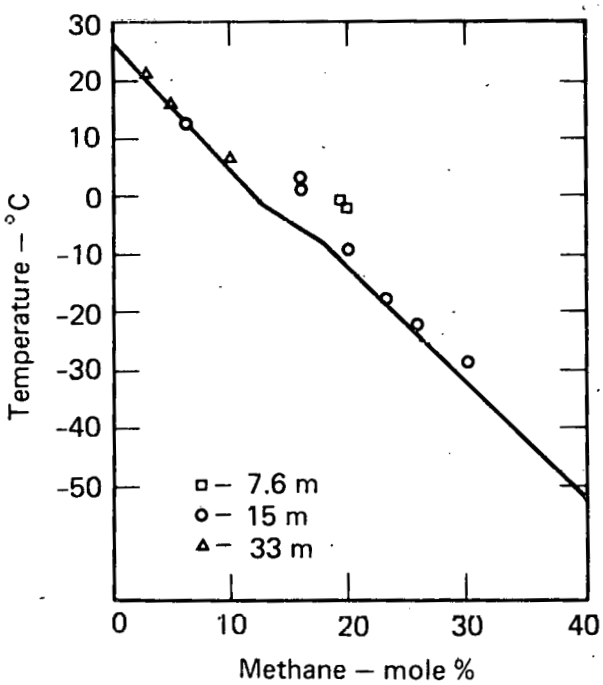

FIG. 5. The expected temperature vs methane concentration (solid curve) and measured data for LNG 20 at various distances from the spill point.

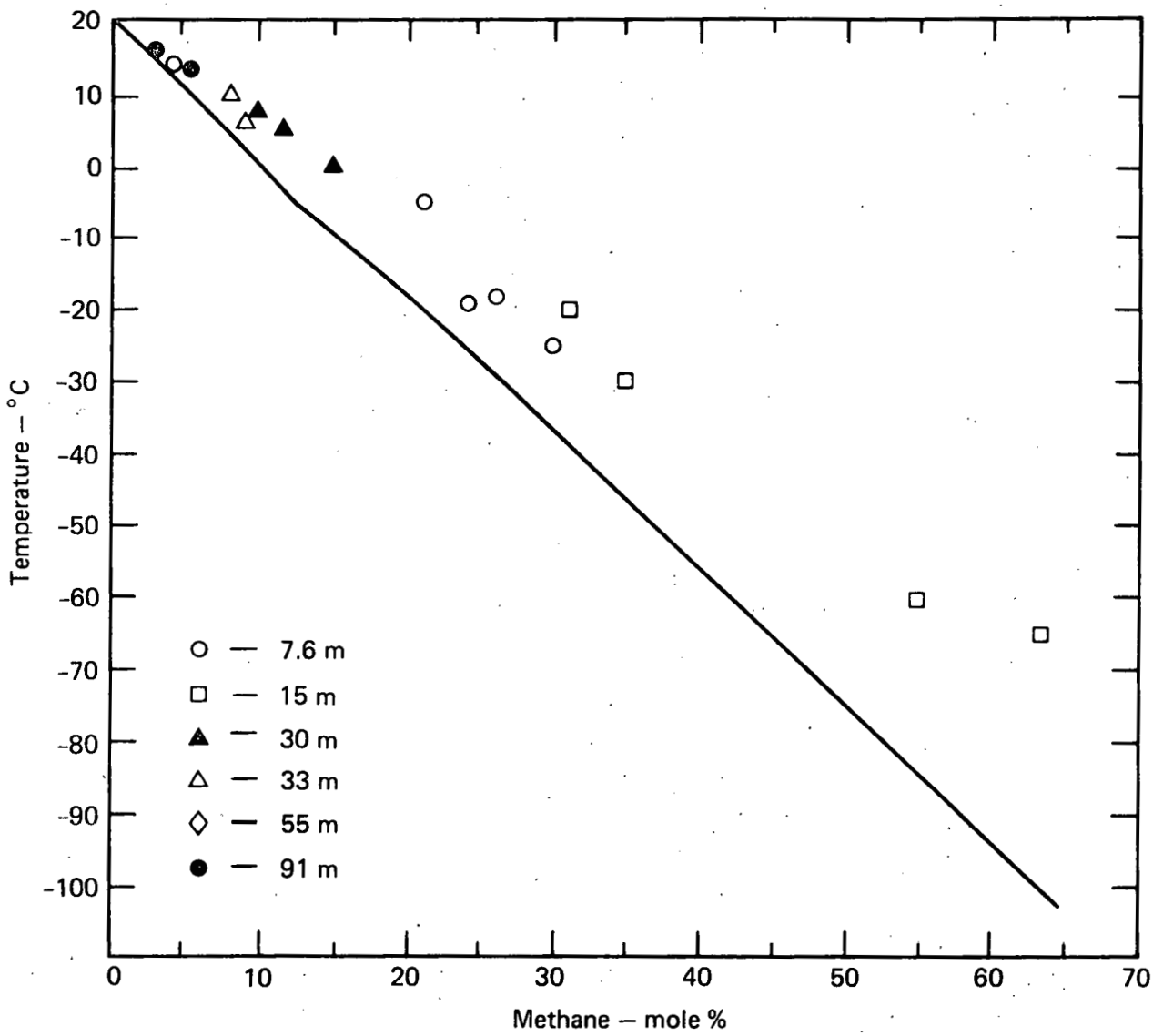

FIG. 6. The expected temperature vs methane concentration (solid curve) and measured data for LNG 21 at various distances from the spill point.

pond, the relative humidity of the air upwind of the pond, the wind velocity, and the temperature of the pond. These factors make it difficult to estimate the magnitude of this effect.

Another possible explanation for the disagreement is that the vapor pressure for water in the pond is much higher than the saturation vapor pressure for the dispersing plume since the pond is warm and the plume is cold. Therefore, any water evaporating from the pool is condensed by the cold gas, increasing the gas temperature. This effect, as in the case of the humid boundary layer, is a dynamic function of many parameters and very difficult to estimate its magnitude. However, we note that in LNG 21 the wind over the pond dropped to a very low value ($\sim$1 m/s), and the vapor cloud had a long residence time over the pond. This test shows the greatest disagreement between theory and experiment, and in particular the data points at about 60% methane would require a humidity of more than 100% in the air to explain the observed difference in the temperature. In LNG 20, where the wind velocity was high, the cloud had a short residence time over the pond, and the theory and experiment in this case are in relatively good agreement. This suggests that the evaporation from the pond may be significantly heating the cloud.

At this time there are insufficient data to determine if these effects are contributing to the disagreement between theory and experiment or if the difference lies elsewhere. On future dispersion tests at China Lake, measurements are planned that will address these questions.

CONCLUSION

Since it is possible that a plume of LNG vapors may become buoyant with the addition of sufficient heat, it is necessary to determine the energy budget of the plume. There are several sources of energy to heat the plume, and each source could be important depending on the plume dynamics and the conditions under which LNG is spilled. Under conditions of sufficiently high temperature and humidity, the condensation of water vapor can cause the plume to become buoyant for mixtures of air and methane on the order of 10% methane and 90% air.

Comparison of theoretical expectations of the effect of humidity on the temperature with experimental measurements for various mixtures of methane and

air indicates that the temperature is higher than expected. This also indicates that there are sources of heat addition to the cloud that are not accounted for by the theory. There are several possible explanations for this effect, however, there are insufficient data to decide the cause of the disagreement. Further work is planned in this area.

REFERENCES

1. D. Mann, general editor, LNG Materials and Fluids, National Bureau of Standards, First Edition, 1977.
2. J. A. Havens, A Description and Assessment of the SIGMET LNG Vapor Dispersion Model, U. S. Coast Guard Report, CG-M-3-79, February 1979, pp. 97-98.
3. C. D. Lind and J. C. Witson, "China Lake Spill Tests," Report L, Liquefied Gaseous Fuels Safety and Environmental Control Assessment Program: A Status Report, DOE/EV-0036, May 1979.
4. R. P. Koopman, L. M. Kamppinen, L. G. Multhauf, G. E. Bingham, and D. N. Frank, "A Review of the 1978 China Lake LNG Dispersion Experiments and Instrumentation," Report K, Liquefied Gaseous Fuels Safety and Environmental Control Assessment Program: A Status Report, DOE/EV-0036, May 1979.

REPORT D

LNG Fire and Explosion Phenomena Research Evaluation

R. C. Corlett

Subcontracted by
Pacific Northwest Laboratory for
the U.S. Department of Energy
under Contract DE-AC06-76RLO 1830

University of Washington
Seattle, Washington 98195

THIS PAGE

WAS INTENTIONALLY

LEFT BLANK

REPORT D

TABLE OF CONTENTS

1.0 SUMMARY

Liquefied natural gas (LNG) fire and explosion phenomena are examined from the viewpoint of estimating hazard characteristics. Such information is needed for decision-making relating to LNG facility siting and operations. This report attempts to delineate and analyze areas where such decisions still cannot be made with confidence, and to recommend the most needed further research.

A necessary starting point is the specification of parameters which control combustion. Representative ranges and some severe case limits are stated. As much as possible, these were based on knowledge of potential release scenarios, and of liquid and vapor dispersion phenomena. However, a significant degree of uncertainty is unavoidable.

1.1 FUEL DISTRIBUTION AND RELATED ASSUMPTIONS

Release volumes on the order of 2500 - 25,000 m^3 are of most interest. Release rates considered vary from instantaneous to continuous. For most purposes, however, instantaneous release over open water leads to fuel distribution parameters for which combustion phenomena are potentially the most hazardous and the most poorly understood. Natural vaporization flux, driven by heat transfer from beneath the released liquid, is assumed to range up to 0.3 $kg/m^2/sec$. Scenarios which involve release of a large liquid volume into a built-up area or release from pressurized storage are not considered.

1.1.1 Vertical Layer Structures

The combustion phenomena of dominant interest are determined by the vertical structure of the LNG vapor cloud. Most important is the thickness of the flammable layer, whose typical range is taken as 3 - 50 m, with 300 m as a severe limit. Other parameters of concern are the total amount of

fuel vapor in concentrations above the lean limit, the velocity of the flammable layer relative to a stationary observer and to the rich layer beneath, and turbulence characteristics.

1.1.2 Pool Fires

The most important pool fire characteristics are the natural vaporization rate and the horizontal dimension up to 1000 m or so.

1.2 RESEARCH EVALUATIONS BY TYPES OF COMBUSTION PHENOMENA

Four types of combustion phenomena are considered separately in the report. These are: ignition, vapor cloud burnup, pool fires, and detonation. Vapor cloud burnup encompasses all aspects of flame development in the vapor cloud and the interaction of combustion-generated buoyancy with the flow patterns within the cloud. Strictly speaking, vapor cloud burnup includes detonation as a special case. In view of public concern with the possibility of detonation, however remote, and the large body of specialized knowledge that has evolved respecting detonation phenomena, this subject is treated separately and extensively.

For each of the four types of combustion phenomena indicated above, the information most needed for hazard evaluation purposes is indicated first, then existing technical understanding is reviewed, and finally salient conclusions and recommendations for research are stated. At the end of the report, the more important recommendations are recapitulated and priorities are stated.

1.2.1 Ignition

LNG vapor-air mixtures within flammability limits are readily ignited by open flame and by most common sparks. Conditions for ignition by hot surface or hot gases are reasonably well understood. Should a flammable mixture envelop a built-up area of a functioning ship, ignition probability is very high. If more precise answers are required, e.g. the probable time to ignition after a flammable cloud reaches a built-up layer, quantification

of the distribution of various types of ignition sources is the most important information not immediately available. No new research on the phenomena of ignition is needed for LNG hazard analysis.

1.2.2 Vapor Cloud Burnup

Concern has been evidenced that a large release of LNG might burn in a "fire-ball" mode. Unquestionably, if several 1000 m^3 of LNG could be vaporized and ignited so as to form a single large fire-ball, injurious thermal radiation would be experienced for great distances. The most important needed information is the extent to which large-scale fire-ball behavior can actually be approached or, more precisely, the maximum length-scale of coherent vapor cloud combustion. Other needed information is the speed of flame spread from a point of ignition to targets at risk, or whether a large liquid spill will become involved rapidly enough to comprise a fully-developed pool fire.

The most important of vapor cloud burnup questions is how rapidly flame spreads through turbulent vapor-air layers of thickness and vertical concentration gradients characteristic of LNG vapor clouds. It appears likely that typical flame spread rates will be only a few m/sec, but new experimental research will be required for resolution. Reasonably straightforward scale modeling principles are available to minimize the size of the required experiments.

An anticipated vapor cloud burnup phenomenon is turbulent diffusive burning of fuel-rich volumes. There would be strong coupling between combustion-generated buoyancy and turbulent diffusion. This coupling is far from well understood scientifically. However, a rational basis is available for extrapolating results of small-scale experiments to realistic conditions.

A characteristic of vapor cloud burnup, which possibly grows in importance as length-scale increases, is the competition between flow induced by combustion-generated buoyancy and turbulent flame spread. The role of such competition is especially important when considering flame spread upstream along a plume. This type of problem is difficult to treat theoretically, but there is a reasonable prospect for useful scale-modeling.

A serious concern is the possible formation of pressure waves capable of structural damage. For simple geometry, ability to calculate pressure wave magnitude is limited primarily by uncertainty in turbulent flame spread rates. Effects of complex geometry need further investigation.

As the involvement length-scale increases, burning vapor clouds pose a thermal radiation hazard. Prediction of thermal radiation from burning vapor clouds is limited primarily by inability to describe the evolution of flame geometry.

1.2.3 Pool Fires

Thermal radiation incident on targets at risk outside the fire involvement area is for practical purposes the one characteristic of LNG pool fires important to decision-makers. This problem can be broken down into determination of fire geometry and description of thermal radiation flux at a perceived flame boundary. Both types of information are available, albeit in highly approximate form. Hazard characteristics are only moderately sensitive to flame geometry parameters and emission flux. Thus, although much scientific work remains to be done toward detailed understanding of pool fire phenomena, additional research in this area is not considered to be a high priority in hazard evaluation.

1.2.4 Detonation

Detonation, as meant in this report, consists of a very strong shock wave followed immediately by a reaction zone in which heat is released. The most important information needed is definition of what, if any, realistically anticipated conditions allow LNG vapor to be mixed with air and detonated. It is well-known that rather special conditions are required for such detonation. The real problem is quantification of the probability of such an unlikely event.

There remains some uncertainty about how much explosive energy would be required to detonate a methane-air mixture. However, it is clear that many kg of explosives would be required. On the other hand, moderate contamination with higher hydrocarbons, such as propane, greatly reduced the initiation requirement.

It is also possible for a deflagration, a low speed combustion wave, to undergo transition to detonation. The transition process may be enhanced by suitable geometric confinement. There is strong theoretical and experimental evidence that such transition to detonations cannot occur under conditions anticipated in typical LNG vapor clouds. However, there are numerous aspects of the phenomena that are incompletely understood, and the impossibility of transition to detonation in LNG vapor clouds is not yet proven.

If, indeed, a detonation can be initiated in an LNG vapor cloud, there are significant uncertainties in predicting the history of subsequent motion. Most importantly, the minimum layer thickness required for propagation, i.e. the quenching thickness, is not established for LNG vapor. The effect of composition stratification is also inadequately understood. Such questions should be answerable by scale modeling experiments using fuels that are relatively easily detonable.

1.3 RECOMMENDATIONS

A few, very large tests will not provide the type of information most needed by the planners. Planning should be biased towards spills of size that would permit a substantial number of well-instrumented and carefully interpreted runs. Scale modeling procedures for critical phenomena should be aggressively pursued. Also, some standardized specifications of initial fuel distribution, ignition characteristics, etc. are needed to define a detailed research program.

The most important class of phenomena requiring research is vapor cloud burnup. Areas which merit further investigation are flame spread in turbulent layered gases, the interaction of gravity and flame spread, and non-detonative pressure wave characteristics. Each of these areas, especially the first-mentioned, may be amenable to a significant degree of scale-down.

Research aimed at detonation phenomena is of lower priority. To provide better understanding of detonation probability, three research activities are recommended. The most important is to ascertain a quenching thickness. Another is to improve understanding of the degree of confinement needed for transition from deflagration to detonation. The third is better knowledge of direct initiation requirements. The first two are amenable to scale-down. The third can be assisted markedly through aquisition of improved chemical kinetic data that will enable reliable theoretical calculations. Facilities to obtain such data are available.

2.0 INTRODUCTION

Liquefied natural gas (LNG) is a fuel of moderate energy density and extreme volatility. It is normally contained by heavily insulated tanks, vessel compartments, etc., and transported by pipe only for relatively short distances, e.g. between tanker vessels and shore storage. Any substantial release of LNG has potential for hazardous rapid combustion.

There are motivations for expanded use of LNG in the next few years. Increases in the number of facilities and operations, and in the scale of LNG inventories, are projected. Responsible government bodies must make decisions respecting siting and operational constraints, to assure public safety with minimal economic and energy penalties.

Such decisions depend on knowledge of release probabilities and understanding of the post-release phenomena. The latter may be categorized as dispersion and combustion. This report evaluates our understanding of the combustion category as needed for decision making relating to hazard evaluation and mitigation.

2.1 SCIENTIFIC PERSPECTIVE

The needed understanding of LNG combustion phenomena is only to a limited degree achievable through testing. The events of concern are accidents. It is necessary to generalize conclusions to a set of plausible cases greatly exceeding that for which test data can be obtained. Moreover, consideration must be given to releases too large for testing. Releases of very large quantities, albeit of low probability, conceivably could lead to catastrophic combustion.

Generalization to untested combinations of variables and, especially, extrapolation to large length-scale require a degree of theoretical understanding. Unwanted combustion typically exhibits a number of complexly coupled phenomena which can be understood only at a rather coarse level of detail. The only feasible scientific approach is to establish what phenomena are dominant, and to rely on idealized theory and experiment for quantitative relations. The result will be an estimate of realistic combustion

behavior. The accuracy of estimates thus arrived at is limited by uncertainty in deduction from postulated scenarios, of parameters appearing in theory or in experimental correlations. Fortunately, most of the hazardous characteristics of unwanted combustion are only moderately sensitive to parameter uncertainty.

This report is presented in the spirit outlined in the preceding paragraph. It attempts to:

- summarize our ability to estimate magnitudes of LNG combustion hazard characteristics
- delineate and analyze areas where such estimates cannot be made with confidence
- recommend most needed further research.

The report is not a compilation of all scientific information bearing on LNG fire and explosion phenomena. Neither is it a programmatic evaluation of on-going research.

2.2 ORGANIZATION OF THIS REPORT

Analysis of any combustion event requires an initial fuel distribution and specification of important environmental characteristics. Section 3 sets forth salient parameters and their assumed ranges. A key assumption is that the LNG is stored at near-atmospheric pressure, thus excluding the high release velocities and adiabatic vaporization encountered when liquefied petroleum gas (LPG) is released from pressurized storage. Sections follow which deal with four major categories of phenomena important to the overall behavior of LNG combustion:

Section 4 - Ignition
Section 5 - Vapor cloud burnup
Section 6 - Pool fires
Section 7 - Detonation

Section 5 includes the important question of the extent to which so-called "fire-ball" behavior may realistically be anticipated following a large LNG release.

Each of the Sections 4 through 7 begins with a statement of the information most needed for hazard analysis, follows with a review of technical understanding, and ends with conclusions and recommendations. Section 8 recapitulates the recommendations and, as limited by the scope of the report, sets priorities. Detailed priorities for recommended further work depend on firmer release/dispersion specifications than presently available. Also, such factors as the importance assigned to events of very low probability but high hazard level must be quantified.

Section 7 is relatively extensive. This reflects the great amount of work that has been devoted over the years to detonation phenomena in general and, recently, to methane-air detonations particularly. It does not imply that detonation is a dominant concern in LNG hazard analysis. The unresolved issues most important for hazard analysis fall within the scope of Section 5.

THIS PAGE

WAS INTENTIONALLY

LEFT BLANK

3.0 FUEL DISTRIBUTION AND RELATED ASSUMPTIONS

This Section sets forth the assumptions respecting fuel distribution and combustion environment which guide the remainder of the report. Ideally, such assumptions should be derived from a spectrum of release scenarios and respective probabilities, and state-of-the-art dispersion analyses reflecting probability distributions of wind and other environmental variables. A further probability distribution of potential ignition sources, in time and space, would make possible derivation of a spectrum of combustion scenarios. Such information is not presently available. The assumptions stated below are judgments based on available factual descriptions of LNG operations, and discussions with various individuals concerned with LNG hazards.

It is remarked that these assumptions are biased away from events for which LNG combustion phenomena are not seriously at issue in hazard analysis. An example would be a ruptured tank volume of only a few 10's of m^3 due, for example, to an LNG truck collision. On the other hand, the assumptions are biased towards events which, at least in theory, could cause tremendous damage, even though occurrence probabilities are small. Thus considerable emphasis is devoted to events that could produce large-scale "fire-ball"-like behavior, or detonation. Public perception of the hazards of such catastrophic events demands clear quantification of occurrence probabilities, at least in an upper-bound sense.

3.1 EXCLUSIONS

- Only scenarios consistent with the current or projected siting and operational policy are considered. Excluded, in particular, is the release of a large volume of liquid into a built-up area, as has occurred in the past[1]. Combined liquid/vapor flow, and boiling, in tunnels, building interiors, etc. is not considered.

- Almost all LNG is contained at near-atmospheric pressure, because temperature variation with pressure is so small, in comparison with the driving temperature differential for heat leaks, that pressurization yields only very small reduction in insulation or refrigeration costs. Only releases from near atmospheric pressure containment are considered. This contrasts with liquefied petroleum gas (LPG) which is typically stored at room temperature and pressures on the order of 10 atm. Releases from pressurized storage exhibit high flow velocities and strong turbulent mixing, with characteristic "fire-ball" behavior[2]. Should LNG be stored under pressure, a release would exhibit behavior similar to an LPG release.
- So-called "boiling explosions", wherein damaging dynamic phenomena may be encountered even in the absence of combustion, are mentioned for completeness in Section 7. However, this type of phenomena can be considered carefully only in the context of liquid flow and boiling phenomena in general. The physical problem properly belongs in the category of dispersion phenomena. Only problem specifications pertinent to hazardous combustion are considered.

3.2 UNDERLYING ASSUMPTIONS

3.2.1 Release Magnitudes

Volumes on the order of 2500 - 25,000 m^3 are of most interest. With the exception of truck or rail transport, all acceptable LNG facilities and operations will probably be sited under the assumption of potential releases of such magnitude. Fire behavior of smaller releases is discussed briefly in Section 6. Although there is no clear upper-bound worst case, 50,000 m^3 (say, two tanker compartments) is appropriate as a severe release.

3.2.2 Release Duration

Raj[3] has given an estimate for the crossover time from instantaneous to continuous release of liquid; for shorter release duration, the liquid flow and boiling phenomena are essentially those of an instantaneous release.

For a 10000 m^3 release and a conservatively high vaporization flux of 0.3 $kg/m^2/sec$, crossover time is approximately 60 sec; this time varies as (release volume)$^{1/3}$ and inversely with vaporization flux. Consideration of release mechanics suggests that instantaneous liquid release is a barely achievable worst case when vaporization flux is high (over open water) but is a reasonable baseline case when low (over land).

For most purposes the assumption of instantaneous liquid release is conservative. An exception arises when considering the possibility that a continuous release might produce a combustible plume connecting distant downstream ignition sources with the source of release, e.g. a tanker with some tanks full and other ruptures but not locally ignited. The major issue is the likelihood of upstream flame propagation along the plume, and is dealt with in Section 5.

3.2.3 Release Site Characteristics

The following are judged representative site specifications of greatest importance.

- release on water of unlimited extent
- near-shore release on water with an on-shore wind component and with sloping beach or sea-wall adequate to prevent on-shore liquid flow
- release from a tank on land in a diked-in area which contains all of the liquid
- release from a tank on land in a diked-in area, with a major escape due to surging or dike breach.

3.2.4 Vaporization

With the possibility of release from pressurized storage neglected, vaporization is heat transfer controlled. Existing data[4] indicates that 0.2 $kg/m^2/sec$. is typical over water. This is consistent with conventionally understood film boiling mechanics. An increased order of magnitude would require a mechanism for self-sustained turbulent mixing of LNG and water. Such a mechanism has been speculatively proposed[5] but the

assumptions are so far unsupported by existing data or theory. In this report, 0.3 kg/m^2/sec. is taken as an upper bound. Over land, although complex transient behavior must occur, time-mean vaporization rates must be much lower.

3.2.5 Wind

The most important range of wind speeds is a few m/sec., say 3-15. For large releases, effects of wind speed below this range are overwhelmed by gravity vapor flow, except at very late stages of dispersion. Wind speed above this range is relatively unlikely. Because high wind speed enhances dilution to safe levels, consideration of the moderate range cited is conservative in a sense. For example, high wind speed reduces plume length for a given spill size. On the other hand, maximum flammable layer thickness increases with increasing wind speed. Increasing flammable layer thickness may exacerbate some aspects of LNG hazardous vapor combustion.

3.2.6 Vapor Dispersion

A number of approximate models have been put forward, and comparatively reviewed by Havens.[6] A relatively complete model has been developed by Science Applications, Inc.[7] Predictive accuracy, in general, appears to be limited primarily by uncertainty in treatment of turbulent phenomena. The uncertainty applies to time-mean transport fluxes and, more severely, to fluctuations of dimension approaching the important (vertical) length scale of the phenomena of interest.

3.3 FUEL CONFIGURATION ASSUMPTIONS

The assumptions outlined above indicate that, prior to ignition, LNG must be distributed in a surface layer that is thin relative to characteristic horizontal dimensions. This becomes more valid the larger the postulated release volume. Vapor combustion phenomena of interest are determined primarily by the local vertical structure of the vapor layer. Of course, realistic prediction of the combustion hazard of a cloud (or plume)

of LNG vapor depends on additional information, such as horizontal dimensions and ignition point. But this is primarily an interpretive step, given a detailed pre-ignition dispersion scenario and understanding of various contributory combustion phenomena as determined by local vapor layer properties. Sections 5 and 7 are written in such spirit. Vapor layer vertical structure and pool fire fuel configuration are addressed separately below.

3.3.1 Vapor Layer Vertical Structure

Most important is the thickness L_F of the flammable layer when local turbulent time-mean fuel vapor mole fraction ξ is between the rich and lean flammability limits, ξ_R and ξ_L, respectively. The working value for ξ_R is 0.14. For pure methane ξ_L is 0.05; however, allowance for spiking with higher hydrocarbons dictates a somewhat lower value, here taken as 0.03.[8]

The flammable layer is mostly air. Its flow properties are essentially those of the ambient surface wind. One important flow property is a characteristic mean velocity $\overline{V}_F$. Another is a characteristic mean relative velocity $\overline{V}_{FR}$ between the flammable and rich layers. Because of gravity flow of the latter, possibly opposite to the wind direction, $\overline{V}_{FR}$ can exceed $\overline{V}_F$.

Beneath the flammable layer, in general, is a richer layer which may potentially feed continued combustion via enhanced mixing as a result of combustion-generated volume expansion and buoyance of the gases in the pre-ignition flammable layer. The fuel availability in the flammable and rich layers together is here characterized by thickness L_T defined, for definiteness, as the equivalent STP methane thickness of all the fuel vapor beneath the ξ_L surface. Examination of the concentration profile from an idealized one-dimensional diffusion analysis[9] shows that the maximum ratio of L_F/L_T is roughly 10, corresponding to disappearance of the rich layer, and is only weakly sensitive to the choice of ξ_L.

Finally, it must be recognized that the flammable layer should exhibit turbulent fluctuations, notably of concentration $\delta\xi$ and of velocity δV_F. The turbulent scale, for definiteness the integral scale L_I, is also important.

Numerical values of the above parameters are tabulated below:

Parameter	Range of Dominant Interest	Severe Limit
L_F (m)	3 to 50	300
L_T (m)	0.1 L_F to 10	30
$\overline{V}_F$ (m/sec)	0 to 15	--
$\overline{V}_{FR}$(m/sec)	0 to 15	20
$\delta \xi/\xi$	0 to 0.5	1
δV_F	0 to max ($\overline{V}_F$, $\overline{V}_{FR}$)	--
L_I	0 to 0.5 L_F	--

3.3.1.1 Comments

An example value of L_F approaching 200 m has been published.[7] Representative maximum values of L_T (vapor cloud formed by a massive release over water) from a variety of sources have been compiled by Havens.(6) With correction to standard temperature, these range past 20 m, hence the selection of 30 m as a severe limit. To maximize L_F, assume a highly unstable atmosphere such that the rich layer is consumed a short distance downwind of the maximum liquid perimeter, and then use the ratio $L_F/L_T = 10$.

It is entirely reasonable to assume that the turbulent mean ξ varies smoothly through the flammable layer. Hence, it appears appropriate always to assume the existence of an equivalence ratio gradient of magnitude at least $(L_F)^{-1}$.

Implicit in developing the severe limits for L_F and L_T is the consideration of the first of the cases stated in Section 3.2.3. For the other cases, notably the third and fourth, the limit values should be smaller.

3.3.2 Pool Fire Fuel Distributions

The following assumptions apply to LNG pools, Section 6. Natural vaporization refers to that independent of flame-to-fuel energy feedback.

3.3.2.1 Major release over open water —

- roughly circular (possible distortion due to contact with ships, shore, piers, etc.)
- maximum radius 1000 m
- maximum duration 600 sec (non-instantaneous)
- natural vaporization rate — up to 0.3 $kg/m^2/sec$

3.3.2.2 Tank release contained by dike —

- roughly square or circular
- maximum side length or diameter 300 m
- depth over 1 m
- negligible natural vaporization

3.3.2.3 Tank release with pool lost from dike —

- possibly erratic shape
- maximum area
  liquid 5×10^5 m^2
  envelope 2×10^6 m^2
- maximum duration 1200 sec.
- natural vaporization rate — up to 0.1 $kg/m^2/sec$.

THIS PAGE

WAS INTENTIONALLY

LEFT BLANK

4.0 IGNITION

Ignition of a cloud of LNG will occur only if a vapor-air mixture within the flammable range, approximately 3 to 14 percent fuel by volume for LNG vapor (Section 3.3.1) comes into contact with a suitable ignition source.

4.1 NEEDED INFORMATION

Information is sought for ascertaining the probability of ignition of a vapor cloud and also, if ignition does occur, for determining the range of probable time and location.

The probability of ignition depends strongly on the spill scenario. For a spill over open water, of a magnitude such that flammable mixtures do not reach land, it is unlikely that ignition will occur except from sources aboard ships, e.g. the ship from which the spill originates. The probability of shipboard ignition is difficult to assess, beyond observing that it appears somewhat similar to probability of ignition that would apply if the flammable mixture were to reach inhabited portions of land. The spill scenario involving a collision between an LNG tanker and another vessel would result in a high probability of ignition. Over land in remote areas, a flammable mixture from a large cloud might well encounter no ignition sources. However, in inhabited areas it appears that the probability of not encountering an ignition source will be very low for a cloud of appreciable extent. Since early ignition may result in a localized fire while late ignition may produce deflagration and pressure waves, which may be more damaging, particularly if they propagate through populated areas, knowledge of the time and location of ignition may be significant in hazard analysis.

4.2 REVIEW

4.2.1 Ignition Modes[10],[11]

Ignition of methane-air mixtures can be produced by a flame, by hot gases, by a hot surface or by a spark.

4.2.1.1 Flame Ignition

Ignition is practically certain if the flammable mixture encounters a flame, even a small one such as the pilot flame of a gas stove. Therefore, ignition times of methane-air mixtures exposed to flames need not be studied in connection with the question of cloud ignition.

4.2.1.2 Hot-gas Ignition

Gases as hot as combustion products in flames exhibit ignition characteristics similar to flame ignition. Hot gases at lower temperature behave similarly to hot surfaces in ignition. Since it seems likely that hot surfaces would be encountered more often than would hot gases at temperatures below flame temperature, hot-surface ignition may be more relevant than ignition by lower-temperature hot gases.

4.2.1.3 Hot-surface Ignition

In ignition by a hot surface, the flammable mixture experiences an auto-ignition process, in the sense that the surface heats the combustible gas and thereby initiates chemical reactions that lead eventually to production of radical species and to combustion. If the surface temperature is below a critical value, a reaction sufficient to produce radical buildup does not occur, and combustion is not observed, there being merely conduction of heat away from the surface through the gas. If the surface temperature is equal to the minimum auto-ignition temperature for the combustible mixture (approximately 530°C for methane-air mixtures and 470°C for propane-air mixtures), the ignition occurs after a long delay time. As the surface temperature is increased further, the delay time decreases. This decrease is quite pronounced, and therefore, in practice, a surface temperature equal to the minimum auto-ignition temperature is sufficient to ignite the flammable mixture.

4.2.1.4 Spark Ignition

In ignition processes, as the rate of energy deposition increases, the ignition time decreases. For very rapid deposition, there is a minimum total amount of energy that must be deposited in the gas to produce ignition. This is the minimum ignition energy, which is relevant for spark ignition. Minimum ignition energies are very small, on the order of 1 millijoule, for mixtures of LNG vapors with air.[12] Energies delivered by sparks in automobile engines, for example, are order of magnitude greater than the minimum ignition energy. Therefore, most sparks encountered by a combustible cloud would produce ignition.

4.2.2 Effects of Chemical Composition

The flammable range varies with content of heavier hydrocarbons; the lower and upper limits both decrease with increasing molecular weight. For example, the flammable range for propane-air mixtures is roughly 2 to 8 percent fuel by volume.[8] Aside from this shift in the flammable range, there is no significant effect of LNG composition on flame or spark ignition. There is a significant effect on auto-ignition (or hot-surface ignition), since ignition temperatures for the higher hydrocarbons are substantially lower. This difference stems ultimately from the fact that the carbon-hydrogen bond is stronger than the carbon-carbon bond, thereby making methane more stable than other hydrocarbons to thermal attack.[13] In flame and spark ignition, the fuel molecule is attacked by energetic chemical species, such as radicals, and the thermal stability is relatively insignificant. In hot-surface ignition, the fuel molecule is attacked thermally, and the stability of methane becomes important.

4.3 CONCLUSIONS AND RECOMMENDATIONS

The preceding considerations indicate that contact of the flammable mixture with nearly any spark or flame will produce ignition. Ignition is less certain upon contact of the flammable mixture with a hot surface, and in this case whether ignition occurs depends on the composition of the LNG, as well as on the temperature of the surface. Although some further research

on auto-ignition of LNG-air mixtures might be justified on the basis of this uncertainty, by far the greatest uncertainty lies in the question of whether a flammable mixture will come into contact with an ignition source, and, if so, when and where the contact will occur. In populated areas, along with hot-surface sources will be spark and flame sources. In general, it seems likely that a flammable cloud in such an area will encounter one of these sources, but the probability of this occurring is not known perfectly. Better quantification of arrangements and accessibilities of spark and flame sources could improve abilities to predict ignitions resulting from LNG spills. Also, uncertainties concerning sensitivities of hazard analyses to ignition probabilities and to ignition times and locations remain and may warrant further investigation.

5.0 VAPOR CLOUD BURNUP

This Section is concerned with the transient combustion of a large cloud of LNG vapor. After ignition, the region of combustion involvement expands due to flame spread and diminishes due to fuel consumption. This region is distorted by wind or by buoyancy-induced convection. Additional gas motion is a consequence of expansion due to combustion heat release. The process ends with the disappearance of the vapor cloud, or with establishment of a pool fire.

As noted in Section 3, a typical large vapor cloud would lie on the water or land surface, and its height would be much less than its horizontal extent. If, due to special initial conditions or to post-ignition convection, the cloud develops comparable vertical and horizontal dimensions and if it becomes fully involved in flame, there would exist what is loosely referred to as a "fire-ball." Recognizing that this is not necessarily the manner in which an LNG vapor cloud would burn, the fire-ball mode has been suggested[14],[15], and dynamic and thermal behavior discussed. Experimentation has been done on laboratory[14] and larger (but still much smaller than realistic)[16] length scales. Participation of a large mass of LNG vapor in a fire-ball would unquestionably constitute a severe thermal radiation hazard.[17]

5.1 NEEDED INFORMATION

An important characteristic of a vapor cloud burnup event is the extent to which large-scale fire-ball behavior is approached, given realistic initial vapor distribution. Even if the complete cloud does not form a fire-ball, the energy potentially available can be so large that local burning concentrations on a length scale substantially smaller than that of the complete cloud may constitute a serious thermal radiation hazard.

A second important characteristic is whether, and how rapidly, flame will spread from the ignition point to targets at risk. An example is whether flame can propagate upstream along a plume to a partially emptied tanker.

Finally, it is necessary to estimate combustion-driven pressure build-up well enough to assess pressure wave hazards, particularly to persons and property beyond the region of direct combustion damage.

5.2 REVIEW

Vapor cloud burnup entails multiple and complexly coupled physical mechanisms. To establish perspective, it is appropriate to consider briefly what constitutes a reasonable approach to understanding of this class of phenomena.

In principle, post-ignition vapor cloud behavior should be calculable by computer field solution of the appropriate partial differential equations. Techniques are evolving for numerical computation of turbulent flows with chemical reaction[18],[19] and buoyancy interactions[20]. Vapor cloud burnup entails turbulent deflagration combined with diffusive burning, distorted by convection. In general, the geometry of the essential features is three-dimensional. A major advance in flow and combustion computing capability is judged necessary before such problems can be confidently treated via field solutions.

An alternative approach is based on establishment of a few critical scenarios which would be subject to definitive field tests. However, for every release/dispersion scenario, it would be necessary to consider a range of ignition times and a variety of ignition locations. The required number of tests would be prohibitive.

The only avenue to decision-making criteria, encompassing a realistically wider spectrum of potential ignition events, is through understanding of important subsidiary phenomena in terms of dominant parameters. Accordingly, five main categories of phenomena are identified and dealt with separately below.

5.2.1 Flame Spread Through Flammable Volumes

There are two major elements in the flame spread problem. The first is determination of the rate of advance of the flame front relative to the local unburnt gas, here referred to as "propagation." Gas volume expansion upon passage of the combustion front disturbs the flow field. Relatively small scale, turbulent distortions are part of the propagation problem. Bulk gas motion due to volume expansion constitutes the second element of the flame spread problem.

5.2.1.1 Propagation

The heart of the propagation problem is the role of turbulence. From a rigorous scientific standpoint, this is far from understood, especially if there are fluctuations in composition in addition to velocity.

Apparently, no experimental investigations of the effect of composition fluctuations on turbulent flame propagation have been reported. In this paragraph, the effect of turbulence on flame propagation into compositionally uniform unburnt gas is reviewed. Lind[21] has measured propagation rate enhancement by turbulence developed upon propagation into a quiescent unburnt gas; the result is propagation S_T at approximately twice the laminar flame speed S_L. The effect of pre-existing turbulence has been reviewed by Andrews et al.[22], and additional measurements reported by Ballal and Lefebvre[23]. Andrews et al. suggest a correlation in terms of a single parameter, namely a turbulence Renolds number (constructed from velocity fluctuation δV and a characteristic turbulence length scale). This suggestion appears to be based on experimental data for high intensity (i.e. high δV) and small scale turbulence. The results of Ballal and Lefebvre show a clear dependence on at least one additional parameter, the velocity ratio $\delta V/S_L$. For the high intensity regime ($\delta V/S_L > 2$) their results suggest that S_T declines as turbulence length scale increases independently. For low intensity turbulence ($\delta V/S_L < 2$) there is a data gap for turbulence integral length scale larger than a few mm. The existing data base is judged consistent with the wrinkled laminar flame concept as applied to turbulence parameters anticipated for LNG vapor

clouds; i.e. $S_T/\delta V$ is of order 1, perhaps as high as 2, and tends to decrease with increasing turbulence scale. An upper bound propagation rate appears to be on the order of a couple m/sec for a low value of the flammable layer speed $\overline{V}_F$ or $\overline{V}_{RF}$; for higher values the corresponding expectation is some fraction, well less than unity, of max ($\overline{V}_F$, $\overline{V}_{RF}$). A more comprehensive data base is needed to evaluate these conjectures.

5.2.1.2 Effects of Expansion-Driven Bulk Gas Flow

A general consequence of volume expansion due to combustion is bulk acceleration of the unburnt gas just ahead of the flame front. Thus the spread rate, defined here as the rate of flame advance in the frame of reference of the local gas before disturbance by combustion, generally exceeds the propagation velocity. Under circumstances where transverse motion to accommodate volume expansion is not possible (i.e. parallel streamline flows) such acceleration might continue indefinitely. However, if the combustible gas layer is of finite thickness and free to expand in at least one transverse direction (i.e. upwards in likely LNG vapor cloud configurations), a steady spread rate is eventually established.

What is the spread rate-propagation rate ratio in an LNG vapor/air mixture with unlimited air above? Small-scale experiments with layered methane/air suggest numbers on the order of 6.[24] However, analytical concepts have been put forward which suggest gravity enhancement such that the ratio increases indefinitely with the thickness L_F of the flammable layer.[25] Whether or not this is true is a critical issue which demands early resolution. It is emphasized that such resolution does not, at least initially, require large scale LNG tests. The critical parameter is the ratio of the propagation velocity to a buoyant velocity, proportional to $(L_F)^{1/2}$. This suggests scale model experiments using fuel/air mixtures with laminar flame speed S_L lower than that of methane/air. It is remarked that S_L is readily lowered well under half that of a stoichiometric methane-air through use of inert diluents, in say, propane-air.

5.2.2 Turbulent Diffusive Burning

After passage of flame through a flammable layer, a degree of residual burning is probable. Because of concentration fluctuations, fuel-rich pockets are likely whenever the mean mixture ratio prior to passage of the combustion front is not too lean. Additionally there may be a large volume throughout which the local mean mixture ratio is too rich to support combustion. Both fuel-rich pockets residual to flame passage and larger volumes of fuel-rich mixture burn diffusively. On any length scale of practical concern there must be substantial turbulence. Turbulence enhances diffusion. Combustion heat release supports a buoyancy-driven flow which generates continued turbulence. This coupling determines the rate of fuel burnout, and the radiative characteristics of the flames. The radiative characteristics of principle interest are rate of growth of the combustion volume, its rate of rise and the effective emission flux at its outer surface.

General theories of coupled turbulent diffusion and combustion generated buoyancy are not available. The point is approaching where some simple cases can be constructively studied by numerical computation. For a reasonably compact (vertical thickness not too different from horizontal extent) fuel cloud fully enveloped in flame, a simple but convincing analysis of the effects of length scale is available and provides a basis for empirical correlation.[15] Although further research can refine the picture, it appears that, if suitable initial conditions for such "fireball-like" burning exist and are known, the features of principal concern to decision makers can be estimated with reasonable confidence.

The crucial question that has repeatedly been brought up in the course of this evaluation is the extent to which coherent diffusive burning is likely to evolve, given a realistic dispersion and ignition scenario. A discussion of this follows.

5.2.3 Envelopment Dynamics

For most circumstances of concern, an LNG vapor cloud at the time of ignition has a vertical thickness much less than its characteristic horizontal dimension. The most likely ignition configuration is a single point, or a few points concentrated in a region recently overrun by the cloud. The probable ignition location is near the edge of the cloud. Two particularly important general questions are the following. Will the entire cloud become involved and, if so, how rapidly? Will a diffusive-burning fireball mode, mentioned above, be established either for the entire cloud remaining after initial burn through of the flammable volume or a relatively small yet perhaps dangerously large fraction of it? Present knowledge does not permit definite answers to questions of this nature, even for specific release scenarios and specific ignition source postulates. A major portion of the uncertainty stems from dispersion uncertainty. But, even for known fuel vapor/air distribution at the time of ignition, there remain questions not now answerable but which should be answerable with improved engineering understanding of the phenomena.

As an important example, consider a wind-driven vapor plume emanating from a large LNG spill over open water which encounters an ignition source a kilometer or so down-wind of the liquid front. The flame spreads slowly upstream against the wind and vapor flow, and relatively rapidly downstream. Since the flammable layer should be thickest over the interior of the plume, the flame spreads across the plume at a rate which depends on the importance of the gravity-controlled effect of layer thickness mentioned in the Section 5.2.1. Eventually a more or less symmetrical front propagating upstream should be established. Behind the front, hot combustion products, perhaps augmented by diffusively burning fuel-rich pockets, form a buoyant column drawing an indraft downstream; i.e. opposite the direction of the flamespread. It is entirely conceivable that this tendency can stall the upstream spreading flame. Suppose, conceptually, that the given plume is scaled up with composition structure homologously preserved. Then the downstream indraft should increase as $(L_F)^{1/2}$, where L_F is the flammable layer thickness. It is then

of crucial importance whether the spread rate relative to the bulk blow of the flammable layer approaches a constant, increases as $(L_F)^{1/2}$, or perhaps increases more rapidly with L_F. This particular issue can be settled by better understanding of gravity influence on flame spread through layered media.

As another example, consider the no wind case with vapor cloud spreading symmetrically over either land or water. The cloud again encounters a point ignition source at its edge. To fully envelop the cloud, a combustion front must propagate across the top or around the perimeter. The effect of layer thickness and orientation or spread rate, especially in the limit of large length scale, again is too poorly known to support a conceptual picture of the envelopment process. Perhaps the cloud in the area of the original ignition burns out or is carried out of the picture by buoyant convection, before the spreading combustion wave completes its travel. Perhaps, as an alternative to a coherent fire-ball on the length-scale of the entire cloud, a smaller moving fireball or a set of localized fireballs appear. Answers applicable to large length-scale phenomena depend on improved characterization of turbulent mixing rates as well as flame spread.

Many other examples can be envisaged. Addition of any significant geometrical complexity can only reduce prospects for useful understanding on the basis of flame spread, buoyant convection, etc. Fortunately, the whole set of envelopment dynamics problems appears amenable to relatively straightforward scale modeling along the same lines outlined in the flame spread subsection. Specifically, assuming flow dimensions large enough to assure strong turbulence, both flame spread and most complex envelopment phenomena should be modeled by reducing the laminar flame speed of the model fuel/air mixture as $(\text{length scale})^{1/2}$. Detailed scale model design has not been formulated as a part of this evaluation, but chances for doing so reliably and conveniently are judged promising.

5.2.4 Pressure Wave Effects

Bulk gas flow because of combustion-generated volume expansion is necessarily associated with pressure variation. Depending on the fuel vapor configuration and ignition characteristics, a great variety of pressure wave phenomena is possible in principle. Detonations, in which the combustion phenomena are strongly coupled with the pressure wave - specifically, via reaction initiation because of temperature increase across a shock, comprise a category treated separately in Section 7. Much more likely are pressure waves of appreciable - and possible damaging - magnitude, in which the temperature rise due to pressure increase is not large enough to significantly couple with combustion chemistry.

It is important to estimate the pressure wave amplitude experienced by targets at risk. This task can be broken down into consideration of a characteristic pressure rise ΔP associated with vapor cloud burnout, and consideration of attenuation as the wave travels to targets outside the cloud. The problem of attenuation outside the cloud is the same as for the case of a detonation, and the comments in Section 7.2.5.2 apply. Estimation of ΔP is discussed below for three classes of conditions.

5.2.4.1 Quasi-steady Flame Spread Along a Flammable Layer

In this case, an estimate for ΔP is

$$\Delta P \simeq \frac{1}{2} \rho_o (S_F)^2$$

where ρ_o is the density of the unburnt gas and S_F is the spread rate in the flammable layer, measured in the frame of reference of the flammable layer undisturbed by combustion. This can be seen by noting that, in the stated reference frame, the stream approaches, but does not achieve, stagnation. This estimate shows that ΔP will reach damaging magnitudes only if S_F reaches 10's of m/sec; i.e. at STP, S_F = 100 m/sec corresponds to $\Delta P \simeq 0.1$ atm. As discussed in Section 5.2.1, values of S_F on this order of magnitude appear unlikely, but the role of turbulence and, especially, the possibility of extreme enhancement as layer thickness L_F reaches large values are unresolved.

5.2.4.2 Blast Wave Development Due to Deflagration Ignition at a Point

A conservative model is a spherically symmetric, combustion-driven pressure wave in a uniform pre-mixed sphere of radius $\sim L_F$. Analyses cited in Section 7.2.1.2 show that magnitude of ΔP depends primarily on the flame propagation speed S_T, and can reach damaging levels only if S_T is several m/sec. Referring again to Section 5.2.1, it is judged that such occurrence is not likely but must be recognized that the role of turbulence is unresolved.

5.2.4.3 Complex Wave Geometry

If suitably shaped solid boundaries are present, pressure waves can be focused to reach magnitudes significantly higher than those stated above. Simultaneous ignition at multiple points can lead to the same effect. Little can be stated in general about such effects. Existing scenarios obviate such concerns. If scenarios which suggest wave interaction effects are put forward, engineering estimates of ΔP should be derivable from appropriate idealized calculations, e.g. 1-dimensional method of characteristic solutions for colliding waves.

There is a potential for scale modeling the complex geometrical aspects of pressure wave buildup. The important scaling parameter is the ratio of a characteristic turbulent spread rate S_F to the speed of sound. Since the latter is essentially constant for practical operations, the scaling rule reduces to preservation of S_F between model and prototype. Better understanding of the dependence of S_F on length (including concomitant dependence of turbulence characteristics) and on fuel characteristics (especially laminar flame speed S_L) is needed before definite pressure wave scale modeling procedures can be proposed.

5.2.5 Thermal Radiation

Thermal radiation potential of burning vapor clouds is determined by flame geometry and the emission characteristics of flame surfaces perceived by targets at risk. Although the emission characteristics of burning vapor clouds have not been extensively studied, they should be predictable to

accuracy within a factor of 2, and probably substantially better, on the basis of general knowledge of fire radiation. For vapor cloud burnout, the uncertainty in flame geometry is much worse than that of emission characteristics. Further comments on emission characteristics appear in Section 6.2.2. Flame geometry will be predictable only to the extent that progress is made in areas discussed in Sections 5.2.1, 5.2.2 and 5.2.3.

5.3 CONCLUSIONS AND RECOMMENDATIONS

The likelihood of "fire-ball" behavior and other hazardous characteristics of vapor cloud burnup depend critically on two incompletely understood classes of phenomena. One is flame spread in turbulent, layered methane-air mixtures. The other is the combined action of flame spread and combustion-induced buoyant flow, in large vapor clouds. Current, but distinctly incomplete, understanding of these phenomena suggests that the length scale of coherent vapor cloud combustion has a limit on the order of 100's of meters. To test this conjecture the following steps are recommended.

- Intermediate scale (e.g. characteristic dimension 2 m wide and deep x 50 m long) experiments on flame spread in turbulent layered methane-air and other mixtures should be carried out to determine the extent that gravity accelerates spread rate. There is good reason to believe that this phenomenon is a member of a much broader class of gravity/spread rate interaction phenomena, all of which can be scaled down through use of fuels with relatively slow laminar flame speeds. This scaling concept can be tested in the course of the intermediate scale flame spread experiments recommended here.
- If the concept can be established, scaling of gravity/flame spread interactions should be applied to clouds of fuel vapor and air to determine the length scale of coherent vapor cloud combustion for release/dispersion scenarios of interest.

The potential for formation of pressure-waves of destructive magnitude is unclear. Certainly such potential is greater than that of the deflagration to detonation transition covered in Section 7. The principle underlying uncertainty is the rate of flame spread in representative layers.

- Pressure magnitudes in flames spreading in layered gases, and deflagration-supported blast waves need additional study. Effects of fuel distribution, geometry of bounding surfaces, and flame acceleration should be investigated theoretically. With better understanding of flame spread phenomena, scale modeling procedures should be sought.

THIS PAGE

WAS INTENTIONALLY

LEFT BLANK

6.0 POOL FIRES

As considered in this section, pool fires are fully involved in flame, and gas-phase transients other than fluctuations are ignored. It is believed that the full involvement assumption is conservative in hazard analysis.

6.1 NEEDED INFORMATION

Thermal radiation incident on targets at risk outside the fire involvement area is for practical purposes the one characteristic of LNG pool fires important to decision makers. Within the fire involvement area, the environment may be assumed fatal to exposed individuals. Property damage within the involvement area, whether by radiation or convection from the LNG flames, or by subsequent burning of ignited auxiliary fuel, is bound to be substantial, but is difficult to calculate in detail and heavily dependent on site details.

A significant problem is the thermal integrity of LNG tanks on trucks or railway cars under post-collision fire conditions. The heating characteristics of small turbulent LNG fires are needed.

6.2 REVIEW

This review is concerned solely with ability to predict radiative exposure external to the involved area. Radiation characterization can be split into two pieces. One piece is determination of the "shape factor" or "view factor" of the fire as viewed by each potential target. This requires enough understanding of fire structure to confidently define flame geometry in an overall (fluctuation-time-averaged) sense. The second piece is the radiation emission flux at the perceived fire surface, together with enough spectral definition to allow calculation of atmospheric attenuation. Assuming modern tank design and reasonable decisions of siting, diking, etc., only large LNG pool fires need consideration.

6.2.1 Fire Geometry

Consider first the flame geometry of large LNG pool fires. This problem is simpler in a number of respects that the geometric evolution of combustion in a vapor cloud. (It is noted that vapor cloud combustion behavior encompasses the interesting question of whether a large liquid spill, especially over open water, becomes involved to an extent that a quasi-steady pool fire can exist, before the liquid is evaporated.) LNG pools are, in cases of primary interest, more or less circular, over water or on land without confining dikes, and more or less square, confined by dikes. If, as here assumed, the envelopment process is complete, the structure and behavior of the fire is independent of ignition mode. Also, the larger the pool and its burning rate, the less susceptible it is to wind distortion. Finally, the principle structural features of turbulent hydrocarbon pool fires are nearly independent of fuel except insofar as fuel characteristics influence the burning rate. And burning rate, expressed as the rate of air required stoichiometrically by the vaporizing fuel, per unit pool area, scales at $D^{1/2}$, where D is the pool diameter (or characteristic horizontal length).[26] Thus decisive testing respecting fire geometry is a reasonable possibility. Furthermore, the extremely rapid burning rate of an LNG pool over open water, which is the most expensive case to test, is especially amenable to reliable scale modeling with relatively slow burning fuels.

For a large symmetrical fire, the most important geometric characteristic is (time-mean) flame height. A secondary concern is flame lean due to wind. A strongly burning symmetric fire in an ambient wind field could generate internal firewhirls which, however, would not influence radiation hazard and, in view of fire location assumptions, would not be expected to contribute to other types of hazard. There exist useful engineering correlations for flame height.[27] In the limit of sufficiently large diameter D, relative to burning rate, most likely an unconfined spill over land, the height ratio of even an LNG fire might be so low that the flames would not be coherent on the length scale D.[26] As such a limit is approached, the engineering

flame height correlation would probably lead to moderately over-estimated shape factors. This problem is also amenable to reduced-scale investigation. For the small amount of wind-lean achievable with large LNG pool fires, the shape factor perturbation would not be large, and adequate correction techniques exist in any case.[28]

A geometric aspect of LNG fires that deserves mention is that the areal distribution of fuel vapor supplied from the pool to the flames may differ from that of pool fires of more conventional fuels. Over open water generally, and perhaps near the front of a pool spreading over land, the local vaporization rate is controlled by heat transfer from below rather than energy feedback from flames. Any tendency to concentrate the local vaporization near the perimeter of a pool relative to the more typical center-biased distribution, at constant net energy release rate, would be expected to decrease flame height and degrade coherency of the flames generally. This is judged a minor consideration respecting hazard analysis.

6.2.2 Radiative Emission Intensity

The radiative behavior of large turbulent flames is not well-understood from first principles, and theoretical approaches are not here discussed. Suffice it to say that there is moderate uncertainty in the emission flux value to be assigned. Typical engineering numbers are in the 12 - 15 W/cm^2[28] range but measurements as high as 22 W/cm^2 have been reported. It is judged that a number around 20 W/cm^2 is conservative for hazard analysis. Also it would appear that the very large fires of most concern are sufficiently thick optically that atmospheric attenuation can be calculated as the basis of grey-body spectral distribution. Certainly, measurement confirming the preceding judgments would be desirable; ultra-large fires are unnecessary for this purpose. Careful measurements from a pool, say 100 m in diameter containing 100-200 m^3 LNG, should be adequate.

6.2.3 An Alternative Approach

A modification of the approach stated above is to develop a value for a fraction χ of the combustion heat release radiated from the flames. May and McQueen report $\chi \approx 0.14$ from their measurements.[29] For a target far removed from an optically thin fire, incident radiative flux depends only on χ, the burning rate, and the distance. Time-integrated radiative flux depends analogously on time-integrated fuel consumption, which is often a directly specified parameter. Of course, no large fire is optically thin to its own dominant radiation. However, the procedure indicated above still applies if the flame height/pool diameter ratio is close enough to unity, to justify its treatment as a point source. Otherwise, fire geometry must still be determined and knowledge of χ is of less direct utility.

6.3 CONCLUSIONS AND RECOMMENDATIONS

For engineering purposes, the uncertainties in large pool fire characteristics are not dramatically large. However, it is pointed out that accurately reproducible data is almost non-existant for length scales above a few 10's of m. Even such first order interpretations as pool energy balances have rarely been carried out and then only with rough precision. The uncertainties due to behavior of a specific fuel such as LNG are outweighed by lack of definite knowledge of pool fire phenomenon in general.

Although pool fire phenomena are beset with many scientific uncertainties, no high priority research is recommended in this area. Some low priority recommendations are listed below in order of importance.

- Further studies should be made of the flame geometry of large pool fires in the weak [burning rate / $\sqrt{(\text{diameter})^{1/2}}$] limit, to improve shape factors estimates for large unconfined LNG pools over land.
- A better data base of thermal radiation from LNG fires of all sizes should be developed. In particular pools on the order of 50 m diameter should be investigated to an extent permitting meaningful statistical descriptions of flame height, and emission flux intensity and spectral characteristics.

- A modest program of fire tests should be incorporated into any evaluation of the function of vehicle LNG tank thermal protection systems under post-collision conditions. Small LNG fires are relatively thin, optically. Hence convective heating would be correspondingly important. The convective heating characteristic of small turbulent fires are not well-understood. A few measurements from well-characterized small LNG spill fires would be worthwhile.
- The distribution of local fuel vaporization in an LNG pool fire contrasts with that of a pool fire fully controlled by energy feedback. This distributional effect should be further studied analytically to assess consequences for hazard analysis.

THIS PAGE

WAS INTENTIONALLY

LEFT BLANK

7.0 DETONATION

As perceived by the public, catastrophic explosion is a potential hazard whenever a large quantity of combustible vapor is released to the atmosphere. Detonation is a particularly destructive type of combustion-generated explosion. There is no evidence of detonation associated with any accidental LNG release to date. Some analysts have concluded that detonation potential can be neglected in LNG hazard analysis.

7.1 NEEDED INFORMATION

Decision-makers need to know under what, if any, realistically anticipated conditions LNG vapor can be mixed with air and detonated. Relevant conditions include the vapor composition (the identify and amount of hydrocarbons other than methane), the spatial vapor distribution (notably the flammable layer thickness L_F), ignition characteristics, and, perhaps, the geometry of solid surfaces which might influence flow and pressure wave behavior.

The severity of detonation imparts greater importance to establishing the probability of occurrence than to the details of the phenomena once detonation is established. Nevertheless, if detonation is at all possible, it is necessary to estimate the damage potential. This is relatively difficult if the geometry is complex.

7.2 REVIEW

Prior to discussing detonation hazards, it is important to clearly distinguish detonations from other types of explosions.

7.2.1 Classification of Explosions

There are three types of explosion hazards associated with spills of LNG.

7.2.1.1 Explosive Boiling

An explosion that does not involve combustion is caused by rapid energy release through phase transition when cold LNG is spilled on water.[4],[5],[30]-[38] This phenomenon, characterized as "explosive boiling," is complicated and deserves further study for purely scientific reasons, since conditions for its occurrence have not been defined precisely. Although an instance has been reported in which the overpressure from an explosion of this type was sufficiently high to break the wall of an aquarium in which an LNG experiment was being performed, current knowledge is adequate to establish with reasonable certainty that potential overpressures are insufficient to initiate combustion. Therefore, explosive boiling appears to have no bearing on the much more hazardous phenomena of combustion and detonation of LNG clouds.

7.2.1.2 Deflagration-supported Pressure Fields

Another type of explosion hazard involves combustion, but not detonation, in the scientific sense of the term. It has been called a nonideal explosion but might better be termed a deflagration-supported shock. The occurrence of this phenomenon stems from the fact that a combustion wave, even a low-speed deflagration, generates pressure waves, mainly through expansion of the hot products of reaction, and these pressure waves coalesce to form shocks that may be quite damaging if the cloud of the combustible mixture is large.[39]-[42] As has been indicated in Section 5, uncertainties concerning the severity of blast waves of this type are sufficiently great to warrant further theoretical and experimental study, especially since typical spark or flame ignitions result initially in a deflagration that will generate these pressure waves. In the present section, the concern with deflagration-supported pressure fields involves only the possibility of their development into a detonation.

7.2.1.3 Definition of Detonation

The most damaging type of explosion is a detonation, which consists of a very strong shock wave followed immediately by a reaction zone in which heat is released.[43] Although this reaction zone sometimes has been termed a deflagration, its structure is very different from that of an ordinary, low-speed deflagration, since heat conduction and diffusion are unimportant in this zone, the reaction being initiated by the increase of temperature associated with the shock. Detonations sometimes have been termed ideal explosions, although some investigators prefer to restrict such terminology to point-source explosions, nuclear explosions or explosions from condensed explosives.

7.2.2 Severity of Detonation

In open geometry detonations produce very severe damage over distances on the order of a few tens of diameters of the combustible cloud.[44]-[47] A detonation in an LNG cloud would travel at about 1800 m/s and carry about 15 atm overpressure,[11] thereby destroying virtually everything in its path, to distances well beyond the edge of the cloud. These detonation properties are known accurately from fundamentals of thermodynamics and fluid dynamics. In complex geometries, the behavior of detonations is much less predictable; this problem area is discussed in detail in Section 7.2.4.

7.2.3 Detonation Initiation

In general, detonations occur either through direct initiation or through transition from deflagration to detonation.

7.2.3.1 Explosive Initiation

The most straightforward way to initiate detonation of a combustible cloud directly is to detonate an explosive charge within the cloud. The term detonability connotes the ease with which detonation can be initiated.

Parameters relevant to detonability may depend upon the means of initiation. For explosive initiation, detonability of the cloud can be evaluated in terms of the amount of explosive needed for producing a self-sustained detonation of the cloud. This amount may be measured in mass per unit area for initiation of a planar detonation by a sufficiently large sheet of explosive, in mass per unit length for initiation of a cylindrical detonation by a sufficiently long line charge, or in mass for initiation of a spherical detonation by a point explosive.[48] Of these three configurations, spherical symmetry is most relevant to cloud initiation in a spill scenario, and much of the available information concerns initiation by essentially a point charge.

- Propane Air It is known that approximately 100 g of tetryl, a typical explosive, is needed to initiate a spherical detonation in a stoichiometric mixture of propane with air.[49]

- Methane-Air Because of the greater chemical stability of methane during thermal ignition, discussed in Section 4, a considerably greater charge is required to initiate a detonation in a stoichiometric mixture of methane with air.[49]-[53] The magnitude of this charge is important because of the relevance of initiation requirements for methane to detonation hazards of LNG spills. The seriousness of the question has prompted a number of investigations during the past few years. Although considerable controversy remains, it appears that a degree of definitiveness in the results has been attained very recently.

  Since initiator requirements for methane-air mixtures are too great to be studied experimentally in the laboratory, one approach has been to test methane-oxygen-nitrogen mixtures enriched in oxygen, to increase reactivity.[54] Linear extrapolation to methane-air in a semi-log graph gave an initiator requirement of 22 kg of tetryl. However, theory shows that the extrapolation should not be linear and that the requirement should exceed 22 kg substantially.[55]-[58] The theory was placed in doubt recently by an observed initiation, outdoors, by about 4 kg of explosive.[59] It should be recognized, however, that this experiment involved initiation of a planar detonation.

Many investigators believe that had the length of the bag containing the combustible mixture in that experiment been longer, say 50 m instead of 12 m, then the detonation most likely would have been observed to decay as it apparently did in some tests. Others disagree. The experiment established that about 65 mg/cm^2 is required to initiate a planar detonation but did not provide the needed information on initiation of a spherical detonation. Thus, it is necessary to resort to theory to obtain the initiation requirement in the spherical case. The best theoretical estimate currently available is an extremely high value, in excess of 1000 kg of tetryl.

If this theoretical value is correct, then it is highly unlikely that direct initiation of a devastating spherical detonation in a stoichiometric mixture of methane and air after a spill in the open ever would be encountered. However, there are uncertainties in the prediction, stemming mainly from uncertainties in rates of chemical reactions at elevated temperatures found behind initiating shock waves in methane-air systems.[13] Further study of the elevated-temperature chemistry definitely seems warranted for the purpose of ascertaining how accurate the prediction is. Nevertheless, it seems unlikely that the uncertainties can be sufficiently great to allow initiation by less than 50 kg of tetryl, an amount difficult to imagine being involved even in an act of sabotage.

- Effects of Chemical Composition It should be noted that addition of relatively small amounts of higher hydrocarbons, such as propane, greatly reduces the initiation requirements for methane clouds.[49],[58] For example, with 20 percent propane in a propane-methane mixture, about 800 g of tetryl would be sufficient to initiate a spherical detonation. Typical compositions of LNG are such that direct initiation will be appreciably less difficult than for methane-air mixtures. Especially hazardous in this respect would be the "heel" of higher hydrocarbons that remains after most of the methane has been boiled off from a spill. The 100 g figure, quoted above for propane, would

be representative of the order of magnitude of the charge required for direct initiation of spherical detonation in the heel. Of course, only a fraction of the initial spill remains combustible when the heel becomes detonable.

7.2.3.2 Transition from Deflagration to Detonation

Direct initiation of a detonation is a relatively improbable event in a spill of LNG. As indicated in Section 4, typical flame and spark sources initiate deflagration instead. Under suitable conditions, deflagrations undergo transitions to detonations. The transition process, which for many years has been subjected to study in mixtures more reactive than methane-air, is quite complex, involving generation and coalescence of pressure waves, flame acceleration, turbulent flame phenomena and local ignitions at hot spots.[60] Since ignition of a deflagration is deemed likely in LNG spills, it is very important to define conditions needed for transition from deflagration to detonation. This is an area worthy of further research, both experimental and theoretical, since many uncertainties remain.[61]-[63]

- Status of Studies of Transition in Methane-Air The largest scales at which transition from deflagration to detonation has been sought systematically in methane-air mixtures are open hemispheres 10 m in radius. It has been established that a turbulent-like flame, traveling faster than a laminar flame, propagates through the methane-air mixture.[21],[64]-[66] No tendency for transition to detonation was observed in the open. Moreover, recent theoretical considerations of nonideal explosions suggest that transition is unlikely, flame accelerations to speeds on the order of sound speed over times on the order of acoustic times being required.[41] However, these theories are not entirely definitive; the process is complex, and further study is needed. Unless these further studies show otherwise, it will remain most logical to assume that transition will not occur in the open.

- Effects of Confinement Many investigators believe that neither winds nor obstacles such as trees or buildings are likely to induce transition to detonation in methane-air clouds. Confinement appears to be needed for focusing pressure waves to produce transition, although direct proof of this belief has not been obtained. These considerations indicate that studies of effects of confinement inside large structures should be of very high priority with respect to the question of detonation potential.

  The degree of confinement needed, and the size of the chamber in which the combustible mixture must be found, are not known at present for methane-air mixtures.[67],[68] Experiments in closed tubes 1 m in diameter have yielded controversial results;[51] it now seems unlikely that a sustained detonation of stoichiometric methane-air mixtures would occur in a long tube of this diameter. Theoretical estimates of required tube diameters have exceeded 50 m. The required size probably lies somewhere between 1 and 50 m, this uncertainty being so great that experiments to establish this size more accurately are desirable. One scenario with a relatively high possibility for detonation development may be a large LNG storage tank, practically empty and situated within a large combustible cloud, with asymmetric ignition of a near-stoichiometric mixture inside the tank. Some investigators have suggested that this is an example of a situation in which a very devastating detonation could develop. It should be noted that there are no grounds to suppose that such a situation is likely to be encountered. Studies directed toward quantifying the magnitude of this problem appear to be warranted.

7.2.3.3 Direct Shockless Initiation

Although there are complex configurations in which some investigators have claimed achieving "direct shockless initiation" of detonation from combustion, such observations have pertained to highly reactive mixtures, not representative of LNG clouds.[69]-[71] Lack of thoroughness of the observations leaves room for questioning the interpretations. Uncertainties are such that, although relevance seems unlikely, further study is warranted.

7.2.4 Propagation and Quenching of Detonations in Complex Geometries

Uncertainties remain concerning histories of detonation motions in complex geometries of types likely to be encountered.

7.2.4.1 Questions Associated with Emergence from Confinement

A detonation developed under confinement must be transmitted successfully to a detonable mixture outside of the structure to cause severe damage to the distant surroundings. There have been only a few preliminary studies of this transmission problem. There are some indications that under suitable conditions turbulent enhancement of combustion can facilitate occurrence of detonation of combustible mixtures at exits to confinement.[70] However, the results are not definitive, and pressure relief at exits may aid in preventing transmission of detonations. More research in this area is needed.

7.2.4.2 Propagation and Quenching in Turbulent Clouds

Even if a detonation leaves a structure, it may not propagate through a combustible cloud. The cloud requires appropriate properties to support a detonation.

- Quenching. Every combustible mixture has a characteristic quenching thickness for detonations,[72]-[75] such that if the thickness of the combustible layer, bounded below by the ground and above by noncombustible gas, for example, is less than the quenching thickness, then the detonation decays and fails to propagate through the cloud. Quenching thickness ranges from less than 0.5 cm for stoichiometric hydrogen-oxygen mixtures to a value possibly well in excess of 1 m for stoichiometric methane-air mixtures. It is important to know the quenching thickness for methane-air mixtures in connection with detonation hazards of LNG spills, and this value is known very poorly at present. Research on quenching thicknesses for detonations therefore seems warranted.

- Stratification Effects. In this last context, it should be observed that turbulent dispersal of combustible gases from LNG spills produces gas mixtures having nonuniform compositions, with portions of the mixture being beyond the combustible range. The size scales of these nonhomogeneities are not well known at present and deserve further study. The stratification is not likely to be sufficiently great to prevent propagation of deflagrations, but it may prevent propagation of detonations. Experiments on detonation of layered methane-air mixtures would be desirable, in an effort to define how small the scale of nonhomogeneity of the combustible mixture must be, and how large the thicknesses of the noncombustible regions must be, to prevent propagation.
- Effects of Chemical Composition. Propagation of detonations is facilitated and quenching made less likely by addition of higher hydrocarbons to methane. Quenching data would be of interest as a function of higher hydrocarbon content, for estimating hazards from LNG clouds of differing compositions. Also, use of more reactive fuels than methane can help to simplify experimental problems of measuring propagation and quenching in nonhomogeneous mixtures of complex geometries, through enabling of propagation to be achieved in experiments of smaller scale. Combined with theory for scaling to less reactive mixtures, the results could be employed for estimating necessary conditions for detonation propagation in LNG clouds.

7.2.5 Calculation of Detonation-Produced Forces on Structures

The pressure and velocity fields produced by detonations must be known if damage to structures in the vicinity of detonations is to be calculated.

7.2.5.1 Inside the Cloud

Since calculation of Chapman-Jouguet detonation pressures and velocities is a matter of well-known thermodynamics and fluid mechanics, being negligibly dependent on chemical kinetics,[43],[60] these calculations are straightforward for locations within a detonable cloud and do not require further investigation.

7.2.5.2 Outside the Cloud

Outside a combustible cloud the pressure and velocity fields decay as distance from the cloud increases. In geometrically symmetrical configurations, these decays can be calculated accurately.[76],[77] There remain some uncertainties and difficulties in achieving high accuracy in such calculations for complex, nonsymmetrical geometrical configurations. Improvements in abilities to make such calculations would be useful in estimating hazards from deflagration-supported pressure fields as well as from detonations.

7.3 CONCLUSIONS AND RECOMMENDATIONS

Specific areas in which unknowns exist and in which further work may be useful have been indicated above. Specific recommendations extracted therefrom appear below and in Section 8. It is difficult to assign a priority to studies of detonation phenomena because this aspect of the subject involves extremes of probability. In general, it may be said that although detonation is not a likely result in an unwanted LNG spill, its potential for devastation is so great that further study of various aspects of the process, as outlined below, is justifiable primarily for the purpose of being able to quantify better how unlikely such an event would be. Within the detonation category, it is easier to assign priorities. The following list is presented in the judged order of decreasing importance.

- Research should be focused on realistic mixtures and configurations of fuel vapor and air. The fuels needing greatest study are mixtures of 1% to 10% of higher hydrocarbons with methane. These are easier to investigate than pure methane and also more relevant to the hazard. The configurations needing emphasis are nonhomogeneous systems, such as layered media.
- Further experiments should be performed on detonation in layered media, with volumes of combustibles separated by volumes of air. The objective should be to ascertain quenching thicknesses for detonation in LNG vapor as a functional mixture composition, notably propane concentration. Once this is accomplished, it should be possible to reduce to manageable

proportions the size of system experiments of realistic fuel/air configuration, through use of propane or propane-methane mixtures. Still greater scale-down might be achievable by substituting hydrogen for hydrocarbons, and this approach should investigated.

- Further studies are needed to improve understanding of the degree of confinement needed for transition from deflagration to detonation in LNG vapors, and of conditions under which a detonation developed under confinement can be transmitted to a surrounding, open, detonable cloud. Since it is widely accepted that appreciable confinement is necessary, studies should be restricted to such conditions. Again, model studies with fuels more reactive than methane would be worthwhile. A few simple geometries should be explored systematically.
- Better knowledge is needed of requirements for direct initiation of detonations in LNG vapor/air mixtures by high explosives. A few large-scale tests would be desirable, e.g., tests of a stoichiometric methane-air mixture in a bag 50m x 2m x 2m with end initiation by a sheet explosive. Of much greater importance than this, however, would be acquisition of improved kinetic data on the reaction rates of the combustible mixtures of interest behind the shock of a Chapman-Jouguet wave. Shock-tube and flow-reactor facilities are available in which the needed data can be generated at relatively low cost. Contents of higher hydrocarbons should be varied in the tests. The results would be relevant to direct initiation as well as to transition from deflagration. Data on autoignition temperatures and autoignition times for mixtures of methane with higher hydrocarbons in air would also be relevant here, for temperatures ranging from slightly elevated values up to values that exist behind shocks preceding the combustion zone in detonations.
- Improvements in methods for theoretically calculating pressure and velocity fields outside detonated clouds in complex geometries may be desirable.

THIS PAGE

WAS INTENTIONALLY

LEFT BLANK

8.0 RECOMMENDATIONS

This Section sets forth relatively high priority research recommendations respecting LNG fire and explosion phenomena. Both general and specific categories of recommendations are given in order of importance.

8.1 GENERAL RECOMMENDATIONS

8.1.1 Field Test Planning

Planning of field tests should be biased towards spills of size that permit a substantial number of well-instrumented and carefully interpreted runs, as opposed to a few relatively large "realistic" burns for which significant parameters are not varied in a known manner, or for which meaningful description of component processes is not possible. The reasoning underlying this recommendation is that confident generalization to a realistically broad set of circumstances depends critically on engineering understanding of component phenomena, e.g. flame spread rate as a function of plume structure.

8.1.2 Scale Modeling

In comparison with work on the scale of even the more modest of suggested LNG field tests, the advantages of experiments small enough to allow plentiful replication, and to facilitate reliable and comprehensive measurements, are very great. There is a powerful incentive for scale modeling. Reasonably straightforward scale modeling approaches to some critical and poorly understood phenomena are set forth in this report. For other phenomena, there appears to be at least a potential for scale modeling. It is recommended that scale modeling of LNG fire and explosion phenomena be investigated systematically. Such investigation would encompass compilation of possible scaling rules and, for the more attractive, experimental design in sufficient detail to allow estimation of costs, practical implementation difficulties, and the quality of results.

8.1.3 Fuel Distribution Scenarios

Some standarized specifications of initial fuel distribution, ignition characteristics and other assumptions governing combustion behavior should be developed. This set is necessary if the probabilities of rare but catastrophic events such as detonations are, even in principle, to be quantified.

8.2 SPECIFIC RECOMMENDATIONS

The collection of phenomena here designated as "vapor cloud burnup" exhibits the greatest uncertainty relevant to LNG fire and explosion hazard analysis. This area should receive top priority in defining further research on unwanted combustion of LNG. In view of public concern and because it is not yet possible, in the judgment of the writer, to guarantee that detonation will not occur, some further work in that area should receive next, but decidedly lower, priority. No high priority work on ignition or pool fires is recommended. Respecting pool fires, however, a need for further research may eventually develop in the light of more detailed specifications of pool configuration and natural vaporization flux distribution.

In Sections 4-7, a number of relatively lower priority research steps are also identified. Some attention should be devoted to dealing with these low priority items as low cost opportunity is presented.

8.2.1 Vapor Cloud Burnup Phenomena

- Flame Spread in Turbulent Layered Gases Intermediate scale (e.g. characteristic dimension 2 m wide and deep x 50 m long) experiments on flame spread in turbulent layered methane air mixtures should be carried out to determine the extent that gravity accelerates spread rate. There is good reason to believe that this phenomenon is a member of a much broader class of gravity/spread rate interaction phenomena, all of which can be scaled-down through use of fuels with

relatively slow laminar flame speeds. This scaling concept can be tested in the course of the intermediate scale flame spread experiments recommended here.

- Scale Modeling of Gravity/Flame Spread Interactions. If the concept can be established, scaling of gravity/flame spread interactions should be applied to complete clouds of fuel vapor and air to determine which release/dispersion scenarios will lead to fireball-like behavior.

- Non-detonative Pressure Wave Characteristics. Pressure magnitudes in flames spreading in layered gases, and deflagration-supported blast waves need additional study: Effects of fuel distribution, geometry of bounding surfaces, and flame acceleration should be investigated theoretically. With better understanding of flame spread phenomena, scale modeling procedures should be sought.

8.2.2 Detonation Phenomena

- Detonation in Layered Gases. Further experiments should be performed on detonation in layered media, with volumes of combustibles separated by volumes of air. The objective should be to ascertain quenching thicknesses for detonations in LNG vapor as a functional mixture composition, notably propane concentration. Once this is accomplished, it should be possible to reduce to manageable proportions the size of system experiments of realistic fuel/air configuration, through use of propane or propane-methane mixtures. Still greater scale-down might be achievable by substituting hydrogen for hydrocarbons.

- Confinement and Deflagration to Detonation Transition. Further studies are needed to improve understanding of the degree of confinement needed for transition from deflagration to detonation in LNG vapors, and of conditions under which a detonation developed under confinement can be transmitted to a surrounding, open, detonable cloud. Since it

is known that appreciable confinement is necessary, studies should be restricted to such conditions. Again, model studies with fuels more reactive than methane would be worthwhile. A few simple geometries should be explored systematically.

- Direct Detonation Initiation Requirements. Better knowledge is needed of requirements for direct initiation of detonations in LNG vapor/air mixtures by high explosives. A few large-scale tests would be desirable, e.g. tests of a stoichiometric methane-air mixture in a bag 50 m x 2 m x 2 m with end initiation by a sheet explosive. The principal need, however, is for improved data behind kinetics that will enable reliable theoretical calculation of direct initiation. There are available shock-tube and flow-reaction facilities in which the needed data can be generated. Focus should be on conditions existing behind the shock of a Chapman-Jouguet wave. Higher hydrocarbon content should be varied.

9.0 ACKNOWLEDGMENTS

Prior to performing the research evaluation presented in this document, efforts were made to solicit inputs from the user industry and from consultants having expertise in these fields. The user industry, including oil companies, pipeline companies and gas companies, was contacted by telephone and subsequently by letter to review in writing conversations that had taken place. The following companies, listed with the responsible individuals, were contacted.

Shell Pipeline Co., Houston, Texas - Dr. George Walker
Mobil Research and Development Co., Princeton, N.J. - Mr. O. M. Slye
Tennessee Gas Pipeline Co., Houston, Texas - Mr. Joseph Guarino
Arco, Los Angeles, California - Mr. Don Wilson
Standard Oil of California, San Francisco, California - Mr. Donald Johnson
Texaco, Houston, Texas - Mr. E. A. Gromatzky
Exxon, Linden, N. J. - Dr. W. G. May

Although individual inputs varied, in general no recent or on-going LNG fire and explosion research was reported. Reference was often made to previous research, including AGA sponsored work, Bureau of the Mines work and reports concerning the 1944 Cleveland disaster. The companies contacted reported varying degrees of interest in LNG. While most felt they were likely to become involved at some point, many were not directly involved with LNG shipment, storage or use.

Contacts were also made with other research organizations that had been or are presently involved in LNG related projects. These contacts were generally in-person, data and document gathering visits. Included among these contacts were:

American Gas Association, Arlington, VA - Mr. L. Sarkes
Applied Technology Corp., Norman, OK - Dr. R. Welker
A. D. Little, Inc., Cambridge, MA - Mr. Don Allen and Dr. P. P. K. Raj
Institute of Gas Technology, Chicago, IL - Mr. P. J. Anderson

Lawrence Livermore Laboratory, Livermore, CA - Dr. W. J. Hogan
Naval Weapons Center, China Lake, CA - Dr. C. D. Lind
Science Applications, Inc., La Jolla, CA - LNG Group - Dr. A. A. Boni, Dr. J. T. Kopecek, Dr. L. H. Teuscher, and Dr. C. W. Wilson

In-depth technical discussions were held at offices of all of these research organizations except American Gas Association and Institute of Gas Technology. These discussions should not in any sense be construed as critiques of programs and activities of the host organizations, but rather as open discussion, between technical professionals, of the type of issues dealt with in this report.

Three consultants were employed to provide technical assistance in preparing part or all of this document. Dr. J. H. Lee of McGill University, and Dr. R. A. Strehlow of the University of Illinois consulted on the topic of detonation. Dr. F. A. Williams of the University of California at San Diego consulted on the topics detonation and ignition and also provided a general critical discussion and manuscript review of the entire document.

F. A. Williams prepared initial drafts of Sections 4 and 7, but R. C. Corlett is solely responsible for the report in its final form.

Comments on the October 1978 draft were received from R. Strehlow (U. Illinois), J. H. Lee (McGill), W. G. May (Exxon), R. Welker (Applied Technology), C. D. Lind (NWC), and J. T. Kopecek and A. A. Boni (Science Applications).

10.0 REFERENCES

1. Liquified Energy Gases Safety, U.S. General Accounting Office EMD 78-28, Volume 1, Chapter 10, July 1978.

2. L. D. Watrous, Fire Journal, Vol. 64, No. 6, p. 10, 1970.

3. P. P. K. Raj, Combustion Science and Technology, Vol. 19, 1979, p. 251.

4. G. Opschoor, Cryogenics, November 1979, p. 629.

5. S. A. Colgate, Fluid-Fluid Explosive Self-Mixing: Hydrodynamic Theory and Application to Disaster Phenomena in Nuclear Reactors and LNG Tankers, New Mexico Institute of Mining and Technology, August 1974.

6. J. A. Havens, Predictability of LNG Vapor Dispersion from Catastrophic Spills onto Water, U.S. Dept. of Transportation/Coast Guard, Washington, D.C., April 1977.

7. W. G. England et al., Proc. 1978 Heat Transfer and Fluid Mechanics Institute, C. T. Crowe and W. L. Grosshandler, eds., Stanford Univ. Press, Stanford, California, 1978. p. 4.

8. H. F. Coward and G. W. Jones, Limits of Flammability of Gases and Vapors, Bulletin 503, U.S. Bureau of Mines, U.S. Govt. Printing Office, Washington, D.C., 1952.

9. H. S. Carslaw and J. C. Jaeger, Conduction of Heat in Solids, 2nd ed., Clarendon Press, Oxford, 1959, p. 54, eq. 3.

10. Basic Considerations in the Combustion of Hydrocarbon Fuels in Air, W. T. Olson, ed., NASA TR 1300, U.S. National Aeronautics and Space Administration, Washington, D.C., 1958.

11. M. G. Zabetakis, Flammability Characteristics of Combustible Gases and Vapors, Bull. 627, U.S. Bureau of Mines, U.S. Government Printing Office, Washington, D. C., 1965.

12. B. Lewis and G. von Elbe, Combustion Flame and Explosion of Gases, Academic Press, New York, 1961.

13. S. S. Penner, et al., Oxidation Rates in the Post-Induction Period for Methane over a Wide Range of Equivalence Ratios, Paper 76-47, Western States Section/Combustion Institute, La Jolla, California, October 1976.

14. J. A. Fay and D. H. Lewis, Jr., Sixteenth Symposium (International) on Combustion, The Combustion Institute, Pittsburgh, Pa., 1977, p. 1397.

15. J. A. Fay, Appendix F of An Approach to Liquefied Natural Gas (LNG) Safety and Environmental Control Research, DOE/EV-002, U.S. Department of Energy, Washington, D.C., February 1978.

16. K. Hasegawa and K. Sato, Experimental Investigation of the Unconfined Vapor-Cloud Explosions of Hydrocarbons, Tech. Mem. of Fire Research Inst., No. 12, Fire Defence Agency, Tokyo, 1978.

17. H. C. Hardee et al., Combustion Science and Technology, Vol. 17, Nos. 5 and 6, 1978, p. 189.

18. C. Dopazo and E. E. O'Brien, Combustion Science and Technology, Vol. 13 Nos. 1-6, 1976, p. 99.

19. A. D. Gosman et al., Sixteenth Symposium (International) on Combustion, The Combustion Institute, Pittsburgh, Pa., 1977, p. 1543.

20. F. Tamanini, Combustion and Flame, Vol. 30, No. 1, 1977, p. 85.

21. C. D. Lind and J. C. Whitson, Explosion Hazards Associated with Spills of Large Quantities of Hazardous Materials - Phase II, NTIS AI A023 505, 1975.

22. G. E. Andrews et al., Combustion and Flame, Vol. 24, No. 3, 1975, p. 285.

23. D. R. Ballal and A. H. Lefebvre, Acta Astronautica, Vol. 1, 1974, p.471.

24. I. Liebman et al., Combustion Science and Technology, Vol. 1, No. 4, 1970, p. 257.

25. M. Kaptein and C. E. Hermance, Sixteenth Symposium (International) on Combustion, The Combustion Institute, Pittsburgh, Pa., 1977, p. 1295.

26. R. C. Corlett and R. A. Williams, Fire Research, Vol. 1, No. 6, June 1979, p. 323.

27. P. H. Thomas, Ninth Symposium (International) on Combustion, Academic Press, New York, 1963, p. 844.

28. L. E. Brown et al., Hydrocarbon Processing, Vol. 53, No. 5, 1974, p. 141.

29. W. G. May and W. McQueen, Combustion Science and Technology, Vol. 7, No. 2, 1973, p. 51.

30. D. S. Burgess et al., Hazards of LNG Spillage in Marine Transportation, NTIS AD 705 078, 1970.

31. D. S. Burgess et al., Hazards Associated with Spillage of LNG on Water, NTIS PB 196 602, 1970.

32. E. Nakamiski and R. C. Reid, Chemical Engineering Progress, Vol. 67, No.

33. S. A. Colgate and T. Sigurgeirsson, Science, Vol. 244, No. 5418, 1973, p.552.

34. T. Enger, Explosive Boiling of Liquefied Gases on Water, Conference Proceedings on LNG Importation and Terminal Safety, National Academy of Sciences, Washington, D.C., June 1972.

35. T. Enger and D. Hartman, Rapid Phase Transformation During LNG Spillage on Water, Third International Conference on LNG, Information Services, Institute of Gas Technology, Chicago, Sept. 1972.

36. D. L. Katz, LNG-Water Explosions, NTIS AD773 005, 1973.

37. W. S. King, NTIS AD A022 226, 1975.

38. G. Opschoor, Investigations into the Explosive Boiling of LNG Spilled on Water, Centraal Technisch Institut TNO, Delft, The Netherlands, October 1974.

39. C. M. Ablow and R. W. Woolfold, Blast Effects from Nonideal Explosions, Final Report, Contract N00017-71-C-4421, Stanford Research Institute, Menlo Park, California, December 1972.

40. A. L. Kuhl et al., Fourteenth Symposium (International) on Combustion, The Combustion Institute, Pittsburgh, Pennsylvania, 1973, p. 1201.

41. F. A. Williams, Combustion Science and Technology, Vol. 12, Nos. 4-6, 1976, p. 199.

42. R. A. Strehlow, "Blast Waves Generated by Constant Velocity Flames," Combustion and Flame, Vol. 24, No. 2, 1975, p. 257.

43. F. A. Williams, Combustion Theory, Addison Wesley, Reading, Mass., 1965, Ch. 6.

44. D. Burgess et al., Hazards of Spillage of LNG into Water, NTIS AD754 498, 1972.

45. D. L. Jaquette, Possibilities and Probabilities in Assessment of the Hazards of the Importation of LNG, NTIS AD A019 353, 1975.

46. F. W. Murray et al., Hazards Associated with the Importation of Liquefied Natural Gas, Rand Corp., June 1976.

47. R. A. Strehlow, Unconfined Vapor Cloud Explosions - An Overview, 14th International Symposium on Combustion, Combustion Institute, Pittsburgh, Pennsylvania, 1973, p. 1189.

48. J. H. Lee, "Initiation of Gaseous Detonations," Annual Review of Physical Chemistry, Vol. 28, 1977, p. 75.

49. A. A. Boni and C. W. Wilson, A Study of Initiation and Propagation of Detonation in Methane/Air and Natural Gas/Air Mixtures, Science Applications Inc., La Jolla, California, June 1978.

50. M. Gerstein et al., Industrial and Engineering Chemistry, Vol. 46, December 1954, p. 2558.

51. S. M. Kogarko, Zh. Tekhn, Fiz., Vol. 28, 1958, p. 1904.

52. S. M. Kogarko et al., International Chemical Engineering, Vol. 6, No. 3, 1966, p. 393.

53. E. B. Vanta et al., Detonability of Some Natural Gas-Air Mixtures, Technical Report AFATL-TR-74-80, Air Force Armament Laboratory, Elgin Air Force Base, Florida, 1974.

54. D. C. Bull et al., A Study of Sperical Detonation in Mixtures of Methane and Oxygen Diluted by Nitrogen, Shell Research Ltd., Thornton Research Centre, Chester, England, May 1976.

55. A. A. Boni et al., Acta Astronautica, Vol. 5, Nos. 11 and 12, 1978, p. 1153

56. A. A. Boni and C. W. Wilson, Mathematical Models of Direct Initiation of Unconfined Gas Phase Detonations, AIAA Paper, 79-0289, 1979.

57. C. W. Wilson and A. A. Boni, Spherical Piston Initiation Model of Gas Phase Detonation, Science Applications, Inc., La. Jolla, California, 1979.

58. A. A. Boni and C. W. Wilson, A Study of Explosion Hazards in Unconfirmed Vapor Clouds, Science Applications, Inc., La Jolla, California, 1979.

59. W. B. Benedick, Combustion and Flame, Vol. 35, No. 1, 1979, p. 89.

60. R. A. Strehlow, Fundamentals of Combustion, International Textbooks, Scranton, Pa., 1968.

61. R. A. Strehlow et al., Combustion Science and Technology, Vol. 6, No. 6, 1973, p. 307.

62. R. A. Strehlow and A. A. Adamczyk, On the Nature of Non-Ideal Blast Waves, Scientific Report, Grant AF-AFOSR-73-2525, Project 9711-02, University of Illinois, Urbana, Illinois, April 1974.

63. H. Matsui and J. H. Lee, On the Measure of the Relative Detonation Hazards of Gaseous Fuel-Oxygen and Air Mixtures, 17th Symposium (International) on Combustion, The Combustion Institute, Pittsburgh, Pennsylvania, 1979, in press.

64. L. H. Josephson and C. D. Lind, Vapor Cloud Explosion Study, Final Report Phase I; Progress Reports Phase II, Naval Weapons Center, China Lake, California, 1974.

65. C. D. Lind, Explosion Hazards Associated with Spills of Large Quantities of Hazardous Materials - Phase I, NTIS AD A0001 242, 1974.

66. C. D. Lind and R. A. Strehlow, Unconfined Vapor Cloud Explosion Study, in Proceedings of the Fourth International Symposium on Transport of Hazardous Cargos by Sea and Inland Waterway, NTIS AD A023 505, October 1975.

67. John H. Lee, On the Detonability of Methane-Air Mixtures, notes, McGill University, Montreal, Quebec, 1978.

68. A. A. Boni et al., Turbulent Combustion, L. A. Kennedy, editor, Progress In Astronautics and Rocketry, Vol. 58, 1978, p. 379.

69. J. W. Meyer et al., Combustion and Flame, Vol. 14, No. 1, 1970, p. 13.

70. R. Knystautas et al., Direct Initiation of Spherical Detonation by a Hot Turbulent Gas Jet, 17th Symposium (International) on Combustion, The Combustion Institute, Pittsburgh, Pennsylvania, 1978.

71. J. Barthel and R. A. Strehlow, AIAA Paper 79-0286, 1979.

72. W. P. Sommers, ARS Journal, Vol. 31, No. 12, 1961, p. 1780.

73. E. K. Dabra et al., Tenth Symposium (International) on Combustion, The Combustion Institute, Pittsburgh, Pennsylvania, 1965, p. 817.

74. T. G. Adams, AIAA Paper No. 73-1196, 1973.

75. F. A. Williams, Combustion and Flame, Vol. 26, No. 3, 1976, p. 403.

76. W. E. Baker, Explosions in Air, University of Texas Press, Austin, Texas, 1973.

77. R. A. Strehlow and W. E. Baker, Progress in Energy and Combustion Science, Vol. 2, 1976, p. 27.

THIS PAGE

WAS INTENTIONALLY

LEFT BLANK

REPORT E

Modeling of Laminar Flames in Mixtures of Vaporized Liquefied Natural Gas (LNG) and Air

C. K. Westbrook

Prepared for the
Environmental and Safety Engineering
Division
U.S. Department of Energy
under Contract W-7405-ENG-48

Lawrence Livermore Laboratory
Livermore, California 94550

THIS PAGE

WAS INTENTIONALLY

LEFT BLANK

REPORT E

TABLE OF CONTENTS

FIGURES

TABLES

SUMMARY

The combustion of fuel-air mixtures resulting from possible liquefied natural gas (LNG) spills is a central problem in the Lawrence Livermore Laboratory (LLL) Liquefied Gaseous Fuels Spill Effects Program. This combustion depends on a variety of factors, including the local fuel-air equivalence ratio, turbulence levels, humidity, characteristics of the ignition source, and many others. Numerical models dealing with the LNG vapor cloud generation and dispersion are being developed as part of this program, and these codes require chemical kinetics submodels to describe the fuel-air burning that might occur in a large LNG spill. Recent work on the development of these chemical kinetics submodels is described in this report.

INTRODUCTION

The combustion of fuel-air mixtures resulting from possible liquefied natural gas (LNG) spills depends on a variety of factors: local fuel-air equivalence ratio, turbulence levels, humidity, characteristics of the ignition source, and many others. Like other portions of the Liquefied Gaseous Fuels Spill Effects Program, this combustion is being analyzed using numerical models to provide a means of predicting the evolution of arbitrary LNG spills. Numerical models dealing with the LNG vapor cloud generation and dispersion are being developed as part of this program.[1-3] These codes require chemical kinetics submodels to describe the fuel-air burning that might occur in a large LNG spill. In this report we describe some recent work concerned with the development of these chemical kinetics submodels.

Flame propagation studies have been carried out using a one-dimensional (1D) model,[4] incorporating the equations of fluid mechanics with chemical kinetics equations of arbitrary complexity. In some of the computations a detailed chemical kinetics mechanism was used, while simplified kinetics mechanisms were used in the remainder of the computations.

The atmosphere in which an LNG spill has occurred will inevitably be turbulent. In modeling the propagation of a flame through a turbulent fuel-air

mixture, we attempt to separate the problems of turbulence modeling from those of chemical kinetics, although the two operators are certain to be coupled to some extent. The kinetics submodel is approached by modeling laminar flame propagation--a problem that is theoretically well defined. When we eventually apply the resulting kinetics model to a turbulent regime, we hope to account for the turbulence by adjusting the thermal and mass transport rates in some appropriate fashion. In the interim we require that our chemical kinetics submodel be able to reproduce experimental data for laminar flames.

DETAILED KINETICS

We examined flame properties for methane-air mixtures at atmospheric pressure using a detailed chemical kinetics reaction mechanism.[5-7] One purpose of these calculations was to provide reliable data to compare with the simplified kinetics schemes. With this detailed kinetics model all available laboratory experimental data on laminar flame speed and flame structure could be accurately reproduced.[8] Effects of variations in ambient pressure, unburned gas temperature, and fuel-air equivalence ratio were all accounted for; although for the simulation of combustion of LNG-air mixtures, only the effects of variations in equivalence ratio are relevant.

Computed results for the laminar flame speed of methane-air at atmospheric temperature and pressure are shown as a function of equivalence ratio by the solid curve in Fig. 1. Note that the maximum value of the laminar flame speed occurs just slightly richer than stoichiometric. Also note that the flame speed becomes quite small for $\phi \leq 0.5$ and for $\phi \geq 1.6$, corresponding quite well with the conventional flammability limits of methane-air. Computed flame speeds with this model are always positive, even outside the experimental flammability limits, because no thermal loss mechanism is included in the model equations. Radiation and other processes render real flames somewhat nonadiabatic. When these heat loss mechanisms exceed the heat production rates in the flame, the flame extinguishes. Therefore, it is argued that a very small computed flame speed corresponds to a nonflammable mixture in practice. Experience seems to indicate, as in Fig. 1, that the upper flammability limit (UFL) and lower flammability limit (LFL) have been reached when the computed flame speed falls below about 5 cm/s.

In addition to reproducing experimental flame speed data, we used the numerical model and detailed reaction mechanism to examine the effects of

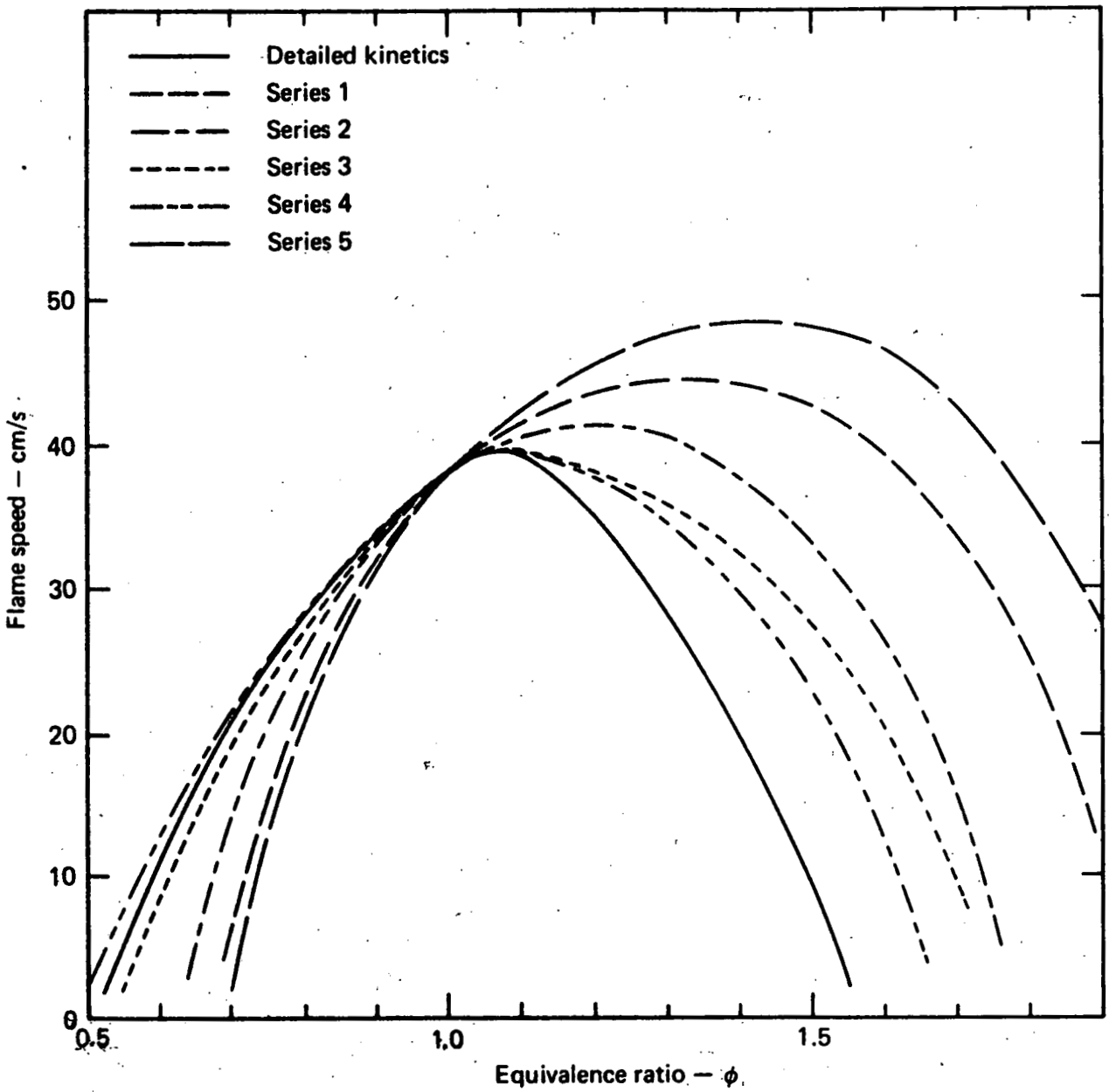

FIG. 1. Computed results for the laminar flame speed of methane-air mixtures at atmospheric temperature and pressure.

adding minor constituents to the unburned fuel. We found that the addition of water vapor to the unburned mixture had virtually no effect on the computed flame speed or flammability limits. The amount of water vapor ranged from five times the saturation limit in normal air down to zero. The reason for this lack of effect seems to be a competition between two factors. The dissociation of water molecules enhances the production rate of free radicals, increasing the flame speed. However, the water also dilutes the fuel-air mixture, lowering its adiabatic flame temperature, tending to reduce the flame speed. These effects very nearly cancel each other, yielding a negligible change in flame speed.

The implications of these particular calculations are important to the LLL test program. If water vapor had a significant effect on flammability limits or flame speed, it would be difficult to generalize data taken at dry desert test sites to humid coastal locations typical of proposed LNG terminals. Fortunately, since water vapor has been found to have little effect on the flame properties under these conditions, flame studies at the Nevada Test Site (NTS) or China Lake, California should be equally valid under other conditions of humidity.

The second minor constituent examined with the detailed reaction mechanism was ethane. Earlier work[5-7] indicated that the presence of 5-10% ethane (typical in LNG) in the primary methane fuel has a profound influence on the detonability of the resulting fuel-air mixtures. We found that in contrast to the results for the problem of detonability, ethane had very little effect on the flame properties of LNG. Fuels were considered in which the amount of ethane ranged from zero to as high as 25%, with methane as the remaining fuel. These results are not surprising in view of several factors. Laminar flame speeds of methane, ethane, propane, and other paraffinic hydrocarbon fuels in air lie in a small range between 38 and about 45 cm/s. The primary physical mechanisms responsible for flame propagation are thermal heat conduction and free radical species diffusion, and both processes take place at about the same rates in all of the flames. In contrast, induction processes that are responsible for the dramatic differences in detonability between methane and ethane play a very small role in flame propagation. For these reasons the addition of ethane to methane has a very small effect on the flammability and flame speed of mixtures of vaporized LNG and air. As a result, it is possible to use flame data for methane-air, which are available

in great detail, to represent flame properties of vaporized LNG in air with very reasonable accuracy.

SIMPLIFIED KINETICS

In the two-dimensional (2D) and three-dimensional (3D) codes being used to model the vapor cloud dispersion and combustion,[1-3] it is essential to use simplified kinetics schemes to represent the chemistry. Detailed kinetics mechanisms are impractical in 2D and 3D because of the large additional number of differential equations that must be solved, and because of the problems of numerical stiffness they introduce into the solutions.

The most common and elementary simple chemical kinetic mechanism consists of a single overall reaction, which for methane can be written

$$CH_4 + 2O_2 \rightarrow CO_2 + 2H_2O \quad .$$

The rate of this overall reaction is a complex function of temperature, pressure, equivalence ratio, and other variables, but it is sometimes possible to average over these parameters in some vague way to arrive at a single expression for the rate. In practice, this averaging amounts to a type of curve fitting, which matches the available experimental data. One drawback of this type of rate fitting is that the resulting expression has only limited applicability,[9,10] and care must be exercised not to use the expression outside its range of validity, which can often be very narrow. For applications such as those of LNG spills in the open air, we are concerned primarily with the effects of variations in local equivalence ratio. Effects of pressure variation are not important because all the spills are assumed to take place at atmospheric pressure, and the unburned fuel-air mixture will not be substantially different from normal atmospheric values (300 ± 50 K). We assume a single global reaction rate of the form

$$k = A \exp(-E_a/RT) [CH_4]^a [O_2]^b \quad ,$$

where A, E_a, a, and b are fitting parameters. For methane oxidation in shock tubes, E_a is of the order of 50 kcal/mole, while the sum a + b depends on pressure and is generally found to lie between 0.7 and 2.[11] In addition to the shock tube data, there is a global expression derived from a study in a

turbulent flow reactor by Dryer and Glassman[12] that is used widely to model methane oxidation. Their rate expression is

$$k = 1.5 \times 10^{13} \exp(-48400/RT)[CH_4]^{0.7}[O_2]^{0.8} \quad .$$

The effective activation energy E_a (48.4 kcal/mole) and the values for a and b (a + b = 1.5) are quite consistent with the expressions derived from shock tube data, even though the pressure, temperature, and fuel-air equivalence ratio regimes in the flow reactor are markedly different from those in the shock tube. Therefore, we have used E_a = 48.4 kcal/mole and a + b = 1.5 for most of the flame models described herein. We allow a and b to vary, as long as a + b = 1.5. (Although in this report we are not concerned with variations of flame speed with pressure, the global kinetics mechanism best reproduces that pressure dependence when a + b = 1.5; so we prefer to maintain that constraint in this study.)

When a, b, and E_a are assigned specific values, the laminar flame speed then depends only on the preexponential term A. This parameter was determined in the following manner. We require that for a stoichiometric (i.e., fuel-air equivalence ratio ϕ equal to unity) mixture of methane and air, the single-step global rate gives the same laminar flame speed as the detailed mechanism (also equal to the experimental value) of 38 ± 3 cm/s. This requirement then fixes the parameters in the global rate expression. With all of these values fixed, the equivalence ratio varies, and the flame speed at each value of ϕ is computed. In Table 1 we list the different rate expressions used, all of which give S_u = 38 cm/s for ϕ = 1.

The sum a + b is equal to 1.5, except for Series 5 in which both a and b were equal to 1. Series 1 uses the values of a and b that were derived by Dryer and Glassman.[12] When the global rate expression of Dryer and Glassman (with $A = 1.5 \times 10^{13}$) was used, the predicted flame speed for ϕ = 1 is approximately 47 cm/s, about 25% larger than the experimentally measured value. The value for A of 1.0×10^{13} in Table 1 gives S_u = 38 cm/s, and the two calculated values of flame speed are consistent with elementary flame theory that predicts $S_u \sim A^{\frac{1}{2}}$ under these conditions. This error of about 25% for S_u with the Dryer and Glassman rate points out an important consideration in this type of modeling study. Flame speed depends on kinetic parameters and transport properties, including thermal conductivity and species molecular diffusion coefficients. Therefore, it is entirely possible that different

TABLE 1. Reaction rate parameters in the global rate expression.

Series	A	a	b	E_a
1	1.0×10^{13}	0.7	0.8	48.4
2	8.5×10^{12}	0.5	1.0	48.4
3	7.25×10^{12}	0.3	1.2	48.4
4	6.7×10^{12}	0.2	1.3	48.4
5	2.4×10^{16}	1.0	1.0	48.4

preexponential kinetic terms are needed in different codes, which may not treat transport effects in the same manner. To resolve this problem in a particular code, we must reproduce the results for the stoichiometric case ($\phi = 1$) by varying A by the method just described. We, therefore, do not recommend specific values for A but rather indicate, within the context of the code (HCT) and the transport coefficients used, which values of A reproduced the stoichiometric mixture flame speed with the given values of a, b, and E_a.

In all flame model calculations reported herein, the transport properties were retained without modification from the detailed kinetic mechanism results described earlier. For each series of calculations using the rates shown in Table 1, the predicted flame speeds are plotted in Fig. 1 as dashed lines, with the results from the detailed kinetic mechanism shown as the solid curve. Series 3 and 4 give quite good agreement with the detailed model results and experiment, while the other series parameters do not. Series 1, 2, and 5 substantially overestimate the flame speed for rich ($\phi > 1$) mixtures and underestimate it for lean ($\phi < 1$) mixtures. In addition to errors in the numerical values, Series 1, 2, and 5 also produce misleading estimates of flammability limits. Using the arguments outlined earlier for relating predicted flame speed to flammability limits, these models (Series 1, 2, and 5) suggest $\phi = 0.7$ for the LFL and $\phi \simeq 2.0$ for UFL. Series 3 and 4 give a value for the LFL of between $\phi = 0.5$ and 0.6, which is quite reasonable and probably overestimates the UFL at $\phi \simeq 1.8$. However, for the applications intended in modeling LNG spills, this UFL is not seriously wrong, and the accuracy in the LFL is much more important.

It appears that the most important term in the rate expression is the exponent a of the methane concentration. As ϕ and the CH_4 concentration increase, the single-step rate also increases. The chemical reason for the eventual decrease in flame speed for $\phi > 1.1$ is that the excess fuel becomes a nearly inert diluent. By including the fuel concentration in the rate expression with only a single term, the model is not able to distinguish between the accelerating effect of having additional fuel and the decelerating effect of dilution. As seen in Fig. 1, the answer lies in keeping the fuel exponent a small so that the increase in reaction rate with fuel concentration remains moderate.

CONCLUSIONS

Within the limitations inherent in the use of a single-step reaction mechanism, it appears that a rate expression (Series 4)

$$k = 6.7 \times 10^{12} \exp(-48400/RT)[CH_4]^{0.2}[O_2]^{1.3}$$

does a creditable job of reproducing flame speed data and flammability limits for methane-air flames in the atmosphere. The parameters for Series 3 also give satisfactory results, although somewhat less accurate than Series 4. The other models, with $a > 0.3$, produced flame speeds and flammability limits that are substantially different from experimental data, and their use is not recommended. Whenever possible, the preexponential term A should be determined for each individual code by requiring that the code reproduce the correct flame speed for a stoichiometric fuel-air mixture under laminar conditions.

As a result of flame speed calculations using the detailed reaction mechanism, we found that the addition of water vapor and ethane, even in relatively large amounts, had very little effect on computed flame speed or flammability limits. Flame propagation in mixtures of vaporized LNG and air can therefore be well described by data for mixtures of methane and air.

REFERENCES

1. B. R. Bowman, "Comparison of Dispersion Models for Spills of Liquefied Natural Gas," *Liquefied Energy Fuels Spill Effects Program Quarterly Report*, October-December 1978, Lawrence Livermore Laboratory, Livermore, Calif., Rept. UCID-17968-78-2 (1978), compiled by W. J. Hogan.
2. D. L. Ermak and B. R. Bowman, "Average Dispersion of a Liquefied Natural Gas Vapor Plume," *Liquefied Energy Fuels Spill Effects Program Quarterly Report*, January-March 1979, Lawrence Livermore Laboratory, Livermore, Calif., Rept. UCID-17968-79-1 (1979), compiled by D. L. Ermak.
3. L. C. Haselman and J. B. Chase, "Computer Simulation of Combustion and Fluid Dynamics in Two and Three Dimensions," *Liquefied Energy Fuels Spill Effects Program Quarterly Report*, January-March 1979, Lawrence Livermore Laboratory, Livermore, Calif., Rept. UCID-17968-79-1 (1979), compiled by D. L. Ermak.
4. C. M. Lund, "HCT-A General Computer Program for Calculating Time-Dependent Phenomena Involving One-Dimensional Hydrodynamics, Transport, and Detailed Chemical Kinetics," Lawrence Livermore Laboratory, Livermore, Calif., Rept. UCRL-52504 (August 1978).
5. L. C. Haselman, C. K. Westbrook, and P. A. Urtiew, "Detonability of Liquefied Natural Gas Vapors," *Liquefied Energy Fuels Spill Effects Program Quarterly Report*, July-September 1978, Lawrence Livermore Laboratory, Livermore, Calif., Rept. UCID-17968-78-1 (1978), compiled by W. J. Hogan.
6. C. K. Westbrook, "An Analytic Study of the Shock Tube Ignition of Mixtures of Methane and Ethane," *Combustion Science and Technology* 20, 5 (1979).
7. C. K. Westbrook and L. C. Haselman, "Chemical Kinetics in LNG Detonations," *Proceedings of the Seventh International Colloquium on Gasdynamics of Explosions and Reactive Systems, Gottingen, West Germany* (August 1979), Lawrence Livermore Laboratory, Livermore, Calif., Rept. UCRL-82293.
8. G. Tsatsaronis, "Prediction of Propagation Laminar Flames in Methane, Oxygen, Nitrogen Mixtures," *Combustion and Flame* 33, 217 (1978).

9. F. L. Dryer and C. K. Westbrook, "Chemical Kinetic Modeling for Combustion Applications," *Proceedings of the AGARD Propulsion and Energetics Panel* Specialists Meeting on Combustion Modeling, Cologne, West Germany (September 1979), Lawrence Livermore Laboratory, Livermore, Calif., Rept. UCRL-81777.

10. F. L. Dryer and C. K. Westbrook, "Detailed Models of Hydrocarbon Combustion," *Proceedings of the DOE Workshop on Modeling of Combustion in Practical Systems, Los Angeles* (January 1978), Lawrence Livermore Laboratory, Livermore, Calif., Rept. UCRL-80096.

11. W. M. Heffington, G. E. Parks, K. G. P. Sulzmann, and S. S. Penner, "Studies of Methane Oxidation Kinetics," *Sixteenth Symposium (International) on Combustion, The Combustion Institute, Pittsburgh* (1977).

12. F. L. Dryer and I. Glassman, "High Temperature Oxidation of CO and CH_4," *Fourteenth Symposium (International) on Combustion, The Combustion Institute, Pittsburgh* (1973).

REPORT F

Chemical Kinetics in LNG Detonations

C. K. Westbrook
L. C. Haselman

Prepared for the
Environmental and Safety Engineering
Division
U.S. Department of Energy
under Contract W-7405-ENG-48

Lawrence Livermore Laboratory
Livermore, California 94550

THIS PAGE

WAS INTENTIONALLY

LEFT BLANK

REPORT F

TABLE OF CONTENTS

FIGURES

TABLES

SUMMARY

The problem of detonability of vaporized mixtures of liquified natural gas and air is addressed, using a characteristic time analysis. Separate numerical models are used to treat the evolution of the blast wave produced by a charge of high explosive and the chemical ignition delay of the fuel-air mixture. These models are combined with experimental data to predict the amount of high explosive required to initiate a detonation of a stoichiometric mixture of methane and air, giving an estimate of 50-100 kg of high explosive in spherical geometry. The effects of minor constituents such as ethane and propane on methane-air detonability are examined, and the mechanism by which these minor constituents kinetically sensitize the fuel is discussed.

INTRODUCTION

In the event of a large scale spill of LNG or other liquefied energy fuel, the liquid fuel will rapidly vaporize and mix with air. As the fuel mixes with air, some portion of the fuel-air mixture may become flammable and/or detonable, depending on a variety of factors which are functions of the spill, spill site, the fuel itself, and many other parameters. In the present work, factors influencing the possibility of detonation of the fuel-air mixtures are examined by means of computer modeling techniques. The type of modeling approach described here is intended to be used in coordination with experimental programs. The models must be validated by means of comparison with experimental data, after which they can be used to assist in the analysis of those experiments and to extrapolate to conditions which are difficult or expensive to achieve experimentally. Model predictions must periodically be verified by means of further experiments. The primary goal of modeling complex systems such as gaseous detonations is to provide additional diagnostic tools to aid in the interpretation of given experiments and to substantially reduce the cost and time requirements of a research program. In addition, model predictions can often indicate potentially fruitful areas for further experimental research or point out potential dangers.

GASEOUS DETONATIONS

Perhaps the most dangerous hazard which can result from an LNG spill is the possibility of an atmospheric gaseous detonation. Detonations can

be produced either by transition from deflagration or by direct initiation from a blast wave. In either case there are quite restrictive conditions which must be satisfied if the detonation is to propagate. The shock wave associated with a detonation compresses and heats a mixture of unreacted gases very rapidly. In the absence of chemical reactions this shock wave would gradually weaken, decaying into a simple compressional sound wave. It is possible to define a characteristic shock wave decay time, in the absence of reaction, as the time required for the shock pressure to fall from one value to some other value. If the shocked gas is reactive, then once the shock wave has compressed and heated the gas, chemical reactions will begin to take place. At the end of a chemical ignition delay period, rapid energy release again heats the mixture and raises its pressure further. The heat and pressure increase from this reaction are needed to counteract the gradual decay of the shock wave. Therefore, a useful measure of the stability of a detonation wave can be derived by comparing the characteristic shock wave decay time with the chemical induction time. If the chemical time scale is longer than the shock decay time, the detonation will weaken, decaying into a sound wave preceding a conventional deflagration. On the other hand, if the chemical time scale is shorter than or comparable to the shock wave time scale, the detonation will be stable and continue to propagate.

Lee (1) has shown that the minimum high explosive charge required to initiate detonation is strongly dependent on geometrical factors and for spherical configurations this blast energy would depend on the cube

of the chemical induction time. Recently Westbrook (2) has developed a kinetic model for the oxidation of methane, ethane and air mixtures. This model makes it possible to calculate chemical induction times with a precision and generality not previously possible. The evolution of high explosive blast waves is computed using a numerical model developed specifically for such conditions (3). The detonation stability and direct initation processes have thus been split conceptually into a fluid mechanical model dealing with the blast wave, and a chemical kinetic model dealing with the induction times. We will describe these two sub-models and show how they have been combined to analyze certain detonation phenomena.

CHEMICAL IGNITION DELAY

A great deal of work has been done in recent years on the ignition of methane in shock tubes, and some studies of the shock tube ignition of ethane and higher alkanes have also appeared. A shock wave is propagated through a reactive gas sample, rapidly raising its density, temperature, and pressure to relatively high values. These post-shock conditions are similar to those which are produced in detonation shock fronts. Under these post-shock conditions the fuel first breaks apart into smaller fragment chemical species. This ignition or induction phase, during which the gas temperature and pressure are nearly constant, is followed by a very rapid oxidation phase during which these fragments react to form final products, with water and carbon dioxide being the most significant. The duration of the ignition phase is much longer than the oxidation phase. In a typical

case, the combined reaction time was 250 μsec, with the final oxidation phase taking less than 1 μsec. The dominance of the ignition period is an important feature of the chemical evolution of these systems. The end of the combined reaction period is characterized by a sharp increase in temperature and pressure as the chemical energy of the fuel is released. This pressure increase during the final fuel oxidation phase reinforces the shock wave in a detonation which is propagating under relatively stable conditions.

A detailed reaction mechanism describing the chemical kinetic evolution of mixtures of methane and ethane has been presented by Westbrook (2) and is given in Table 1. This model reproduces experimental data reported by Burcat et al. (4) for the ignition delay of $CH_4/O_2/Ar$ and $C_2H_6/O_2/Ar$ mixtures. These results are summarized in Fig. 1, in which the logarithm of the induction time is plotted as a function of reciprocal temperature. The upper solid line represents the experimental data for methane and the lower solid line shows the experimental data for ethane. Computed induction times are indicated as dashed lines, with the key indicating the relative fuel fractions of methane and ethane, respectively. From Fig. 1 it is clear that the model reproduces very well the data of Burcat et al. for the pure fuels.

With the mechanism validated at both ends of this compositional spectrum, the model was then used to investigate the evolution of mixtures of methane and ethane, combined first with stoichiometric amounts of oxygen. Particular attention was directed towards the compositional range which is closest to that encountered in normally-occurring LNG, with approximately 90% CH_4 and 10% C_2H_6. While the kinetic mechanism is not yet able to deal with propane

or higher alkane species, there is both experimental and theoretical evidence to suggest that as far as kinetic sensitization and induction delay are concerned, propane and ethane behave quite similarly.

This study of the induction period of methane-ethane mixtures demonstrated several very significant points. First, the addition of quite small amounts of ethane (5-10%) to methane very sharply reduced the induction time of the composite fuel relative to that of pure methane as shown in Fig. 1. This reduction is also illustrated in Fig. 2, in which the induction time at several post-shock temperatures is plotted as a function of fuel composition. For example, when ethane is 5% of the fuel, the induction time is roughly half that for pure methane. This reduction in induction time by a factor of two would correspond to a reduction in the critical energy for direct initiation of a detonation by a factor of eight (Lee (1)). This effect is quite large and illustrates dramatically the need for detailed chemical kinetic analysis of these systems. In an important sense, the chemical behavior of LNG, at least as far as its detonability is concerned, appears to be dominated by minor constituents such as ethane.

This work was able to determine the detailed chemical mechanism for the fuel sensitization process. Methane itself is difficult to detonate, due primarily to its very long chemical induction time. The CH_4 molecule is unusually stable, with the hydrogen atoms bound tightly to the carbon atom. In addition, when a hydrogen atom is abstracted, the resulting methyl radicals (CH_3) are even more difficult to consume. Rather than being oxidized directly, methyl radicals combine together to form ethane ($CH_3 + CH_3 \rightarrow C_2H_6$). Much of methane consumption thus proceeds through

ethane. The hydrogen atoms in the ethane molecule are more easily abstracted than in methane, and the consumption of ethane is much more rapid than methane. When ethane is present initially, more hydrogen atoms are available, and these hydrogen atoms initiate the chain branching reactions which rapidly consume the available fuel. The kinetic process by which small amounts of ethane can dominate the consumption of methane and dramatically reduce the induction times, not only explains all of the experimental data but also demonstrates conclusively the inadequacy of so-called thermal sensitization mechanisms. Crossley et al. (5) reached the same conclusion as to the inadequacy of the thermal sensitization mechanism, based on purely experimental results. The consumption of the two fuels occurs simultaneously, and it is through the free radical chain branching reactions that the coupling occurs, not through a sequential release of heat.

It was also shown (2) that the same degree of kinetic sensitization occurs for fuel-air mixtures which are not stoichiometric. This conclusion is significant since wide ranges in local fuel-air equivalence ratio would be expected in an actual LNG spill. In addition, the presence of water vapor in the air was found to have a negligible effect on the computed induction delay times.

In addition to the earlier kinetic modeling work already described, we have carried out another series of shock tube ignition delay time calculations to examine the effects of changes in the amount of inert diluent which is present along with the fuel and oxygen. For the sake of illustration we consider here the results for stoichiometric methane-oxygen

mixtures with different amounts of dilution; results for fuel mixtures of methane and ethane and for non-stoichiometric mixtures are very similar. The experimental work of Burcat et al. (4) used argon as the diluent, and the mole fraction of argon was five times that of the oxygen. This was done in order to better approximate the heat capacity of air than if greater dilution were used. In the new series of calculations, the amount of argon diluent was varied by ± 50%, with ignition delay times computed for each composition at a variety of initial post-shock temperatures. The ignition delay times for some of these mixtures are plotted in Fig. 3 as functions of reciprocal temperature. The effective activation energy appears to increase slightly with increasing argon dilution. The computed results at 1500 K and at 1900 K are summarized in Fig. 4 as functions of dilution. The ignition delay time can be seen to be proportional to the ratio $[Ar]_o/([O_2]_o + [CH_4]_o)$, with the constant of proportionality changing with temperature.

RELATING SHOCK DECAY TIMES TO INDUCTION TIMES

A considerable amount of experimental information is available on the detonability of fuels which are either pure methane or primarily methane, in oxygen and in air. These experiments have been carried out under nearly unconfined, atmospheric conditions and with carefully defined amounts of fuel and oxidizer. In one series of experiments, Bull and co-workers (6) used stoichiometric mixtures of methane and oxygen, diluted with varying amounts of nitrogen. In each case they determined the minimum amount of high explosive required to initiate a steady detonation in an

unconfined spherical configuration. One goal of their study was to use results at low nitrogen concentrations, where the experiments were simpler to perform, to extrapolate to conditions with large amounts of nitrogen (as in normal air) where the experiments could not be carried out. In the second series of experiments reported by Bull et al. (7,8), critical masses of high explosive were determined for various mixtures of methane and ethane in air. This data, shown in Fig. 5, displays the same rapid sensitization of methane by ethane described earlier. Again the data were extrapolated to the limit of pure methane in air, with both extrapolations indicating that approximately 22 kg of high explosive would be required to detonate a methane-air mixture.

Comparisons were made with these two sets of experiments in a series of model calculations. For each mixture selected a one-dimensional finite difference hydrodynamic numerical model was used to calculate the evolution of the time-dependent shock wave produced by spherical charges of high explosive for charge masses ranging from 10 gm to 22 kg. The shock decay time was defined somewhat arbitrarily as the time required for the shock to decay from 20 to 10 bars. This pressure range was selected primarily because the Chapman-Jouguet pressure for a detonation in atmospheric LNG-air is approximately 16 bars. The result of these calculations was a relation between charge mass and shock decay time and is shown in Fig. 6. The shock decay time was found to vary as the cube root of the charge mass, as would be expected from analytic treatments of spherical shock front decay. At the same time, chemical induction times were calculated

for each mixture. In these kinetics calculations, the initial post-shock density was held fixed at 6×10^{-3} gm/cm^3 and the initial post-shock temperature was varied over a wide range. The results of the induction time calculations for the CH_4 - C_2H_6 mixtures in air are plotted in Fig. 7. By equating the chemical induction time with the shock decay time, a correlation was established between the critical mass of high explosive and the initial post-shock temperature of the reactive gas mixture. This procedure is illustrated by the three large dots in Figs. 5-7, showing the effect of fuel composition on critical high explosive mass characteristic shock decay time, and induction time. An entirely analogous procedure was carried out for the experimental data (6) in which the nitrogen content varied. Finally, the characteristic temperature correlations were extrapolated in both cases to estimate the relevant induction time for methane-air. This procedure is illustrated in Fig. 7 by the three sets of dashed lines leading from the large dots to the line representing methane-air. The dashed lines represent reasonable upper and lower limits for the extrapolation based on the data in Fig. 5, and the central dashed line shows a straight line extrapolation. Translating the intersection points back into critical charge masses gives values of 24 kg and 100 kg. The corresponding values based on the other set of experimental data gives a range of 50-100 kg of high explosive.

The choice of a characteristic pressure decay time based on a decrease of the shock pressure from 20 to 10 bars is of course somewhat arbitrary. An interesting correlation can be derived in a somewhat different fashion from that described above, requiring only that the shock decay time depend

on the cube root of the charge mass. The fuel mixture with 70% CH_4 - 30% C_2H_6, at an initial post-shock temperature of 1400K was chosen for reference. From Fig. 7, the induction time is 33 μs. From Fig. 5, the experimental data show that the critical high explosive mass for detonation initiation for this mixture is 360 gm. These two points, together with the assumption of a cube root dependence of pressure decay time on charge mass, allow us to use the other data of Fig. 5, all at 1400K initial temperature, to predict the dependence of critical charge mass on composition. The result of this process is illustrated by the dashed curve in Fig. 5 which shows a remarkable agreement between predicted and experimental results. The extrapolation of this predicted curve to pure methane in air gives a high explosive mass of 106 kg. Data points quoted by Boni, et al. (9) are also indicated in Figure 5 and are consistent with the predicted curve. The use of a constant initial post-shock temperature reflects the fact that the Chapman-Jouguet conditions for methane and ethane are very similar, so that the post-shock conditions which lead to a propagating detonation should be the same for all mixtures of fuels. The temperature of 1400K was used because it provided the best fit to the portion of Fig. 5 for which experimental data are available.

The extrapolations carried out in this type of analysis have used temperature as a variable because this dependence is rather weak. The predicted critical charge mass for pure methane in air is quite sensitive to the extrapolation method, so that the range quoted of 24-106 kg must be regarded as somwhat uncertain. However, there appears to be no way to justify a predicted charge mass of more than 1000 kg suggested by Boni

et al. (10). Boni et al. (10) used a coupled fluid mechanics-chemical reaction model in their study, while the present study has decoupled the two processes, but it seems unlikely that the large differences in predictions for methane-air could be attributed solely to this one factor. In addition, the chemical reaction model used in the present work is considerably more sophisticated and more reliable than that used by Boni et al. In this light, no explanation can be given for the disagreements between the present results and those of Boni et al.

It must be emphasized again that while there is considerable theoretical interest in the initiation of a detonation in methane-air, there is some reason to question how relevant that situation is to practical LNG safety. Since LNG contains appreciable amounts of minor chemical species which have been determined, both experimentally and in our modeling studies, to significantly modify its chemical behavior, predictions of LNG detonability made on the basis of studies of pure methane can be seriously misleading. As noted earlier, with only 5% of the fuel consisting of ethane, the induction time is half that of pure methane. This translates into a reduction of a factor of eight in the amount of high explosive needed to detonate such a mixture, and with a "typical" LNG composition of 90% CH_4 and 10% ethane, propane and other species, the critical mass is even smaller. In addition, the process of differential boiloff, in which the more volatile component methane evaporates first, will mean that the composition of the LNG vapor resulting from a typical spill will be progressively richer in these minor constituents. This effect would further reduce the required high explosive mass to initiate a detonation.

The kinetic modeling presented here, as well as that discussed earlier by Westbrook (2), suggests that several types of fuel modification might be used to increase the chemical induction time of LNG-air mixtures, thereby reducing the detonability of the mixtures. If some additive were included in the fuel which could serve as a means of capturing H atoms, the chain branching of these systems would be sharply reduced. Similarly, if the amounts of minor constituents such as ethane or propane could be removed or at least significantly reduced, the results in Fig. 1 indicate that the induction time would again be sharply increased. In addition, a chemically inert diluent species could be added to the LNG. Although in the computations described earlier argon was the diluent, any such inert diluent would produce similar results. The need to be able to liquefy the diluent at about the same temperature as the LNG would place restriction on the choice of diluent. Any of these processes could significantly enhance the safety of handling and using the fuel, so long as the process being used had no other effect detrimental to the safety or end use of the fuel.

CONCLUSION

It is important to consider that typical LNG is composed not only of methane, but that approximately 10% of LNG is made up of ethane, propane, and other species. The induction time calculations described here show that this 10% makes a great deal of difference in the induction time and therefore in the detonability of LNG. Studies which have not or do not take this composition into account may not be applicable to the question

of the detonability of LNG vapor. These impurities or minor constituents play a major role in determining the induction time and detonability of LNG. The purely kinetic model described here has been validated by comparison with experimental data and can be reliably applied to other sets of conditions which have not received experimental attention. This was done to examine the possible effects of the presence of water vapor and effects of inert dilution and fuel stoichiometry, in addition to variations in fuel composition. Finally, the characteristic time analysis described was used to correlate available experimental data on unconfined detonations. Extrapolations were made to estimate that a high explosive mass of 24-106 kg would be required to detonate a stoichiometric methane-air spherical cloud.

REFERENCES

1. Lee, J. H., Initiation of Gaseous Detonation, Annual Reviews of Physical Chemistry 28, 75 (1977).
2. Westbrook, C. K., An Analytical Study of the Shock Tube Ignition of Mixtures of Methane and Ethane, Combustion Science and Technology, (1979), Also available as U. of Calif., Lawrence Livermore Labs. Report UCRL-81507, July 1978.
3. Wilkins, M., Calculation of Elastic-Plastic Flow, University of California Lawrence Livermore Laboratory Report UCRL-7322 (1969).
4. Burcat, A., Scheller, K., and Lifshitz, A., Shock-Tube Investigation of Comparative Ignition Delay Times for C_1-C_5 Alkanes, Combustion and Flame 16, 29 (1971).
5. Crossley, R. W. Dorko, E. A., Scheller, K., and Burcat, A., The Effect of Higher Alkanes on the Ignition of Methane-Oxygen-Argon Mixtures in Shock Waves, Combustion and Flame 19, 373 (1972).
6. Bull, D. C., Ellsworth, J. E., Hooper, G., and Quinn, C. P., A Study of Spherical Detonations in Mixtures of Methane and Oxygen Diluted with Nitrogen, J. Phys. D 9, 1991 (1976).
7. Bull, D. C., Ellsworth, J. E., and Hooper, G., Initiation of Spherical Detonation in Hydrocarbon/Air Mixtures, presented at the Sixth International Colloquium on Gasdynamics of Explosions and Reactive Systems, Stockholm, Sweden (1977).
8. Bull, D. C., Elsworth, J. E., and Hooper, G., Susceptibility of Methane-Ethane Mixtures to Gaseous Detonation in Air, Combustion and Flame 34, 327 (1979).

9. Boni, A. A., and Wilson, C. W., A Study of Detonation in Methane/Air Clouds, presented at the Sixth International Colloquium on Gasdynamics of Explosions and Reactive Systems, Stockholm, Sweden (1977).

10. Boni, A. A., Su, F. Y., and Wilson, C. W., Numerical Simulation of Unsteady Combustion and Detonation Phenomena, AIAA Paper 78-947, presented at the AIAA/SAE 14th Jount Propulsion Conference, Las Vegas (1978).

Table I

Methane-ethane oxidation mechanism. Reaction rates in cm^3-mole-sec-kcal units, $k = AT^n \exp(-E_a/RT)$

	Reaction	Rate			Reference (See Westbrook[2])
		log A	n	E_a	
1	$CH_4 + M \rightarrow CH_3 + H + M$	17.1	0	88.4	Hartig et al. (1971)
2	$CH_4 + H \rightarrow CH_3 + H_2$	14.1	0	11.9	Baldwin et al. (1970)
3	$CH_4 + OH \rightarrow CH_3 + H_2O$	3.5	3.08	2.0	Zellner and Steinert (1976)
4	$CH_4 + O \rightarrow CH_3 + OH$	13.2	0	9.2	Herron (1969)
5	$CH_4 + HO_2 \rightarrow CH_3 + H_2O_2$	13.3	0	18.0	Skinner et al. (1972)
6	$CH_3\ HO_2 \rightarrow CH_3O + OH$	13.2	0	0.0	Colket (1975)
7	$CH_3 + OH \rightarrow CH_2O + H_2$	12.6	0	0.0	Fenimore (1969)
8	$CH_3 + O \rightarrow CH_2O + H$	14.1	0	2.0	Peeters and Mahnen (1973)
9	$CH_3 + O_2 \rightarrow CH_3O + O$	13.4	0	29.0	Brabbs and Brokaw (1975)
10	$CH_2O + CH_3 \rightarrow CH_4 + HCO$	10.0	0.5	6.0	Tunder et al.
11	$CH_3 + HCO \rightarrow CH_4 + CO$	11.5	0.5	0.0	Tunder et al.
12	$CH_3 + HO_2 \rightarrow CH_4 + O_2$	12.0	0	0.4	Skinner et al. (1972)
13	$CH_3O + M \rightarrow CH_2O + H + M$	13.7	0	21.0	Brabbs and Brokaw (1975)
14	$CH_3O + O_2 \rightarrow CH_2O + HO_2$	12.0	0	6.0	Engleman (1976)
15	$CH_2O + M \rightarrow HCO + H + M$	16.7	0	72.0	Schecker and Jost (1969)
16	$CH_2O + OH \rightarrow HCO + H_2O$	14.7	0	6.3	Bowman (1975)
17	$CH_2O + H \rightarrow HCO + H_2$	12.6	0	3.8	Westenberg and deHaas (1972a)
18	$CH_2O + O \rightarrow HCO + OH$	13.7	0	4.6	Bowman (1975)
19	$CH_2O + HO_2 \rightarrow HCO + H_2O_2$	12.0	0	8.0	Lloyd (1974)
20	$HCO + OH \rightarrow CO + H_2O$	14.0	0	0.0	Bowman (1970)
21	$HCO + M \rightarrow H + CO + M$	14.2	0	19.0	Westbrook et al. (1977)
22	$HCO + H \rightarrow CO + H_2$	14.3	0	0.0	Niki et al. (1969)
23	$HCO + O \rightarrow CO + OH$	14.0	0	0.0	Westenberg and deHaas (1972b)
24	$HCO + HO_2 \rightarrow CH_2O + O_2$	14.0	0	3.0	Baldwin and Walker (1973)
25	$HCO + O_2 \rightarrow CO + HO_2$	12.5	0	7.0	Westbrook et al. (1977)
26	$CO + OH \rightarrow CO_2 + H$	7.1	1.3	-0.8	Baulch and Drysdale (1974)
27	$CO + HO_2 \rightarrow CO_2 + OH$	14.0	0	23.0	Baldwin et al. (1970)

Table I

Methane-ethane oxidation mechanism. Reaction rates in cm^3-mole-sec-kcal units, $k = AT^n \exp(-E_a/RT)$ cont'd

	Reaction	Rate			Reference
		log A	n	E	
28	$CO + O + M \rightarrow CO_2 + M$	15.8	0	4.1	Simonaitis and Heicklen (1972)
29	$CO_2 + O \rightarrow CO + O_2$	12.4	0	43.8	Gardiner et al. (1971)
30	$H + O_2 \rightarrow O + OH$	14.3	0	16.8	Baulch et al (1973a)
31	$H_2 + O \rightarrow H + OH$	10.3	1	8.9	Baulch et al. (1973b)
32	$H_2O + O \rightarrow OH + OH$	13.5	0	18.4	Baulch et al. (1973b)
33	$H_2O + H \rightarrow H_2 + OH$	14.0	0	20.3	Baulch et al. (1973b)
34	$H_2O_2 + OH \rightarrow H_2O + HO_2$	13.0	0	1.8	Baulch et al. (1973b)
35	$H_2O + M \rightarrow H + OH + M$	16.3	0	105.1	Baulch et al. (1973b)
36	$H + O_2 + M \rightarrow HO_2 + M$	15.2	0	-1.0	Baulch et al. (1973b)
37	$HO_2 + O \rightarrow OH + O_2$	13.7	0	1.0	Lloyd (1974)
38	$HO_2 + H \rightarrow OH + OH$	14.4	0	1.9	Baulch et al. (1973b)
39	$HO_2 + H \rightarrow H_2 + O_2$	13.4	0	0.7	Baulch et al. (1973b)
40	$HO_2 + OH \rightarrow H_2O + O_2$	13.7	0	1.0	Lloyd (1974)
41	$H_2O_2 + O_2 \rightarrow HO_2 + HO_2$	13.6	0	42.6	Lloyd (1974)
42	$H_2O_2 + M \rightarrow OH + OH + M$	17.1	0	45.5	Baulch et al. (1973b)
43	$H_2O_2 + H \rightarrow HO_2 + H_2$	12.2	0	3.8	Baulch et al. (1973b)
44	$O + H + M \rightarrow OH + M$	16.0	0	0.0	Moretti (1965)
45	$O_2 + M \rightarrow O + O + M$	15.7	0	115.0	Jenkins et al. (1967)
46	$H_2 + M \rightarrow H + H + M$	14.3	0	96.0	Baulch et al. (1973b)
47	$C_2H_6 \rightarrow CH_3 + CH_3$	19.4	-1	88.3	Pacey (1973)
48	$C_2H_6 + CH_3 \rightarrow C_2H_5 + CH_4$	-0.3	4	8.3	Clark and Dove (1973)
49	$C_2H_6 + H \rightarrow C_2H_5 + H_2$	2.7	3.5	5.2	Clark and Dove (1973)
50	$C_2H_6 + OH \rightarrow C_2H_5 + H_2O$	13.8	0	2.4	Greiner (1970)
51	$C_2H_6 + O \rightarrow C_2H_5 + OH$	13.4	0	6.4	Herron and Huie (1973)
52	$C_2H_5 \rightarrow C_2H_4 + H$	13.6	0	38.0	Lin and Back (1966)
53	$C_2H_5 + O_2 \rightarrow C_2H_4 + HO_2$	12.0	0	5.0	Cooke and Williams (1971)
54	$C_2H_5 + C_2H_3 \rightarrow C_2H_4 + C_2H_4$	17.5	0	35.6	Benson and Haugen (1967)

Table I

Methane-ethane oxidation mechanism. Reaction rates in cm^3-mole-sec-kcal units, $k = AT^n \exp(-E_a/RT)$ cont'd.

	Reaction	Rate			Reference
		log A	n	E	
55	$C_2H_4 + O \rightarrow CH_3 + HCO$	13.0	0	1.1	Davis et al. (1972)
56	$C_2H_4 + M \rightarrow C_2H_3 + H + M$	14.0	0	98.2	Just et al. (1977)
57	$C_2H_4 + H \rightarrow C_2H_3 + H_2$	13.8	0	6.0	Benson and Haugen (1967)
58	$C_2H_4 + OH \rightarrow C_2H_3 + H_2O$	14.0	0	3.5	Baldwin et al. (1966)
59	$C_2H_4 + O \rightarrow CH_2O + CH_2$	13.4	0	5.0	Peeters and Mahnen (1973)
60	$C_2H_3 + M \rightarrow C_2H_2 H + M$	16.5	0	40.5	Benson and Haugen (1967)
61	$C_2H_2 + M \rightarrow C_2H + H + M$	14.0	0	114.0	Jachimowski (1977)
62	$C_2H_2 + O_2 \rightarrow HCO + HCO$	12.6	0	28.0	Gardiner and Walker (1968)
63	$C_2H_2 + H \rightarrow C_2H + H_2$	14.3	0	19.0	Browne et al. (1969)
64	$C_2H_2 + OH \rightarrow C_2H + H_2O$	12.8	0	7.0	Vandooren and VanTiggelen (1977)
65	$C_2H_2 + O \rightarrow C_2H + OH$	15.5	-0.6	17.0	Brown et al. (1969)
66	$C_2H_2 + O \rightarrow CH_2 + CO$	13.8	0	4.0	Vandooren and VanTiggelen (1977)
67	$C_2H + O_2 \rightarrow HCO + CO$	13.0	0	7.0	Browne et al. (1969)
68	$C_2H + O \rightarrow CO + CH$	13.7	0	0.0	Browne et al. (1969)
69	$CH_2 + O_2 \rightarrow HCO + OH$	14.0	0	3.7	Benson and Haugen (1967)
70	$CH_2 + O \rightarrow CH + OH$	11.3	0.68	25.0	Mayer et al. (1967)
71	$CH_2 + H \rightarrow CH + H_2$	11.4	0.67	25.7	Mayer et al. (1967)
72	$CH_2 + OH \rightarrow CH + H_2O$	11.4	0.67	25.7	Peeters and Vinckier (1975)
73	$CH + O_2 \rightarrow CO + OH$	11.1	0.67	25.7	Peeters and Vinckier (1975)
74	$CH + O_2 \rightarrow HCO + O$	13.0	0	0.0	Jachimowski (1977)
75	$CH_3OH + M \rightarrow CH_3 + OH + M$	18.3	0	80.0	Westbrook and Dryer

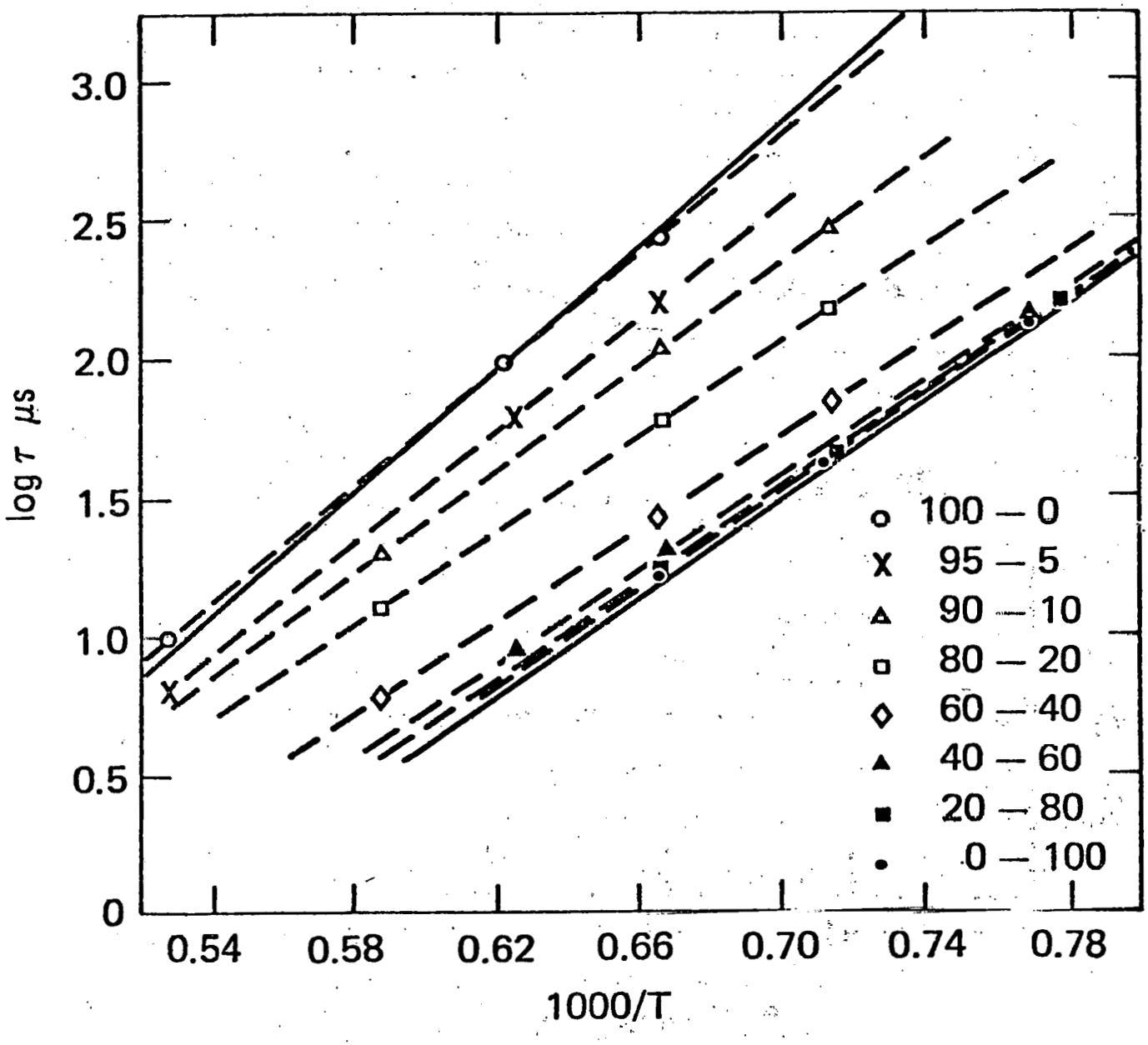

Figure 1. Logarithm of the chemical induction time (in μs) at different temperatures. Dashed lines represent computed cases, with the key giving the CH_4-C_2H_6 percentages respectively. Upper solid line shows experimental data for CH_4, lower solid line for C_2H_6.

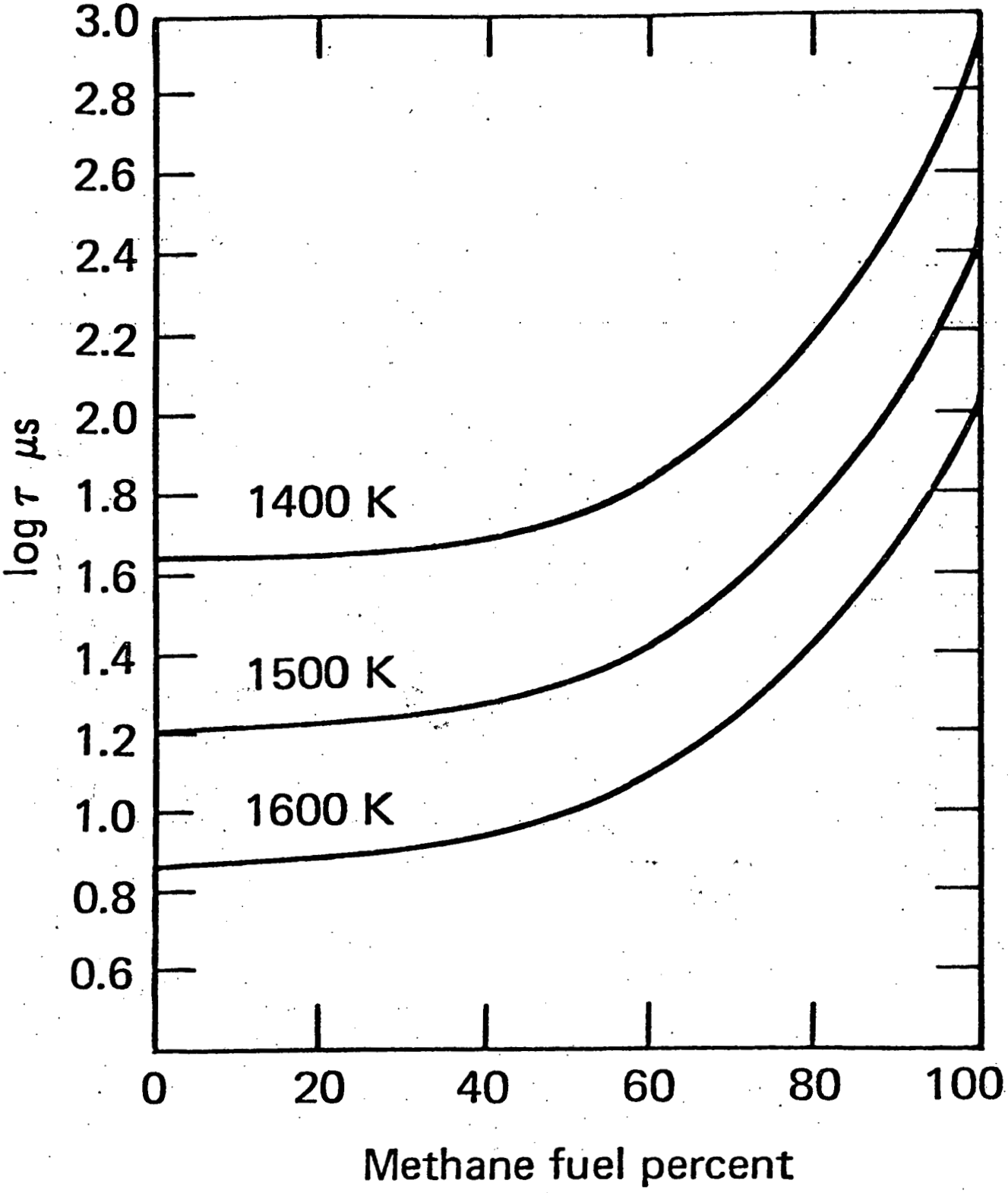

Figure 2. Logarithm of chemical induction time (in μs) at selected post-shock temperatures, showing the effect of fuel composition. Remaining fuel is ethane.

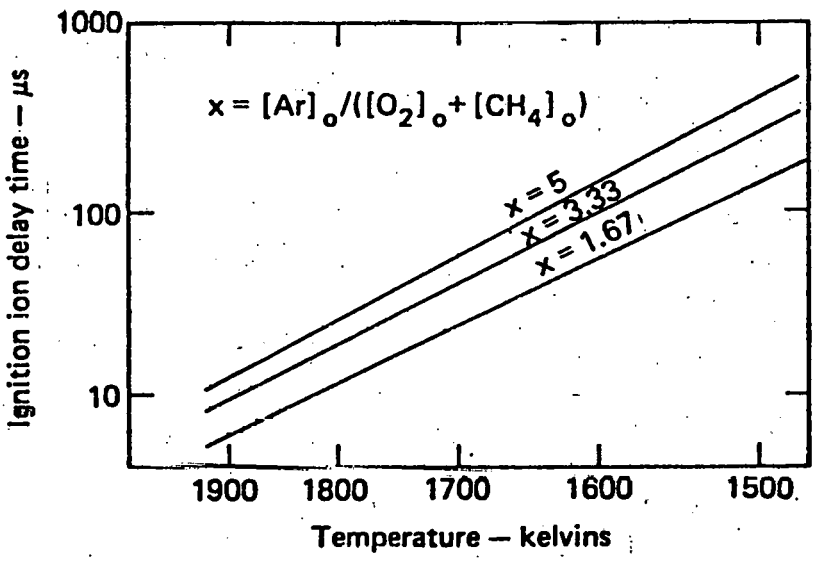

Fig. 3 Ignition delay times as functions of temperature for different amounts of Argon dilution.

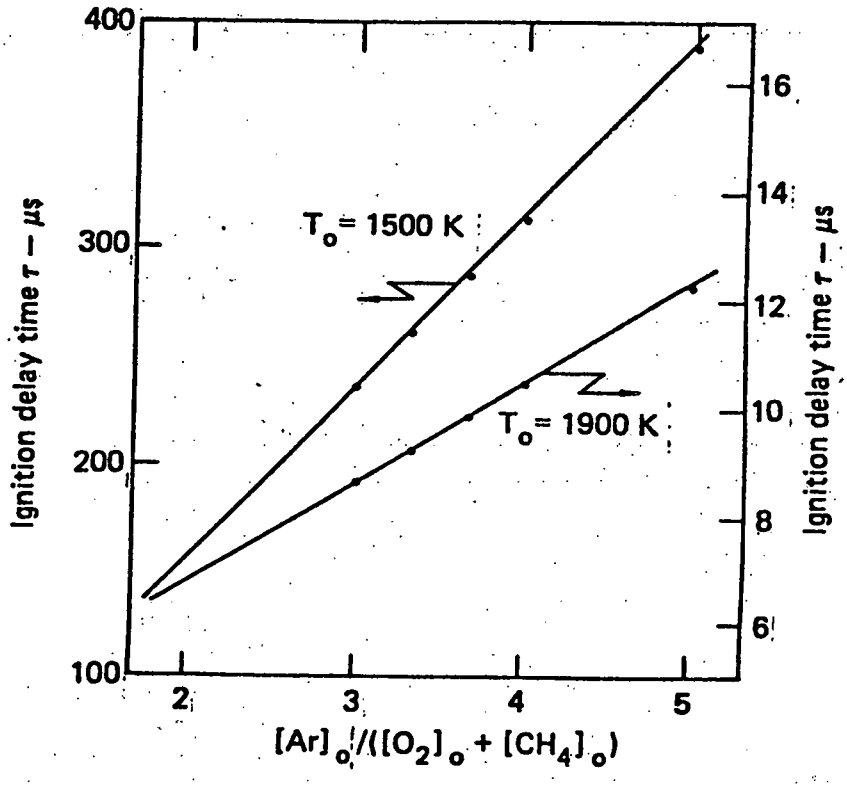

Fig. 4 Ignition delay times as functions of Argon dilution, evaluated for T_o = 1500K and 1900K.

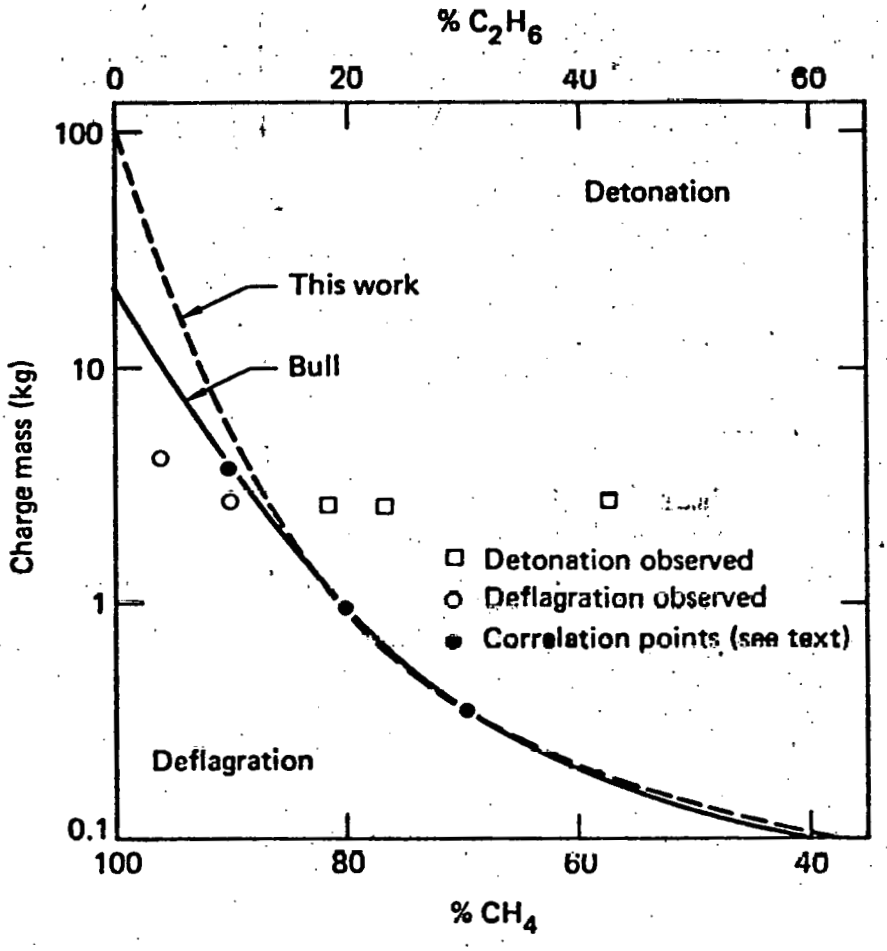

Fig. 5 Detonation thresholds as functions of composition.

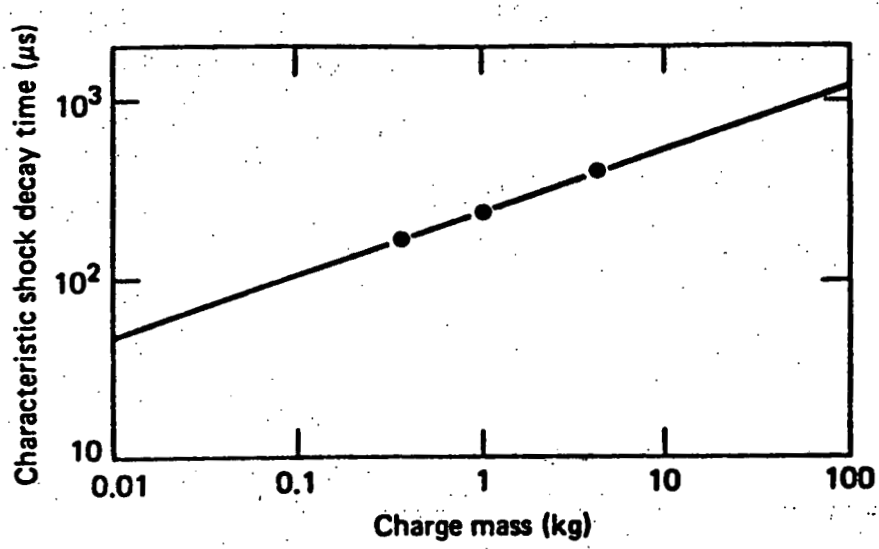

Fig. 6 Shock decay times (20-10 bars) for varying high explosive charge masses.

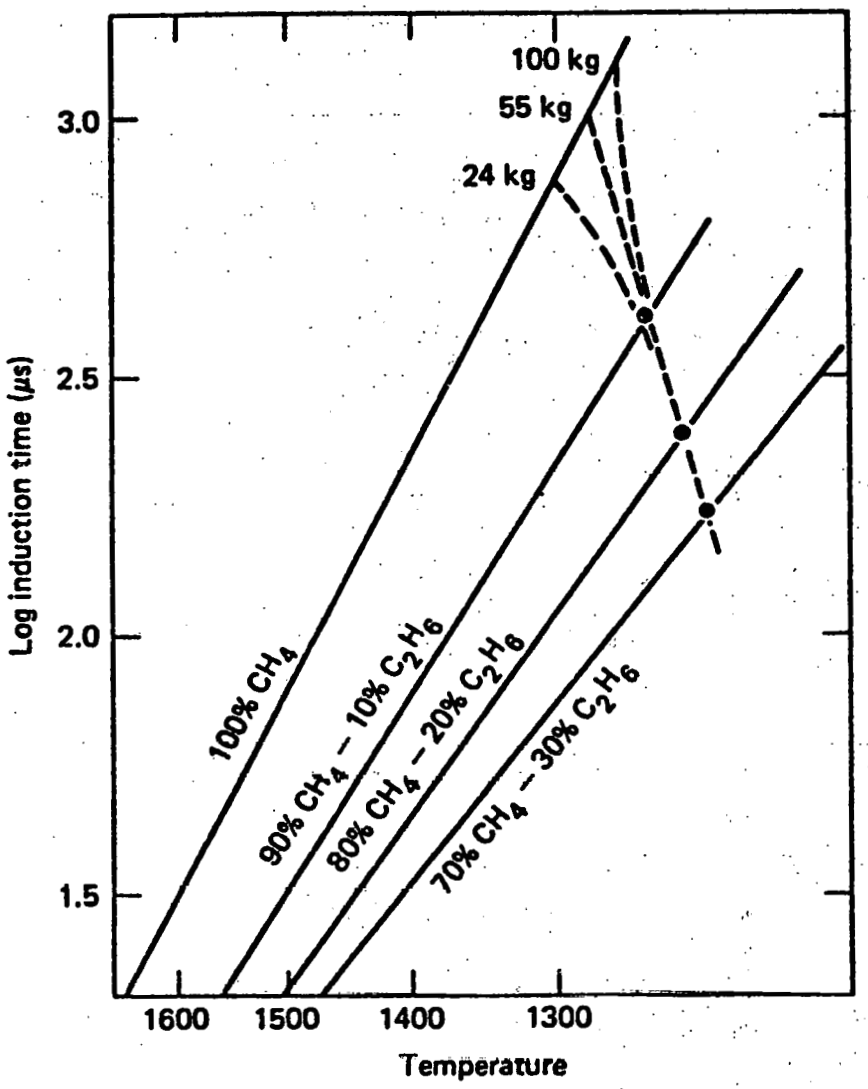

Fig. 7 Logarithm of chemical induction time (in μs) for various fuel mixtures, showing the points used to extrapolate to pure methane.

REPORT G

Effects of Cellular Structure on the Behavior of Gaseous Detonation Waves under Transient Conditions

P. A. Urtiew
C. M. Tarver

Prepared for the
Environmental and Safety Engineering
Division
U.S. Department of Energy
under Contract W-7405-ENG-48

Lawrence Livermore Laboratory
Livermore, California 94550

THIS PAGE

WAS INTENTIONALLY

LEFT BLANK

REPORT G

TABLE OF CONTENTS

FIGURES

TABLES

SUMMARY

Increased concern about the detonability of gaseous mixtures in unconfined clouds renewed our interest in the behavior of the detonation process under various transient conditions, such as a nonuniform distribution of pressure, temperature, or composition. In readjusting itself during such a transient state, the process may either survive and continue as a detonation wave or may weaken so fast that it transforms into a simple deflagration wave. A similar transient condition may be imposed on the wave by letting it pass through an area change. Here again, the wave may either survive or weaken to a point of its extinction.

Assuming that the cellular structure of the detonation wave is responsible for its existence and its uniqueness, we investigated the effect of variation in the cross-sectional area of the tubes on the cell size and on the survival of the detonative process during the transition. Comparison was made with the results of other investigators who performed similar experiments for different reasons.

The results show that it is not the tube diameter nor the initial pressure of the medium that controls the survival of the wave but that it is (1) the number of cells available to endure losses from flow effects generated by the transient conditions and (2) the number of cells remaining to regenerate new cells to revive the detonation process.

INTRODUCTION

Recent advances in the field of gaseous detonation have renewed interest in one of the relatively untouched areas of the detonative process, that is, its behavior under transient conditions when one or more of the controlling variables is not constant. Such transient conditions are met when a detonation wave experiences a change in composition, pressure, temperature, or confinement. The process begins to adjust itself to a new set of conditions and undergoes a change in structure. It also begins to reveal its characteristic features. Knowledge of such details of the character of the wave may lead us to a better understanding of the process and, in particular, of the link between chemistry and hydrodynamics in a detonation wave.

The last few decades have been very fruitful in providing information about the nature of the detonative process and the essential features of its cellular structure. Full details about the subject may be found in the comprehensive reviews of Oppenheim et al. (1963), Strehlow (1968), Lee et al. (1969), and Lee (1977). It is believed that the cellular structure of gaseous detonations has been proven beyond any doubt and that any new findings connected with the behavior of the detonation process must be associated, one way or another, with this cellular structure.

One important finding that emerged from all investigations during the last few decades is that the cellular structure not only exists but is essential to the detonative process. Its size and regularity are characteristic of a particular combination of initial conditions, such as composition, pressure, and temperature. Variation of these conditions causes the cell size to change and attain a new size that is characteristic of the new set of conditions. Differences in confinement (such as in the tube diameter) or the lack of any confinement (as in the case of spherical detonations), if kept constant during the process, will have no effect on the characteristic cell size. However, should the detonation wave enter an area change, the cell size will immediately be affected by the change and will reveal some of the transient features of the phenomenon. Local variations in these conditions, including those of the cross sectional area, will cause enhancement of the detonative process or weakening of it with a possibility of a complete extinction.

The first records of a detonation wave traveling into both gradual and abrupt changes of the cross-sectional area were shown by Voitsekhovsky et al. (1963). Their records were taken with an open-shutter technique, and changes in cell size and even complete loss of cellular structure are quite evident. Strehlow and his group at the University of Illinois have gathered an enormous amount of valuable information on the cellular structure and have

contributed significantly to our present understanding of the phenomenon. Their experiments (Strehlow et al., 1972) with an adjustable wedge inside the tube also reveal the effects caused by the change in the cross-sectional area and by the variation of the cell size as the detonation wave propagates through such an area change.

Our earlier unpublished experiments, in which an area change in the path of a detonation wave was produced by a wedge inserted into the 2.54 x 3.81-cm rectangular tube, also revealed some interesting results such as different threshold pressures for transition at different orientations of the wedge. Similar experiments with a convergent-divergent tube were performed the same year by Lee et al. (1965). However, it is his recent study with Matsui (Matsui and Lee, 1978) on the transition of detonation from a planar geometry into a spherical one that stimulated the present work and led us to study the effects of cellular structure of the detonation wave on its transition from a tube of constant cross section into an expanded geometry.

THE EFFECTS

If we examine the records of Strehlow et al. (1972) and Voitsekhovsky et al. (1963), as well as unpublished experiments of

Urtiew and Oppenheim (1965), we find that as the detonation wave progresses into an area change the cell size either gets smaller or larger depending on whether the detonation wave propagates, respectively, into a contraction or expansion of the tube. This process is qualitatively illustrated in Fig. 1.

When the wave enters a convergent section (Fig. 1a), an oblique shock or a compression fan is generated at the corner or at its gradual convergence. The flow behind the front is affected and the wave becomes slightly overdriven. At the same time at the wave front, the triple-intersection point nearest the converging wall meets a reflecting surface sooner than it would under constant area flow, and it reflects at higher pressure. Therefore, the cells become smaller. The effect is propagated radially into the tube, continuously changing the cell size.

When the wave enters a divergent section (Fig. 1b), it encounters a rarefaction wave centered at the corner or spread around a gradual expansion (not shown). At the same time, the triple-intersection point nearest the wall does not find a reflecting surface in time for a regular enforcement of the detonation process and thus becomes weaker and weaker. Both of these effects must work hand in hand, because loss of reflecting surface alone would not prevent the wave from generating a new explosion point near the would-be reflection point and thereby continue the process, as it does in spherical detonations. On the

other hand, rarefaction alone (depending on its strength) may only weaken the process, which will still carry on until marginal conditions are attained.

In the case of tube expansion, the strength of the rarefaction, namely, the amount of pressure drop across the wave, depends on the amount of expansion, i.e.,

$$\Delta p = f(\delta) \quad , \tag{1}$$

where δ is the angle of divergence. Rarefaction is an isentropic process propagating at a local velocity of sound. In a uniform flow, the sound velocity would be constant and the rarefaction wave would travel along a characteristic curve toward the center of the tube. In the case of a detonation wave with the cellular structure, local velocities of sound vary so much within the cell that interaction between the detonation front and the incoming rarefaction wave becomes very complex. The question of original strength becomes very important. The rarefaction wave may not be sufficiently strong to overcome the effect of burning as it propagates through individual cells and may cease to exist at some point along its path and toward the center of the flow.

TRANSITION OF DETONATION FROM PLANAR TO SPHERICAL GEOMETRY

Consider the case of transition from a plane geometry into a hemispherical one, which represents the case where $\delta = 90°$. This case does not produce the strongest rarefaction wave at the corner, but it represents a simple case that may be compared with experimental studies of Matsui and Lee (1978). Unlike the rarefaction caused by a plane shock wave, the effects of a rarefaction wave generated by a detonation wave will gradually diminish as it propagates towards the centerline of the hemisphere until, if the original tube diameter is large enough, the effects become so small that the wave begins to regenerate new cells as if it were a portion of a spherical detonation wave. The criterion for survival is, then, the diameter of the tube or, rather, how much of the inner core of the detonation wave will remain unaffected by the rarefaction wave and how well it will be able to reestablish the detonation process in a spherical geometry.

To determine the relationship of the inner-core diameter, d_o, with the critical diameter of the tube, d_c, let us relate the energy required for initiation of a spherical wave with the work done by the core of the wave on the undisturbed gas outside of the tube. If we consider the geometry as illustrated in Fig. 2, the work done (WD) by the core on the outside gas will have the following approximate expression:

$$WD = \int_{o}^{t_c} P\, u\, A\, dt \quad , \tag{2}$$

where P and u represent the Chapman-Jouguet (C.J.) pressure and particle velocity, A is the area of the inner core, and

$$t_c = \frac{\ell}{z}\left(\frac{r_c - r_o}{D}\right) \tag{3}$$

represents the time required by the head of the rarefaction wave to reach the outer edge of the core at r_o. There, ℓ and z are the cell size dimensions in length and width, respectively, and D is the detonation velocity of the wave.

Integrating Eq. (1), one obtains an expression for the work done:

$$WD = \pi\, P_{CJ} u_{CJ} r_o^2 \left(\frac{\ell}{z}\right)\left(\frac{r_c - r_o}{D}\right) \tag{4}$$

or

$$WD = \left(\frac{\pi P_{CJ} u_{CJ}}{8D}\right)\left(\frac{\ell}{z}\right)\left(\frac{d_c}{d_o} - 1\right)\ d_o^3 \tag{5}$$

In essence, this work done on the outside gas by the inner core of the wave is the energy required to initiate a detonation

process in a hemispherical geometry. To compare its value with the experimental value of Matsui and Lee (1978) for the spherical case, we must take 2 WD and express it in terms of d_c as follows:

$$E_c = 2\ WD = \frac{\pi P_{CJ} \gamma_{CJ}}{4D} \frac{\ell}{z} \left[\left(\frac{d_c}{d_o} - 1 \right) \left(\frac{d_o}{d_c} \right)^3 \right] d_c^3 \qquad (6)$$

As expected, E_c is proportional to d_c^3 provided the term in the square brackets remains constant. If we assume various values for the ratio of d_c/d_o, the expression in the square brackets attains a maximum value of 0.15 when the ratio of d_c to d_o is set equal to 1.5, which agrees quite well with experimental records of Lee (1979). Using this value for the ratio of d_c/d_o, setting $\ell/z = 2$, and calculating the CJ parameters for each of the mixtures investigated by Matsui and Lee (1978), we can compare our calculated energy values with theirs by plotting both values against their experimentally determined values of the critical diameter, d_c. All calculated values are tabulated in Table 1, while the plot of E_c versus d_c is shown in Fig. 3.

The agreement between the two sets of values is quite evident, indicating that not only our expression for the critical energy is correct but also that the assumption of $d_c/d_o = 1.5$ is valid. Figure 3 also reveals that, while all the points of the fuel-air mixtures lie on the same straight line, they do fall below the extended fuel-oxygen line. This may be because of the chemical

difference between the fuel-oxygen and fuel-air mixtures or simply because of erroneous, although consistent, extrapolation of the d_c versus N_2/O_2 curves to N_2/O_2 for air (Matsui and Lee, 1978). The critical energy for initiation of methane-air detonations resulted in the value of 1.74×10^8 J, which falls slightly below the line but within the range of the predictions made by Bull et al. (1976) and recently by Westbrook and Haselman (1979). However, the resulting value falls far below that of Boni et al. (1978).

Recently Vasiliev (1978) suggested a formula for an estimate of the energy required to initiate a cylindrical detonation wave. Taking his value of 0.1 J/cm for a stoichiometric oxy-acetylene mixture at initial pressure of 0.1 atm and scaling it to spherical geometry at P_0 = 1 atm with the cell size z = 2 mm, we get a number that agrees very closely with our number of $E_c = 3.6 \times 10^{-4}$ J. Furthermore, his relative values of energy required to initiate cylindrical detonation in other hydrocarbon mixtures, including that of methane-air, when plotted against Lee's experimental d_c, fall on a straight line with a quadratic slope, as one would expect for cylindrical geometry. This all suggests that our estimate of energy for initiating a spherical detonation is in good agreement with those found by others.

QUANTITY OF CELLS NEEDED FOR TRANSITION

In their experimental investigation, Matsui and Lee (1978) found that, for a transition of a gaseous detonation from a planar geometry into a spherical one, the critical diameter of the tube is related to the initial pressure by

$$P_o = a\, d_c^{\alpha} \quad , \tag{7}$$

where a and α are constants for each particular mixture. Earlier studies on the cell size dependence on initial pressure (Strehlow and Engel, 1969) yielded

$$P_o = b\, z^{\beta} \quad , \tag{8}$$

where again b and β are constants for each particular mixture. An algebraic manipulation leads to a combined expression

$$n = \frac{d_c}{\pi} = KP^{\gamma} \quad , \tag{9}$$

where n stands for the number of cells present across the critical diameter of the tube, and K and γ are new constants related to the previous ones by

$$K = a^{-1/\alpha}\, b^{1/\beta} \text{ and } \gamma = \frac{1}{\alpha} - \frac{1}{\beta} \quad . \tag{10}$$

For the four mixtures common to both studies, values of all constants are listed in Table 2. The numbers in brackets for the oxy-hydrogen system represent a slight correction, which may be introduced by drawing another line through the experimental points of Strehlow and Engel (1969). The values of γ in Table 2 are much less than one, and therefore the effect of initial pressure is minimal. If this is true for the other explosive mixtures as well, then it apparently is not the initial pressure or the diameter of the tube that determines the criterion for the transition but the cell size z. Also important is the number of cells available to suppress the incoming rarefaction wave and to generate new cells, which will receive the detonation process. The above results seem to indicate that for each mixture a particular number of cells is required for that purpose.

Of interest here is the sign before the exponent γ. In contrast to acetylene-oxygen, ethylene-oxygen, and methane-oxygen mixtures (where a lower initial pressure increases the number of cells required across the critical diameter), the hydrogen-oxygen mixture has the opposite effect, i.e., the number of cells decreases as the initial pressure decreases.

EXTRAPOLATION OF n AND z TO CH_4-AIR MIXTURE

At one atmosphere initial pressure, the value of K in Eq. (9) represents the number of cells needed across the critical diameter for a transition of detonation to take place. As noted in the previous section, this value of n varies inversely with the susceptibility to detonation. Plotting this value of n (see Table 2) against the critical diameter reveals the interesting fact that, with the exception of the oxy-hydrogen mixture, the values for all the hydrocarbon fuels indeed fall on a straight line. This line may then be extended to the critical diameter of the least detonable mixture, methane-air. This remarkable correlation of n and z for the available hydrocarbon-oxygen mixtures is illustrated in Fig. 4. The extrapolation of the straight lines to the critical diameter of CH_4-air results in n = 105 and z = 9 cm for that mixture.

EFFECT OF GEOMETRY AND INITIAL PRESSURE

Thus, a transition of detonation from a cylinder to a hemisphere is assured if a core of the detonation wave remains unaffected by the rarefaction wave and is large enough to supply the necessary amount of energy to the undisturbed gas for a hemispherical initiation (i.e. $E_c \sim d_c^3$, with $d_o = 0.67\ d_c$ and a different n for each particular gaseous system).

If, instead of an open hemisphere, the cylinder ends in a circular cone with a solid angle smaller than 2π steradians (i.e., where $\delta < 90°$), the rarefaction generated at the corner will be weaker and both d_c and d_o will become smaller: first, because of a weaker rarefaction and, second, because of a smaller energy requirement as a result of a smaller solid angle of expansion. To the first approximation, this new critical core diameter may then be expressed as

$$d_{o\delta} = d_{oo} + \left(d_o - d_{oo}\right) \frac{\delta}{90} \quad , \tag{11}$$

where $d_{o\delta}$ is the core diameter for any expansion where $o < \delta < 90$, and d_{oo} is the minimum-constant-area tube diameter (δ=o) capable of supporting a detonation wave, which in terms of a cell size can be expected to be of the order of z/2.

If the geometry is kept the same while the initial pressure P_o is lowered, then, as noted earlier by Matsui and Lee (1978), one needs a larger d_c. Because during the derivation of Eq. (6) no particular value of initial pressure was stipulated, the ratio of $d_c/d_o = 1.5$ must still hold and, therefore, d_o will also be larger. Following Strehlow and Engel (1969), z will also be larger, but the number of cells, $n = d_c/z$ and $k = d_o/z$, will remain in the same proportion, although slightly different from the atmospheric condition because of a small effect of initial pressure in Eq. (9).

On the E_c - d_c plot of Fig. 3, the effect of initial pressure shows a quadratic behavior. This is so because, while D and u remain almost invariant with P_o, P_{CJ} and d_c vary as P_o and $1/P_o$, respectively. This causes $P_{CJ} \sim 1/d_c$ and $E_c \sim d_c^2$. The effect of P_o on the E_c - d_c relationship is illustrated in Fig. 3 for the hydrogen-oxygen system. The other systems are expected to follow suit.

COMPARISON OF THE DETONATION KERNEL TO THE DETONATION CELL

It is of interest to compare the expression for the critical energy with that derived earlier by Lee and Ramamurthi (1976) for the spherical geometry and to correlate their findings of the critical detonation kernel R_s^* with the dimensions of the detonation cell.

Taking Lee's expression for the critical energy,

$$E_c = \frac{1}{3} \frac{\pi}{\gamma^2 - 1} \rho_o c_o^2 M_s^{*2} R_s^{*3} \quad , \tag{12}$$

and equating it to our critical energy equation (3), we get the expression for the critical diameter

$$d_c^3 = \frac{4\ D\ \rho_o c_o^2\ M_s^{*2}\ R_s^{*3}}{3\ P\ u\left(\gamma^2 - 1\right)\ \frac{\ell}{z}\left(\frac{d_o}{d_c}\right)^3\left(\frac{d_c}{d_o} - 1\right)} \quad . \tag{13}$$

This expression can be simplified by setting

$$P_{CJ} = \frac{\rho_o\ D^2}{\gamma + 1} \quad , \tag{14}$$

$$U_{CJ} = \frac{D}{\gamma + 1} \quad , \tag{15}$$

$$M_{CJ} = \frac{D}{C_o} \quad . \tag{16}$$

Then

$$d_c^3 = \frac{4}{3}\ \frac{(\gamma + 1)}{(\gamma - 1)}\ \frac{z}{\ell}\ \frac{1}{\left[\left(\frac{d_o}{d_c}\right)^3\left(\frac{d_c}{d_o} - 1\right)\right]}\ \frac{M_s^{*2}}{M_{CJ}^{\ 2}}\ R_s^{*3} \tag{17}$$

Introducing typical values for a hydrocarbon fuel, we may set

$$\gamma \cong 1.2; \quad \frac{\ell}{z} \cong 2; \quad \left[\left(\frac{d_o}{d_c}\right)^3\left(\frac{d_c}{d_o} - 1\right)\right] = 0.15; \quad \frac{M_s^*}{M_{CJ}} \cong 0.7;$$

and get the value of the detonation kernel in terms of the critical diameter d_c,

$$R_s^* = 0.3469\ d_c \quad . \tag{18}$$

If we now take Lee's argument that the detonation kernel size, R_s^*, is comparable to the cell length, ℓ, we would get only one set of d_c and d_o, i.e.,

$$\text{if } R_s^* = \ell, \quad \text{and} \quad \ell = 2z, \quad \text{then} \quad \begin{matrix} d_c = 5.77z, \\ d_o = 3.84z. \end{matrix} \tag{19}$$

However, if $d_c > 5.8\ z$, as it appears from the records of Lee, and is approximately equal to 12 z, as suggested by Voitsekhovsky et al. (1963), then R_s^* is on the order of 4.16 z or 2.08 ℓ. This does not diminish the significance of the detonation kernel concept; however, it does change its relationship to the characteristic cell size.

Table 3 lists the values of R_s^* for the five mixtures described earlier. The values of the detonation kernel are given in terms of the cell length ℓ as obtained from combining Eqs. (6) and (13), with the assumption that $\ell/z = 2$. Note that for the acetylene-oxygen mixture, which was the main working medium for

Lee and his group, the critical size of the detonation kernel R_s^* is indeed very close to the cell length ℓ. The other four mixtures, ethylene-oxygen, hydrogen-oxygen, methane-oxygen, and methane-air, result in R_s^* equal to approximately 1.39 ℓ, 5.2 ℓ, 2.98 ℓ, and 18.21 ℓ, respectively. Again note that following its direct proportionality with n, the critical size of the detonation kernel R_s^* varies inversely with the susceptibility to detonation. This observation may be useful in determining proper values for other explosive mixtures in the series.

SPHERICAL INITIATION OF DETONATION

If, as previously noted in Eq. (18), the critical size of the detonation kernel R_s^* is uniquely related to the critical diameter d_c, one can use the values listed in Table 3 to evaluate the physical size of R_s^* and make a comparison with the blast initiation radius computed with the numerical techniques as used by Westbrook and Haselman (1978).

For this purpose, the numerical model described by Wilkins (1969) was used to calculate the distances at which a blast wave initiated by a charge of high explosives would decay to pressures covering the range of CJ pressures for most fuel-oxygen and fuel-air mixtures. The results are shown in a reduced form in Fig. 5, where pressure is plotted as a function of the radius normalized by

the cube root of the critical energy. The solid line represents the decay of pressure following a release of energy from a charge into an inert atmosphere. When the explosive charge is set off in an explosive medium, then the energy of the medium itself also contributes to the total energy release and the decay of the blast wave is somewhat slower, increasing the radius at which a particular pressure is attained. This effect is illustrated in Fig. 5 by a broken line, which is somewhat arbitrary because it is based on estimates made for several pressures.

Also included in Fig. 5 are the points representing the values of the detonation kernel R_s^* reduced by $E_c^{1/3}$ for the five mixtures described above. The agreement is rather remarkable. This confirms the original notion of Lee and Ramamurthi (1976) about the R_s^*. They said that for each particular mixture, there is a certain minimum distance R_s^* wherein the chemical energy released by the medium is comparable to the energy released by the source; so that the subsequent shock motion will be strongly coupled to the chemical processes and a detonation wave is sustained. However, their postulate that the size of the detonation kernel is comparable to the cell length is true only for a mixture of the acetylene-oxygen. Other explosive hydrocarbon mixtures have their relative R_s^*/ℓ ratios in the order of their susceptibility to detonation.

In view of this finding, one can invoke another criterion for the self-sustenance of the detonation wave: to continue the existence of the detonative process, one must have, in each particular mixture, a certain number of cells around the periphery of the sphere and that number can be found from

$$N_c = \frac{2\pi R_s^*}{z} \quad . \tag{20}$$

This number is also listed in Table 3.

Thus, initiation of spherical detonation will occur if, at the proper radius from the center of the blast wave, i.e., the radius of the detonation kernel R_s^*, the decay of the wave matches that of the decay through the individual cell of the detonation wave. If the initial charge is too small, then the decay will be too steep and the detonative process will fail.

This criterion for spherical initiation of detonation can also be attributed to the amount of angular expansion of the cell as the wave propagates radially outward. For each particular mixture, there is a certain maximum of such angular expansion at which a new cell must be initiated or the process will decay to its extinction. Such angular expansion may be expressed in terms of

$$\theta = tg^{-1} \frac{z}{R} \quad ; \tag{21}$$

whose value for each of the five mixtures is also listed in Table 3. Also note that plotting θ versus d_c on the log-log scale will result in a straight-line relationship.

Of course, these are purely physical observations of the phenomenon and cannot be considered as fundamental criteria for the process. Here the chemistry of the medium plays the most important role. The decay of the wave is inherently connected with the induction time of a certain molecule or group of molecules that, if retained in a thermodynamic state for a sufficient length of time, will autoignite and thereby start a new local explosion. This results in a new cell. Being an unsteady process, it does not lend itself to an easy analytical treatment. Therefore, observations such as those made here are considered very helpful and informative.

CONCLUSION

The object of this work was to study the effect of the cellular structure of the detonation wave on the transition of the process into expanded geometries. Previous observations revealed that for each initial pressure there is a characteristic cell size and a critical diameter from which a transition of detonation is possible. We have demonstrated the effect of the cellular structure by showing there must be an inner core of the wave, consisting of a critical number of cells unaffected by side rarefactions, to ensure the transition of the detonation process.

In this study, the work done on the outer gas by that inner core of the wave was compared with the critical energy for spherical initiation. The agreement was remarkably good. Extrapolation of data on the log-log plot of critical energy versus critical diameter led to a prediction of the critical energy needed to initiate detonation in a pure methane-air mixture. A plot of the characteristic cell size and critical number of cells needed for transition also led to quantitative estimates of these values for the methane-air mixtures. In fact, if we consider values for the whole range of mixtures from the most to the least susceptible to detonation (acetylene-oxygen and methane-air, respectively) and find them to fall on a straight line over several decades on a log-log plot, we can predict the behavior of any other explosive mixture, provided one of the parameters becomes known.

Comparison of our results on the critical energy of initiation with those previously reported by Lee and Ramamurthi (1976) led to a slightly different view on the physical significance of the detonation kernel and, in particular, its correspondence to the length of the detonation cell. While the size of the kernel is essentially unique in that the chemical energy contained within is comparable to the source energy released by the initiator charge, the size of the kernel is not the same as the characteristic length of the detonation cell. As reported here, the kernel size varies according to the susceptibility of the explosive mixture to

detonation. The detonation kernel, however, agreed well with the size of the radius at which numerical calculations predicted the blast wave would decay to the detonation pressures of the gaseous mixture.

ACKNOWLEDGMENTS

One of the authors (PAU) wishes to thank Professor J. H. Lee for his several fruitful discussions of the subject and, in particular, for his original suggestion to look into the "work-done" concept. We are also grateful to our colleagues, Len Haselman and Fred McMurphy for providing numerical calculations for Fig. 5 and Table 1, respectively.

REFERENCES

Boni, A. A., Wilson, C. W., Chapman, M. and Cook, J. L. (1978) A study of detonation in methane/air clouds, Acta Astronaut., 5, 1153-1169.

Bull, D. C., Elsworth, J. E., Hooper, G. and Quinn, C. P. (1976) A study of spherical detonation in mixtures of methane and oxygen diluted with nitrogen, J. Phys. D., 9, 1991-2000.

Lee, J. H. S. (1977) Initiation of gaseous detonation, Ann. Rev. Phys. Chem., 28, 75-104.

Lee, J. H., Knystautas, R. and Lee, B. H. K. (1965) Structure of gaseous detonations in a convergent-divergent channel, AIAA J., 3, No. 9, 1785-1787.

Lee, J. H., Soloukhin, R. I. and Oppenheim, A. K. (1969) Current views on gaseous detonation, Astronaut. Acta, 14, 565-586.

Lee, J. H. and Ramamurthi, K. (1976) On the concept of the critical size of a detonation kernel, Combust. Flame, 27, 331-340.

Matsui, H. and Lee, J. H. (1978) On the measure of the relative detonation hazards of gaseous fuel-oxygen and air mixtures, Seventeenth Symposium (International) on Combustion, The Combustion Institute, Pittsburgh, Pa.

Oppenheim, A. K., Manson, N. and Wagner, H. Gg. (1963) Recent progress in detonation research, AIAA J., 1, No. 10, 2243-2252.

Strehlow, R. A. (1968) Gas phase detonations: recent developments, Combust. Flame, 12, No. 2, 81-101.

Strehlow, R. A., Adamczyk, A. A. and Stiles, R. J. (1972) Transient studies of detonation waves, Astronaut. Acta, 17, No. 4-5, 509-527.

Strehlow, R. A. and Engel, C. D. (1969) Transverse waves in detonations: II. Structure and spacing in H_2-O_2, C_2H_2-O_2, $C_2H_4O_2$ and CH_4-O_2 systems, AIAA J., 7, No. 3, 492-496.

Vasiliev, A. A. (1978) Estimate of the energy to initiate a cylindrical detonation, Fiz. Gor. Vzryva, 14, No. 3, 154-155.

Voitsekhovsky, B. V., Mitrofanov, V. V. and Topchian, M. E. (1963) Struktura Fronta Detonatsii v Gazakh, Izd. Sib. Otd. AN SSSR, pp. 97-103. (Translation: The Structure of a Detonation Front in Gases, Foreign Technol. Div. Rept. FTD-MT-64-527 (1966).)

Westbrook, C. K. and Haselman, L. C. (1979) Chemical Kinetics in LNG Detonations, Lawrence Livermore Laboratory, UCRL-82293.

Wilkins, M. (1969) Calculations of Elastic-Plastic Flow, Lawrence Livermore Laboratory, UCRL-7322.

THIS PAGE

WAS INTENTIONALLY

LEFT BLANK

TABLE 1. Detonation Parameters and Critical Values of Energy and Diameter for Various Explosive Mixtures

Fuel	Oxid	Fuel	E_c[a]	d_c[a]	P	D	u	c	δ	E_c
Source		(Vol %)	(J)	(cm)	(atm)	(m/s)	(m/s)	(m/s)	-	(J)
C_2H_2	O_2	40	3.83×10^{-4} 5.9×10^{-3} 10×10^{-3}	(0.25)[b] 0.09	41.42	2728.54	1235.08	1493.46	1.18	3.6×10^{-4}
C_2H_4O	O_2	40	1.2×10^{-2}	0.28	43.55	2499.78	1145.73	1354.05	1.16	1.07×10^{-2}
C_2H_4	O_2	33.3	7.2×10^{-2}	0.52	38.78	2584.57	1182.18	1402.38	1.16	6.16×10^{-2}
C_3H_6	O_2	25	2.03×10^{-1}	0.7	43.22	2559.75	1172.33	1387.43	1.16	1.66×10^{-1}
C_3H_8	O_2	22.2	5.77×10^{-1}	1.0	42.72	2539.57	1165.69	1373.87	1.17	4.76×10^{-1}
C_2H_6	O_2	28.6	1.07	1.3	38.85	2544.80	1167.99	1376.81	1.15	9.52×10^{-1}
H_2	O_2	66.7	1.58	(1.9)[b] 2.0	18.90	2848.83	1297.15	1551.68	1.13	1.66
CH_4	O_2	40	5.07×10	(3.2)[b] 5.0	31.73	2544.78	1167.33	1377.45	1.14	4.42×10
C_2H_2	Air	12.5	1.29×10^{2}	8.0	20.01	1927.90	856.38	1071.52	1.19	1.08×10^{2}
C_2H_4O	Air	12.3	7.62×10^{3}	30.0	19.79	1852.26	818.05	1034.21	1.20	5.56×10^{3}
C_2H_4	Air	9.5	1.2×10^{5}	80.0	17.82	1816.10	797.98	1018.12	1.20	9.46×10^{4}
C_3H_6	Air	6.6	7.55×10^{5}	150.0	17.82	1786.99	782.28	1004.71	1.21	6.2×10^{5}
C_3H_8	Air	5.7	2.52×10^{6}	220.0	17.26	1759.78	768.54	991.23	1.22	1.89×10^{6}
C_2H_6	Air	5.7	5.09×10^{6}	280.0	16.96	1766.56	772.49	994.07	1.21	3.84×10^{6}
H_2	Air	29.6	4.16×10^{6}	280.0	14.80	1915.61	853.54	1062.07	1.16	3.42×10^{6}
CH_4	Air	12.3	2.28×10^{8}	1020.0	15.96	1763.88	770.11	993.77	1.21	1.74×10^{8}

[a]Values taken from Matsui and Lee (1978).

[b]Values in parentheses taken from Voitsekhovsky, et al. (1963).

TABLE 2. Parameters of Eqs. (4) to (7) for Four of the Explosive Mixtures Common to Studies of Matsui and Lee (1978) and Strehlow and Engel (1969).

Fuel	Oxid	a	α	b	β	K^a	γ
C_2H_2	O_2	0.167	-0.882	0.025	-1.057	4.31	-0.188
C_2H_4	O_2	0.668	-0.918	0.0265	-1.44	8.0	-0.395
H_2	O_2	1.91	-0.928	0.135	-0.74 (-0.83)	30.0 (22.4)	+0.274 (+0.13)
CH_4	O_2	4.6	-0.95	0.29[b]	-1.0[b]	17.2	-0.05

[a] K = n at P = 1 atm.

[b] Estimated on basis of other mixtures diluted with 50% argon.

TABLE 3. Critical Parameters Evaluated in Present Study for Five Explosive Mixtures, Including that of Methane Air

Fuel Source	Oxid	d_c[a] (cm)	n[b]	$z = d_c/n$ (cm)	$\ell = 2z$ (cm)	R_s^*[c]	R_s^*[d] (cm)	N_c[e]	θ[f]
C_2H_2	O_2	0.09	4.3	0.021	0.042	0.74 ℓ	0.031	9.27	34.11
C_2H_4	O_2	0.52	8.0	0.065	0.13	1.39 ℓ	0.18	17.40	19.85
H_2	O_2	2.01	30.0	0.067	0.13	5.2 ℓ	0.67	62.83	5.71
CH_4	O_2	5.0	17.2	0.29	0.58	2.98 ℓ	1.72	37.27	9.57
CH_4	Air	1000.0	105.0	9.0	18.0	18.21 ℓ	327.0	228.3	1.57

[a] M&L-78

[b] M&L-78, S&E-68

[c] $n/2(0.347)$

[d] $n/2(0.347)\ell$

[e] $\frac{2\pi R_s}{z}$

[f] $tg^{-1}\frac{z}{R_s}$

THIS PAGE

WAS INTENTIONALLY

LEFT BLANK

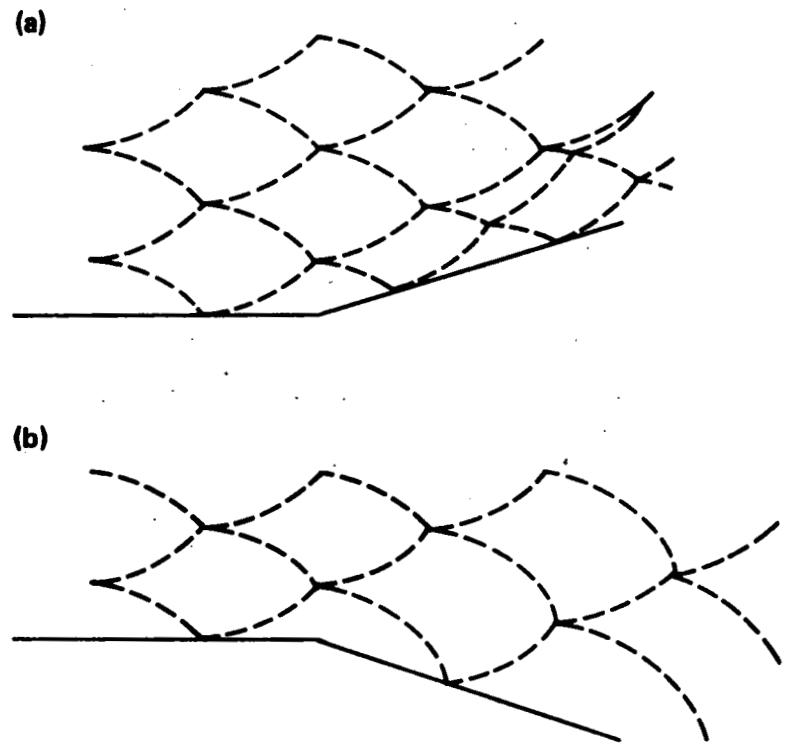

FIGURE 1. Sketch of a Cellular Detonation Wave Entering (a) Convergent Section and (b) Divergent Section.

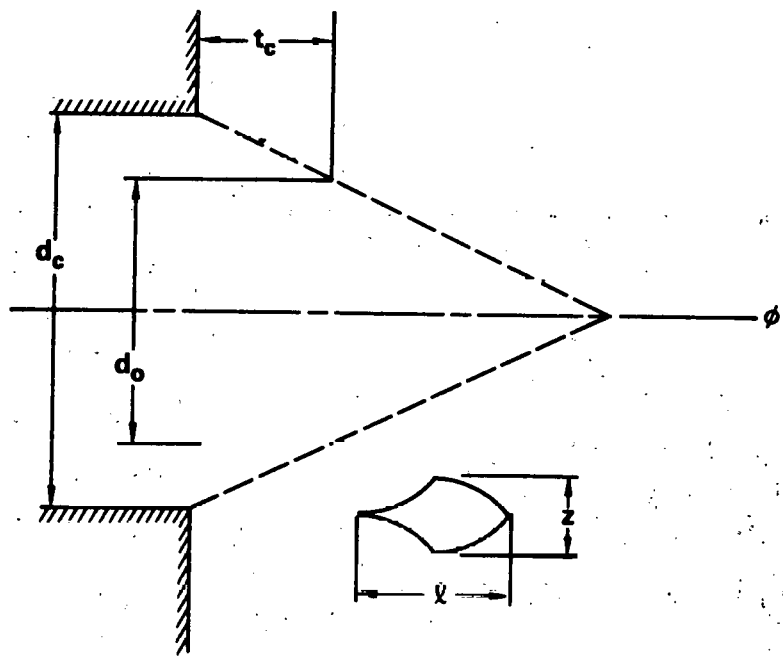

FIGURE 2. Sketch of Geometry for Determining the Work Done, According to Equation (3).

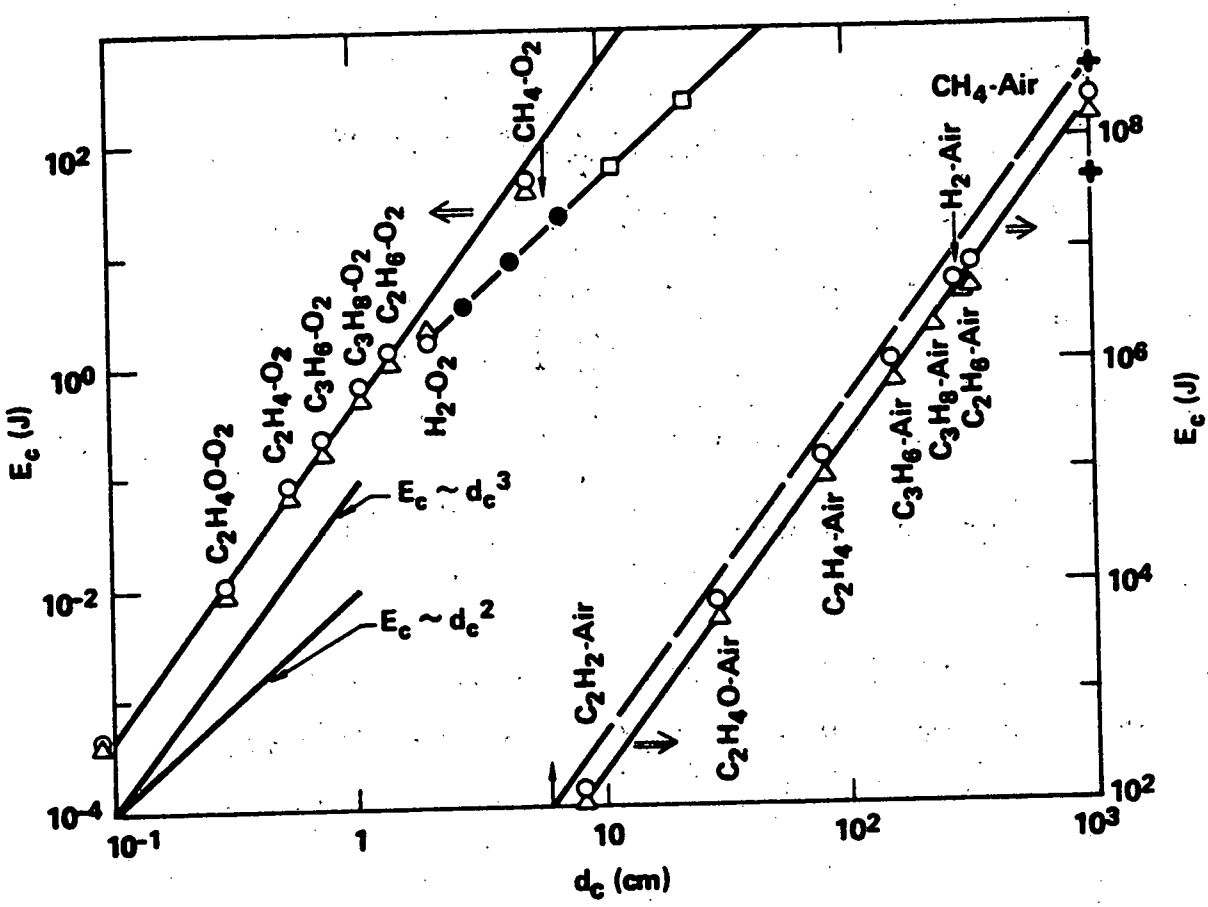

FIGURE 3. Critical Energy of Initiation As a Function of the Critical Diameter (○, values reported by Matsui and Lee (1978); △, present values obtained by Eq. (3); □, effect of P_o on E_c - d_c variation; +, range of prediction between Bull et al. (1976) and Westbrook and Haselman (1979)).

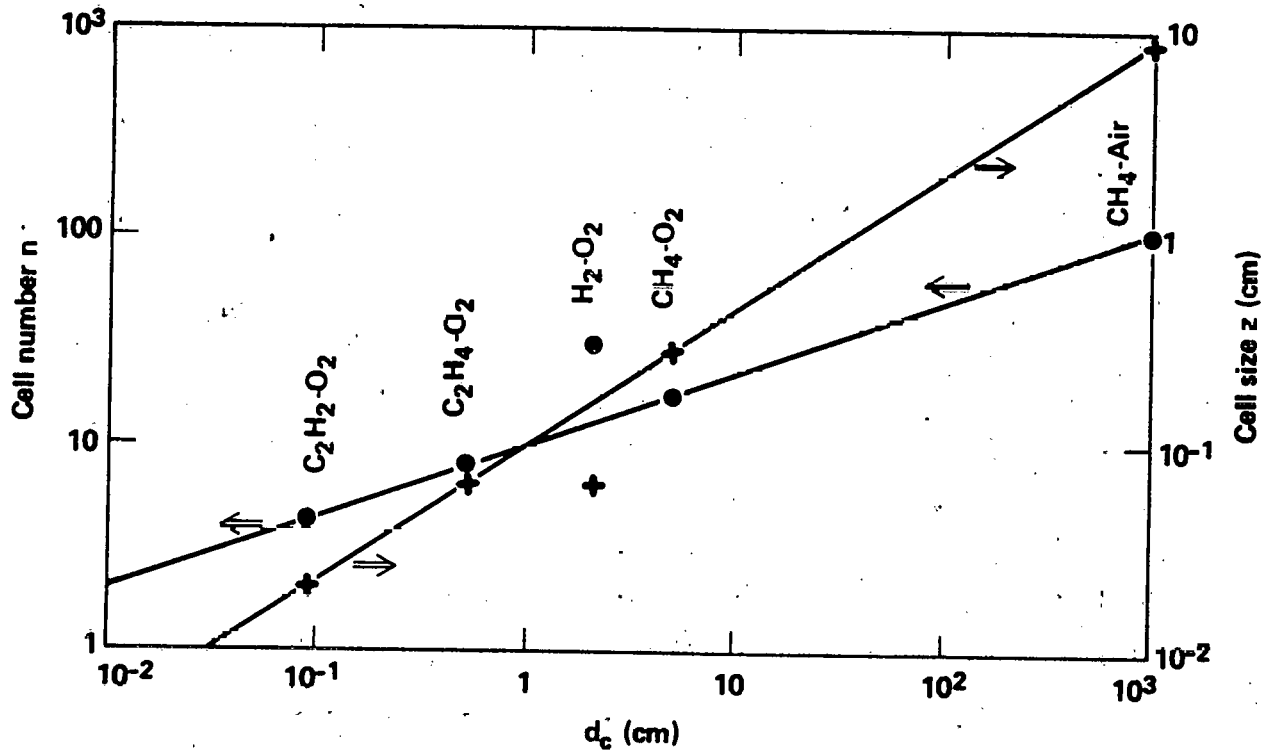

FIGURE 4. Plot of the Cell Size z and Cell Number n as a Function of the Critical Diameter for Various Mixtures.

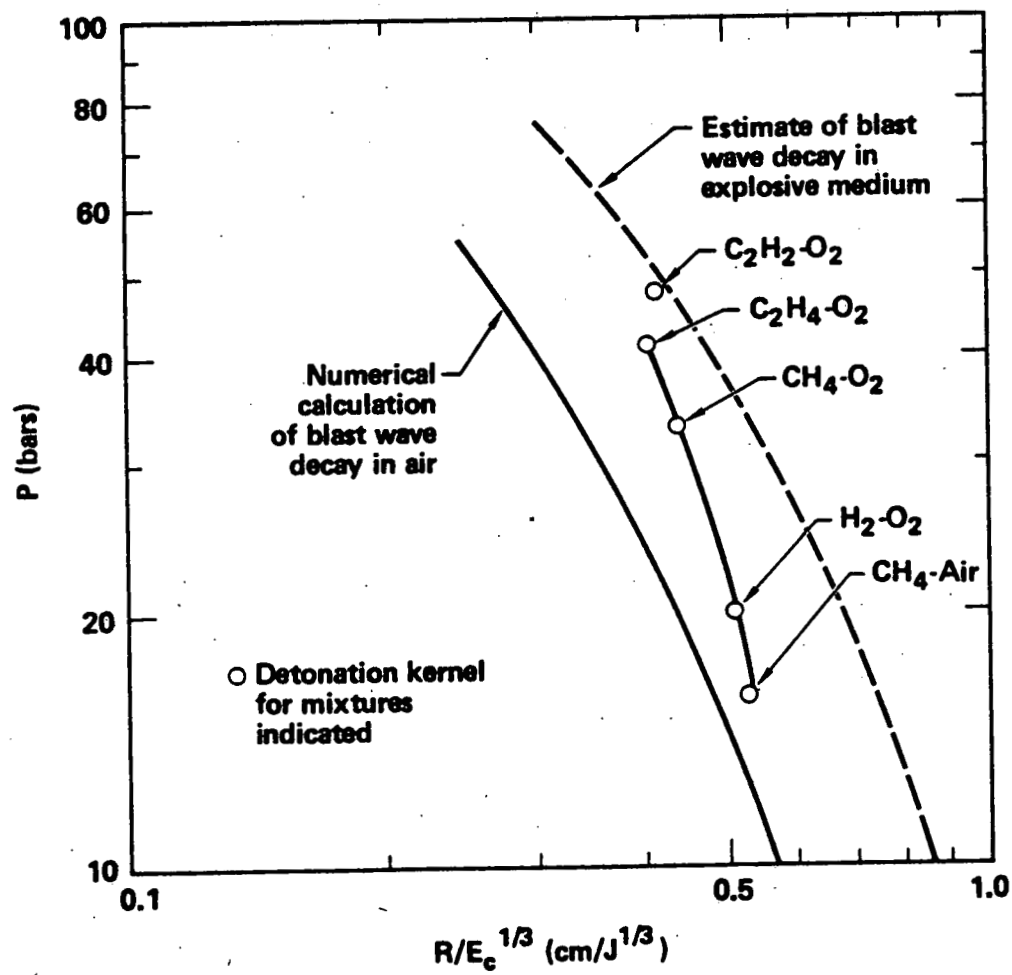

FIGURE 5. Plot of Blast Pressure P Versus the Reduced Radius $R/E_o^{1/3}$.

REPORT H

Computer Simulation of Combustion and Fluid Dynamics in Two and Three Dimensions

L. C. Haselman
J. B. Chase

Prepared for the
Environmental and Safety Engineering
Division
U.S. Department of Energy
under Contract W-7405-ENG-48

Lawrence Livermore Laboratory
Livermore, California 94550

THIS PAGE

WAS INTENTIONALLY

LEFT BLANK

REPORT H

TABLE OF CONTENTS

SUMMARY

This report gives a brief overview of computer codes developed by LLL to simulate unsteady gaseous combustion and fluid dynamic processes. Areas of application include pool fires, fireball formation and burn, and dispersion of fuel vapors both with and without wind.

Two codes are under development; the TDC (two-dimensional code) which models combustion and fluid dynamics in an axisymmetric or a two-dimensional Cartesian coordinate system, and the COM3 code, which uses a three-dimensional Cartesian coordinate system. Both codes use state-of-the-art finite differencing methods to solve the viscous hydrodynamic conservation equations. Although it is, in principle, feasible to obtain an accurate solution to these equations, in practice, the number of zones required is too great for even the largest computers. Thus coarse grids are used with subgrid-scale gas motions being simulated by a turbulence model. Because turbulence models are inherently empirical, the computer models must be chosen carefully and validated against experimental data.

Preliminary computations have been made of pool fires and fireball formation using the TDC code; however, these calculations cannot yet be considered predictive. The primary application of the COM3 code will be plume combustion.

OVERVIEW OF COMPUTER CODES

For several years we have been developing computer codes for simulating unsteady gaseous combustion and fluid dynamic processes. These include the TDC (two-dimensional combustion) code, which models combustion and fluid dynamics in an axisymmetric or a two-dimensional Cartesian coordinate system, and the COM3 code, which uses a three-dimensional Cartesian coordinate system. Although originally intended for reciprocating internal combustion engines,[1] these codes were developed with sufficient generality to be easily adaptable to other fields of combustion, including many problems of interest for liquefied energy fuels (LEF). Areas of application include pool fires, fireball formation and burn, and dispersion of LNG vapors both with and without wind.

Both TDC and COM3 use state-of-the-art finite differencing methods[2,3] to solve the viscous hydrodynamic conservation equations. These equations may be written as follows:

Conservation of mass

$$\frac{\partial \rho}{\partial t} + \vec{\nabla} \cdot (\rho \vec{v}) = S$$

Conservation of momentum

$$\rho \frac{\partial \vec{v}}{\partial t} + \rho \, (\vec{v} \cdot \vec{\nabla}) \, \vec{v} = - \vec{\nabla} P + \vec{F} + \vec{\nabla} \cdot \overline{\overline{\tau}} + S_v$$

Conservation of energy

$$\rho \frac{\partial \epsilon}{\partial t} + \rho \, (\vec{v} \cdot \vec{\nabla}) \, \epsilon + P \, \vec{\nabla} \cdot \vec{v} = - \vec{\nabla} \cdot q + \overline{\overline{\tau}} : (\vec{\nabla} \vec{v}) + W$$

Conservation of species

$$\rho \frac{\partial Y}{\partial t} + \rho \, (\vec{v} \cdot \nabla) \, Y_i = \vec{\nabla} \cdot (\rho D_i \vec{\nabla} Y_i) + S_i + K_i$$

where ρ, $\vec{v}$, Σ, and Y_i are the density, velocity, internal energy, and mass fraction of the $\underline{i}$th species. $\bar{\bar{\tau}}$ is the viscous stress tensor, q is the heat flux from thermal diffusion, $\vec{F}$ is an external body force, and S, S_v, S_i are sources of mass, momentum, and species, respectively. W and K_i are the rates of change of energy and species due to chemical reactions. D_i is the species diffusion constant.

Also needed is an equation of state for the fluid. In most cases this will be an ideal gas equation of state given by

$$P = (\gamma-1)\ \rho\ \epsilon$$

where γ is the ratio of specific heats.

In addition to the basic differential equations, there are constraints needed to satisfy overall continuity. These are:

$$\Sigma\ Y_i = 1$$

$$\Sigma\ S_i = S$$

$$\Sigma\ K_i = 0$$

$$\Sigma\ \vec{\nabla} \cdot (\rho D_i \vec{\nabla} Y_i) = 0 \quad .$$

From these equations are derived differencing equations in time and space. Although it is technically feasible to use these differencing equations to achieve an accurate solution to the differential equations, in practice the number of zones needed to define the grid is so great as to be prohibitive for even the largest computers. Coarse grids are therefore used, the subgrid-scale gas motions being simulated by a turbulence model. Since turbulence models are inherently empirical and rely on a data base for validity, one must be careful in applying them to LEF to choose appropriate models and validate them against experimental data. An important part of the modeling effort is to determine that the model correctly accounts for turbulence on several different scale sizes and under different initial conditions, so the code may be used to extrapolate to large-scale spills for which there are no experimental data.

In applying TDC and COM3 to wind dispersion of LEF vapors, preliminary numerical sensitivity studies have shown the problems to be inherently three-dimensional. Thus, most of the effort in this area must be directed toward COM3. One aspect that can be studied two-dimensionally is the gravity spread of vapors under calm conditions.

In addition to the basic conservation equations, models are needed for the phenomena that will affect the dispersion of LEF vapors. These include pool spread and vaporization, humidity, heat addition due to radiation from the ground and sun, and convective heat transfer from the ground or water. To simulate combustion processes, one must solve equations for the kinetics of the chemical reaction of the fuel and oxidizer. Such chemical kinetics for even the simplest hydrocarbons are extremely complex, requiring the simultaneous solution of a large set of differential equations. Because a large amount of computer time would be needed for accurately solving the chemical kinetics in two and three dimensions, these calculations are not practical at present. The approach now used is a simplified scheme whereby one adjusts the parameters until the results agree with experiments or with more accurate calculations by complex nondimensional or one-dimensional chemical kinetic models. This is an acceptable and computationally efficient method for chemical kinetics; however, it does not have the generality of the more complex method and may not yield accurate results if applied to situations other than that for which it was developed.

There are two types of chemical kinetics used by TDC. The first is a one-step reaction scheme in which the fuel plus oxidizer goes to products and the reaction rate is controlled by

$$\frac{dC_i}{dt} = -AT^{\delta}e^{(-B/T)}C_i^{\alpha}C_2^{\beta}$$

where C_i is the molar fuel concentration, C_2 is the molar oxygen concentration, T is the temperature, and A, B, α, β, and δ are constants. The second is a more sophisticated model from Creighton[9] that reacts methane with oxygen to produce intermediate radicals, which then react with oxygen to produce products. In COM3 it is expected that only the simple one-step scheme will be used, at least initially.

Most practical combustion problems involve the propagation of a turbulent flame. The interaction between the turbulence, which may be created by the flame or associated with the medium through which the flame propagates, leads to flame velocities that are significantly faster than laminar flame velocities. The interaction between the flame and the turbulence is a complex process that is only qualitatively understood. At present there is no adequate model to predict turbulent flame velocities, so these velocities must be determined experimentally. If one knows the turbulent flame velocity, the various parameters in the chemical kinetics and the turbulence models in TDC and COM3 can be adjusted to produce the observed flame velocity; the codes then can be used to study the fluid dynamic motions resulting from that flame velocity.

Two combustion applications for which TDC may be used are pool fires and fireball formation. It may also have limited utility in studying plume burn. Preliminary calculations of these phenomena have been done with TDC; however, these calculations cannot yet be considered predictive. The primary combustion application for COM3 will be plume combustion.

REFERENCES

1. C. K. Westbrook and L. C. Haselman, "Computer Modeling of Automotive Engine Combustion," Proceedings National Computer Conference, Anaheim, California, June 1978.

2. R. B. Debar, Fundamentals of the KRAKEN Code, Lawrence Livermore Laboratory, Livermore, CA, Internal Document UCIR-760 (1974). Readers outside the Laboratory who desire further information on LLL internal documents should address their inquiries to the Technical Information Department, Lawrence Livermore Laboratory, Livermore, California 94550.

3. L. C. Haselman, TDC-A Computer Code for Calculating Gaseous Combustion in Two Dimensions, Lawrence Livermore Laboratory, Livermore, California (report in preparation).

4. J. R. Creighton, "A Two-Reaction Model of Methane Combustion for Rapid Numerical Calculations," Paper 77-44, Western States Section, The Combustion Institute, Stanford, CA, October 17-18, 1977.

REPORT I

LNG Release Prevention and Control

P. J. Pelto
E. G. Baker
T. B. Powers
S. L. Weber
G. H. Holter
A. M. Schreiber

Prepared for the
Environmental and Safety Engineering
Division
U.S. Department of Energy
under Contract DE-AC06-76RLO 1830

Pacific Northwest Laboratory
Richland, Washington 99352

THIS PAGE

WAS INTENTIONALLY

LEFT BLANK

CONTENTS

TABLES

FIGURES

1.0 SUMMARY

This report summarizes results of the LNG Release Prevention and Control (RPC) Task in the LNG Safety Studies Project conducted by Pacific Northwest Laboratory (PNL). The basic objective of the RPC task is to develop an adequate understanding of LNG release prevention and control systems and the factors which may nullify their usefulness.

Scoping assessments have been completed of the typical release prevention and control systems used in LNG facilities. Summaries of these assessments are included in this report. Building upon the scoping assessments more detailed assessments of a reference LNG import terminal and peakshaving facility release prevention and control systems have been initiated. Release prevention systems have been emphasized and the progress to date is described. A study of LNG fire and vapor control systems has been initiated. Future plans in this area are discussed.

The scoping assessments have identified some general areas which merit consideration in more detailed analyses. These include human factors in LNG operations, LNG storage tank operations, and data gathering. Separate studies have been initiated in these areas and future plans are described.

THIS PAGE

WAS INTENTIONALLY

LEFT BLANK

2.0 INTRODUCTION

The LNG industry employs a variety of release prevention and control mechanisms which contain LNG during transfer and storage and which detect and control an LNG release if it occurs.

The LNG Release Prevention and Control Task in the LNG Safety Studies Project was initiated in late FY-1978 with a basic objective of developing an adequate understanding of LNG release prevention and control systems and the factors which may nullify their usefulness. Some more specific objectives include:

- Identifying the important features and possible weak links of release prevention and control systems.
- Identifying data needs and information gaps in the release prevention and control area and providing recommendations for obtaining the necessary additional information through data gathering, analytical studies and experimental studies.
- Identifying potential areas where release prevention and control systems can be effectively improved in terms of safety and cost/benefit.

A staged approach has been selected to accomplish the study objectives. A reference description of each type of LNG facility is developed. This system description is used to perform a scoping or first level analysis (initially a preliminary hazards analysis followed by a failure mode and effect analysis) to identify information needs and potential release prevention and control areas which may merit more detailed study. The feasibility and methods of of obtaining the required additional information are investigated and a decision is made whether to perform a more detailed assessment (possibly a refined failure mode and effect analysis or, if the system detail and data warrant it, a fault tree/event tree type analysis). In conjunction with this assessment, analytical and experimental studies are recommended to fill information gaps.

This report summarizes the status of this project as of the second quarter of FY-1980. (The reader is referred to DOE/EV-0036 for an earlier status report.)

The scoping assessments for each of the basic types of LNG facilities have been completed. These include:

- Export Terminal
- Marine Vessel
- Import Terminal
- Peakshaving Facility
- Truck Tanker
- Satellite Facility

These assessments consist of a reference system description, a preliminary hazards analysis (PHA), and a list of representative release scenarios. The emphasis of the scoping assessments is the release prevention area. Summaries of the scoping assessments are given in Section 3. After reviewing the scoping assessments, a decision was made to concentrate on the import terminal and the peakshaving facility for the more detailed analysis phase. A summary of ongoing work on these two facilities is given in Section 4. Section 5 discusses planned work for the remainder of FY-1980.

3.0 SCOPING ASSESSMENTS

This section presents a summary of the scoping assessments of the release prevention and control systems of the basic types of LNG facilities. The initial emphasis of the scoping assessments is the release prevention area. The basic objectives are to identify important release prevention features that may merit more detailed study and to identify data needs and information gaps.

Each scoping assessment report includes a reference system description, a preliminary hazards analysis (PHA), and a list of representative release scenarios. The system description outlines the basic process flow, plant layout, and process description. The PHA identifies the critical release prevention operations. The list of representative release scenarios provides a format for discussing potential initiating events, effects of the release prevention and control systems, information needs, and possible design changes to prevent or reduce the consequences of a potential release. The representative release scenarios will form the basis for the next stage of analysis.

The scoping assessments of the import terminal and the peakshaving plant are summarized in a fair amount of detail. The export terminal, marine vessel, and satellite facility scoping assessments are briefly summarized.

3.1 SCOPING ASSESSMENT OF LNG IMPORT TERMINAL RELEASE PREVENTION AND CONTROL SYSTEMS

3.1.1 Reference Import Terminal System Description Summary

This section provides a brief summary description of each of the major operations included in the import terminal. More detail is included in the reference import terminal system description which is not included here but will be published in the final report. Figure 1 illustrates the basic operations in the import terminal. They are the marine terminal, the storage system, and the vaporization system.

Marine Terminal

The marine terminal for the LNG import facility consists of a dock and a 6,000-ft trestle supporting a roadway and four transfer lines. The four major transfer lines include a 42-in. main LNG transfer line from the trestle to the

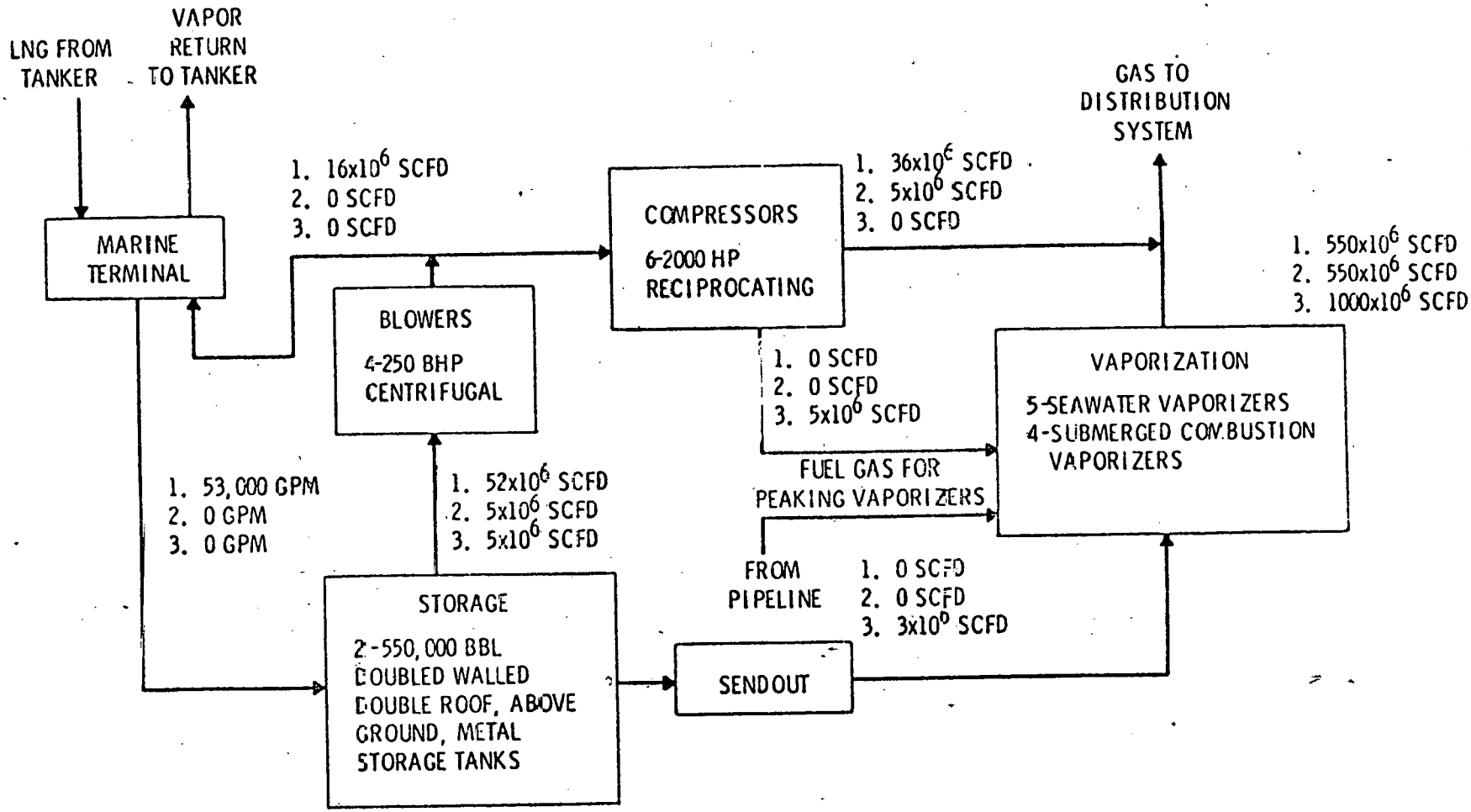

1. TANKER UNLOADING
2. NORMAL OPERATING CONDITIONS
3. PEAKING OPERATIONS, NO TANKERS UNLOADING

FIGURE 1. Block Flow Diagram for Reference LNG Import Terminal

LNG storage facility, a 16-in. vapor return line to maintain adequate pressure in the ship's storage tanks, a 4-in. LNG recirculation line to maintain the LNG unloading transfer lines cold when not unloading a vessel, and a 10-in. Bunker "C" fuel oil line.

Four 16-in. diameter articulated LNG loading arms are located on deck at the terminal. The loading arms connect with a 24-in. transfer line. Two sets of four 24-in. lines connect to a 42-in. header which ties into the 42-in. transfer line.

The marine terminal includes enough berths to accommodate two vessels, one on each side of the trestle. However, only one ship can unload at a time. A control tower overlooking the ship unloading operations is also included at the terminal.

Storage System

LNG storage consists of two flat-bottom, double-walled, above-ground LNG storage tanks with a capacity of 550,000 bbl each. The inner tank is constructed of 9% nickel-steel which possesses excellent low temperature ductility. The outer tank is constructed of carbon steel, which possesses a very poor low temperature ductility. The dimensions of the tank are as follows:

inner diameter:	230 ft
outer diameter:	239 ft
inner shell height:	75 ft, 1 in.
outer tank shell height:	85 ft
overall tank height:	130 ft, 6 in.

The high liquid level of LNG in the tank is approximately 74 ft, 10 in.

Expanded perlite, a nonflammable material, is maintained in the annular space between the inner and outer shells as insulation. A resilient fiberglass blanket is wrapped around the outside of the inner shell to alleviate perlite compaction due to normal movement of the inner shell. Foamglass blocks, a load-bearing insulation, are employed as insulation for the tank bottom.

A 4-ft thick reinforced concrete slab supports each tank. An electrically heated sandbed is located between the tank and the concrete slab. This prevents

the soil from freezing beneath the tank and causing frostheave. Engineered fill is located directly beneath the slab.

The tanks are designed to withstand instantaneous wind gusts up to 104 mph, earthquakes of up to 7 on the Richter scale, and a maximum horizontal acceleration of 0.21 g. All piping to the inner tank enters through the roof of the storage tank.

A concrete dike wall surrounds each storage tank. Each dike will hold approximately 1-1/3 times the capacity of one storage tank. The inside of the dike wall is lined with insulating material to reduce the evaporation rate of LNG in the event of a tank failure.

A weather shield extends from the top of the concrete dike to the outer tank roof in order to keep precipitation from falling into the annular space.

Normal tank boiloff and vapors from LNG tanker unloading are handled by a vent gas compressor system. Storage tank pressure is maintained by returning vapors from the vent gas compressor. Excess vapors are compressed by fuel gas and pipeline compressors to be used as fuel or for delivery to the gas transmission pipeline.

Vaporization System

Vaporization for the import terminal includes two major types of vaporizers: falling-film open-rack seawater vaporizers and submerged combustion gas-fired vaporizers. These vaporizers provide the plant with a total output capacity of 1 billion scfd of gas.

Baseload vaporization occurs in five falling-film open-rack seawater vaporizers with a total capacity of 550 MMscfd. LNG is introduced through manifolds at the bottom of banks of vertical panels constructed of special extruded fins. The LNG passes upward inside the tubes where it is heated by the water which falls as a film over the outside of the panels. LNG emerges in its gaseous form at the top.

The falling water film used in this design gives extremely high heat transfer coefficients, which reduces the amount of ice formed, thus maintaining high performance. With this open type of system the amount of ice which is formed

does not interfere with the flow of water. The panels of finned tubes and all parts in contact with the LNG are made of aluminum alloy, which maintains its strength at low temperature.

For standby or peaking vaporization, four submerged gas-fired vaporizers are used having a total capacity of 450 MMscfd. The gas-fired vaporizers are used approximately 800 hours per year.

The gas-fired vaporizers are designed such that the burners exhaust hot combustion gases downward through a downcomer and into a water bath below the liquid surface. The exhaust forms bubbles in the water causing turbulence. mixing, and a "lifting" action. This lifting action forces the water up at a high velocity through an annular space created by a weir around the downcomer. The water flows over the top of the weir and into the more quiescent tank. A heat exchanger tube coil for the LNG is located in the annular space between the weir and the downcomer where it is scrubbed by the warm gas-water mixture thus transferring the heat to the LNG and vaporizing it. The vaporizers consume between 1.5% and 2.0% of the LNG vaporized as fuel.

The inlet piping, all piping that comes in contact with the LNG feed stream inside the vaporizers and outlet piping to the first flange are all stainless steel construction on both the seawater and gas-fired vaporizers. An independent containment dike is included in the seawater vaporizer area to accommodate any LNG release that might occur.

Compressors and Sendout Pumps

This section of plant includes all the equipment operating at high pressure up to 1300 psig. There are ten major compressors at the facility: four, centrifugal boiloff compressors which take suction of the storage tanks and boost the gas to 10 psig; three two-stage reciprocating fuel gas compressors which take gas from the boiloff compressors and increase its pressure to 150 psig; and three, two-stage, reciprocating pipeline compressors which compress the gas to 1300 psig. Only the boiloff compressors run cold. A fuel gas preheater heats the boiloff before it enters the fuel gas compressors.

Each storage tank contains two submerged primary sendout pumps which boost the LNG to 60 psig. These are followed by 10 secondary pumps. The secondary pumps are submersible, pot-mounted, 15-stage units which raise the LNG up to 1330 psig.

Safety Systems

The plant emergency shutdown system (ESD) has three shutdown circuits: the Master Emergency shutdown (MES), the Vaporizer Emergency Shutdown (VES), and the Loading Emergency Shutdown (LES). These systems automatically shutdown and isolate portions of the facility or the whole facility in the case of the MES. It takes about 30 seconds to shutdown the plant once the ESD is activated. The shutdown systems are activated by detectors located throughout the plant, by certain process control variables or by the plant operator.

Combustible gas detectors, UV flame detectors and temperature sensors are located throughout the plant area. These detectors activate alarms which indicate the exact location of a spill or fire on a graphic panel in the control room.

The fire control system consists of fixed and portable dry chemical extinguishers, expansion foam systems, and a fire water system.

3.1.2 Reference Import Terminal System Level Analysis

The purpose of the system level analysis is to identify those sections of the import terminal that are most critical with respect to release prevention and control. This was accomplished by identifying the flow rate and inventory of LNG or LNG vapor in the appropriate area to be considered. Containment/confinement barriers which prevent spills or releases were identified.

Process operating conditions including flow rates, temperature, pressure, and pipeline sizes for all sections of the import terminal are presented in Table 1.

Marine Terminal and Unloading System

The primary hazards involved in handling LNG at a marine terminal are the flammability of the gas and the cold temperature of the liquid.

TABLE 1. System Capacities and Flow Rates

System	Component	Number of Components	Flow Rate		Operating Condition	
			In	Out	Pressure (psig)	Temperature (°F)
Marine Terminal and Unloading System	42-in. LNG transfer line	1	53,000 gpm	53,000 gpm	100	-258
	4-in. LNG recirculation line	1	1,500 gpm	1,500 gpm	60	-258
	16-in. vapor return line	1	16 MMscfd	16 MMscfd	10	-152
Storage	Storage tank	2	53,000 gpm	4,550 gpm	0.8	-258
Sendout Pumps	Primary in-tank pumps	2/tank	4,000 gpm	4,000 gpm	60	-258
	20-in. tank outlet line	1/tank	4,000 gpm	4,000 gpm	60	-258
	Secondary pumps	10	8,550 gpm	8,550 gpm	1,300	-252
	25-in. secondary pump sendout line	1	8,550 gpm	8,550 gpm	1,300	-252
Vaporization System	Seawater vaporizers	5	4,550 gpm	550 MMscfd	1,300	-252 to 30
	Submerged gas-fired vaporizers	4	3,720 gpm	450 MMscfd	1,300	-252 to 30
Compressors	Boiloff compressor	4	26-52*MMscfd	26-52 MMscfd	10	-200 to 152
	Fuel gas compressor	3	5-36 MMscfd	5-36 MMscfd	150	285
	Pipeline compressor	3	5-36 MMscfd	5-36 MMscfd	1,300	120

* Flowrate during unloading operations.

The unloading section includes two primary methods by which LNG or natural gas can be potentially released from the system:

- leak or rupture in valves, pipes, fittings, loading and transfer arms, etc.
- pressure relief valve discharges from transfer lines

A containment system is located under the unloading platform to hold all spills from the loading arms. Transfer line drain valves are included in the transfer line so it can be drained into the containment system under the dock. Any release of LNG between the terminal and shore would fall into the ocean. A containment barrier follows the ship unloading line from shore to the storage tanks. Because of the size of the transfer line and the high flow rates a single leak or break can result in a large spill. The maximum release in the marine terminal area is approximately 880,000 gallons for a large rupture of the 42-in. transfer line.

Storage System

There are three primary methods for a potential release in the storage area:

- storage tank failure
- leak or rupture from inlet or outlet piping, flanges, valves, fittings, etc.
- atmospheric discharge from a relief valve

The inner container of the LNG storage tanks is constructed of 9% nickel steel, suitable for operating at cryogenic temperatures. The outer tank is constructed of carbon steel and is susceptible to fracture if contacted with any LNG or cold vapors. Each LNG storage tank has an insulated concrete dike wall to contain any spills of LNG from the tank. Failure of the inner tank would eventually lead to failure of the outer tank. Flow rates into and out of each tank are included in Table 1.

Each tank has pressure and vacuum relief valves to protect against failure of the tank from overpressure and underpressure. An auxiliary gas supply system also protects the tanks from underpressure. Activation of the master emergency shutdown automatically stops all flows into and out of the tanks and isolates them from the rest of the plant.

LNG Vaporization System

Vaporization occurs in two types of vaporizers, falling-film open-rack seawater vaporizer, and submerged gas-fired vaporizer. The gas-fired peaking vaporizers operate approximately 30 days/yr. Table 1 gives inventories, flow rates, and process operating conditions for each type of vaporizer.

Primary methods for a potential LNG and LNG vapor release include:

- leak or rupture from inlet and outlet piping, valves, flanges, fittings, etc.
- leaks from vaporizer heat transfer tubing or coils

A containment dike surrounds the vaporizer area to contain any spills that might occur there. The vaporizers are connected to the Vaporizer Emergency Shutdown (VES) circuit. When activated, this system shuts down the feed pumps to the vaporizers, isolates the vaporizers from the rest of the plant and vents all gas handling equipment to the vent header. The VES is automatically activated by the loss of seawater flow, by high water temperature, by low outlet gas temperature, and by UV flame detectors in the area. It also can be activated manually from the vaporizer area as well as the control room. Activation of the MES automatically activates the VES.

The maximum release in this area would probably result from a failure of the 24-in. liquid transfer line from the secondary pumps to the vaporizers. A release of 105,000 gal of LNG is estimated as the maximum spill size that can occur from this area. This assumes the VES is not activated or fails to function properly. If the VES operates as designed the spill would be limited to 23,000 gallons. Failure of the VES can also result in failure of the vaporizer outlet lines in the event of loss of seawater or fuel gas. The cold LNG could then contact the carbon steel outlet lines and cause them to crack.

Compressors and Sendout Pumps

The hazards involved with operation of this equipment are the cold temperature of the LNG, the flammability of the LNG vapor, and the high pressure at which some of the components operate.

There are two general means by which LNG or LNG vapor can be potentially released from these systems:

- failure of piping, valves, fittings, etc.
- failure of the compressors or pumps

When activated, the Master Emergency Shutdown (MES) and the Vaporizer Emergency Shutdown (VES) stops the LNG sendout pumps and isolates them from the storage tank and the vaporizers. The MES also stops and isolates the compressor systems. The secondary pumps are located in their own diked area which has a dry chemical fire extinguishment system and high expansion foam system.)

The maximum spill in this area of the plant is approximately 23,000 gallons assuming the MES is activated promptly and functions as designed. The spill could be as large as 100,000 gallons if the system has to be shutdown manually.

3.1.3 Reference Import Terminal Component Level Analysis

Information generated from the system level analysis indicates a significant release could come from any of the four systems analyzed. The largest releases could come from the storage and ship unloading systems.

A preliminary hazards analysis has been completed on each system previously discussed. The preliminary hazards analysis for the major components in each system analyzed are presented in tabular form. This includes potential hazards, effects, and existing preventive controls. The PHA for the unloading system is given in Table 2.

Unloading

The unloading system may be the most critical system at the terminal. Extremely high flow rates combined with natural forces such as, large waves, winds, earthquakes, etc., that could be encountered with this system make it an area of safety interest.

The following components were determined to be the most important with respect to release prevention and control.

- The 42-in. Diameter Transfer Line. This line includes various valves, expansion joints and other fittings. A leak or rupture in this line could result in a large spill.

TABLE 2. Preliminary Hazards Analysis for the Marine Terminal

Component	Potential Hazard Condition	Effect	Existing Preventive and Control Measures
16-in. loading Arm	Fissure or break	LNG release	A spill containment system is provided under the loading arms
			Closing at appropriate loading arm block valve
			LNG remaining in line is drained
24-in. pipe prior to air-operated valve	LNG surge	Possible increase in pressure	Regulation of ship's pumps, release through pressure relief valve in 24-in line
	Fissure or break	LNG release	A spill containment system is provided under the loading arms
			Closing of appropriate loading arm block valve
			LNG remaining in line is drained
16-in. loading arm	Bad flange connection with ship	LNG release into water	Shutdown of pumps
24-in. pipe directly after air-operated valve	Fissure or break	LNG release	Activation of loading ESD system unless there are valves in the liquid header to isolate each 24-in. line from each other
42-in. liquid header	Fissure or break	LNG release	Drainage of LNG remaining in the lines
Air-operated valve	Failure to close if break occurs in the line rupture	LNG release and unable to isolate 24-in. line and loading arms	Loading ESD system activated
			Drainage of LNG remaining in the lines
	Rupture	LNG release	Activation of loading ESD system
Unloading lines	Blockage or restriction of line	LNG flow is backed up or stopped	Closing of appropriate valves to isolate problem if not in main liquid header
			Pressure buildup released through pressure safety valve
			Drainage of LNG in line
42-in. liquid transfer line	Fissure or break	LNG release	Activation of marine ESD system
			Remaining LNG is drained

TABLE 2. (contd)

Component	Potential Hazard Condition	Effect	Existing Preventive and Control Measures
16-in. vapor return line	Fissure or break during recycle to cooldown lines	LNG release	Loading ESD system is activated, drain LNG
	Fissure or break during vapor return	LNG vapor release	Isolation of damage by closing appropriate block valves
			Activate loading ESD system
	Increased vapor return flow rate	Pressure buildup	Activation of the inline pressure safety valve
Vent gas compressor	Failure to operate (all)	No vapor return to ship	Activation of the loading ESD system
LNG tanker	Any hazardous condition		Release of loading arms from ship
			Activation of the loading ESD system
Marine trestle	Large winds or earthquake	Possible collapse of trestle	Activation of Master ESD System
4-in. recirculation line during recirculation	Fissure or break	LNG release	Isolation of damage by closing appropriate valves
			Shutdown of primary pumps
			Drainage of LNG
Valves in dock drain lines	Rupture or leak	LNG release to dock drain	Activation of the loading ESD system
	Failure to open	Can't drain loading arms	
	Failure to close	LNG release to dock drain	Activation of the loading ESD system
9% Ni-steel inner barrier	Fissure or break	LNG leakage into annular space	Activation of Master Emergency Shutdown System
		Possible collapse of exterior barrier	LNG spill can be contained by an insulated concrete dike capable of holding 1.34 times the tank capacity
Insulation	Heat leak	Pressure buildup	Boiloff compressors handle smaller amounts of pressure buildup
			Buildup in boiloff line can be handled by the vent stack header
			Pressure relief valves discharge vapor to the atmosphere in the case of an excessive pressure buildup

TABLE 2. (contd)

Component	Potential Hazard Condition	Effect	Existing Preventive and Control Measures
Carbon steel outer barrier	Fissure or break	Heat leak could crack and collapse the tank	LNG spill contained by an insulated concrete dike
		Pressure gradient from inner tank to annulus due to vapor release of annulus	A pressure gradient equilibrated by the vapor return line
Electrical heater for storage tank	Failure to operate	Possible soil freezing resulting in frost heaving, storage tank collapse, LNG spill, possible dike collapse	Activation of Master Emergency Shutdown System
Vent gas compressor	Failure to operate (all of them, no backup available)	Unable to return vapor to the storage tank, possible under-pressurization	Activation of Master ESD System If the pressure drops below 0.15 psig, a backup gas system supplies LNG from the gas transmission pipeline to the storage tank If the pressure reaches 0.031 psig, three 12-in. vacuum relief valves open to the atmosphere
	Fails to turn off	Overpressurization	Activation of MESD If pressure reaches 1.5 psig, three 12-in. pressure valves open to the atmosphere Pressure of vacuum safety valves are frequently checked to insure operation
Storage tank and dike	Large earthquake (7 on Richter scale)	Large LNG spill	
Loading Emergency Shutdown System	Fails to activate upon demand	The unloading system would not shutdown automatically in an emergency	Operator detects malfunction and responds

- The Loading Arms and Ship Coupling Mechanism. The ability of the loading arms to maintain their mobility is important. Redundant sensing devices are included with each arm that detect excessive motion and automatically activate the Loading Emergency Shutdown, (LES) system. The thermal stresses the arms undergo is of safety interest as they are repeatedly warmed and cooled. A good connection between the loading arm and ship is also important.

- The Loading Emergency Shutdown (LES) System. This system can limit and control the amount of release that can occur. However, if this system does not operate properly and a manual shutdown is necessary, this can result in a significant increase in the amount of LNG released.

Storage

Components of primary interest as identified by the PHA are as follows:

- Pressure Control System. This system includes the boiloff compressor, the pressure/vacuum relief valves, and pressure controllers and indicators on inlet and outlet lines.

- LNG Level Indicators and Alarms. These components sound an alarm in the control room and activate the Master Emergency Shutdown System to prevent overfilling the storage tank.

- Outer Shell. This carbon steel shell protects the inner shell and insulation from the environment and surroundings.

- Annular Space Insulation. This prevents excessive boiloff of LNG vapors. The insulation also protects the carbon steel outer tank from being exposed to the cryogenic temperature of the LNG.

- Inner Shell. This 9% nickel-steel is continually exposed to cryogenic temperatures. Thus, any failure of this tank could result in a complete storage system failure and release large quantities of LNG and LNG vapor.

Vaporization

Primary components of interest related to release prevention and control include the following:

- The Temperature Controllers and Alarms. These are probably the most important components related to release prevention and control in this system. The temperature controllers indicate the vaporized LNG temperature and adjust the incoming LNG flow rates, the seawater inlet rate in the seawater vaporizers, and the air/fuel rates and ratios in the gas-fired vaporizers. Any malfunction of these controllers could result in a hazardous situation possibly releasing significant quantities of LNG or LNG vapor.
- Vaporizer Inlet Lines. A leak or rupture in any vaporizer inlet line releasing cold LNG could possibly cause failure of other components in the system that are not designed to withstand the extreme cold.

Compressors and Secondary Pumps

Because of the high pressures and large flow rates a pipe failure in these areas can result in a large release and could spray cold liquid or vapor and result in failure of carbon steel components in the area. Components of primary interest with respect to release prevention and control are given below.

- Emergency Shutdown System. Proper operation of the ESD system can prevent or significantly reduce the size of releases in the vaporizer area.
- Secondary Pumps and 24-in. Sendout Line to Vaporizers. This system not only accommodates a large LNG flow rate, but operates at a very high pressure (1280 psig). A leak could spray LNG and possibly cause failure of some other component.
- Fuel Gas Preheater. Failure of the fuel gas preheater or temperature controllers could allow cold vapors to reach carbon-steel components resulting in the release of LNG vapor.

3.1.4 Conclusions and Recommendations

The scoping assessment of the import terminal has identified some important release prevention features that may merit more detailed study. The storage section and the unloading section of the import terminal have the potential for the largest LNG releases. Key storage section components include the inner and outer tank structure, the pressure control system, and the liquid-level

indicators and alarms. Important unloading section components include the transfer line, the loading arms and coupling mechanism, and the loading emergency shutdown system.

Utilizing the results of the scoping assessment, a list of representative release scenarios was developed and is shown in Table 3. It is recommended that these scenarios form the basis for a more detailed assessment of the import terminal release prevention and control systems. As an initiating point for a more detailed assessment, a preliminary analysis of these release scenarios was performed. Potential initiating events, effects of the release prevention and control systems, information needs, and potential design modifications which could prevent or reduce the consequences of a potential release were examined.

TABLE 3. Representative Release Events for an LNG Import Terminal

1. Failure of nine percent nickel-steel inner storage tank.
2. Failure of carbon-steel outer barrier for LNG storage.
3. LNG release from 16-in. loading arms.
4. Failure of 42-in. liquid transfer line from unloading dock to the storage tanks.
5. Failure of 20-in. LNG transfer line storage to the secondary pumps.
6. Failure of the 24-in. transfer line from the secondary pump to the vaporizers.
7. Seawater vaporizer failure.
8. Submerged combustion vaporizer failure.
9. Failure of vaporizer exit lines.
10. Failure of pipeline inlet compressor line.
11. Failure of 16-in. vapor return to ship's tanks.
12. Failure of 30-in. vapor line from pipeline compressors to gas transmission pipeline.

In performing the scoping assessment several areas requiring additional information were identified. Some of these are outlined below.

- Component Stresses from Thermal Cycling. Many components such as the storage tanks, valves, unloading arms, and transfer lines undergo a number of thermal cycles. Exactly how many cycles each component is designed to withstand needs to be determined.
- Terminal Piping Network. Details such as diameter, length, wall thickness, and materials of construction are needed for the components that make up the terminal piping.
- Structural Mechanics of the Storage Tank. The effect on the structural integrity of the tank relative to hazardous conditions is of major importance. Such conditions include overpressure, overfilling, and fire or explosion in the tank or nearby. A more detailed description of the heatup and cooldown procedures is necessary for a complete analysis to be accomplished.
- LNG Vaporizer Process Control. More details on the temperature and flow controllers are needed. Potential hazards and release prevention details relative to these controls are also needed. Additional details on the startup and shutdown procedures are required to complete the analysis in this area.
- Failure Rate Data. The scoping assessment of the import terminal did not explicitly consider the potential release frequency. A more detailed study of the export terminal release prevention, detection, and control systems must carefully consider the likelihood of the release initiating event and the reliability of the release detection and control systems. Due to the lack of operating experience of LNG facilities, little data is available for LNG equipment failure rates.

The next phase of the assessment of the import terminal release prevention and control systems is to perform more detailed analyses on the areas identified in this scoping assessment. The representative release scenarios will form the basis of this analysis. Additional emphasis will be placed on analyzing the effectiveness of the release detection and control systems.

3.2 SCOPING ASSESSMENT OF LNG PEAKSHAVING FACILITY RELEASE PREVENTION AND CONTROL SYSTEMS

3.2.1 Reference Peakshaving Facility System Description Summary

This section provides a brief summary description of each of the major operations included in the peakshaving facility. More detailed information is included in the reference peakshaving facility system description which is not included here but will be published in the final report. Figure 2 illustrates the basic operations in the peakshaving facility. They are gas treatment, liquefaction, storage, vaporization, and transfer and transportation operations.

Gas Treatment System

Natural gas from the pipeline first enters a filter separator to remove any free liquids. The 500-psia gas then passes through one of two molecular sieve adsorbers where moisture and CO_2 are removed. Each adsorber is capable of handling up to about 12 million scfd of gas. After passing through the adsorber, the gas is filtered to remove dust. About half the treated gas ($\sim$6 million scfd) is routed as feed to the liquefaction unit and the rest of the gas is used to regenerate the off-line adsorber. The regeneration gas is first heated to about 550°F in a gas-fired salt bath heater and is then passed through the off-line adsorber. Next, the regeneration gas is filtered to remove dust, cooled in a fan cooler, and passed through a separator to remove free liquids. The gas is then compressed back to line pressure (about 870 psia), cooled in another fan cooler to under 120°F, and then reintroduced into the pipeline.

Liquefaction System

After treatment, the natural gas is cooled and liquefied in a mixed refrigerant cycle to provide LNG for storage. The liquefaction unit is comprised of a cold box, refrigerant compressor and coolers, and refrigerant storage. The cold box contains heat exchangers, separator vessels, and associated piping and instrumentation, all enclosed in an insulated shell. All cold box equipment is constructed of stainless steel, except for the heat exchanger tubing which is aluminum. The natural gas feed enters the cold box

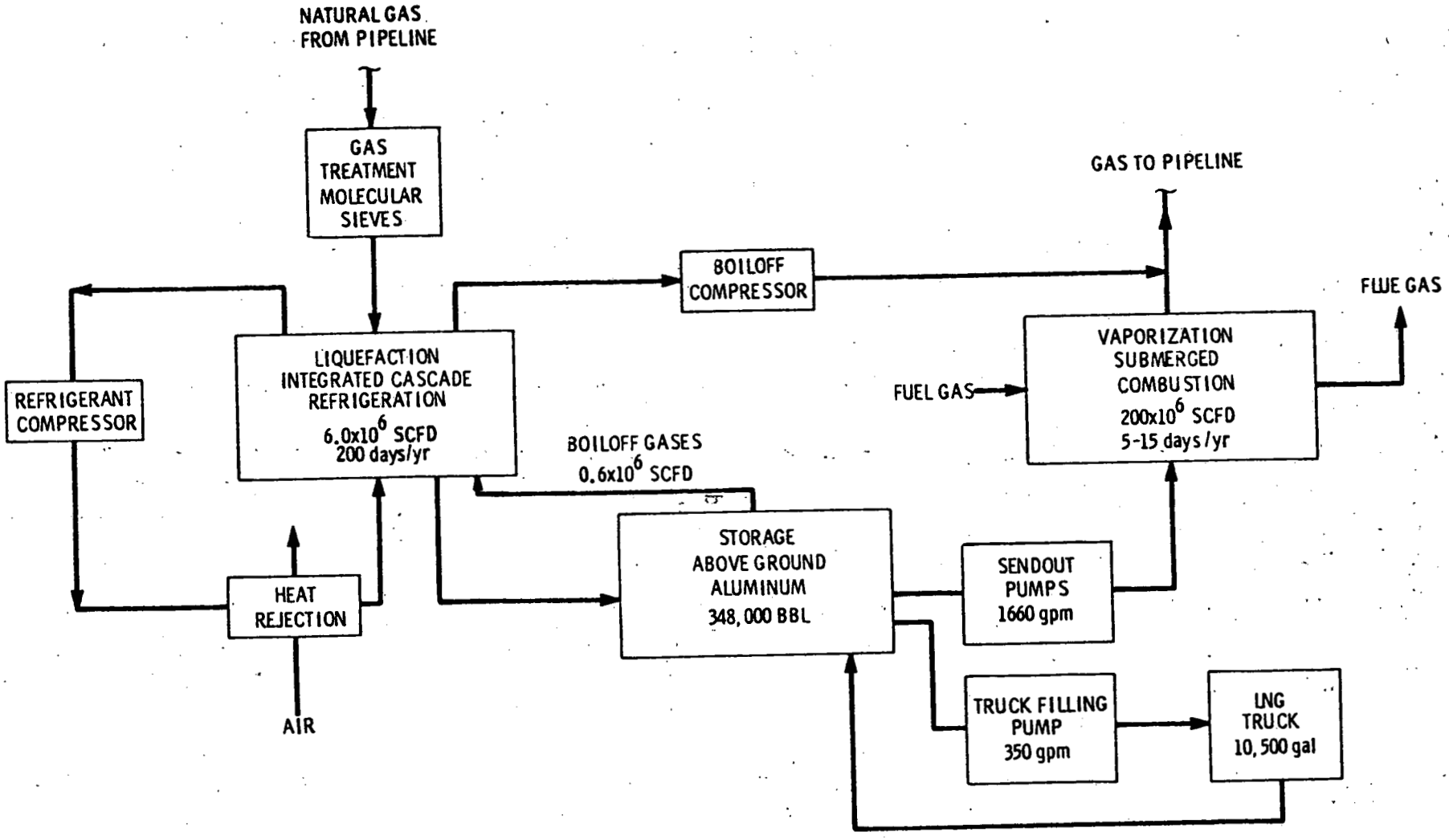

FIGURE 2. Block Flow Diagram for Reference LNG Peakshaving Plant

at about 500 psia and is passed through a series of six heat exchangers where it is progressively cooled until it is liquefied. The liquefied gas leaves the cold box at about -260°F and about 475 psia. It is let down to slightly above atmospheric pressure (~1 psig) as it is introduced into the storage tank.

The mixed refrigerant, which is made up of nitrogen, methane, ethylene, propane, butane, and pentane, is cooled and condensed in stages and then expanded to provide cooling in the cold-box heat exchangers. The refrigerant is then recompressed by a two-stage compressor with inter-and after-fan coolers for heat rejection. The boiloff gases from the LNG storage tank also provide cooling for the refrigerant in three cold-box heat exchangers.

Storage System

The LNG from the liquefaction system is stored in a flat-bottomed, double-walled, aboveground storage tank with a capacity of about 350,000 bbl. The inner shell of the tank is constructed of an aluminum-magnesium alloy which has excellent low temperature ductility. The outer shell of the tank is made of carbon steel. The tank dimensions are:

inner tank diameter:	164 ft
outer tank diameter:	173 ft
inner tank height:	97 ft
outer tank height:	134 ft.

The annular space between the inner and outer tank walls is filled with expanded perlite insulation, with a resilient fiberglass blanket adjacent to the inner wall to protect the perlite from excessive pressure due to expansion and contraction of the inner tank wall. The ceiling of the inner tank is a metal deck suspended from the roof of the outer tank. Perlite insulation is spread evenly over the deck. Open pipe vents are installed in the deck so product vapor can circulate freely in the insulation space to keep the insulation dry. The outer tank rests on a concrete ringwall foundation while the inner tank rests on load-bearing insulation placed on the foundation soil. Electric resistance heating coils prevent the soil underneath the tank from freezing.

The storage tank is designed to operate at 1.0 psig, with a maximum design pressure of 2.0 psig. The maximum external design pressure is 1.0 ounce gauge. Tank pressure is controlled by adjusting the boiloff compressor recycle rate. The tank is equipped with two pressure relief valves which vent to the atmosphere. In the event of an underpressure, gas from pipeline is brought back into the tank and, if underpressure limits are still exceeded, two vacuum relief valves admit air to the tank. In the event of an emergency, the tank is isolated by internal blockvalves on the inlet and outlet liquid lines. The liquid level in the storage tank is monitored by a servo-powered, displacer-type liquid level device and a differential pressure gauge.

Boiloff gases from the storage tank are heated, compressed to pipeline pressure by one of two compressors, and cooled prior to discharge to the pipeline. Each compressor is capable of handling 1.2 million scfd of gas. The boiloff gas design rate is about 0.6 million scfd, with an additional 0.3 million scfd of flash gas during liquefaction. During liquefaction, the boiloff and flash gases are routed to the coldbox to provide extra cooling, as described previously.

Vaporization System

LNG is pumped from the storage tank to the vaporizers by three vertical submerged, pot-mounted pumps. With one pump as a spare, the total rated send-out capacity for two pumps is about 200 million scfd (1660 gpm) at a discharge pressure of about 900 psia. In the vaporizers, the LNG is vaporized in tube bundles submerged in a heated water bath, after which the vaporized natural gas is reintroduced into the pipeline. The vaporizers, rated at 50 million scfd each, burn natural gas and bubble the resulting combustion gases through a water bath to heat the tube bundles and thus vaporize the LNG. With three vaporizers in service and one held as a spare, total vaporization capacity of the plant is 150 million scfd. All vaporization equipment normally carrying LNG is constructed of cryogenic materials, to the first flange on the vaporizer outlet.

Transportation and Transfer System

Specially designed truck trailers can be used to transport LNG both to and from peakshaving facilities. Truck transport is mainly used to supply LNG either to satellite facilities without liquefaction capability or to temporarily isolated sections of pipeline. A peakshaving facility would likely receive LNG only when its liquefaction unit is inoperative for an extended period of time.

The type of truck trailer used for LNG transport consists of an inner vessel of 5083 aluminum and an outer vessel of carbon steel. The annular space is filled with perlite and maintained at a pressure of 50 microns to insulate the inner vessel. The inner vessel is designed for a maximum working pressure of 70 psig but typically operates at only slightly above atmospheric pressure. The numerous pressure relief valves on the liquid and vapor piping all exhaust to a common elevated vent stack. Remotely operated shutoff valves are installed in the liquid lines. The trailer has a capacity of about 10,500 gallons and weighs about 60,000 lbs when full.

The trucking terminal at the peakshaving plant is diked and trenched for spill retention. Trucks are loaded and unloaded through 3-inch-diameter flexible metal hoses which connect directly to stainless steel pipes at the terminal. The hoses are drained after each loading/unloading prior to disconnection.

Small LNG sendout pumps are used to load the trailers; pump capacity is 350 gpm, yielding a filling time of about 1/2 hour. Boiloff vapors from loading the trailer are returned to the storage tank through a 2-inch vapor return line. Weight scales and two overflow trycock valves indicate the liquid level in the trailer.

Trucks can be unloaded by pumping but are more often emptied by using the vapor pressure above the liquid. If the vapor pressure is insufficient for good transfer, a small amount of LNG is vaporized in the pressure buildup coil and routed to the top of the tank to provide sufficient pressure.

Safety Systems

Combustible gas detectors, UV flame detectors, and temperature sensors are located throughout the plant area. In the event of off-standard conditions, these detectors activate alarms in the control room. They can also be set to automatically activate the emergency shutdown system or the fire control system.

The emergency shutdown system has two circuits: the Master Emergency Shutdown (MES) and the Vaporizer Emergency Shutdown (VES). The systems can be activated either automatically by detector alarms or manually by the plant operators, and they take about 30 seconds to shut down the plant. Upon activation, the MES:

- de-energizes normal plant electrical circuits, while leaving essential plant electrical equipment energized
- closes valves at the plant boundaries to isolate the plant from the pipeline
- isolates the LNG tank and dike area from the rest of the plant
- sets all control valves in their failsafe positions
- vents gas from all gas-handling equipment and lines via the relief header to the vent stack.

The VES, when activated, shuts down the vaporizers and the LNG sendout pumps, isolates the vaporizers from both the pumps and the pipeline and also isolates the pumps from the LNG storage tank, and vents gas from all equipment and lines to the vent stack. Both the MES and VES are energized by separate "Uninterruptable Power Supplies" which trip the shutdown systems if they fail.

The fire control system consists of fixed and portable dry chemical fire extinguishers, high expansion foam systems, Halon fire extinguishing systems, and a fire water system. Automatic venting and isolation systems help to prevent accumulations of flammable gas mixtures in enclosed areas and facilitate extinguishment of any fires.

The LNG storage tank and sendout pumps share a spill basin that drains into a diked impoundment basin. The dike walls average 17 ft in height. The impoundment basin is capable of holding about 480,000 bbl, or 1.37 times the capacity of the storage tank. High expansion foam generation systems installed in the spill basin can be activated either manually or automatically. The trucking terminal is also diked and trenched and is equipped with several dry chemical extinguishers. The spill basin capacity is greater than that of a tank trailer plus the loading/unloading transfer lines.

3.2.2 Reference Peakshaving Facility System Level Analysis

The purpose of the system level analysis is to identify those sections of the peakshaving facility that are the most critical with respect to release prevention and control. The evaluation of each system is based largely on two factors:

1. the quantity of a potential release due to either the inventory or the flow rate, and
2. the probability of a release as determined by subjective judgment.

Process operating conditions, including capacities, flow rates, temperatures, and pressures, are presented in Table 4 for major components of the gas treatment, liquefaction, storage, vaporization, and transportation and transfer systems.

Gas Treatment System

The primary hazard associated with the gas treatment system is the flammability of the natural gas being handled. There are three primary methods for a potential natural gas release from the system:

- adsorber vessel failure
- leak or rupture in inlet or outlet piping, flanges, valves, fittings, etc.
- tube failure in the regeneration gas heater.

TABLE 4. System Process Operating Conditions

System	Major Components	Number of Components	Component Capacities	Flow Rates In	Flow Rates Out	Operating Conditions Pressure	Operating Conditions Temperature
Gas Treatment	Adsorbers	2	17,000 scf	12.3 MMscfd	12.3 MMscfd	500 psia	68°F
Liquefaction	Cold Box	1	--	6.3 MMscfd	6.3 MMscfd (50 gpm)	485 psia	-257 to 106°F
Storage	Storage Tank	1	348,000 bbl	6.3 MMscfd (50 gpm)	200 MMscfd (1660 gpm)	15.8 psia	-257°F
	Sendout Pumps	3	--	200 MMscfd (1660 gpm)	200 MMsfcd (1660 gpm)	900 psia	-257°F
	Boiloff Compressors	2	--	0.9 MMscfd	0.9 MMscfd	870 psia	120°F
Vaporization	Submerged Combustion Vaporizers	4	--	150 MMscfd (1245 gpm)	150 MMscfd	900 psia	-257 to 70°F
Transportation and Transfer	Truck Trailer	1	10,500 gal	42 MMscfd (350 gpm)	42 MMscfd (350 gpm)	15 psia	-257°F

When activated, the Master Emergency Shutdown (MES) system isolates the gas treatment system from both the pipeline and the rest of the plant (except the liquefaction system), after which gas contained in the system is vented via the relief header to the vent stack. However, assuming the MES fails, it could take up to about 10 minutes to isolate the gas treatment system. Normal system flow during this time would result in a release of 85,000 scf of gas. This coupled with a system holdup of about 34,000 scf, gives a maximum release of 119,000 scf of natural gas.

Liquefaction System

The liquefaction system contains both natural gas and LNG. Besides the flammability hazard, there is also the hazard associated with the cryogenic temperature of the LNG. The liquefaction system also contains a mixed refrigerant with hazards similar to those of the LNG.

The primary method by which LNG or natural gas can be potentially released from the system is a leak or rupture in piping, flanges, valves, fittings, etc. The primary methods of refrigerant release are:

- leak or rupture in piping, flanges, valves, fittings, etc.
- failure of separator vessel or refrigerant compressor.

When activated, the MES isolates the liquefaction system from the rest of the plant (except the gas treatment system.) Thus, the maximum release of natural gas and LNG from the liquefaction system is the same as that from the

gas treatment system, 119,000 scf. The maximum release of refrigerant in the system is 3000 gallons, which is the cycle fluid storage capacity in the system. The largest refrigerant storage tank is 10,000 gallons.

Storage System

There are three principal methods for a potential release in the storage area:

- storage tank failure
- leak or rupture in inlet or outlet piping, flanges, valves, fittings, pumps, etc.
- atmospheric discharge from a relief valve.

The inner shell of the LNG storage tank is constructed of an aluminum-magnesium alloy which can withstand cryogenic temperatures. The outer tank is constructed of carbon steel and is susceptible to fracture if contacted with any LNG or cold vapors. Thus, failure of the inner tank would eventually lead to failure of the outer tank.

Activation of the MES system stops any flows into and out of the tank and isolates the tank from the rest of the facility. The maximum release from the storage system is the total capacity of the tank, which is 348,000 bbl of LNG. A pipe break in a 12-in. outlet line which leaks for 10 minutes before the block valve is closed would result in a leak of about 23 MMscf (280,000 gal).

Vaporization System

Vaporization takes place in four gas-fired, submerged combustion vaporizers. The vaporizers have the capacity to empty the storage tank in about 15 days of operation.

Primary methods for a potential LNG or LNG vapor release from the vaporization system are:

- leak or rupture in inlet or outlet piping, flanges, valves, fittings, etc.
- failure of vaporizer heat transfer tubes.

The Vaporizer Emergency Shutdown (VES) system, when activated, shuts down the vaporizers and the LNG sendout pumps, isolates the vaporizers from the rest of the plant, and vents all gas-handling equipment and lines to the vent stack. The maximum release from the vaporization system would occur if the VES failed and the system had to be shut down manually, taking up to 10 minutes. Normal flow through the system during this time could result in a release of up to 1.0 MMscf of LNG and LNG vapor.

Transportation and Transfer System

LNG releases in the transportation and transfer system may occur at the truck terminal or during transport on public roads. Primary methods for a potential LNG release at the terminal are:

- leak or rupture in inlet or outlet piping, flanges, valves, fittings, etc.
- failure of the double-shell tank trailer.

A failure of the trailer (due, for instance, to overpressurization) would result in a maximum release of 10,500 gallons of LNG. The probability of such a release is low. The probability of a leak in a transfer line is medium due to the operator interface. Such a leak continuing for ten minutes at the normal loading rate would release 3,500 gal of LNG.

The primary method for release in transport is failure of the trailer due to collision or overturning. Overturning accidents for LNG trailers are relatively frequent because of their high center of gravity. However, the probability of a release is low because of the excellent integrity of the double-shell trailer construction.

3.2.3 Reference Peakshaving Facility Component Level Analysis

The purpose of the component level analysis is to identify those components that are most critical with respect to release prevention and control for each of the systems. The system level analysis indicates that a significant release could come from any of the five systems. The largest releases could come from the storage and vaporization systems.

A preliminary hazards analysis (PHA) has been completed for each system previously discussed. The PHA analyzes the major components with regard to potential hazard conditions, effects, and existing preventive and control measures. Each PHA is presented in tabular form. The PHA for the storage system is given in Table 5.

Gas Treatment System

The gas treatment system is one of the less critical systems in the peak-shaving facility with regard to release prevention and control. This is because of the relatively low flow rates and the relatively small holdup in this system as compared to other systems in the facility.

The following components of the system are judged to be the most important with respect to release prevention and control:

Regeneration Gas Heater. This component contains heat exchanger tubes which carry natural gas. If a tube ruptures or leaks, natural gas is released in close proximity to the unit's gas-fired burner, and a subsequent fire or explosion is possible. The probability of such a tube failure is judged to be medium.

Molecular Sieve Adsorbers. These are large vessels (about 20 ft high by 5.5 ft in diameter) that contain gas under pressure (about 500 psia). Thus, the gas holdup in these vessels is significant. If a vessel ruptures or leaks, this holdup gas would be released along with any additional gas flowing into the system before the feed lines are closed. The probability of adsorber vessel failure is judged to be low because of design and maintenance considerations.

Master Emergency Shutdown (MES) System. When operating properly, this system limits the size of a release. However, if the system does not operate properly and a manual shutdown is necessary, the amount of natural gas released can be significantly increased.

TABLE 5. Preliminary Hazards Analysis for the Storage System

Subsystem or Component	Potential Hazard Condition	Effect	Existing Preventive and Control Measures
Startup-Shutdown Operations			
1. Storage Tank	Inadequate nitrogen purge	Possible explosive mixture when filling with LNG	• Startup procedure • Operator expertise
2. Purge Ring	Fails closed during purging process	Overpressurization and possible failure of outer tank, possible flammable gas mixture between shells	• High P alarm on tank • P relief valves
3. Inner Tank	Cooldown monitoring system fails or is inaccurate	Tank fills too fast, resulting in rapid cooldown with possible failure of inner tank and release of LNG	• Startup procedure • Operator expertise • Spill basin
4. Downcomer	Disperses LNG unevenly	Nonuniform cooldown of inner tank resulting in possible tank failure and release of natural gas or possible stratification and rollover	• Cooldown monitoring instrumentation • Operator attention • Spill basin
5. Storage Tank	Heatup with hot natural gas too rapid	Overpressurization and possible failure of tank with release of natural gas	• Tank monitoring instrumentation • P relief valves • Heatup procedure/operator expertise
		Thermal shock fails inner tank, LNG released to outer tank which subsequently fails and releases LNG	• Tank monitoring instrumentation • Heatup procedure/operator expertise • Spill basin
6. Combustible Gas Detector System	Fails, results in inadequate nitrogen purge	Possible explosive mixture when air admitted to tank	• Purging procedure • Operator expertise • Maintenance and inspection
Steady State Condition			
1. Liquid Discharge Line	Line ruptures or leaks	LNG released	• Block valves in line and in tank outlet • MES/VES • Spill basin
2. Sendout Pumps	Pump ruptures or leaks	Pump leaks to pump vessel, no release	• Low discharge P alarms on pumps, MES/VES • Maintenance and inspection
3. Sendout Pump Vessel	Vessel ruptures or leaks	LNG released (severity greatly increased if pump fails in conjunction)	• Vessel integrity • Block valves in line and in tank outlet • Combustible gas detector alarm • MES/VES • Spill basin
4. Vapor Return Line from Pumps	Line ruptures or leaks	Natural gas released	• Piping integrity • Combustible gas detector alarm • MES/VES

TABLE 5. (contd)

Subsystem or Component	Potential Hazard Condition	Effect	Existing Preventive and Control Measures
Steady State Condition			
5. Tank Foundation	Settles Nonuniformly	Outer tank fails, inner tank cannot support load and fails, LNG released	• Integrity of foundation • Maintenance and inspection • Spill basin
	Heating coil system fails	Frost heaving fails tank, LNG released	• T instrumentation/operator attention • Maintenance and inspection • Spill basin
6. LNG Fill Line	Line ruptures or leaks	LNG or natural gas released	• Piping integrity • Maintenance and inspection • Spill basin • Combustible gas detector alarm
7. High Level Liquid Alarm System	Fails, and operator does not notice dangerous condition on liquid level gauge	LNG overflows and leak to outer tank, which is failed by cold and releases LNG	• Operator expertise/attention • Temperature instrumentation would indicate unusual condition • Spill basin
8. Inner Tank Shell	Leaks or ruptures due to structural failure or earthquake	LNG leaks to outer tank, which is failed by cold and releases LNG	• Construction standards • Maintenance and inspection • Spill basin
	Inner shell moves off-center	Forces due to perlite compaction fail tank, LNG released	• Linear movement indicators • Strain gauges • Spill basin
9. Outer Tank Shell	Shell fails or leaks	Loss of insulation, heating of LNG and release and release of natural gas	• Pond T instrumentation on tank • Fire control systems
	Plan crashes into tank	Possible rupture of tank with release of LNG and/or natural gas and probable fire	• Spill basin • Fire control systems
	Sabotage, bomb explodes	Probable rupture of tank with release of LNG and/or natural gas and probable fire	• Security measures • Spill basin • Fire control systems
	Rollover	Rapid increase in vaporization and over-pressurization, possible failure of tank dome and release of natural gas	• P and T instrumentation • Tank loading and mixing procedures
	Inner shell fails	LNG leaks to outer tank, which fails due to cold and releases LNG	• Construction standards • Maintenance and inspection • Spill basin
10. Suspended Insulated Deck	Fails and falls into tank along with insulation	Extreme cold fails outer tank dome and natural gas is released, debris may foul outlet valves	• Structural integrity of deck • Operator attention
11. Boiloff Heat Exchangers	Fail	Cold fails carbon steel lines and natural gas is released	• Low T alarm/operator attention • Combustible gas detector alarm • Maintenance and inspection

TABLE 5. (contd)

Subsystem or Component	Potential Hazard Condition	Effect	Existing Preventive and Control Measures
Steady State Condition			
12. Boiloff Compressors	Compressor ruptures or leaks	Release of natural gas	• Block valves either side of compressor • Combustible gas detector alarm • Maintenance and inspection
	Cannot handle boiloff gases fast enough	Pressure buildup in storage tank, possible rupture of tank and release of natural gas	• Adequate compressor design • Maintenance and inspection • High P alarm on tank • P relief valves on tank
13. Compressor Aftercooler	Leaks or ruptures	Release of natural gas	• Block valves either side of aftercooler • Combustible gas detector alarm • Maintenance and inspection
	Fails to adequately cool the compressed boiloff gases	Shutdown of boiloff compressors, leading to pressure buildup in tank and possible rupture	• Adequate aftercooler design • Maintenance and inspection • High P alarm on tank • P relief valves on tank
14. Tank Pressure Relief Valve	Fails open	Release of natural gas, possible explosive mixture if air enters tank	• Maintenance and inspection • Tank P instrumentation/operator attention
	Fails closed	Pressure buildup in tank, possible failure of tank dome and release of natural gas	• Maintenance and inspection • High P alarm on tank • Boiloff system can help reduce P
15. Tank Vacuum Relief Valve	Fails open	Possible release of natural gas, possible explosive mixture as air enters tank	• Maintenance and inspection • Tank P instrumentation/operator attention
	Fails closed	Possible outer tank failure due to vacuum, with release of natural gas	• Maintenance and inspection • Tank P instrumentation/operator attention • Low P switch/natural gas inlet valve interlock
16. Purge Ring	Fails open	Natural gas released through roof deck, perlite insulation, and purge ring	• Maintenance and inspection
17. Recirculation Line from Pump to Storage Tank	Ruptures or leaks	Release of LNG	• Piping integrity • Pump/MES interlock • Spill basin • Combustible gas detector alarm
18. Vapor Return Line from Pump to Storage Tank	Ruptures or leaks	Release of natural gas	• Combustible gas detector alarm • Pump/MES interlock • Piping integrity
19. Tank Outlet Valve	Fails open and outlet line fails before secondary valve	Release of tank contents	• Spill basin • Maintenance and inspection
20. MES	Fails on demand	Flows not stopped automatically in an emergency	• Operator attention/manual shutdown

Liquefaction System

The liquefaction system is another of the less critical systems in the peakshaving facility because of its relatively low flow rates and relatively small holdup.

System components of primary concern regarding release prevention and control are as follows:

Temperature and Liquid Level Instrumentation and Controls. These are probably the most important components related to release prevention and control in this system. The temperature controller in the LNG outlet line ensures that the LNG is sufficiently cold before it is sent to the storage tank. If the controller fails and warmer LNG or natural gas is introduced into the storage tank, excessive flashing will occur in the storage tank resulting in increased tank pressure. If this increased pressure cannot be controlled by the boiloff system, the pressure relief valves will open and release LNG vapors. In the refrigerant system, temperature and liquid level instrumentation protects against carryover of liquid refrigerant to the carbon steel compressor suction piping. If carryover occurs, brittle failure of the piping accompanied by release of refrigerant is likely. Minor malfunctions of instrumentation and controls are highly probable but, because of design considerations, the probability of malfunctions resulting in the aforementioned releases is judged to be medium.

Heat Exchangers and Vapor-Liquid Separator Vessels. Leaks or ruptures in these vessels would result in the release of refrigerant to the cold box and possibly to the environment. The probability of vessel failure is judged to be low because of design and maintenance considerations.

MES System. When activated, this system limits the size of a release. However, if the system fails and a manual shutdown is required, a much larger release can occur.

Storage System

The storage system is probably the most critical in the peakshaving facility with regard to release prevention and control. This is due to the large LNG inventory in this system.

Storage system components of primary concern with respect to release prevention and control include the following:

Inner Tank Shell. Failure of this component would cause the maximum release of LNG or LNG vapor (up to 348,000 bbl of LNG). The probability of a failure of the inner tank shell is judged to be low because of design considerations.

Annular Space Insulation. This component is important because it prevents excessive boiloff of LNG vapor and protects the carbon steel outer shell from cryogenic temperatures and subsequent failure. The loss of insulation is judged to have a low probability due to design and operational factors.

Outer Tank Shell. This carbon steel shell provides a vapor-tight seal and protects the inner shell and annular insulation from the environment. Failure of the outer tank shell would result in large vapor releases and could possibly result in the failure of the inner shell. The probability of such a failure is judged to be low.

Tank Discharge Line to Pumps. Failure of this line could result in the maximum release for this system if no valves functioned to shut off tank flow. The probability of the line failing is judged to be low because of the types of failure mechanisms considered.

Storage Tank Pump Vessel. If the pump vessel were to fail and the feed valves to the vessel were open, a large LNG release (14,000 gal) could occur. The probability of the pump vessel failing is judged to be low.

Pressure Control System. This system includes the boiloff compressor and heat exchangers, the pressure/vacuum relief valves, and pressure controllers and indicators on inlet and outlet lines. Failure of this system could result in over or underpressure in the storage tank which could lead to tank failure and the subsequent release of at least part of the tank contents. Failure of individual components (e.g., relief valves failing open) could result in the uncontrolled release of LNG vapors. Failures of individual components are judged to have low to medium probabilities; the probability of system failure resulting in the failure of the storage tank is low.

Vaporization System

Because of the relatively high flow rates through this system, it is one of the more critical systems in the facility with respect to release prevention and control.

The PHA identifies the following system components as being most important in terms of release prevention and control:

Vaporizers. These components contain a number of heat exchanger tubes. If one or more of these tubes fail, LNG is released to the vaporizer and a subsequent fire or explosion is possible. The probability of a heat exchanger tube failure is judged to be medium.

Natural Gas Discharge Line From Vaporizer. If this carbon steel line fails (possibly from cold LNG or vapors), LNG vapors or LNG will be released. The probability of this line failing is judged to be low considering the temperature control shutdown subsystem.

Vaporizer Water Bath Tank. If the tank fails, the loss of water could result in either heat exchanger tube failure or discharge line failure. The probability of the tank failing is judged to be low.

Temperature Controller on Discharge Line. If this controller fails, the discharge line could fail. The probability of the controller failing is judged to be medium.

Transportation and Transfer System

The transportation and transfer system is one of the less critical systems in the peakshaving facility. The PHA identifies the following system components judged to be most important with respect to release prevention and control:

Double Shell Truck Tank. Failure of this component causes the maximum release of LNG for this system (10,500 gal). Furthermore, the release may occur on public roads where few or no release control measures are available and numerous sources of ignition are present. The probability of a failure is low because of the extreme ruggedness of the double-shell tank.

Truck Pressure Relief Devices. These components are important because their failure in an overpressure situation could lead to failure of the tank. The probability of simultaneous failure of these components is low because of the redundancy of devices.

Valving and Valve Controls. Failure of these devices due to rear-end collision would completely stymie emergency response measures, possibly leading to a slow but total release. The probability of such a failure is low because of judicious valve placement.

Operator Interface

Although the plant operators are not traditionally viewed as plant components, they are essential to the proper operation of the plant. The interface between operator actions and plant operations is therefore a critical factor relating to release prevention and control.

Operators perform a number of diverse tasks at the peakshaving facility, most of which relate to release prevention and control either directly or indirectly. During normal plant operations, the operators run the plant within set limits and standards to prevent conditions that may lead to releases. During off-standard conditions, the operators must respond appropriately to alarms, indicators, and other signals to prevent releases from occurring or to limit releases in progress. Plant inspection and maintenance is also important to identify and remedy conditions that may lead to subsequent releases.

Because of the number of operator tasks performed at the facility, the probability of operator error is judged to be medium to high. The probability of LNG or natural gas releases resulting from operator errors varies from a high probability of no release to a low probability of a maximum release.

3.2.4 Conclusions and Recommendations

The scoping assessment of the LNG peakshaving facility has identified some important release prevention features that may merit more detailed study. The storage system and the vaporization system have the potential for the largest LNG releases from the facility. Key storage release prevention components include the inner and outer tank structure, the pressure control system,

the tank discharge line, and the storage tank pump vessel. Important vaporization system release prevention components include the vaporizer heat exchanger tubes and water bath tank, the vaporizer discharge line, and the temperature controller on the discharge line. In addition, the operator interface can have a significant effect on release prevention for all systems in the facility.

Utilizing the results of the scoping assessment, a list of representative release events was developed and is shown in Table 6. The release events for transportation and transfer are shown separately in Table 7. It is recommended that these events form the bases for a more detailed assessment of the peak-shaving facility release prevention and control systems. As an initiating point for a more detailed assessment, a preliminary analysis of these release events was performed. Potential initiating events, effects of the release prevention and control systems, information needs, and potential design modifications which could prevent or reduce the consequences of a release were examined.

In performing the scoping assessment, several areas requiring additional information were identified. Some of these are outlined below.

- Component Stresses from Thermal Cycling. Many plant components (including the storage tank, piping, valves, and heat exchanger tubes) undergo thermal cycles during operation. These cycles produce stresses that can result in eventual component failure. Information is needed on the number of thermal cycles these various components can withstand prior to failure.
- Plant and Component Construction Details. Additional information concerning the construction of the plant and its individual components would allow more complete and detailed analysis. Needed details include such things as construction materials, thicknesses, dimensions, valve placement, and equipment configurations.
- Structural Mechanics of the Storage Tank. The effects of hazardous conditions on the structural integrity of the tank are of major importance. Such conditions include overpressure, overfilling, and fire or explosion in the tank or nearby. A more detailed description of the heatup and cooldown procedures is necessary for a complete analysis to be accomplished.

TABLE 6. Representative Release Events for an LNG Peakshaving Facility

1. Gas supply line from pipeline fails.
2. Molecular sieve adsorber vessel fails.
3. Heat exchanger tube in regeneration gas heater fails.
4. LNG piping in cold box fails.
5. Refrigerant compressor suction line fails.
6. Refrigerant storage tank fails.
7. LNG storage tank fails.
8. LNG outlet line from storage tank fails.
9. LNG vapor vented through relief valves after overpressurization of storage tank.
10. Sendout pump vessel fails.
11. LNG supply line to vaporizers fails.
12. Vaporizer heat exchanger tube fails.
13. Natural gas line from vaporizers fails.

TABLE 7. Representative Release Events for Transportation and Transfer Operations

1. Liquid line from storage to the truck loading station fails.
2. Flexible loading/unloading hoses fail.
3. Vapor return line from the truck loading station to storage fails.
4. Liquid line from the truck unloading station to the storage tank fails.
5. Truck LNG tank fails.
6. Trailer pressure buildup coil fails.

- Failure Rate Data. The peakshaving facility scoping assessment considered release frequency in a qualitative manner. A more detailed study of the release prevention and control systems must carefully consider the likelihood of the release initiating event and the reliability of the release detection and control systems. Due to the lack of operating experience at LNG facilities, little data is available for LNG equipment failure rates.
- Operator Interface. Reliability information on operator tasks performed at the facility is needed.

The next phase of the assessment of the LNG peakshaving facility release prevention and control systems is to perform more detailed analyses on the areas identified by this scoping assessment. The representative release events will form the bases of this assessment. Additional emphasis will be placed on analyzing the effectiveness of the release detection and control systems.

3.3 SCOPING ASSESSMENT OF LNG EXPORT TERMINAL RELEASE PREVENTION AND CONTROL SYSTEMS

The scoping assessment of the export terminal has identified some important release prevention features that may merit more detailed study. The storage section and the loading section of the export terminal have the potential for the largest LNG releases. Key storage section components include the inner and outer tank structure, the pressure control system, the internal shutoff valves, and the liquid-level indicators and alarms. Important loading section components include the transfer line, the loading arms and coupling mechanism, and the loading emergency shutdown system.

Utilizing the results of the scoping assessment, a list of representative release scenarios were developed and is shown in Table 8.

In performing the scoping assessment several areas requiring additional information were identified. Some of these are outlined below.

- Emergency Shutdown (ESD) System. Of particular interest are the location and number of detectors that activate the ESD, how quickly the shutdown occurs, exactly what equipment is shutdown and what valves are closed, and details on the inspection, testing, and maintenance of the system.

TABLE 8. List of Representative Release Scenarios for an LNG Export Terminal

1. Rupture of the 36-in. main transfer line between the loading pumps and the dock.
2. Rupture of the 24-in. liquid outlet line between the storage tank and the first block valve.
3. Rupture of the 16-in. loading arms.
4. Storage tank pressure relief valves open.
5. Storage tank vacuum relief valves open.
6. Inner tank is overfilled with LNG.
7. Complete failure of storage tank.
8. Rupture of 18-in. feed gas line in liquefaction train.
9. Rupture of 20-in. mixed refrigerant liquid piping between high pressure separator and main cryogenic heat exchanger.
10. Rupture of 10-in. nozzle to propane/mixed refrigerant exchanger.
11. Failure of a refrigerant compressor (propane or mixed refrigerant).
12. Rupture of 12-in. transfer line from liquefaction area to the storage tanks.
13. Rupture of outlet nozzle or piping on refrigerant storage tanks (propane, ethylene).

- Plant Piping Network. Details, such as diameter, length, wall thickness, and material of construction are needed for the piping, vessels, valves, loading arms, expansion joints, etc., that make up the plant piping.
- Structural Mechanics of Storage Tanks. A key factor in this area is the effect of various hazard conditions on the structural integrity of the tank. Such conditions include overpressure, overfilling the inner tank, and a fire or explosion in another area of the plant. The effect of heatup and cooldown on the tank, the potential problems encountered during these transitions, and the correct heatup and cooldown procedures are necessary for more detailed analysis.

- Failure Rate Data. The scoping assessment of the export terminal did not explicitly consider the potential release frequency. A more detailed study of the export terminal release prevention, detection, and control systems must carefully consider the likelihood of the release initiating event and the reliability of the release detection and control systems. Due to the lack of operating experience of LNG facilities, little data is available for LNG equipment failure rates.

3.4 SCOPING ASSESSMENT OF LNG MARINE VESSEL RELEASE PREVENTION AND CONTROL SYSTEMS

The scoping assessment of the marine vessel has identified some important release prevention features that may merit more detailed study. The largest potential spills of LNG occur when one or more of the cargo tanks rupture. Failure or misoperation of the cargo handling system generally result in smaller spills. Important cargo storage tank components include the primary tank structure, the outer and inner hulls, the cargo tank hull indicators, and safety valves. Important cargo handling system components include the liquid header, crossover line, valves, and the emergency shutdown system. The human element is also a factor during tanker loading and unloading. Crewman and operator training and good communications between ship and terminal personnel are particularly important.

Utilizing the results of the scoping assessment, a list of representative release scenarios was developed and is shown in Table 9.

TABLE 9. Representative Release Scenarios for an LNG Marine Vessel

1. Ship sinks and all five cargo tanks rupture from overpressure.
2. Rupture or leak in one of the LNG cargo tanks.
3. Cargo tank is overfilled.
4. Pressure safety valves relieve to the atmosphere.
5. Rupture or leak in the liquid cargo system.
6. Rupture or leak in the vapor handling system.
7. Release of LNG or natural gas from ship due to misoperation of the cargo handling system.

In performing the scoping assessment several areas requiring additional information were identified. Some of these are outlined below.

- Collision Probability. Several analytical methods have been applied to Coast Guard Collision data to determine the probability of an LNG vessel being involved in a collision. These methods usually include a safety factor for LNG vessels to account for the additional navigation and safety equipment on board, and the special navigational procedures used. Additional research and analysis is needed to develop a standard method for calculating these probabilities.
- Effects of a Collision on an LNG Vessel. While the critical velocity for penetration of the storage tanks has been calculated, little attention has been given to the effects of a collision on other portions of the ship such as the cargo handling system and the propulsion system.
- Cargo Handling System. A complete piping and instrument drawing of the cargo handling system is needed.
- Effects of Spills, Fires, and Explosions. The effect of these events on the structural integrity of the ship, on the cargo handling system, and the cargo tanks needs to be determined.
- Failure Rate Data. The scoping assessment of the marine vessel did not explicity consider the potential release frequency. A more detailed study of the marine vessel release prevention, detection, and control systems must carefully consider the likelihood of the release initiating events and the reliability of the release detection and control systems. Due to the lack of operating experience of LNG facilities, little data is available for LNG equipment failure rates.

3.5 SCOPING ASSESSMENT OF LNG SATELLITE FACILITY RELEASE PREVENTION AND CONTROL SYSTEMS

The scoping assessment of the LNG satellite facility has identified some important release prevention features that may merit more detailed study. The storage system and the transportation and transfer system of the satellite facility have the potential for the largest LNG releases. Key storage reaction

components include the inner and outer tank structure, the pressure control system, the tank discharge line, the LNG recirculation line, the storage tank pump vessel, and the boiloff heaters. Important transportation and transfer system release prevention components include the double shell truck tank, the operator interface, and the pressure relief devices.

Utilizing the results of the scoping assessment, a list of representative release events was developed and is shown in Table 10.

TABLE 10. Representative Release Events for an LNG Satellite Facility

1. Liquid line from storage to the truck loading station fails.
2. Flexible loading hoses fail.
3. Vapor return line from the truck loading station to storage fails.
4. Flexible unloading hoses fail.
5. Liquid line from the truck unloading station to the satellite storage tank fails.
6. Truck LNG tank fails.
7. Trailer pressure buildup coil fails.
8. Satellite storage tank fails.
9. Exit gas line from the boiloff heaters fails.
10. Liquid discharge line from the satellite storage tank prior to the sendout pumps fails.
11. Sendout pump vessel fails.
12. Liquid recirculation line from the sendout pumps fails.
13. Vapor return line from the sendout pumps fails.
14. Liquid line to the vaporizers fails.
15. Vaporizer heat exchanger tubes fail.
16. Natural gas line from the vaporizers fails.

In performing the scoping assessment several areas requiring additional information were identified. Some of these are outlined below.

- Thermal cycle stresses. Information is needed on the number of thermal cycles the storage tank and various sizes of pipes or tubing can take prior to failure.

- Operator interface. Reliability information on operator tasks related to loading, transport, and unloading is needed.
- LNG line relief valves. Reliability information for operation of LNG line relief valves is needed.
- Boiloff system. Additional information concerning the entire boiloff system such as construction materials, valve placement, and temperature controllers are needed.
- Storage tank. Information concerning discharge valving for the tank is needed.
- Vaporizers. Information concerning the vaporizer internals such as diameter of tubes, number of tubes, tube configuration, and flowrates is needed. Information concerned with vaporizer tube corrosion problems is needed.
- Failure rate data. The satellite facility scoping assessment considered release frequency in a qualitative manner. A more detailed study of the release prevention and control systems must carefully consider the likelihood of the release initiating event and the reliability of the release detection and control systems. Due to the lack operating experience of LNG facilities, little data is available for LNG equipment failure rates.

THIS PAGE

WAS INTENTIONALLY

LEFT BLANK

4.0 MORE DETAILED ASSESSMENT OF IMPORT TERMINAL AND PEAKSHAVING FACILITY RELEASE PREVENTION SYSTEMS

The scoping assessments summarized in Section 3.0 form the basis for a more detailed assessment of release prevention and control systems. An important output of the scoping analyses was representative lists of release scenarios. Using these lists as a starting point, a study analyzing the effectiveness of the release prevention, release detection, and release control systems was initiated for the reference import terminal and peakshaving facility. The primary emphasis is on the release prevention systems. The representative release scenarios will be quantified in terms of release frequency and release quantity using the best available information. Alternative process options and equipment designs will be examined to assess their effect on release frequency or quantity.

4.1 IMPORT TERMINAL ANALYSIS

A failure modes and effects analysis (FMEA) has been completed for each process area of the reference import terminal. The scoping assessment indicated that the storage section and the unloading section have the highest potential for large LNG releases. Consequently, these areas received special emphasis in the analysis. The FMEA assists in identifying those component failure modes which are critical with respect to release prevention and estimates the failure rates.

A simplified fault tree/event tree analysis has been completed for the majority of the representative release events. Simple fault trees are used to estimate the frequency of the release event. Event trees are helpful in evaluating the post release events (effect of detectors, emergency shutdown systems, etc.)

Critical system components have been identified on a preliminary basis. These are defined as the components which have the most direct effect on the frequency or quantity of release. Some examples include the loading areas, expansion bellows, storage tank, level detectors, pressure controller, block valves, and the operator. Improvements in the operating performance of these types of components could be achieved by such areas as:

1. improved maintenance and testing
2. use of redundant components
3. advanced or novel design
4. additional automation if operator response is critical

The next phase of the import terminal release prevention analysis will evaluate the effect of various alternative designs and operating procedures using the representative release events and the fault/event trees that have been developed.

4.2 PEAKSHAVING ANALYSIS

The peakshaving facility release prevention analysis generally parallels that of the import terminal. A failure modes and effects analysis has been completed for the storage system and the vaporization system. An analysis of the representative release events identified by the scoping assessment has been initiated. The next phase of analysis is to complete the quantification of the representative release event frequency and release quantity. The effect of alternative designs and operating procedures will then be evaluated.

4.3 FUTURE PLANS

The planned work for FY-1980 includes: 1) Extend the scoping assessment to include more detailed analyses with additional emphasis on the release detection and control areas; 2) establish a data gathering program to support the above analyses; 3) initiate a study of LNG facility fire and vapor control systems; and 4) initiate a study of human factors in LNG release prevention and control. Some details on this work are discussed below.

Work performed to date has concentrated on release prevention. A complete mitigation strategy for LNG accident scenarios includes release prevention, release detection, release control, vapor control, fire prevention, fire detection, fire control, and damage control. It is anticipated that the LNG release prevention analyses will be completed at the end of FY-1980. Release detection and control system analyses will be included on a preliminary basis. The emphasis of future work in the project will be on the engineering aspects of vapor control and fire prevention and control.

A study of LNG fire and vapor control systems has been initiated with the basic objective of assessing the current knowledge and LNG industry practices relating to fire and vapor control systems. Fire protection systems include such systems as fire hydrants, dry chemical extinguishing systems, halon extinguishing systems, water deluge systems, and high expansion foams. Vapor control systems include use of diking systems, water curtains, and high expansion foams. This study will review existing models which analyze potential fire conditions and vapor dispersion within an LNG facility and the effectiveness of the designed fire and vapor control systems. Results of this evaluation will form the basis for future work on LNG vapor control and fire prevention and control.

The scoping assessments identified some general areas which merit consideration in more detailed analyses. These include human factors in LNG operations, LNG storage tank operations, and data gathering. Separate studies have been initiated in each of these areas.

The objective of human factors study is to identify possible gaps in the use of existing information in applying human reliability and engineering in the design and operation of LNG facilities. Human interaction is essential to the operations, testing, and maintenance of LNG release prevention and control systems and consequently is a significant factor in an analysis of their effectiveness. The degree of human involvement varies with the type of facility. Shipping operations require a great deal of human involvement while some satellite facilities are designed for periods of unmanned operation. Some typical LNG operations where human operators perform key functions include the purging of process equipment and vessels, the initial cooldown of process and storage equipment, maintenance and testing operations, and fire extinguishment. Human engineering is extensively applied in military systems and in the aerospace, nuclear and chemical industries. Data from these sources will be reviewed to determine possible needs and opportunities for applying this knowledge in LNG. The results of this study will provide input to the evaluations of equipment and process options planned in the LNG release prevention and control project.

LNG storage tank operations are included in each of the LNG facilities under study in this project. Based on a contained inventory basis and the

magnitude of potential releases, LNG storage tank operations merit careful analysis. Information on various storage tank designs and preliminary safety comparisons will be performed for alternative storage tank designs. Both internal incidents (such as weld failure or overfilling) and external hazards (such as adjacent fire or earthquake) will be considered.

A small data gathering effort was initiated in FY-1979. A more rigorous and formalized data gathering effort was initiated to support the FY-1980 release prevention and control analyses. This will provide an organized source file of LNG release prevention and control equipment characteristics and operating procedures.

REPORT J

The Feasibility of Methods and Systems for Reducing LNG Tanker Fire Hazards

D. S. Allan
P. K. Raj
P. Athens
E. G. Pollak
N. M. Laurendeau
A. A. Fowle

Prepared for the
Environmental and Safety Engineering
Division
U.S. Department of Energy
and the Department of Commerce,
Maritime Administration,
Office of Commercial Development
under Contract DE-AC-02-78EVO4734

Arthur D. Little, Inc.
Cambridge, Massachusetts 02140

THIS PAGE

WAS INTENTIONALLY

LEFT BLANK

REPORT J

TABLE OF CONTENTS

TABLES

SUMMARY

The objective of this effort was to identify and evaluate new and novel concepts for reducing the hazards presented by LNG tanker transits of navigable waters in the United States. The study also included a preliminary assessment of the technical feasibility and the costs associated with the concepts that were identified.

This study considers tankers that transport about 125,000 cubic meters (m^3) of LNG, which are expected to dominate the LNG shipping trade and, in fact, are currently the largest ships in service. Ships of both the membrane and free-standing tank design were considered.

A rapid spill of the entire contents of one LNG cargo tank ($\sim$25,000 m^3) was generally used as the basic accidental event. This volume is characteristic of a potential spill expected by the collision of a large ship with an LNG tanker. In risk studies performed for various projects, the collision accident has been considered as representative of the most hazardous occurrence deemed credible.

The principal approaches to reducing LNG tanker hazards are modifications to the ship and/or its cargo so that the magnitude of the fire would be decreased should a spill occur. Generally, there is little that can be accomplished by fire fighting or inerting the flammable vapor once a large spill has occurred. Methods that might be retrofitted to ships already built are regarded to be of particular importance because many of the ships that will be used in the U.S. LNG trade over the next 10 to 20 years may be either under construction or already in service.

THIS PAGE

WAS INTENTIONALLY

LEFT BLANK

1.0 INTRODUCTION

Liquefied Natural Gas (LNG) tankers present a fire hazard to surrounding areas as they enter United States ports. These hazards derive from the possibility that a major tanker accident could result in a large spill of a very volatile and flammable cargo.

In this program methods of reducing these fire hazards are identified and evaluated. They include:

- Methods of reducing the rate and/or quantity of LNG that might be released in an accident;
- Techniques for altering the physical or chemical state of the cargo;
- Systems for protecting the tanker and crew from the thermal effects of a large fire and methods of disposing of the cargo from a damaged and disabled tanker (so as to prevent the escalation of an accident that involved the spill of the contents of only one of several LNG containers on board the tanker).

In addition, because the hazards that are to be reduced depend upon the time of occurrence of ignition of spilled cargo, a detailed investigation of the propensity for ignition to take place at the time of a collision impact was carried out.

The entire program has now been completed, and the final report has been submitted to the sponsor for printing. It is expected that copies of the report will become available during June of 1980.

A summary of the work performed in this program is presented here.

THIS PAGE

WAS INTENTIONALLY

LEFT BLANK

2.0 HAZARD-REDUCTION METHODS

2.1 HAZARD REDUCTION

The penetration of an LNG cargo tank of an existing tanker, such as could happen in a major collision, is apt to result in the release of the entire contents of the tank within a few minutes. In fact, the spill time has been estimated to be so short that the modeling of spill hazards in most prior risk estimates assumes, for reasons of simplicity (and conservatism), that the LNG spills instantaneously.

To establish the gains to be made by slowing down the rate of release and/or limiting the total amount that is released in a single spill, estimates have been made of the resultant decrease in pool fire and vapor cloud hazards. An example of the results of these estimates is presented in Table 2.1. The table shows that by reducing the spill size to only 1,000 m^3 rather than 25,000 m^3, and by causing the spill to occur at a constant rate over a period of some 30 minutes or more rather than near instantaneous, the thermal radiation hazard from a pool fire would be so curtailed that significant thermal effects would remain essentially within the vicinity of the spill; i.e., within about 400 feet of the center of the spill. The size of the potential vapor cloud (under adverse meteorological conditions) would also be diminished; however, it would still present a hazard some 4500 feet from the center of the spill. Greater reductions are theoretically possible, but become more difficult and expensive to achieve.

2.2 METHODS

We have considered four different ways in which the accidental spill quantity or rate of release of LNG may be reduced. Each is described below:

(1) Partitioning of Existing Tank Designs - Cargo tanks may be divided into separate compartments so that when a collision occurs only the LNG in the compartment that is accidentally penetrated would be released. To partition tanks in this manner, however, requires that

TABLE 2.1

THERMAL RADIATION AND VAPOR CLOUD HAZARDS
FOR
DIFFERENT SPILL SIZES AND SPILL DURATIONS

Spill Size, m^3	Spill Duration, min.	Distance of Harmful Thermal Radiation from Pool Fire, m*	Maximum Travel of Vapor Cloud, Km**	Maximum Half Width of Vapor Cloud, m
25,000	"instantaneous"	2100	20	700
	10	900	10	300
	30	550	3.2	150
10,000	"instantaneous"	1500	14	500
	10	600	7.5	200
	30	350	2.7	100
1,000	"instantaneous"	660	5	200
	10	190	2.8	70
	30	120	1.4	35

* distance from center of spill where radiation = 5 kW/m^2. Raj (1977) and Appendix A, "The Feasibility of Methods and Systems for Reducing LNG Tanker Fire Hazards," Allen et al. in press (to be available through NTIS).

** Maximum travel distance of unignited flammable vapor cloud assuming flammable limit is 5% methane in air, atmosphere condition F; Germeles and Drake (1975) and Appendix B, "The Feasibility of Methods and Systems for Reducing LNG Tanker Fire Hazards," Allan et al., in press.

the bulkheads be structurally capable of withstanding the liquid forces when one compartment is emptied, and the increased heat input to the liquid in the remaining compartments would also have to be accommodated.

A review of the designs of LNG tankers already built or under construction indicates that there are several difficulties associated with this approach. It does not appear feasible to insert bulkheads or partitions in existing membrane systems within a reasonable cost since the membrane linings will not in themselves provide adequate support. The free standing spherical containers will support partitions but because of the increased difficulties in analyzing stresses in such a system there is some possibility that the classification of the tanks would be changed; thus introducing the requirement that a full secondary cryogenic barrier be introduced. This would not appear to be practical.

Only the self supporting rectangular tanks of the Conch design may be receptive to the installation of partitions without introducing other severe problems, but there is a limited number of ships of this configuration. In any event, either a large number of partitions or a complex and expensive design would be required in order to achieve large reductions in spill quantity. Partitioning of tanks may be most cost effective, however, when combined with other approaches such as the addition of filler material that would restrict the outflow of LNG.

(2) Multi-tank Ship Designs - There are two ship designs that utilize a large number of smaller cargo tanks being proposed for LNG trade. One of these being offered by Verolme uses 3,400-m^3 uninsulated vertical cylinders located in groups within insulated holds in the ship. The major effort by Verolme at present is concentrated on a large vessel design, with a payload of 330,000 m^3. Spillage of LNG by penetrating the ship in a collision would be greatly reduced, but the flooding of the hold in such a case may create venting problems for the undamaged containers.

The other ship design referred to as the OCEAN PHOENIX uses a complex system of partially compartmented multi-lobed vessels for LNG containment at pressures in the 40 to 70 psi range. This design provides the advantage of reduced spill rates in an accident, but bursting of pressurized vessels due to thermal exposure could result in explosions and possible propagation of the failure to other tanks.

Since both of these ship designs are being proposed as competitive alternatives to existing ship configurations, their cost may be near that of ships now being built of similar capacity.

(3) Insertion of Open Cell Filler Material - The object of this approach would be to restrict the flow of LNG from the container by requiring it to pass through small restrictions within an open celled filler material that has been placed in the tank. This principle has been applied to small flammable liquid containers using open-cell foams or rolled-up sections of expanded aluminum to form a cell-like structure within the tank. Only a few percent of the container volume is occupied by the filler material. Additional analysis is required, however, before the loss of cargo space and the restriction of outflow from an LNG tank may be established.

A variation of this approach utilizing much less filler would be the installation of partitions of material suspended as curtains which would tend to block tank openings created by ship collision penetrations. The rate of outflow would be reduced by the impedence offered by the small passages through which the LNG would have to travel.

This approach appears to warrant further investigation, at least as a potential hazard reduction technique that might act as a retrofit for the free standing tank designs.

(4) Combine Cellular Filler Material with Compartmentalization - This approach offers the opportunity of reducing both the rate and quantity of spill. It also might allow the cellular material to be applied only to those compartments that are most vulnerable to

penetration during an accident, thus reducing the loss in cargo space and cost.

2.3 OTHER METHODS OF REDUCING TANKER FIRE HAZARDS

Other techniques that are considered for achieving reduced levels of fire hazards from LNG tanker spills are described in the sub-sections that follow.

2.3.1 Gelled LNG

Experiments have demonstrated that LNG can be transformed to a gel using small percentages of either water or methanol. The gels have been shown to evaporate at a slower rate (on a unit area of heat transfer surface basis) than the liquid, and it is predicted that the spreading rate of the gel on water (on spilling from a cargo tank) would be less than that of LNG as well. The maximum size of the evaporating pool may also be reduced. It has been estimated, using the results of small-scale experiments that the maximum distance that a vapor cloud might travel when gel is spilled in water would be about one-fourth that if the same amount of LNG were spilled. The effect of gelling of LNG on hazards from pool fires has not been estimated, but significant decreases might be expected.

The extent of actual benefits to be derived, however, requires an evaluation of the effect of scale on pool size and evaporation rates. It would also appear that additional development work on the manufacturing process is also required so as to better establish feasibility and cost.

2.3.2 Methanol

The conversion of methane, the primary component of natural gas, to methanol has been considered in the past as a means of reducing the cost of transportation. Methanol could be shipped in slightly modified, conventional (crude oil) tankers, which are much less costly than LNG ships. The savings in transportation, however is not large enough to compensate for the increased costs associated with energy losses incurred in the conversion of natural gas to methanol and the later transformation of methanol back to a synthesis gas. This trade off also has become less attractive as the result of the increases in gas prices that have been experienced in recent years.

Methanol would be safer to transport. It is miscible with water and when spilled would disperse in water quite rapidly to the point where the resultant mixture would no longer be flammable. Methanol also has a relatively low vapor pressure so that vapor cloud hazards would be greatly diminished. Large quantities spilled and mixed with water would adversely affect the aquatic environment, and could be toxic to humans who obtain water from sources along shipping routes.

The methanol approach, then, offers the opportunity of achieving safer transport, but at an increased cost. This would probably be true even if markets were developed for the direct use of methanol or as a gasoline extender and the costly reconversion to synthesis gas were to be eliminated. However, if the cost of LNG tankers were to be increased for safety reasons, the methanol route might become more attractive, particularly for projects requiring long shipping distances. The implementation of a methanol import project would require a large capital investment, some risk, and an extended period of time before it could be put in operation.

2.3.3 Flame Suppressants

In concept, extinguishants, such as halons, could be mixed with LNG and render it non-flammable. In practice, however, excessive amounts would be required. Uniform mixtures of the suppressant and vapor

could not be achieved, and the separation and difficulties associated with the complete removal of the extinguishant at the receiving terminal might result in trace (but hazardous) quantities being present in the gas send-out. This concept is considered impractical.

2.3.4 Solid Natural Gas

If natural gas were to be shipped as a solid instead of a liquid, the spillage of cargo during the most severe of collisions would be expected to be minimal and the hazards to the surroundings greatly reduced, if not completely eliminated. The basic technology for converting the liquid to solid exists so that the prime consideration for shipping natural gas as a solid reduces to the increase in costs related to facilities and energy for converting liquid to solid (and back to liquid again at the receiving terminal) relative to the benefits to be derived from the hazard reduction that is achieved. Some of the increased costs associated with conversion might be alleviated, however, by the potential use of lower cost single hulled (but insulated) tankers for transporting the solid.

2.4 SYSTEM COSTS

Generally speaking, improvements in safety are accompanied by increased costs, and this appears to be true for all of the LNG tanker fire reduction concepts that have been reviewed in this study. In this preliminary evaluation we consider very approximate indicators of costs and benefits so as to identify areas of potential interest and to eliminate totally infeasible concepts.

As an indicator of hazard reduction (benefits) that may be achievable with one or more approaches, we assume that the best that might be attained is that equivalent to the effect of the previously mentioned 1,000-m^3 spill over a period of 30 minutes.

For a cost baseline, we have used the costs associated with a somewhat typical LNG project consisting of a billion standard cubic feet per day project, with the LNG shipped from Algeria to Texas. The baseline costs are shown in Table 2.2.

TABLE 2.2

ESTIMATE OF COSTS FOR
LIQUEFYING, TRANSPORTING, AND REGASIFYING LNG
(ARZEW, ALGERIA TO TEXAS)

1 BSCF/Day

		Cost in Dollars	Percent of Total Cost	
Cost of Gas		$0.50/M SCF		.181
Liquefaction				
Fuel	.075		.027	
Operating Costs	.103		.037	
Capital Charges	.662	.84	.240	.304
Shipping				
Fuel	.030		.011	
Boil-Off	.092		.033	
Capital Charges (vessel)	.790		.286	
Fixed Costs	.225	1.137	.081	.412
Receipt and Regasification		.285		.103
TOTAL		2.762/M SCF		1.000

Using this baseline, we estimate that the cost of gas at send-out might be increased by as much as 1 percent of the total (some 3¢/MSCF) for tank partitioning and for multi-tank vessel concepts. A value of less than 0.5 of 1 percent increase might be reasonable for the concept involving the hanging wall of expanded metal used to impede the outflow of LNG.

Since industrial processes for making gelled or solid LNG in quantity have not been developed, the costs associated with these concepts are more uncertain than the above methods for reducing the rate and quantity of spill. However, assuming that new and unique plants would have to be built for both concepts, and new ship designs and terminal facilities developed for solid LNG, the incremental increases in cost of gas might be as much as 15 percent for the two concepts.

It is also estimated that the achievement of the improved safety attainable by transporting methanol instead of LNG might require as much as a 10 percent, or more, increase in cost per unit of energy delivered.

The economic impact of cost increases of the magnitude presented here will also require considerable analysis. One perspective, however, is to compare the potential reduction in monetary loss attainable by significant improvements in safety with the cost of employing these improvements. If, for example, one were to assume that a hazard-reduction concept could achieve a decrease in the total losses that might occur in a single major accident of $100 million (including property loss plus losses associated with the ship itself), and if it is further assumed that the yearly probability of such an accident occurring is unusually large, say of the order of 1 chance in a 1000 per year, then the prorated yearly savings would be about $100,000. Clearly, the hazard reduction concepts considered here would greatly exceed this value and, on this basis alone, might not be considered to be cost-effective.

This, however, does not consider the indeterminate value of losses associated with injuries and fatalities that might result from a major accident nor does it take into account the possibility that the overall impact of the incremental increase in cost of gas might be considered to be low relative to the potential benefits.

3.0 VULNERABILITY OF LNG TANKERS AND CREWS TO FIRES

3.1 VULNERABILITY OF SHIP AND CREW

Most of the published work on the safety of LNG tankers has centered on hazards presented to personnel and property external to the tanker itself. However, a large pool fire from a 25,000-m^3 spill of LNG might cause extensive damage to the ship and either severely or fatally injure the crew as well. The fire exposure might either directly or indirectly cause failures of cargo tanks that are not damaged in the initial phases of the accident and, at the very least, may result in a severely damaged and immobile vessel with no trained crew to assist in its salvage.

A preliminary review of the vulnerability of ship components to fire from a large LNG spill indicates that fire exposure may cause the hull plates to buckle or warp, or perhaps rupture the external protection of the cargo containers and compromise their insulation. Piping, deck machinery, life boats, and communication and navigation equipment may be severely damaged and glass windows may be destroyed during the early phases of such an exposure. If the latter occurs, hot gases may enter certain areas and adversely affect the ship's controls.

On existing tankers, most, if not all, of the critical locations for the ship's operations may be exposed to the thermal effects of fire. This includes positions within enclosures, but which become vulnerable due to hot gases entering through window openings, as well as exposed locations on deck.

3.2 PROTECTION OF SHIP AND CREW

Thermal insulation offers an opportunity to reduce greatly the critical damage caused by fire. Water deluge systems would also provide protection, but the reliability of pumps and water distribution systems

is questionable, particularly if the ship were severely damaged in a collision. Protecting the hull would be extremely difficult, but thermal damage to an unprotected hull would not be expected to be great enough to cause the ship to sink. The cargo tank covers, piping, critical enclosures (including windows), and other equipment could, at least in theory, be protected by thermal insulation. Conventional insulating materials may not be adequate for some components, however. In the case of protective enclosures for crew members, special insulation would be required. On the basis of a conservative criterion that living space must be maintained at 100°F or lower for exposure to a fire of one hour, special insulative coatings of the intumescent and/or transpirational cooling type would be required. Laboratory-tested coatings that appear adequate for these purposes are available.

4.0 CARGO DISPOSAL AND PLANNING

4.1 SALVAGE AND DISPOSAL

Past shipping accidents with other cargos indicate that possibly the remaining cargo would have to be off-loaded from a severely damaged LNG tanker at some location other than a loading or unloading terminal. Either the tanker would be incapable of being moved to a terminal or being moved may be deemed to be too hazardous.

Currently, no satisfactory method exists for the emergency off-loading of cargo from LNG tankers other than at terminals, unless an empty tanker that could receive the cargo happens to be nearby. Equipment and procedures need to be developed for off-loading or disposal of a damaged LNG tanker. In this study, we have considered the transfer of cargo to other ships, the disposal of cargo by ship flares or combustors aboard ship, and eventual disposal after the cargo has been transferred by pipeline to some location external to the vessel.

The transfer of cargo from a disabled LNG tanker in or near a U.S. port to another carrier during an emergency does not represent a very likely solution, since it would be rare for another vessel to be available and close enough to effect the transfer within the short interval of time (several days) as demanded by the urgency of the situation. Burning the LNG on board the tanker at the high rates needed to empty the ship in a short time would be difficult, if not impossible, to accomplish with flares, because of the potential thermal damage that could be effected by the large flames. Combustion equipment that would provide for burning aboard ship with little or no thermal hazard cannot be accommodated aboard existing ships, and would occupy excessive space on new tankers.

The transfer of cargo to platforms located at an appropriate distance from the damaged tanker, however, offers an opportunity of burning LNG at high rates without endangering the LNG carrier. A matrix of small flares, or a series of waste heat boilers, mounted on a barge might be used for disposal. The development of flexible metal hoses for transferring the LNG from the ship to the barges at a distance represents a formidable undertaking, but appears to be feasible.

Another simpler but, perhaps, limited method -- also requiring flexible transfer lines -- would be the discharge and ignition of LNG on the water at an adequate distance from the tanker. This would eliminate the need for barges and associated burner equipment to be continuously on standby at each port. Controlled pool burning of the LNG could be accomplished satisfactorily if a location could be found in which thermal hazards would not endanger nearby property.

4.2 CONTINGENCY PLANNING

Appropriate and timely responses to LNG tanker accidents may prevent the escalation of the consequences of an accident. Contingency planning is necessary to achieve proper response and to conserve labor and funds in carrying out any plan. In this report, requirements for contingency planning for major LNG tanker accidents are considered, and primary inputs to these plans are discussed.

5.0 IGNITION DURING AN IMPACT COLLISION

The effectiveness of spill control methods depends upon whether ignition of the spilled cargo occurs at the time of impact and a pool fire takes place or ignition occurs only after an unignited vapor cloud travels some distance and enters a populated area (see Table 2.1). Because the evidence that ignition will occur at the time of impact (although generally considered to be true) is limited, the mechanisms by which ignition could occur were examined in this study.

The statistics of past accidents involving collisions with tankers carrying flammable liquids were examined. It was found that a significant fraction (about 0.3) of the collisions where cargo was spilled resulted in immediate ignition. Where it could be determined that there was a significant penetration of the flammable liquid carrier by an impacting ship, immediate ignition occurred in almost 100 percent of the accidents. Hence, ignition sources appear to be present when there is a substantial impact of one ship with another.

The potential causes of ignition were then analyzed using empirical and analytical data on the ignition of flammable gases. It was found that hot surfaces created by frictional impact of two colliding ships are the most likely sources of ignition for LNG spill accidents. The sliding of one steel surface against another under the forces that would occur in a substantial impact collision would cause the surfaces to be heated, momentarily, to the melting point of the steel ($\simeq$ 1500°C). These surfaces when exposed will be large enough and remain sufficiently hot over a long enough period of time to cause ignition of flammable methane-air mixtures.

This determination was confirmed by a series of experiments in which thin strips of inert metal were rapidly heated to elevated temperatures, approaching the melting point of steel. The surface areas, temperatures, and times to ignition were consistent with the analysis and supported theoretical correlations developed in this study.

Although this work demonstrated that ignition sources may be present in an impact collision, consideration must also be given as to whether these sources will, in fact, be exposed to flammable mixtures of methane and air during an accident. For example, ignition may have been more likely in collisions of tankers carrying flammable liquids since the vapor space in the cargo tanks may have contained flammable mixtures of vapor and air at the time of the collision. This would not be true for LNG carriers, and flammable mixtures would have to form after the cargo is released and the vapors external to the tank mix with air.

The results of a first order analysis are unclear as to whether, in fact, flammable mixtures of methane and air will come in contact with hot surfaces long enough for ignition to take place. By the nature of the collision impact, the exposed hot surfaces will tend to form in the region between the two hulls of the LNG vessel being impacted; an area where mixing of the spilled cargo vapors with air may be insufficient for significant volumes of flammable mixtures to occur.

A more detailed analysis of the structural deformation of the impacting ships and of the fluid mechanics associated with the discharges of cargo and its mixing with air is needed before the likelihood of ignition at the time of impact for an LNG tanker accident can be predicted with reasonable certainty.

REPORT K

Safety Assessment of Gelled LNG

M. I. Rudnicki
E. M. Vander Wall

Prepared for the
Environmental and Safety Engineering
Division
U.S. Department of Energy
and the Department of Commerce,
Maritime Administration,
Office of Commercial Development
under Contract DE-AC-03-78EV02057

Aerojet Energy Conversion Company
Sacramento, California 95813

THIS PAGE

WAS INTENTIONALLY

LEFT BLANK

REPORT K

TABLE OF CONTENTS

FIGURES

TABLES

1.0 SUMMARY

This project involved the characterization of gelled LNG (GELNG) with respect to process, flow, and use properties and an examination of the degree of safety enhancement attainable by gelation. The investigation included (1) an experimental examination of gel properties and gel safety characteristics as well as (2) an analytical study involving the economics and preliminary design of an industrial scale gelation system.

The safety-related criterion for the successful application of gelled LNG is the substantial reduction of the Maximum Distance to the Lower Flammability Limit (MDLFL). This will be achieved by first, gel inhibition of the hydrodynamic pooling and spreading of the spill, and second, the suppressed thermal transport properties of the GELNG relative to those of LNG.

Experimental work on this contract revealed the superiority of water over methanol as a gelling agent for LNG on the basis of the minimum gelant required to obtain a given gel structure. Yield stresses were measured over a range of gel conditions and were found to increase with increasing gelant content. Similarly, determinations of rheological characteristics were conducted, revealing effects of gelant concentration in the carrier gas and end product GELNG. Gels flowed easily through flow coils, exhibiting shear thinning with no evidence of gel structure degradation even after repeated shearing. Gel expulsion from tanks was found to be dependent on tank surface area. Expulsion efficiencies greater than 90 percent of those exhibited by LNG were obtained for gels using a tank with a surface area to volume ratio as large as 8.5 ft^{-1}. There was little difference found between boiloff rates of LNG and GELNG under simulated storage conditions of low and moderate heat flux. Five gallon unconfined spills showed that gelation significantly increases total spill vaporization times and decreases maximum spill spread areas. Vaporization rates determined from 0.4 gallon confined spills on sand, concrete, and water were also found to be lower for gels than for LNG. Rates were decreased as much as five fold at some points along the vaporization

rate vs time curves for sand and concrete spill tests. Rates were found to decrease by more than two times at some points along water spill vaporization rate curves. It was found that 2 weight % gelant GELNG could not be driven through a simulated crack, even at up to 20 psig driving pressure; LNG was found to flow freely at lower pressures.

The industrial scale gelation study evaluated a design capable of producing 11,000 gallons (LNG tank truck) of gel in two hours. The increased cost of gelation using this equipment was estimated at $\$0.23/10^6$ Btu for plants with liquefaction facilities.

The technical results of this study are supportive of the conclusion that gelation of LNG will reduce, relative to ungelled LNG, the hazard associated with a given size spill. Parameters of interest to the LNG facility operator (such as pumpability) are not significantly affected by gelation, and the impact on LNG delivery cost appears to be small, about 5%. Thus, the initial assumption that gelation would provide a practical means to enhance safety is supported by the results of this study. Larger scale, comparative spill tests of LNG and GELNG are now required to confirm the safety aspects of use of the gelled material.

2.0 INTRODUCTION

The projected importation of large quantities of LNG into the U.S., as a result of the domestic natural gas shortage, has generated considerable public concern and resistance because of the potential danger of catastrophic explosion or asphixiation from vapor clouds formed by the rapid evaporation of accidentally spilled LNG. Projections of LNG imports of about 5 billion cfpd in 1980 and over 10 billion cfpd by 1990 indicate that, by 1990, ships will be off-loading at the rate of five ships per day with about 15 LNG carriers in U.S. ports at all times. Therefore, the potential for accidental spills resulting from collision, etc., cannot be considered negligible. The consequences of a major spill, especially in a populated and/or industrial area, are totally unacceptable.

The gelling of LNG inhibits the free-flowing character of the liquid and, by so doing, reduces the spread area and rate of evaporation from a given amount that is accidentally spilled. In concept, this could result in a reduction in the magnitude of a pool fire or of an unignited vapor cloud. The relative advantage of gelling, of course, depends upon the reduction in risk and the cost associated with its achievement.

Successful experiments with the gelling of cryogenic fluids were carried out many years ago, and the ability to gel LNG was demonstrated by Aerojet[1] in 1970. The gelling of LNG as a means of reducing shipping hazards has been examined by Shanes[2].

The objective of the program reported herein was to characterize gelled LNG for process, flow, and use properties and to explore safety enhancement through the use of GELNG. To attain the objective, a five-task technical program was carried out as follows:

Task 1 - Gel Preparation
Task 2 - Gel Characterization
Task 3 - Safety Evaluation Tests
Task 4 - Preliminary Design of Industrial-Scale Gelation System
Task 5 - Preliminary Economic Assessment

3.0 EXPERIMENTAL RESULTS AND DISCUSSION

Experimental work performed on the program was directed toward completion of the first three tasks. Accordingly, the results are presented under the following headings: 3.1, Task 1-Gel Preparation; 3.2, Task 2-Gel Characterization; and 3.3, Task 3-Safety Evaluation Tests.

3.1 GEL PREPARATION

Performance of the gel preparation task served two distinct functions. It produced gels for the characterization and safety evaluation task and furnished information concerning gelant selection.

The batch gel production facility assembled under this task allowed for the preparation and evaluation of approximately four-liter quantities of gel. A total of approximately 90 gels were prepared for characterization and safety testing.

Methane and two distinct LNG compositions containing heavier hydrocarbons were selected for gelation studies. The two LNG compositions were designated LNG A and LNG B, with LNG A containing nominally 93% CH_4 and 7% C_2H_6 and LNG B containing nominally 85% CH_4, 10% C_2H_6, and 5% C_3H_8.

Two gelant candidates, methanol and water, were investigated with respect to properties exhibited by gels produced using each gelant. The data show that significantly more gelant was required for methanol gels to obtain the same degree of structure as water gels. For this reason, water gelant gels dominated the investigations in this program.

Gels prepared using a variety of gelant injection stream concentrations were characterized according to yield stress and rheological properties. The trends observed in this set of tests made it evident that gels required less gelant to attain a given structure when prepared using a lower gelant injection concentration. A gelant injection stream concentration of 25 volume percent was used for the majority of the experimental work. This concentration was chosen in order to provide adequate dispersion without requiring excessively long gelation times.

3.2 GEL CHARACTERIZATION

Physical characteristics of LNG gels and their variation with gelant content, gel composition, gelant type, and method of preparation were examined. Gels were characterized according to six properties: (1) yield stress; (2) rheological characteristics; (3) flow characteristics under simulated transfer conditions; (4) expulsion behavior; (5) gel aging characteristics; and (6) boil-off rates under simulated storage conditions.

3.2.1 Yield Stress

Yield stress measurements were made approximately 90 gels using the weighted sphere method. The method involved the determination of

the maximum weight sphere that could be supported by a given gel. Four glass spheres of the same diameter, containing various amounts of mercury to provide a range of weights, were employed.

It is important to note that yield stresses determined by the weighted sphere method actually represent a yield stress range. This range corresponds to yield stress values between the maximum weight supported and the minimum weight which fails to be supported. Since values listed in this report are determined from the maximum supported weight, they represent minimum yield stress values.

Under the conditions of similar composition and preparation methods, yield stresses for LNG and methane gels were found to increase with gelant content over the range of conditions investigated. This can perhaps best be seen through an examination of each of the three sections of Table 1. Over these condition ranges the observed yield stress trend was evident with only a few minor exceptions.

A comparison between the three sections of Table 1 reveals that yield stresses were less for LNG gels than for methane gels when the gels compared were of similar gelant content with similar preparation histories. Yield stresses for the two types of LNG gels examined did not differ significantly over the range of conditions investigated.

Two gelant candidates, water and methanol, were examined with respect to the yield stresses exhibited by their corresponding gels. LNG A gelled with methanol required significantly more gelant to achieve yield stresses corresponding to those measured for gels gelled with water.

Yield stress measurements were made on gels with differing preparation histories. The specific variation in gel preparation involved changes in the gelant concentration in the injection gas stream. Yield stresses increased with decreasing gelant concentration for gels of similar composition, of similar gelant content, and of the same gelant type.

3.2.2 Rheological Characteristics

Two types of tests were performed to characterize LNG and methane gels according to their rheological properties. Both types of

TABLE 1

YIELD STRESS DATA FOR METHANE AND LNG GELS AT 102 K PREPARED USING APPROXIMATELY 25 VOL % WATER GELANT IN THE INJECTION GAS STREAM

Approximate LNG Composition of Gel (Vol. % as Gas)				Volume % Gelant in Injection Gas Stream	Wt. % Gelant	Yield Stress ($dynes/cm^2$)
Methane	Ethane	Propane	Gelant			
84	11	5	Water	25	3.3	771
85	10	5	Water	25	3.5	771
88	8	4	Water	26	3.8	771
85	10	5	Water	25	4.0	270
85	10	5	Water	25	4.1	771
77	15	8	Water	25	4.3	973
81	13	6	Water	25	4.3	973
84	11	5	Water	25	4.4	973
85	10	5	Water	26	4.6	973
85	10	5	Water	25	6.5	973
93	7	0	Water	24	2.2	<270
90	10	0	Water	25	2.6	<270
91	9	0	Water	24	2.8	<270
93	7	0	Water	25	2.8	<270
89	11	0	Water	25	2.9	270
93	7	0	Water	25	2.9	270
93	7	0	Water	25	3.0	270
93	7	0	Water	25	3.0	270
91	9	0	Water	25	3.1	270
93	7	0	Water	25	3.1	270
93	7	0	Water	25	3.2	270
93	7	0	Water	25	3.5	270
93	7	0	Water	26	3.6	771
93	7	0	Water	25	3.6	771
88	12	0	Water	24	3.7	270
93	7	0	Water	25	3.8	771
93	7	0	Water	25	4.0	270
89	11	0	Water	26	4.1	771
93	7	0	Water	25	4.1	973
85	15	0	Water	24	4.4	771
93	7	0	Water	25	4.6	771
87	13	0	Water	26	4.7	1311
91	9	0	Water	25	4.7	973
93	7	0	Water	25	5.5	973
100	0	0	Water	25	1.6	<270
100	0	0	Water	25	1.9	270
100	0	0	Water	25	2.7	270
100	0	0	Water	25	2.9	771
100	0	0	Water	26	3.5	771
100	0	0	Water	25	3.6	771
100	0	0	Water	25	3.7	771
100	0	0	Water	25	3.8	973
100	0	0	Water	25	4.3	973
100	0	0	Water	25	4.3	>1311
100	0	0	Water	25	4.6	1311

testing involved flowing gels through coiled tubes under isothermal conditions. One test type was designed to provide characteristic flow data by measuring shear rates for gels flowed under selected constant shear stresses, while the other test type involved determinations of the degree of gel structure degradation resulting from repeated flow cycles at high shear rates.

Shear rates were determined in the isothermal gelation enclosure using a flow loop consisting of coiled copper tubing. After gel preparation, the gelation vessel was pressurized to a preselected value, and a valve was opened to allow flow through the loop. The volume of gel flowing through the tubing was recorded as a function of time. Typical results are plotted in Figure 1.

All gels subjected to characteristic flow testing showed shear-thinning (apparent viscosity decreases as shear rate increases). This was true regardless of gelant content of the gel, LNG composition of the gel, gelant type employed, or injection gelant concentration.

Flow characteristics were found to vary with gelant content according to the following trends: (a) Apparent viscosity at a given shear rate increased with gelant content. (b) The degree of shear thinning showed a weak tendency to increase with gelant content. See Figure 1 for typical results.

Data was obtained for gels belonging to three different categories with respect to hydrocarbon composition, including gels containing only methane, gels containing methane and ethane (LNG A type gels), and gels containing methane, ethane and propane (LNG B type gels). Flow characteristics were found to vary with the hydrocarbon compositions of gels according to the following trends: (a) Methane gels had higher apparent viscosities at low shear rates and exhibited a greater degree of shear thinning than corresponding LNG gels (i.e., gels containing heavier hydrocarbons), and (b) LNG A type gels exhibited higher apparent viscosities at given shear rates than LNG B type gels even when methane mole percentages were similar.

Flow characteristics were investigated for two gelant candidates, water and methanol. Apparent viscosities for methanol gelant type LNG gels

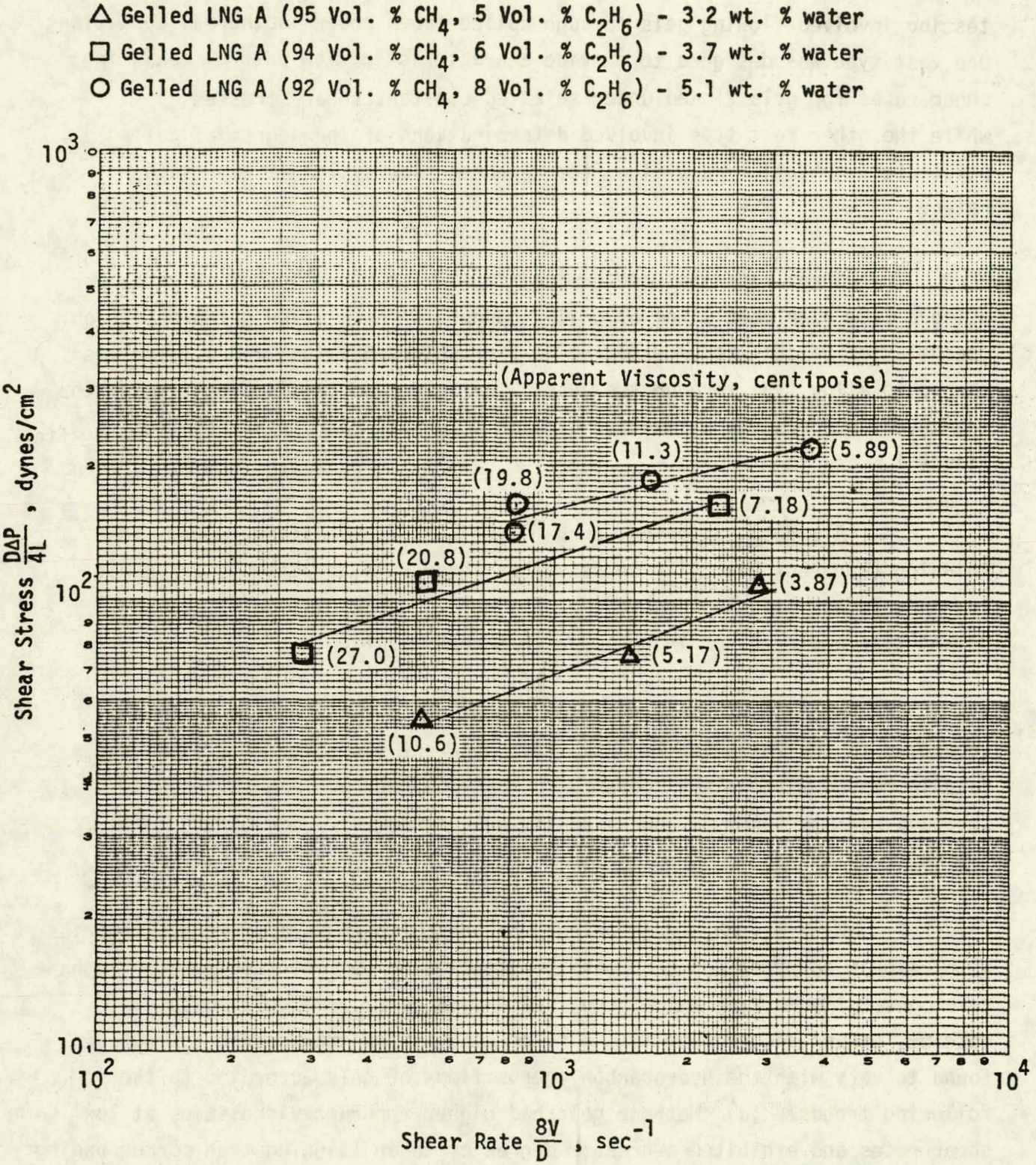

Figure 1. Characteristic Flow Curves of Gelled LNG A at 102 K Prepared Using 60 Vol. % Water Gelant in the Injection Gas Stream

were significantly lower than those for corresponding water gelant type gels even at much higher gelant contents.

The preparation variable examined with respect to rheology was injection stream gelant concentration. Apparent viscosity at a given shear rate increased with decreasing injection stream gelant concentration.

Shear degradation testing was performed using the characteristic flow test apparatus. Gels were subjected to five flow cycles from the preparation vessel to the receiving vessel and back at shear rates greater than 3000 sec^{-1}. Yield stress measurements were made before and after flowing to determine the degree of gel structure degradation. Two LNG A gels were subjected to shear degradation testing. One of the gels was a 3.5 weight percent water gel with a yield stress of 270 $dynes/cm^2$. The other gel was a 4.7 weight percent water gel with a yield stress of 771 $dynes/cm^2$. No evidence of shear degradation was noted for either gel.

3.2.3 Flow Characteristics Under Simulated Transfer Conditions

Flow characteristics of LNG A and GELNG A were determined under comparable nonisothermal conditions by flowing both substances through a controlled heat transfer apparatus. The apparatus consisted of a sixteen inch long stainless steel tube with a .18 inch inner diameter. The tube was fitted with an external jacket through which a measured, ambient temperature gaseous nitrogen flow was passed to simulate thermal conditions associated with material transfer.

Transfer tests using LNG A and LNG A gel containing 3.5 weight percent water gelant were performed. Flow rates determined from the tests were 2630 cc/min for LNG and 1516 cc/min for the gel. This gel transfer rate was as expected considering the experimentally-determined apparent viscosities and the higher temperature conditions involved in these tests. No problems were encountered in GELNG transfer.

3.2.4 Expulsion Behavior

Three types of tests were conducted to investigate expulsion behavior. One set of tests examined maximum expulsion of gels as a function of yield stress, gelant content, and gel composition. A second test set involved expulsion behavior at a constant driving pressure. The third test type probed the relationship between vessel surface area and expulsion efficiency.

Maximum expulsion tests utilized a transparent pyrex expulsion vessel with surface area to volume ratio of $0.28 cm^{-1}$. Tests were initiated with the preparation of gel in the expulsion vessel. The initial gel volume was noted and expulsion was initiated by pressurizing the vessel with helium. Gel was expelled through the transfer tube to a point outside the environmental enclosure using variable driving pressures up to 20 psig. After expulsion had been completed, the remaining gel was allowed to settle in the expulsion vessel and the final volume was recorded. The data shows that expulsion efficiencies for gels are slightly lower than those for LNG. In addition, expulsion efficiencies decrease slightly with increasing gelant content and with increasing yield stress for gels with similar LNG compositions.

Constant pressure expulsion tests were performed using the same test apparatus and basically the same procedure as for the maximum expulsion tests. Constant pressure tests differed by utilizing a constant driving pressure of 7 psig to expel the gel rather than a variable pressure. The results indicate lower expulsion efficiencies for gels driven by a constant 7 psig pressure than for similar gels expelled using a variable driving pressure up to 20 psig.

Increased surface area expulsion tests were conducted using a 700 cc transparent pyrex expulsion vessel with a full vessel surface area to volume ratio equal to $0.89\ cm^{-1}$. The initial gel volume in the expulsion vessel was recorded and expulsion was started by pressurizing the vessel with helium. Results indicated that expulsion efficiencies are much lower than might be expected on the basis of the maximum expulsion test noted above. Findings suggest that expulsion efficiencies for LNG gels are strongly dependent on vessel surface area exposed to the gel. It is probable that

tanks with smaller surface area to volume ratios would have expulsion efficiencies more comparable to those for LNG.

3.2.5 Gel Aging Characteristics

Two sets of gel aging tests were conducted. Each set involved the static storage of three compositionally different gels under isothermal conditions near their boiling points. A methane gel, an LNG A gel, and an LNG B gel were selected for storage in each test set. The first test set was monitored for over 24 hours, while the second set had a test duration in excess of 100 hours. No visual changes were noted in any of the gel samples over any of the monitored test periods.

3.2.6 Boil-Off Rates Under Simulated Storage Conditions

No significant difference was observed between boil-off rates for LNG and those for LNG gels under static storage conditions at low heat fluxes corresponding to approximately 18 Btu/ft^2 and 70 Btu/ft^2. At three distinct insulating regimes, corresponding to LNG heat fluxes between 114 Btu/ft^2 hr and 317 Btu/ft^2 hr, gels tested were found to have slightly higher boil-off rates than LNG. This is counter to the trend seen during spills, in which high heat fluxes are encountered. The mechanisms involved in this result are not known at this juncture. Additional testing at higher heat fluxes is recommended to clarify this issue.

3.3 SAFETY EVALUATION TESTS

Safety evaluation tests were directed toward defining the relative safety characteristics of GELNG with respect to those of LNG. The three types of tests selected to achieve this goal were spill behavior tests, leakage behavior studies, and boil-off behavior determinations.

3.3.1 Task 3.1 - Spill Behavior

Three types of tests were used to evaluate spill behavior. Simulated one dimensional spills, unconfined land spills, and unconfined

water spills were performed using both LNG A and GELNG A.

Simulated one dimensional spill tests were conducted using a modified version of a spill apparatus designed under the direction of Professor R. C. Reid at M.I.T. The apparatus provided a controlled, virtually one dimensional environment for investigating small scale spills on water. It consisted of a 10 foot long section of clear Pyrex pipe with a 6 inch internal diameter. Before initiating testing, the pipe was half filled with deionized water. Approximately one quart of the test sample was then introduced into the system through the entry port. Small scale water spills using liquid nitrogen, LNG and GELNG were conducted. Both liquid nitrogen and LNG spills produced vapor clouds which were visible for less than 2 minutes. In contrast, GELNG samples showed evidence of gas evolution eight minutes after the spill.

Six unconfined land spills were conducted. These tests included two liquid nitrogen equipment check out spills, one LNG A spill, and three GELNG A spills. All gels tested showed a significant increase in total vaporization time and a decrease in maximum spill spread area. This is evident from the spill test results given in Table 2. A qualitative view of vapor cloud dispersion behavior and spill vaporization rates is provided by the time sequenced photographs of land spill testing presented in Figures 2 and 3 for LNG and GELNG, respectively.

One LNG A spill and one GELNG A spill were conducted on water. Total vaporization times were nearly the same for both unconfined water spills. The gel, however, exhibited a decrease in maximum spill spread area compared to that for LNG. Review of the spill technique and results of the water spill tests leads to the conclusion that the test series should be redone using less violent spilling onto the water surface. This would be more nearly representative of marine spill scenarios.

3.3.2 Leakage Behavior

Two categories of leakage tests were conducted using both LNG and GELNG. One test type involved the determination of leakage rates

Table 2

UNCONFINED LAND SPILL TEST RESULTS

Parameter						
Test Number	1	2	3	4	5	6
Substance Spilled	LN_2	LNG[2]	GELNG[1],[3]	GELNG[1],[4]	LN_2	GELNG[1],[5]
Mass Spilled (lbs)	36.5	21.5	6.0	18	30	21.5
Volume Spilled (gal)	5.4	5.8	1.6	4.9	4.4	5.6
Wind Direction	SW	SW	NE	SSE	SSE	WNW
Wind Speed (mph)	2.5-3	2	2-3	5-10	5-10	0.5
Average Ambient Temperature (°F)	59	59	51	54	54	70
Relative Humidity (%)	45	45	80	65	65	45
Approx. Maximum Spill Spread Area (sq. ft.)	41	67	13	44	50	49
Approx. Spill Vaporization Time (min.)	0.3	0.2	(10.7)[6]	(5.8)[7]	0.3	(7.0)[8]
Visible Vapor Cloud Dissipation Time (min.)	1.8	1.4	(7.5)[6]	(4.3)[7]	1.4	5.5
Ground Conditions	Dry	Dry	Moist	Wet	Wet	Dry

---

(1) All gels were prepared using approximately 25 volume percent water vapor gelant in the injection gas stream.

(2) The LNG composition as volume % gas was 93% CH_4 and 7% C_2H_6.

(3) The LNG gel used was a 5.5% by weight water gel with a yield stress of ~973 dynes/cm^2. The LNG composition of the gel as volume % gas was 93% CH_4 and 7% C_2H_6.

(4) The LNG gel used was a 3.1% by weight water gel with a yield stress of ~270 dynes/cm^2. The LNG composition of the gel as volume % gas was 93% CH_4 and 7% C_2H_6.

(5) The LNG gel used was a 3.5% by weight water gel with a yield stress of ~270 dynes/cm^2. The LNG composition of the gel as volume % gas was 93% CH_4 and 7% C_2H_6.

(6) The spilled gel was ignited after 7.5 minutes and burned for an additional 3.2 minutes.

(7) The gel was ignited after 4.3 minutes and burned for an additional 1.5 minutes.

(8) The remaining gel was ignited after 7.0 minutes and burned less than 0.1 minutes.

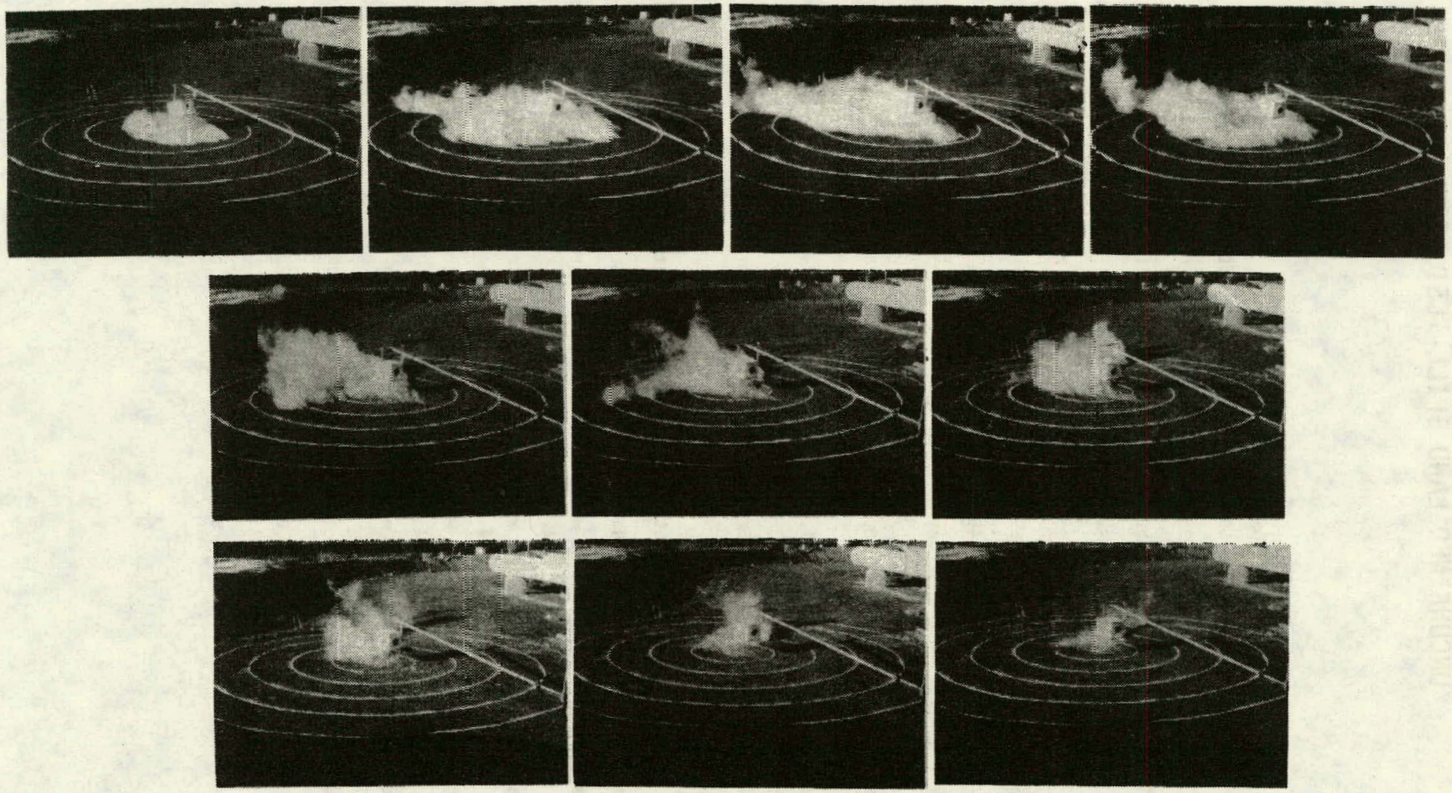

INITIAL 20 SECONDS OF TESTING AT 2 SECOND INTERVALS

Figure 2 Unconfined LN_2 Land Spill - Test #1

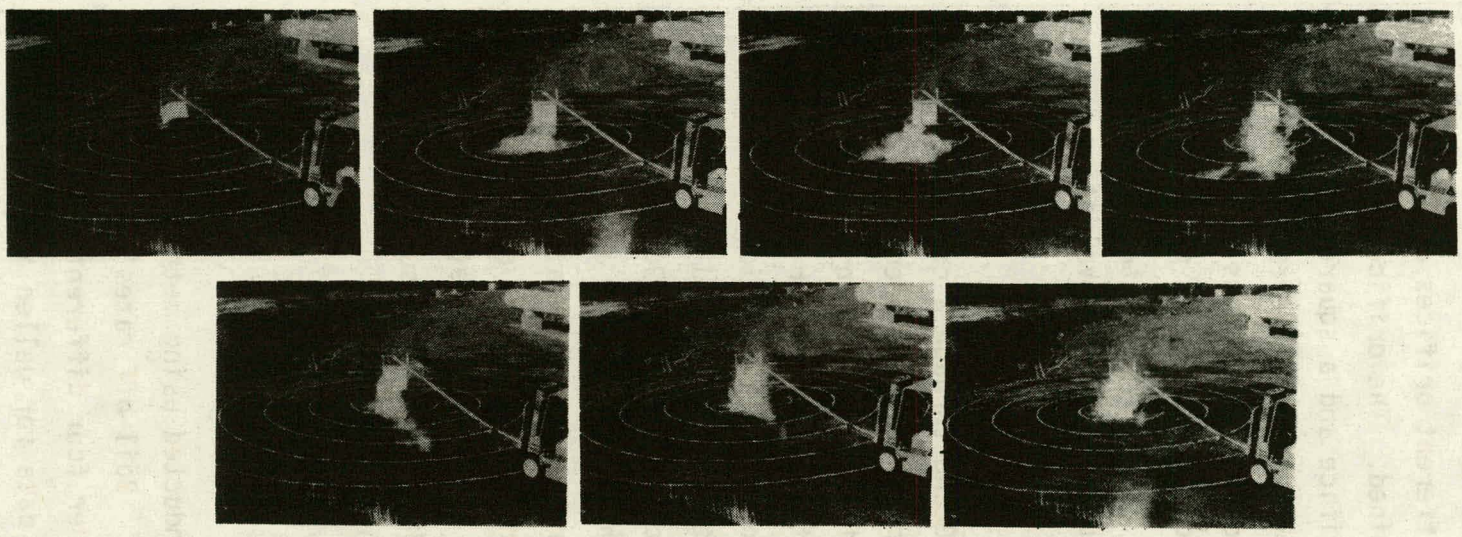

INITIAL 14 SECONDS OF TESTING AT 2 SECOND INTERVALS

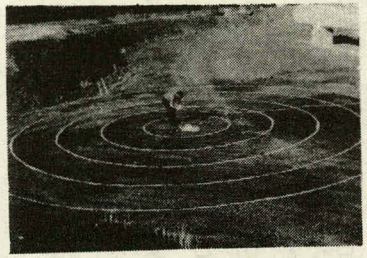

After 7.5 min.

After Ignition

Figure 3 Unconfined Gelled LNG Land Spill - Test #3

through orifices, while the second test type examined leakage through a crack in a fitting.

Leakage rates through two different orifices at a driving pressure of approximately 10.5 psig were determined. The orifices involved in the tests were a .128 inch diameter round orifice and a square orifice .132 inch on a side. Both orifices were tested in three different leakage environments (air, water, and air-water interface). Comparisons between leakage rates for LNG and GELNG under similar conditions reveal mixed results which are probably attributable to experimental error. More data, particularly at lower driving pressures, would be valuable in evaluating these comparative rates.

Leakage behavior of LNG and GELNG through a crack was investigated with an experimental setup very similar to that used for orifice leakage determinations. The crack was formed by notching a brass pipe fitting and then stress cracking it along the notch by over-torqueing a threaded pipe into the fitting threads. Microscopic examination showed the crack to be an opening with an approximate length of 0.38 cm and a maximum width of .060 cm. LNG A flowed through the crack at a rate of 964 g/min at a driving pressure of 10.5 psig, while gels with gelant content as low as 2.0 weight percent showed no detectable flow through the crack at the same driving pressure. In addition, a 2.0 weight percent gel showed no detectable flow at a driving pressure of 20 psig. All gel tests in this set showed a small initial flow of material through the crack upon tank pressurization. This initial flow was followed immediately by flow cessation.

3.3.3 Boil-Off Behavior

Boil-off rate testing was conducted using methane, LNG A, LNG B, methane gels, LNG A gels, and LNG B gels. Boil-off rates for contained spills of various sizes were examined under four different sets of spill conditions in order to obtain comparative data for gelled and ungelled material under each set of conditions. The four spill types employed were contained spills on water, on land, on land in the presence of an ignition source and on concrete.

Boil-off rate determinations for contained spills on water were performed using a 4 inch deep, 20 inch by 19.5 inch rectangular aluminum spill pan suspended from a 100 pound capacity load cell. During vaporization, the output of the load cell was continuously recorded to determine mass versus time relationships. The contained spill apparatus is shown in Figure 4. Sixteen water spill tests were conducted. Typical results are presented in Figure 5. General characteristics of the methane and LNG vaporization curves are similar to those observed by Shanes[2]. Vaporization rates, however, are lower than those observed by Shanes. It is evident that gelation significantly reduces the confined water spill vaporization rates of methane, LNG A, and LNG B. Further, gels prepared by methods used in this study required greater than 4.4 weight percent water gelant to significantly reduce LNG vaporization rates for contained water spills.

The apparatus employed for confined water spill testing was also used for confined land spill boil-off rate determinations. Instead of water, the aluminum pan was filled with silica sand. For the confined land spills, as was the case for water spills, it is evident that gelation significantly reduces the vaporization rates of methane, LNG A, and LNG B. Land spill vaporization rates are effectively reduced for even the lowest water content gel tested (2.8 weight percent).

Boil-off rate tests for confined land spills in the presence of an ignition source were conducted in the same manner as confined land spill tests except that an electrical resistance heated nichrome wire ignition source was placed in the vicinity of the spill. Data for one LNG A and one GELNG A land spill vaporization test in the presence of an ignition source are plotted in Figure 6. Material combustion increases the length of time that both LNG A and GELNG A exhibit high land spill vaporization rates. In addition, it is evident that gelation significantly reduces confined land spill vaporization rates for LNG A even when a spill ignition source is present.

An apparatus similar to the one used for boil-off rate determinations on water was employed to obtain vaporization rates on concrete. A rectangular concrete spill basin replaced the water spill surface in this

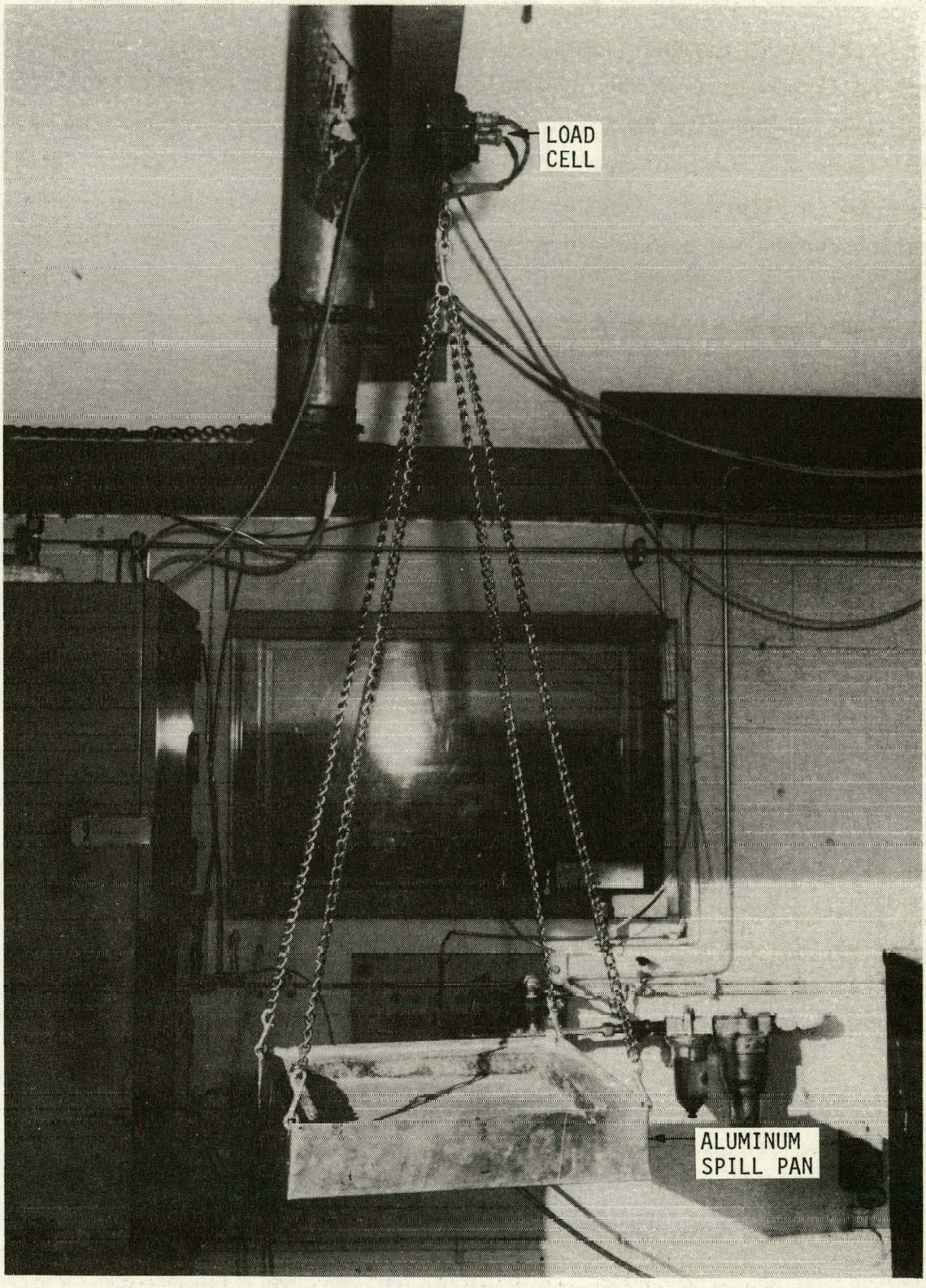

Figure 4 Confined Spill Vaporization Apparatus

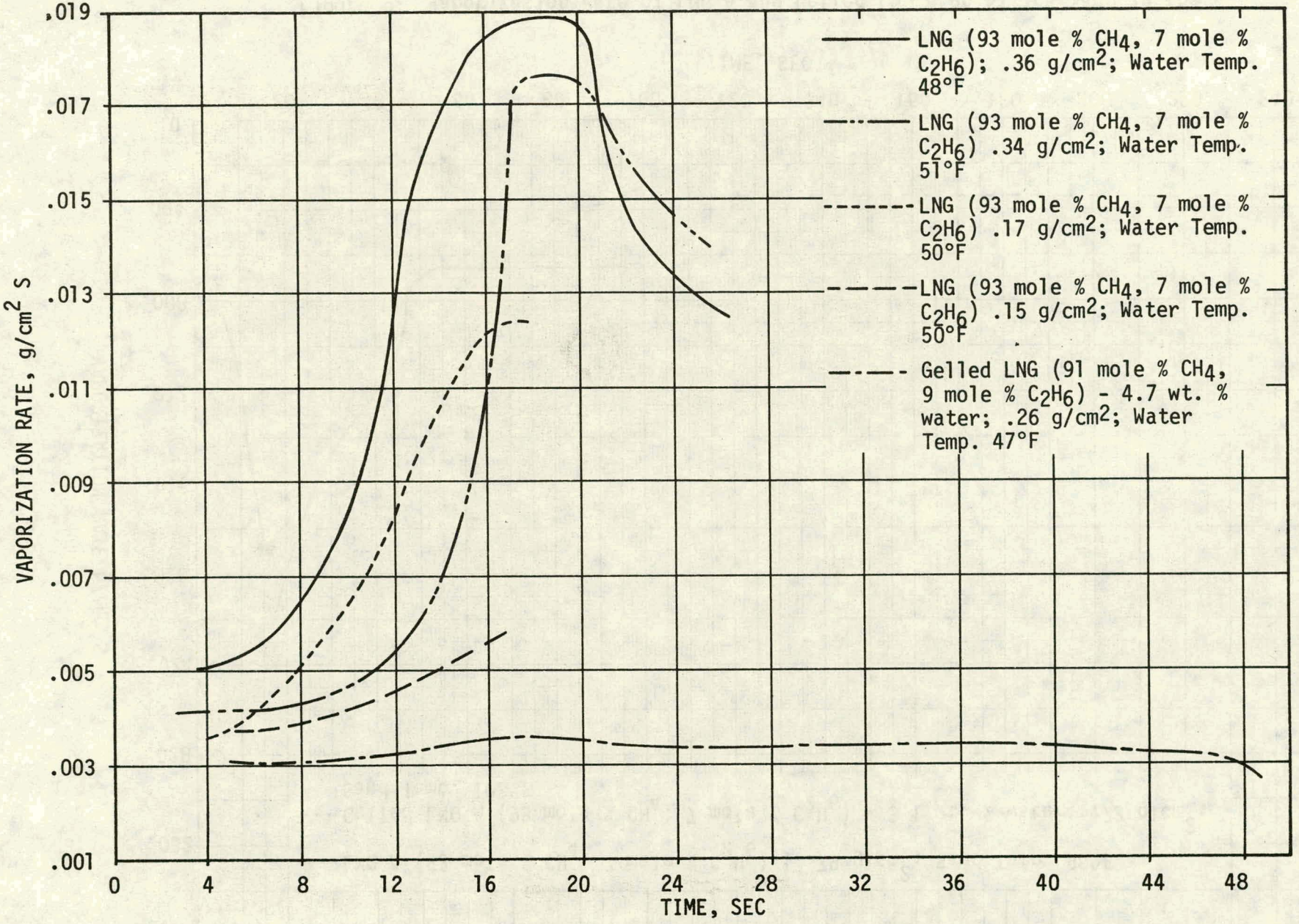

Figure 5 Vaporization Rate of LNG A and LNG A Gels on Water

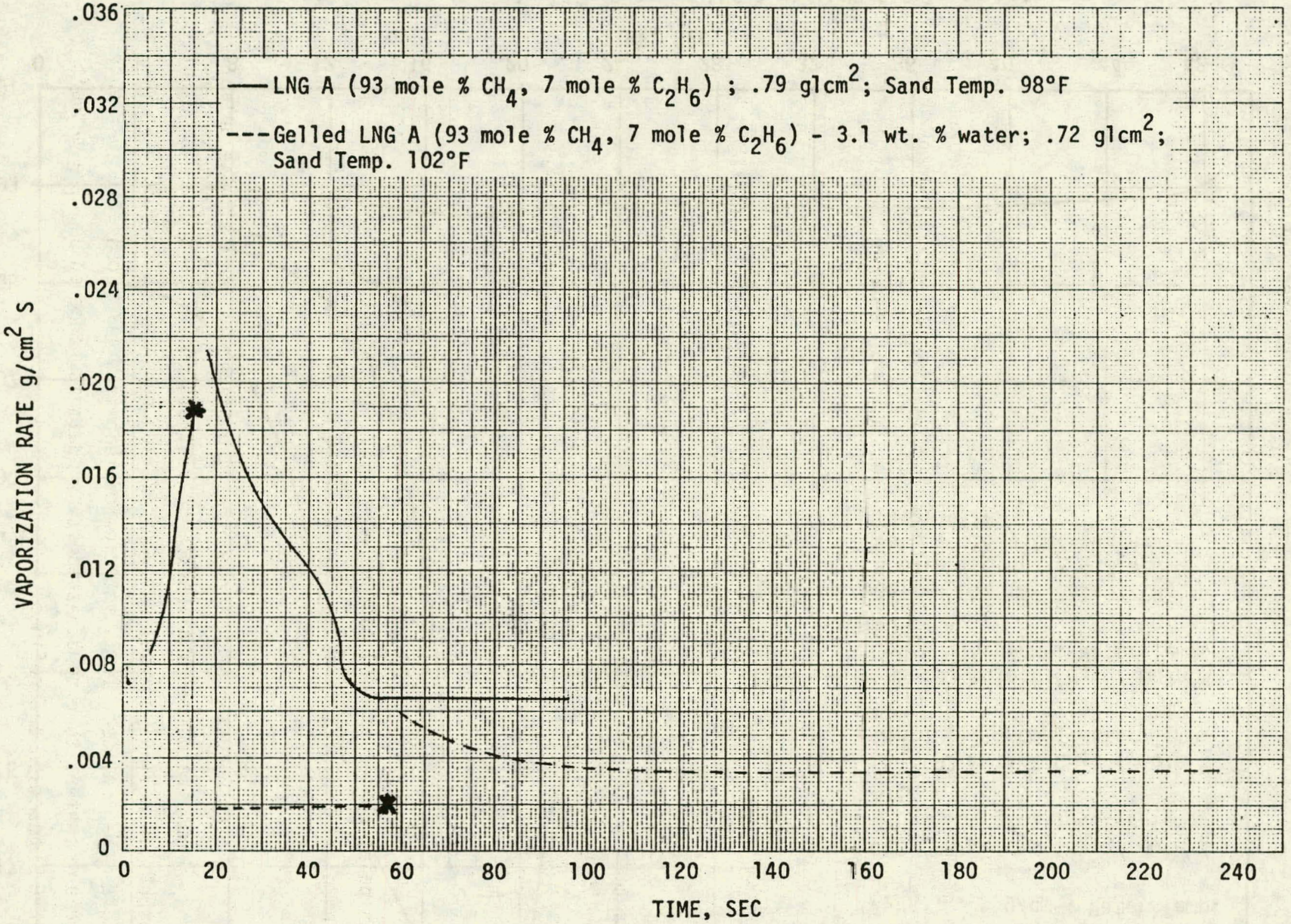

Figure 6. Vaporization Rate of LNG A and Gelled LNG A on Silica Sand in the Presence of an Ignition Source

set of tests. It was found that gelation significantly reduces concrete spill vaporization rates for methane, LNG A, and LNG B. All LNG A gels tested exhibited reductions in vaporization rate over LNG A even at gelant contents as low as 1.9 weight percent. Vaporization rates for gels increased with decreasing gelant content.

4.0 INDUSTRIAL SCALE GELATION PROCESS STUDIES

Industrial scale gelation studies were performed to obtain a preliminary assessment concerning the feasibility and costs of the LNG gelation process on a large scale. The results constitute work conducted under Tasks 4 and 5 of the program and are presented under the following headings: 4.1, Task 4 - Preliminary Design of an Industrial Scale Gelation System and 4.2, Task 5 - Preliminary Economic Assessment.

4.1 PRELIMINARY DESIGN OF AN INDUSTRIAL SCALE GELATION SYSTEM

The system designed in this task consists of the equipment required to convert LNG to the gelled form, GELNG. Auxiliary equipment (e.g., regasification gelant removal) for integrating the gelation system into an overall LNG facility is not covered in the design, although such factors are considered in the subsequent economic evaluation.

The GELNG output capacity of the system is chosen to provide filling of an 11,000 gallon LNG truck in less than two hours. The specific design point chosen is 6800 gallons/hour. For application to a peak shaving plant, this converts to just over 600 m^3 per day produced for storage.

The required GELNG properties are stated in terms of the gelant content of 5%. Data from small-scale spill tests indicates that a 5% gelant concentration will give excellent vaporization performance for GELNG in both land and water spills. It is anticipated that it will be possible to reduce the gelant content to 2 to 3% as additonal data is gathered and the methods of GELNG production are refined.

The basic continuous gelation concept selected is for the direct injection of a gaseous gelant feed stream into the LNG as it is transferred to the LNG truck or peak shaving storage tank. The continuous gelation plant schematic is shown in Figure 7. LNG is transferred to a pre-process surge tank at a rated input of 10,000 gal/hr. An LNG pump raises the process stream pressure to overcome system losses. The pumped LNG then flows through the preconditioner unit to achieve the necessary conditions for the gelation step. The control point for the process stream occurs at the output of the preconditioner. The preconditioning of the LNG is monitored and controlled by the sensors and valves through the main process control panel. The conditioned LNG then enters the gelator/separator unit. The gelant is dispersed in the LNG in a continuous manner, producing GELNG (6800 gallons/hour rated capacity) and natural gas vapor. The latter, saturated and at atmospheric conditions, is returned for reliquefaction.

4.2 PRELIMINARY ECONOMIC ASSESSMENT

A preliminary economic assessment has been made based upon the gelation plant design described above. Included are capital and operating costs for the gelation plant as well as the major economic impacts on the overall processing of GELNG (e.g., reliquefaction of gelator-produced natural gas).

The objective of the economic assessment is to calculate the increment of cost to each unit of gas delivered for a plant incorporating gelation relative to that of an unmodified LNG plant. Thus, much simplification of the calculation is valid.

The estimation of impacts on the existing facility requires some assumptions about how the integration of the gelation plant would be accomplished. For simplicity, it is assumed that a liquefaction facility exists with sufficient capacity to handle the return of gas from the gelation plant. The associated reliquefaction costs are thus attributed to extra energy costs. It is necessary to provide for gelant removal in the eventual revaporization of GELNG. A capital item has been included to account for this; it is assumed that no additional operating costs of significance are incurred by this addition.

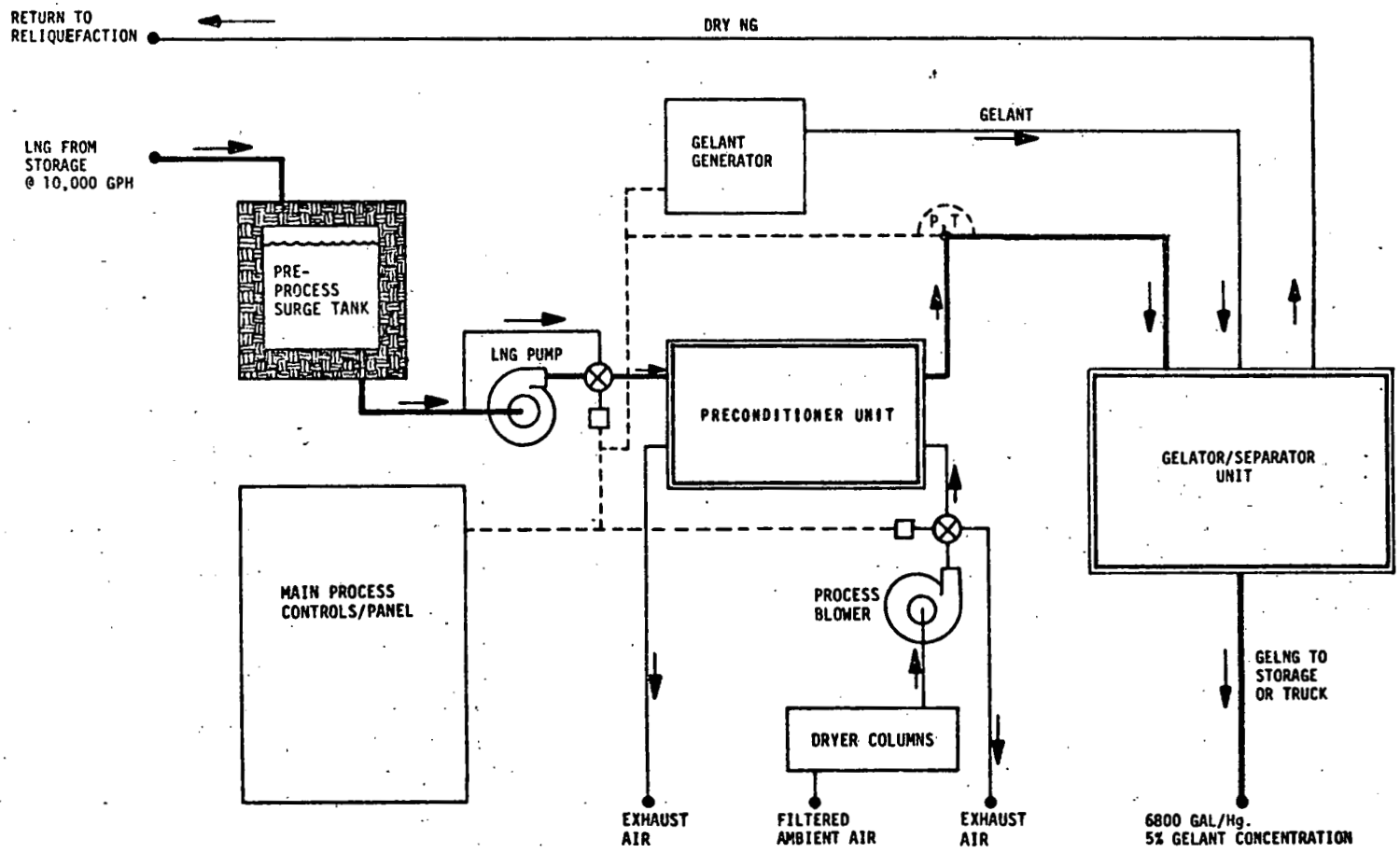

Figure 7. Continuous Gelation Plant Schematic, Conversion of LNG to GELNG

The capital cost of equipment ($1,040,000) converts to a yearly plant cost equivalent of $11.80/hour, as contrasted to the much larger operating cost of $116/hour. The combined effect is an incremental cost in the delivery of natural gas of $0.23/$10^6$ Btu, mostly attributed to operating costs. This can be compared to the basic cost of NG at the distribution point of about $4.25/$10^6$ Btu. Thus, the added cost of gelation would be just over 5% for the conditions and assumptions of this study. The addition of liquefaction capacity, if required, would have a minor impact on this result.

It is a conclusion of this cost study that the operating costs are the dominant cost factor in the increase in per-unit cost. Trade-offs which decrease the annual operating cost for increased initial capital costs would seem justified in future design/economic studies.

5.0 RECOMMENDATIONS

The following recommendations are made for futher work:

(1) Comparative evaluation of GELNG versus LNG in large- scale (40 m^3) tests at NWC, China Lake or other test site.

(2) Extending the evaluation of rheological characteristics to both higher and lower shear rates.

(3) Conducting leakage tests with perforation-type orifices.

(4) Further examination of crack leakage to establish conditions under which GELNG will flow through a crack (crack size, driving pressure).

(5) A comparative spill, spread, burn, and extinguish test series for LNG and GELNG at Brooklyn Union Gas Company's Hellsgate Fire-fighting School with the cooperation of the New York Municipal Fire Department; 40 m^3 is recommended.

(6) Unconfined water spill tests in which the cryogen is introduced gently onto the water surface to more nearly represent the marine spill scenario.

(7) Further testing at increased heat flux to establish conditions under which GELNG begins to demonstrate superiority over LNG.

(8) Additional, controlled unconfined land spill rate tests.

References

1. Vander Wall, E. M., "Investigation of the Stability of Gelled Methane for Use in a Jet Engine", Aerojet General Co., Contract NAS 3-14305, NASA CR-72876, March 1971.

2. Shanes, L. M., "The Structure and Rheological Properties of Liquefied Natural Gas Gelled with Water and Methanol Clathrates", Doctoral Thesis Digest, Department of Chemical Engineering, Massachusetts Institute of Technology, August 1977.

REPORT L

A Four Band Differential Radiometer for Monitoring LNG Vapors

J. M. Conley
J. J. Simmonds
R. A. Britten
M. Sinha

Prepared with Interagency Support for the
National Aeronautics and Space Administration
under Contract NAS-7-100

Jet Propulsion Laboratory
California Institute of Technology
Pasadena, California 91103

THIS PAGE

WAS INTENTIONALLY

LEFT BLANK

REPORT L

TABLE OF CONTENTS

FIGURES

TABLES

Summary

The Jet Propulsion Laboratory (JPL) developed a Two Band Differential Radiometer (TBDR) for monitoring methane that was successfully tested during the LNG spill tests held in the fall of 1978. The TBDR design was modified to measure absorption at four wavelengths allowing the determination of four parameters of the LNG cloud. This Four Band Differential Radiometer (FBDR) is described in this Status Report. This report provides details of the FBDR design and estimated performance together with a summary of recent development, testing and design verification activities.

Fabrication and assembly of the FBDR engineering model was completed in January 1980 and routine operation of the instrument has been achieved. Absorption data for methane, ethane and propane have been collected with gas-to-air ratios of about 5, 15 and 30% at six wavelengths. Final analysis of these results will be the basis for selecting the four wavelengths to be used in the field units.

A production prototype will be built and used for final system integration testing. Detailed opto-mechanical design of the prototype sensor is complete and fabrication of optical and mechanical components has begun. The final electronic packaging design has also been started. After verification that system integration and overall design compatibility meets performance requirements, the production of ten field instrument systems will begin.

Introduction

During 1978 the Jet Propulsion Laboratory developed a Two Band Differential Radiometer (TBDR) for monitoring methane concentration at the Liquified Natural Gas (LNG) spill tests conducted by the U. S. Coast Guard and the Department of Energy. That instrument measured the absorption by the LNG cloud at two wavelengths in the near infrared, one at a methane absorption band and a second at a spectral window. It was successfully tested at the Fall, 1978, spill test conducted at China Lake, California (1). Following the 1978 tests, it was recognized that a capability for differentiating methane from ethane and propane was desirable. The design of the TBDR is now being modified to measure the absorption at four wavelengths, allowing the determination of four parameters of the LNG cloud. The baseline design of the Four Band Differential Radiometer (FBDR) calls for the measurement of methane, ethane, and propane. The fourth channel is utilized to correct for variations of source intensity or of broadband extinction in the optical path. The spectral region of the 2.0 to 2.5 μm bands of methane, ethane, and propane was selected because of the availability of inexpensive components and high performance room temperature detectors. For example, crown glass transmits well here, the lamp is a readily available commercial component, and the lead sulfide detectors yield specific detectitives of $\geq 10^{10}$ at low cost.

This report gives some details of the design considerations and estimated performance of the FBDR. In addition, the development, testing and design verification activities undertaken during the period August 1979 to April 1980 are described. Finally plans are summarized for the construction of a production prototype, the production of tar field units and support of field testing at the China Lake Test Facility.

Instrument Description

Figure 1 is a preliminary isometric sketch of the instrument sensor, which is contained in a sealed housing of approximate dimensions 5.4 x 13 x 20 cm. The source is an incandescent lamp operating at a temperature of approximately 1850 K. The source beam is chopped by a motor driven blade and exits the sensor housing through a condensor lens which is the optics entrance pupil. The sensor is deployed in the region of the spill and is immersed in the LNG vapor cloud during the spill test. Thus, the absorption region, rather than being a cell as in laboratory instruments, is external to the sensor in the path defined by the external mirrors. Nominally, four passes are made for a total path length of 60 cm. Upon re-entering the housing through a window, the beam is split by the partially silvered mirrors indicated in the drawing, and field lenses image the entrance pupil on the detectors. Four PbS detectors are mounted in the T-shaped detector block, each integral with an interference filter. The detector assembly, consisting of the mounting block, detectors, detector masks and interference filters are temperature controlled with a thermoelectric cooler in order to stabilize the responsivity of the detectors and the pass bands of the filters.

Figure 2 illustrates the instrument in block diagram form. The PbS detectors are followed by the necessary signal conditioning, digitizing and interface circuits. The test facility at China Lake provides data acquisition, recording, and reduction.

Principle of Operation

Ideally, the instrument would utilize three absorption bands, each of which absorbs for one of the three gases, and a fourth band, a "window," absorbed by none of the three. None of the four bands would be absorbed by ambient atmospheric gases or water vapor. Additionally, the bands would be spectrally adjacent such that differential effects, for example, those due to scattering and lamp temperature changes, would be small. No such bands could be found for these gases in the visible and near infrared. There are, however, bands which are absorbed strongly by one or two of the hydrocarbons and less strongly by the other(s). There are also regions approximating windows, where the absorption is small for all three gases.

Had it been possible to find ideal absorption bands, it would have been possible to derive gas concentrations from absorption data in a computationally trivial manner. The observed deviations from the ideal lead to greater mathematical complexity.

In all of the bands studied ethane and propane showed absorption properties which follow Beer's law:

$$I = I_o \exp (-\alpha c \ell)$$

where I_o is the intensity of the incident light, I is the transmitted intensity, α is the absorption coefficient $(\text{atm cm})^{-1}$, c is the gas concentration (atm), and ℓ is the path length (cm).

At six of the bands studied, methane absorption also follows Beer's law, but for two bands studied the absorption is described by an equation of the form

$$I = I_o \exp (- \beta c^{2/3} \ell)$$

where β is an empirical constant.

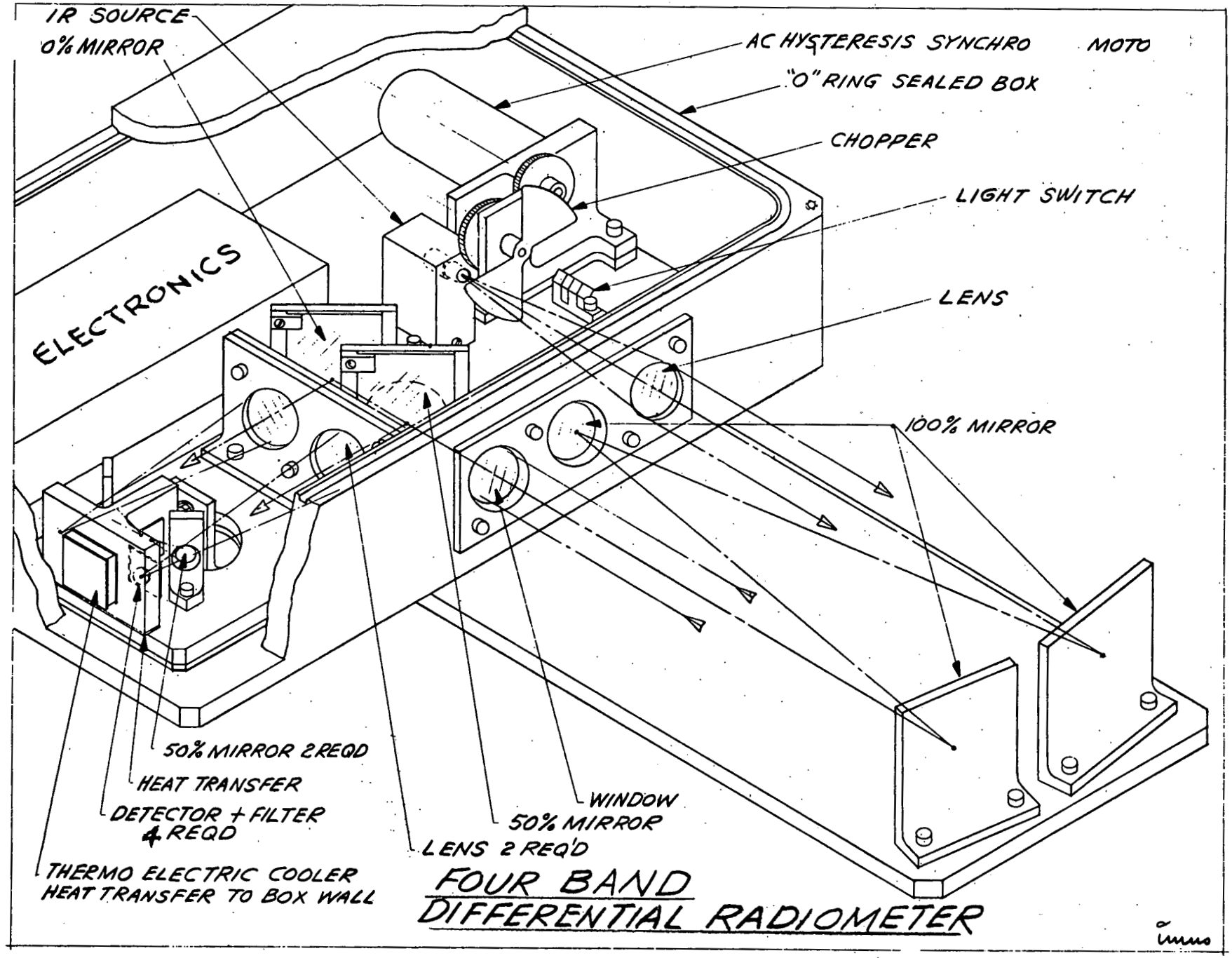

Figure 1. FBDR Conceptual Drawing

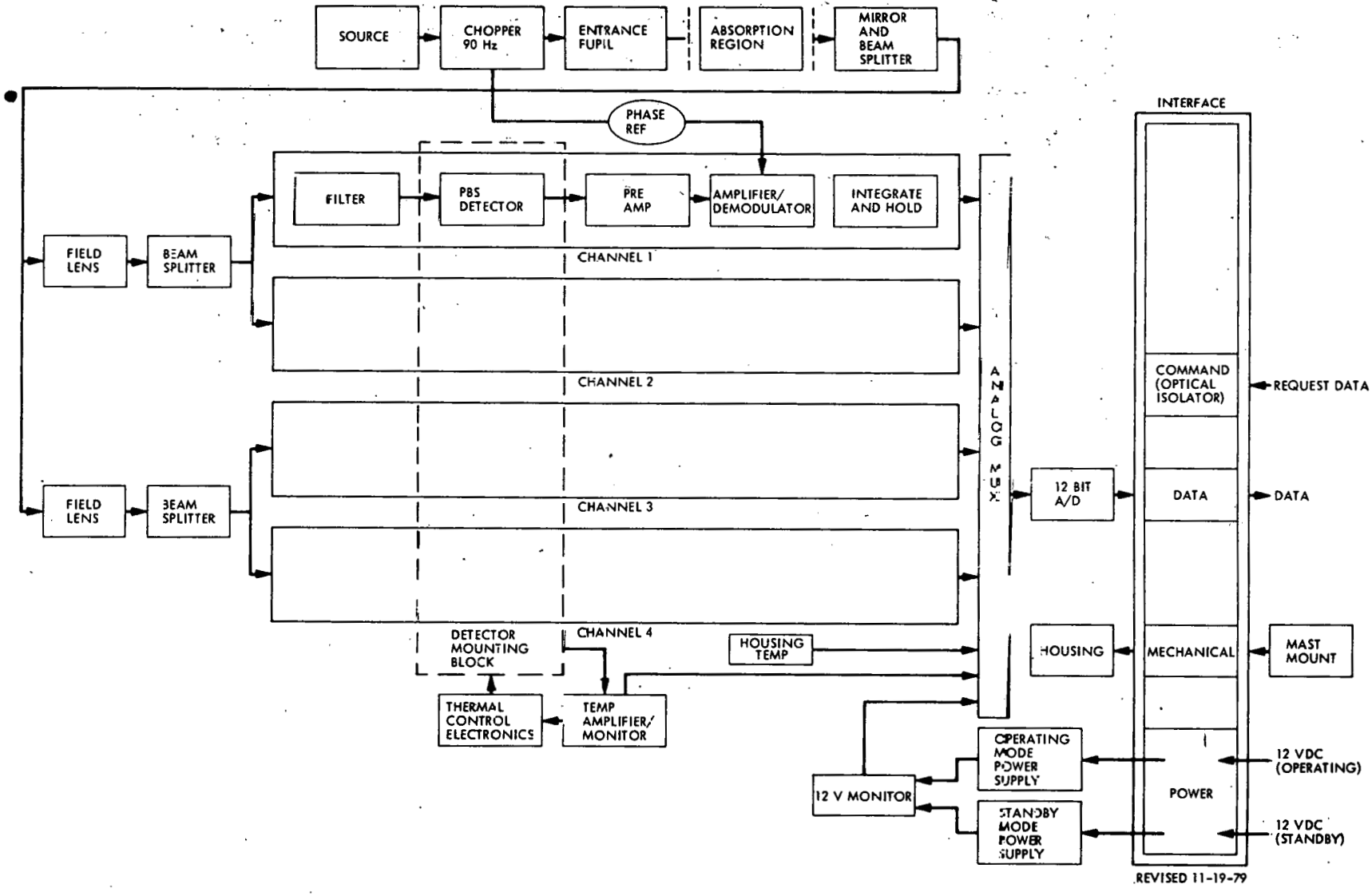

Figure 2. (FBDR) Four Band Differential Radiometer Block Diagram

For mixtures of the three gases the combined absorption in a given band j (j = 1, 2, 3, 4) is described by a general equation

$$I_j = I_{oj} \exp\left[-\ell \quad \beta_j c_1^{2/3} - \ell \sum_{k=1}^{3} a_{jk} c_k \right]$$

where c_1 is the concentration of methane and c_2 and c_3 are the concentrations of ethane and propane respectively. This general equation is simplified by the fact that for each band j either $\beta_j = 0$ or $a_{j1} = 0$. Compensating for changes in lamp brilliance and/or detector sensitivity is accomplished through a ratioing technique. The band most closely approximating a window is designated "r" and is used as a reference. Thus

$$\left(\frac{I_j}{I_r}\right) = \left(\frac{I_{oj}}{I_{or}}\right) \exp\left[-\ell \, (\beta_j - \beta_r) c_1^{2/3} - \ell \sum_{k=1}^{3} (a_{jk} - a_{rk}) c_k \right]$$

for $j \neq r$.

Even though they are non-linear, these three simultaneous equations in three unknowns can be solved in closed form. The process entails finding solutions of a cubic equation in one unknown and then rejecting those solutions which make no physical sense because they imply a negative partial pressure for one of the three gases. A simple iterative method of solving the equations has also been demonstrated by computer.

For convenient field test and calibration of the instrument, it is also required to have on-line solutions of these equations. The instrument support equipment will include a microcomputer to calculate the concentrations of methane, ethane, and propane from the absorption data supplied by the FBDR. Real-time operation is not required for this support function since it is reasonable to wait for several seconds for the concentration display. However, it may later be required to process the data with a microcomputer in real time in which case fast and simple algorithms will be desirable.

Performance Requirements

The TBDR used in the Fall, 1978 spill tests performed well. The offset and gain of the amplifier were stable but the rapid sensor temperature change which occurred at the incidence of the cold LNG cloud caused the responsivity of the detectors to change rapidly. The reference channel cannot be immediately

utilized to correct for this effect since the detector temperature coefficients are not identical. An advantage of the instrument, however, is that such changes can be calibrated out when a non-absorbing path again occurs. Since the test duration was short, it was possible to interpolate the responsivity drift throu the period of temperature change for the 1978 spills.

The performance requirements for the FBDR include immersion in the LNG cloud for much longer periods than did the earlier ones. It is therefore necessary to stabilize the temperature of the PbS detectors. To minimize the average power required, the operating temperature was selected to be 20°C. A lower temperature would have resulted in better noise performance but the spill instrumentation system is power limited because of portability requirements and the 20°C temperature results in suitable performance. Table I is a summary of other performance requirements of the FBDR.

FBDR PERFORMANCE REQUIREMENTS SUMMARY

TABLE I

LNG vapors measured	Methane Ethane Propane
Measurement threshold	0.4% volume of any of the three vapors
Range	Threshold to 50% volume
Accuracy	0.2% or 10% of concentration, whichever is greater
Measurement output during spill	Seven 16 bit words per measurement
Sampling rate	10 measurements per second
Operating temperature range in calibration	-5 to +60°C internal temperature
Total power (sum of mast mounted sensor and surface chassis)	25 watts maximum
Mass of mast mounted sensor	1.8 kg
Absorption region length	15 cm
Number of passes in absorption region	4
Interfering gases	Performance of the instrument will not be degraded by the normally presen atmospheric gases (O_2, N_2, CO_2, Ar and water vapor below saturation)

Design Considerations

Weight, Power, Volume:

The LNG spill site system is designed to allow maximum portability for rapid compliance to changes in wind direction. The FBDR will be mounted on light weight masts and operated from batteries. For this reason, it is important that the instruments be lightweight, of small cross section, and have low power requirements. It is expected that the weight estimates in Table I will be met and that the instrument power will be less than that shown in the table.

Signal to Noise Ratio:

The sensor output signal in the absence of absorbing gas is a 10 volt square wave deflection from each detector corresponding to the difference between the fully irradiated and the dark detector as the chopper blade rotates. A small amount of gas in the absorption region reduces the amplitude of this signal in proportion to the fractional absorption. Thus, the information is in the form of the difference between two large signals. The demodulator rejects the DC component of the signal and accurately yields the difference signal, proportional to absorption, which may be as small as one part in 1,000 of full scale at the threshold of the instrument. Although the signal processing task and the requirements for detector stability are demanding, the technique has the advantage that the effects of detector noise are small in the presence of the the large irradiance available from the tungsten lamp. The calculated signal to noise ratio, based upon a detector NEP of 1.2×10^{-11} watts/Hz $^{1/2}$, is 10^4 for the 5 Hz bandwidth required for the 10 measurement per second sampling rate. This S/N has been verified by laboratory measurements.

Number of Detectors:

The temptation is strong to use a single detector and sample the four bands sequentially. This option has not been exercised because nonsimultaneity of sampling could result in some complex form of aliasing if the turbulence spectrum of the cloud contains appreciable energy at frequencies greater than one half the sampling frequency. Lacking a detailed knowledge of the cloud turbulence, the sampling of the four bands has been kept simultaneous, obviating potential problems external to the instrument design. The instrument output is thus representative of the gas composition at the time of the sampling. Of course, aliasing is still possible in the reconstructed waveforms but the individual measurements will be correct.

Temperature:

The ambient temperature seen by the instrument housing will vary from an extreme high at 47°C (the record high temperature at China Lake) to a low of -20°C within the LNG cloud. The insolation, ground effects, and power dissipation further influence the sensor temperature. A thermal analysis indicates that the maximum housing temperature will be 60°C and that response of the housing to the cold LNG cloud will be moderately fast ($\tau \simeq 5$ minutes).

Based upon the temperature coefficient of responsivity of the PbS detectors of 4%/^{o}C (2) and a requirement that the relative sensitivity of the four channels remain constant to one part in 5000 to meet the threshold and accuracy requirements, the detector temperature must be held stable to approximately 0.005^{o}C throughout the ambient temperature range for unmatched detectors. This requirement may be relaxed by an order of magnitude by matching detectors and even further if sensitivity is sacrificed for operation in fog. The detector thermal control circuit must also meet this stability requirement as the housing temperature passes through the control temperature and the junction current direction is reversed to switch between the cooling and heating modes. A thorough program to test this control was planned with an engineering model of the sensor. The effect of ambient temperature on lamp radiance was also investigated.

The following sections describe FBDR development testing and design verification activities that have taken place since August 1979.

FBDR ENGINEERING MODEL

The FBDR engineering model shown in Figure 3 has been designed and fabricated based upon the considerations presented above. The fabrication and assembly was completed in January 1980 and testing of the unit has proceeded.

The instrument is operating routinely at signal-to-noise ratios (measured at the demodulator output) of approximately the design value which is required to give accuracy of gas measurement beyond the limits of flammability of the three gasses of interest. The thermal control servo system has been demonstrated to maintain the temperature of the four lead sulfide detectors at the control temperature ($+20^{o}C$) to within $0.03^{o}C$ through the ambient temperature range of -20 to $+60^{o}C$. This level of control coupled with the use of detectors with matched responsivity coefficients ($\%\Delta R/^{o}C$) gives adequate control of responsivity non-linearities between the four detectors so as not to be a limiting factor in the system's performance.

The Engineering Model has been used to collect absorption data for methane, ethane, and propane at gas-to-air ratios of approximately 5, 15, and 30% at six wavelengths that appeared most promising in the breadboard testing. Additional detailed calibration data will be taken to extend the range of the absorption data base since the absorption characteristics at some wavelengths are non-linear and must be determined experimentally rather than by simple applications of Beer's Law. Final analysis of these results will culminate in the selection of the final four wavelengths to be employed in the FBDR field units and the necessary calibration coefficients for data reduction during the LNG Spill Tests.

Data analysis algorithms and supporting software have been written to reduce the instrument data to gas concentration. Considerable effort has taken place to develop suitable mathematical relations to resolve individual gas concentrations from the complex functional form that is taken by the absorption characteristics of the three gasses. The resulting software will enable a microprocessor with limited speed and memory capability to carry out data reduction in near real-time. These programs are being used successfully to reduce Engineering Model data output and will be incorporated into the design of the on-board microprocessor system of the Support and Calibration Equipment (SCE). The SCE will then be used in the field to reduce test data during calibration verification.

The analog-to-digital conversion, multiplexing and interface circuits have been integrated into the system and design verification is proceeding. Preliminary test results indicate acceptable performance.

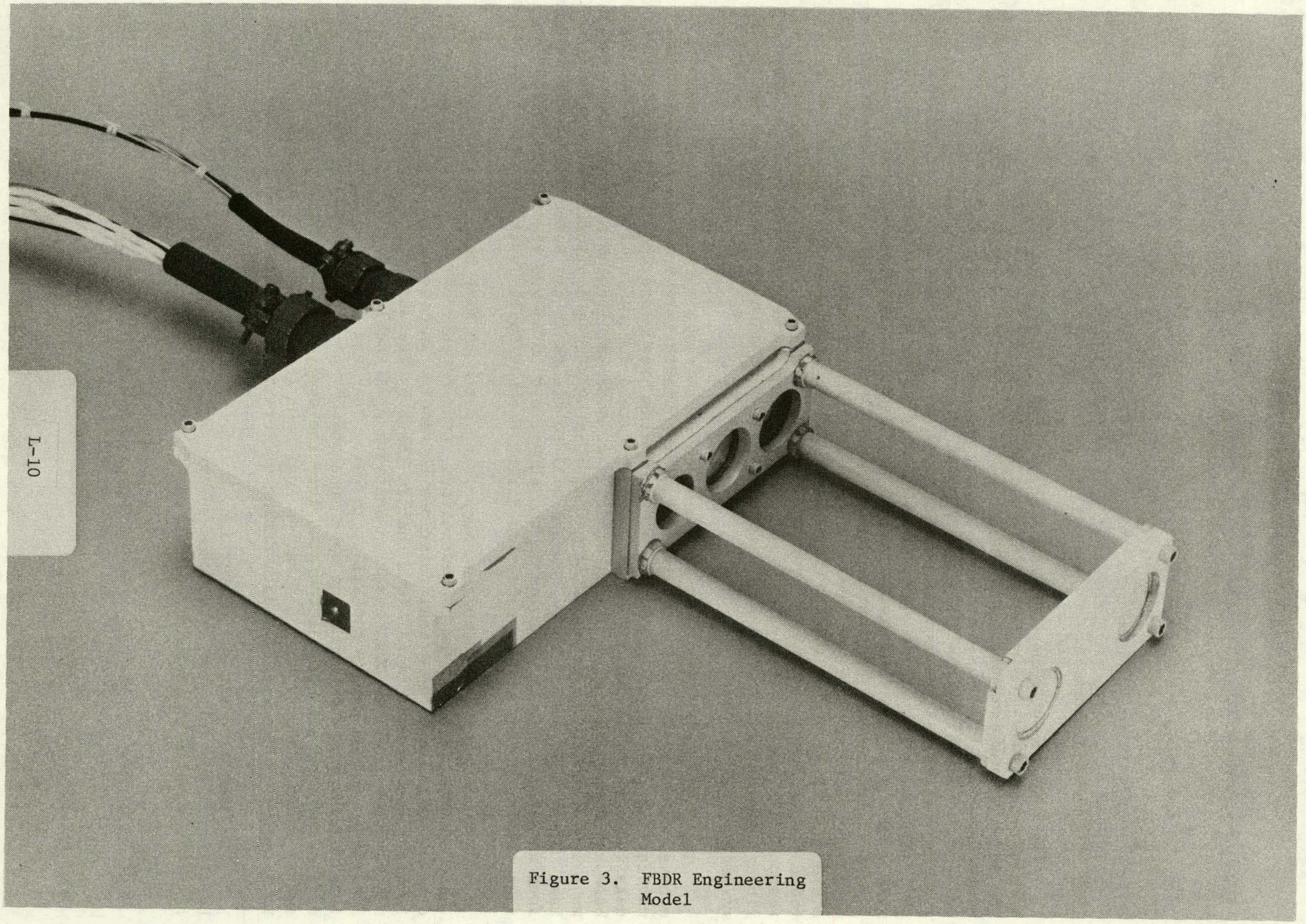

Figure 3. FBDR Engineering Model

An additional interface to a dedicated mini-computer system has been worked to allow automated data acquisition and reduction until the SCE is operational.

Full-up system level testing of the Engineering Model instrument was begun the week of April 7, 1980.

FBDR PRODUCTION PROTOTYPE

A production prototype will be built as a final verification of design changes resulting from Engineering Model testing and efforts to make instrument production more economical. It will be used for final system integration testing and be the first unit actually used in the field at China Lake.

The detailed opto-mechanical design of the prototype sensor has been completed and the fabrication of optical and mechanical components of the system has begun.

Only slight differences exist in the optical design of the prototype from that of the Engineering Model. A computer-aided ray-based analysis of the optical design was carried out to optimize the system throughput at the wavelengths of interest and to establish the level of manufacturing tolerances required to most economically meet the performance requirements. The alignment criteria for assembly of the Prototype and Production Units were determined. The design has also been modified to give decreased sensitivity to vibration and misalignment which might occur during transport and handling as the instrument stations are repositioned in the field array. Heaters have been incorporated on the exposed optical surfaces to minimize the possibility of fogging at these surfaces when the instrument reenters a warm ambient environment after being enveloped in the cold LNG cloud for some period of time.

The modifications to the electronic design are also slight. Additional bandwidth limiting in the signal conditioning circuitry as well as more precise frequency control in the chopper and demodulator have been designed to give added reliability and performance margin to the FBDR system. Final electronic packaging design (printed wiring board layout, etc.) has begun.

Final assembly and acceptance testing of the Production Prototype Unit is scheduled for early June 1980. System integration testing with Lawrence Livermore Laboratories data acquisition system will be carried out in mid-June at the China Lake LNG Spill Test Facility.

Design, assembly, and test of the micro-processor based SCE is scheduled to be completed in time for use during the prototype integration testing at China Lake.

PRODUCTION FIELD UNITS AND SUPPORT OF FIELD TESTING

After system integration and overall design compatability with the performance requirements and the Livermore system have been verified, production of ten field instrument systems will begin. The completion and integration of the ten field units into the China Lake System ready to support the LNG Spill Tests is currently scheduled for early September 1980.

JPL plans to propose providing additional field support and assistance in data reduction and analysis for the subsequent spill test cycles. Additionally, while no hardware has been incorporated, space has been allotted in the ground electronics enclosure to allow integration of a microprocessor to do real-time data reduction for the FBDR system if that development effort is funded.

References

1. Hinkley, E. D., Monitoring of LNG Vapors, Phase I Report, Jet Propulsion Laboratory, (31 March 1979).

2. Humphrey, J. N., Optimum Utilization of Lead Sulfide Infrared Detectors Under Diverse Operating Conditions, Applied Optics 4, 6, 665-675 (June 1965).

REPORT M

A Battery-Powered, Differential Infrared Absorption Sensor for Methane, Ethane and Other Hydrocarbons

G. E. Bingham
C. H. Gillespie
J. H. McQuaid

Prepared for the
Environmental and Safety Engineering Division
U.S. Department of Energy
under Contract W-7405-ENG-48
and for the
National Science Foundation
under Grant DEB 77-16327

Lawrence Livermore Laboratory
Livermore, California 94550

m.i

THIS PAGE

WAS INTENTIONALLY

LEFT BLANK

REPORT M

TABLE OF CONTENTS

FIGURES

SUMMARY

This report presents the performance goals, design considerations, and physical details of the miniature infrared absorption sensor being developed for the U.S. Department of Energy's Liquefied Natural Gas Spill Safety Program. The sensor is lightweight, battery-powered, portable, self-contained, and able to interface readily with large-array data systems. Essentially a precision infrared differential spectrometer capable of operating over the full range of gas concentrations expected in the spill diffusion tests, the sensor is expected to cost less than $7,000 per unit. The present design of this open-cell, fast-response sensor allows it to measure two components, but it can be modified to measure additional components at a reduced sampling frequency. To minimize temperature effects and power consumption, the sensor has a single-source, single-detector design which includes a rotating chopper-filter wheel. A CMOS microprocessor interfaced with a fast arithmetic chip is used to linearize sensor output and correct for component interference.

INTRODUCTION

Our purpose in this effort has been to develop a small, portable, accurate gas sensor for array deployment during LNG spill dispersion tests, capable of operating over the full range of expected gas concentrations and within the extremely dense fogs created when liquid methane (-164°C) comes in contact with humid air and liquid water. Goals are to meet all requirements with a sensor that can be produced inexpensively and adapted easily to other purposes, such as monitoring other gases with middle-infrared absorption bands. This development is a significant step forward in the state of the art of ir hydrocarbon sensors and should find significant application, for example, in oilfield and refinery pollutant monitoring, where such gases are generated.

The sensor described here is a direct evolution of the miniature portable CO_2 sensor developed by this Laboratory[1] with funding from the National Science Foundation (Grant DEB 77-16327) and the DOE carbon dioxide program (RPIS 003032). It uses the same design philosophy and many of the components previously developed for these programs. A prototype CO_2 sensor modified to sense methane was successfully demonstrated in the LNG spill tests at the U. S. Naval Weapons Center, China Lake, during September and October 1978.[2]

OPERATIONAL DESIGN GOALS

The LNG sensor must be battery-powered and small enough for several such devices to be mounted on a lightweight, portable, aluminum mast. It must operate in an explosive atmosphere and maintain its sensitivity and accuracy in the presence of extremely cold, dense fog in which it must function for up to 20 min. Sensor optical elements should not have to be cleaned after each test but can be covered between tests to protect them from rain and windblown sand. Optical coatings should be hard enough to withstand nonabrasive scrubbing without loss of transmission or reflection. Image sizes on optical surfaces should be large enough not to be significantly degraded by a single large water droplet.

The sensor electronics, not included in the optical head, must reside in the same electronics enclosure as the tower data acquisition and transmission system, whose power and communications facilities are used by the sensor. Each sensor must also be capable of independent operation without the data station or the other sensors. Provision must be made for local and remote control, front panel control and display, and an internal status monitor. Specific operational design goals are as follows:

- Battery power: less than 15 W total.
- Warmup time: fast (<5 min).
- Capability: multigas: methane and ethane-propane (0.1-100% methane, 0.1-25% ethane-propane).
- Sampling rate: 5/s per channel.
- Optical unit weight: less than 1 kg.
- Total optical sensor head volume: <500 cm^3.
- Output: linearized in % concentration.

SENSOR WAVELENGTH CONSIDERATIONS

Methane and several other atmospheric gases have strong absorption bands in the near- and middle-ir region.[3] Methane has infrared absorption bands at 2.4, 3.4, and 7.7 μm (see Fig. 1). Since strong water vapor and nitrous oxide absorption bands also occur in the 7.7-μm region, we considered only the 2.4 and 3.4 μm regions. Two other spectra-dependent absorption characteristics become apparent from comparable infrared spectrometer scans for the major components of natural gas in these two absorption regions (see Figs. 2 and 3). First, percent transmission in the 3.4-μm band is significantly lower for each gas than in the 2.4-μm band. Second, component separation is much cleaner in the 3.4-μm band, where methane and ethane enjoy areas of nearly independent absorption. Figure 1 also shows that a water vapor absorption band exists on the short-wavelength side of the 3.4-μm methane band, and long-path measurements indicate that some water vapor absorption occurs coincident with methane and ethane because of the tail of this band. However, at the short path lengths used in this sensor, these effects should be small and can be measured and corrected for as part of the differential scattering correction.

The requirement that the sensor operate in dense fog also affects our choice of wavelength. For clouds and mature fogs, transmission is nearly independent of wavelength (see Fig. 4).[4] That is because the particle distributions in these fogs show a wide range of droplet sizes, with a peak concentration at a radius of about 3 μm and with a significant number of much larger particles (see Fig. 5). The large droplets form over tens of minutes by the collision of smaller droplets. In the dispersion tests, however,

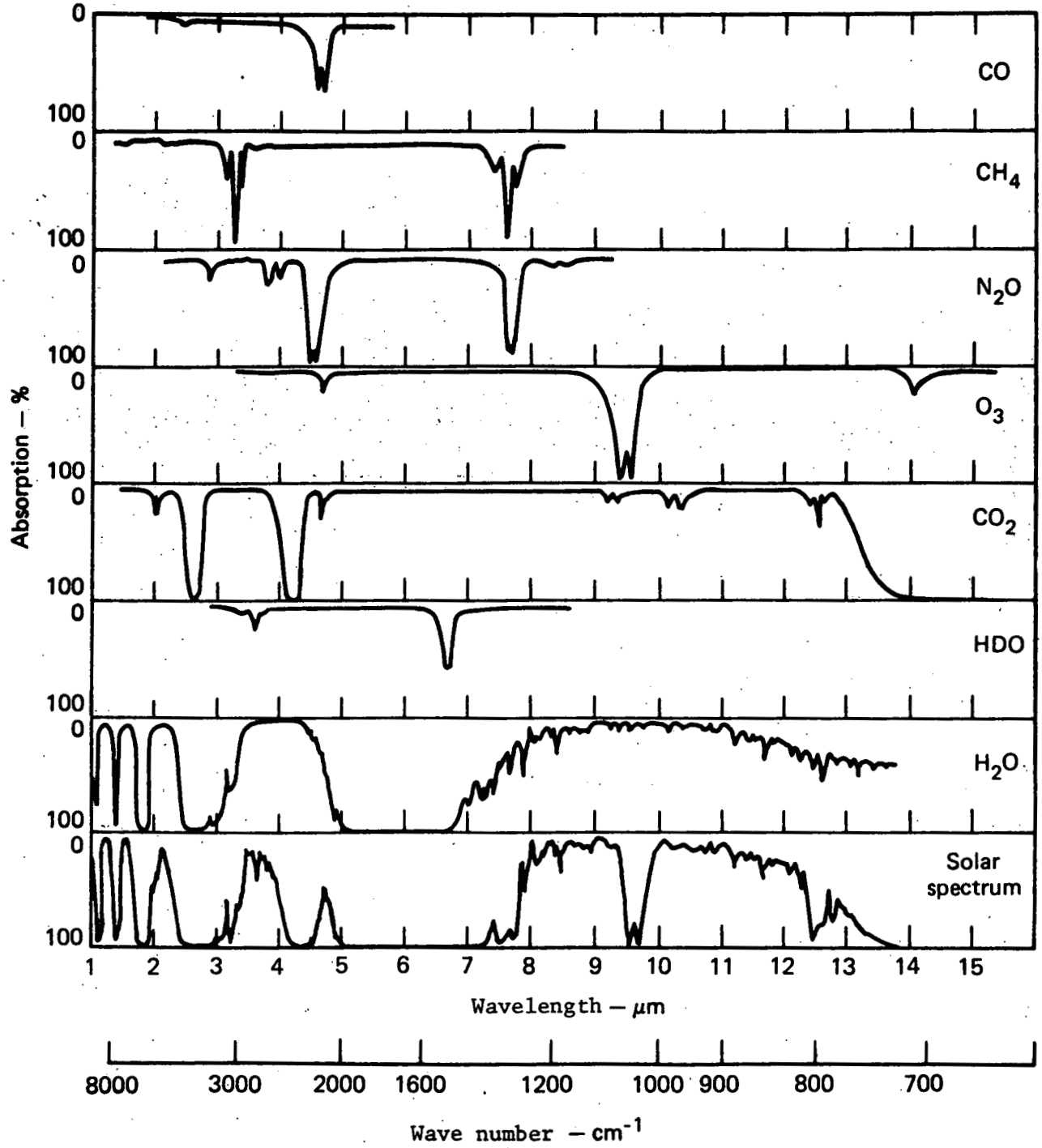

FIG. 1. Low-resolution comparison of absorption ir spectra showing methane vs other major atmospheric gases. (From Fig. 6-59, p. 228, of Ref. 3.)

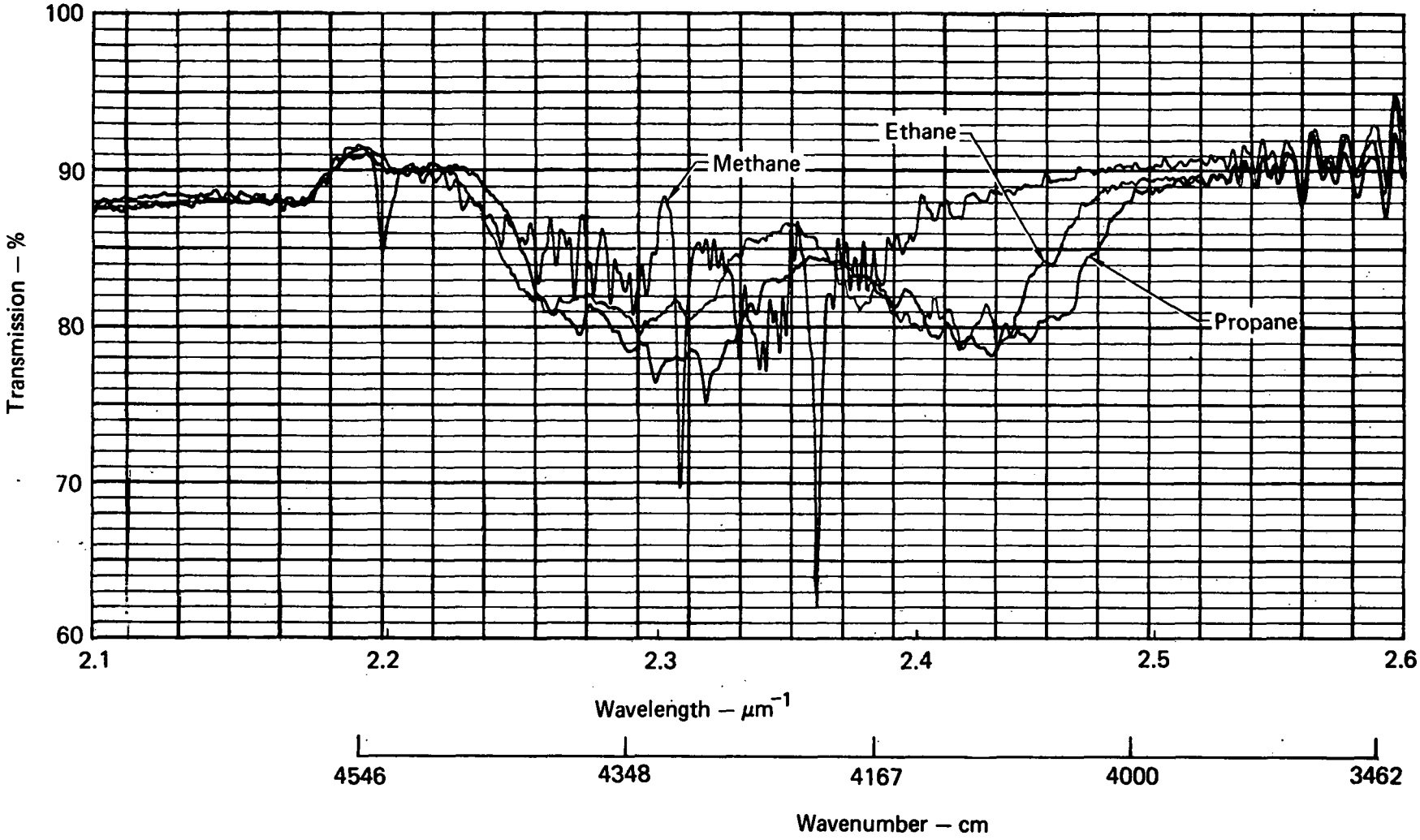

FIG. 2. Methane, ethane, and propane transmission in region of their 2.4-μm absorption band. Data are for 100% concentrations in a 1-mm cell.

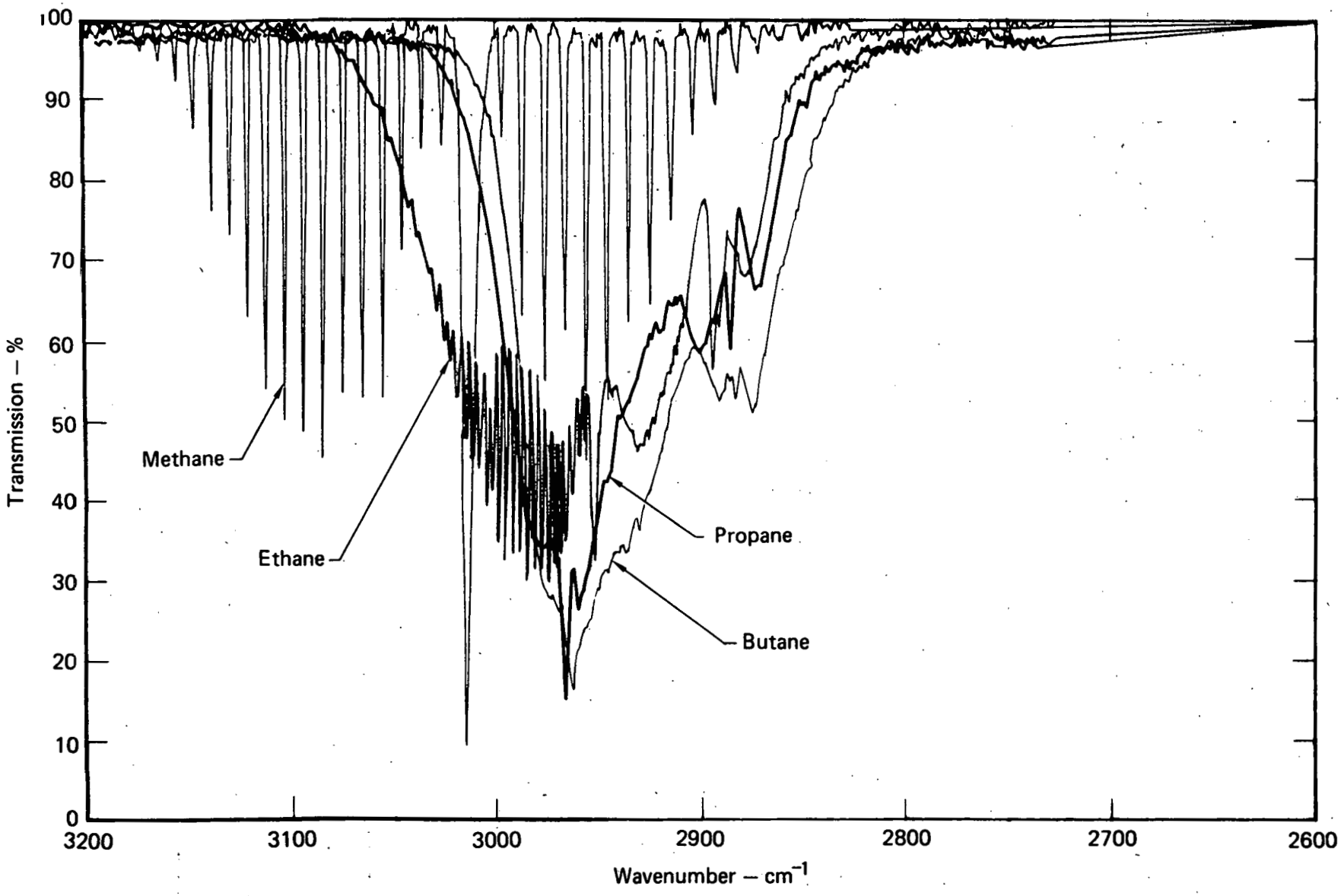

FIG. 3. Methane, ethane, propane, and butane transmission in region of their 3.4-μm absorption band. Data are for 100% concentrations in a 1-mm cell.

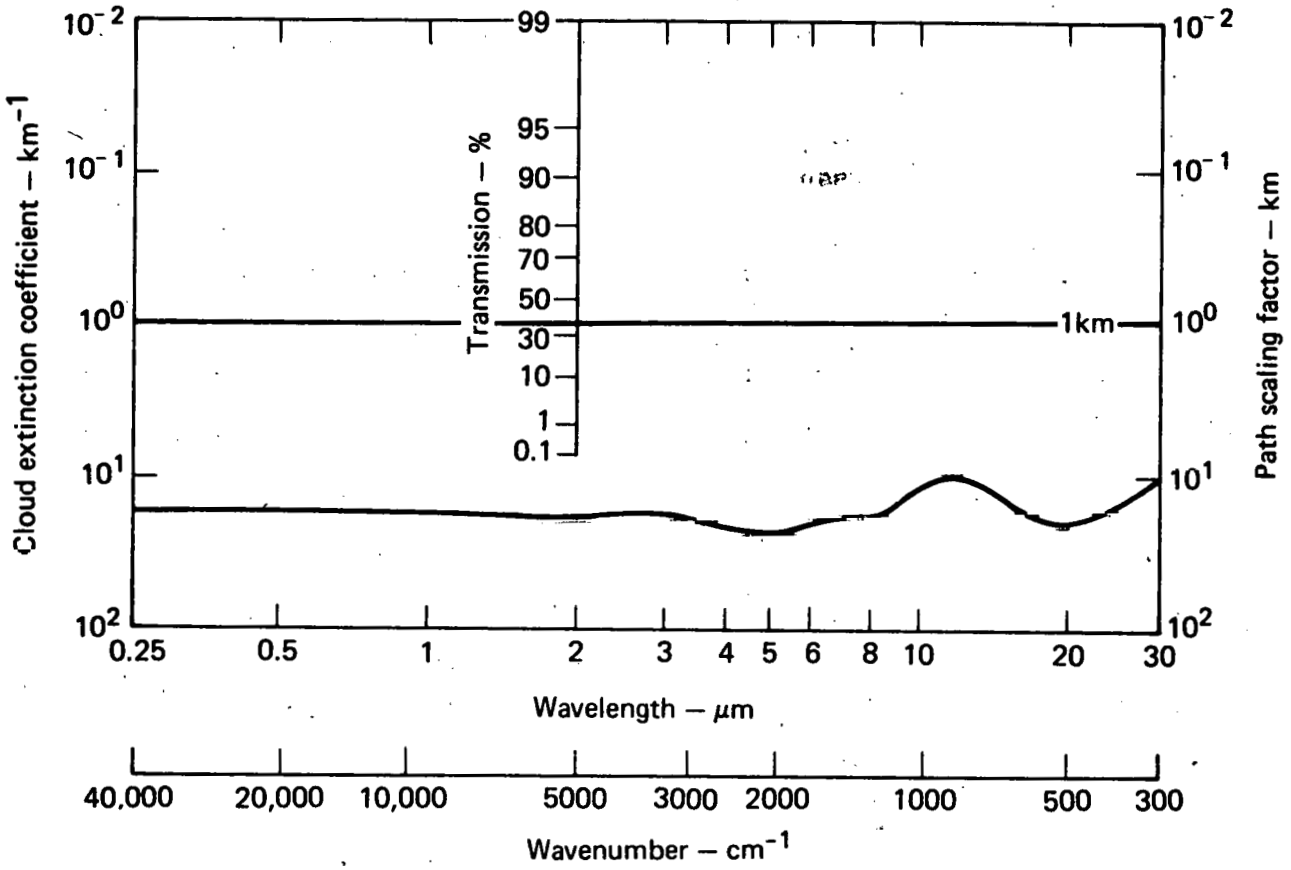

FIG. 4. Attenuation of radiation due to broad spectrum aerosol. (From Fig. 33, p. 79, of Ref. 4.)

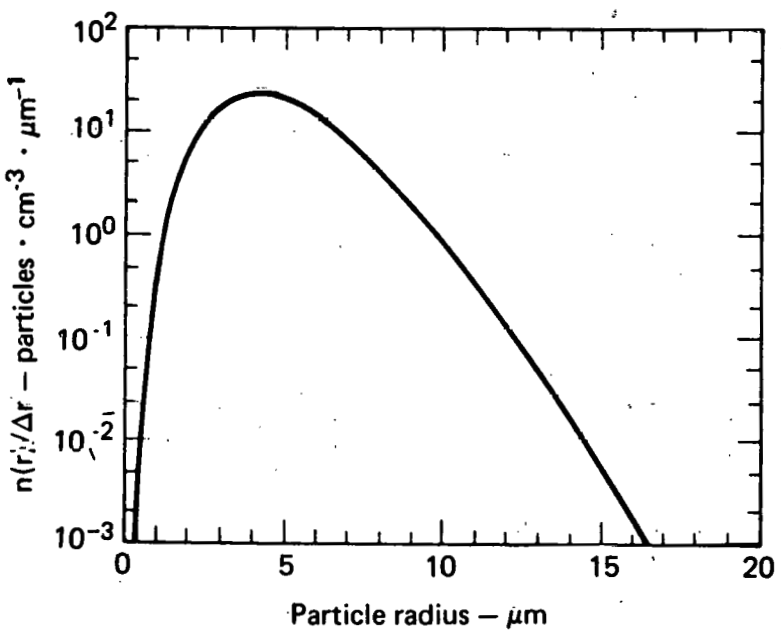

FIG. 5. Cloud droplet size distribution typical of that in cumulus clouds and in heavy mature fogs. (From Fig. 34, p. 80, of Ref. 4.)

individual droplet half-lives will probably be of the order of a few minutes, and the peak will probably be at a significantly smaller ratio. Laboratory measurements of new fogs created using liquid nitrogen and water show very few, if any, particles larger than 1 μm in radius. Since no measurements have been made of the number density and size distribution under open-air spill conditions, we are forced to assume that fogs in open air will be similarly composed.

If we assume that the fog will be composed largely of ice crystals smaller than 1 μm in radius, differential scattering becomes important. If we assume that the size distribution in new fog can be approximated by an atmospheric aerosol model[5] shown in Fig. 6, then both differential scattering and aerosol absorption (largely water absorption; see Fig. 7) favor operation (i.e., higher transmission) at the 3.4-μm wavelength. From an optics standpoint, an instrument operating on the 2.4-μm band is cheaper to build, because it can use readily available glass lenses and an incandescent source. However, the long paths demanded at this wavelength are incompatible with the requirement for operating in the fog. For this reason, we have chosen to design our instrument to operate on the 3.4-μm absorption band.

Figure 3 shows that areas of semi-independent absorption for methane and ethane occur in the 3.4-μm band. In the 3085 cm^{-1} (3.24 μm) region, moderate methane absorption occurs, while ethane absorption is weak. A region very sensitive to ethane with only weak methane and propane absorption occurs at 3030 cm^{-1} (3.30 μm). A sensor with approximately equal sensitivity to ethane and propane can be built using a filter operating at 2900 cm^{-1}

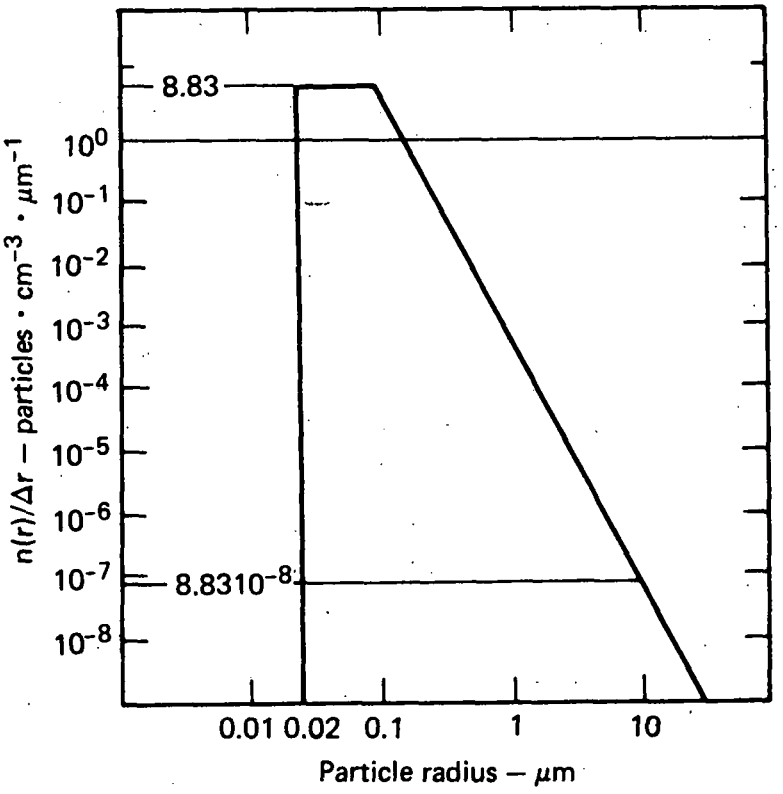

FIG. 6. Aerosol size distribution typical of continental aerosol, which may also be similar to that found in cryogenically created young fogs. (From Fig. 1, p. 11, of Ref. 5.)

(3.45 μm). However, absorption of each species is not totally independent in any of these areas; at high concentrations, the ethane tail intrudes into the 3085 cm^{-1} area (see Fig. 8(a)), and methane absorption becomes significant in the 3030 and 2900 cm^{-1} regions (see Fig. 8(b)).

To normalize the optical system for component and electrical drift and for attenuation by fog, we need a reference wavelength not attenuated significantly by any of the natural gas components. Because of the water vapor band on the shorter wavelength side, we have chosen our measurement reference at 3.85 μm. It is necessary to move this far from the 3.4-μm band because of significant absorption by propane and butane at wavelengths close to our measurement wavelengths. The problem with establishing reference and measurement wavelengths so far apart arises from differential scattering from aerosols in the measurement path. For particles much smaller than the wavelength of interest, differential scattering varies as λ^{-4} (Rayleigh scattering). For particles of the same order as the wavelength, it varies as λ^{-2} (Mie scattering). Since the fog particles will have some distribution and will approach the same order as the wavelength as the fog grows, we expect scattering and absorption to affect our system somewhere between these values.

To adjust for any differential scattering that may occur in the system, the sensor includes a second reference filter, located between the water absorption band and the methane band at about 3.05 μm (3280 cm^{-1}). The use of this filter is described below. Since some water vapor absorption also occurs at this wavelength, the filter can also be used to correct the measurement ratios for changes in background water vapor concentration occurring during the spill.

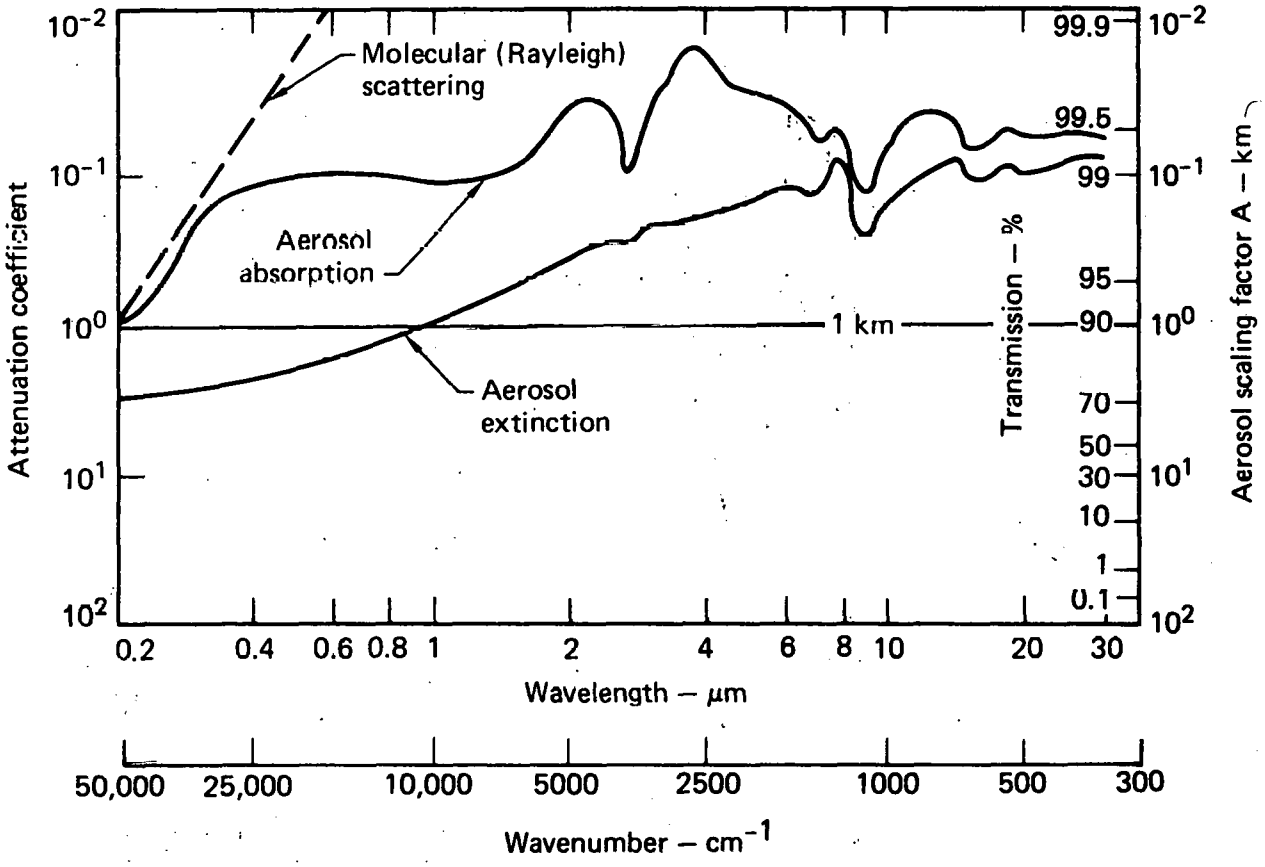

FIG. 7. Effect of atmosphere aerosol distribution on ir extension in mid-ir region. (From Fig. 2, p. 14, of Ref. 5.)

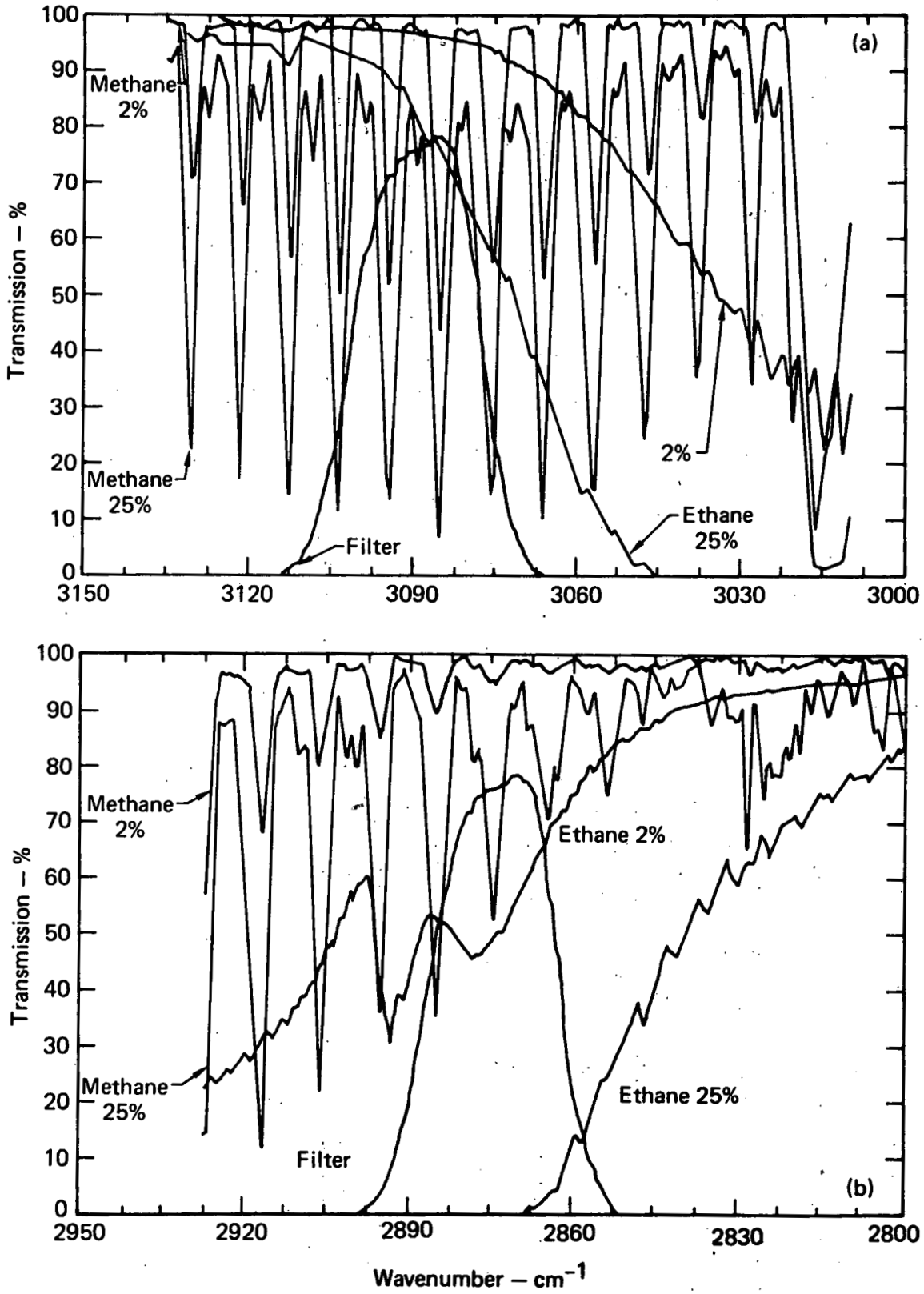

FIG. 8. High-resolution transmission spectra for methane and ethane concentrations in area of filters that will be used to determine their concentrations: (a) 3.24-μm filter for methane concentrations; (b) 3.48-μm filter for ethane concentrations.

The thick fog associated with the spill will greatly reduce the total power reaching the detector at all wavelengths. In controlled experiments using boiling water over liquid nitrogen, scattering coefficients have been observed[6] for 3.39-μm radiation as high as 0.34 cm^{-1}. Therefore, the sensor must have enough dynamic range to make accurate measurements when more than 60% of the radiation transmitted from the source has been lost due to scattering out of the beam. Inaccuracies caused by the change in path length because of scattering out of the beam and then scattering back into the collection aperture can be minimized but not totally eliminated. Cryogenically generated fogs easily qualify as multiscattering media.

Fortunately, high fog concentrations are also associated with high methane concentrations and, in areas where fog is expected, the sensor path length can be shortened by an order of magnitude and still meet performance specifications. Two easily interchangeable optical absorption cells have been designed for the sensor, one with a 25-cm absorption path length and the other with only 2.5 cm.

MEASUREMENT STRATEGY

To make accurate measurements under these adverse conditions, the full power of the system microprocessor must be used. To allow for correction of as many effects as can be physically identified and measured, a high-speed calculator chip, the AM9511A, has been interfaced with the CMOS microprocessor. The combination of microprocessor and arithmetic chip can handle the logarithmic and power law calculations fast enough to allow for conversion of each individual data point before averaging. This is important since a scheme that averages the absorption measurements before linearizing is taking a linear average of a log-varying function, which can lead to serious measurement error in a rapidly varying function.

The anticipated measurement sequence is as follows:

1. Voltages (V_i) representing transmission through the three measurement filters and the reference filter in the optical head are transferred to the microprocessor. These values are determined in this order: reference measurement, fog and water vapor measurement, methane measurement and ethane measurement. (A sensor providing four samples/s could also measure propane. The propane filter would be scanned last.)

2. The transmission voltages are then multiplied by a normalizing factor to correct for variations in transmitted power caused by filter bandwidth and differential source emission. This factor, T_i, is determined empirically with no gas or fog present in the absorption path.

3. Transmission ratios are made for each adjusted measurement with the reference, resulting in three new values:

$$V_f/V_r = r_f;\ V_m/V_r = r_m;\ V_e/V_r = r_e.$$

4. The measurement ratios (r_m, r_e) are corrected for differential scattering from fog and for water vapor effects, using empirically determined multiplicative factors F_m and F_e. These constants, specific for each gas measurement filter ratio, are determined empirically by using the sensor prototype in a chamber with various aged, cryogenically generated fog concentrations. The constants are stored in a look-up table, the proper value being determined by the corrected transmission ratio of the fog and reference filters.

5. The scattering-corrected methane and ethane ratios (r_i') are put into a linear algebra routine to correct for mutual interference absorption,

yielding a pair of totally corrected ratios (R_m and R_e) ready to convert to concentration. Since the constants used in the linear algebra routine are not really constants but vary with concentration, empirically determined sets of coefficients are stored in a look-up table accessible by using the value of the ethane ratio (r_e') and the methane/ethane ratio (r_m'/r_e').

6. Linearization algorithms are now applied to the final corrected ratio. We expect these routines to resemble those used to determine the methane concentration from measurements by the initial (CO_2) prototype at China Lake in 1978. That expression took the form

$$C(V/v) = \left(\frac{l_n(R_m)}{2.077}\right)^{1.536}$$

The microprocessor with the AM9511A should be able to perform these calculations in 30-50 ms, well within the 200 ms available between samples.

7. Once the logarithmic and power law operations have been removed from the data, true averages and other linear statistics can be obtained. This work could be performed by the sensor's processor or sent to the data system for development.

LNG SENSOR DESIGN

To achieve the above goals and measurement strategy, the LNG sensor is designed in two packages: a small, lightweight optical head assembly and the electronic control and processing unit. We intend that no reference voltages be present in the cable connecting these packages. For this reason the optical head, which is about the size of a 12-oz soft drink can (see Fig. 9), contains several electronic circuits. The long-path absorption cell adds about 8 cm to the length of the optical head.

The physical layout of the electronic control and processing unit is not settled yet, pending completion of the tower data acquisition system design. The prototype unit will use a single plane wire-wrap format with display and keypad on the same plane as the microprocessor. Two-way communication with the tower data station processor is expected to start, stop, and possibly change the averaging time of the LNG sensor.

Optical Head Arrangement

Figure 10 shows the main mechanical and optical components of the LNG sensor. The key to success of any low-power miniature ir sensor is its source. Two years of joint Lawrence Livermore Laboratory and industry effort have gone into the present source design. Light bulbs aren't efficient mid-infrared sources. Laser systems, when available, are large, power-hungry, and difficult to maintain in the field. The most efficient available source is a blackbody radiator. Blackbodies have large source areas, high emissivity, and can be made quite small. They are stable over long periods and can be accurately controlled. However, they typically lose a lot of heat to their surroundings. Our main challenge has been to insulate the small 600 to 1000°C slug that forms the blackbody radiator from the rest of the electromechanical system: the better the insulation, the lower the power consumption of the source and the cooler the rest of the package.

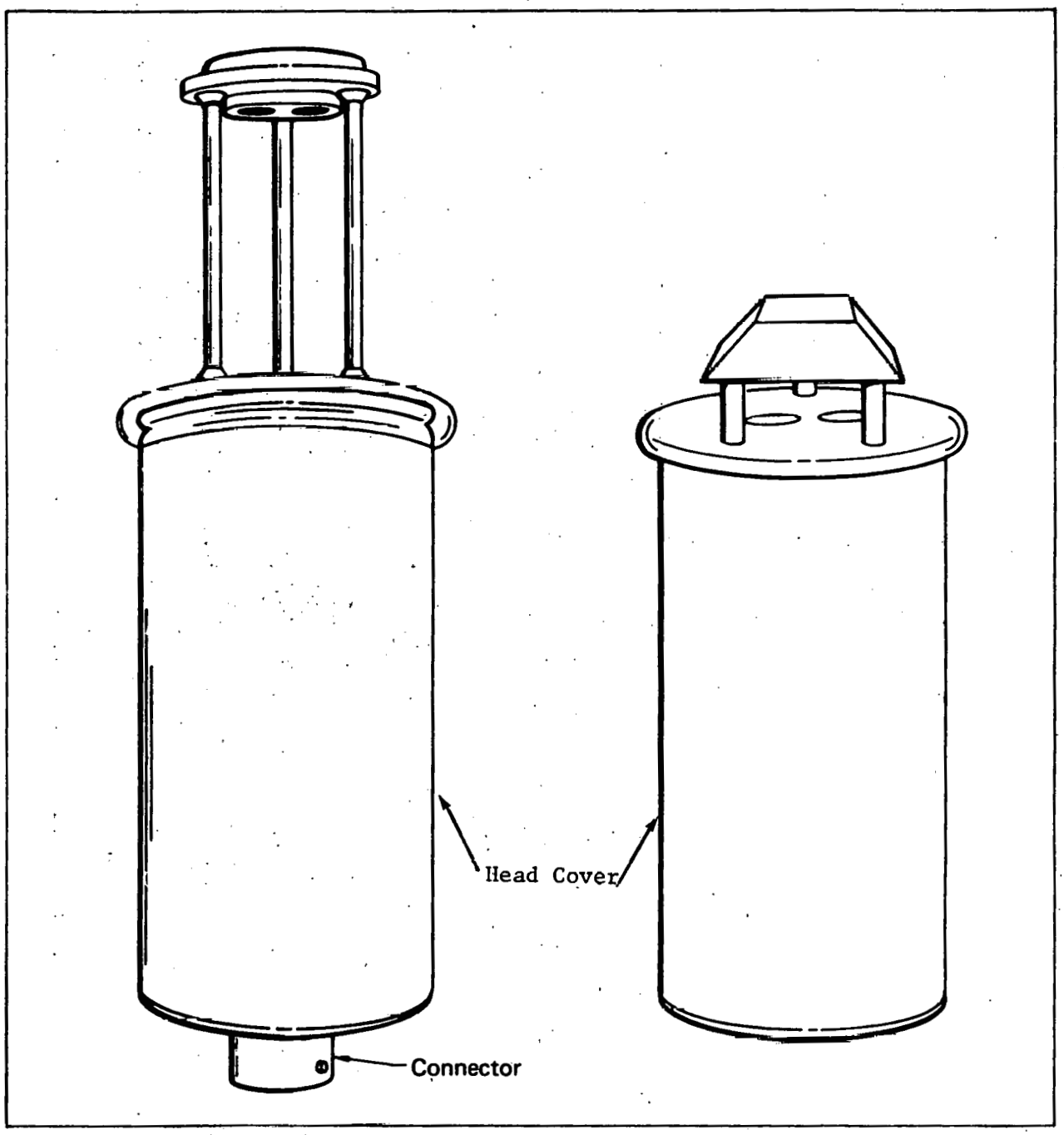

FIG. 9. Concept drawings of optical head assembly showing large- and short-path absorption cells. The cover over the head assembly is about the size of a 12-oz soft drink can.

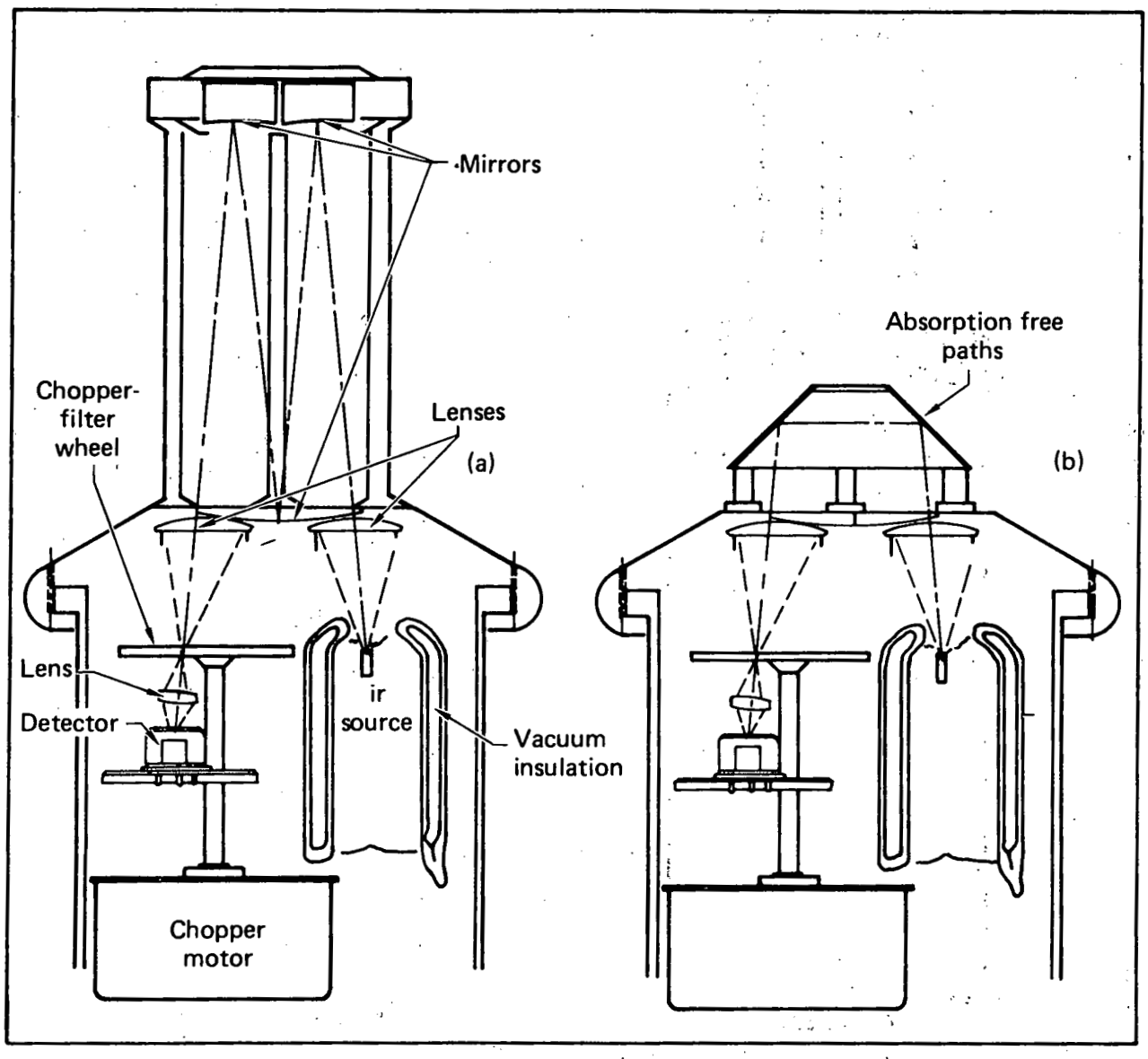

FIG. 10. Main mechanical and optical components of optical head assembly: (a) 25-cm folded-path absorption cell for low concentrations; and (b) 2.5-cm absorption cell, using a nonabsorbing prism, for use at higher concentrations.

Our present source design uses an inverted quartz-glass vacuum Dewar with a small hole in the bottom for radiant emission. This device uses about 50% less power than the source used during the 1978 China Lake tests. The Dewar has a 28-mm O.D. and is about 45 mm long. Radiation is emitted in an f 1.3 cone through a thin sapphire window. The window, epoxied to the outside of the Dewar, is easily changed; it prevents any low-temperature condensibles emitted from the source from contaminating the main collecting lens and minimizes convective cooling of the blackbody cone.

The main collecting lens gathers source radiation at f 1.5 and transmits it to the first relay mirror at f 4.0. From this mirror, the radiation is reexpanded to lens size and reflected off a spherical mirror polished into the top of the sensor. From this point, it is reflected to a second relay mirror adjacent to the first and then through a second collection lens on the head. This lens focuses the f 4.0 beam back to an f 1.5 cone and images the 1-mm^2 source area on the rotating chopper-filter wheel. Leaving the filter wheel the expanding cone, is apertured to remove stray light and refocused on the detector's active area. Computer ray traces of the optical system indicate that the system is nearly diffraction-limited, providing an almost perfect 1:1 image of the source onto the detector.

With the long-path absorption cell, the smallest image outside the can is the diameter of the relay mirrors (1.2 cm). Using this inverted-white-cell design greatly reduces the effect of large droplet concentration on mirror reflectivity. The mirrors in the long-path cell are nickel-coated aluminum with a hard gold overcoat.

Where significant fog concentrations are expected, the long-path cell is supplanted by the short-path 2.5-cm cell, which is basically a nonabsorbing bridge between the two lenses on top of the LNG sensor. Radiation enters the prism 1.25 cm above the output lens is reflected internally through the prism and then back into the optical sensor head. To minimize liquid water effects, a fine wire-mesh screen could be put around the optical bridge to cause particle collisions and prevent large droplets from entering the absorption path. The minimum beam size with the short-path cell is about 2 cm. A photograph of the LNG prototype sensor with both the long- and short-path absorption cells is shown in Fig. 11.

The optical head could be protected by an inexpensive fire-protection system: an insulated can on a vertical rail above it. If the can were suspended by a low-temperature-fuseable link, fire melting the link would drop it down over the head, protecting the head from radiation and short exposures to flame.

Electrical Design

As noted, the first design principle is absence of voltage-critical signals on the cable between the optical head assembly and the electronic control and processing unit, so the cable length can be varied. The electrical design has three other governing principles:

- To digitize the detector signal as close to detector as possible.
- To use CMOS components to reduce power consumption and volume.
- To design for long life, low maintenance, and high stability.

Figure 12 is a block diagram showing circuits and electrical relationships between the optical head assembly and electronic control and processing unit.

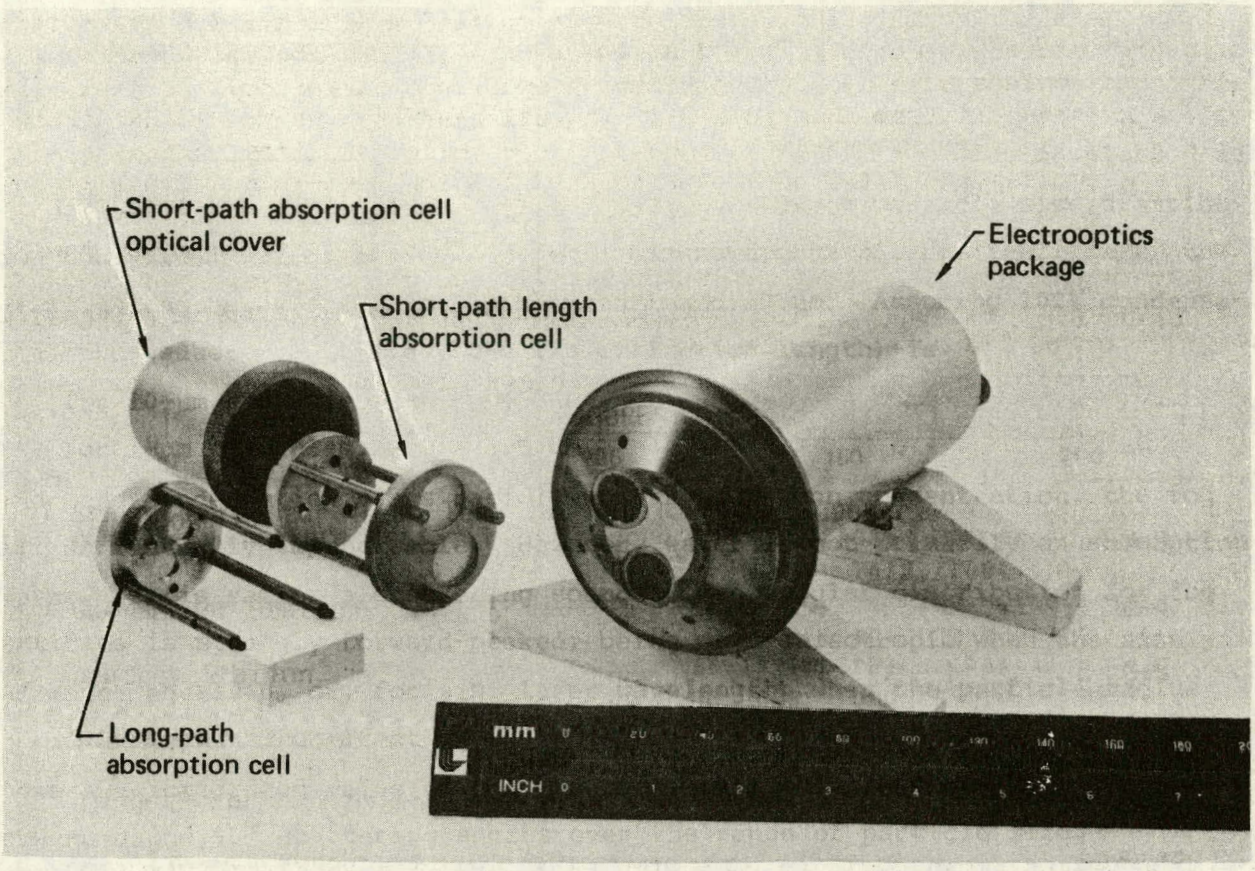

FIG. 11. LNG prototype sensor showing electrooptical compartment and both long-path and short-path external sample cells. Cap screws over short-path cell to eliminate absorption in path between two optical wedges.

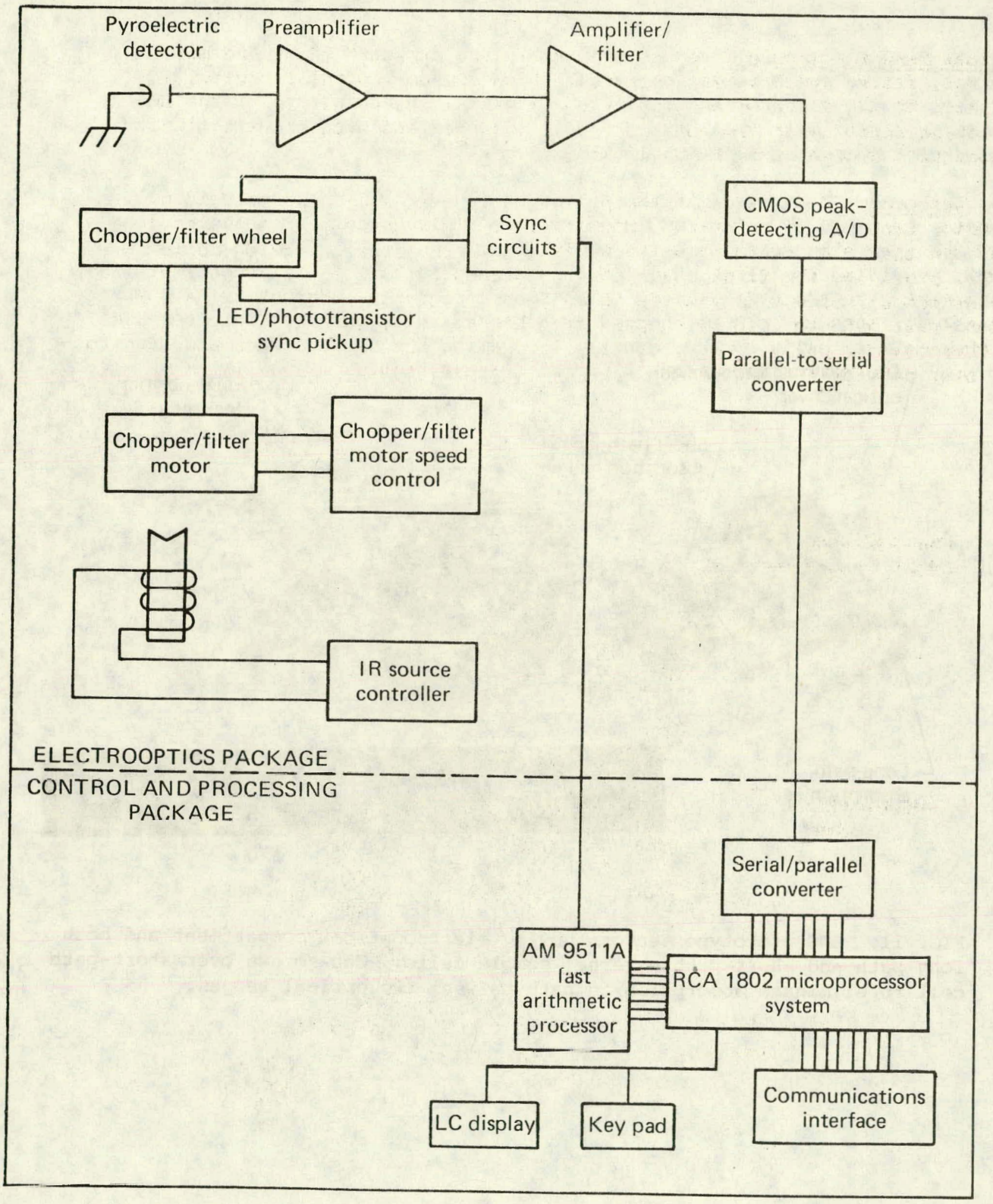

FIG. 12. Block diagram of sensor electronics showing circuit distribution between optical head and electronic control and processing unit.

tical Head Electronics. In this assembly are expected to be the motor control, filter synchronization circuit, and source control circuits, in addition to the detector and amplifier circuits. A photograph of the LNG prototype sensor with the long-path cell attached and with the electronic compartment uncovered is shown in Fig. 13.

Detector. Being used in the prototype is a 1- x 1-mm pyroelectric detector marketed by Molectron (Model P171). This detector is mounted in a T-05 can that also contains a low-noise 10^{12}-Ω resistor and a low-noise J-FET, providing the first stage for the preamplifier. In this configuration, the detector response is limited to a signal frequency of about 20 Hz. While a lead-salt detector can be chopped at a higher rate, the PbSe detector must be thermoelectrically cooled, greatly increasing the sensor power and adds to the heat dissipation requirements of the optical head.

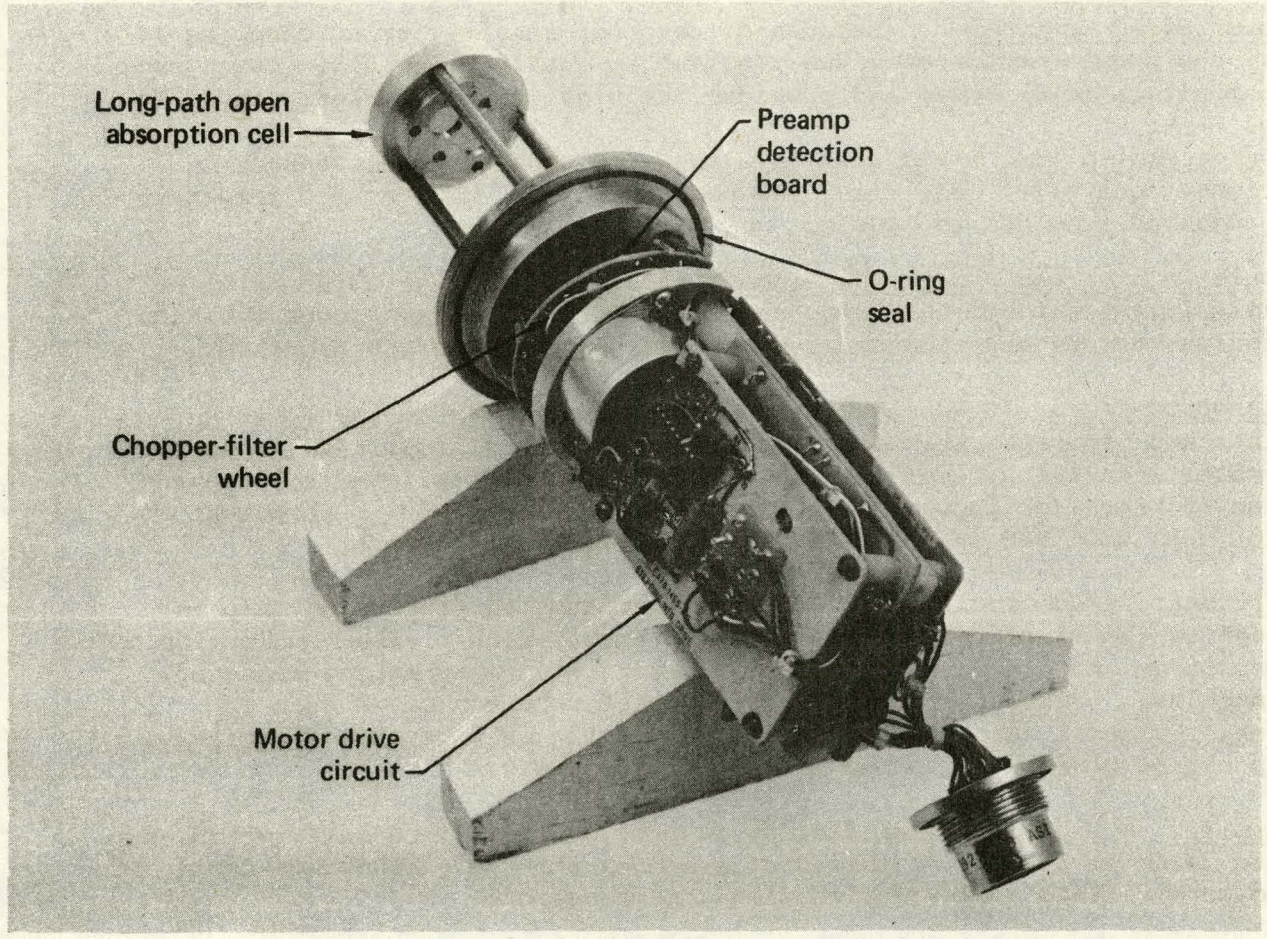

FIG. 13. Prototype LNG sensor with electrooptical compartment cover removed. Stepper motor and drive circuit are clearly visible, along with chopper-filter ıeel. Long-path absorption cell is shown on sensor.

Amplifier-Filter Section. A single detector-amplifier section is used so that electronic drift is ratioed out of the measurements. The amplifier raises the detector output voltage from the millivolt level to the full range of the analog-to-digital (A/D) converter (10 V). Out-of-band noise suppression is achieved by a "gated-integration" amplifier and filter.

Peak-Detecting A/D Converter. The amplifier is followed by a peak-detector sample-hold circuit. The peak detector is reset by a zero-crossing circuit and tracks the amplifier signal unit it peaks. At this point, the peak detector holds the signal level until a conversion-complete signal is received from the A/D converter, which is a 12-bit CMOS single-chip converter made by Beckmann (7556 MCU) and having both series and parallel outputs.

Filter Synchronization Circuit. A LED/photo transistor pair and a hole in the filter wheel are used to synchronize the signal processor with the proper filter. A simple pattern-recognition routine in the processor could be used on initial startup and would suffice if the signal were never totally lost. In dense fog, unfortunately, the possibility exists for completely attenuating the signal; hence, the need for positive synchronization.

Motor Speed Controller. Because of detector sensitivity to chopping rate changes, the chopper motor must run constant to within 0.1-0.01%. The speed control monitors motor speed and provides the high initial current needed for startup.

Source Controller. This unit is a two-wire, constant-resistance, proportional controller regulating the source to ±1°C. The source temperature can be adjusted from 600 to 1000°C.

Electronic Control and Processing Package. This package, as noted, will be physically located within the tower data enclosure. It draws power from the data-station battery and communicates through the data-station processor.

Microprocessor. An RCA 1802 microprocessor controls the sensor, linearizes and separates its output, and monitors its status. The processor communicates with the optical head through the serial interface and with the data-station processor through a separate, yet to be defined, interface. The processor uses CMOS RAM and EPROM to minimize power consumption.

Arithmetic Processor. An AM 9511A fast-arithmetic processing chip is interfaced to the microprocessor to expedite computations. The combination is easy to program and can do number-processing at rates approaching those of larger machines. Since the arithmetic processor consumes 1.7 W when in operation, a circuit has been developed to turn the chip on and off quickly. The chip can be powered up to one microprocessor cycle.

Display. A liquid crystal display is provided for field calibration and checkout. A small key pad or series of switches will be included on the front panel to permit field communication with the processor.

PROTOTYPE TESTING

Calibration of the LNG prototype, configured as described in this report and using standard gases, has been completed. The sensor has also been

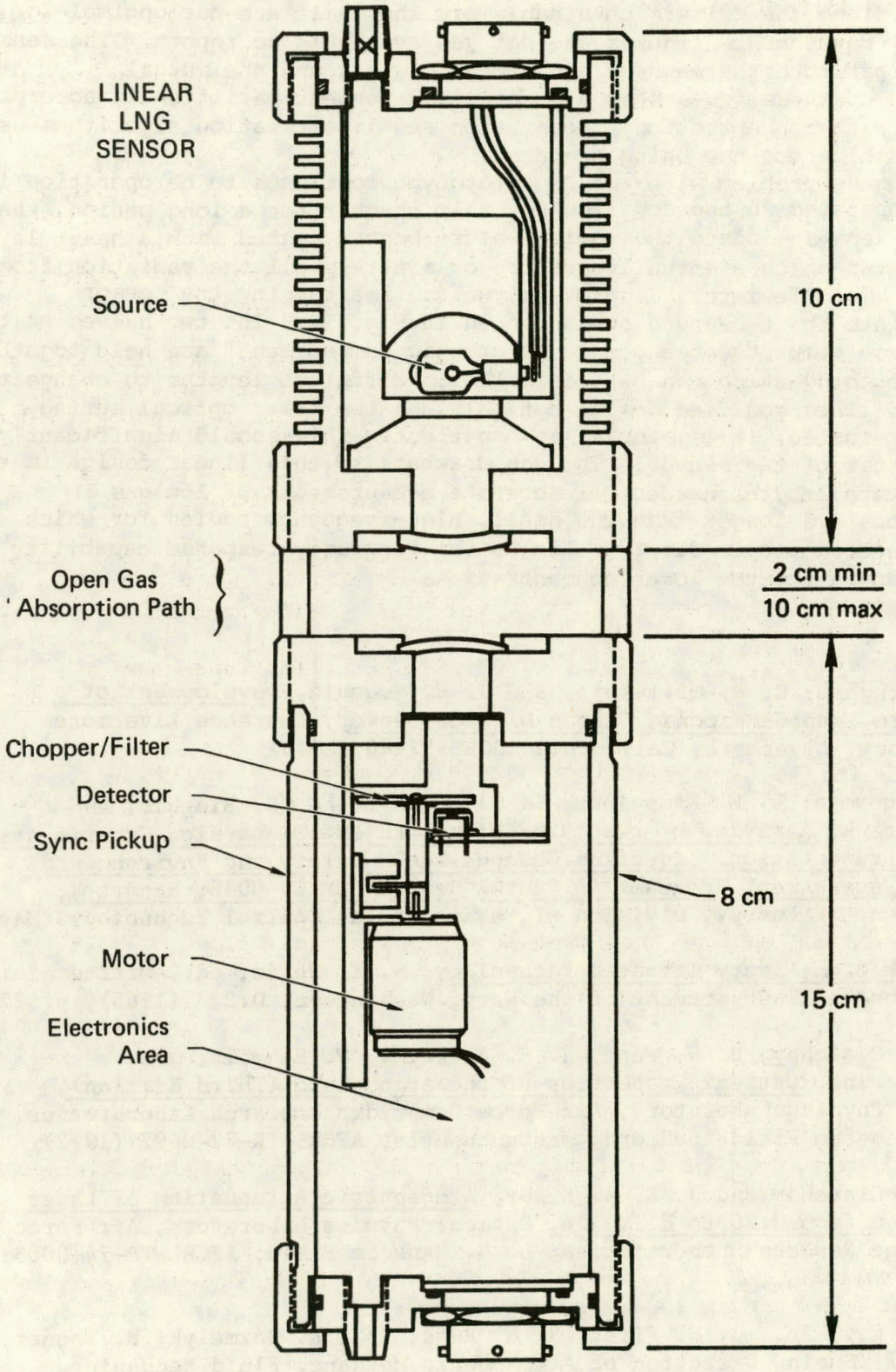

FIG. 14. Linear design for LNG sensor that uses same parts as folded-path design but has only two optical surfaces exposed to fog.

operated in a fog chamber with both the long- and short-path absorption cells installed. Since the filters obtainable off the shelf are not optimal for our needs, final performance figures are not yet available to report. The sensor did verify that both the methane and ethane signals and the mutual interference of these gases show a power-law-dependent variation in absorption coefficient with concentration. Separation and linearization algorithms using the relationships are now being prepared.

The biggest problem with the LNG prototype continues to be operation in fog. When operated in the fog (ice crystal) chamber for a long period, the windows and lenses--indeed the whole sensor--become coated with a heavy layer of liquid water which eventually absorbs or scatters all the radiation from the source. To alleviate this problem, we are rearranging the sensor components into the two-ended design shown in Fig. 14. The two halves of the sensor (source compartment and opto-electronic compartment) are held together by an open bushing which can be fabricated in different lengths to change the path length. This modified design not only has two fewer optical surfaces to become water-coated, it is simpler to construct. This should significantly reduce the cost of the sensor. The one drawback to this linear design is that the longer path lengths needed for accurate measurements of low gas concentrations are longer than the small, high-frequency eddies for which studies have been proposed. This limits the frequency response capability of the sensor design at the lower concentrations.

REFERENCES

1. G. E. Bingham, C. H. Gillespie, and J. H. McQuaid, Development of a Miniature, Rapid-Response Carbon Dioxide Sensor, Lawrence Livermore Laboratory, Livermore, California, UCRL-52440 (1978).

2. R. P. Koopman, L. M. Kamppinen, L. G. Multhauf, G. E. Bingham, and D. N. Frank, A Review of the 1978 China Lake LNG Dispersion Experiments and Instrumentation, Liquefied Gaseous Fuels Safety and Environmental Control Assessment Program: A Status Report DOE/EV-0036, Report K, Department of Energy, Division of Environmental Control Technology (May 1979).

3. Handbook of Military Infrared Technology, W. T. Wolfe, ed., Office of Naval Research, Department of the Navy, Washington, D.C. (1965), p. 228.

4. R. A. McClatchey, R. W. Fenn, J. E. A. Selby, F. E. Volz, and J. S. Garing, Optical Properties of the Atmosphere (Third Edition), Optical Physics Laboratory, Air Force Cambridge Research Laboratories, L. G. Hanscom Field, Bedford, Massachusetts, AFCRL-TR-72-0497 (1972).

5. R. A. McClatchey and J. E. A. Selby, Atmospheric Attenuation of Laser Radiation from 0.76 to 31.25 μm, Optical Physics Laboratory, Air Force Cambridge Research Laboratories, L. G. Hanscom Field, AFCRL-TR-74-0003 (1974).

6. C. F. Dewey, Jr., J. H. Flint, R. M. Russ, Jr., R. Dezmelyk, R. Fenner, and M. I. Stein, Detection of Atmospheric Methane, Fluid Mechanics Laboratory, Massachusetts Institute of Technology, Cambridge, Massachusetts (1979).

REPORT N

Remote Sensing for Diagnosing Vapor Dispersion in Spills of Liquid Energy Fuels

L. G. Multhauf
A. M. Frank
R. O. Koopman

Prepared for the
Environmental and Safety Engineering
Division
U.S. Department of Energy
under Contract W-7405-ENG-48

Lawrence Livermore Laboratory
Livermore, California 94550

THIS PAGE

WAS INTENTIONALLY

LEFT BLANK

REPORT N

TABLE OF CONTENTS

FIGURES

TABLES

SUMMARY

The measurement of gas concentrations in Liquid Energy Fuel (LEF) dispersion clouds by remote LIDAR sensing is an attractive alternative to the use of *in situ* instruments in regions where the gas concentration level is low. A comparison of Raman and DIAL LIDAR has shown that Raman LIDAR is best suited to measure the concentration levels of interest in the LEF progr The LIDAR systems are limited primarily by the opaque fog produced by the evaporation of a cryogenic liquid fuel. The limitation is most severe for methane, for which LIDAR is not useful for concentrations above the flammability range. However, it is in this low concentration region that the spatial extent of the cloud is large and not easily covered with an array. Comparison is made between a "fence" of *in situ* instruments proposed for 40-m^3 spills at China Lake (a row of 10 *in situ* instrument stations) and a Raman LIDAR system of similar cost designed to cover the same area of the cloud. LIDAR offers substantially higher spatial resolution and coverage that better allows for wind variations. A feasibility test of the Raman LIDAR instrument on a 5-m^3 spill at China Lake has demonstrated the usefulness of the technique.

INTRODUCTION

As a means of determining the effects of a large-scale accidental spill of Liquefied Natural Gas (LNG), the Lawrence Livermore Laboratory (LLL) is developing the calculational capability to determine how the liquid spreads, vaporizes, and disperses under varying weather conditions. In order to experimentally verify the accuracy of models, it will probably be necessary to conduct and diagnose spills in the 200 to 1000 m^3 range. The maximum spill size will be chosen such that results can be extrapolated with confidence to the capacity of presently operating LNG tankers.

Diagnosing planned experimental spills of 40 m^3, and subsequent spills of 200 m^3 or more, will require an extensive array of *in situ* instruments that may cost several million dollars. Remote sensing is a means of potentially reducing the cost, and/or of providing better coverage than a more extensive *in situ* array could provide.

LNG is predominantly methane. However, the heavier hydrocarbons are important because they are much more readily detonable. They also have higher boiling temperatures than methane, and therefore tend to be concentrated in the vapor boiled off after most of the methane has evaporated. A remote sensor must therefore be capable of determining the time-varying concentration level of several hydrocarbon species, especially methane (CH_4), ethane (C_2H_6), and propane (C_3H_8). To be more generally useful in the LEF program, it should be adaptable for gases of future interest as well.

There are two LIDAR (a laser ranging technique named by analogy to RADAR) systems currently in use for measuring gas concentrations[1] that are potentially applicable to the LEF program: DIAL (a differential infrared absorption technique) and Raman. Both have been used to measure hydrocarbon concentrations. The two methods are compared in this report.

The feasibility of using Raman LIDAR on LNG spills was evaluated on a 5-m^3 China Lake spill in September 1978. The expected performance was verified, and the observed relationship between hydrocarbon concentration and fog was consistent with calculations. Test results are described in this report.

We propose that a Raman LIDAR system be built to diagnose the large volume, low concentration region on 40-m^3 spills. For spills of this size, LIDAR is competitive in cost, and superior in performance to the alternative *in situ* instruments. When larger spills are conducted, a LIDAR system will result in a significant reduction in total diagnostic cost.

INFRARED ABSORPTION AND RAMAN SCATTERING

Molecular excitations appear in three spectral regions:

- Visible-ultraviolet: electronic excitations
- Infrared: vibrational excitations
- Microwave: rotational excitations

Not all molecules have discrete electronic states (methane, for example), and spherical top molecules have no rotational Raman structure. However, all molecules have vibrational levels by which they can be identified. The infrared structure will look qualitatively as shown in Fig. 1, where the width of the rotational structure is shown greatly exaggerated. Symbols used are as follows:

u = vibrational quantum number

J = rotational quantum number

ν_0 = incident photon energy

I_0 = incident photon flux

$\Delta\nu_0$ = energy shift in photon energy produced by Raman interaction

T = transmission

Q = designation for $\Delta u = +1$ vibrational excitation

o,s = designations for rotation-vibration branches produced by the ensemble of $\Delta J = \pm 2$ transitions.

Widths and amplitudes of all lines in the spectrum are temperature-dependent.

Molecular structure can be measured in both absorption and emission (Raman) spectroscopy. In absorption spectroscopy a photon, normally in the infrared (ir), is absorbed when its energy corresponds to that of a molecular excitation level. A Raman interaction is not absorptive, but produces a shift in the incident photon energy equal to the excitation energy of the molecular level. Since this reaction has a cross section with a λ^{-4} dependence, it is useful only with energetic (normally uv) photons. The incident photon energy can be shifted either up or down depending on whether the interaction excites or de-excites the level. Selection rules for the major transitions are given in Fig. 1.

Figure 1 shows the Q branch of one vibrational mode. Some molecules have several. In general, the number of vibrational degrees of freedom is

Linear molecules: $3n - 5$,

Nonlinear molecules: $3n - 6$,

where n is the number of atoms in the molecule. Diatomic molecules have only one vibrational state. Methane (n = 5) has nine. However, degeneracies reduce the total number of states (to four for CH_4). Of the nondegenerate states, some are "infrared" (absorption) inactive, because the excitation

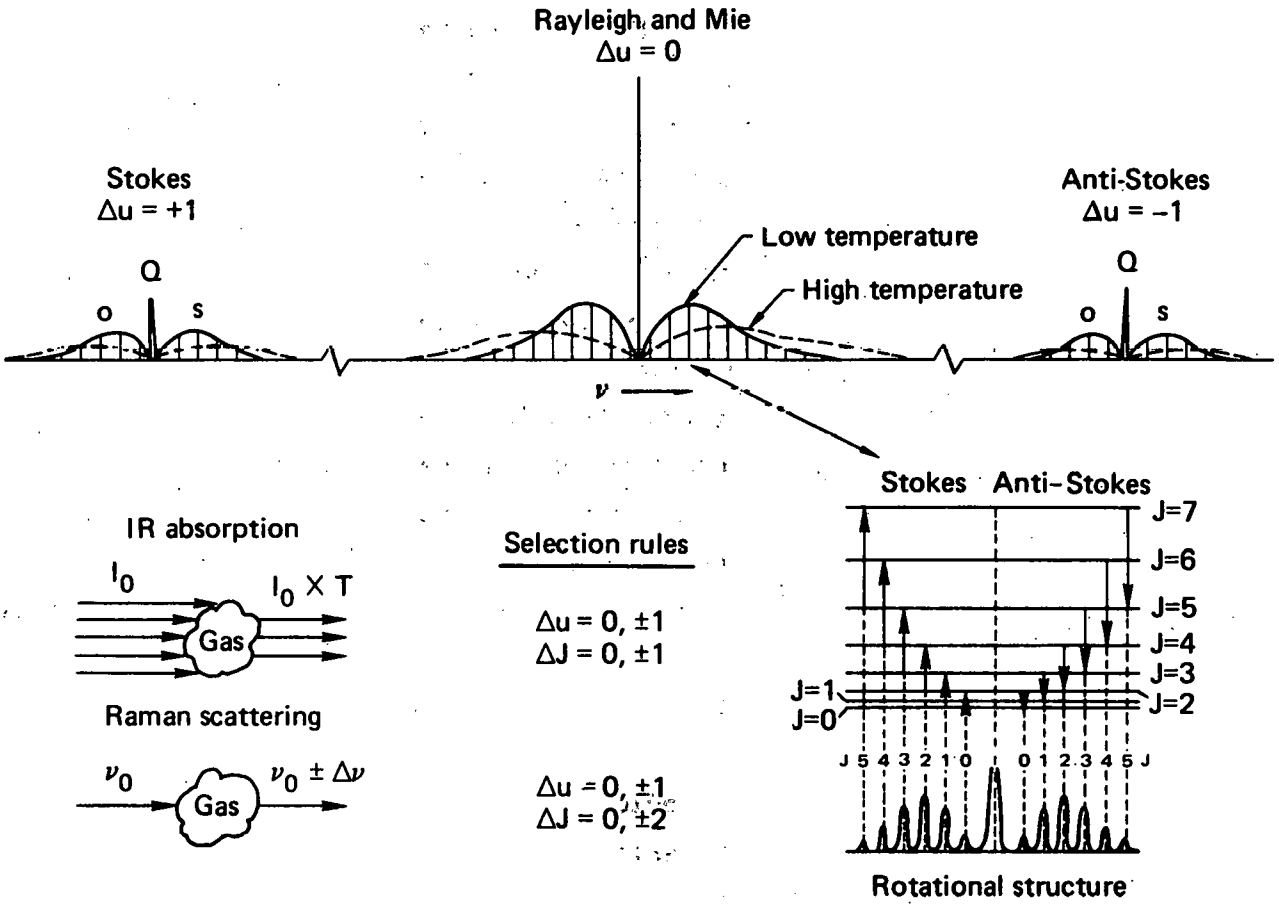

FIG. 1. Molecular excitation.

produces no change in dipole moment. Others are Raman inactive due to the absence of a change in polarizability. Most states have complex fine structure resulting from rotation-vibration interactions. In addition, weak states appear due to overtones (multiples of vibrational frequencies resulting from anharmonicities in the interatomic potential), combinations (of different vibrational modes), and combined rotation-vibration interactions.

There are several vibrational modes that appear in hydrocarbon molecules with frequencies not strongly dependent on the particular molecular specie. These frequencies are called "group frequencies."[2] The strongest group is always identifiable with the C-H stretch vibration. Unfortunately, the strongest lines from different hydrocarbon species nearly overlap. Therefore, the C-C stretch lines can be important signatures, especially in Raman spectra since they are the second most intense lines. Figures 2 through 4 give both absorption (top) and Raman (bottom) spectra of CH_4, C_2H_6, and C_3H_8, respectively.[3]

DIAL--DIFFERENTIAL ABSORPTION LIDAR

As the foregoing discussion has indicated, there are two ways of using molecular ir structure to identify materials. The first is to pass infrared radiation through a sample and measure the absorption spectrum. The second is to use visible or uv radiation and measure the Raman spectrum. A single-ended absorption scheme is shown schematically in Fig. 5., which is taken from Ref. 4. The laser frequency must be tuned to the precise frequency of a narrow absorption peak of the gas sample of interest. When the gas is introduced into the sample cell, the signal attenuation is measured, and can be related directly to the gas concentration. This system was used by Stanford Research Institute to measure methane.[4] The results are shown in Fig. 5.

If this system is to be used in an uncontrolled environment, a second laser frequency immediately adjacent to the absorption peak can be used to measure the backscatter efficiency and the effect of interferences from other gaseous species (hence, the term "differential").

If range information is required (as it is in a LIDAR measurement), two additional complications are introduced. First the laser must have a pulse width narrow enough to give the desired spatial sampling length, and second,

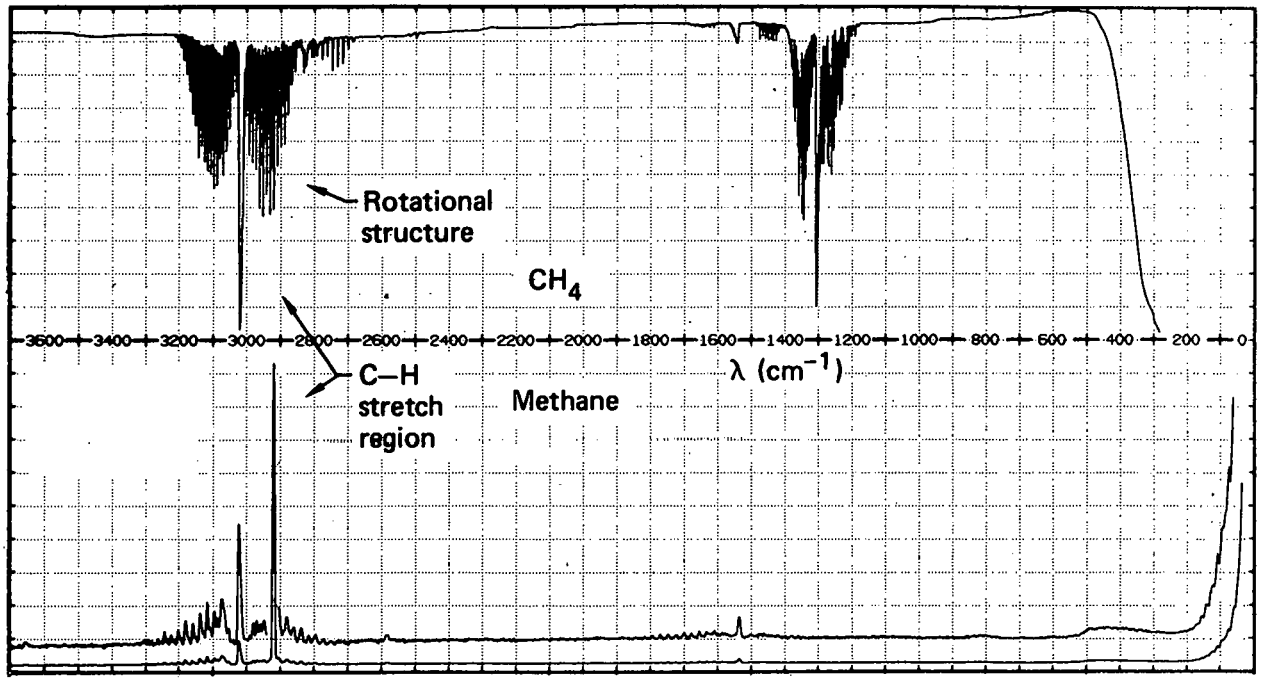

FIG. 2. Infrared absorption (top) and Raman (bottom) spectra of methane.

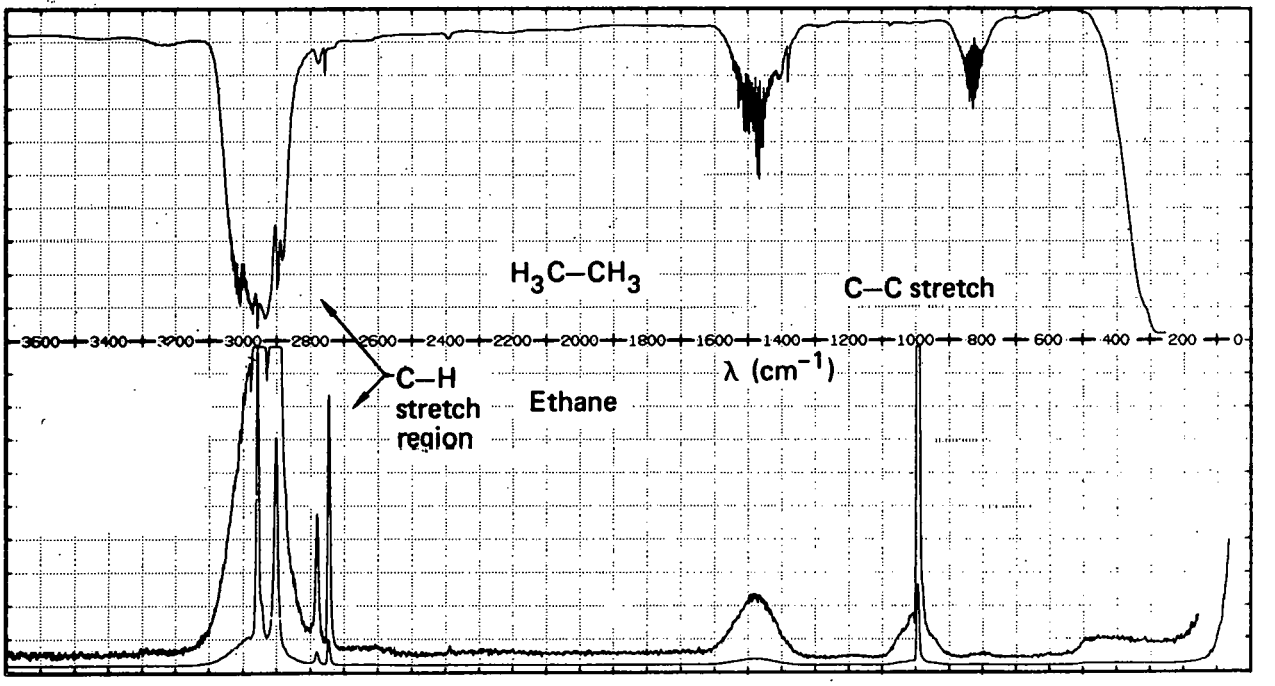

FIG. 3. Infrared absorption (top) and Raman (bottom) spectra of ethane.

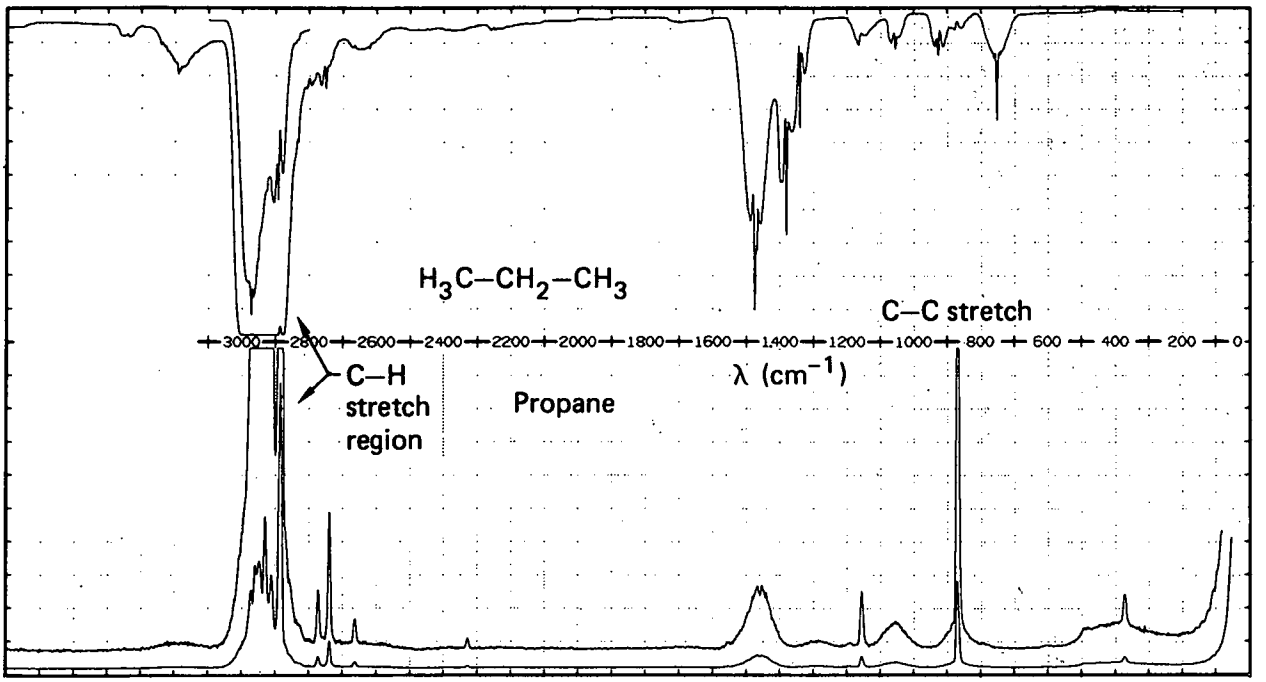

FIG. 4. Infrared absorption (top) and Raman (bottom) spectra of propane.

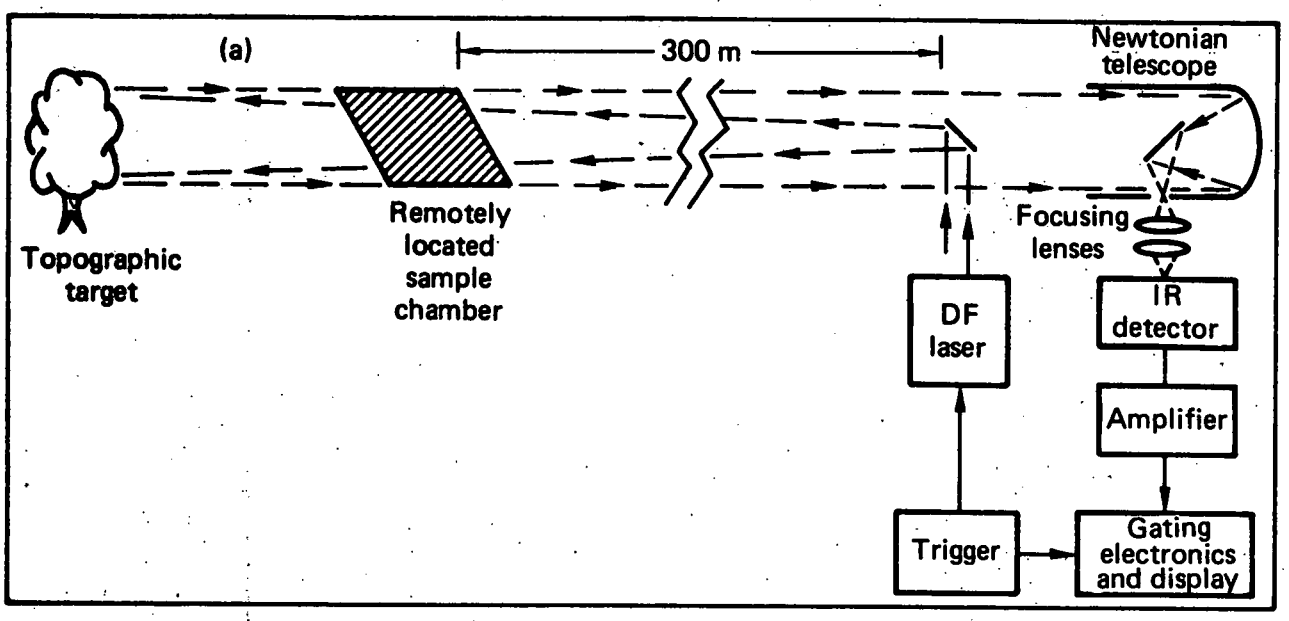

Experimental apparatus

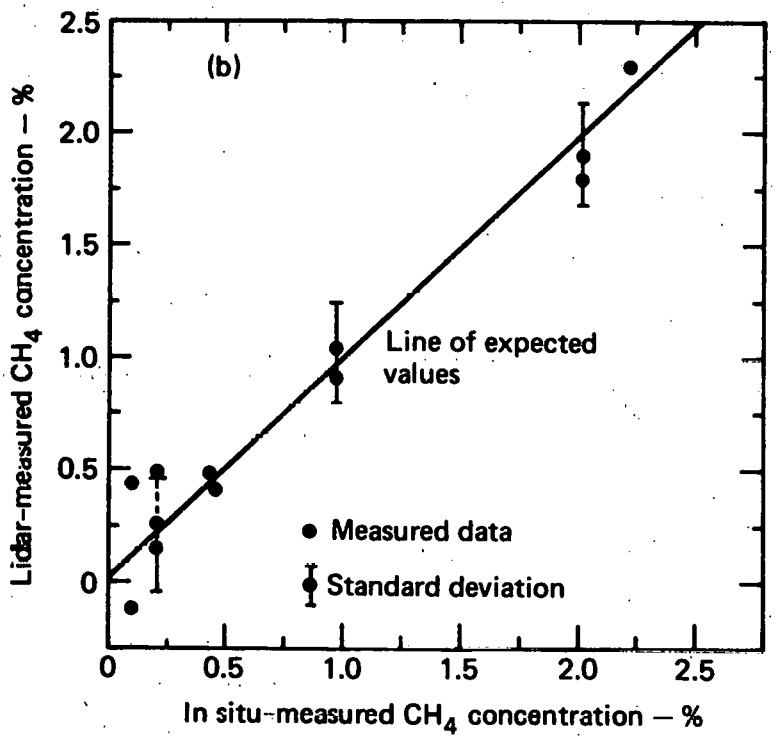

FIG. 5. Infrared absorption LIDAR: (a) experimental apparatus, (b) measured values.

the laser power must provide an adequate backscattered signal from Mie (particulate) scattering interactions. (Molecular scattering has a λ^{-4} cross section dependence, and is therefore too weak for backscattering at infrared wavelengths.) A DIAL system is shown schematically in Fig. 6.

The return signal in a DIAL measurement is given (assuming single scattering) by the expression

$$P_r(R) = P_0 \left(\frac{c\tau}{2}\right) \beta(R)\ \varepsilon_0 \varepsilon_r \Omega(R) Q\ e^{-2\int_0^R \alpha\,(r)\,dr} \quad ,$$

where

R = distance of a range cell,

$P_r(R)$ = power in the signal returned from backscatter events at R,

P_0 = transmitted laser power,

c = speed of light,

τ = time width of the laser pulse,

$\beta(R)$ = average volume-backscatter coefficient at R,

ε_0 = efficiency of transmitter,

ε_r = efficiency of receiving optics and spectrometer,

$\Omega(R)$ = solid angle of receiving optics relative to the scattering point (at R),

Q = detector quantum efficiency,

$\alpha(r)$ = volume extinction (scattering plus absorption) coefficient.

A laser frequency must be chosen with these conditions:

- α is due predominantly to the gas specie of interest.
- α has the right magnitude.
  a) if α is too large, there will be an inadequate return signal from within the cloud.
  b) if α is too small, there will be little absorption, and hence little accuracy in the deduced gas concentration.

The extinction coefficient is given by

$$\alpha(r) = \sum \sigma_i N_i(r) \quad ,$$

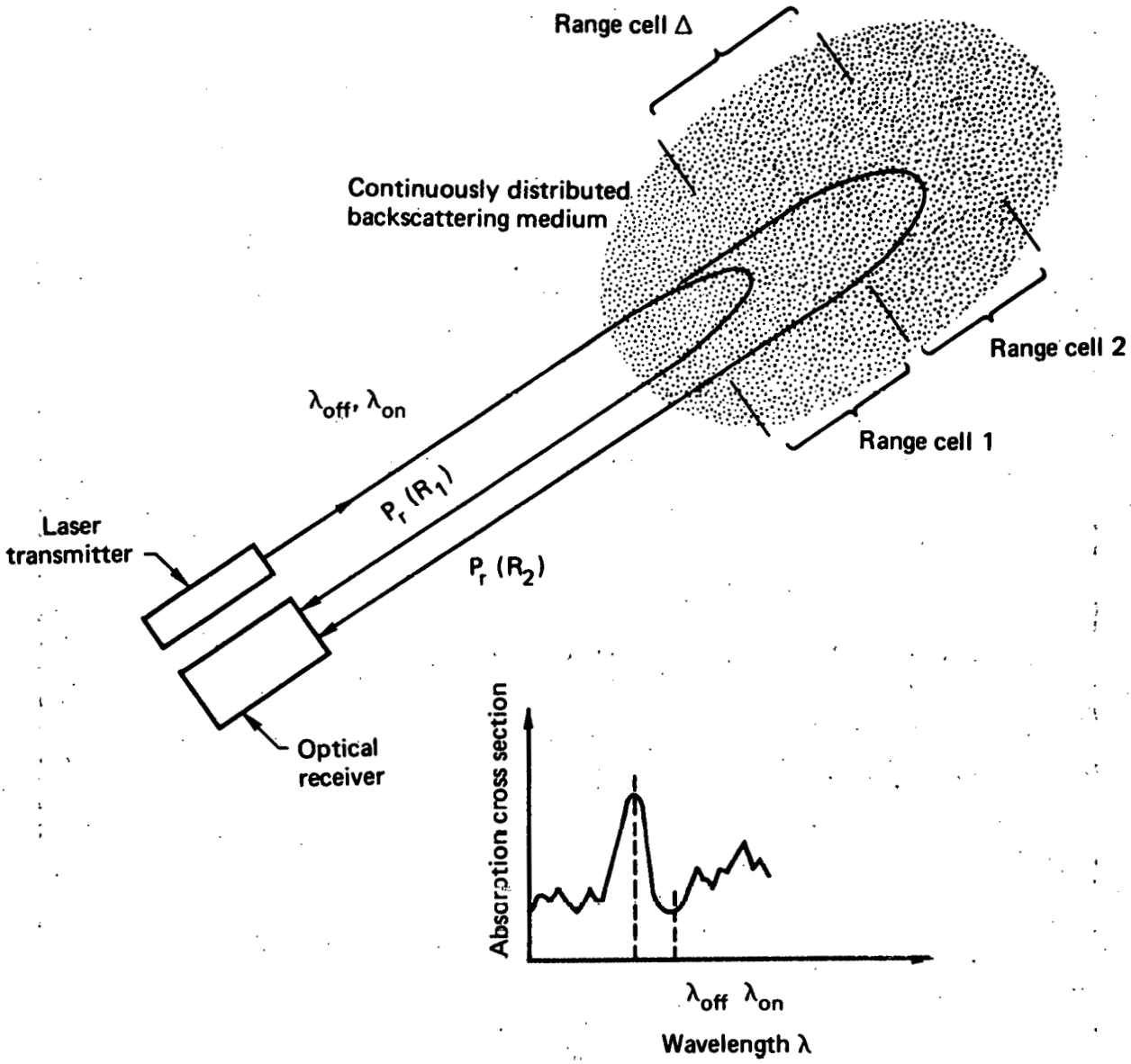

FIG. 6. Differential absorption LIDAR--DIAL.

where

σ_i = extinction cross section for gas specie i.

$N_i(R)$ = number density for gas specie i.

Ignoring interfering species and backscatter uncertainties, concentrations could be derived from a measurement at a single laser frequency using the expression

$$\bar{N}(R) = \frac{1}{2\sigma\Delta R}\left[\ln P_r(R) - \ln P_r(R+\Delta R) - \frac{2\Delta R}{R}\right] ,$$

where it is assumed in computing an average concentration, that the backscatter coefficient is essentially constant across a range cell. If an adjacent frequency can be found that is off the absorption peak of interest, but for which the cross sections for backscattering and extinction by interfering species are unchanged, then these effects can be measured and eliminated. The concentration for the specie of interest is then given by the expression

$$\bar{N}(R) = \frac{1}{2\sigma\Delta R}\left[\ln P_r(\lambda,R) - \ln P_r(\lambda,R+\Delta R) - \ln P_r(\lambda+\Delta\lambda,R) + \ln P_r(\lambda+\Delta\lambda,R+\Delta R)\right] .$$

The uncertainty in the results is given by

$$\frac{\Delta\bar{N}(R)}{\bar{N}(R)} = \frac{\left\{\left[\frac{\Delta P_r(\lambda,R)}{P_r(\lambda,R)}\right]^2 + \left[\frac{\Delta P_r(\lambda,R+\Delta R)}{P_r(\lambda,R+\Delta R)}\right]^2 + \left[\frac{\Delta P_r(\lambda+\Delta\lambda,R)}{P_r(\lambda+\Delta\lambda,R)}\right]^2 + \left[\frac{\Delta P_r(\lambda+\Delta\lambda,R+\Delta R)}{P_r(\lambda+\Delta\lambda,R+\Delta R)}\right]^2\right\}^{1/2}}{\ln P_r(\lambda,R) - \ln P_r(\lambda,R+\Delta R) - \ln P_r(\lambda+\Delta\lambda,R) + \ln P_r(\lambda+\Delta\lambda,R+\Delta R)}$$

or, for a system limited by Poisson statistics,

$$\frac{\Delta N(R)}{\bar{N}(R)} = \frac{\left[\frac{1}{P_r(\lambda,R)} + \frac{1}{P_r(\lambda,R+\Delta R)} + \frac{1}{P_r(\lambda+\Delta\lambda,R)} + \frac{1}{P_r(\lambda+\Delta\lambda,R+\Delta R)}\right]^{1/2}}{\ln P_r(\lambda,R) - \ln P_r(\lambda,R+\Delta R) - \ln P_r(\lambda+\Delta\lambda,R) + \ln P_r(\lambda+\Delta\lambda,R+\Delta R)} .$$

For a linear system, the dynamic range is given simply by the minimum and maximum detectable signals. DIAL, however, is not linear and, in addition, the measurement capability must be adequate to cover the necessary signal range from the front to the back range cells. Therefore, the dynamic range of the recording system must substantially exceed the range of concentrations to be measured.

The required system dynamic range depends on a number of factors, including the atmospheric visibility, which gives a measure of the backscatter efficiency. The relationship between system dynamic range and range of concentration coverage cannot be given in a simple analytical form, but one can obtain some feel for it from the following example of its use on a hypothetical LNG dispersion test:

- Requirements
  - --Range of concentrations to be measured = 10 (e.g. 1 to 10%, 2 to 20% etc., depending on choice of absorption peak)
  - --Maximum uncertainty = a factor of 2
  - --Number of range cells = 20
- Conditions
  - --No interference from other species
  - --Visibility = 50 km
  - --Distance between LIDAR and LNG cloud = 2 km
  - --Laser wavelength = 1 μm
- Result
  - --System dynamic range must be 500:1 or greater
  - --Laser energy must be ~1 J over the measuring time interval.

A system dynamic range of 500:1 is achievable. However, the requirements are barely adequate, and it may be difficult to find appropriate absorption peaks that have essentially no interference from other gas species. In addition, the requirement of a large laser per gas specie of interest (or perhaps two, if a separate background channel is required for each specie) causes DIAL LIDAR to look unattractive in comparison to Raman LIDAR for LNG applications.

This analysis has assumed a time-domain system for obtaining range information. A system could be constructed using a CW laser and a heterodyne detection system. Range information could be obtained using Fourier frequency analysis with a detection scheme proposed by Hirschfeld.[5] No further

description will be given here, as the system capabilities are not changed significantly from those of the system described. If a system were constructed, however, the heterodyne approach might be preferred.

Before proceeding to a discussion of Raman LIDAR, we should consider DIAL in regard to optical penetration of the fog produced by the cold gas vapor (methane evaporates at a $-161.5^{\circ}C$). Raman LIDAR requires the use of blue light or uv radiation, neither of which can be expected to penetrate the fog. Might not the ir radiation of a DIAL system penetrate better (just as long-wavelength yellow headlights are used in fog in preference to white)? One can give a "no" answer without going into the details of Mie scattering by noting that DIAL requires Mie backscattering to work at all. If the backscatter coefficient is large enough to permit measurements in regions of the cloud with no fog (i.e., from the small particulate content of clear air), then the laser radiation will certainly not penetrate a fog cloud. This is in agreement with Mie scattering theory for spherical particles. (In the auto driver analogy, longer-wavelength headlights do not penetrate significantly better, but the angular distribution is more forward-peaked, and hence there is less reflected light to blind the driver.)

RAMAN LIDAR

Raman LIDAR has several advantages over DIAL LIDAR:

- It is a simpler system because it does not require multiple laser frequencies that must be carefully tuned.
- It may be usable on burn tests.
- It may provide temperature data.
- Initial analysis is easier because it does not require high resolution spectra of all gases of interest.

The disadvantage of Raman LIDAR is that it will be difficult to detect much below 1% average concentrations in 9-m range cells, especially for ethane and propane (and CO_2 and O_2 in burn tests).

The return signal from a Raman LIDAR is given by

$$P_r(R) = P_0 T(\lambda_0)\ T(\lambda_r)\ \varepsilon_0 \varepsilon_r \Omega(R) \Delta R \frac{d\sigma(180^{\circ})}{d\Omega} N\ ,$$

where

$T(\lambda_0)$ and $T(\lambda_r)$ = atmospheric transmission factors for the incident laser and return Raman scattered wavelengths,

$d\sigma(180^\circ)/d\Omega$ = differential Raman cross section at 180° for the gas specie of interest,

N = specie concentration.

Other symbols are the same as in the previous section.

The atmospheric transmission and the Raman cross section are both strongly wavelength-dependent, the transmission falling off rapidly in the uv, and the cross section at longer wavelengths, producing a distinct optimum in the wavelength response. For path lengths of interest for LNG diagnostics, the optimum wavelength is about 350 nm. The return Raman signal will be frequency-shifted for different gas species of interest by the amounts shown in Fig. 7. All of the lines shown can be resolved except perhaps for the hydrocarbons near 3000 cm^{-1}, which will, in general, be dominated by methane in LNG vapors. The N_2 line is convenient for examining temperature-dependent rotational structure, and for verifying system operation.

The cross section for Raman backscattering is

$$\frac{d\sigma(180^\circ)}{d\Omega} = \frac{2\pi^2 h\,(\nu_0 - \nu_j)^4\, g_j\, P_j}{c\,\nu_j\,\left|1-\exp(-hc\nu_j/kT)\right|},$$

where

ν_0 = laser frequency in cm^{-1},

ν_j = frequency shift of the j state in cm^{-1},

g_j = degeneracy of j state,

P_j = polarizability term associated with state j.

Several backscatter cross sections measured at 347.2 nm and 488.0 nm are given in Table 1.

The analysis of a Raman system is relatively straightforward in that it is linear, with sensitivity limited primarily by photon statistics. To maximize the sensitivity, components must be as large and efficient as feasible.

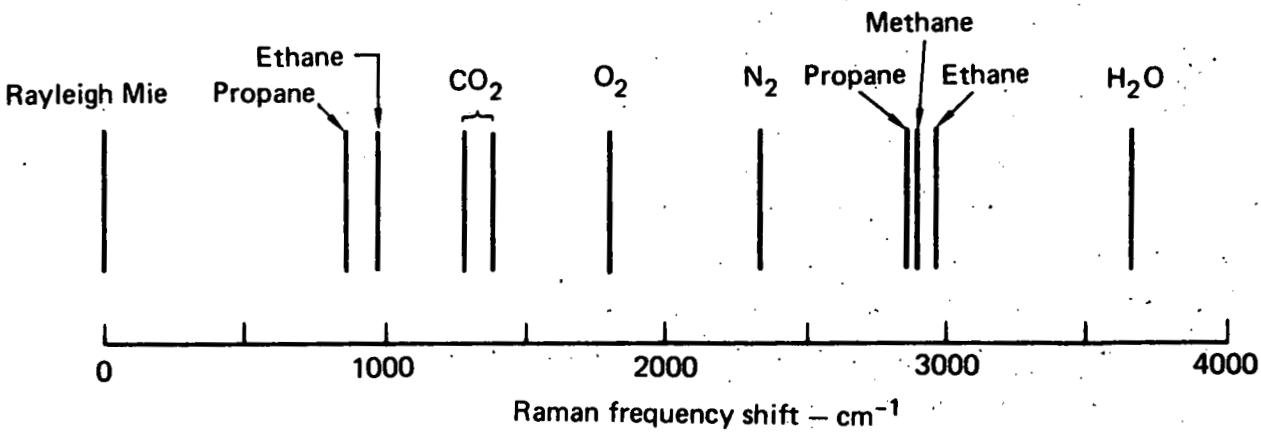

FIG. 7. Raman frequency shifts of gas species in an LNG cloud.

TABLE 1. Raman cross sections of gases.[a]

Compound	Formula	Raman line shift $\Delta\nu$, cm^{-1}	Relative cross section compared to nitrogen	Cross section at 4880 A and 180° observation angle cm^2 molecule^{-1}	Cross section at 3472 A and 180° observation angle cm^2 molecule^{-1}
Carbon dioxide	CO_2	1286	0.80	5.62×10^{-30}	2.37×10^{-29}
Carbon dioxide	CO_2	1388	1.18	8.30×10^{-30}	3.52×10^{-29}
Ethane	C_2H_6	988	2.96	2.08×10^{-29}	8.59×10^{-29}
Ethane	C_2H_6	2954	5.50	3.87×10^{-29}	1.79×10^{-29}
Methane	CH_4	2914	7.15	5.02×10^{-29}	2.36×10^{-28}
Nitrogen	N_2	2331	1.00	7.03×10^{-30}	3.18×10^{-29}
Oxygen	O_2	1555	1.21	8.51×10^{-30}	3.64×10^{-29}
Propane	C_3H_8	867	5.08	3.57×10^{-29}	1.47×10^{-28}
Propane	C_3H_8	2887	6.21	4.37×10^{-29}	2.04×10^{-28}
Water	H_2O	3652	3.24	2.28×10^{-29}	1.17×10^{-28}

[a]Taken from Ref. 6.

Specifications that appear reasonable with presently available equipment are listed in Table 2. The laser and telescope could be larger, but only with a significant increase in cost. The laser-beam divergence and telescope acceptance angle must be small to permit operation with daylight, or flame background. The spectrometer efficiency is high, and would require some effort to build. Details of specifications will be discussed further in a later section of this report.

Based on these specifications (the laser being a frequency tripled YAG), and assuming a 1-km distance between LIDAR and LNG vapor, the following is the rate of detector photoelectrons produced by gases at 1% concentration levels:

CH_4 N = 120/s,
C_2H_6 N = 65/s,
C_3H_8 N = 88/s,

which indicate that statistically significant information can be obtained down to a fraction of a percent concentration.

TABLE 2. Specifications for a Raman LIDAR system.

E(laser) $\geq$ 0.15 J/pulse - 10 pps, $\leq$ 10 ns/pulse
d(telescope) $\geq$ 35 cm
Beam divergence $\lesssim$ 0.1 mrad
Telescope acceptance cone ~0.1 mrad
λ(laser) - 300 nm to 400 nm
Data channels $\geq$4 (CH_4, C_2H_6, C_3H_8, N_2)
ε(telescope-spectrometer) = efficiency ~0.5
Q = detector quantum efficiency $\geq$ 0.3
Digitizer frequency $\geq$ 267 m bits/sec (8 bit words, 30 ns/word)
Memory $\geq 1.64 \times 10^4$ words (128 $\times$ 128)
Control system--real-time variation in scanning
Data system--data collection, storage, averaging, display, plotting
Portability--move in one day or less

In a dispersion test, there will be a background due to scattering of sunlight from air or from the cryogenically produced fog. The sky radiance at 396.0 nm (methane Stokes line using a tripled YAG source) is approximately 5×10^{-6} W/nm$\cdot$cm^2 sr. Assuming a 1.0-nm resolution, and the system specifications of Table 2, the number of detected background photoelectrons is

N(sky radiance) = 6/s.

If a fog is present, background light may be predominantly from the scattering of sunlight in the fog. To get a rough estimate of this source, assume that sunlight entering the cloud (ϕ^{396}nm ~ 0.12 W/cm$^2\cdot\mu$m) is multiply-scattered until it is emitted uniformly from the cloud surfaces. Then the radiance of scattered light is ~3×10^{-6} W/cm$^2\cdot$nm sr, which is similar to the 5×10^{-6} W/nm$\cdot$cm^2 sr shown above for air scattering. We conclude that the proposed system will be usable in peak daylight conditions without serious background due to scattered sunlight.

One of the advantages of Raman LIDAR listed at the beginning of this section is its potential for measuring concentrations before and during burn tests, and for measuring gas temperatures. During burn tests, most *in situ* instruments will have to be removed from the burn area. The LIDAR can make measurements until the cloud is ignited so that the condition of the cloud

immediately prior to ignition will be known. It may also be possible to make LIDAR measurements during the burn. Raman LIDAR has been used for measurements in both flames and rocket exhaust gases.[6] However the reported results are not sufficiently quantitative to allow extrapolation to a burning LNG cloud. Laboratory measurements of cross sections and flame backgrounds will be necessary to determine the feasibility of Raman LIDAR for this application.

Temperature measurements are also possible in principle. There are several temperature-dependent spectral quantities, some of which are as follows:

At low temperatures (dispersion tests)

- Width of the rotational envelope
  - --around the Rayleigh line
  - --around the Q line

At high temperatures (burn tests)

- Q lines Stokes-Anti-Stokes ratio
- Q line width
- Rayleigh line width
- Q line ratios

At low temperatures, the intensity of data around the Q line (of N_2) would be too weak to obtain temperatures with better than 10 to 20°C accuracy. The rotational envelope about the Rayleigh line is 200 times stronger but discrimination against the intense Mie scattering is a problem that will require further investigation.

At high temperatures there are several potentially useful temperature-dependent quantities. However there are very few high temperature laboratory measurements to base an analysis on. Block Engineering[6] has used the ratio of the 1286- and 1388-cm^{-1} lines of CO_2 to measure temperatures below about 600°C. At higher temperatures, other line ratios might be useful. However, laboratory measurements will be required to determine if there is a feasible technique.

EFFECTS OF CRYOGENICALLY PRODUCED FOG

Before proceeding to describe the China Lake feasibility test, we should consider the effects that can be expected from the fog produced by the cold

LNG vapor. If air is cooled to below the dew point, water will be condensed, thereby keeping the relative humidity from exceeding 100%. If the air is then heated by turbulent mixing, the fog will begin to evaporate, until at the dew point it disappears. Actually this is an oversimplification, because it does not account for radiant heating or the persistence of a fog below 100% relative humidity. But it does give a first-order indication of the relationship between temperature, hydrocarbon concentration, and fog density. A program to relate the two was written with these conditions:

Input parameters

- Initial temperature, density, and specific heat for air and the chosen hydrocarbon specie
- Initial relative humidity
- Saturation water vapor density vs temperature
- Final equilibrium temperature, T_{eq}

Energy exchange terms

- Temperature change due to air-hydrocarbon mixing
- Condensation of water vapor
- Solidification of water vapor

The output is

- Concentration of hydrocarbon in the mixed gas at T_{eq}.

Curves of methane concentration and water condensation as functions of equilibrium temperature are shown in Fig. 8, with initial conditions being those of China Lake during the dispersion test that will be described in the next section. For these conditions--a typical warm September evening (81°F) with water content of air (29% relative humidity) also typical for summer months--concentrations above about 9% will be mixed with fog.

How far can we expect the laser light to penetrate the fog? An estimate can be obtained from Mie-scattering theory.[7] According to Mie theory for spherical dielectric particles with an index of refraction of 1.33 (water), the intensity of unscattered light is given by

$$I = I_0 \, e^{-\gamma \ell} \quad ,$$

where

$$\gamma = \int_0^\infty (\pi a^2) \, N(a) Q(a) \, da \quad ,$$

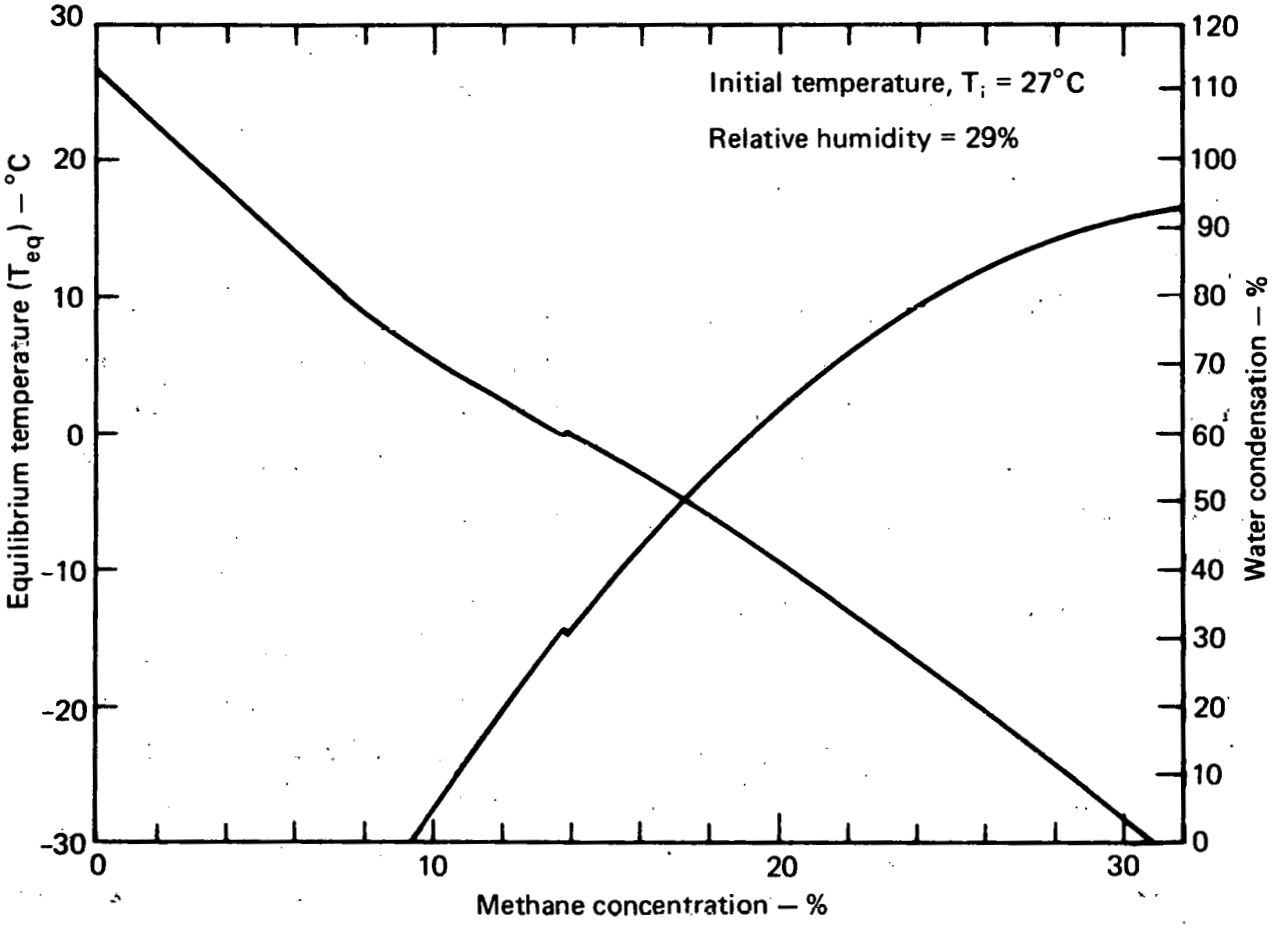

FIG. 8. Equilibrium temperature and water condensation versus methane concentration for conditions of China Lake LNG spill test.

πa^2 = geometrical cross section of a particle of radius a,

$N(a)$ = density of particles of radius a,

$Q(a)$ = efficiency factor for particles of radius a.

Expressed in terms of the "size parameter" $2\pi a/\lambda$, λ becomes

$$\gamma = \frac{\lambda^3}{8\pi} \int_0^\infty \alpha^2 N(\alpha)\ Q(\alpha)\ d\alpha \quad .$$

The physics of Mie scattering is contained in the efficiency factor plotted as a function of the size parameter in Fig. 9. The exact particle-size distribution for a cryogenically produced fog is unknown, but a large fraction of the particles can be expected to lie between 1 and 10 μm. Assuming 100% condensation, the value of γ^{-1} (i.e., the 1/e extinction length) is

for 10-μm particles, γ^{-1} = 450 cm,

for 1-μm particles, γ^{-1} = 3.5 cm.

Since the condensation rises rapidly with hydrocarbon concentration, the fog will be virtually impenetrable. However, water is not primarily an absorption source, but is rather a scattering source. The angular distribution for fog particles is strongly forward-peaked, being most anisotropic when the size parameter equals 6, or, for a N_2 laser wavelength, when the particle radius equals 0.34 μm. The effect of the anisotropy is indicated in Fig. 10., which shows the integrated value of the Mie cross section between 0 and 45°, and between 0 and 90° scattering angles over the range of particle sizes calculated by Blumer.[8,9] For comparison, integrated values are shown for isotropic scattering also.

Because of the weak absorption, one would expect to detect Raman return signals in a LIDAR measurement even after the light has scattered in the fog. However, the Raman interaction will be at some unknown location reached by multiple Mie scattering, and the information will not be useful in any quantitative sense.

The foregoing discussion indicates the most serious limitation of a LIDAR system. Even for the weather conditions of our China Lake feasibility test, we should not expect to cover fully the range of flammability concentrations of methane. In the winter months, when the air is cooler, LIDAR is even more limited. Figure 11 gives a band of methane concentration values that should be associated with the onset of fog condensation. The limits are based on

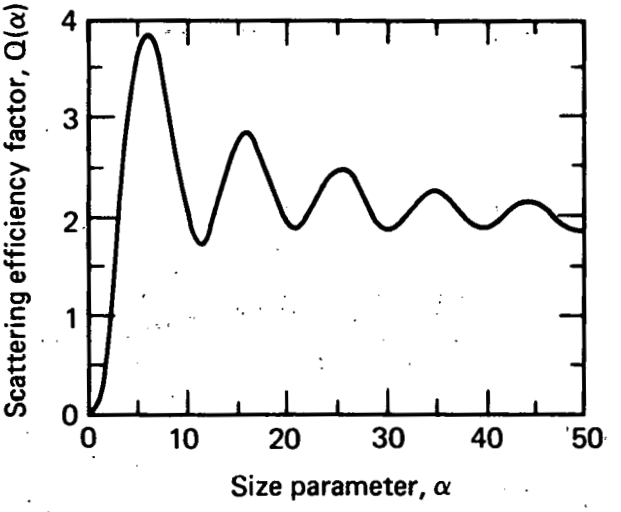

FIG. 9. Mie scattering efficiency factor.

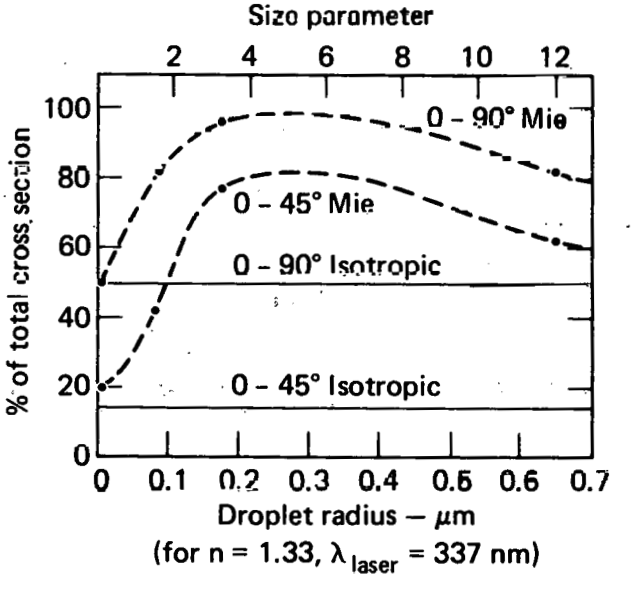

FIG. 10. Mie scattering integrated over forward angles. (Angular values for points shown were calculated by Blumer.[8,9])

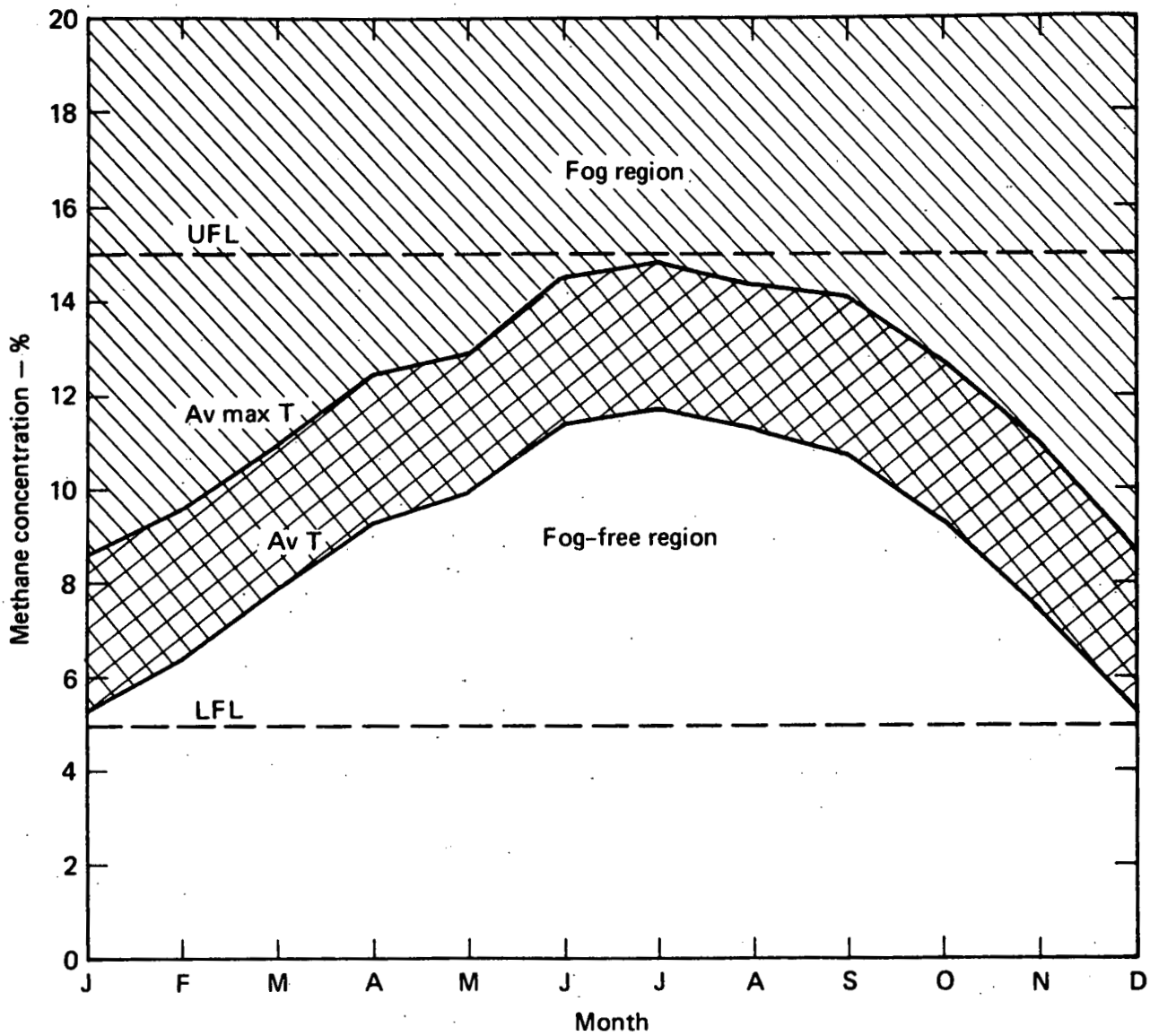

FIG. 11. Fog versus methane concentration for different months of the year at China Lake.

monthly average, and average maximum temperatures at China Lake. Between noon and sunset, temperatures rarely drop below the average values shown. On most days, the average temperature is exceeded during morning hours as well. However, there will be days during the winter months when a LIDAR system would likely not measure significantly above the lower flammability limit (LFL). The usefulness of LIDAR is much greater when the fuels are ethane or propane, as Fig. 12 indicates. This results from the combination of higher boiling temperatures and lower flammability ranges. For propane in particular, even during the coldest months, the entire flammability range can be diagnosed without interference from fog.

LIDAR FEASIBILITY TEST AT CHINA LAKE

The construction at LLL of even a simple LIDAR system for a feasibility test would have required a significant investment of time and effort. Therefore, a contract was given to Computer Genetics Corporation (CGC) to field their existing instrumentation and mobile van on a 5-m^3 LNG dispersion test at China Lake. The corporation's system was capable of measuring total hydrocarbons at eight range-gated positions across a vapor cloud. Specifications for the CGC system are given in Table 3. The system did not incorporate a

TABLE 3. CGC Raman LIDAR specifications.

P(laser) = 0.2 W (1 mJ/pulse, 200 pps, Δt = 10 ns)
λ(laser) = 337 nm (N_2)
Beam divergence 2 to 10 mrad (~1-m diam at spill)
d(Raman telescope) = 20 cm
d(elastic β telescope) = 5 cm
Raman telescope acceptance angle $\lesssim$ 10 mrad
Elastic β telescope acceptance angle $\lesssim$ 10 mrad
Data channels--2 (not simultaneous)
Filters--374.0 ± 1.5 nm (hydrocarbons) 365.8 ± 1.5 nm (nitrogen)
Q = PM (RCA 8850) quantum efficiency ~0.3
Memory--1024 words and cassette tape

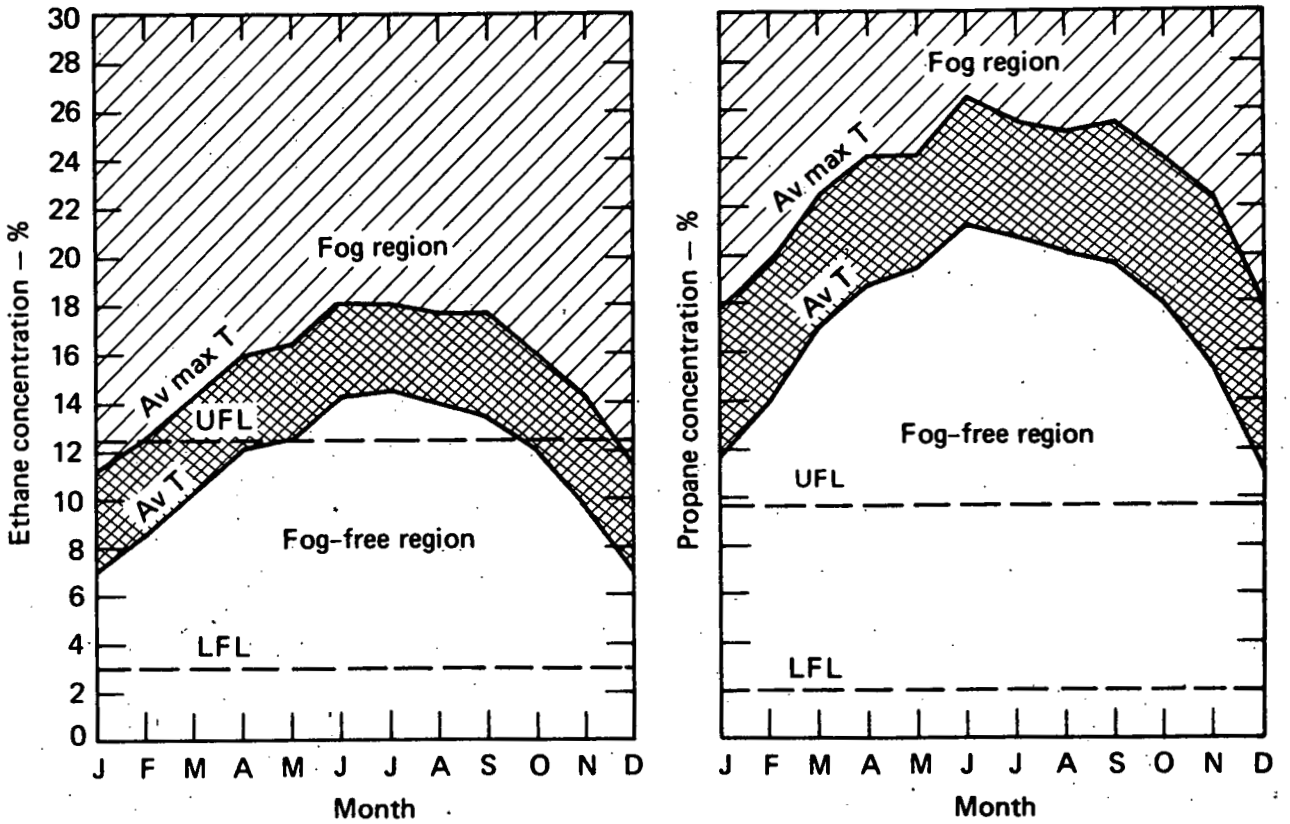

FIG. 12. Fog versus ethane and propane concentrations for different months of the year at China Lake.

scanning capability. Also, the test had to be performed at night because of the low laser power, and large laser-divergence and telescope-acceptance angles. However, the system was adequate to provide a test of the usefulness of a remote measuring system. A block diagram of the CGC LIDAR system is shown in Fig. 13.

The LIDAR van, with N_2 laser and receiving telescope, was situated relative to the LNG spill pond as shown in Fig. 14. Near the pond, the laser beam was 0.6 m above the ground (2.4 m above the water level). The total path length from the van to a reflector across the pond was 135 m. The laser emitted pulses of 10-ns duration (3.0 m spatially). The Raman-scattered light was gated to produce eight return signals per laser pulse, corresponding to the eight 9-m regions shown on the figure. The signals were digitized and recorded in a computer memory for later analysis. The presence of fog in the laser path was monitored by recording on an oscilloscope, an elastically back-scattered component of the laser light. The oscilloscope face was photographed with an 8-mm motion picture camera to provide a permanent record.

A complete description of the China Lake test is contained in a final report prepared by CGC.[10] In the following, a summary of the data is given along with an analysis of its significance.

Examples of scope traces used to determine fog backscattering are given in Fig. 15. The first figure shows the black target return signal (no fog). From this and a scale calibration of 200 ns per major division, the location of the fog can be determined. The position of the fog as a function of time after the spill is indicated in Fig. 16. Some of the data are from within or behind fog regions, as is indicated in the figure. In some of these areas, the density of the fog was low enough that accurate concentration data could have been derived. However, for this test the method of recording fog attenuation made accurate corrections to the Raman data difficult, so we have not attempted to make them.

Concentration data are shown for each range cell in Figs. 17 and 18. Zero time corresponds to the beginning of the spill. Each point represents a 0.92-s average of the Raman return signal. The data points fluctuate rapidly, probably due primarily to vertical turbulence.

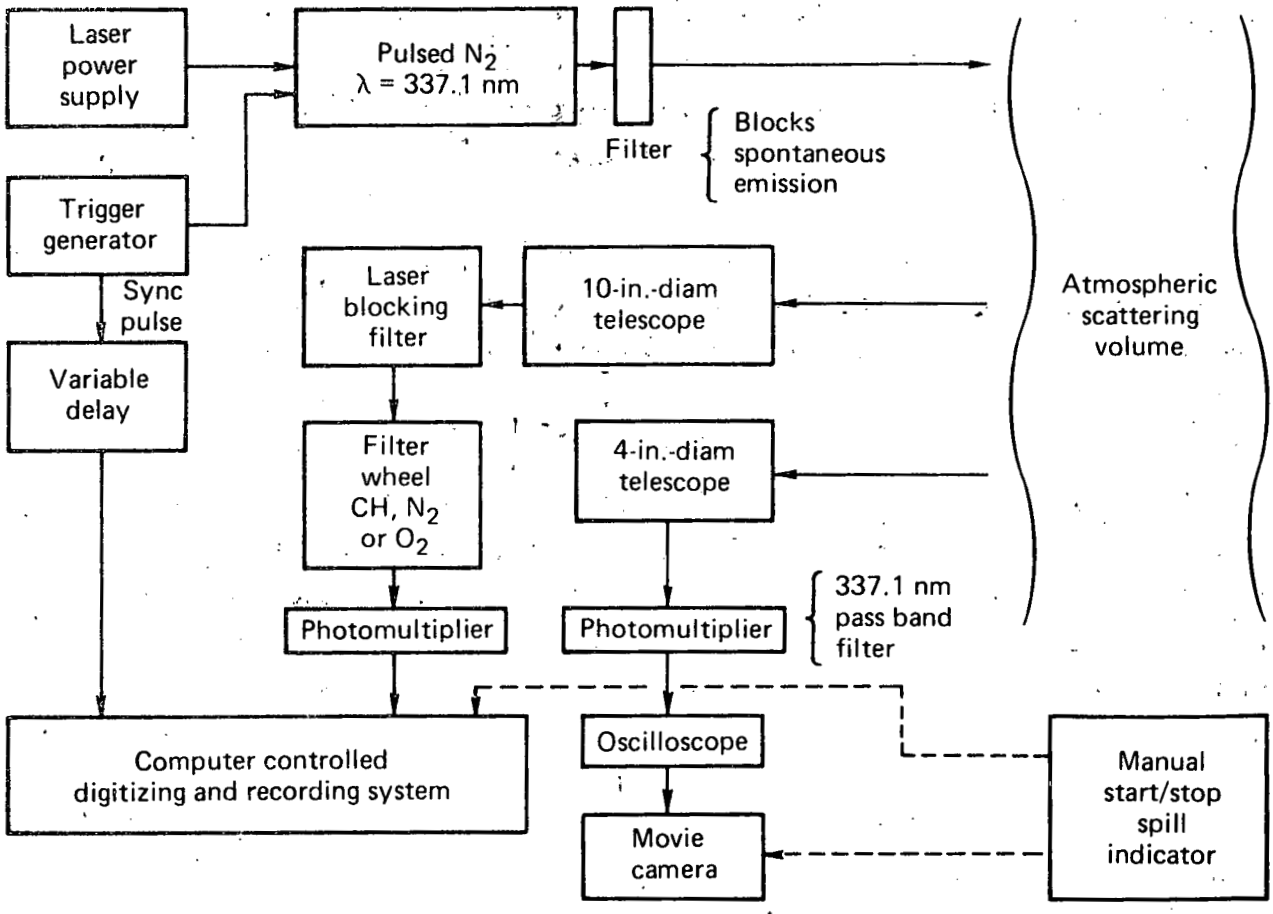

FIG. 13. Block diagram of CGC Raman LIDAR system.

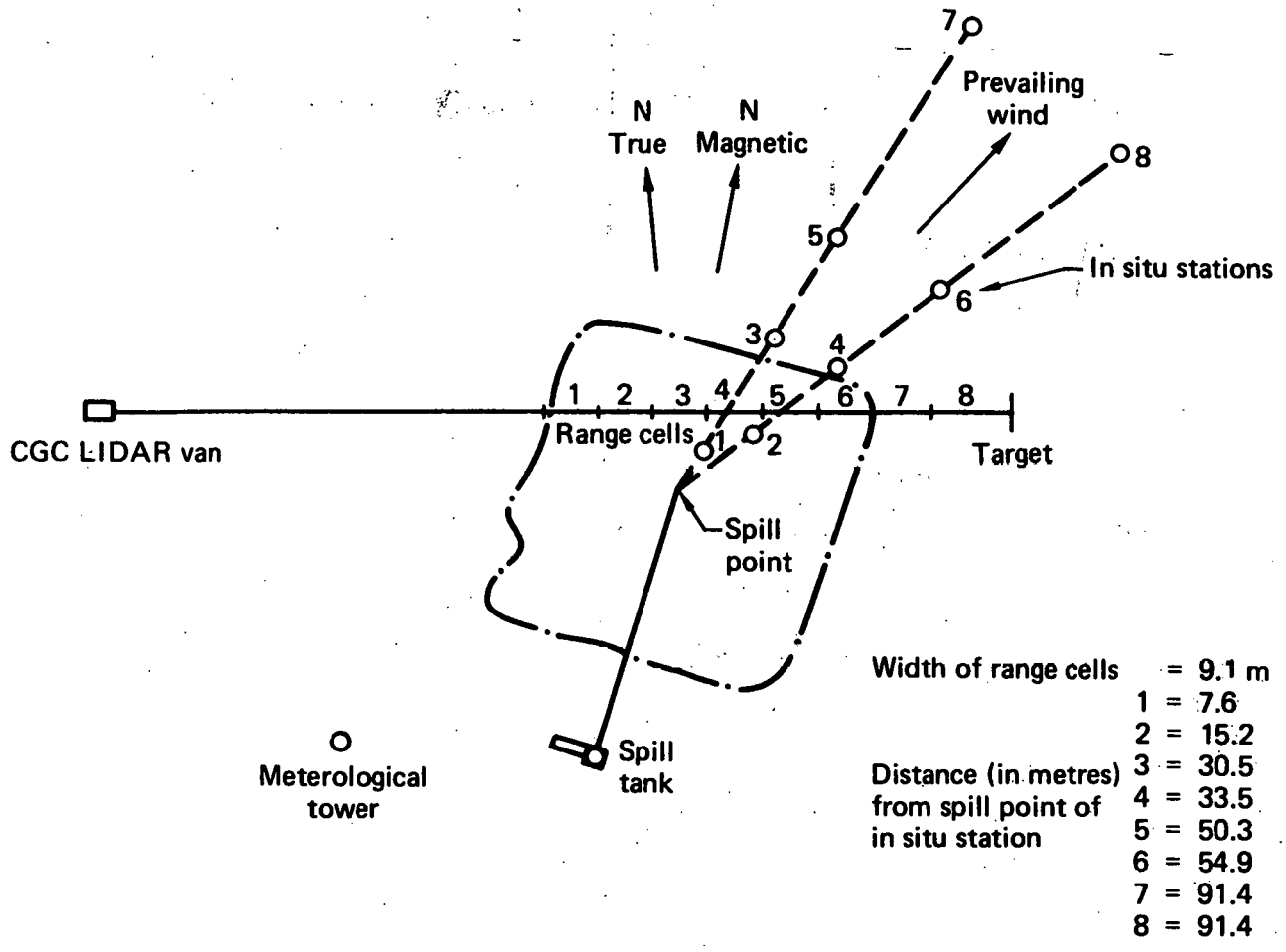

FIG. 14. China Lake LNG spill site plan.

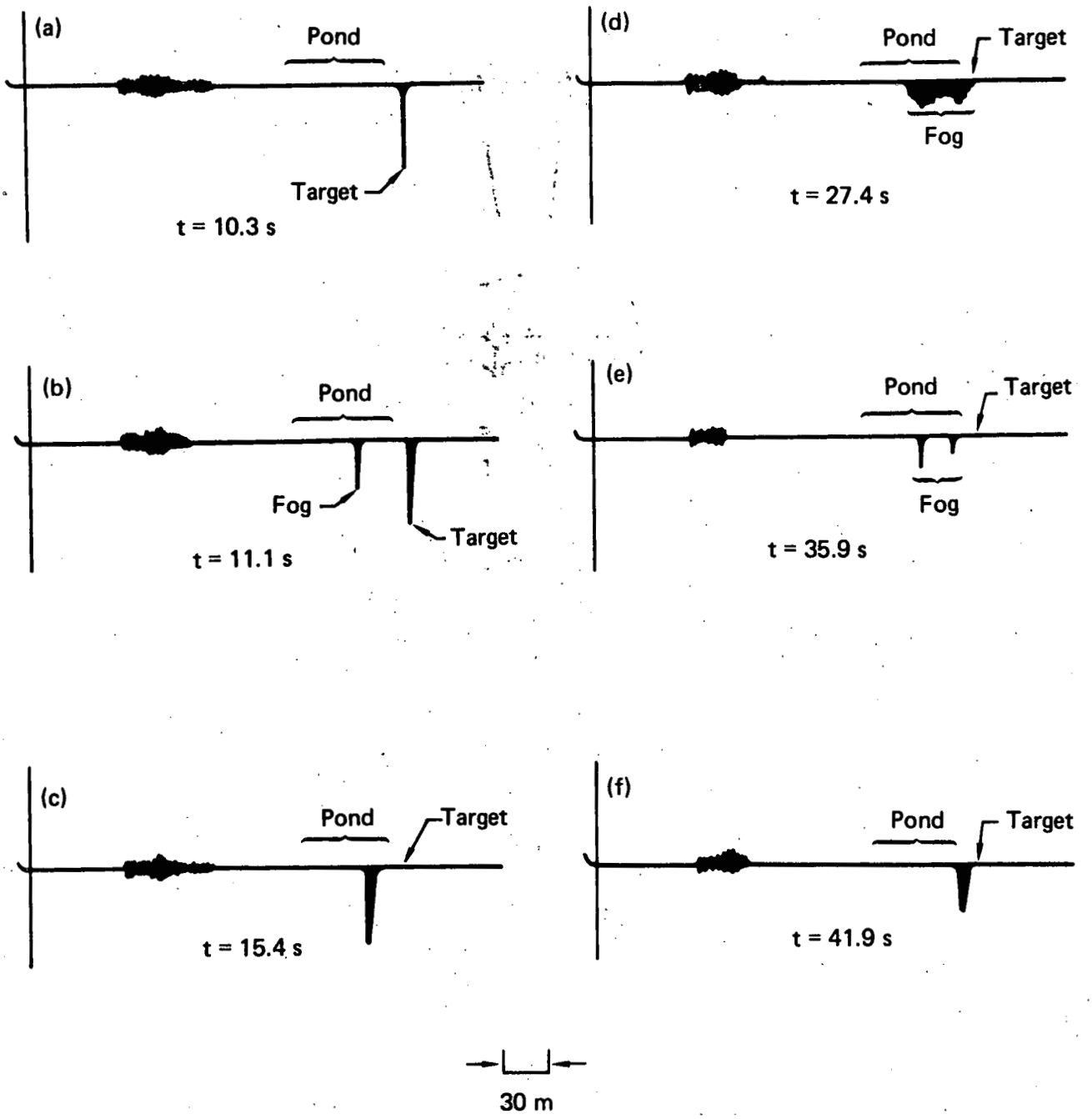

FIG. 15. Drawings of oscilloscope traces of laser return signals indicating the presence and position of the fog. t = 0 s is the beginning of the spill.

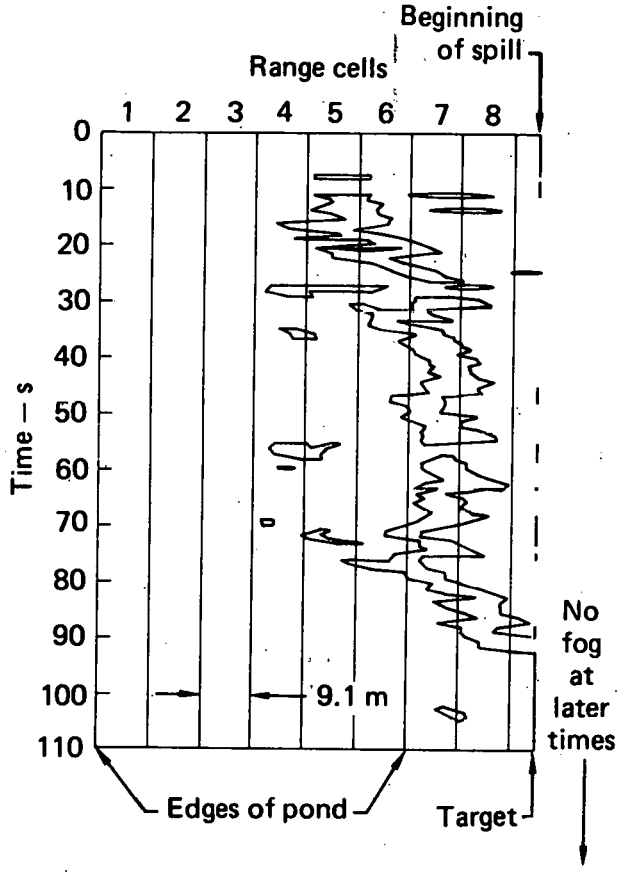

FIG. 16. Location of fog during 5 m^3 LNG spill at China Lake.

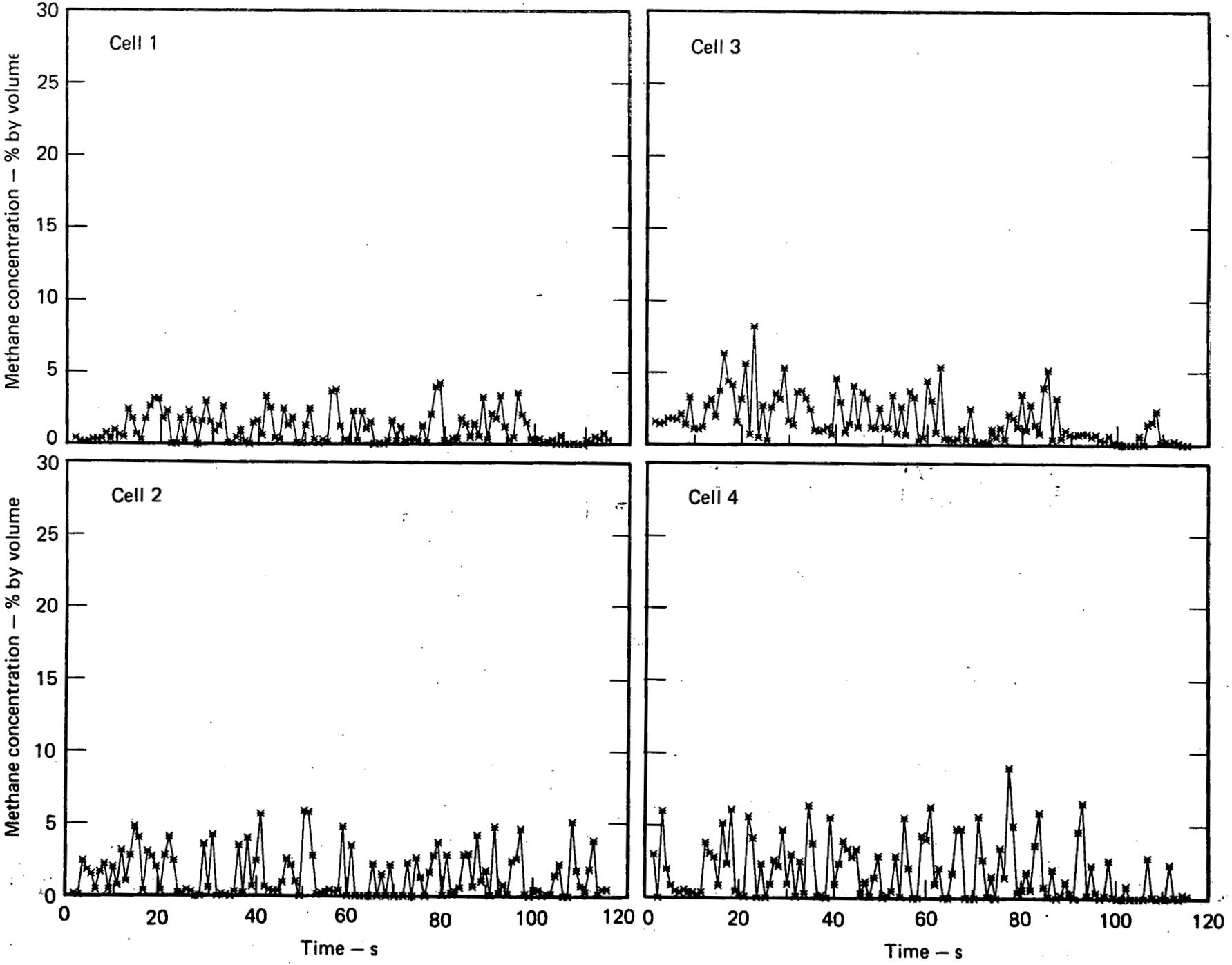

FIG. 17. Measured methane concentrations for range cells 1 to 4.

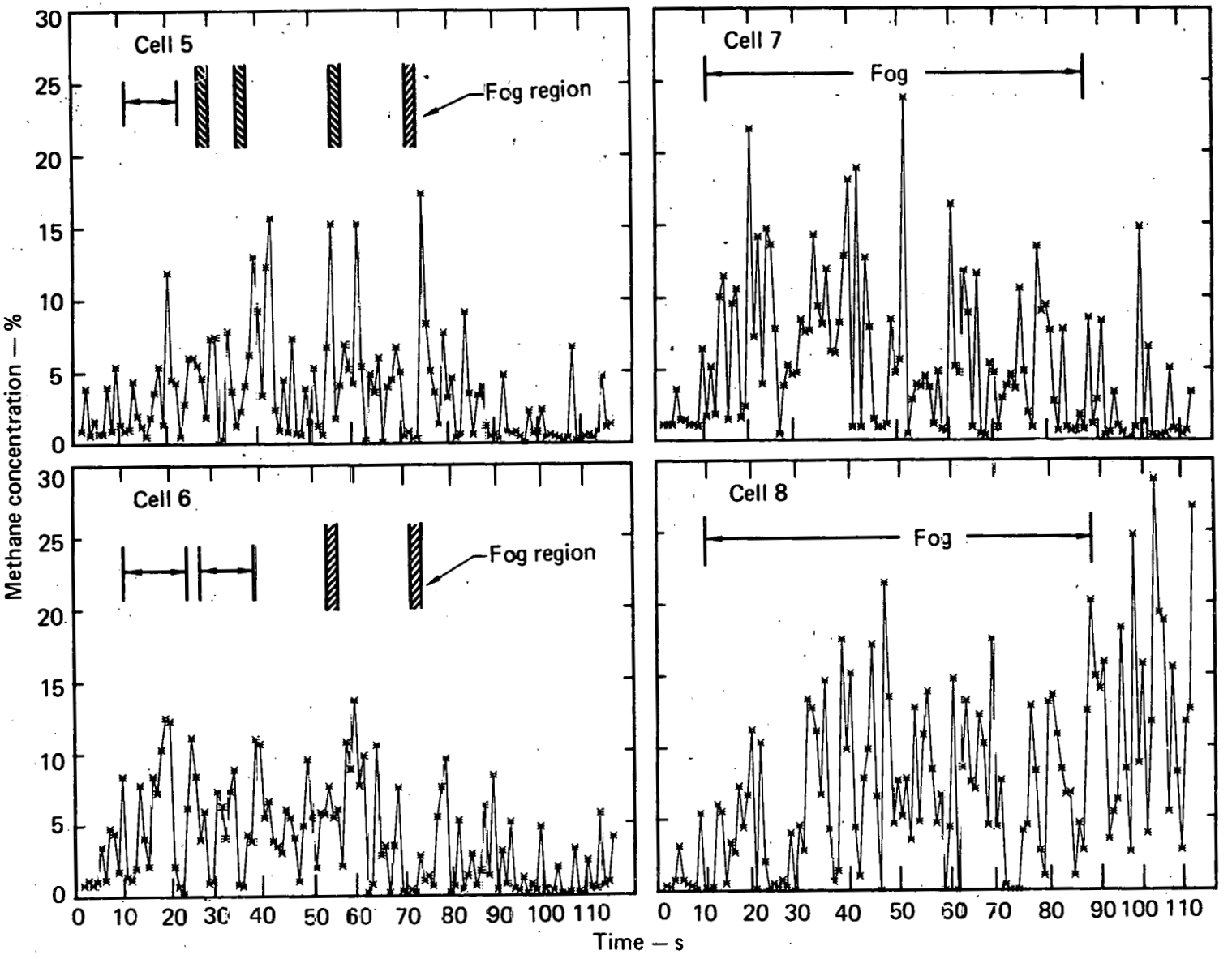

FIG. 18. Measured methane concentrations for range cells 5 to 8.

Due to limited magnetic tape storage capacity, data beyond 97 s were averaged over 18.4-s intervals. During that time, the cloud had drifted so that it was largely in or beyond range cell eight. As a result, only in region eight was there a significant hydrocarbon concentration. Figure 19 shows data from region eight averaged over 18.4-s intervals and extending to 207 s.

Examining range cells that are just ahead of the fog (see Fig. 20), we find that concentrations in clear air extend to as high as 14%. (Data for $t > 95$ s are not included, for reasons given below.) This exceeds the calculated 9% peak concentration for the temperature and humidity conditions at the time of the spill. This is encouraging, especially considering that spatial and temporal averaging undoubtedly lowered peak concentration levels.

The relationship of measured hydrocarbon concentrations to the presence of fog appears to change at late times. After 95 s, almost no fog appears, even though the apparent hydrocarbon concentration level increases to as high as 29% (see Fig. 20). A plausible explanation for this is that differential boiloff is causing heavy hydrocarbons to appear late in the spill. As indicated in the previous section, concentration levels producing fog are higher for the heavy hydrocarbons because their boiling points are considerably higher than that of methane. Under the weather conditions of the spill, calculated levels of the onset of fog condensation are 11% for ethane and 17% for propane (vs 9% for methane). It should be noted that the system was not calibrated for the heavier hydrocarbons, so the reported levels, which assume a methane gas, cannot be directly applied to other hydrocarbons, for which cross sections over the spectral width covered are higher by a factor of 2 to 5. Future measurements should incorporate separate calibrated ethane and propane channels.

It is interesting to find that flammable mixtures extend beyond one edge, and nearly to the other edge of the pond. Even at that, both LIDAR and *in situ* instruments missed much of the late time data due to the variability of the wind direction over even the 2- to 3-min duration of the spill. With a LIDAR system, the range of coverage is easily increased to allow for the variation observed.

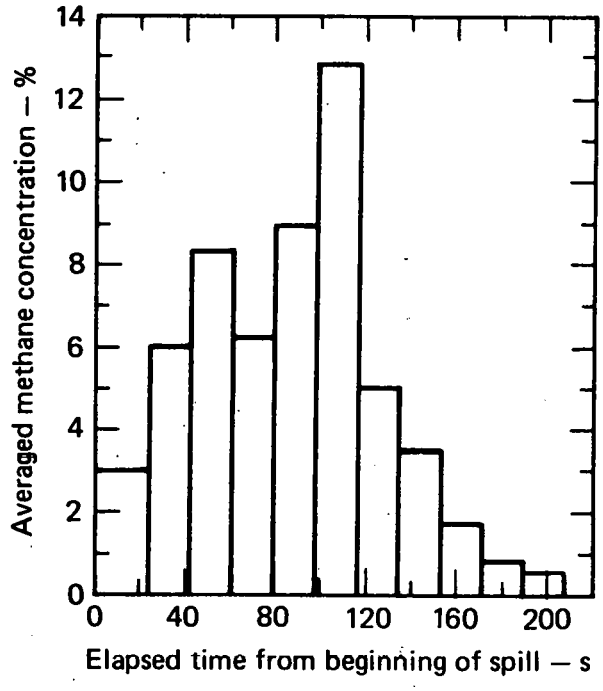

FIG. 19. Methane concentrations in range cell 8 with 19 s time windows.

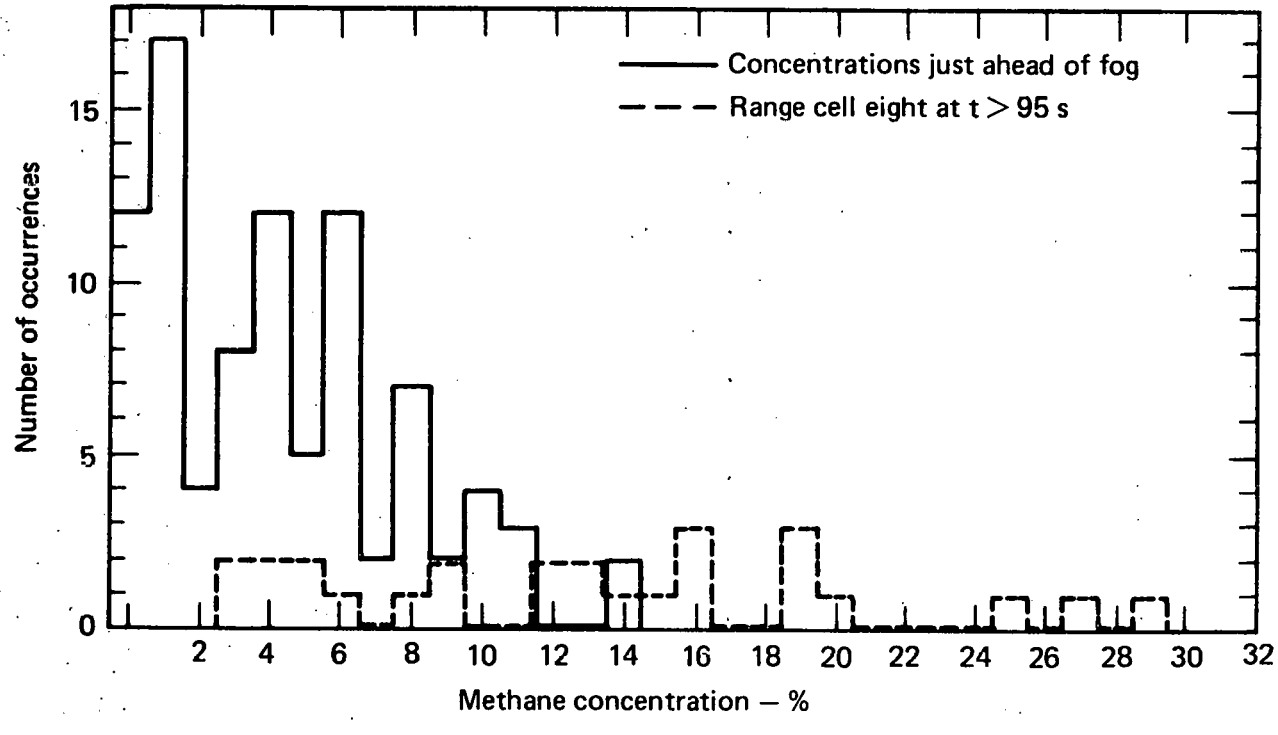

FIG. 20. Histogram of methane concentration levels measured in range gates just ahead of the fog, and of methane (or methane equivalent) levels at late times when a fog no longer appeared.

No detailed comparison of *in situ* and LIDAR data can be made due to the spatial averaging nature of the LIDAR, and to the 1.8-m depression of the pond, which prevented the laser beam from being located at the same height as the nearest *in situ* sensors. Average concentrations from the LIDAR are about one-third those of nearby, but lower *in situ* instruments (range gate 4 vs stations 1 and 3, and range gate 5 vs stations 2 an 4). This is consistent with the height distribution of the one relevant *in situ* station (No. 3, with sensors at 1.5 and 3.0 m above the pond level).

PROPOSED RAMAN LIDAR SYSTEM

The test of a Raman LIDAR system at China Lake demonstrated both its advantages and disadvantages. The principal advantage of LIDAR over *in situ* instruments is spatial coverage. The LIDAR system at China Lake provided adequate time resolution, and a spatial coverage comparable to that of the entire *in situ* array. This was true even though the LIDAR system was not designed expressly for this application, and therefore fell far short of the spatial coverage it was capable of providing with some relatively minor additions. During the 4-min dispersion period, the wind changed direction by at least 20°. The LIDAR system, properly designed, would follow the cloud without requiring a compromise in resolution. With *in situ* sensors spaced relatively far apart, as they will have to be in the future large-scale tests, significant concentration fluctuations may occur between sensors. A LIDAR system integrates scattered light from all of the gas within range cells. Taken together, the range cells give a 30-cm-diam tube of gas spanning the cloud that is completely sampled with a single laser pulse. With the addition of vertical scanning, horizontal tubes from discrete vertical positions can be measured. The tubes form a plane through which the gas flow is monitored. Knowing the flow characteristics of the dispersing gas cloud through the plane will be extremely important for comparison of model calculations with experiments.

The principal disadvantage of LIDAR is that it is unable to penetrate the dense fog associated with LNG spills. Due to the low boiling point of methane, LIDAR is limited to concentrations below the upper flammability limit

(UFL), and approaching the LFL for some winter days. For most other gases, including propane, LIDAR will not be seriously limited. And LIDAR would provide a compensating advantage in expanding the range of wind conditions under which spills could be conducted.

The spatial averaging nature of LIDAR has been cited as an advantage. This could also be a disadvantage in a region of large concentration fluctuations. *In situ* instruments could determine fluctuations with a volume resolution of about 10 cm^3. LIDAR is limited by a sample volume of about 1 m^3.

Is LIDAR worth building for the LEF program, and for the LNG diagnostics in particular? We feel the answer is yes, because LIDAR, in spite of limitations on the detectable concentration range, can cover most of the dispersing gas cloud. It presently appears that, for the most effective comparison of spill test results and model calculations, it will be necessary to follow the gas to concentrations levels substantially below the LFL. This greatly increases the volume to be covered, and the attractiveness of LIDAR. The strengths and weaknesses of the LIDAR seem to complement those of the *in situ* instruments. We believe that an ideal system for dispersion measurements of LEF spills would consist of *in situ* instruments relatively close to the spill point and a LIDAR for measurements near and below the LFL contour.

As presently planned the *in situ* array of instruments will cover the dispersion cloud in four "fences," one of which is shown in Fig. 21. A "fence" will consist of approximately 10 instrument towers to map concentration levels at some radial distance from the spill point. The cost of a fence will be about $400,000. We propose to replace one fence with a LIDAR system. Consider a fence located at a distance from the spill point corresponding to the maximum width of the LFL contour line, as shown in Fig. 21. This 40-m^3 spill has been modeled under conditions of a 4-m/s wind, and a 16-m^3/min spill rate.[11] The distance from the spill point and maximum width of the LFL are predicted to be about 400 and 128 m, respectively. Between contour lines, the maximum concentration given by the model is 7%. If the wind direction was stable and known in advance, the 10 towers would cover the cloud with a 13-m transverse resolution. However, experience to date at China Lake suggests that at least 30° be allowed for variations in wind direction. This adds

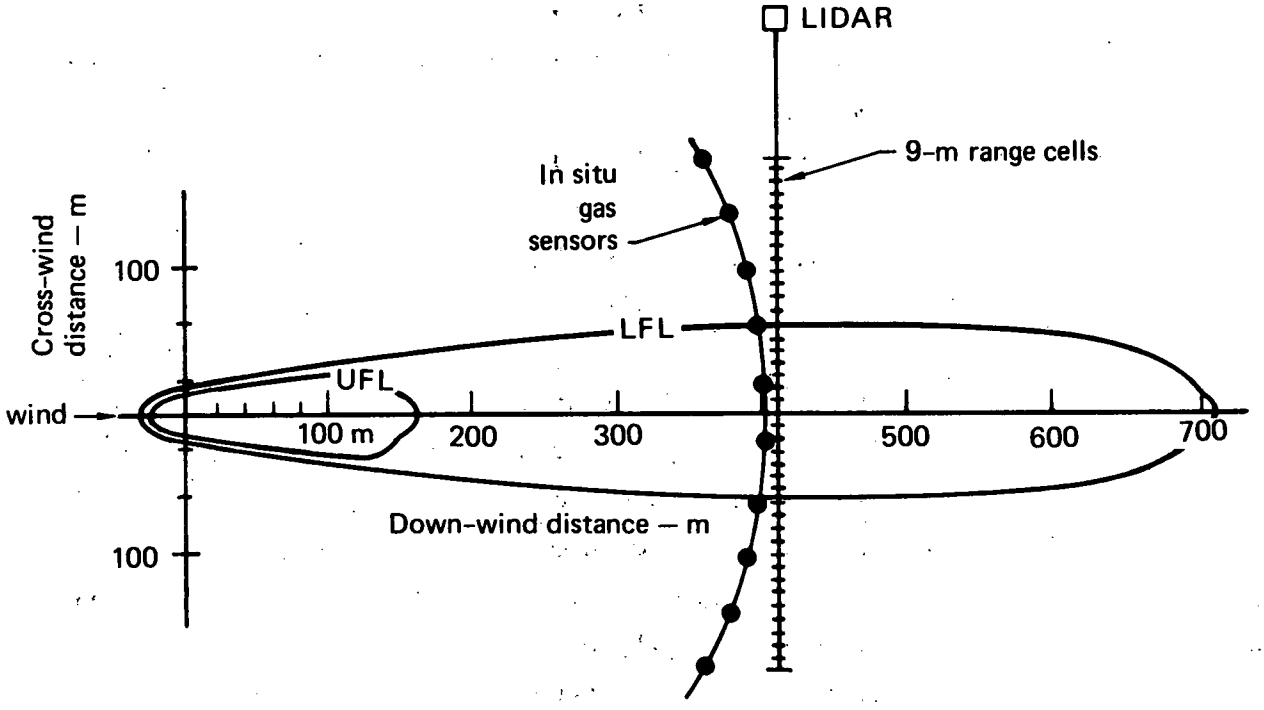

FIG. 21. LIDAR compared to *in situ* instrument "fence" with superimposed model calculation of a 40 m^3 LNG spill.

214 m to the transverse coverage, for a total fence width of 342 m. The resolution becomes 38 m, with normally only three to four stations appearing within the LFL contours.

A LIDAR system could be built for $400,000 that would cover the same region with 9-m range cells. For the same model as just mentioned, 14 cells would fall within the cloud, giving four times the coverage of the *in situ* array. The system would include vertical scanning, and channels for methane, ethane, and propane. If necessary to allow for wind variations, the range coverage could be increased over that assumed for the *in situ* array without loss of resolution. In addition to the improved coverage, the use of LIDAR of 40-m^3 spills would provide valuable experience for larger spills, where the cost savings of LIDAR will be of major importance.

The proposed LIDAR system consists of a laser and a receiver. For a Raman LIDAR the receiver includes a telescope, spectral analyzer, detectors, and electronics for control, data recording, analysis and display (see Fig. 22). Both the laser and receiver are concentrically aligned and aimed at the target through a common scan mirror. The entire system, except for the scan mirror, would be mounted in a mobile van. The scan mirror would be mounted separately for mechanical isolation.

Specifications for the Raman LIDAR system based on state of the art technology were given earlier and are summarized in Table 2. The major components will now be described.

LASER

The initial requirements for the laser are for 0.15 J/pulse at 300 to 400 nm. Additional requirements for range resolution limit the pulse length to 10 ns. A reasonable scanning speed requires at least a 10-Hz repetition rate for an average power of 1.5 W.

Of the various lasers commercially available, tripled YAG appears to come closest to the required performance. The best commercial, tripled YAG laser delivers aboaut 0.10 J/pulse and 10 pulses/s (1-W average) at 354 nm. Typical pulse lengths are 8 ns. It is possible that the output power could be increased to aboiut 0.20 J/pulse and the pulse rate increased to perhaps as high

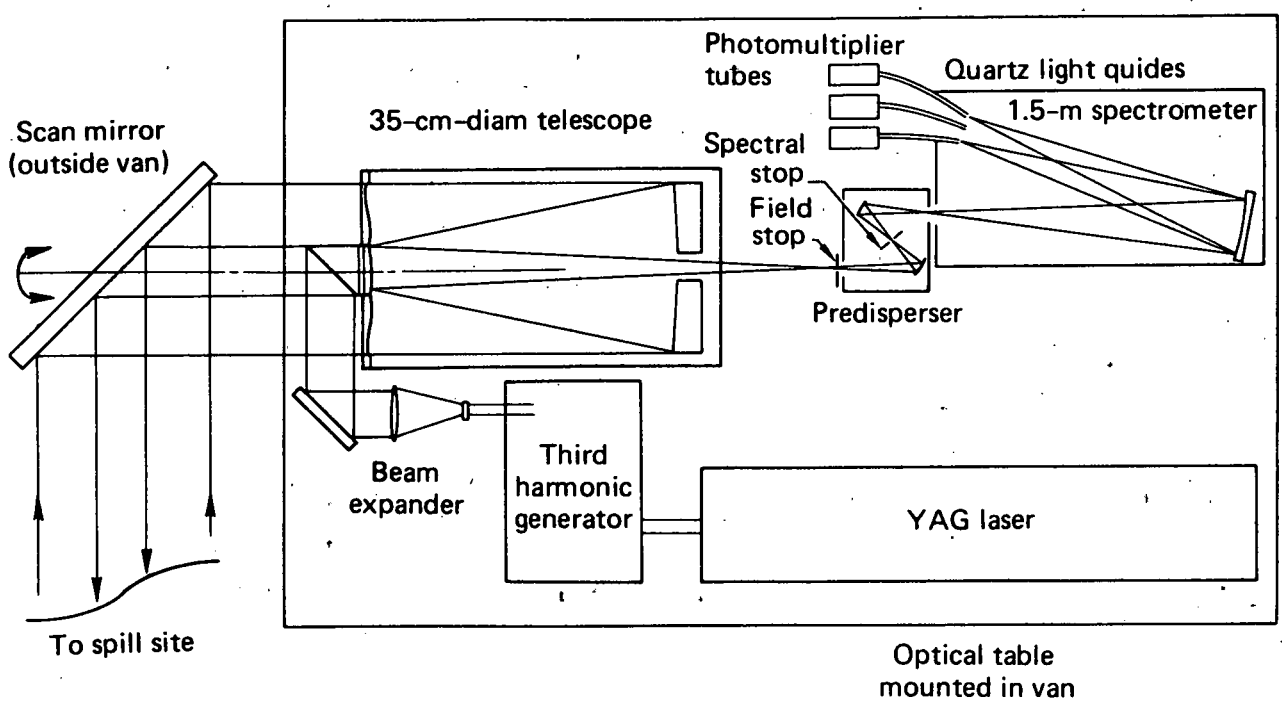

FIG. 22. Optical system layout for proposed Raman LIDAR.

as 20 or 30 Hz. A significant advantage of the tripled YAG is its high reliability and continuous operation capabilities. Ruggedized versions are available that would be ideal for field use.

Two other pulsed lasers that meet the wavelength requirements were also considered. The rare gas halide, or excimer lasers, can currently produce about 0.1 to 0.2 J/pulse at up to 20 Hz from xenon fluoride at 350 nm, or from xenon chloride or 308 nm. These lasers have just come onto the market, and currently have several major disadvantages. The pulse length is about 20 ns, thereby limiting range resolution. The beam quality is quite poor, thus limiting the amount of energy that can be propagated. They are TEA lasers containing very high voltage discharges, making them electrically noisy and subject to severe breakdown problems. The highly reactive gases involved cause some maintenance problems and, therefore, TEA lasers tend to be less reliable than the solid state lasers. However, a considerable amount of research is being done on excimer lasers, and the properties of commercially available units can be expected to improve.

The doubled ruby is capable of as much as 1 J/pulse outputs in the uv, and it has been used in LIDAR systems. However, its poor thermal characteristics limit its repetition rates to less than one pulse per minute, which is inadequate for this application.

RECEIVER

A modular approach is used for the receiver. Optically it consists of three units, the telescope, analyzer and detectors. Each unit is designed to take advantage of current technology and be adaptable to new technology as it becomes commercially available.

1. Telescope

The only experimental constraints on the telescope are the aperture and field of view. The amount of light collected is proportional to the square of the aperture diameter; 1/3 m is considered the minimum acceptable diameter. The largest telescopes available "off the shelf" have apertures of about 35 cm. Larger telescopes up to 1-m diam were considered, but the cost impact on the total LIDAR system is quite large.

The best commercially available telescope is a Schmidt-Cassegrain with an aperture of 35 cm and a focal length of 3.9 m. The corrector plate in the Schmidt telescope is a transmission element, that must be transmissive in the uv. Telescopes are available with the plate made of BK-7, for which the optical transmission is greater than 0.95 at 350 nm, and improves at longer wavelengths.

The field of view of the telescope must be kept as small as possible to minimize the background radiation from ambient light, yet it must be sufficiently large to encompass the entire laser beam. Atmospheric turbulence will cause the laser beam to expand at a divergence of about 25 μrad (i.e., a 10-cm-diam beam will double in size in 4 km). This number is from actual experience at NTS and is subject to considerable fluctuation depending on conditions.[12] A field of view of 100 μrad appears to provide a reasonable minimum diameter. This gives a 10-cm-diam circle at a range of 1 km.

The field of view is established by a field stop in the focal plane of the telescope. The image diameter of the field would be 0.39 mm. The resolution limit of the telescope is 5 μrad (0.02 mm in the image plane), a small fraction of the field of view.

Probably the most critical tolerance will be internal alignment of the telescope and coalignment with the laser. To maintain a 100 μrad field, the internal and external laser alignment should be maintained within 10 μrad. This tolerance suggests using a fixed telescope with a separate mechanically isolated scan mirror.

2. Analyzer

Three analyzer techniques have been considered: spectrometers, filters, and Fabrey-Perot etalons. Figure 7 shows a series of Raman shifts for the interesting constituents. The basic requirement is that every specie be resolved, if possible, using the C-H stretch lines.

The use of filters is the simplest analyzer technique, but both the resolution and throughput are limited. A series of filters could be used as dichroics to look at several lines (Fig. 23). The typical minimum bandwidth of filters in the 300-to-400-nm range is about 1.5-nm FWHM. Typical transmissions are 10%. With a great deal of effort the bandwidth can be reduced to 1.0 nm and the transmission increased to 20%.

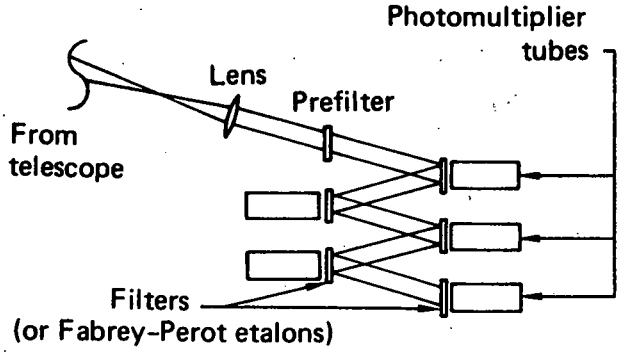

Filter analyzer

(Fabrey-Perot alternative)

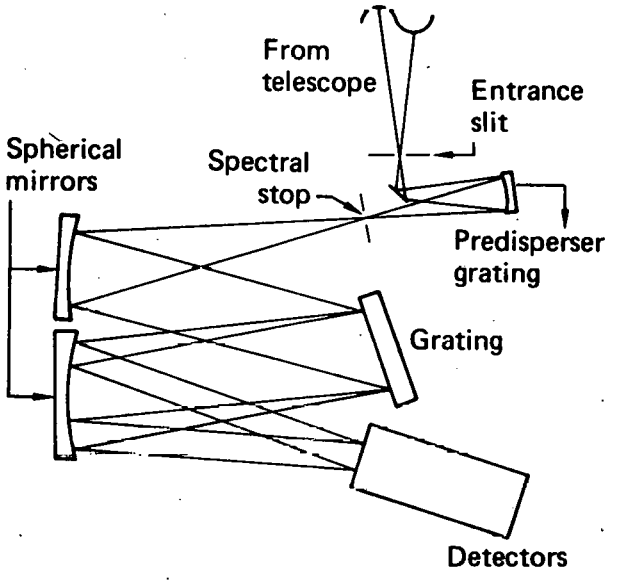

Double spectrometer

FIG. 23. Analyzer concepts.

A grating spectrometer is probably the most efficient analyzer. Holographic gratings are available with up to 3600 g/mm and efficiencies of 70 to 80%. For a given grating and spectrometer length, the resolution will be limited by the entrance slit of 0.39 mm, which gives the 100 μrad field of view. For example, a 1.5-m spectrometer using a 3600 g/mm grating would have a resolution of about 0.06 nm.

A single spectrometer should be adequate to discriminate between the Raman signals, and the more intense Rayleigh and Mie scattering. A good holographic grating has a stray light (ghost) level of about 10^{-5}. If required, this could be improved by a double spectrometer configuration (Fig. 23), which would reduce stray light to 10^{-9}.

Gratings are typically polarization-specific, so that a spectrometer also tends to be a polarizer. This effect can be used to advantage in that both the sky light and the Raman light are polarized. Sky light is typically polarized horizontally. The amount of polarization is dependent on the line-of-sight orientation with respect to the sun, being maximum at 90°. Multiple scattering, such as from a cloud, is generally not polarized. Raman radiation for a symmetric molecule will be completely polarized in the direction of the pump laser. A nonsymmetric molecule could give some depolarization depending on the orientation of the transition. By using a vertically polarized laser and a polarization specific receiver, the ratio between sky light and Raman signal can be substantially enhanced.

Another analyzer that deserves consideration would be configured like the filter scheme, but with the filters replaced by Fabrey-Perot etalons. This would improve the resolution and thereby make it possible to resolve the C-H stretch lines of different hydrocarbon species. To do this, a finesse of 20 would be required. (Finesse is the ratio between the resolution and free spectral range.) Although theoretically such etalons can have transmissions well above 50%, in practice this is difficult to achieve due to the extreme flatness requirements. The most limiting requirement will be stability and calibration. The extreme physical and thermal stability limitations ($< \lambda/200$) would require an active, closed-loop calibration system. Because of the limited free spectral range, a Fabrey-Perot etalon would have to be used with an auxiliary filter or spectrometer.

In conclusion, a spectrometer is the most versatile analyzer that has both high efficiency and the resolution needed to separate the hydrocarbon C-H lines. With filters, the C-C and C-H hydrocarbon lines could be separated, but the higher cross-section C-H lines could not be used to measure the heavy hydrocarbons. In addition, the low efficiencies of the filters would severely limit their usefulness. Fabrey-Perot etalons have extremely high resolution capabilities, but the difficulty of fabrication and operation would probably preclude their use for this application.

3. Detectors

The photomultiplier is clearly the most sensitive detector in the 350-to-400-nm region. Several types of photocathodes are available in the 20-to-30% quantum efficiency range. The gallium arsenide reflective photocathodes are the most efficient, being nominally about 30% (best performance 40%). These reflective photocathodes are generally deep inside the tube making coupling difficult. One vendor is now making a semitransparent GaAs photocathode that is only slightly less efficient. The bialkali and multialkali cathodes are about 20 to 25% efficient. These are semitransparent, coated directly on the inside of the tube face making coupling substantially easier.

When used with the filter analyzers, the semitransparent photocathode tubes would be placed behind the appropriate filters. For the reflective cathodes, auxiliary focusing lenses would have to be used between each filter and tube. For the spectrometer, a mask would be placed in the image plane with a series of mirrors or quartz light conduits directing various band-pass segments to each tube. Again, auxiliary lenses would be necessary for the reflective photocathodes.

An alternate detector concept usable only with the spectrometer would be to couple the image plane to a streak tube that is mated to a vidicon camera. This would eliminate the need for active electronic range gating of a group of PMT's by providing a complete spectrum-versus-time matrix. This approach would probably not provide the sensitivity of photomultiplier tubes, because only the semitransparent photocathodes could be used. However it would allow the integration of several laser pulses to be done directly by the superposition of light on the vidicon.

4. System Transmission

Transmission estimates for each subsystem are given in Table 4. These estimates are based on using dielectric reflector coatings with a reflectivity of 0.99. (Some coatings are available with reflectivities as high as 0.998.) Antireflection coatings on transmission elements give transmission efficiencies of 0.995 per surface. Gratings are based on a 0.80 ruling efficiency and a 0.90 reflective coating.

TABLE 4. Optical transmission of LIDAR components.

Subsystem		Transmission	
Transmitter			
• Collimator		0.98	
• Mirrors (turning and scan)		0.98	
			0.96
Receiver			
• Telescope (and scanner)			
--Obscuration		0.96	
--Mirrors (4)		0.96	
			0.92
Analyzer			
• Single grating (double)		0.72 (0.52)	
• Mirrors (4)		0.96	
• Auxiliary lens		0.99	
			0.68 (0.49)
Total receiver transmission	Single spectrometer		0.63
	Double spectrometer		0.45

5. Data Storage, Analysis, and Display

There are two approaches to digitization of data. One uses a high-frequency fast-sampling ADC with an integrating front end. The second approach would use simple low-frequency ADC's for each range gate, as employed in the CGC system shown schematically in Fig. 13. Either approach would allow, with commercially available equipment, range resolution even higher than proposed in this report. The choice between the two approaches would depend on the number of range cells to be analyzed.

Data analysis and display is a straightforward application of commercially available or LLL-designed equipment. In particular, equipment designed for data gathering in nuclear weapons testing, utilizing LSI-11 microprocessors with large core memories and image display routines, could be adapted for this application.

SYSTEM COSTS

A $400,000 estimate for the total cost of the LIDAR system was given earlier. The estimate was derived from a detailed analysis of component costs, as shown in Table 5. Both performance and cost estimates are based on commercially available components and subsystems that can be integrated with little engineering design effort. Proven state-of-the-art technology is used, and no development items are considered.

For a comparison with the *in situ* sensors, this estimate assumes four data channels measuring methane, ethane, propane, and nitrogen. Additional data channels could be added as required to monitor the fog boundary, combustion products, etc. The cost of additional channels is relatively small, resulting primarily from the increased data handling equipment required.

Hardware costs are all taken either from catalog listings, manufacturers quotes or recent procurement experience. Manpower estimates are based on an average burdened cost of $70,000 per FTE year.

TABLE 5. LIDAR system costs.

Equipment	Source of estimate	Cost, thousand of dollars
Laser		
YAG	Molectron quote	45
Optics		
35-cm telescope	Celestron quote	6
Special coatings	Recent experience	3.5
Scan mirror	Recent experience	5
Miscellaneous optics, mounts		10
Spectrometer		
Predisperser	Quotes	3.5
Grating	Catalogue	10-20
Rotary table with accessories	Catalogue	3.5
Detectors		
PM tubes	Catalogue	10
Tube bases	Catalogue	2
Power supplies	Catalogue	5
Hardware		
Scan mirror mount	Carson Instr. quote	10
Bench	NRC catalogue	5
Van with ac and power		15
Electronics (4-channel system)		
Biomation 8100	Catalogue	46
Tape units	Quotes	12
Interface	Recent purchase	8
LSI II computer	Recent purchase	3
Floppy disk	Recent purchase	1
LSI II scanning interface	Recent purchase	5
TEK 4012	Catalogue	5-6
TEK hard copy	Catalogue	4-6
Versatek printer	Catalogue	2
Miscellaneous		13
Total equipment		240

TABLE 5. (Continued.)

Manpower	FTE FY80	Cost (at 70/FTE) in thousands of dollars
Systems engineer/physics	0.5	
Systems technician	0.5	
Mechanical design/drafting	0.2	
Mechanical shop/optics shop	0.3	
Electronics engineer	0.2	
Electronics technician	0.2	
Programmer	0.3	
Total manpower	2.2	154
Total cost		394

LIDAR FOR LARGER SPILLS

For 40 m^3 spills, LIDAR is cost competitive with the *in situ* instruments it replaces. For larger spills there is a significant cost advantage in using LIDAR. If the spill size were increased to 1000 m^3, the fences of *in situ* sensors would be increased in both length and numbers. The proposed LIDAR system would accommodate the increased fence length with additional range cells. This requires only the detection of scattered light over a longer time interval, with at most, a minor addition to data-handling equipment.

Additional downwind coverage (multiple fences) could be added either by using multiple LIDAR systems or by adding a horizontal scanning capability to the proposed system.

Additional LIDARs similar to the one proposed could be added at approximately $400,000 per unit. A LIDAR with a horizontal scan capability would be more difficult to build, and would cost between $1 and $1.5 million. In the

long run, however, a two-axis scanning LIDAR may be the most cost-effective system as it would provide a three-dimensional map of a majority of the cloud volume. Scanning additional volume without sacrificing data at any sampled point would require a significant increase in the data collection rate. Since the system proposed here is photon-limited, the increase can be accomplished only by an increase in laser power and/or telescope and scan mirror size. Neither a larger laser nor a telescope is available "off the shelf." However, both are within the current state-of-the-art.

The telescope and scan mirror could be increased to provide a 1-m aperture with technology available to several vendors. The increased size and speed of a scan mirror mount would require substantial engineering effort, but is within the capability of commercial suppliers.

Laser power could be increased to about 1 J/pulse using either of two approaches. The first is based on an established technique of multiplexing parallel solid-state amplifiers from a common oscillator. This would incorporate the laser proposed for the smaller system.

The alternative is use of a single large rare-gas halide laser system. This alternative is less certain because it depends on advances in the technology of rare gas halide lasers. However, much research is currently being done in this area.

A larger system would require changes in the spectrometer, and in the control and data-recording electronics. The increased size and complexity would also increase the effort involved in integrating the components into a workable system. This would result in increased LLL manpower effort, and increased lead time for development.

ACKNOWLEDGMENTS

Several people gave helpful input to the LIDAR analysis. We especially wish to thank D. Redhead, H. Koehler and W. Wakeman of LLL, S. Klainer of the Lawrence Berkeley Laboratory, L. Jelsma of Arizona State University, R. Byer of Stanford University, and D. Murcray of the University of Denver.

REFERENCES

1. For a general description, see E. D. Hinkley: *Laser Monitoring of the Atmosphere* (Springer-Verlag, Berlin, 1976).
2. N. B. Colthup, L. H. Daly and S. E. Wiberley; *Introduction to Infrared and Raman Spectroscopy* (Academic Press, New York, 1975).
3. Raman/IR Atlas of Organic Compounds, B. Schrader and W. Meier, Eds. (Verlag Chemie, Weinheim, 1974), vol. 1.
4. E. R. Murray, J. E. van der Laan and J. G. Hawley, Applied Optics 15, No. 12 (1976).
5. T. Hirschfeld, private communication (February 1979).
6. S. Klainer, Lawrence Berkeley Laboratory, private communication (November 1978).
7. E. J. McCartney, *Optics of the Atmosphere* (Wiley, New York, 1976).
8. H. Blumer, Z. f. Phys. 38, 119 (1926).
9. H. Blumer, Z. f. Phys. 38, 304 (1926).
10. D. A. Leonard and B. Caputo, Remote Sensing of LNG Spill Vapor Dispersion Using Raman LIDAR, Computer Genetics Corporation, 18 Lakeside Office Park, Wakefield, Mass. 01880, for Lawrence Livermore Laboratory, Livermore, Calif., Rept. UCRL-13984 (1979).
11. L. Hazelman, private communication (March 1979).
12. J. Coutts, private communication (February 1979).

REPORT O

The LLL Data Acquisition System for Liquefied Gaseous Fuels Program

J. Baker

Prepared for the
Environmental and Safety Engineering
Division
U.S. Department of Energy
under Contract W-7405-ENG-48

Lawrence Livermore Laboratory
Livermore, California 94550

THIS PAGE

WAS INTENTIONALLY

LEFT BLANK

REPORT O

TABLE OF CONTENTS

FIGURES

TABLES

THE LLL DATA ACQUISITION SYSTEM FOR LIQUEFIED GASEOUS FUELS PROGRAM

SUMMARY

A data acquisition system is being developed by EG&G, Inc., and the Electronics Engineering Department of LLL for use during upcoming liquefied natural gas (LNG) dispersion tests. The system will employ 51 battery-powered complementary metal-oxide semiconductor (CMOS) data acquisition units to measure gas concentration, wind direction and speed, temperature, humidity, and heat flux.

Data acquired by the CMOS data acquisition units will be telemetered via UHF radio links to a trailer-based microcomputer command, control, and data recording system (CCDRS). In the CCDRS, wind data will be displayed graphically. All data will be recorded on disk units for subsequent analysis at the Livermore time-sharing system computer facility.

INTRODUCTION

The Liquefied Gaseous Fuels (LGF) Program is scheduled to begin dispersion tests in May 1980 at the Naval Weapons Center, China Lake, California. These tests will involve spills of liquefied natural gas in quantities up to 40 m^3. Up to 51 stations will be measuring the wind direction and speed, gas concentration, temperature, heat flux, and humidity to provide data for verification of computer models of the dispersion of the gases. The stations will be located in an area approximately 500 m wide by 2000 m long. They must be portable and consume little power. Approximately 700 channels of analog or digital signals must be recorded for periods of 1/2 hour or more for each test. Safety requires that the wind direction and velocity be displayed graphically before and during the tests. A commercial data acquisition system is not available which will meet the needs of the LGF

Program; therefore the Field Test Systems Division (FTSD) of the LLL Electronics Engineering Department was asked to undertake the development of the necessary system. FTSD personnel determined the system requirements and then undertook the design of the system.

The overall system design is now complete. Most of the detailed designs are complete, and much of the necessary electrical and electronic components have been ordered.

REQUIREMENTS

The following are the basic requirements of the data acquisition system:

1. To graphically display wind data from the weather stations before and during the spill tests so that the test director can be sure that the gas will drift over the data acquisition units.
2. To record wind data from twenty weather stations and six turbulence stations from 15 min before the spill test until 15 min after the spill test.
3. To receive a signal (contact closure) indicating the start of the spill test for timing of the gas sensor data acquisition system.
4. To record data from twenty-five gas sensor stations during the spill tests in addition to the weather and turbulence data.

The sensor array for the 40-m^3 experiments at China Lake is shown in Fig. 1. Calculated gas concentration contours from the COM3 code are also shown in Fig. 1. Figures 2 through 4 show schematic diagrams of a gas sensor station, a weather station, and a turbulence station.

The signal sources at the weather stations are the two-axis anemometers. They will measure wind direction and speed at twenty locations on the site. All of these measurement locations are shown in Fig. 1 except the two furthest upwind anemometers. Wind vectors will be averaged over a 10-s period, then transmitted to the trailer-based data recording system and displayed on a cathode ray tube (CRT) display unit.

Gas concentration and temperature will be measured at three different heights at each of the gas sensor stations. Some stations will also have

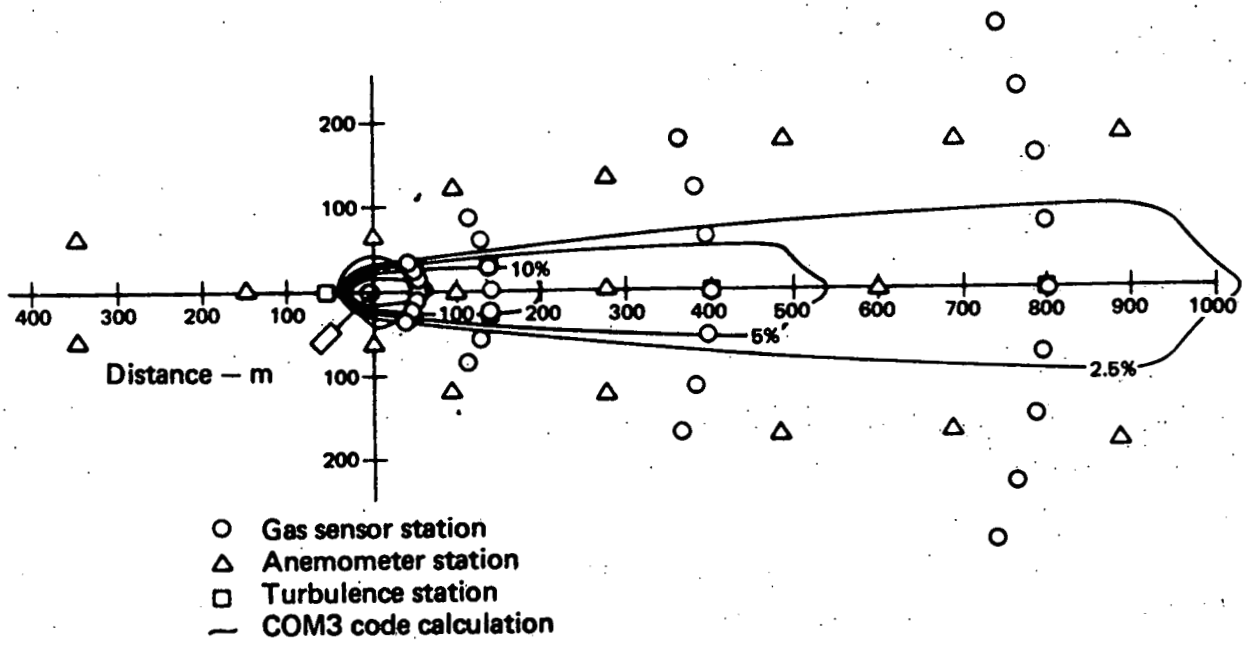

FIG. 1. Sensor array for 40-m^3 tests at Naval Weapons Center, China Lake.

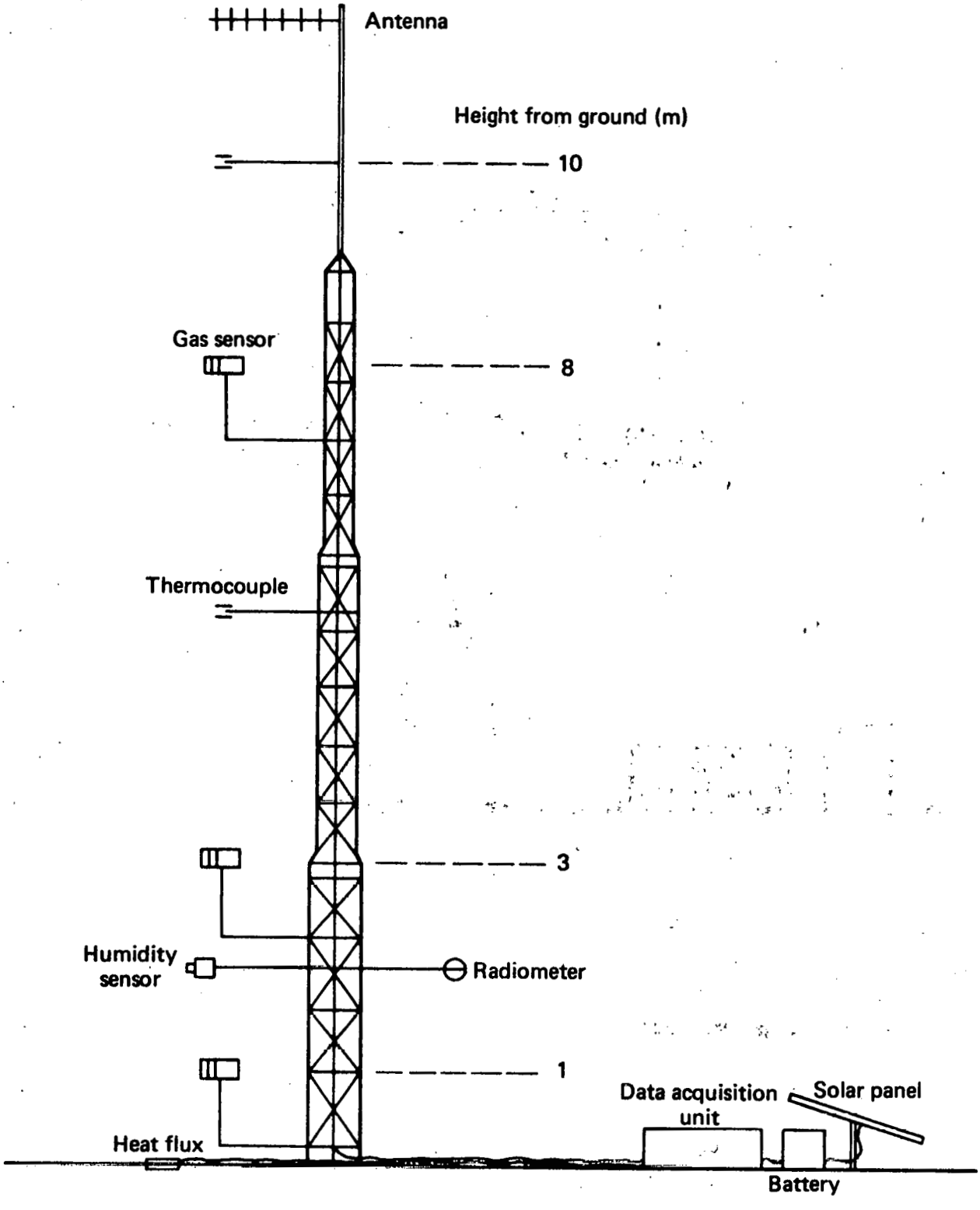

FIG. 2. Gas sensor station.

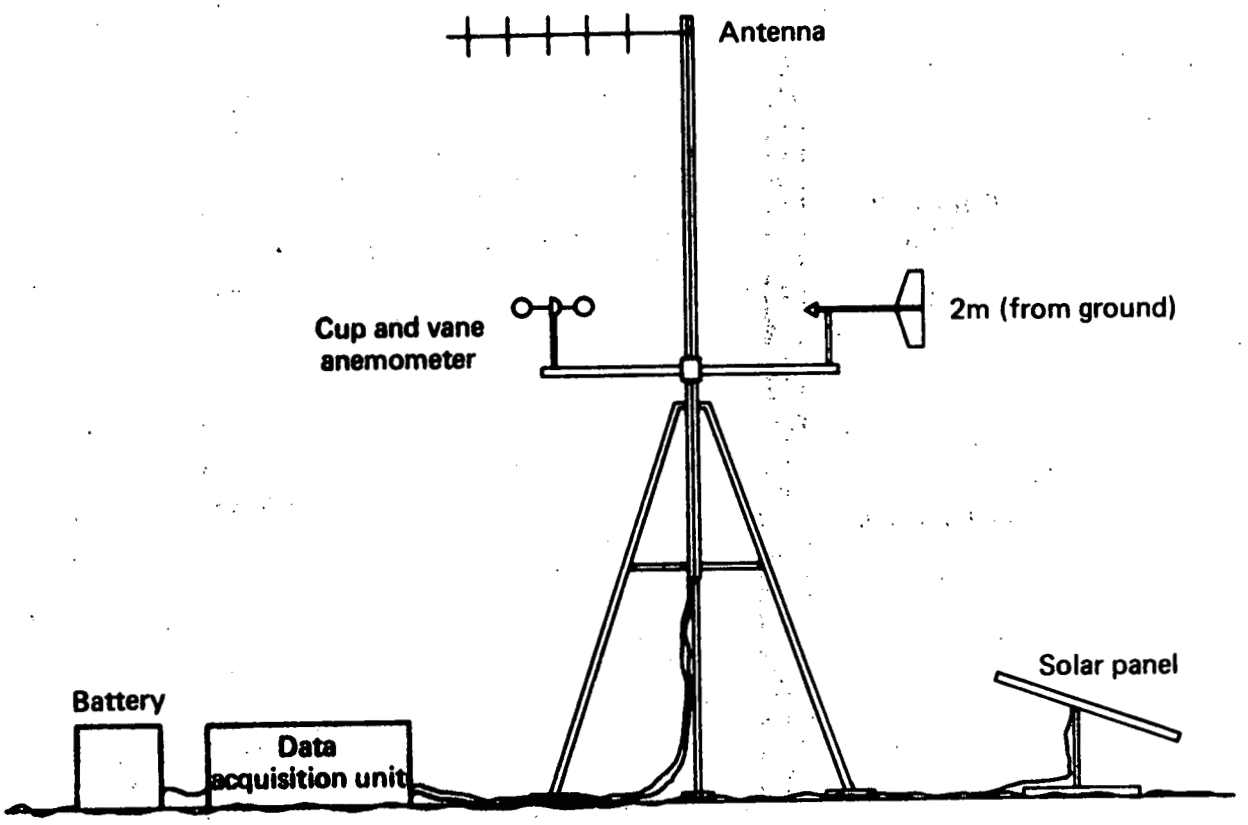

FIG. 3. Weather station.

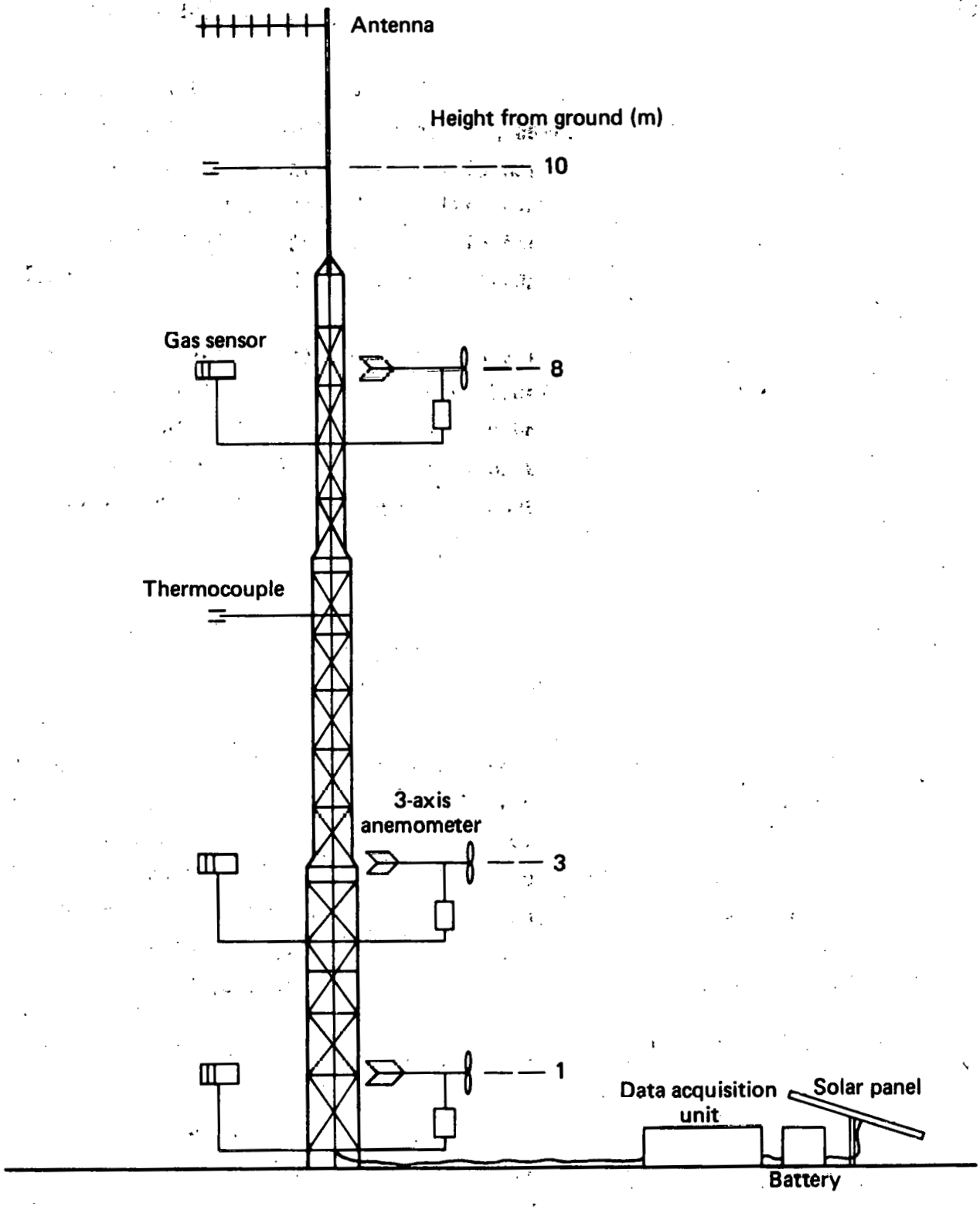

FIG. 4. Turbulence station.

humidity sensors, heat flux sensors, and radiometers. Measurements will be made once per second and the data recorded in the trailer for subsequent analysis.

Wind velocity, gas concentration, and temperature data will be acquired at three different heights, five times per second at five of the turbulence stations. The sixth turbulence station will acquire wind velocity and temperature only. This unaveraged data will also be recorded.

Altogether, approximately 700 channels of data must be recorded for periods of one-half hour or more. Tables 1 through 3 show the overall signal requirements.

Other requirements are portability and low power consumption. Previous dispersion tests indicated that portability was a necessary requirement because of the variability of the wind direction. Low-power-consuming components are necessary for the data acquisition units because they are battery-powered. The large area covered by the array precludes the use of power cables and commercial power.

MICROCOMPUTERS TO CONTROL SYSTEM

Commercially available microcomputers will be used in the data acquisition, data recording, and display. They will be programmed to perform system self-test and calibration, to initiate the data acquisition, to acquire and to transmit the data to the recording system, to receive and to record the data, and to display the wind direction and velocity. Communications between the microcomputers will be carried out by means of a UHF command and data telemetry system. Because of the large and variable distance between data acquisition units, each will have its own command receiver and data transmitter. Figure 5 shows a block diagram of the overall system.

DATA ACQUISITION STATIONS

The data acquisition units will be of three types: weather stations (20), gas sensor stations (25), and turbulence stations (6). All of the stations will employ the Intersil IM6100 low-power CMOS microprocessor. The IM6100 microprocessors will be supplied to LLL by Pacific Cyber/Metrix as the

TABLE 1. Data from gas sensor stations.
(25 Stations: 1 sample/s; data not needed in trailer during test.)

Signal source	Range	Accuracy	Signal type	No. of channels
Six thermocouples, Type K	-150 to +70°C	0.1°C	Analog 12 bits	6
IST gas sensor	0 to 25%	10% of reading	Analog 8 bits	1
LLL gas sensor (methane, ethane, fog, reference)	0 to 100%	1%	Digital 12 bits	4
Humidity	0 to 100%	± 3%	Analog 8 bits	1
JPL gas sensor (methane, ethane, propane, reference)	0 to 50%	1%	Digital 12 bits	4
Time (2 words)	0 to 14,400 s (4 hrs)	1 s	Digital 12 bits	2

TABLE 2. Data from weather stations.
(20 stations: 5 stations upwind, 15 stations downwind, 1 sample/s; data averaged over 10; data must be transmitted to command trailer from at least 10 stations during test within 10 s of real time.)

Signal source	Range	Accuracy	Signal type	No. of Bytes/s
Anemometer (two-axis)	0 to 359° 0 to 50 m/s	0.7° 0.05 m/s	Analog 12 bits	2/s
Time (2 words)	0 to 14,400 s	1 s	Digital 12 bits	2/s
				4 bytes/s

TABLE 3. Data from turbulence stations (6 stations: 5 with gas sensors, 5 samples/s, begin acquiring data 15 minutes before spill.)

Signal source	Range	Accuracy	Signal type	No. of channels
Three thermocouples, Type K	-150 to +70°C	0.1°C	Analog 12 bits	22.5/s
Three LLL gas sensors (methane, ethane, and fog)	0 to 100%	1%	Digital 12 bits	22.5/s
Three JPL gas sensors	0 to 50%	1%	Digital 12 bits	30/s
Three anemometers (3-axis)	-45 to +45°	0.04°	Analog 12 bits	22.5/s
	-50 to +50°	0.05°	Analog 12 bits	
	0 to 13 m/s	0.006 m/s	Analog 12 bits	
Time (2 words)	0 to 14,400 s	0.1 s	Digital 12 bits	
				98 bytes/s

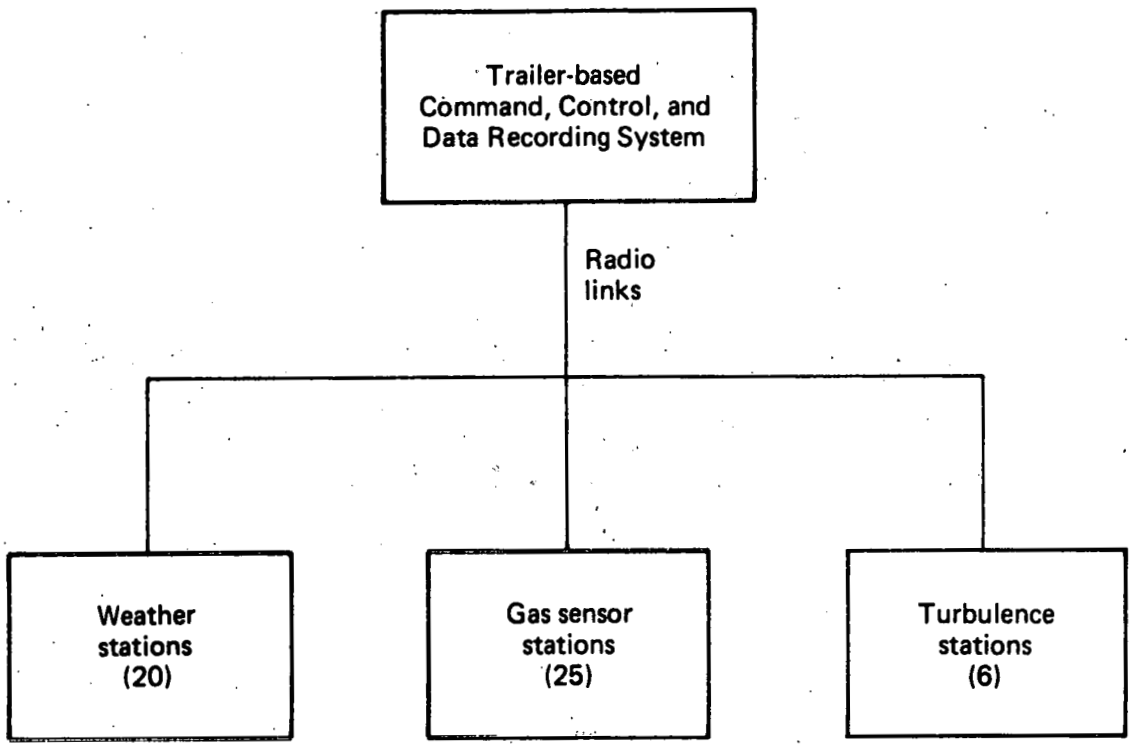

FIG. 5. Block diagram of overall LEF data acquisition system.

result of a competitive bid on an LLL specification. Pacific Cyber/Metrix will provide the microprocessor systems with up to 8,500 twelve-bit words of read/write memory, 3000 words of read-only-memory, three parallel input channels, two parallel output channels, five serial input/output (I/O) channels, and a 16-channel multiplexed analog-to-digital converter (ADC).

We will install these microprocessors in a military-type enclosure along with instrumentation amplifiers, power supplies, radio transmitter/receivers, and other components. Each of the stations will include a low-power UHF command receiver and data transmitter. Analog signals, such as the thermocouples, three-axis anemometers, humidity sensors, etc., will be digitized by the 16-channel multiplexed analog-to-digital converter. Power will be provided by gelled-electrolyte 12-V storage batteries with solar cell rechargers. The dc converters will generate the 5-Volts, $\pm$ 15 Volts, and other dc voltages required by the microprocessors. Figure 6 is a block diagram of the turbulence data acquisition unit.

The UHF command and data telemetry system will operate in the 406 to 420 MHz band. Commercial (Monitron Corporation) wide-band (50-kHz) transmitters and receivers will handle the data channels which will send data asynchronously up to 19.6 kbaud. The asynchronous mode permits the use of standard universal asynchronous receiver/transmitter (UART) integrated circuits at both ends of the communication channels. Narrow-band (3-kHz) transmitters and receivers will be used for the command links and the lower baud-rate weather systems data channels. A three-level binary (pseudo-ternary) interface was designed at LLL to connect the microprocessors to the radio units. This interface permits ac-coupled transmitters to send the pulse-coded modulated (PCM) data by eliminating dc components.

The CMOS microprocessors will be commanded to begin acquiring data by a trailer-based command, control and data recording system (CCDRS). The weather stations will acquire ten 1-s samples of the wind direction and speed, they will convert these to north and east vectors, and they will average them. Upon command from the CCDRS, each of the twenty weather station microprocessors will transmit its data to be recorded and displayed and will begin acquiring new wind direction and speed data.

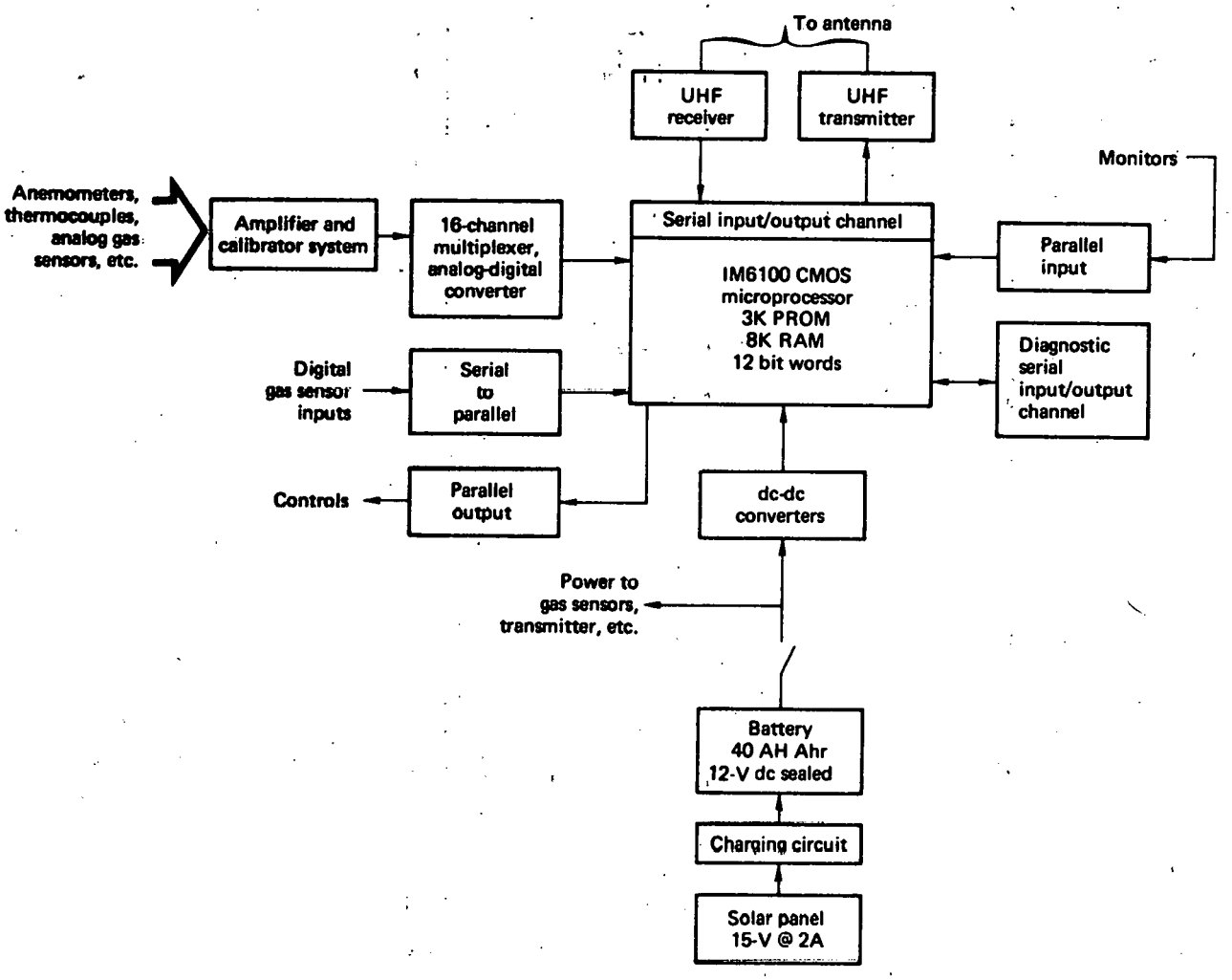

FIG. 6. Block diagram of turbulence data acquisition unit.

The gas sensor stations will be commanded by the CCDRS to acquire data at five samples per second from gas sensors, thermocouples, etc., to average that data, and to transmit the 1-s averages to the CCDRS, upon command, approximately every 60 s. The data will be recorded only and not displayed.

The turbulence stations will acquire data from gas sensors, three-axis anemometers, and thermocouples five times per second and will transmit the data to the CCDRS approximately every 10 s upon command. The data will be recorded in the CCDRS trailer only.

The microprocessors will be programmed in a "high-level" assembly language using LLL-developed "structured macros," such as "IF-THEN-ELSE" and "LOOP-UNTIL" constructs similar to those used in ALGOL and other modern languages.

COMMAND, CONTROL, AND DATA RECORDING SYSTEM

The overall system will be controlled by the microcomputer-based CCDRS. Digital Equipment Corporation LSI-11 microcomputers located in the CCDRS trailer will be programmed by EG&G, Inc., personnel to command the portable data acquisition units to acquire, to average, and to transmit the gas sensor and other data back to the CCDRS system where it will be recorded for future analysis on the Livermore time-sharing system (LTSS). Figure 7 is a block diagram of the CCDRS. All timing and sequencing will be controlled through the CCDRS microcomputers. Each major subsystem (the weather stations, the gas sensor stations, and the turbulence stations) will communicate its data to its respective LSI-11 front end processor (FEP). The data will be stored on the 10-M byte disk memory unit attached to the FEP. The weather station FEP will also communicate wind vectors to the attached Tektronix 4025 graphics terminal. Following each test, the data will be retrieved from the disks and re-recorded on magnetic tape to be read on the LLL LTSS for data processing. The graphics terminal will also permit "quick looks" at the recorded data following each test.

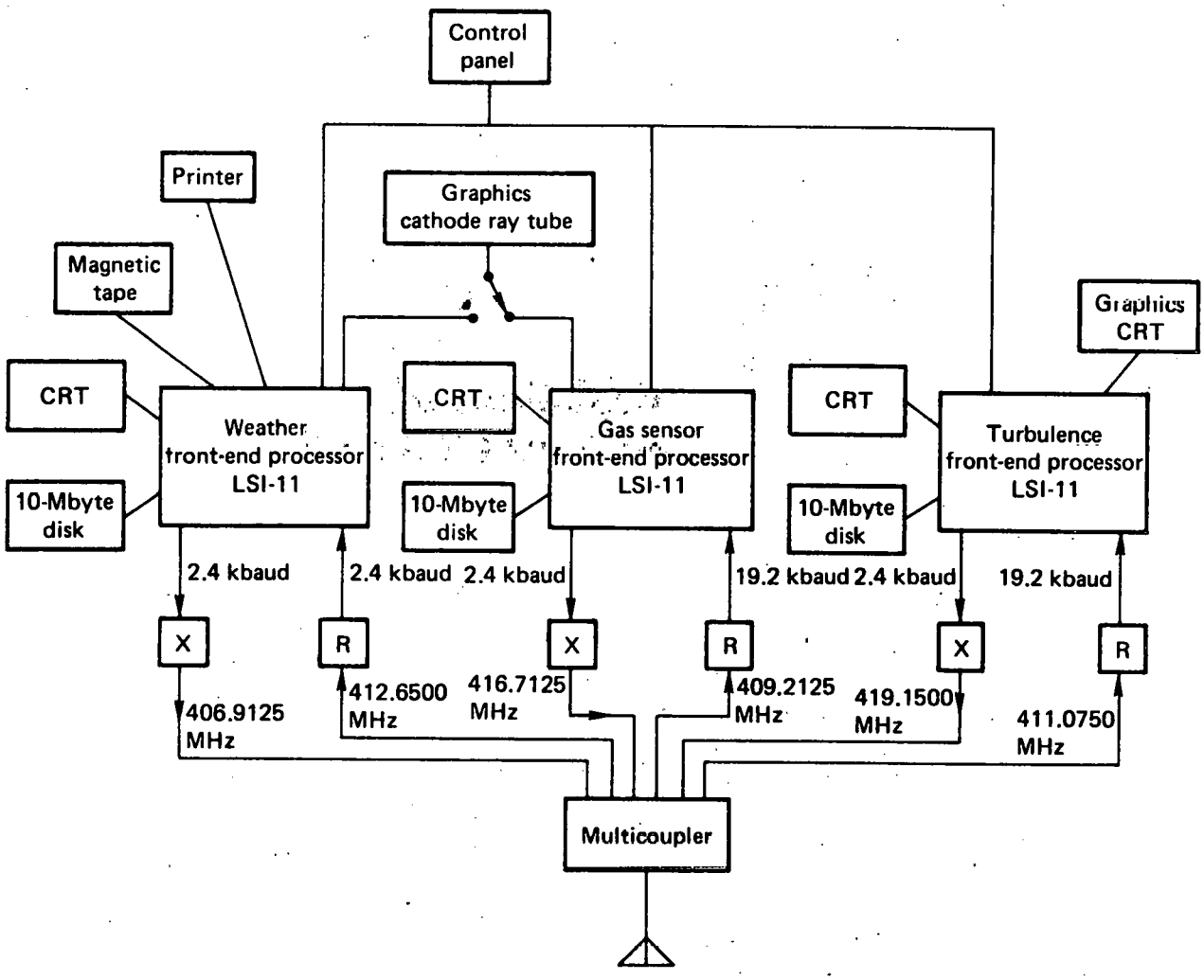

FIG. 7. Block diagram of command, control, and data recording system (CCDRS).

REPORT P

Data and Calculations of Dispersion on 5-m^3 LNG Spill Tests

R. P. Koopman
B. R. Bowman
D. L. Ermak

Prepared for the
Environmental and Safety Engineering Division
U.S. Department of Energy
under Contract W-7405-ENG-48

Lawrence Livermore Laboratory
Livermore, California 94550

THIS PAGE

WAS INTENTIONALLY

LEFT BLANK

REPORT P

TABLE OF CONTENTS

FIGURES

TABLES

Data and calculations of dispersion on 5 m^3 LNG spill tests

SUMMARY

A series of liquefied natural gas (LNG) spill and dispersion experiments was carried out at the Naval Weapons Center at China Lake. These spills were nominally 5 m^3 of liquid spilled on a water pond under various wind conditions (3 to 10 m/s). The objective of the experiments was to evaluate sensors for field use in the detection of downwind hydrocarbon concentrations. The concentration data are shown as a function of time at various stations downwind from the spill point. These data are compared with calculations made by ATMAS, a computer model that uses wind field measurements as input then solves the advection diffusion equation for the downwind concentration as a function of time. The comparisons of data with ATMAS are quite good. It is concluded that ATMAS is a useful model; however, a more detailed description of the wind field (more measurements), a better model of the source (liquid pool spread and boil off of vapor), and the inclusion of variable density and temperature effects are required for better comparison with the data. The objective of the experiments, to evaluate sensors, was accomplished and has led to a selection of instruments to be placed in the field for larger (40 m^3 and more) spill and dispersion experiments to be conducted in the future.

INTRODUCTION

During a 3-month period in the early fall of 1978, an experimental team from the Lawrence Livermore Laboratory (LLL) participated in a series of four liquefied natural gas (LNG) spill experiments at the Naval Weapons Center (NWC) at China Lake, California. These experiments were conducted at the request of the Division of Environmental Control Technology of the Department of Energy as part of their Liquefied Gaseous Fuels Safety and Environmental Control Assessment Program. The main reason for our participation was to evaluate instruments—primarily gas concentration measuring devices—which might be used on future larger scale spill experiments. A report discussing this instrument evaluation was recently published as a part of the DOE report[1] on the status of liquefied gaseous fuels (LGF) safety research. The intent of this report is to present the dispersion data taken during the experiments and to compare the data with computer model calculations.

Each of the four experiments (referred to as Avocet 1 through Avocet 4 in this report[2]) involved the release of about 5 m^3 of liquefied natural gas through an 8-in. pipe onto a pond of water at a rate of about 5 m^3/min. The LNG, being very cold (111 °K) and less dense than water, formed a rapidly evaporating liquid pool on top of the water surface. As the vapor was formed, it mixed with the atmosphere and traveled downwind away from the source. A typical experiment lasted from 2 to 3 min. from the beginning of the LNG release until the trailing edge of the vapor cloud passed the last sensor. Data were collected for about 5 min.

Comparison of the measured concentration data with model predictions was significantly hindered by fluctuations in the wind speed and direction during the experiments since most transport models assume a constant wind velocity. Even when averaged over 10-s intervals, the wind speed varied by as much as a factor of 3 and the wind direction

shifted by as much as 60° during a single test. To overcome this difficulty, we attempted to simulate plume dispersion using an atmospheric transport model that generates a three-dimensional, time-varying windfield from the wind velocity data taken during the experiment. The simulations were generally quite good and provided a useful tool for interpreting the field data and understanding the effects of wind variations on the vapor plume.

EXPERIMENTAL CONFIGURATION AND INSTRUMENTATION

The experimental array was laid out such that most of the instruments would be exposed to the gas cloud during a spill test and could be evaluated under field conditions. The array of eight stations was laid out as shown in Fig. 1 and supplemented by *in situ* instruments fielded by Jet Propulsion Laboratory (JPL) and NWC and a LIDAR (an optical analog to RADAR) fielded by Computer Genetics Corp. A schematic drawing of the instrument placement at each LLL station is shown in Fig. 2 for the third and fourth tests (Avocet-3 and Avocet-4). The thermocouples, shown at 3.7 and 4.6 m, were at 0.3 and 1 m for the first two tests (Avocet-1 and Avocet-2). The anemometer at station 9 was moved in on the pond, to station 2, and station 4 was moved 7 m north-east from the edge of the pond to the top of the pond lip for Avocet-3 and Avocet-4. The array was designed for instrument evaluation, not dispersion measurements, and this has caused some problems in interpreting the data relative to dispersion calculations.

Each station had one or more gas sensors, grab samplers, and thermocouples, all of which were used in some way to measure the concentration of the gas. We designed the grab sampler system to verify the performance of the gas sensors. Grab samples were taken at the same location as the gas sensor samples. Evacuated bottles were opened at pre-programmed intervals to sample from the gas stream. The contents of the bottles were analyzed with a mass spectrometer and compared with the gas sensor output over the same time interval and are plotted in the figures showing gas sensor output.

Stations 1 and 2 were located on the spill pond about 7.6 and 15.2 m from the spill pipe, respectively. They were single-level gas sensor stations using, in addition to a grab sampler, a Shell sensor. This instrument was developed and loaned to us by Shell Research Ltd. of England. It operates on the principle of heat loss from a filament exposed to the gas stream and to the resulting unbalance in a bridge circuit that occurs when a gas with a specific heat different than air flows past the filament. The response time of the sensor appeared to be about 0.7 s, as determined by laboratory calibration. Gas samples were drawn through tubing immersed in a warming bath to raise the gas temperature to ambient before reaching the sensor. The instrument calibration was extremely sensitive to flow rate changes and had to be checked before and after each experiment.

Stations 3 and 6 were triple-level stations, located about 30 m and 55 m from the spill pipe, respectively. Grab samplers, thermocouples, and TSI sensors were located at the 1 m and 2.4 m levels, and only thermocouples and grab samplers were at the 0.45 m level. Thermocouples were moved to 3.7 m and 4.6 m for the third and fourth tests (Avocet-3 and Avocet-4). Gas samples were drawn through tubing coiled in a water bath to warm the samples and vaporize water droplets before reaching the gas sensors or the grab samples.

The TSI gas sensor, manufactured by Thermo-Systems Inc. of St Paul, Minnesota, consists of a thin-film anemometer element (two in our case) in a gas stream whose flow velocity is determined by a sonic nozzle downstream. Since sonic velocity is sensitive to gas composition ($v_{CH4} = 1.3\ v_{air}$), the anemometer can be used as a gas sensor. The instrument response was very fast, in about 10 ms, and the calibration was quite stable over the test series.

Station 4 was a single-level station (0.9 m high) with a grab sampler, two thermocouples, and a non-dispersive, infrared (IR) gas analyzer custom built for us by Anarad, Inc. The IR instrument was capable of distinguishing between methane, ethane, and propane with only a small amount of "cross talk" between the various gas species and provided our first quantitative evidence of the differential boiloff of the different hydrocarbons from the pool. The gas sampled by this instrument was also warmed, and water droplets were evaporated by passing it through coiled tubing in a water bath. The response time was several seconds.

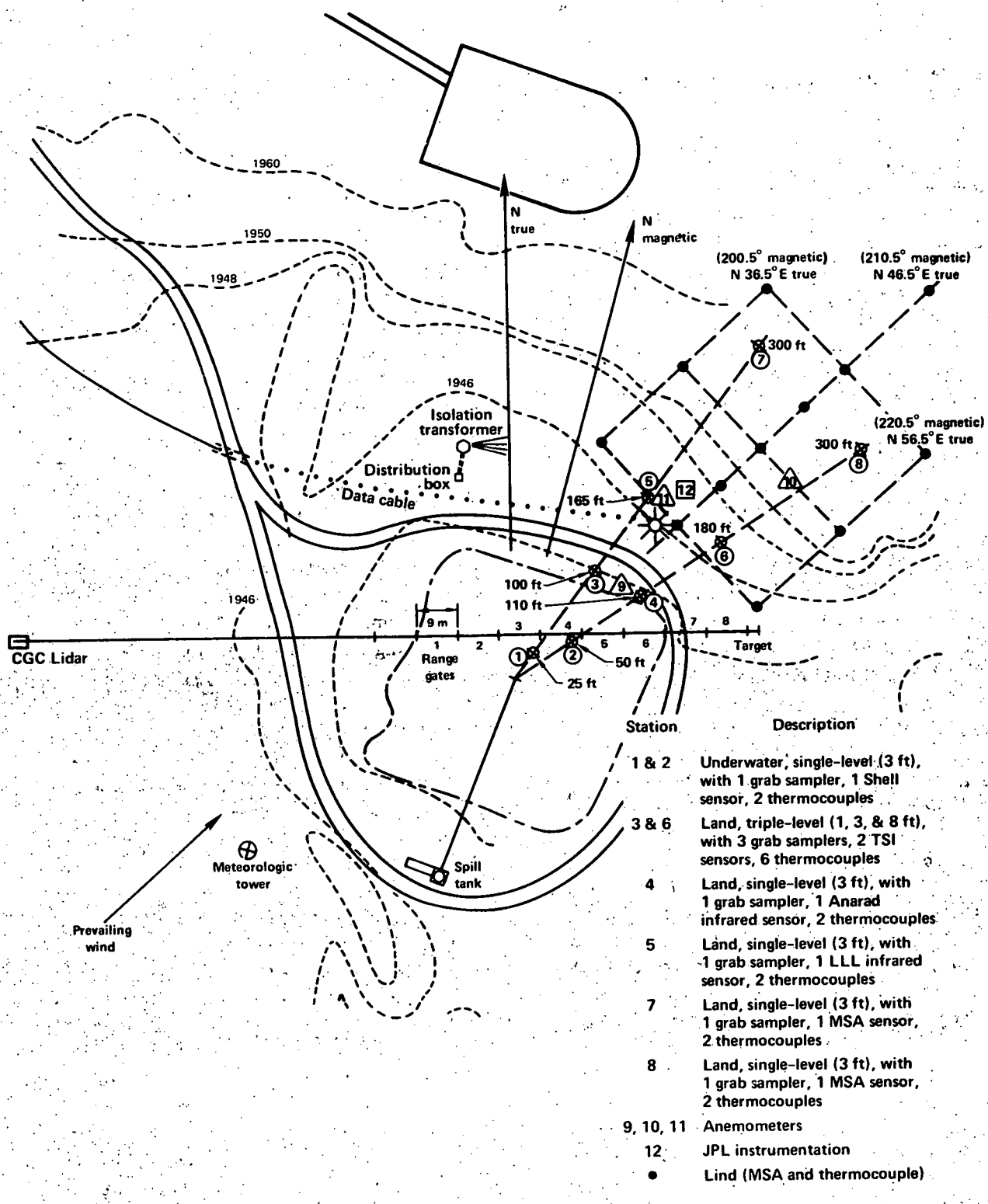

Station	Description
1 & 2	Underwater, single-level (3 ft), with 1 grab sampler, 1 Shell sensor, 2 thermocouples
3 & 6	Land, triple-level (1, 3, & 8 ft), with 3 grab samplers, 2 TSI sensors, 6 thermocouples
4	Land, single-level (3 ft), with 1 grab sampler, 1 Anarad infrared sensor, 2 thermocouples
5	Land, single-level (3 ft), with 1 grab sampler, 1 LLL infrared sensor, 2 thermocouples
7	Land, single-level (3 ft), with 1 grab sampler, 1 MSA sensor, 2 thermocouples
8	Land, single-level (3 ft), with 1 grab sampler, 1 MSA sensor, 2 thermocouples
9, 10, 11	Anemometers
12	JPL instrumentation
•	Lind (MSA and thermocouple)

FIG. 1. Site plan for the 1978 liquefied natural gas (LNG) spills at China Lake.

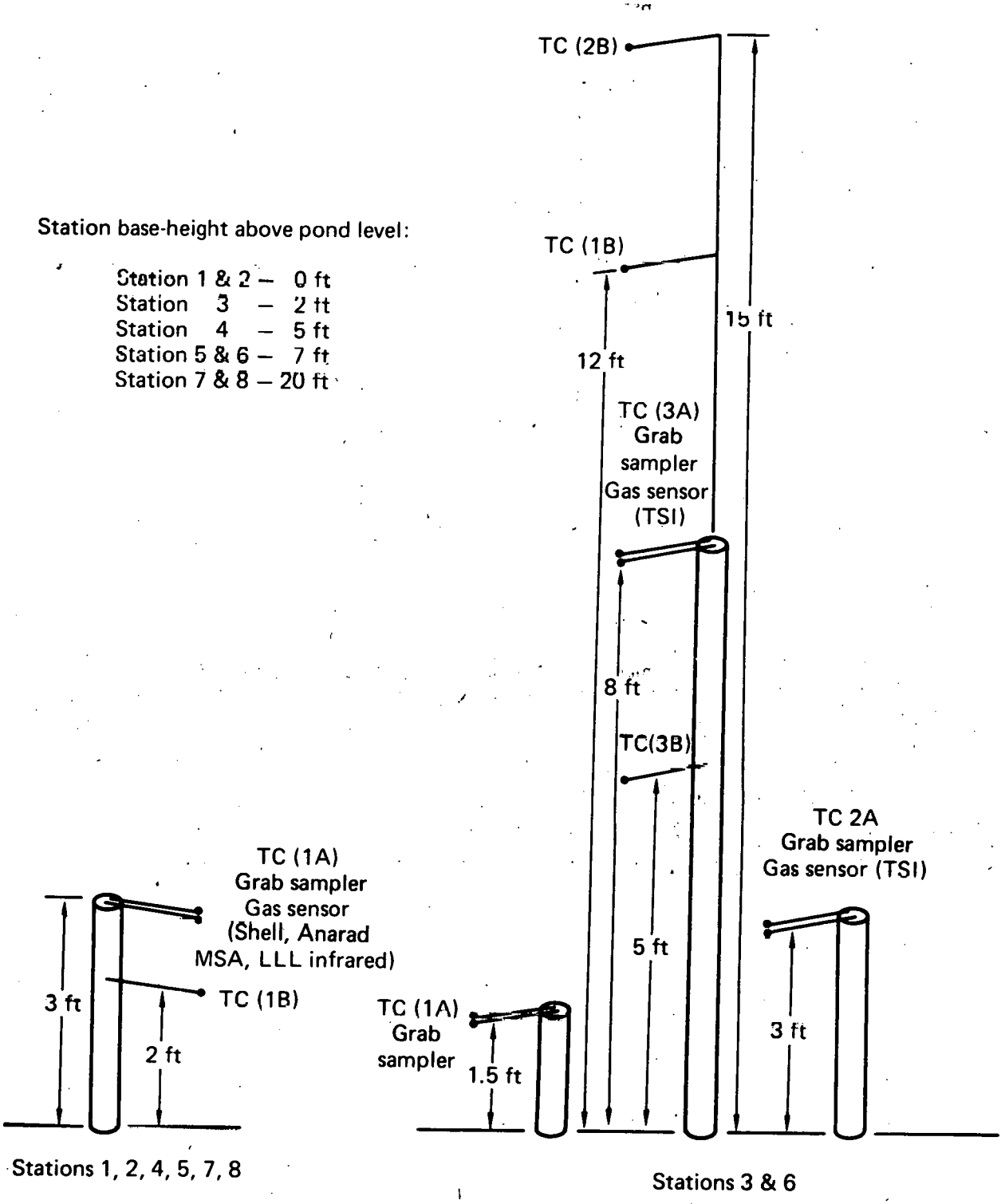

FIG. 2. Locations of the thermocouples (TC), grab samplers, and gas sensors (TSI, MSA, Anarad, or LLL infrared) for LNG-20 and LNG-21.

Station 5 was also a single-level station (1 m) with a gas sensor, grab sampler, and two thermocouples. The sensor used at this station was a miniature, rapid response, infrared gas sensor prototype developed for the DOE CO_2 program[3] and modified to detect methane. No attempt was made to separate the various hydrocarbon species because of time limitations. The sensor operates on the principle of differential absorption, with one of the filters centered on a methane line and the reference filter centered nearby on a background region. The ratio of these two measurements is then essentially independent of water vapor, water droplets, or dust in the absorption cell. The sensor has a full scale response of 5 Hz and operates non-thermostated in environments with temperatures from −20° to +40°C. This was the only truly portable sensor used in these tests. The sample cell was small and open to the environment so that pumps and water baths were not required.

Stations 7 and 8 were single-level stations (1 m), each with a grab sampler, a Mine Safety Appliances (MSA) gas sensor and two thermocouples. The MSA sensor operates on the principle of combustion of the flammable gas on a catalyst coated filament and can be used to detect gas concentrations only up to the stoichiometric concentration (10% for methane).

Three propeller, bivane, fast-response, anemometers were set up at stations 9, 10, and 11 at 1 m above the ground. These were used for general wind field tracking and to follow the rapid fluctuations in wind speed and direction. In addition to these, the NWC facility had a meteorological tower on the south-west side of the spill pond with two 2-axis cup and vane anemometers at 2 m and 10 m above the ground.

For one test, Avocet-2, a Raman LIDAR was fielded by Computer Genetics Corp. to make remote concentration measurements. The LIDAR used a pulsed laser to excite the gas and time-gated the Raman scattered return signal to obtain concentration measurements in a series of 9-m-long range gates across the gas plume. The orientation of the LIDAR and the position of the range gates are shown in Fig. 1. The laser beam was about 2 m above the pond level.

ATMAS COMPUTER MODEL

Computer simulations of each experiment were conducted using the atmospheric transport model ATMAS[4] to aid in the analysis of the measured concentration data. The ATMAS code is a three-dimensional computer model that was developed for another LLL program to predict the transport of trace species emitted to the atmosphere from quasi-area sources. A major advantage in using the code to analyze the field data is that it can simulate a three-dimensional, time-varying wind field from the meteorological data obtained at different locations within the region of interest. The use of a variable wind-field model rather than a constant wind velocity model allows for a more realistic simulation of the true wind field.

Species transport in the ATMAS code is governed by the atmospheric advection-diffusion equation

$$\frac{\partial c}{\partial t} = \nabla \cdot K \nabla c - \nabla \cdot \vec{U} c \ , \qquad (1)$$

where c is the species concentration, t is time, ∇ is the divergence operator, K is the eddy diffusion coefficient, and $\vec{U}$ is the mean advection velocity. As governed by this equation, transport is the result of only two processes. The advective process represents transport by the average wind velocity where the velocity has been averaged over a length of time Δt. The diffusion process is assumed to approximate the effects of atmospheric turbulence occurring on time scales shorter than the wind velocity averaging time Δt.

To solve the transport equation, ATMAS uses a particle-in-cell method.[5,6] These methods represent the mass of the emitted species by marker particles whose trajectories through space are calculated from an equation of motion derived from the advection-diffusion equation. The array of marker particle locations presents a three-dimensional representation of the plume mass distribution. The species concentration at any point in the plume is approximated by the average concentration within an incremental volume surrounding the point and is calculated by summing the number of marker particles within that incremental volume.

The marker particle equation of motion is

$$\vec{r}(t + \Delta t) = \vec{r}(t) + \vec{U} \cdot \Delta t + \vec{R}(\Delta t) \ , \qquad (2)$$

where $\vec{r}(t)$ is the marker particle location at time t, $\vec{U}$ is the marker particle advection velocity, and $\vec{R}$ is a diffusive displacement. The advection velocity at each grid point is calculated from the measured wind velocity at several station locations in the region by using d^{-1} interpolation-extrapolation, where d is the horizontal distance from the grid point to the data station location. The horizontal components are assumed to increase with height according to the power law

$$U = U_0(z/z_0)^p \qquad (3)$$

The vertical component of the advection velocity is assumed to be zero. Individual marker particle velocities are interpolated from the advection velocities at the surrounding grid points. In the Avocet simulations, a new advection field was calculated every 10 s. The value of the exponent p was set equal to 0.1, the average value obtained from the wind velocity measurements taken at the two heights on the NWC meteorological tower in each experiment.

The vertical and horizontal diffusive displacements are calculated in two different ways, both derived from Eq. (1). The vertical diffusive displacement is given by Ref. 7 as

$$R_z(\Delta t) = \frac{-K_z}{C} \cdot \frac{\partial C}{\partial z} \cdot \Delta t \doteq \frac{K_z \cdot z \cdot \Delta t}{\sigma_z^2} \qquad (4)$$

where

$$\sigma_z^2(s) - \sigma_z^2(0) = 2 \int_0^s \frac{K_z}{U} ds = as^b \ ,$$

z is the marker particle height relative to the plume centerline, s is the downwind distance that the particle has traveled, and the coefficient a and exponent b are empirical constants. The relationship between σ and K in Eq. (4) is obtained by assuming the shape of the plume to be Gaussian in the vertical direction. In the horizontal directions, a Monte Carlo method is used, which does not depend on the shape of the plume. The horizontal diffusive displacements are random displacements chosen from a Gaussian distribution function with a mean value of zero and a mean square value of $2 \cdot K_H \cdot \Delta t$.[8] The form of K_H is the same as that for K_z, namely,

$$K_H = (1/2)\, a \cdot b \cdot U \cdot s^{b-1} \ , \qquad (5)$$

where different values of a and b are used in the horizontal and vertical directions.

In the Avocet simulations, the dispersion constants were selected on the basis of measurements of the LNG vapor plume concentration rather than measurements of the stability of the atmosphere. The vertical diffusion coefficient was taken to be constant, $b = 1$. The value of "a" was set equal to 0.044 and was calculated from the concentration measurements at the two heights (0.9 and 2.4 m) on station 6 by assuming the vertical concentration distribution to be Gaussian. Estimates of the vertical dispersion constants were made for all four experiments and found to be nearly the same so that the above values were used in each calculation. The horizontal dispersion rate was chosen in a similar manner. In Avocet-2, stations 3 and 5 lay just beyond the plume edge through most of the experiment. The values of a and b were adjusted so that the edge of the calculated plume behaved similarly. This estimate of the horizontal dispersion rate was made only for Avocet-2; however, the same values of a and b were used for all experiments and were $a = 0.0072$ and $b = 1.76$. These dispersion rates correspond to the Pasquill-Gifford dispersion categories E and F, that is, stable conditions with low dispersion rates.

To complete the description of the dispersion model, one must also specify the LNG vapor source and the boundary conditions. For the first three experiments a constant emission rate for a fixed time period was used. The shape of the source was uniform and circular in the horizontal plane and Gaussian in the vertical direction with a standard deviation of 0.25 m and the centerline of the Gaussian distribution at ground level. The source emission rate and horizontal radius were different in each experiment and are summarized in Table 1. For the fourth test, it was necessary to try to simulate a vapor source that was observed to change size during the course of the spill because of changes in

TABLE 1. A summary of the 1978 China Lake dispersion tests.

Avocet	1 (LNG-18)	2 (LNG-19)	3 (LNG-20)	4 (LNG-21)
Date	31 Aug	13 Sep	9 Nov	20 Nov
Time	14:56	19:37	15:26	15:11
Temperature	35.8°C	21.1°C	26.8°C	20.1°C
Rel humidity	16%	29%	15%	21%
Spill volume	4.39 m^3	4.52 m^3	4.5 m^3	4.2 m^3
Spill duration	67 s	59 s	77 s	53 s
Source rate (g/s)	2.058×10^4	2.384×10^4	2.234×10^4	44.0[a]
Spill radius (m)	7.22	7.81	6.82	Variable[a]
Boiloff time (s)	90	80	85	120

[a]For Avocet-4, the source rate is in units of $g/m^2 \cdot s$ to accomodate a pseudo-pool spread which increases in time:

Pool radius (m)	3	5	8	11	15
Time block (s)	0-22	22-40	40-60	60-85	85-120

wind velocity. The simulation was done by turning on a series of sources with successively larger areas during the course of the spill. The boundary conditions at the top and sides of the grid were open; that is, marker particles that travel out of the grid do not return. At the bottom of the grid the boundary is reflective so that particles do not exit the grid or deposit on the ground surface.

The ATMAS code has several methods for displaying the plume concentration. Contour plots of the plume showing the concentration isopleths at a height of 1 m above the ground are made at regular time intervals during the simulation. Graphs of concentration versus time for each of the measurement station locations are also presented. A qualitative description of the plume shape and location is given by three views (one each in the x, y, and z directions) of the plume in the form of dot plots of the marker particle locations. Each of these methods is used in the analysis of the measured concentration data presented in the following section.

Before discussing the results, a final comment should be made regarding the use of the ATMAS model in this analysis. The ATMAS model has significant deficiencies when applied to LNG vapor cloud dispersion in the atmosphere; namely, it does not consider effects due to density and temperature variation in the cloud. However, the model does attempt to simulate a spatial and time-varying wind field as encountered in the LNG spill experiments. We used this code to help overcome the difficulties in analyzing the concentration data that were due to changes in the wind field and to evaluate the impact of these changes on plume movement.

THE EXPERIMENTAL DISPERSION DATA AND COMPARISON WITH ATMAS CALCULATIONS

Experimental concentration data from the Avocet series of experiments are presented in this section and compared with ATMAS calculations. The gas concentration data have been smoothed using a multiple-pass, two-point averaging technique. This eliminated most of the high frequency noise and, unfortunately, the high frequency data as well. However, the high frequency data are not necessary for comparisons with our computer calculations, which are 10-s averages. The experimental data are shown in all the figures as dots with grab sample results superimposed as bullets (●). ATMAS results are indicated by the dashes (——).

AVOCET-1

A typical orientation of the plume relative to the sensor array is shown in Fig. 3. This plot shows the contours of constant concentration at 60 s after the spill. For this experiment, the wind carried the plume to the left of the center of the sensor array. The mean wind speed and direction and the standard deviations of these quantities are shown in Table 2. The range in wind speed varied from a maximum at station 11 of 7.33 m/s to a minimum of 0.62 m/s at station 10. During the course of the experiment, the wind direction, averaged for 10 s,

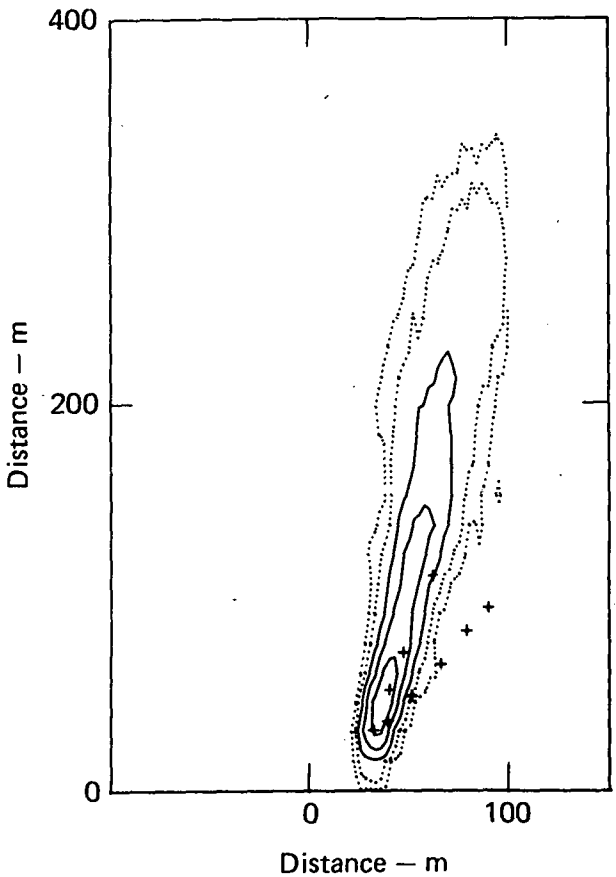

FIG. 3. Concentration isopleths of Avocet-1 plume at 60 s. The contours correspond to concentrations of 0.585, 5.85, 29.2, 87.7, and 175 g/m^3.

varied from 155° to 207°, relative to magnetic north at the different stations. The estimated maximum extent of the lower flammability limit (33 g/m^3 at 300 K) for this case was about 380 m.

Figure 4 shows the gas concentration data from the Shell sensor and grab samples at station 1 versus time plotted with the ATMAS calculation. This calculation used upwind meteorological data as input to ATMAS in addition to the three meteorological stations down-wind. The general agreement is reasonably good; however, the detailed structure of the experimental data is not reproduced by ATMAS. This structure is probably due to local wind variations. A similar plot is provided for station 2 in Fig. 5 and shows good agreement with the data. The grab sample results agree very well with the Shell sensor output at both of these stations and confirm that the sensors were working properly.

In Fig. 6a the agreement between calculation and data for station 3, at the 1-m level, is seen to be poor. Gas concentration data at the 2.4-m level are shown in Fig. 6b. Since this station was in the middle of the dispersing plume, one might expect better agreement. Grab sample results do not agree with the TSI sensor data at the 1-m level but do agree at the 2.4-m level. The disagreement at the 1-m level was probably caused by miswiring of the grab sampler, which was later corrected.

Problems with both the Anarad infrared gas sensor at station 4 and the LLL infrared gas sensor at station 5 kept them from taking any reliable data on this experiment. The measurements at station 6, shown in Figs. 7a and 7b show a peak in gas concentration at about 80 s., which is not reproduced by the ATMAS calculation which was nearly zero here. The grab sample results agree well with the TSI gas sensor data. However, most of the time both devices saw no gas at this station. Station 6 was apparently at the edge of the plume (see Fig. 3) and small shifts in wind direction could make large changes in gas concentration at this point. The MSA sensors for stations 7 and 8 had not arrived from the manufacturer at the time of this experiment. Grab sample data, however, indicates concentrations of about 5% at 90 s after the start of the spill at station 7. This is in good agreement with the ATMAS calculation shown in Fig. 8, which also indicates that the grab sampler missed most of the gas plume at this station.

AVOCET-2

Avocet-2 is a particularly interesting experiment because of the large effect of wind shifts on the gas concentration measured at the instrument stations. These shifts occur locally both in the wind

TABLE 2. Average and standard deviations in wind speed and direction for Avocet-1 for time interval 0 - 125 s.

Station	Speed (m/s)	Standard deviation of speed (m/s)	Direction (deg)	Standard deviation of direction (deg)
9	3.81	0.81	188	13.1
10	2.38	1.28	179	16.8
11	5.76	0.87	190	12.9

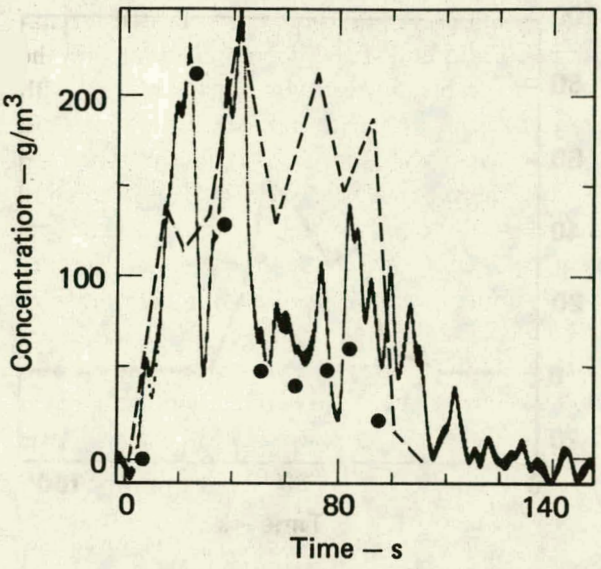

FIG. 4. Avocet-1 concentration vs time at station 1. Continuous data from SHELL1C (dots), grab samples (●), and ATMAS calculation (——).

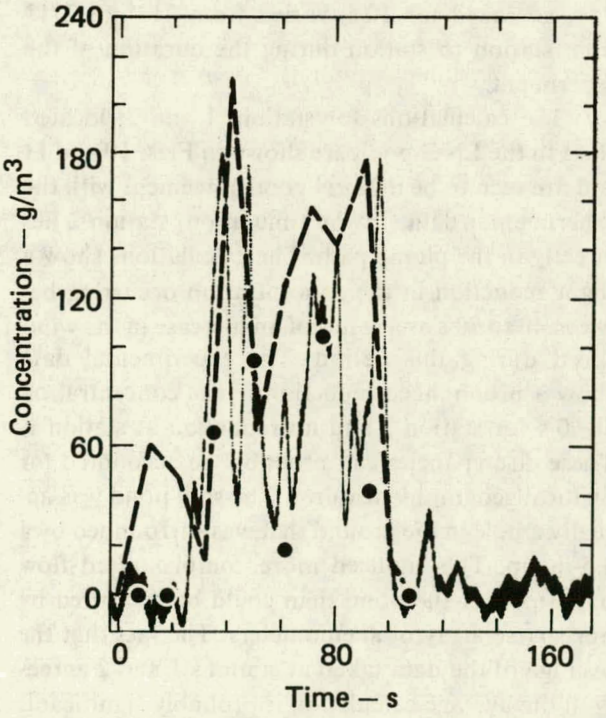

G. 5. Avocet-1 concentration vs time at station 2. Continuous data from SHELL2C (dots), grab samples (●), and ATMAS calculation (——).

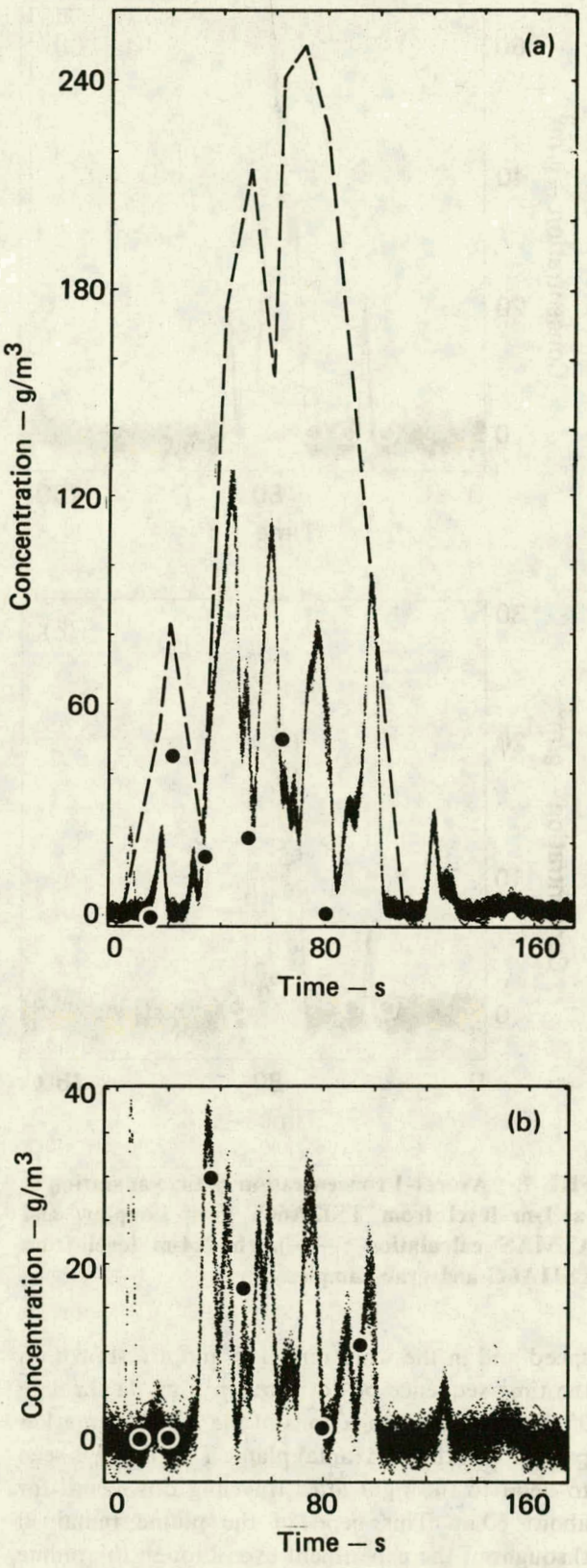

FIG. 6. Avocet-1 concentration vs time at station 3. (a) 1-m level, from TSI2A3C (dots), grab samples (●), and ATMAS calculation (——). (b) 2.4-m level from TSI1A3C and grab samples.

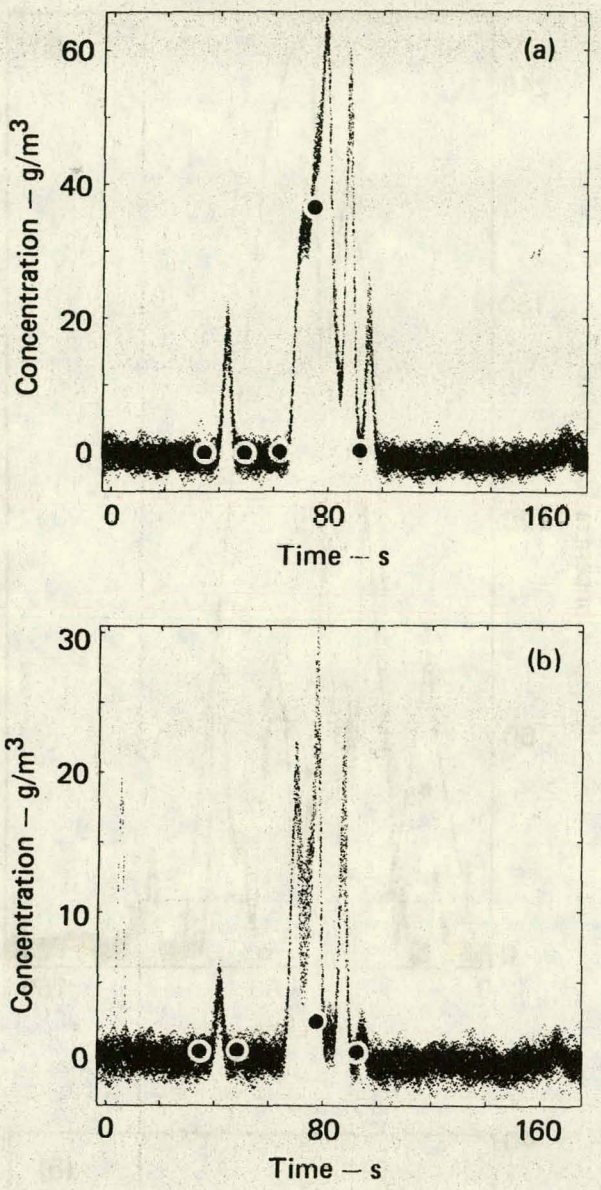

FIG. 7. Avocet-1 concentration vs time at station 6. (a) 1-m level from TSI2A6C, grab samples, and ATMAS calculation (——). (b) 2.4-m level from TSI1A6C and grab samples.

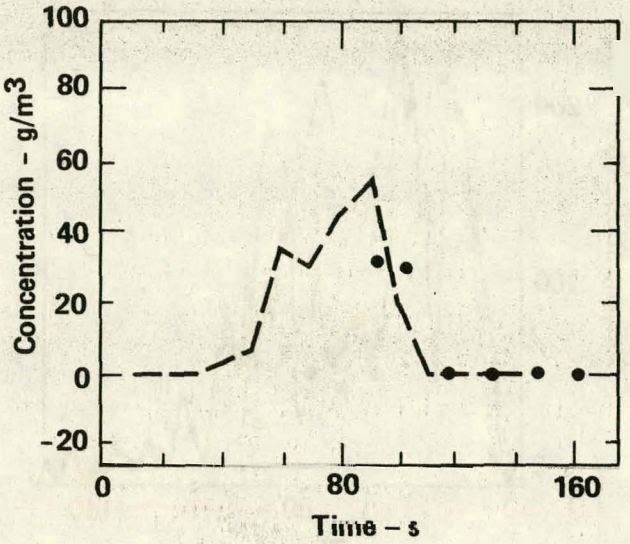

FIG. 8. Avocet-1 concentration vs time at station 7 from grab samples (●), and ATMAS calculation (——).

speed and in the wind direction and are shown on the time sequence of dot plots in Figs. 9a through 9f. The dots are projections of the ATMAS marker particles on the horizontal plane. The plume is seen to bend to the right after traveling downwind for about 60 m. This bend in the plume remained throughout the experiment even though the plume position shifted considerably during the experiment. While there is some uncertainty over the reason for the bend in the plume, it is believed to be due to the hill in this area. Upwind meteorological data were not available as input for this experiment so that only data from anemometer stations 9, 10, and 11 were used. The mean and standard deviations in velocity and direction for Avocet-2 are shown in Table 3. Wind velocities for this experiment ranged from a maximum of 5.49 m/s at station 11 to a minimum of 0.34 m/s at station 10. The wind direction, averaged for 10 s, varied from 213° to 271° from station to station during the duration of the experiment.

The calculations for stations 1 and 2, located close to the LNG pool, are shown in Figs. 10 and 11 and are seen to be in fairly good agreement with the experimental data. In the simulation, station 2 lies directly in the plume path. The calculations show a slight reduction in the concentration occurring between 40 to 70 s as a result of an increase in the wind speed during this period. The experimental data show a pronounced reduction in the concentration at 60 s for station 2 and no reduction at station 1. These discrepancies can probably be accounted for by local geographic features. The spill pond was actually a hole in the ground that was surrounded by a 1.5-m lip. This induced more complex wind flow patterns over the pond than could be measured by our sparse array of anemometers. The fact that the average of the data taken at stations 1 and 2 agrees with the average calculation is probably significant.

Stations 3 and 5 appear to lie on the edge of the plume for most of the experiment. This makes comparison between experimental data and calculation

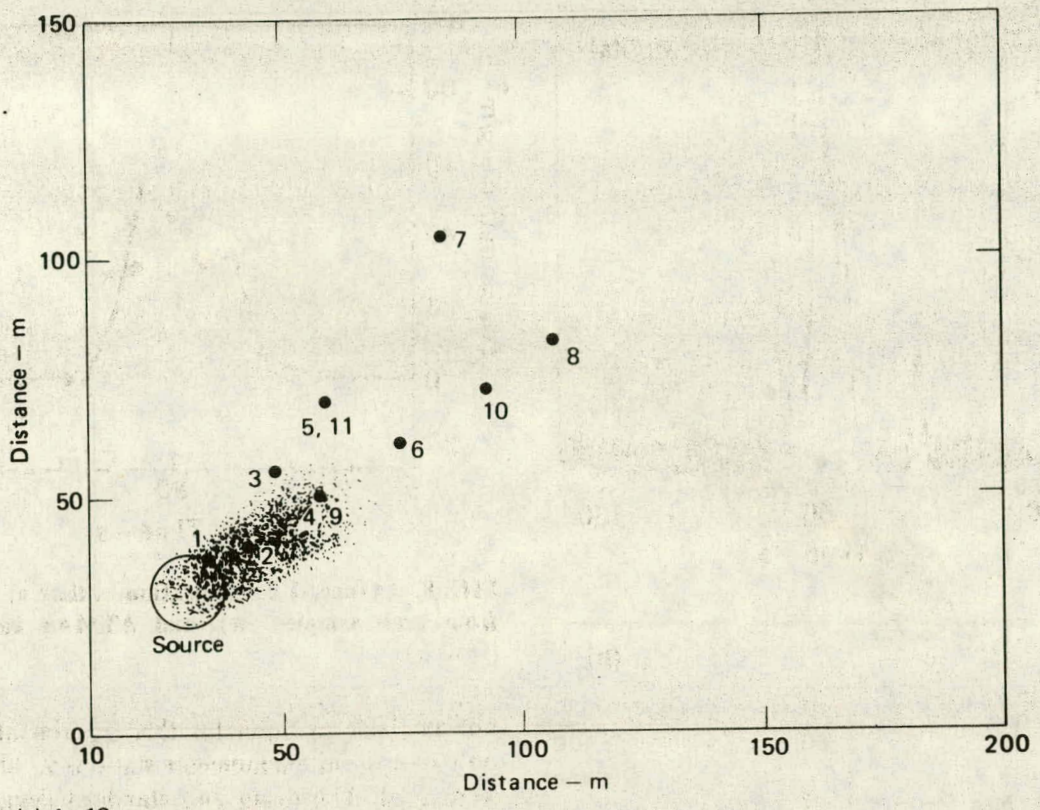

(a) At 10 s

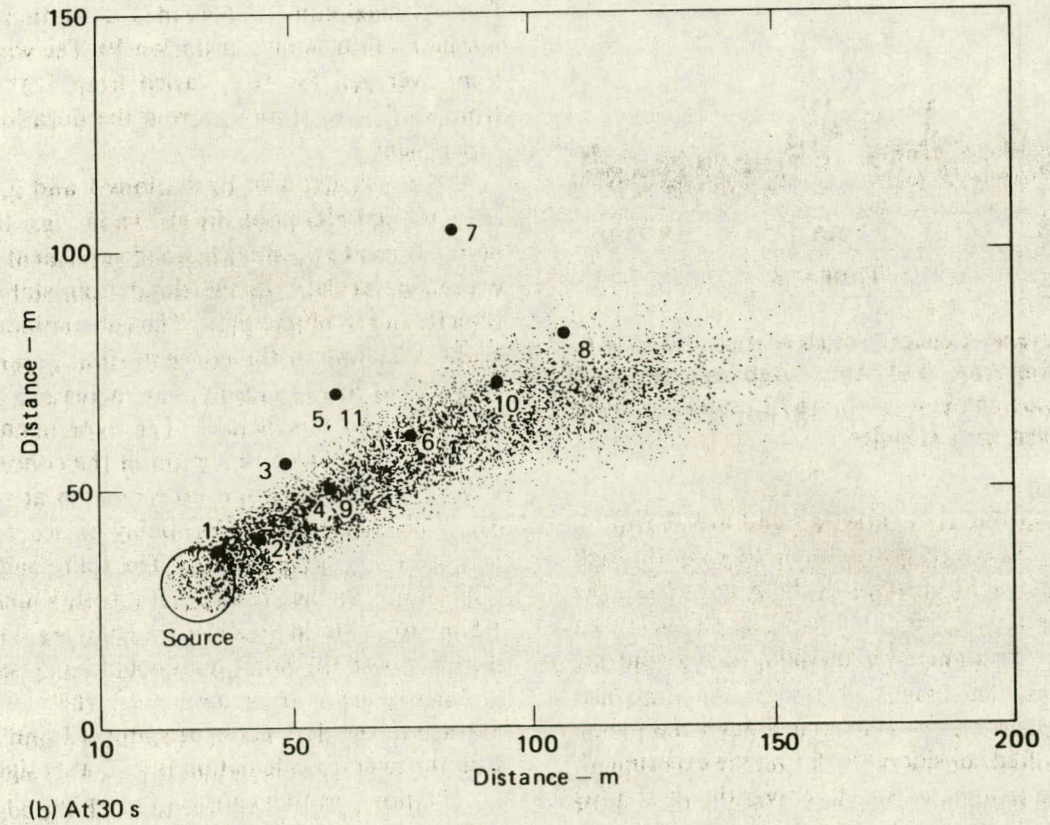

(b) At 30 s

FIG. 9. Top view of dot plots for LNG plume Avocet-2 at various times.

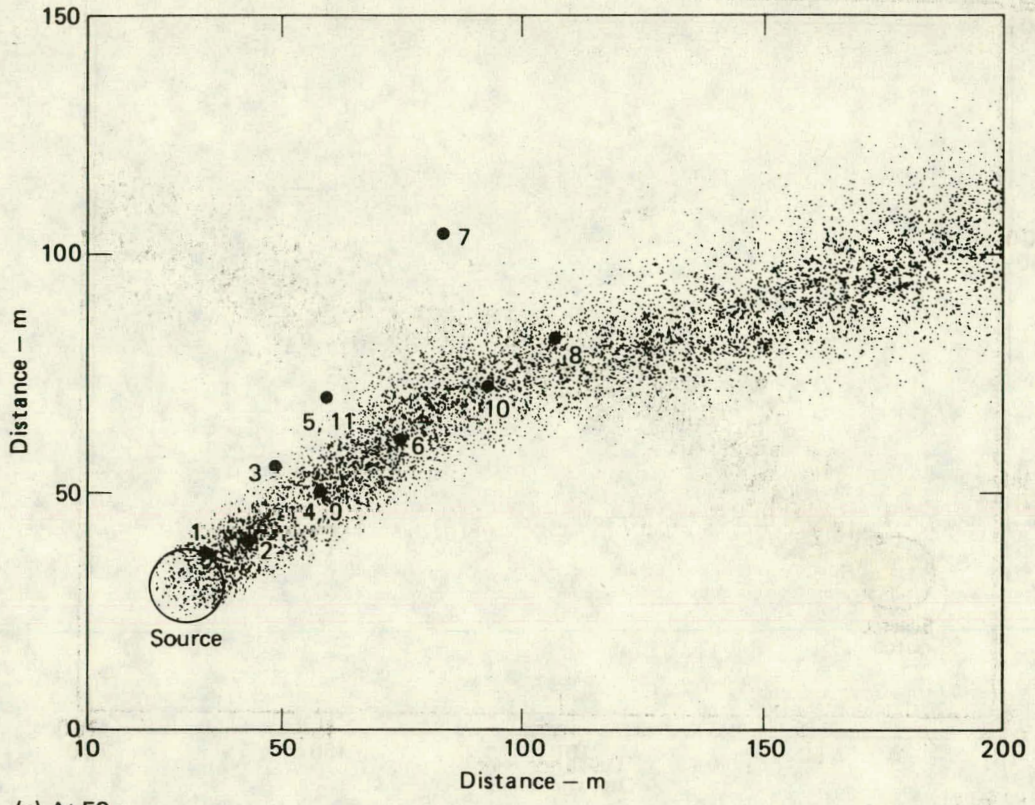

(c) At 50 s

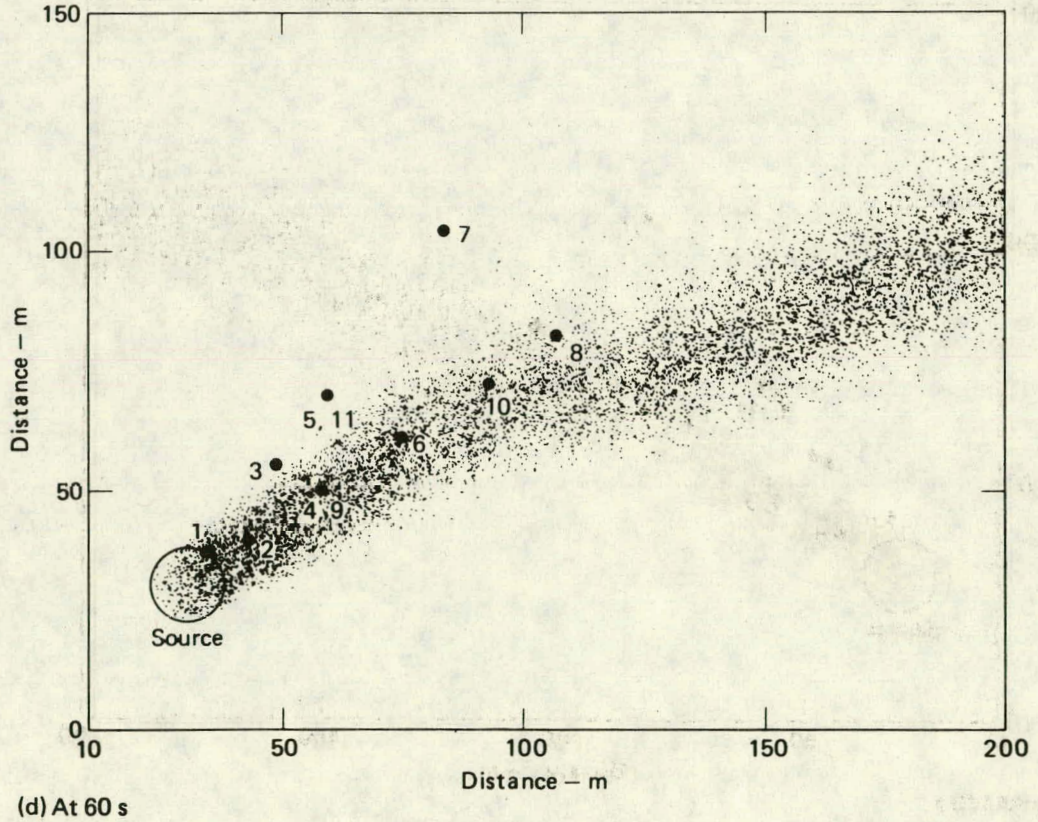

(d) At 60 s

FIG. 9. (Continued)

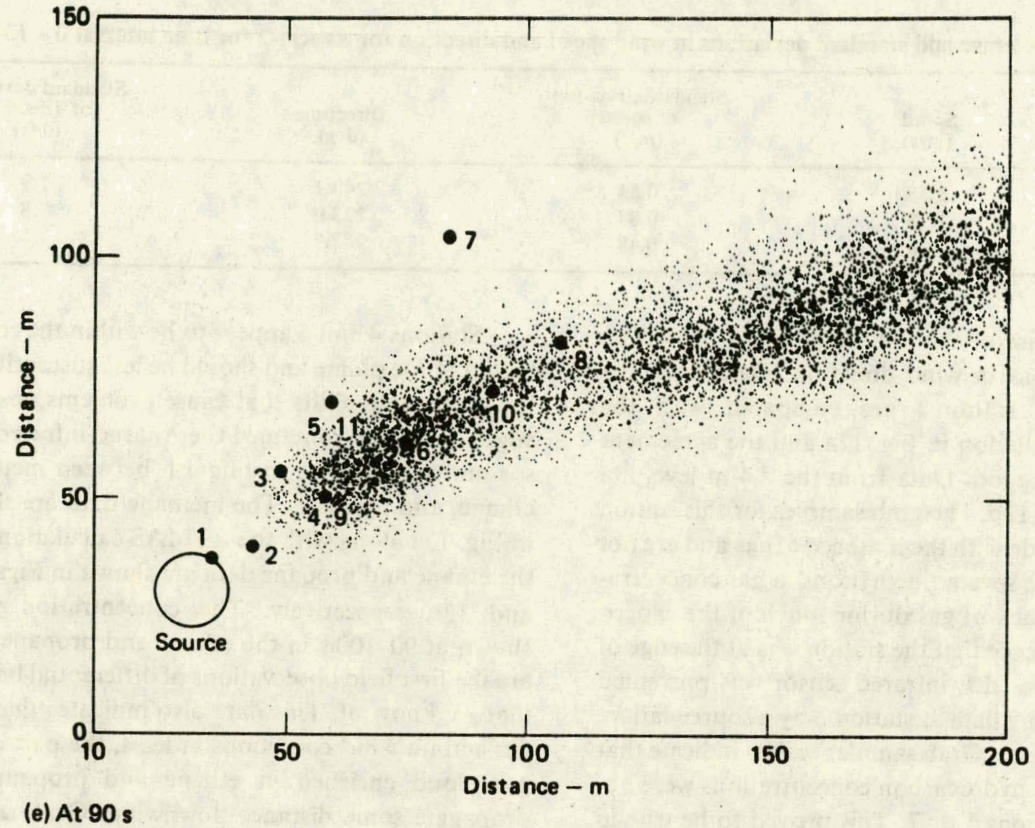

(e) At 90 s

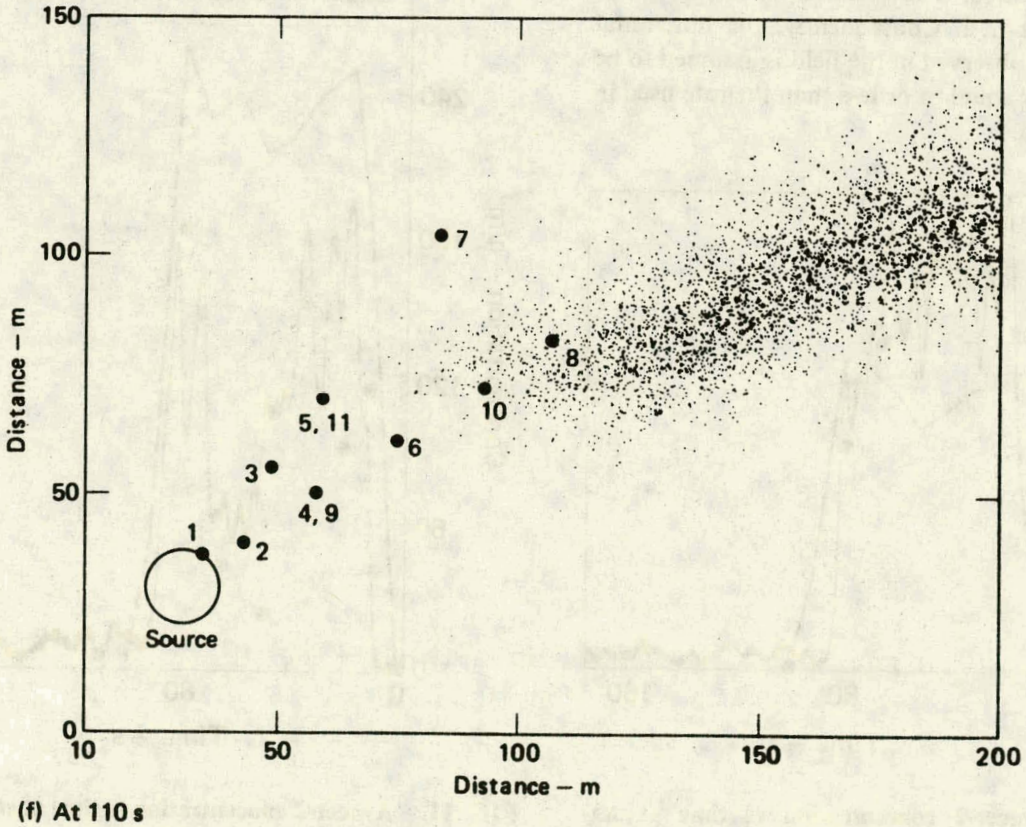

(f) At 110 s

FIG. 9. (Continued)

TABLE 3. Average and standard deviations in wind speed and direction for Avocet-2 for time interval 0 - 130 s.

Station	Speed (m/s)	Standard deviation of speed (m/s)	Direction (deg)	Standard deviation of direction (deg)
9	3.58	0.54	240.1	7.9
10	1.98	0.84	223.0	7.8
11	4.95	0.48	262.7	7.6

difficult because of the very large effect caused by slight variations in wind direction. Data from the 1-m level at station 3 are compared with the ATMAS calculation in Fig. 12a and the agreement is reasonably good. Data from the 2.4-m level are shown in Fig. 12b. The grab samples for this station did not coincide with the presence of gas and are not presented. The severe fluctuations in gas concentration and the lack of gas during much of the experiment are evidence that the station was at the edge of the cloud. The LLL infrared sensor was prevented from taking any data at station 5 by a source failure within the sensor. Grab sampler results indicate that no significant hydrocarbon concentrations were observed at stations 5 or 7. This proved to be true in the simulation also. When the horizontal diffusion rate was increased, a low concentration level appeared at station 5. Consequently, the horizontal diffusion rate observed in the field is assumed to be approximately equal to or less than the rate used in the simulation.

Stations 4 and 6 appear to lie within the central region of the plume and should be less susceptible to the small wind shifts that cause problems near the edges. Station 4 contained the Anarad infrared sensor and was able to distinguish between methane, ethane, and propane. The methane data are shown in Fig. 13a along with the ATMAS calculation, and the ethane and propane data are shown in Figs. 13b and 13c, respectively. The concentration peaks shown at 90–100 s in the ethane and propane data are the first field observations of differential boil-off that we know of. This data also indicates that, under certain wind conditions at least, the part of the gas cloud enriched in ethane and propane can propagate some distance downwind. Grab sample

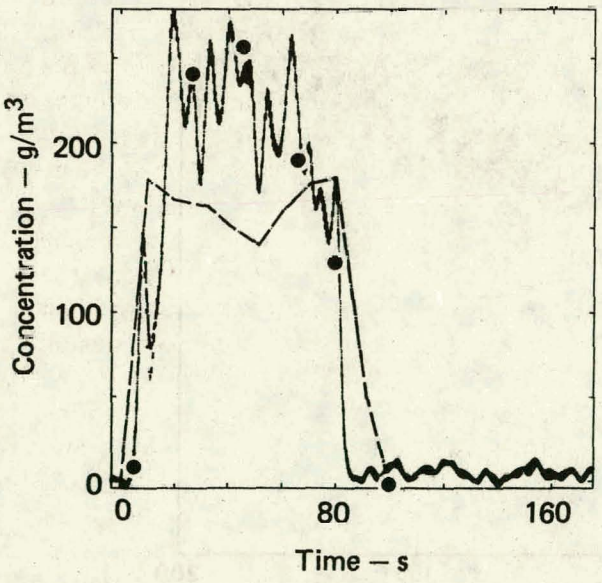

FIG. 10. Avocet-2 concentration vs time at station 1. Continuous data from SHELL1C (dots), grab samples (●), and ATMAS calculation (——).

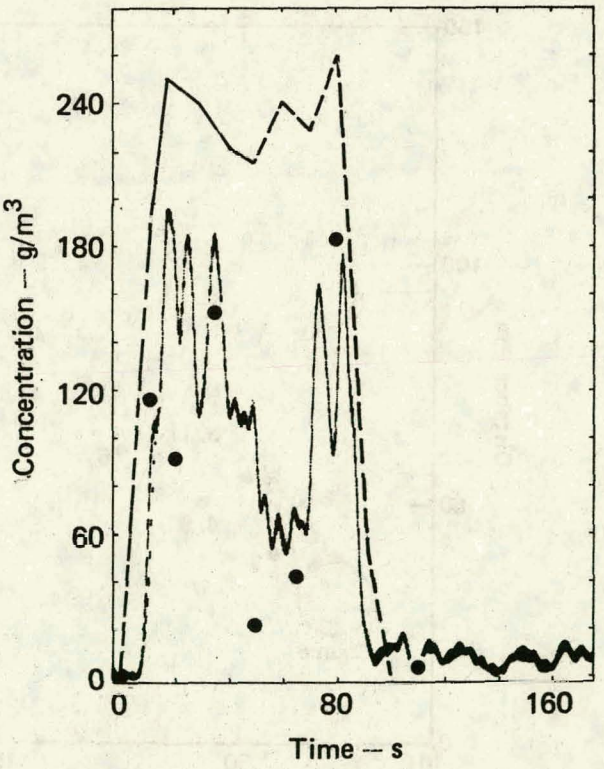

FIG. 11. Avocet-2 concentration vs time at station 2 from SHELL2C (dots), grab samples (●), and ATMAS calculation (——).

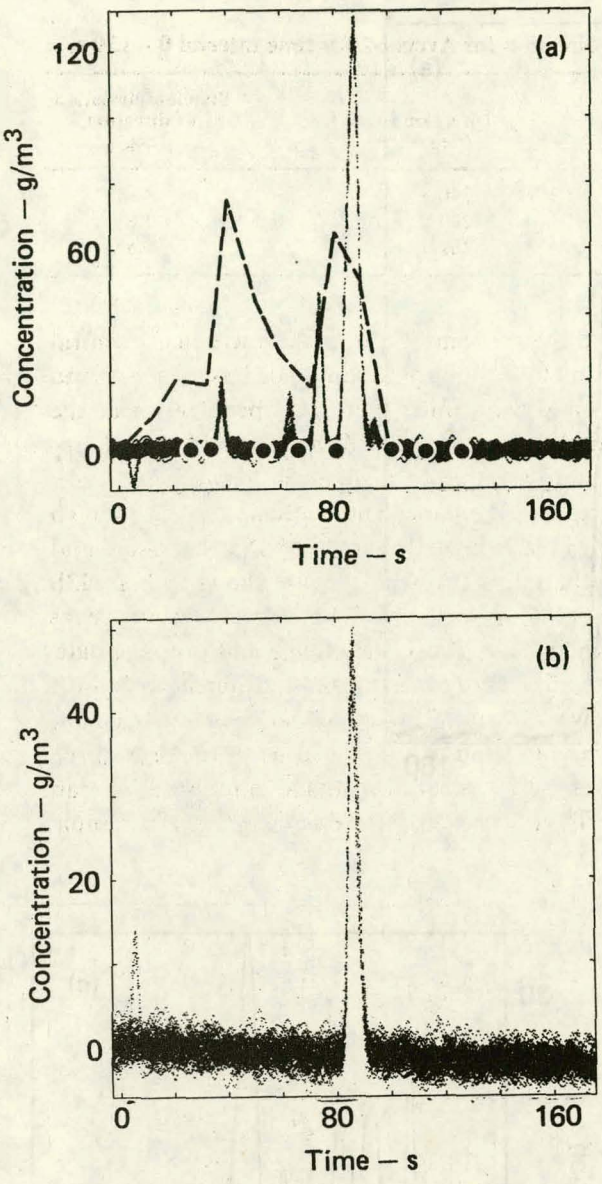

FIG. 12. Avocet-2 concentration vs time at station 3. (a) 1-m level from TSI1A3C (dots), grab samples (●), and ATMAS calculation (——). (b) 2.4-m level from TSI2A3C.

data also revealed evidence of differential boil-off and the subsequent propagation of an enriched part of the cloud downwind. A comparison of grab sample data with a simple differential boil-off model was reported in Ref. 9.

The agreement between the methane data and the calculation is not too bad; however, the calculation does significantly over-predict the concentration at station 4 and at the 1-m level at station 6 as can be seen in Figs. 13a and 14a, respectively. Data from the 2.4-m level at station 6 are shown in Fig. 14b. The pronounced drop in concentration observed in the data at station 2 does not appear in the data at stations 4 and 6. But it does appear in the calculation at these stations. It is probably the result of local acceleration of the wind between 60 and 80 s after the start of the spill, which was seen by the anemometers but which apparently was not transmitted to stations 4 and 6.

The grab samplers at stations 4 and 6 were triggered early by a large gas cloud formed during the cool-down of the spill pipe prior to the spill. Consequently, no grab sample results are available for comparison with the sensor results from these stations.

Both the calculated and experimentally observed concentrations at station 8 have two significant peaks as shown in Fig. 15. The grab sample results also show these two peaks and agree well with the data if the 5-s delay characteristic of the MSA sensor is subtracted from the data. The dot plot projections of the simulated plume onto the horizontal plane (Figs. 9a through 9f) show that these peaks are due to changes in the wind direction causing a rotation of the entire plume. Initially, station 8 lies just outside the plume on the left side (Fig. 9b). Forty seconds into the experiment the plume begins to move over station 8 causing the concentration at this station to rise. After 60 s the plume rotates away from station 8 (Fig. 9d) and thereby completes the first concentration peak. The plume remains on the east side of station 8 for 20 s and then begins to move back over the station resulting in a second concentration rise (Fig. 9e). The second peak decays as the back end of the vapor cloud moves over the station and beyond the test region (Fig. 9f). This behavior is also observed at station 3. The rotational motion of the plume resulting from changes in the mean wind direction appears to provide the correct explanation for the observed double peaks in the concentration. The simulation does produce, however, an enlarged first peak at station 8 in comparison to the experimental data.

The maximum extent of the lower flammability limit (LFL = 33 g/m^3) occurs at about 110 s into the experiment. The simulation predicts a maximum distance to the LFL of about 320 m; however, with no experimental data at this distance, this prediction remains unverified.

This test was done specifically at night so that the CGC LIDAR, which was sensitive to the solar background, could be used. The trajectory of the

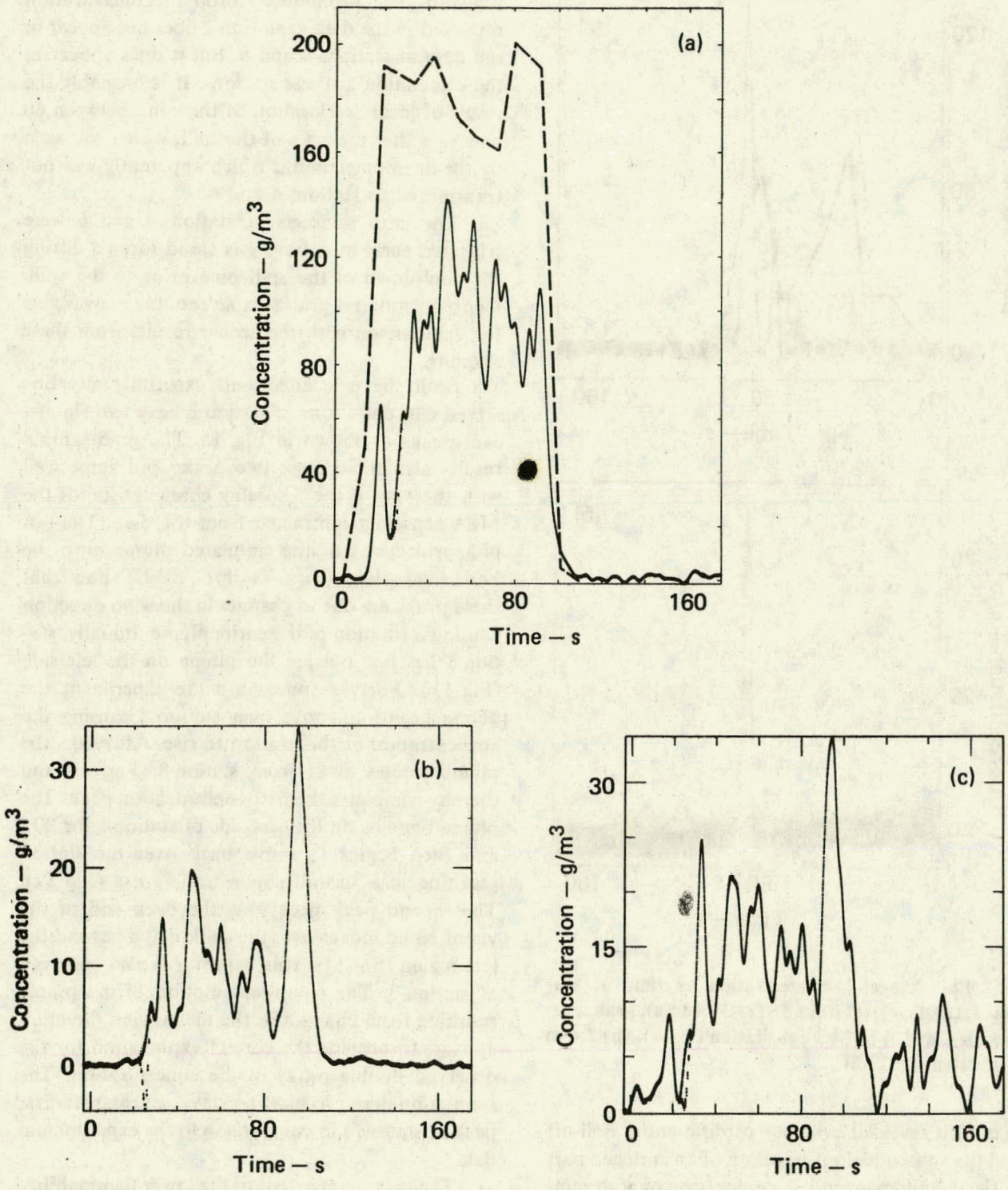

FIG. 13. Avocet-2 concentration vs time at station 4. (a) Methane concentration from IR4-MC (dots), grab samples (●), and ATMAS calculation (——). (b) Ethane concentration. (c) Propane concentration.

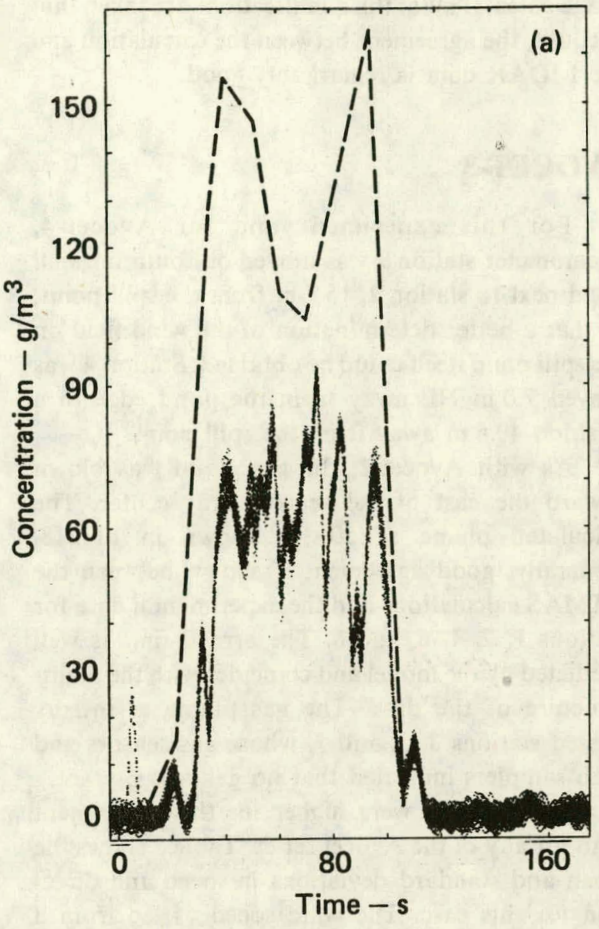

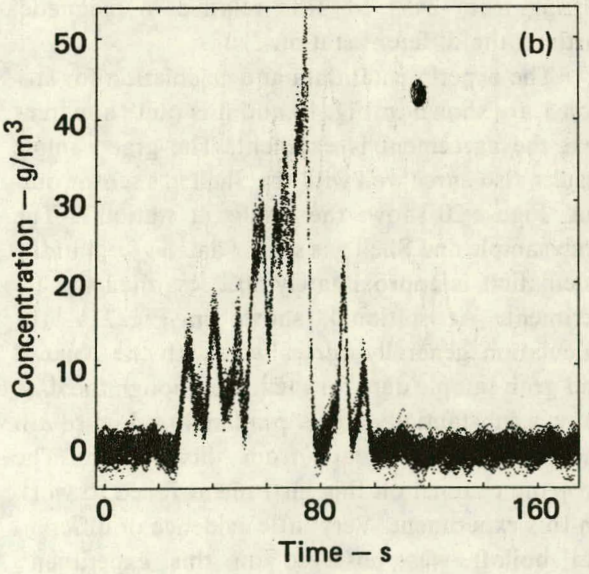

FIG. 14. Avocet-2 concentration vs time at station 6. (a) 1-m level from TSI1A6C (dots) and TMAS calculation (——). (b) 2.4-m level from TSI2A6C.

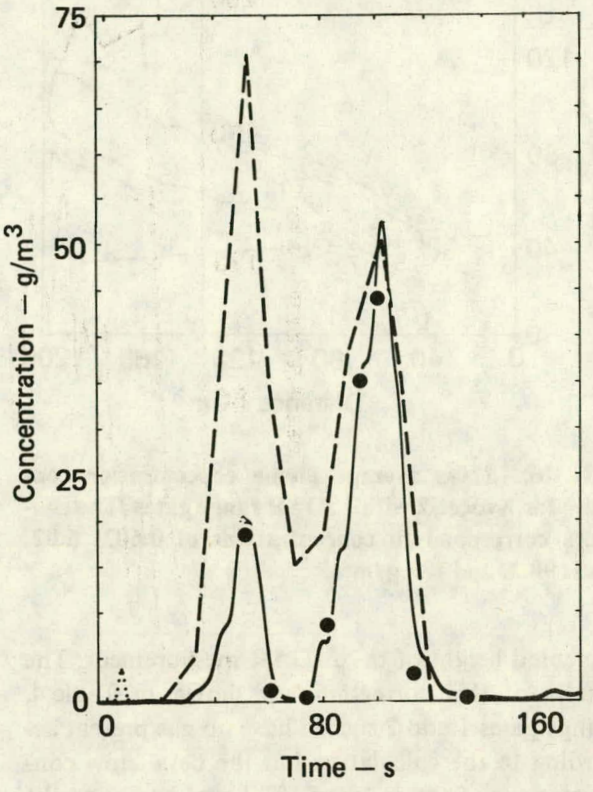

FIG. 15. Avocet-2 concentration vs time at station 8 from MSA (dots), grab samples (●), and ATMAS calculation.

laser beam through the plume, with the range gates marked, is shown in Fig. 16. The average concentrations measured over 120 s in each range gate are given in Table 4, and the concentration data for each range gate as a function of time, with the fog interference shown, is given in Figs. 17a and 17b. The measurements are averages over the length of the 9-m range gate and over 1 s.

The LIDAR was not able to penetrate the fog associated with the higher gas concentrations. Multiple scattering of the laser light by the water and ice particles caused time delays that effectively put the Raman return from these photons into more distant range gates. This skewed the average concentrations shown in Table 4 toward range gates 7 and 8.

In addition to the fog problem, the laser beam crossed the pond approximately 2.1 m above the water level, making a direct comparison with either the *in situ* sensor data or the ATMAS calculations difficult. Using the vertical dispersion coefficients given earlier in this report it is possible to apply correction factors to approximately account for the

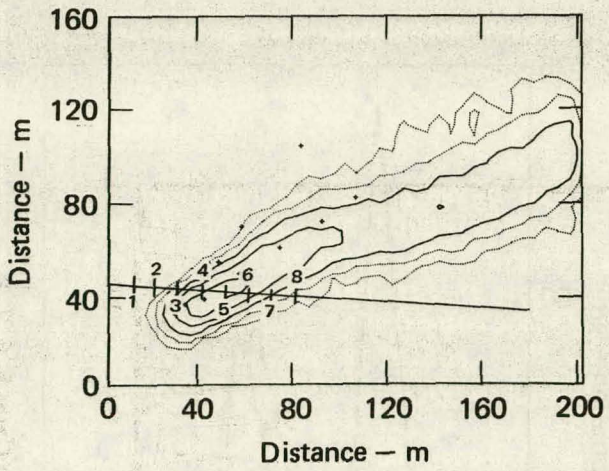

FIG. 16. 120-s average plume concentration contours for Avocet-2 with LIDAR range gates. The contours correspond to concentrations of 0.602, 6.02, 30.1, 90.2, and 181 g/m^3.

increased height of the LIDAR measurement. The results of this correction are shown in Table 4. Range gates 1 and 2 should have no gas present according to the calculation but the data show concentrations of the order of 1%. Local eddies on the spill pond, non-Gaussian behavior of the gas cloud close to the spill point, or an undefined systematic error of 0–1% in the LIDAR measurement are all possible contributors to the discrepancy. The calculation shows some gas in range gate 3 but not as much as the LIDAR measures. Range gates 4 and 5 lie in the middle of the calculated plume and show very good agreement between measurement and calculation. The agreement is good for range gate 6, but fog is starting to interfere with the LIDAR measurements. The measurements in range gates 7 and 8 are totally unreliable due to the addition of counts from multiple scattering in other range gates. If all of the qualifications are taken into account, the agreement between the calculation and the LIDAR data is remarkably good.

TABLE 4. Average methane concentrations over 120 s from the LIDAR measurement and ATMAS calculation.

Range gate	120-s average concentration (%) (Measured)	(Calculated)	Fog interference
1	1.03	0	none
2	1.45	0	none
3	1.74	0.3	none
4	1.75	2.3	none
5	3.41	4.5	slight
6	3.85	3.4	more
7	5.11	1.2	extensive
8	7.41	0.3	extensive

AVOCET-3

For this experiment and for Avocet-4, anemometer station 9 was moved out onto the spill pond next to station 2, 15.2 m from the spill point, so that a better determination of the wind field on the spill pond itself could be obtained. Station 4 was moved 7.0 m NE away from the pond edge to a position 40.5 m away from the spill point.

As with Avocet-2, the gas cloud was blown toward the east of the sensor array center. The calculated plume at 50 s is shown in Fig. 18. Generally, good agreement is shown between the ATMAS calculations and the experimental data for stations 1, 2, 4, 6, and 8. The arrival time is well predicted by the model and coincides with the major structure of the data. The gas plume essentially missed stations 3, 5, and 7, whose gas sensors and grab samplers indicated that no gas was present.

Wind speeds were higher for this experiment than for any of the Avocet series. Table 5 shows the mean and standard deviations in speed and direction for this case. The wind speed varied from a maximum of 12.7 m/s to a minimum of 4.8 m/s, shifting from 245° to 218° relative to magnetic north at the different stations.

The experimental data and calculation for station 1 are shown in Fig. 19 and it is quite apparent that the agreement is excellent. The grab sample results also agree well with the Shell gas sensor output. Figure 20 shows the results at station 2. The grab sample and Shell gas sensor data agree, but the calculation is approximately 50% less than the experiment. At station 4, shown in Fig. 21a, the calculation generally agrees well with the Anarad and grab sample data for methane, though the data show a substantially higher peak at 40 s. Figure 21b shows the ethane data from this station. The propane channel on this instrument failed to work on this experiment. Very little evidence of differential boiloff was observed on this experiment, probably because of mixing caused by the very high winds. The agreement between calculation and data is also very good at station 6, as can be seen in Fig. 22a. Data from the 2.4-m level at station 6 are shown in Fig. 22b.

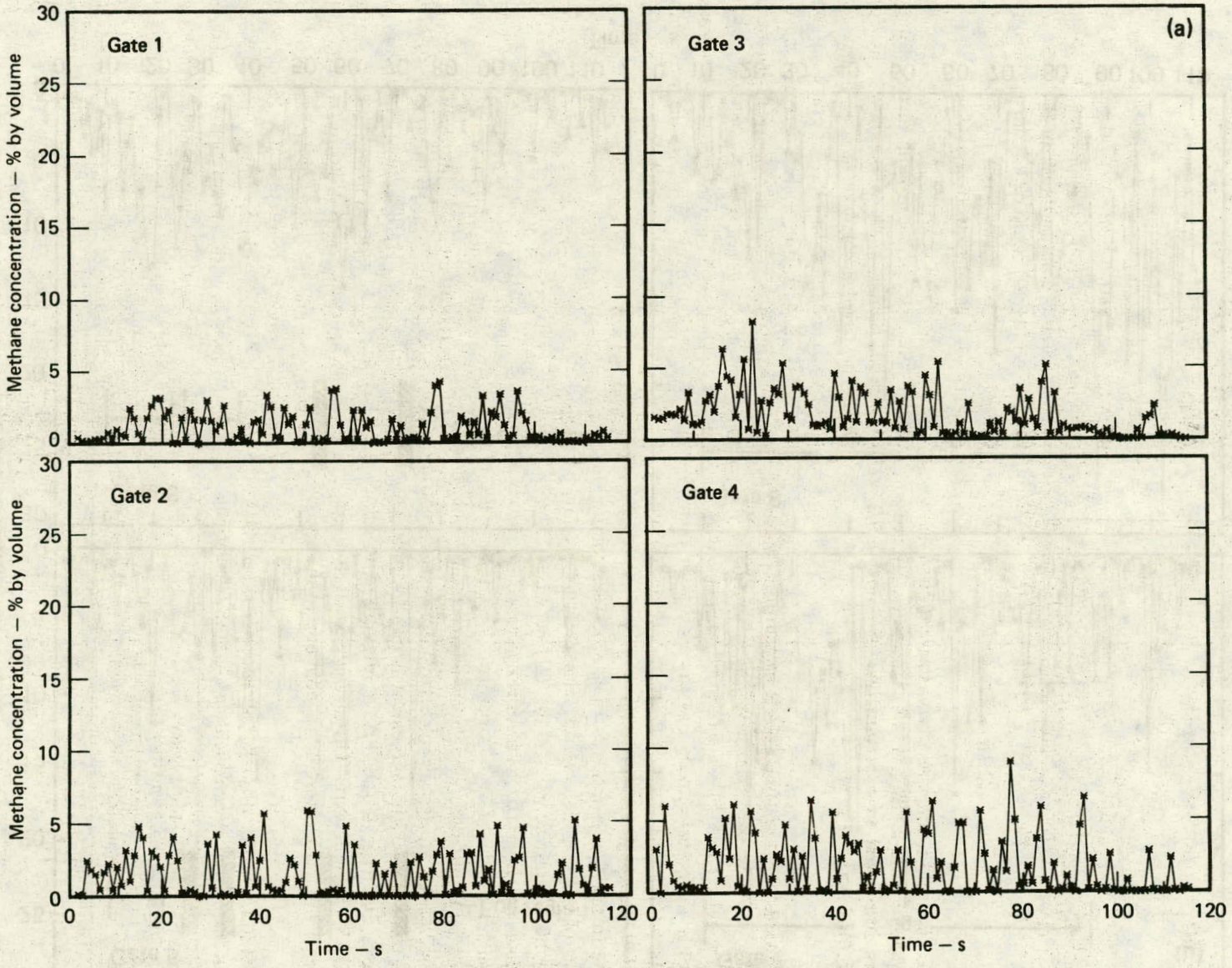

FIG. 17. Methane concentrations vs time in LIDAR range gates. (a) Gates 1, 2, 3, 4. (b) Gates 5, 6, 7, 8.

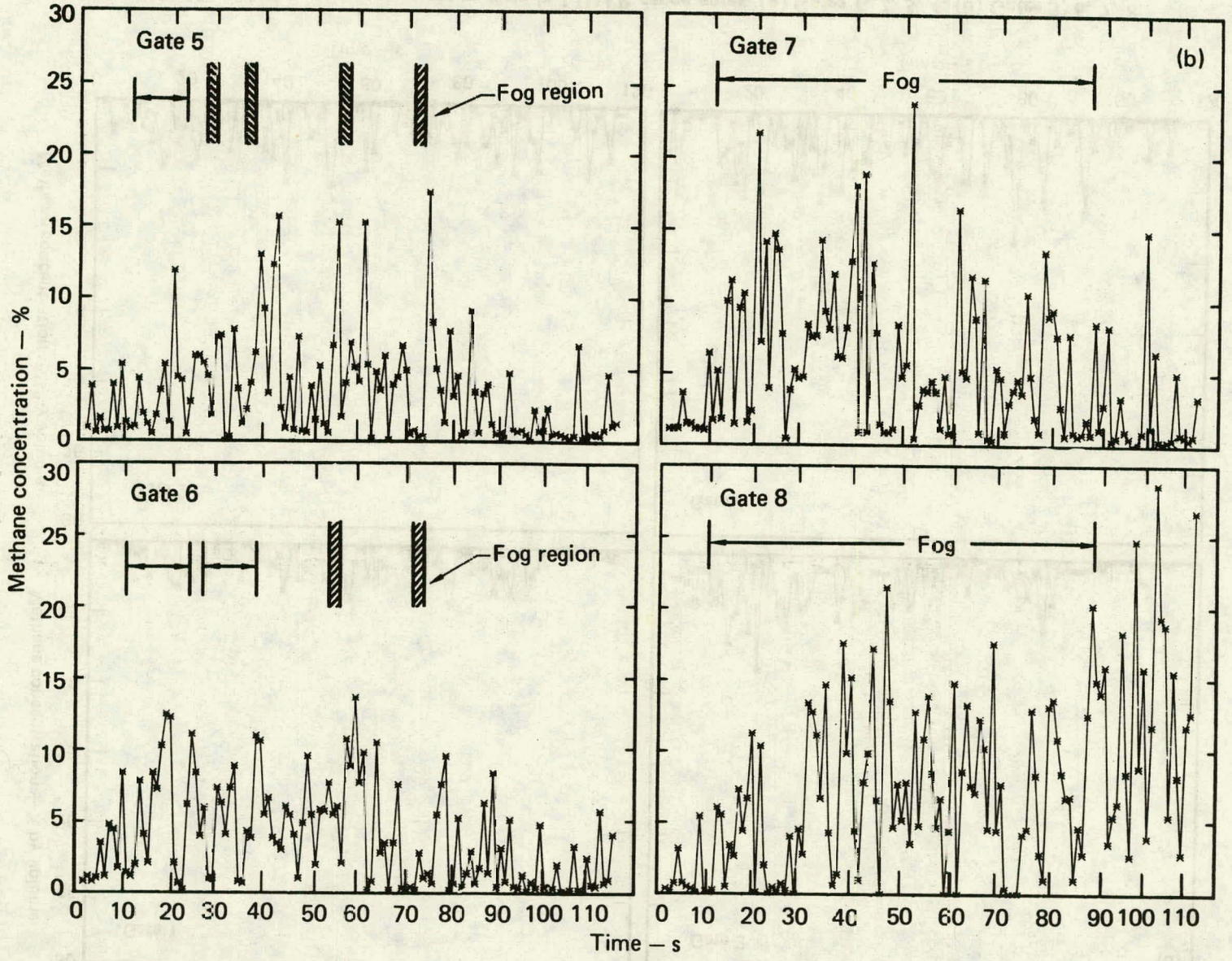

FIG. 17. (Continued)

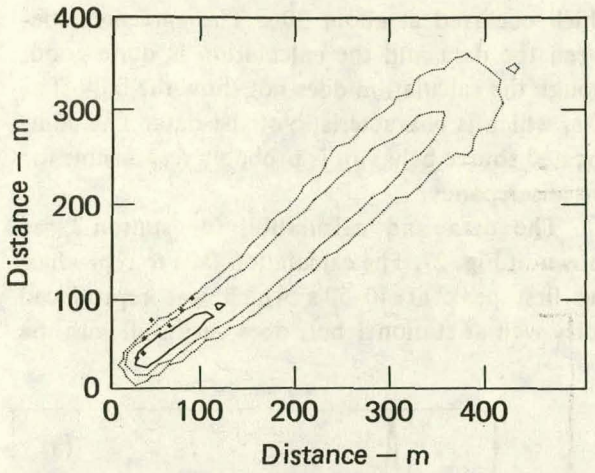

FIG. 18. Concentration isopleths of Avocet-3 plume at 50-s. The contours correspond to concentrations of 0.654, 6.54, 32.7, 98.0, 196 g/m^3.

The observation that the calculated concentrations tend to be somewhat lower than the measured concentrations might suggest an adjustment to the dispersion coefficient; however, the two-level measurement of concentration at station 6 indicates essentially the same value for the vertical dispersion coefficient as used for Avocet-1 and Avocet-2. A distinct difference between this experiment and the other three is the persistently higher wind speed and relatively constant wind direction; however, no apparent difference in cloud height is noted.

Data and calculation for station 8 are shown in Fig. 23. The peak at 40 s is well reproduced by the calculation whereas the later peaks are not. The MSA sensor proved to be sensitive to the high wind velocities (up to 14 m/s) that occurred during this experiment. That sensitivity is shown in Fig. 24. No gas was present at this station during the experiment, as confirmed by the grab samples, so all of the signal is due to wind. Wind probably also accounts for most of the signal seen in Fig. 23 after 80 s; however, grab sample results do show the presence of some gas. One must remember that there is a 5-s delay between the grab sampler results and the MSA output when comparing these two. The calculated maximum extent of the lower flammability limit is about 120 m from the spill point at about 50 s after the spill valve is opened.

AVOCET-4

This experiment showed evidence of behavior not observed in the previous three experiments. Initial attempts to do ATMAS calculations of this experiment showed significant disagreement with the experimental data. Examination of the film of the experiment and anemometer data taken on the spill pond showed that the wind speed on the pond dropped steadily to zero during the first 90 s of the spill, in addition to changing direction significantly. As the wind speed approached zero, the LNG vapor cloud spread farther over the water surface than had been observed in the other experiments. This may indicate an increase in LNG pool size but since no actual measurements of pool size or boil-off rate were made, it is not possible to determine directly what the vapor source parameters should be. For this calculation, an expanding pool was modeled crudely by turning on and off sources with successively larger areas as a function of time. The pool radius increased to a maximum of 15 m in an attempt to approximate the observed extent of the pool spread. The rate per unit area remained constant such that the total vapor evolution rate increased with time. The calculated plume at 10-s intervals is shown in Figs. 25a through 25o. As in Avocet-1, the wind came more from the south-southeast during the early part of the experiment, shifting to the south-southwest at about 40 s.

The meteorological stations for this experiment were at the same location as for Avocet-3. Table 6 gives the mean and standard deviations of the wind speed and wind direction for these stations. The maximum and minimum wind speeds encountered during the experiment were 5.3 m/s and 1.07 m/s

TABLE 5. Average and standard deviations in wind speed and direction for Avocet-3 for time interval 0 - 125 s.

Station	Speed (m/s)	Standard deviation of speed (m/s)	Direction (deg)	Standard deviation of direction (deg)
9	7.92	1.35	235.3	9.07
10	5.77	0.81	221.3	9.44
11	10.61	1.54	232.3	9.06

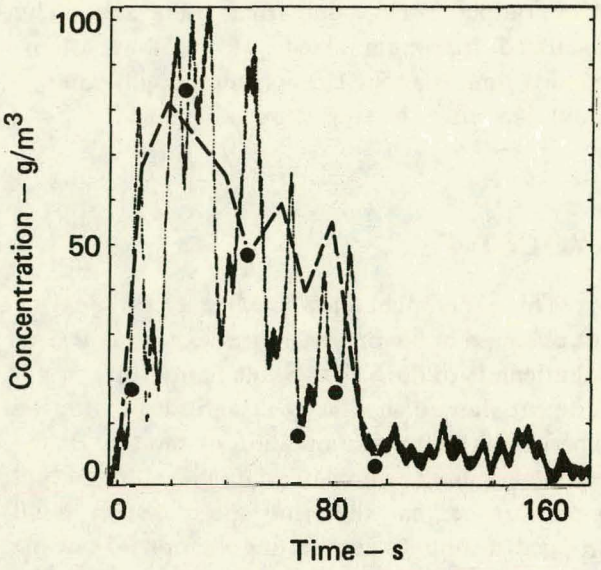

FIG. 19. Avocet-3 concentration vs time at station 1. Continuous data from SHELL1C (dots), grab samples (●), and ATMAS calculation (——).

respectively. The wind direction, averaged for 10 s, varied from 150° to 208°, relative to magnetic north at different stations.

Data from the Shell sensor and grab sampler at station 1 and the ATMAS calculation are shown in Fig. 26. The very high peak concentration measured by the Shell sensor is verified by the grab sampler and must be due to the change in wind direction,

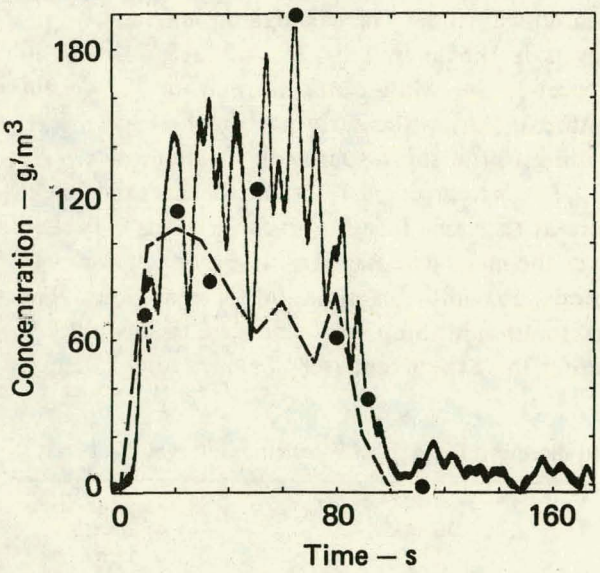

FIG. 20. Avocet-3 concentration vs time at station 2 from SHELL2C (dots), grab samples (●), and ATMAS calculation (——).

which occurred at about 30 s. The agreement between the data and the calculation is quite good, though the calculation does not show the fall-off at 60 s, which is characteristic of the data. The complicated source behavior is probably responsible for this discrepancy.

The data and calculation for station 2 are shown in Fig. 27. The calculation fails to reproduce the first peak at 40–50 s which was reproduced fairly well at station 1 but, does very well with the

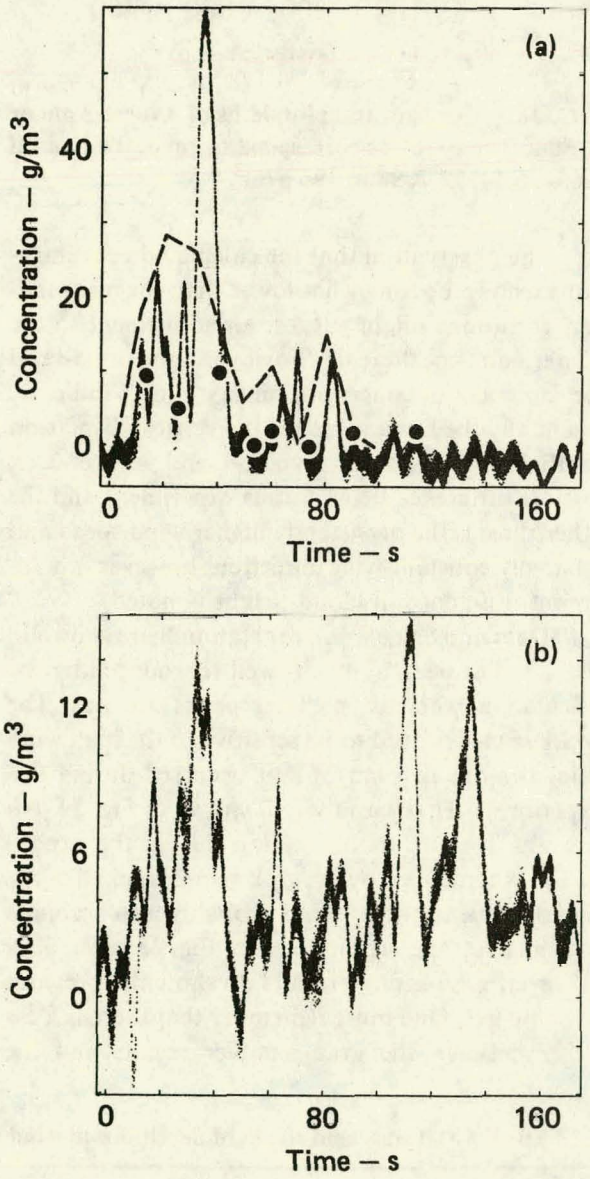

FIG. 21. Avocet-3 concentration vs time at station 4. (a) Methane concentration 1-m level from IR4-MC (dots), grab samples (●), and ATMAS calculation (——). (b) Ethane concentration from IR4-EC.

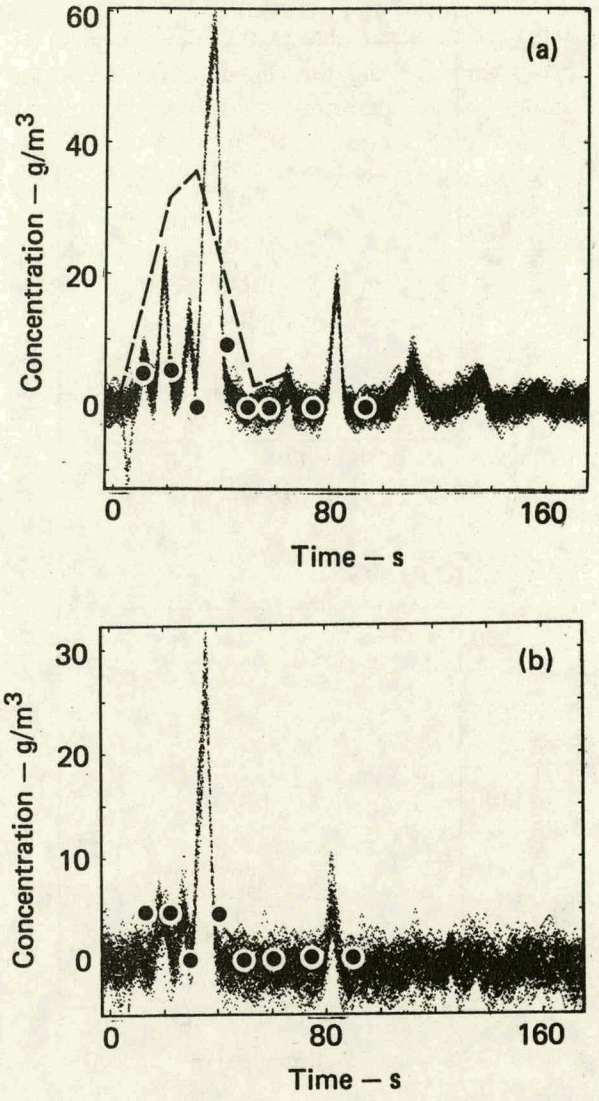

FIG. 22. Avocet-3 concentration vs time at station 6. (a) 1-m level from TSI1A6C (dots), grab samples (●), and ATMAS calculation (——). (b) 2.4-m level from TSI2A6C.

second peak at 90 s, which was not observed at station 1. The peak at 90 s was probably due to the dramatic drop in wind speed and shift in direction that occurred at that time. The stations on the water (1 and 2) were sensitive to changes in the vapor source size and rate. In addition, it appears that the source parameters were in turn sensitive to changes in wind speed and direction. The grab sampler at this station failed to operate properly.

Data from the TSI sensors and grab samplers at station 3 at the 1- and 2.4-m levels are shown in Figs. 28a and 28b, respectively. The ATMAS calculation for the 1-m level is also shown in

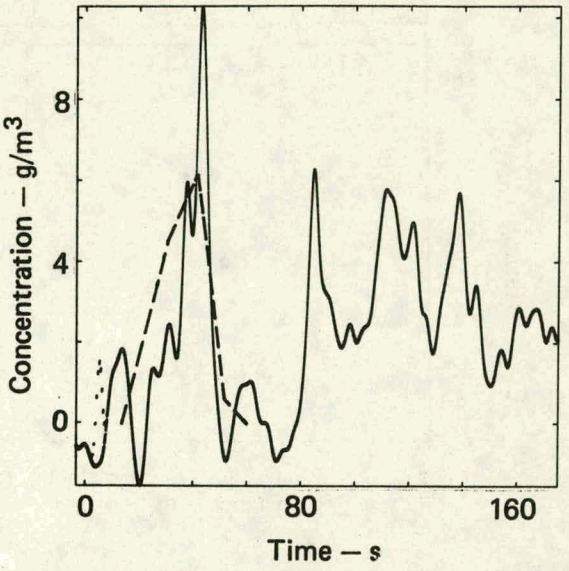

FIG. 23. Avocet-3 concentration vs time at station 8 from MSA (dots) and ATMAS calculation (——).

Fig. 28a and, as with station 2, missed the first peak, but did reproduce a second major peak at 90 s. This second peak appeared more dramatically at the 2.4-level, shown in Fig. 28b.

Data from the Anarad IR gas sensor at station 4 for methane, ethane, and propane are shown in Figs. 29a, 29b, and 29c, respectively. The grab sample data are also plotted and show good agreement with the gas sensor output. The ATMAS

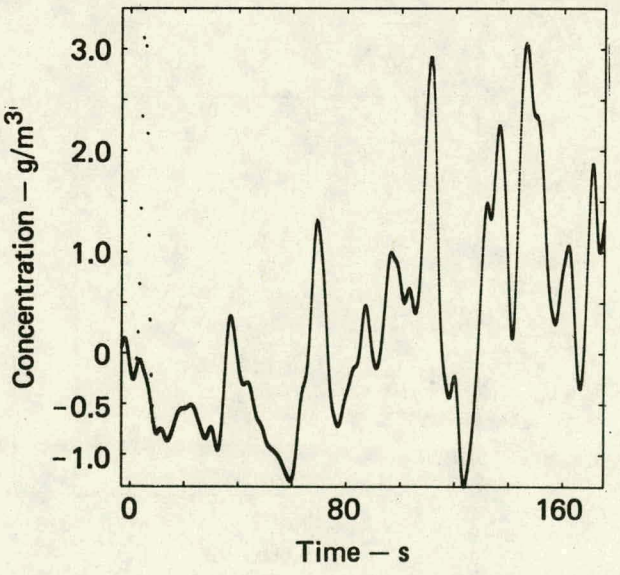

FIG. 24. Avocet-3 concentration vs time at station 7 from MSA. ATMAS showed zero concentration at this station.

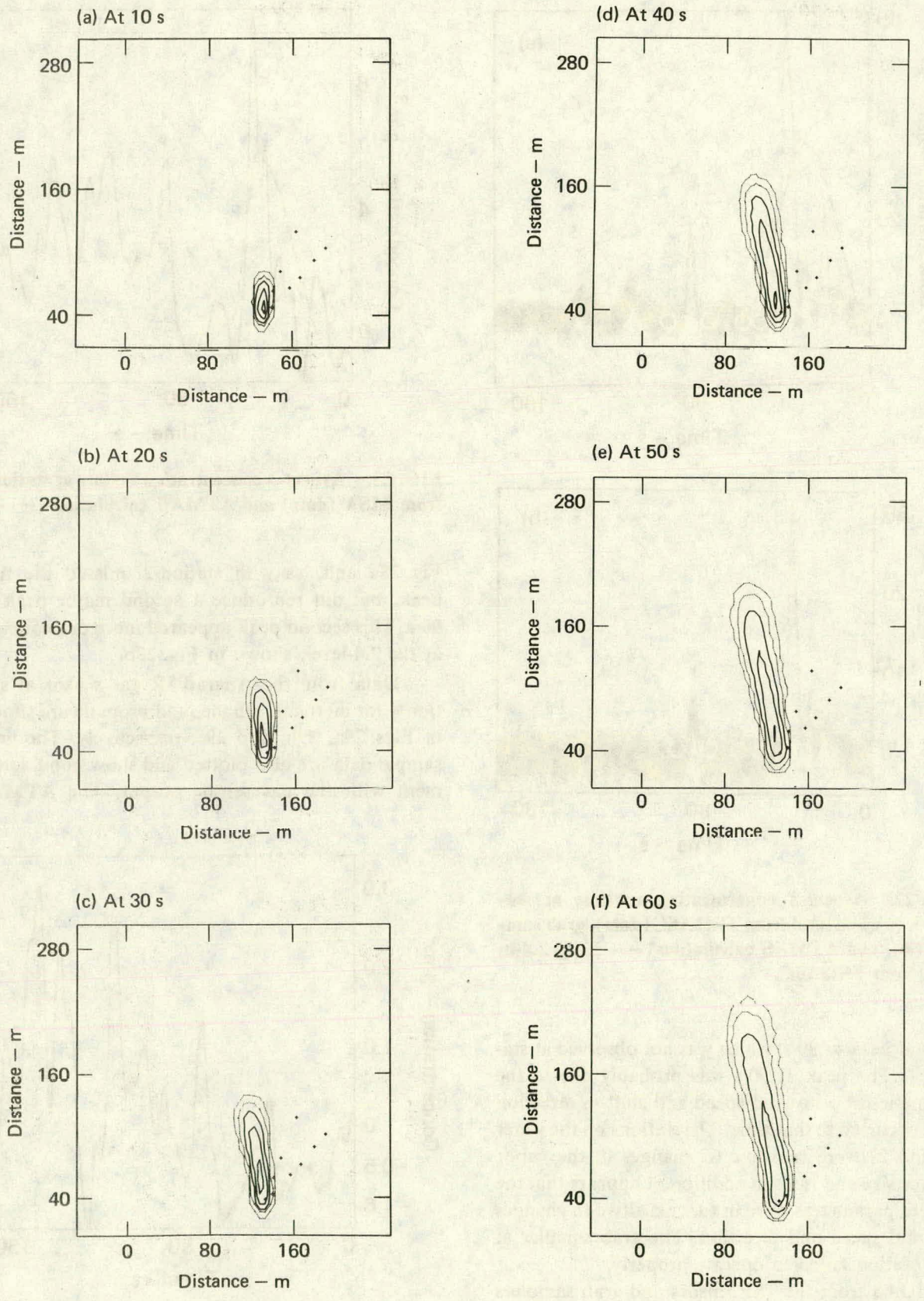

FIG. 25. Concentration isopleths at various times for Avocet-4 plume. The contours correspond to concentrations of 0.617, 6.17, 30.8, 92.5, and 185 g/m^3.

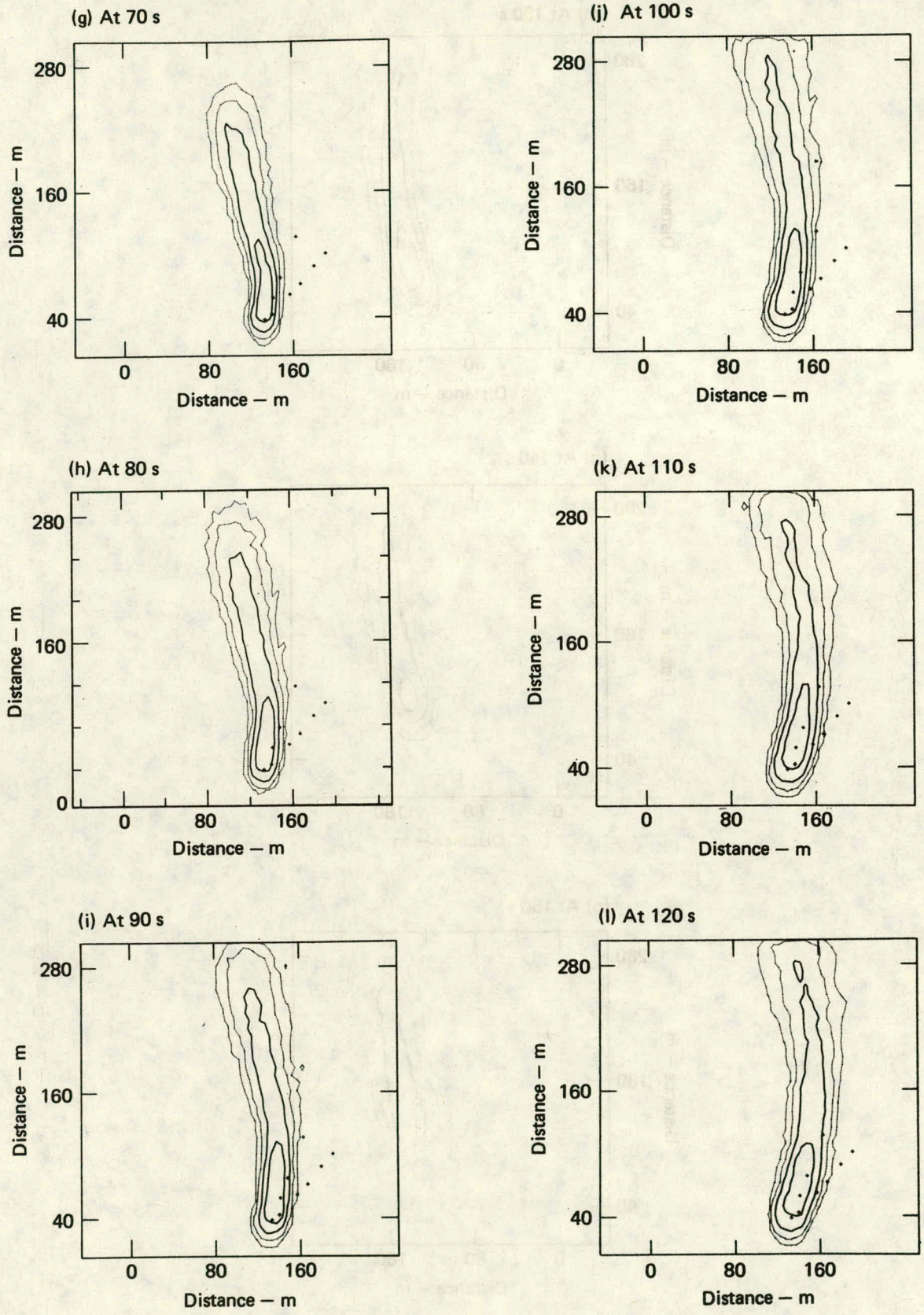

FIG. 25. (Continued)

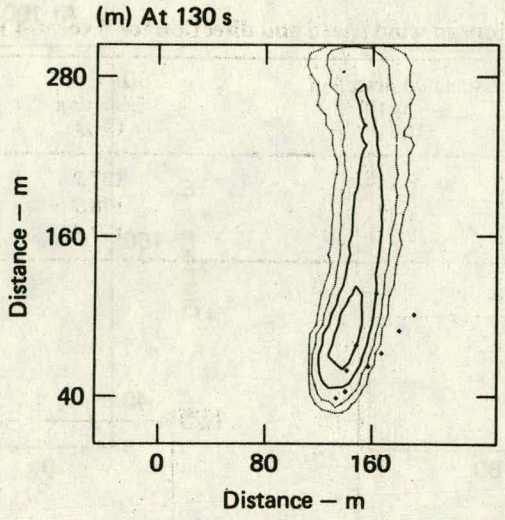

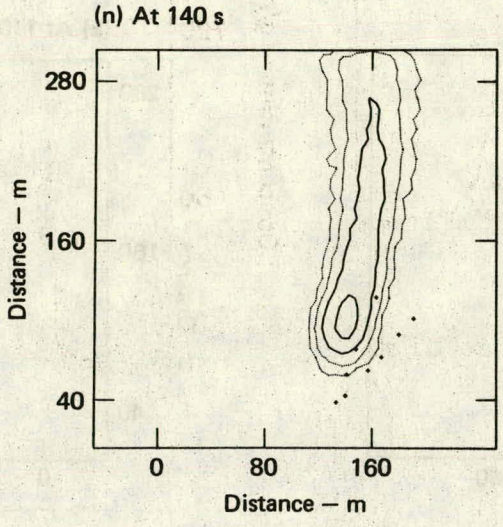

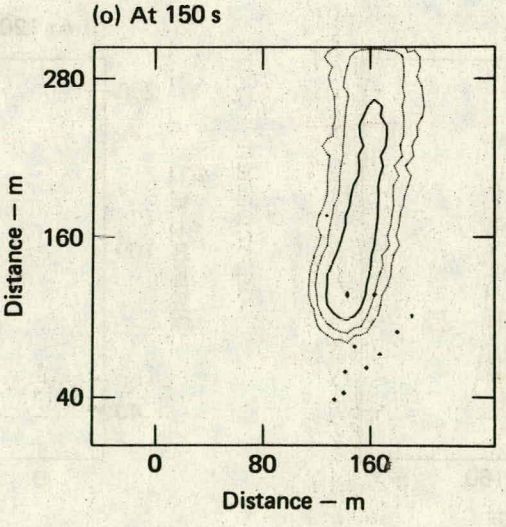

FIG. 25. (Continued)

TABLE 6. Average and standard deviations in wind speed and direction for Avocet-4 for time interval 0 - 125 s.

Station	Speed (m/s)	Standard deviation of speed (m/s)	Direction (deg)	Standard deviation of direction (deg)
9	2.83	0.72	187.2	14.6
10	1.91	0.84	178.9	18.4
11	4.12	0.57	177.0	10.5

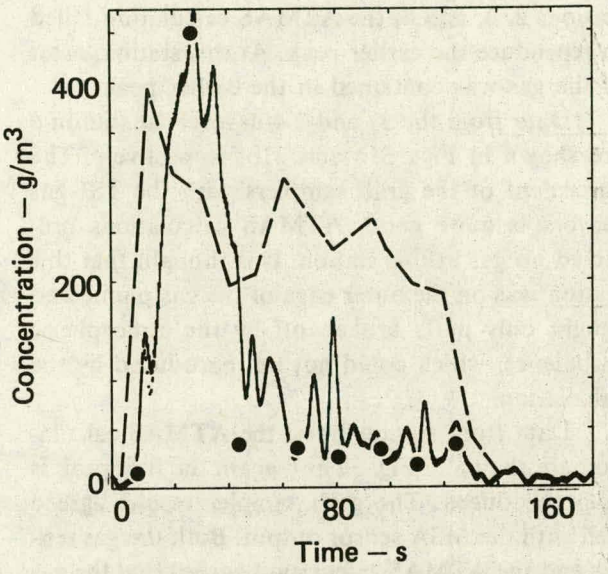

FIG. 26. Avocet-4 concentration vs time at station 1. Continuous data from SHELL1C (dots), grab samples (●), and ATMAS calculation (——).

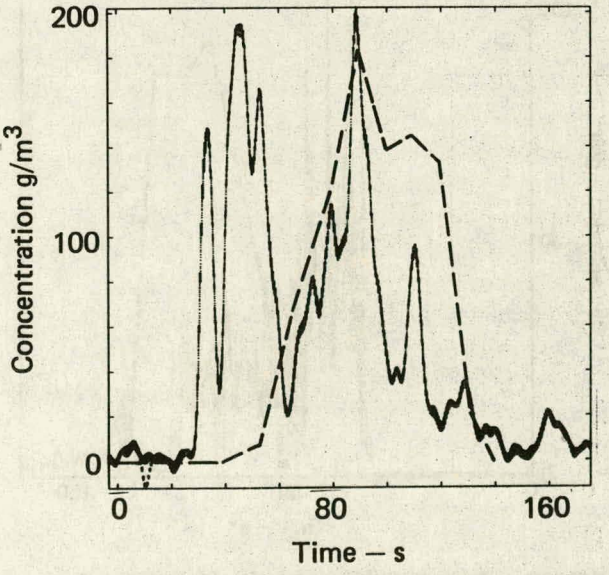

FIG. 27. Avocet-4 concentration vs time at station 2 from SHELL2C (dots) and ATMAS calculation (——).

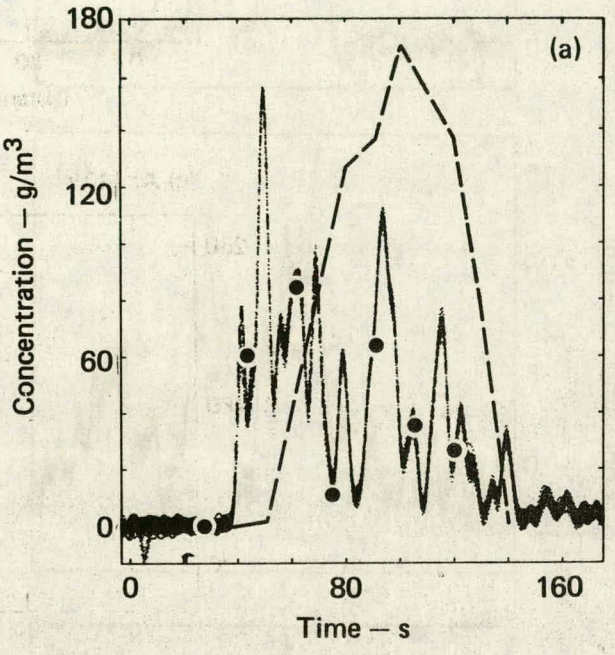

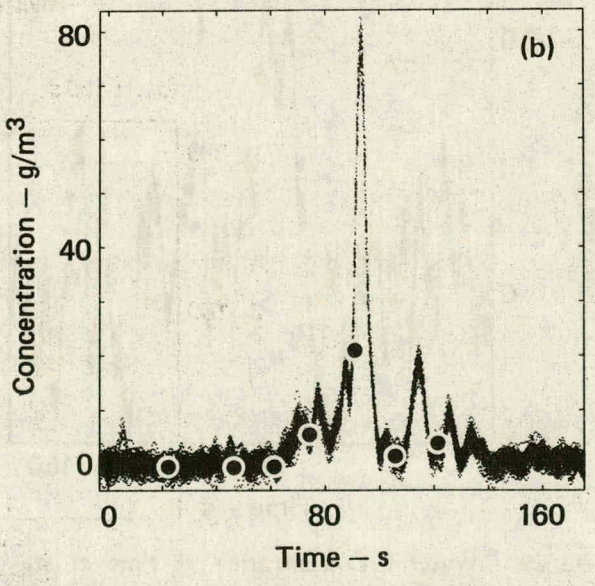

FIG. 28. Avocet-4 concentration vs time at station 3. (a) 1-m level from TSI1A3C (dots), grab samples (●), and ATMAS calculation (——). (b) 2.4-m level from TSI2A3C.

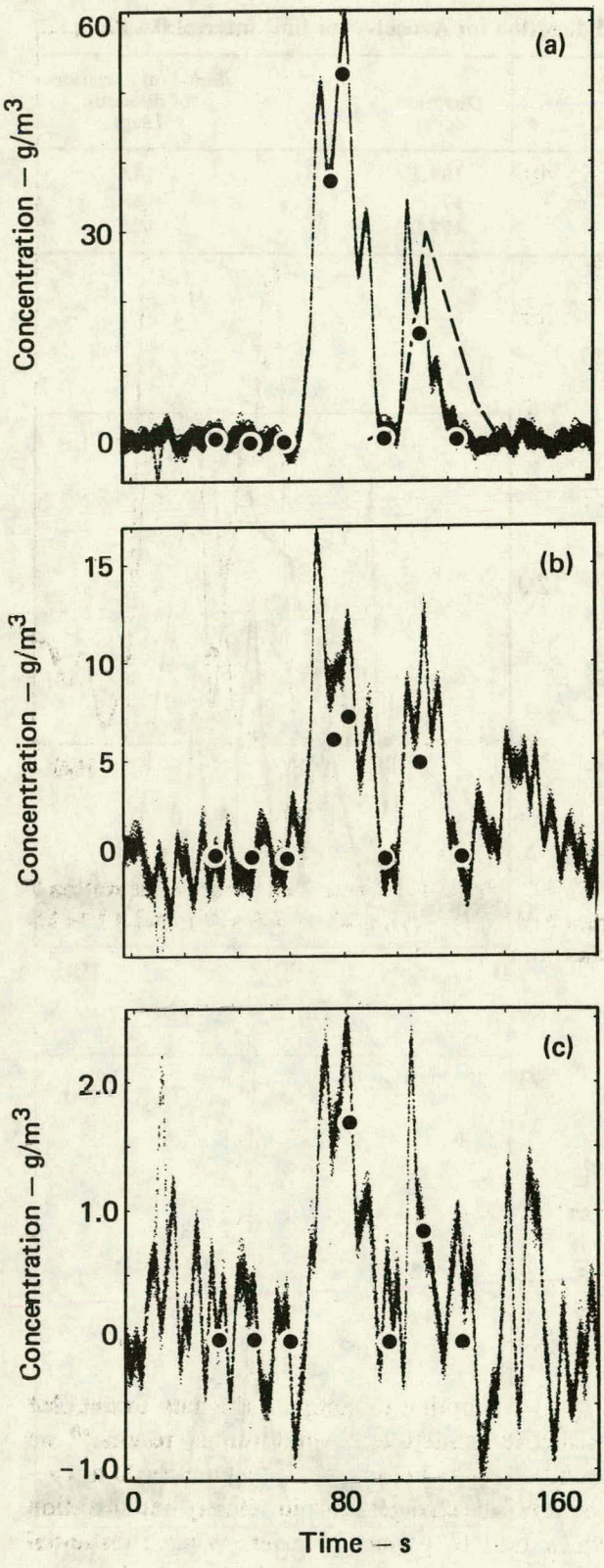

FIG. 29. Avocet-4 concentration vs time at station 4. (a) Methane concentration from IR4-MC (dots), grab samples (●), and ATMAS calculation (——). (b) Ethane concentration from IR4-EC. (c) Propane concentration from IR4-PC.

calculation for methane is shown in Fig. 29a, and, as at stations 2 and 3, does not reproduce the first peak, which appears to be due to a wind shift on the pond at about 30 s. The calculation does reproduce the second peak, which arrived at this station at about 110 s.

The LLL-IR sensor worked well on this test and produced the data shown in Fig. 30. Agreement with the grab samplers was quite good, but as with stations 2, 3, and 4, the ATMAS calculation failed to reproduce the earlier peak. At this station, most of the gas was contained in the earlier peak.

Data from the 1- and 2.4-m levels at station 6 are shown in Figs. 31a and 31b, respectively. The agreement of the grab samplers with the TSI gas sensors is quite good. ATMAS calculations predicted no gas at this station. It is thought that this station was on the outer edge of the gas plume and caught only puffs broken off by the atmospheric turbulence, which could not be reproduced by the calculation.

Data from station 7 and the ATMAS calculation are shown in Fig. 32 and again the first peak is not reproduced. The grab sampler results agreed well with the MSA sensor output. Both the gas sensor and the ATMAS calculation agreed that the gas cloud missed station 8.

The maximum distance to the lower flammability limit was calculated to be about 240 m from the spill point for this test.

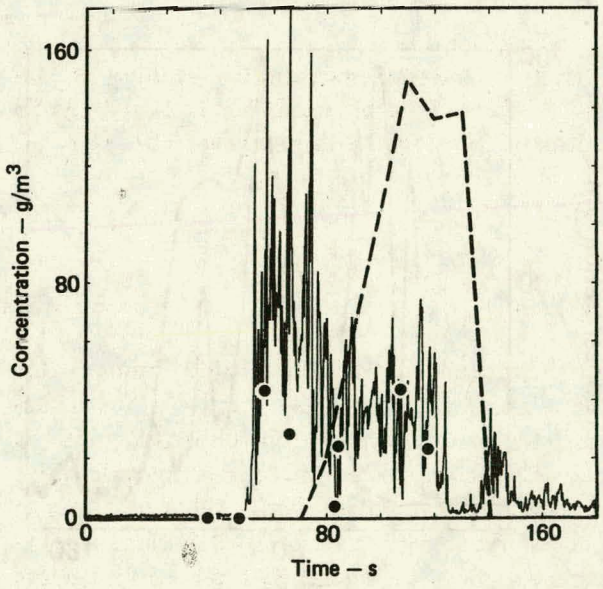

FIG. 30. Avocet-4 concentration vs time at station 5 from LLL-IR sensor (dots), grab samples (●), and ATMAS calculation (——).

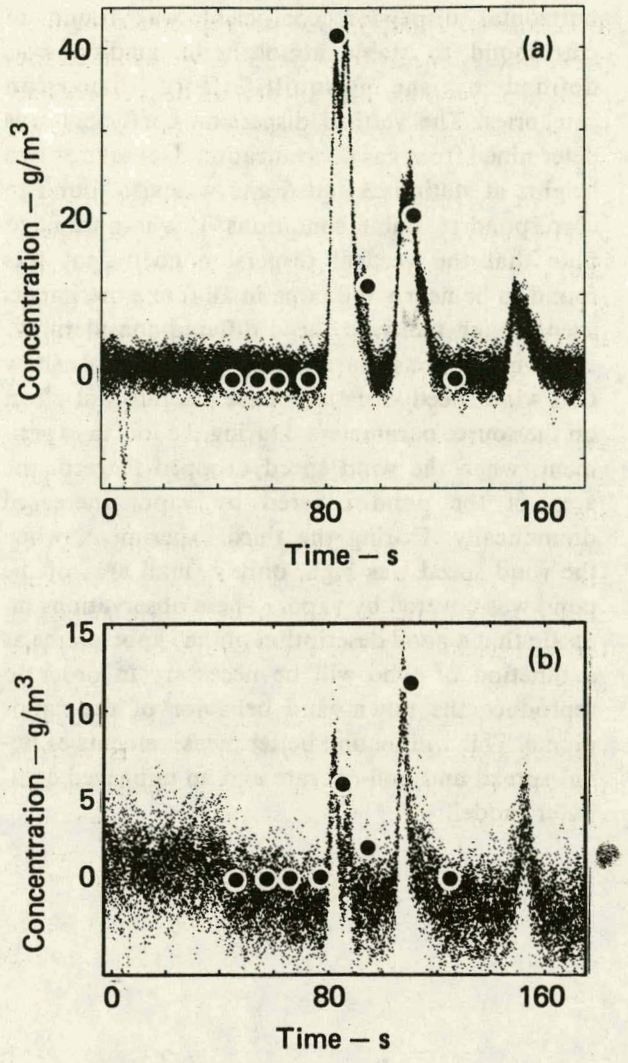

FIG. 31. Avocet-4 concentration vs time at station 6. (a) 1-m level from TSI1A6C. ATMAS calculated zero. (b) 2.4-m level from TSI2A6C.

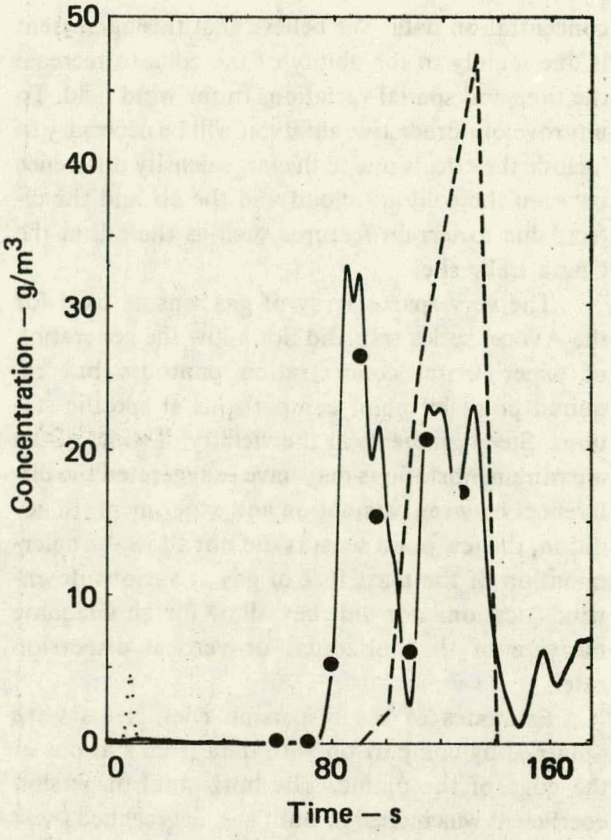

FIG. 32. Avocet-4 concentration vs time at station 7 from MSA7C (dots), grab samples (●), and ATMAS calculation (——).

CONCLUSIONS

These experiments were intended primarily for the evaluation of gas sensors and were used successfully for this purpose. In addition, the data has been used to try to learn more about the dispersion process and what measurements will be necessary to understand dispersion from larger spills. These experiments have shown clearly the need for a large array of instruments to measure both the gas concentration and the wind field. Therefore, we are building just such an array for the 1980 40-m^3 spill experiments.

In attempting to compare the data to detailed predictive models and wind tunnel results,[10] we found difficulty because these techniques do not account for the changes in wind velocity and direction which lead to plume meander. When substantial plume meander does occur during an experiment, as it did in three out of four of the experiments reported here, it becomes necessary to use a transport code that includes wind field variations.

Our first attempt shows promise in that, in general, the ATMAS predictions conformed to the

concentration data. We believe that this agreement is due mainly to the ability of the code to recreate the time and spatial variations in the wind field. To improve our predictive ability, it will be necessary to include the effects due to the large density difference between the cold gas cloud and the air and the effects due to terrain features such as the hill at the China Lake site.

The very sparse array of gas sensors used for the Avocet series tests did not allow the generation of experimental concentration contours but required point by point comparisons at specific stations. Steep gradients in the vicinity of some of the measurement stations may have exaggerated the differences between calculation and experiment. In addition, the few point sensors did not allow the determination of the mass flux of gas at various down wind locations nor did they allow for an adequate measure of the horizontal or vertical dispersion rate.

Estimates of the dispersion coefficients were obtained by comparison with data from stations at the edge of the plume. The horizontal dispersion coefficient was increased until gas just reached these stations at the plume edge. Using this approach, the horizontal dispersion coefficient was found to correspond to stable atmospheric conditions as defined by the Pasquill-Gifford dispersion categories. The vertical dispersion coefficient was determined from gas concentration data take at two heights at stations 3 and 6 and was also found to correspond to stable conditions. It is important to note that the vertical dispersion coefficient was found to be nearly the same in all four experiments even though the wind speed differed considerably.

Observations, particularly on Avocet-4, show that wind speed variations have a significant effect on the source parameters. During the fourth experiment, when the wind speed dropped to zero, the area of the pond covered by vapor increased dramatically. During the third experiment, when the wind speed was high, only a small area of the pond was covered by vapor. These observations indicate that a good description of the vapor source as a function of time will be necessary in order to reproduce the down-wind behavior of the vapor plume. This will require better measurements of liquid spread and boil-off rate and an improved computer model.

REFERENCES AND NOTES

1. *Liquefied Gaseous Fuels Safety and Environmental Control Assessment Program: A Status Report,* U.S. Dept. of Energy, Assistant Secretary for Environment, Division of Environmental Control Technology, DOE/EV-0036, May, 1979, Report K.
2. These four tests are part of a series of tests conducted at the Naval Weapons Center. In this series they are identified as LNG-18 to LNG-21.
3. G. E. Bingham, C. H. Gillespie, J. H. McQuaid, *Development of a Miniature, Rapid-Response Carbon Dioxide Sensor,* Lawrence Livermore Laboratory, UCRL-52440 (1978).
4. D. L. Ermak, R. A. Nyholm, R. Lange, *ATMAS: A Three Dimensional Atmospheric Transport Model to Treat Multiple Area Sources,* Lawrence Livermore Laboratory, UCRL-52603 (1978).
5. A. A. Amsden, *The Particle-In-Cell Method for the Calculation of the Dynamics of Compressible Fluids,* Los Alamos Scientific Laboratory, Los Alamos, NM, LA-3466 (1966).
6. R. Lange, "ADPIC - A Three-Dimensional Particle-In-Cell Model for the Dispersal of Atmospheric Pollutants and Its Comparison to Regional Tracer Studies," *App. Meteor.* **17**, 320–329 (1978).
7. R. Lange, *PATRIC-A Three Dimensional Particle-In-Cell Sequential Puff Code for Modeling the Transport and Diffusion of Atmospheric Pollutants,* Lawrence Livermore Laboratory, UCID-17701 (1978).
8. S. Chandrasekhar, "Stochastic Problems in Physics and Astronomy," *Rev. Mod. Phys.* **15**, 1-89 (1943), see also pp. 24–25, 40–41.
9. *Liquefied Gaseous Fuels Safety and Environmental Control Assessment Program: A Status Report,* U.S. Dept. of Energy, Assistant Secretary for Environment, Division of Environmental Control Technology, DOE/EV-0036, May 1979, Report A.
10. D. E. Neff, R. N. Meroney, "Dispersion of Vapor from LNG Spills—Simulation in a Meteorological Wind Tunnel of Spills at China Lake Naval Weapons Center, California," Colorado State University, Wind Engineering Program, March 1979.

REPORT Q

Experimental Plan for 40-m^3 Liquefied Natural Gas (LNG) Dispersion Tests

R. P. Koopman

Prepared for the
Environmental and Safety Engineering
Division
U.S. Department of Energy
under Contract W-7405-ENG-48

Lawrence Livermore Laboratory
Livermore, California 94550

THIS PAGE

WAS INTENTIONALLY

LEFT BLANK

PREFACE

The development of this experimental plan has been a cooperative effort and includes the contributions of many people both inside and outside of LLL. It evolved through a series of group discussions within the LLL LGF Program and was supplemented by input from C. D. Lind on the China Lake facility, J. M. Conley on the JPL infrared sensor, and W. Ginsberg on the EG&G infrared imaging overflights.

THIS PAGE

WAS INTENTIONALLY

LEFT BLANK

REPORT Q

TABLE OF CONTENTS

FIGURES

TABLES

SUMMARY

An experimental team from the Lawrence Livermore Laboratory (LLL) will soon begin a series of liquefied natural gas (LNG) experiments at the Naval Weapons Center (NWC), China Lake, California. These experiments will involve spilling $40m^3$ of LNG onto a pond and measuring the characteristics of the gas plume as it disperses downwind. A large array of instruments has been developed to make measurements of gas concentration, temperature, humidity, wind velocity, and heat balance and to telemeter the data back to a data recording trailer. Experiments will be performed for various wind speeds and various spill rates over a five-month period.

INTRODUCTION

In May of 1980 a Lawrence Livermore Laboratory (LLL) experimental team will begin a series of dispersion experiments at the Naval Weapons Center (NWC) liquefied gaseous fuels spill facility at China Lake, California. These experiments, along with an earlier series on pool fires and a later series on vapor burns, are a joint effort between LLL and NWC personnel. The LLL team assumes leadership for the vapor generation and dispersion experiments and the NWC team for the pool fires and vapor burn experiments. This report contains the LLL plan for the vapor generation and dispersion experiments.

These experiments are part of a larger Department of Energy (DOE) program to assess safety problems associated with liquefied gaseous fuels, beginning with liquefied natural gas (LNG). The field program consists of a series of spill experiments, starting at 40-m^3 and increasing as necessary to satisfy the program goals. The hallmark of the program is the close coupling between the experimental work and the computer and physical modeling. To insure close coupling occurs, it is necessary to intensively instrument the experiments so that sufficient quantitative data are gathered to gain an understanding of the relative importance of the various physical phenomena occurring and to make detailed comparisons with computer and wind tunnel models. The results of this combined experimental and analytical approach are computer models that contain the physics important to LNG dispersion and that have been verified by detailed comparison with experiments over a range of spill sizes. Some of the experiments discussed here are designed to provide answers directly, and some provide answers only when coupled with computer model calculations.

We currently believe that 40-m^3 spill experiments represent a minimum size at which the dispersing LNG vapor cloud is expected to have an influence on the atmospheric boundary layer resembling that of a large spill. The experiments are designed to investigate this effect by measuring those quantities that either indicate the amount of dispersion occurring as a function of time and distance or those that

indicate the physical phenomena influencing the dispersion. More specifically, a major goal of the experimental program is to measure gas concentrations downwind of the spill point, which is done for a series of wind speeds and stability conditions, spill sizes, and spill rates. This requires a detailed knowledge of the wind field in which the vapor is dispersing. Measurement of gas concentrations close to the spill point will be used to characterize the vapor source early in the experimental series. Later, direct measurements on the pool itself will be made.

Concentration fluctuations will be examined as a function of downwind distance and atmospheric conditions. The significance of these fluctuations on the flamability of the cloud will be addressed. Our earlier work at China Lake indicates that the high density of the cold cloud may inhibit vertical mixing, which is an important effect that will be investigated further. The overall energy balance of the cloud also affects its dispersal. Measurement of heat flux, temperature, and water content will be used to determine this energy balance. Our earlier work has also determined that the last vapor to boiloff is significantly enriched in heavy hydrocarbons, and the upcoming experiments will determine the persistence of this enriched region downwind.

DATA REQUIREMENTS

GAS CONCENTRATION

Gas concentration measurements constitute the backbone of the experimental program. They are needed to determine the characteristics of the dispersing cloud for comparison with model calculations. The measurements must be extensive, so that three-dimensional concentration contours may be reconstructed from the data. This does not require fast instrument response. Current plans call for 25 of the 30 stations to make measurements that are averaged over 1 to 5 seconds and used for plume definition. To determine the effect of turbulence induced mixing and to examine concentration fluctuations near the flammability limit, fast response (5-10 samples/second) measurements will be made at five of the 30 stations.

The need to be able to reconstruct the gas cloud requires an extensive array of gas sensors. The sensor array will be laid out in such a manner that the entire mass of gas passing through each radial arc of sensors can be determined as a function of time. Figure 1 shows the initial instrument array for these tests with calculated plume contours superimposed upon it for a 30 m^3 per minute spill. (The two furthest upwind anemometer stations at 600 meters

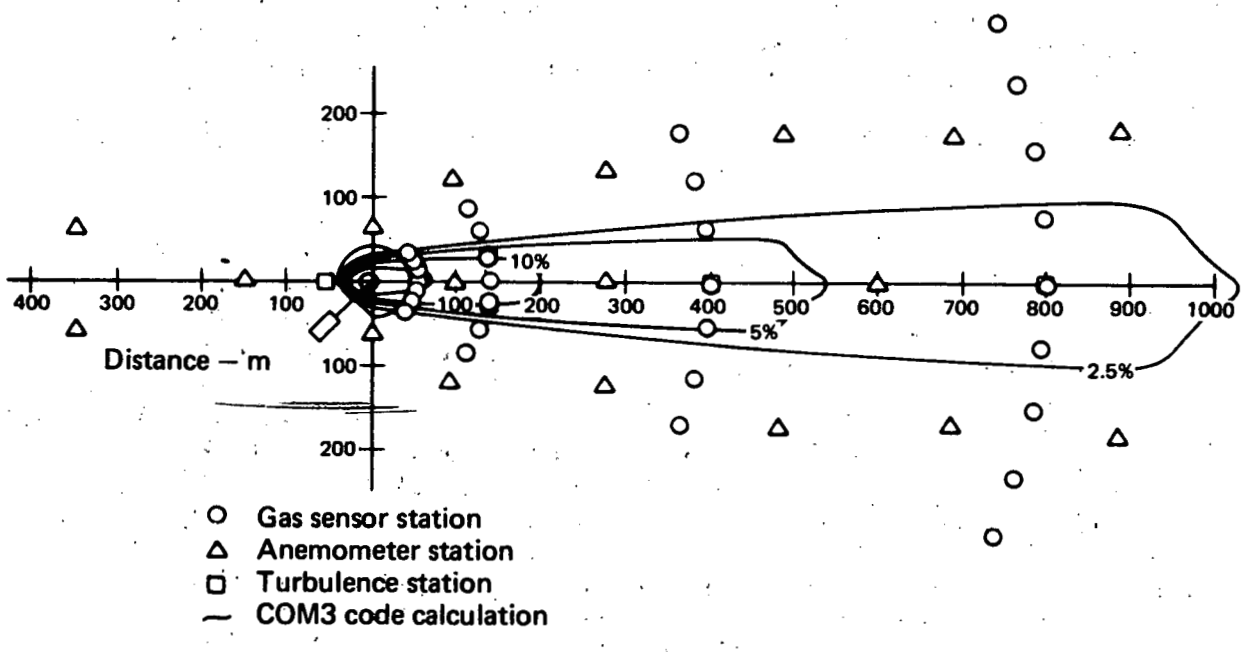

FIG. 1. Far field dispersion array for 40-m^3 spill tests at China Lake.

and 800 meters are not shown in this figure.) To measure the vertical dimension of the dispersing LNG plume, each station will have gas sensors at three vertical locations, up to a maximum height of 10 meters. Figure 2 shows the vertical dimension of the instrument array with calculated concentration profiles for a 30 m^3 per minute spill superimposed.

As the LNG evaporates, the remaining liquid becomes increasingly rich in the higher boiling temperature, heavier hydrocarbons. These boiloff after the methane and produce an enriched region of the vapor cloud. To track this enriched region downwind, gas sensors capable of distinguishing between methane, ethane, and propane will be used. It should not be necessary for all of the gas sensors to be capable of separating the hydrocarbon species. Current plans call for only some of the instruments in each arc to have this capability.

TEMPERATURE AND HEAT FLUX

Temperature measurements will be needed for model/data comparisons, since some code calculations are done in terms of mass fraction and the experimental measurements in terms of volume fraction. The temperature measurements will also help us to understand the heating of the cloud as it disperses downwind. It is important that all heat transfer into and out of the cloud be understood, since it will contribute to the dispersion and the lower flamability limit (LFL) distance by changing the buoyancy. Temperature also serves as an indicator of the presence of the cold gas. If adiabatic mixing of the cold gas with the air and the condensation and freezing of the water vapor in the air were the only sources of heat input into the vapor cloud, then temperature could be related directly to the gas concentration. At present, it appears that this cannot be done. It may, however, still be possible to use temperature measurements to interpolate roughly between concentration measurements to better define the vertical concentration profile.

POOL SPREAD AND VAPOR GENERATION RATE

Measurements of maximum pool size have been made for spill volumes up to 10 m^3. Measurements of vaporization rate as a function of time have not been made for other than laboratory scale experiments. It is important, for realistic model predictions, that the time-dependent behavior of the vapor source be known. (This includes both pool radius and vaporization rate.) Ice formation may change

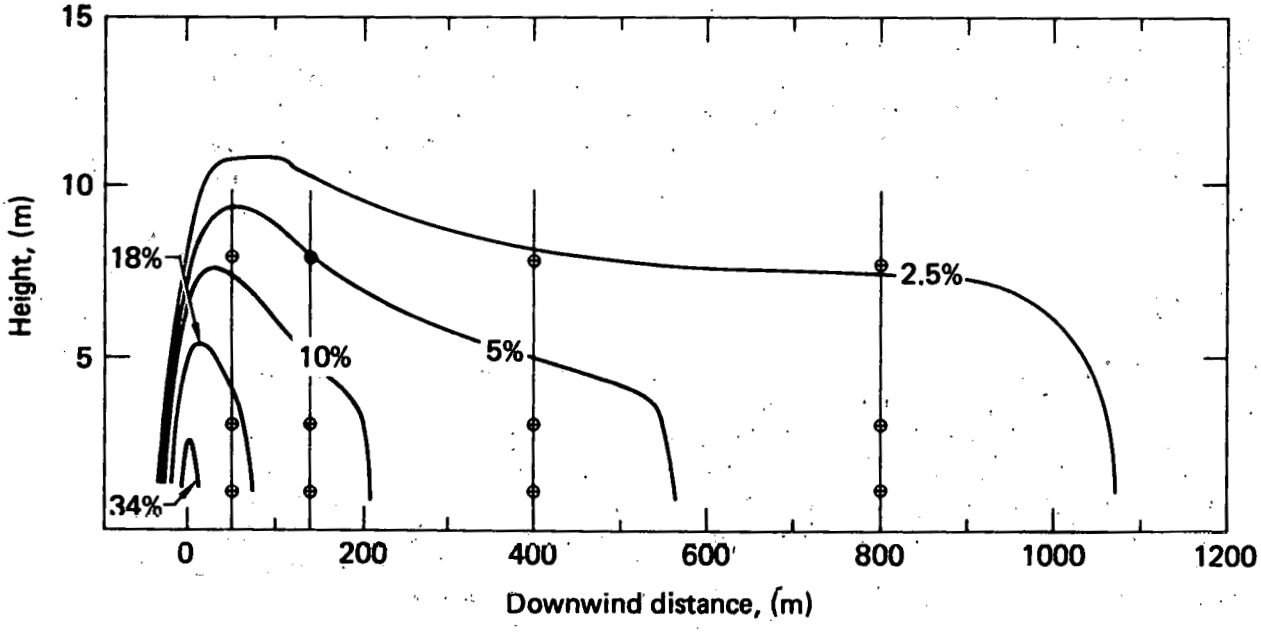

FIG. 2. Calculated vertical gas cloud profile with measurement stations shown.

the vapor generation rate with time or may simply change the effective pool area. Pool spread and vaporization rate are strongly dependent on spill rate and spill volume. Other important parameters are spill velocity and configuration, temperature, surface roughness of the spill pond, the composition of the LNG, and possibly wind velocity.

As soon as manpower becomes available, a program for measuring pool spread and vapor generation will be established. This will include the development of instruments for measuring LNG in the presence of dense clouds of LNG vapor and water droplets, both as a function of time and over an irregular area.

Vapor explosions are a means of generating a large vapor cloud in a very short time, and their study properly falls within this area. Only a very small effort, if any, will go into studying these at China Lake in FY-80. If they occur frequently, an effort will be made to determine how much energy is involved and how effectively the LNG is vaporized.

WIND FIELD

Wind provides the principal driving force for the dispersion of the gas. For small scale spill experiments the gas cloud is rapidly torn apart by atmospheric turbulence. For large scale experiments we expect the cold gas cloud to modify the atmospheric turbulence and to stay together in a more contiguous mass as it entrains air at its boundary and drifts downwind. There is some evidence that even for 5-m^3 spills the presence of the cold cloud may effect the atmospheric mixing, at least in the vertical direction.

Normal wind field fluctuations plus those induced by the complex terrain at the China Lake Site can be partially compensated for by carefully mapping the wind field in which the gas cloud disperses. This kind of information is necessary for comparing dispersion data with computer model calculations that do not include terrain features and variations in wind direction. To obtain this information it will be necessary to cover the area in which the gas cloud disperses with an array of approximately evenly spaced anemometers.

In addition to measurements of the wind field, it will be necessary to measure the rapid fluctuations associated with turbulence at a number of points within the dispersing cloud. The purpose of these measurements will be to characterize the normal atmospheric turbulence before the test, determine the effect of the cold gas cloud on this turbulence, and characterize the turbulence induced mixing of the gas with the air as the cloud passes.

Dispersion data for steady, low wind speeds and severe inversion conditions, where some dispersion codes predict the LFL distance to be the longest, do not exist. Wind tunnel tests also indicate that a steady 2-m/s wind may produce the maximum dispersion distance condition but have trouble at such a low wind speed. Our ability to take such data at China Lake is limited by safety requirements for the operation of the facility and by the infrequent occurrence of such conditions.

HUMIDITY

Condensation of water vapor in the air can provide a significant source of heat for the cold gas cloud. The amount of heat that can be transferred in this way depends on the amount of water vapor in the air. At the China Lake site the amount of water vapor in the air downwind of the spill pond may be significantly larger than upwind due to evaporation from the pond in the hot, dry desert conditions. There is also an indication that the spill process itself may add a significant amount of water to the gas plume. Comparison of data from last year's tests at China Lake with adiabatic mixing model calculations indicates a discrepancy that may be due to this added water vapor or some other source of heat input into the cloud. Since the ultimate dispersion distance is going to depend strongly on the amount of heat input, a serious attempt will be made to determine the source of the additional heat. This will involve temperature, heat flux, and radiometric measurements as well as humidity measurements within the dispersing gas cloud.

OPERATIONS

In addition to the dispersion and vapor generation data needs discussed in this report, there will be operational data requirements. The NWC team, as operators of the spill facility, will record the data concerned with the operation, such as spill volume, spill duration, LNG composition, and meteorological tower data. We will also rely on NWC to provide photographic coverage of the experiments similar to that provided last year. Since these tests are substantially larger than those done last year, however, some provision should be made to photograph further downwind so that a complete record of the dispersion of the visible cloud will be obtained.

INSTRUMENTS AND STATION REQUIREMENTS

GAS SENSORS

The requirements discussed in this section are based largely on our experience at China Lake last year. Most of the instruments considered were used in the field, and our ranking of the instrument strongly reflects the field experience. For the instruments not used in the field, the rankings are based on estimates obtained from comparison with similar instruments and from laboratory tests. A summary of the gas sensors we evaluated is given in Table 1.

Considering that the array of instruments will look like that shown in Figure 1, that the stations will look like those shown in Figure 3, and that some of the stations will have to be moved before each test to accommodate different experimental goals and shifts in the mean wind direction, we decided that the instruments and the stations should be portable and lightweight. In addition, since there will be 50 or more stations involved in the tests, it will be necessary that each instrument be easily calibrated or that the calibration be easily checked remotely and that the instrument be stable over periods of many days or weeks. The instruments must require only a minimum of maintenance.

Since the instrument stations may each be thousands of meters from the data acquisition trailer and from a source of power, we determined that power and data cables would be more costly than batteries and rf telemetry. The need for mobility also makes cables impractical. Battery-powered systems then become necessary, and they require that the instruments have low power consumption. This eliminates systems without miniaturized, low power, solid-state electronics (CMOS) and systems that depend on power-consuming pumps.

To keep the data rate within the range easily handled by rf telemetry and the computers, it may be necessary to do real time data processing within the stations or the sensors themselves to compress the data before shipping it back to the data acquisition trailer.

The nature of the dispersing cloud also adds requirements for the instruments. The cold cloud produced by the vaporizing LNG condenses essentially all of the atmospheric water vapor close to the spill pond. The instruments must be able to function within this very dense fog and must not be adversely affected by the cold gas associated with it. The fog causes problems for optical instruments and for instruments based on the thermodynamic or chemical properties of the gas. It appears that there are methods of dealing with these problems, more or less successfully, for most of the instruments evaluated.

TABLE 1. Gas sensor capabilities.

Sensor	Portability	Stability	Power Consumption	Response Time (sec)	Maintenance	Separate HC species	Fog, dust, temperature sensitivity	Cost[d]
TSI	Poor[c]	Good	High[c]	<0.1	Low	No	High	Med
MSA[a]	Good	Good	Low	5	Low	No	Low	Low
Shell	Poor	Poor	High	0.7	High	No	Low	(Med?)
ANARAD IR	Poor	OK	High	2-3	Low	Yes	High	High
LLL-IR (Bingham)	Good	Good	Low	0.2	Low	Yes	Low	High
IST[b]	Good	OK	Low	2-9	Low	No	Low	Low
LIDAR	Good	Good	High	0.1-1	?	Yes	High	High
MIT-LASER (Dewey)	Good	?	Low	<0.1	High	No	Low	High
JPL-LASER	Poor	?	High	<0.1	High	No	Low	High
JPL-IR	Good	?	Low	0.1	Low	Yes	High	High
Thermocouple	Good	Good	Low	0.1	Low	No	Low	Low
Grab sample	Poor	Good	High	0.6-10	High	Yes	Low	Med

[a] For concentrations below 10% only.
[b] For concentrations below 25% only.
[c] Miniaturized low power electronics now available.
[d] Low <$1000
Med <$5000
| >$5000

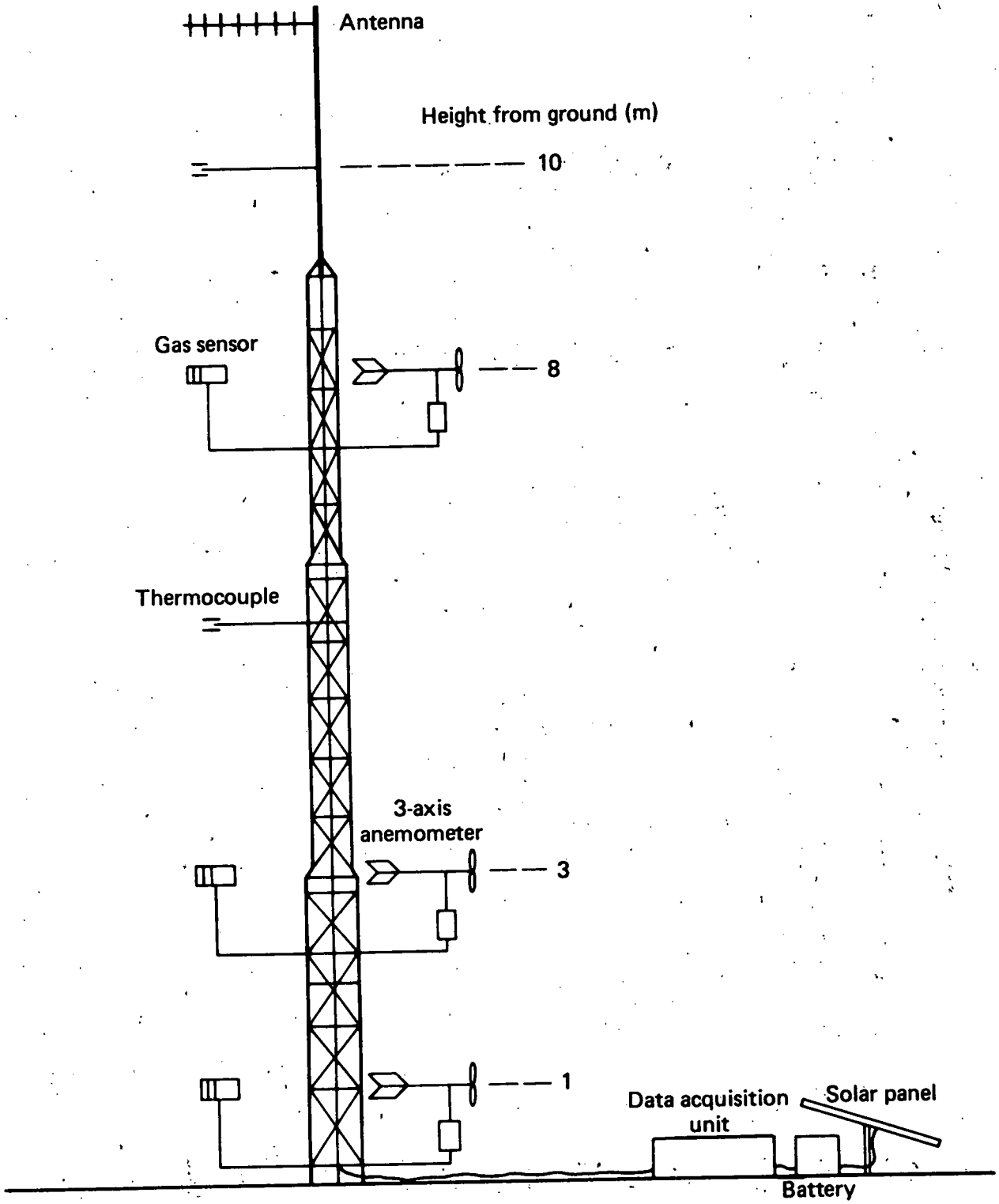

FIG. 3. Turbulence station.

The gas cloud has associated with it significant concentration fluctuations due to turbulence. These fluctuations can occur over times as short as 0.2 seconds. Since turbulence and its effect on mixing and dispersing the gas is a major area of interest in these experiments, fast response gas detectors will be necessary at some stations. It will not, however, be necessary to have fast detectors at all stations, since the principal purpose of the array will be to determine the time-dependent concentration contours of the gas cloud, with a resolution of only 1 to 10 seconds necessary for comparison with computer model calculations. Current plans call for about five of the 30 gas sensor stations shown in Figure 1 to be fast response stations with a sampling frequency of 5-10 Hz. The remaining stations will either use slower responding instruments or will average over several measurements such that their measurement frequency will be effectively about 1 Hz or less.

Since methane vapor enriched in heavier hydrocarbons is considerably more explosive than methane alone, it will be one of our experimental goals next year to follow the enriched portion of the cloud produced by the differential boiloff of these heavier hydrocarbons downwind to see how rapidly it disperses. To do this we must have hydrocarbon sensors capable of distinguishing methane from ethane and propane. It will not be necessary for all of the gas sensors to have this capability on every test, but it may be necessary to run several tests under similar conditions with the multiple species sensors clustered in different regions of the cloud for the different tests. Alternatively, it may be desirable to have one multiple species sensor at each station to track the enriched region of the cloud. The vertical profile would then have to be determined on a separate series of tests. The instrument stations are being designed so that such changes can be made easily in the field.

We currently believe that it is not necessary to distinguish between ethane and propane, but that it will be sufficient to simply measure the sum of the two species. This is due primarily to the fact that they both have a very similar effect on the detonability of the gas mixture. Last year's measurements at China Lake also showed that the two species evaporate at about the same time and show the same concentration fluctuations with time, immediately downwind of the spill pond. For future work with other liquefied fuels, however, separation of ethane and propane as well as the detection of other species will be desirable. Consequently, the multiple hydrocarbon detector is being designed to be highly adaptable.

We currently believe that the LLL-IR, JPL-IR, and the IST (International Sensor Technology) gas sensing instruments will provide the best combination of measurement capabilities over the whole array. The MIT laser-based device appears to be particularly well suited for deep-fog, fast-time response measurements but has not been available for evaluation. Therefore, it will not be considered for this test series. LIDAR looks promising for measurements outside of the fog and would be very useful for the far-field dispersion experiments. The cost figures shown in the last column of Table I are based either on the known cost of commercially available hardware or estimates of the cost of manufacturing ten or more of the developmental sensors. Low cost instruments are defined to be those costing less than $1000, medium between $1000 and $5000, and high are those costing more than $5000 per instrument. Since the Shell sensor is not a commercially available instrument, its cost is uncertain; but based on our experience with other instruments, it appears to fall into the medium cost category. The cost of the JPL-IR instrument is not known at this time, but it is likely to fall into the high cost category.

In addition to in situ measurements of gas concentration, an attempt will be made to image the cloud from above and from the side using infrared imaging or scanning systems. The ground-based work will be performed by NWC personnel and the overflights by EG&G, Las Vegas. Both efforts will involve the use of optical filters centered on a strong methane absorption band in the infrared to inhance the imaging systems capability to detect methane. If this can be done efficiently it should be possible to see the cloud in the infrared substantially farther down wind than it would be visible to the eye. This would be of great help in trying to reconstruct the cloud, after the experiments, for comparison with models.

TEMPERATURE AND HEAT FLUX

Temperature measurements will be made at each gas sensor or humidity sensor location using thermocouples. The time reponse of the thermocouple will be matched to that of the other instrument and sampled at the same rate. In addition, temperature measurements may be made vertically between gas sensors to help establish the vertical concentration profile. Heat balance measurements will be made at several locations within the dispersing gas cloud using radiometers. These radiometers will measure both the incident solar radiation and reemitted radiation from the ground. Heat flux plates, just under the soil surface, will be used to determine the total heat flux from the ground.

POOL SPREAD AND VAPOR GENERATION RATE

Initially this will be determined indirectly from the concentration measurements designed for source definition and near field dispersion. In addition, NWC may provide thermocouple measurements in the spill pond or other source definition measurements. Later in the test series, we plan to field some instrumentation designed specifically to measure pool spread and vaporization rate. Imaging and acoustic techniques will be considered for the determination of the pool size as a function of time. Instrumentation and techniques for measuring either pool spread or vaporization rate have not yet been investigated.

WIND

The array of wind measurement stations planned for a typical spill test is shown in Figure 1. The 15 station downwind array is designed to cover the area of gas cloud dispersal uniformly. There will be an additional five upwind stations along the prevailing wind direction (only three of which are shown in Figure 1). These will be used in a predictive way to determine when the wind field is such that the gas cloud is most likely to pass over the sensor array. The output from the anemometers, except for the turbulence stations, will be displayed in the control trailer in real time so that decisions about when to spill the LNG can be made.

Out of the 26 wind stations, 20 are designed to do the wind field mapping, and six will be fast-response turbulence stations. A turbulence station is shown in Figure 3, and one of the anemometer stations is shown in Figure 4. Five of these turbulence stations will also have high speed gas sensors, thermocouples, and three-axis, fast-response anemometers at three levels, making 5 to 10 measurements per second. The sixth will be immediately upwind of the pond and have only fast response anemometers and thermocouples. These stations will be used for the detailed characterization of the turbulent mixing of the gas and the air. The five downwind stations will be located at different positions within the cloud depending on the purpose of the experiment. They will generally be distributed within the cloud, but may be clustered together for a special series of turbulence correlation measurements, or placed across the cloud at varying downwind distances to examine the effect of the cloud on the wind profile. Good quality cup and vane anemometers will be used at the wind field mapping stations and propeller bivane anemometers at the turbulence stations.

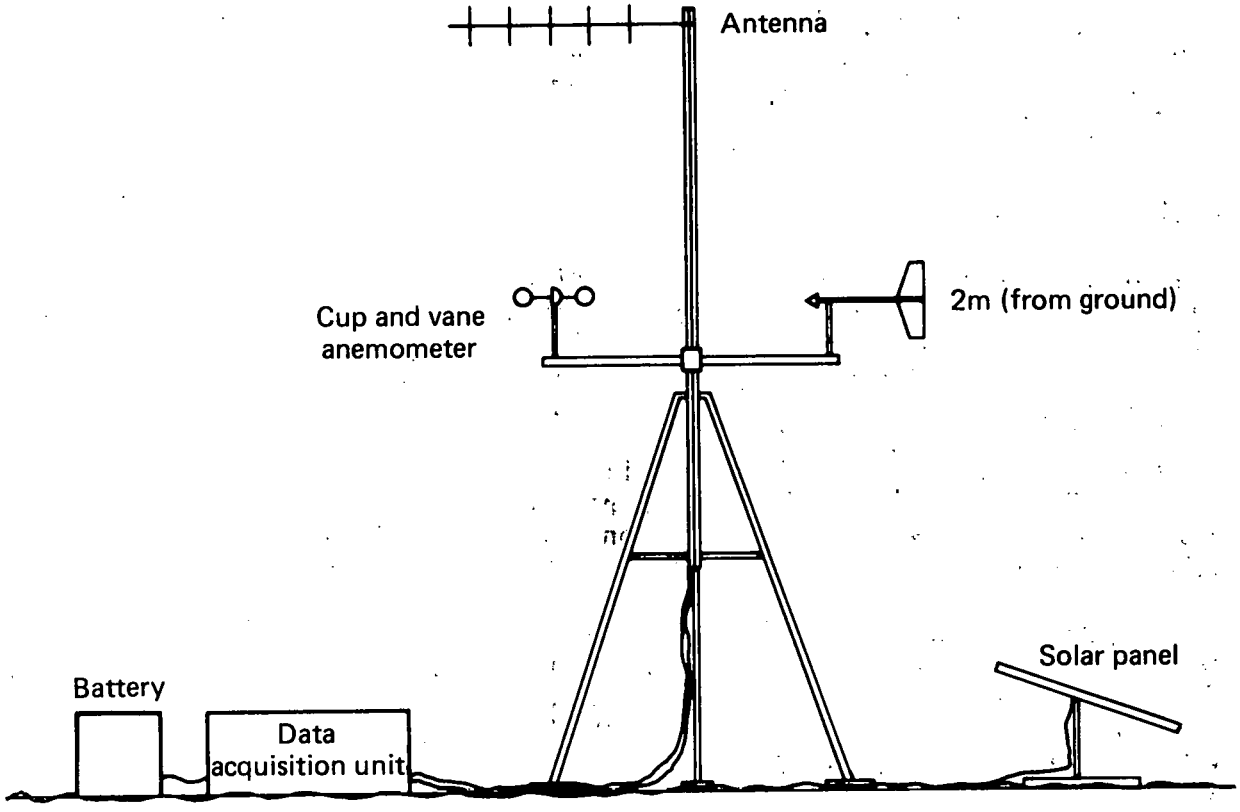

FIG. 4. Anemometer station.

HUMIDITY

Humidity measurements will be made upwind of the spill pond to obtain the background humidity level and at several locations downwind of the pond to determine the environment into which the gas cloud is dispersing. Measurements will be made during the spill to determine if the spill process itself is adding water to the cloud. These measurements will be made using a commercial device whose resistance changes proportionately with water vapor content in a heated sensor developed here to work in dense cryogenic fog. It is necessary to warm the air to vaporize the water droplets and ice particles produced by the cold LNG vapor cloud in order that a true measurement of total water content be obtained.

DATA ACQUISITION SYSTEM REQUIREMENTS

As with the instrument and station requirements, the data system requirements discussed here are based largely on our experience at China Lake last year and the extrapolation of this experience to a large array of stations. Many of the requirements are based on the operational need to deal efficiently with a very large amount of data from a large number of instruments dispersed over a large area.

The data acquisition hardware associated with each station is shown in Figure 5. The stations are designed to store data in a local buffer memory that will be emptied and transmitted to the data acquisition trailer when polled by the computer. There will be some ability to compress or average data within the station and check or calibrate detectors before tests. Fast detectors with multiple nonlinear outputs, such as the LLL-IR or the JPL-IR detectors, should have their own ability to linearize and average their signals if the data rates to be transmitted are to be kept reasonable. Slow, single-output, nonlinear detectors such as the IST will not need to be averaged. The stations will accommodate both digitized and analog input, with the analog input digitized before being stored. The communication link between the trailer and the stations will be two-way so that the stations can be turned on, checked out, and calibrated on command and can send data back at a high rate when polled.

A schematic of the system in the data acquisition trailer is shown in Figure 6. The system has been designed to be modular so that it can expand to accommodate additional stations or additional special function instrumentation. It is designed around a series of LSI-11 microcomputers. There will be a worker computer dedicated to the six high frequency turbulence stations, one dedicated to the 23 remaining low frequency gas concentration stations, and one dedicated

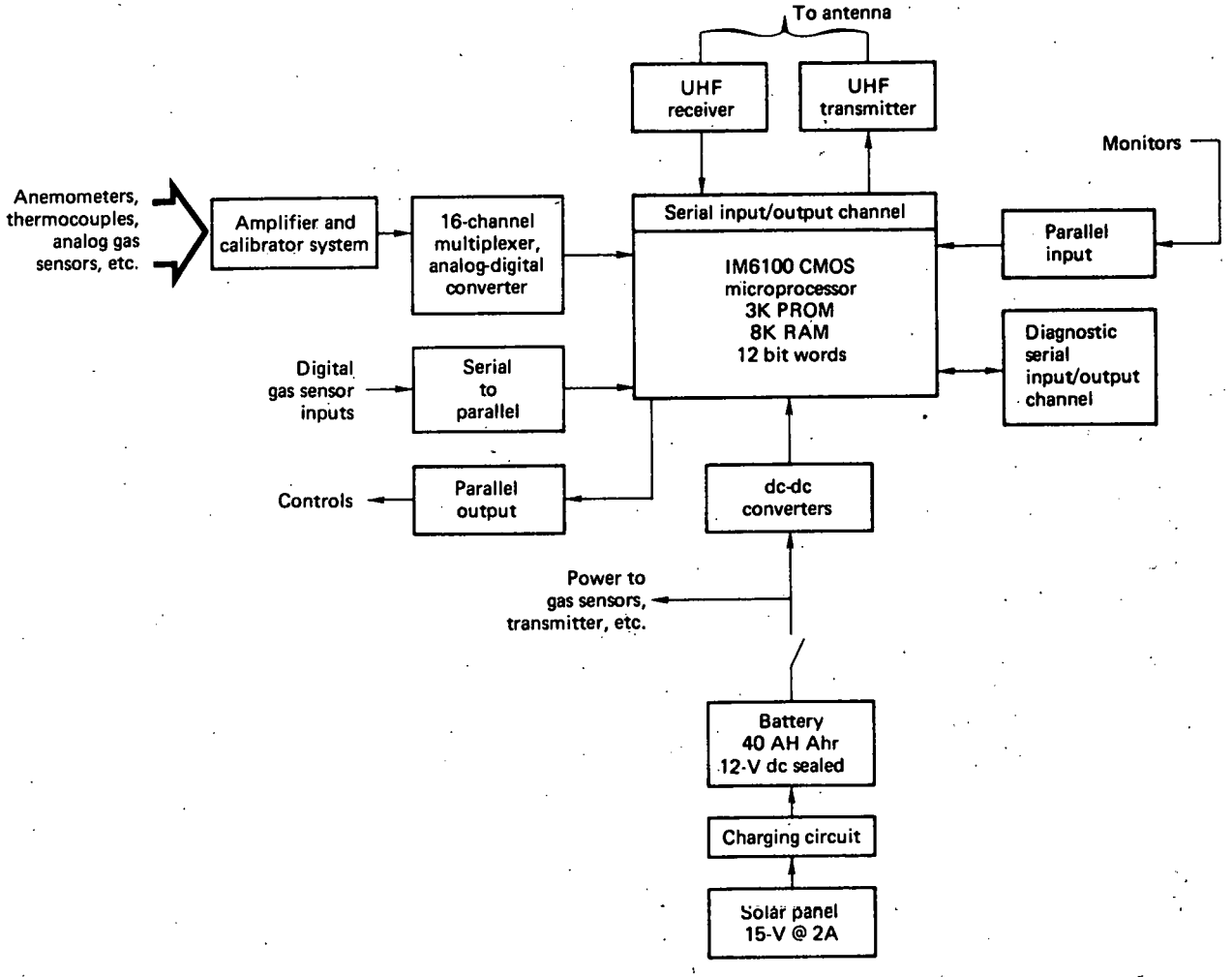

FIG. 5. Gas sensor data acquisition unit block diagram.

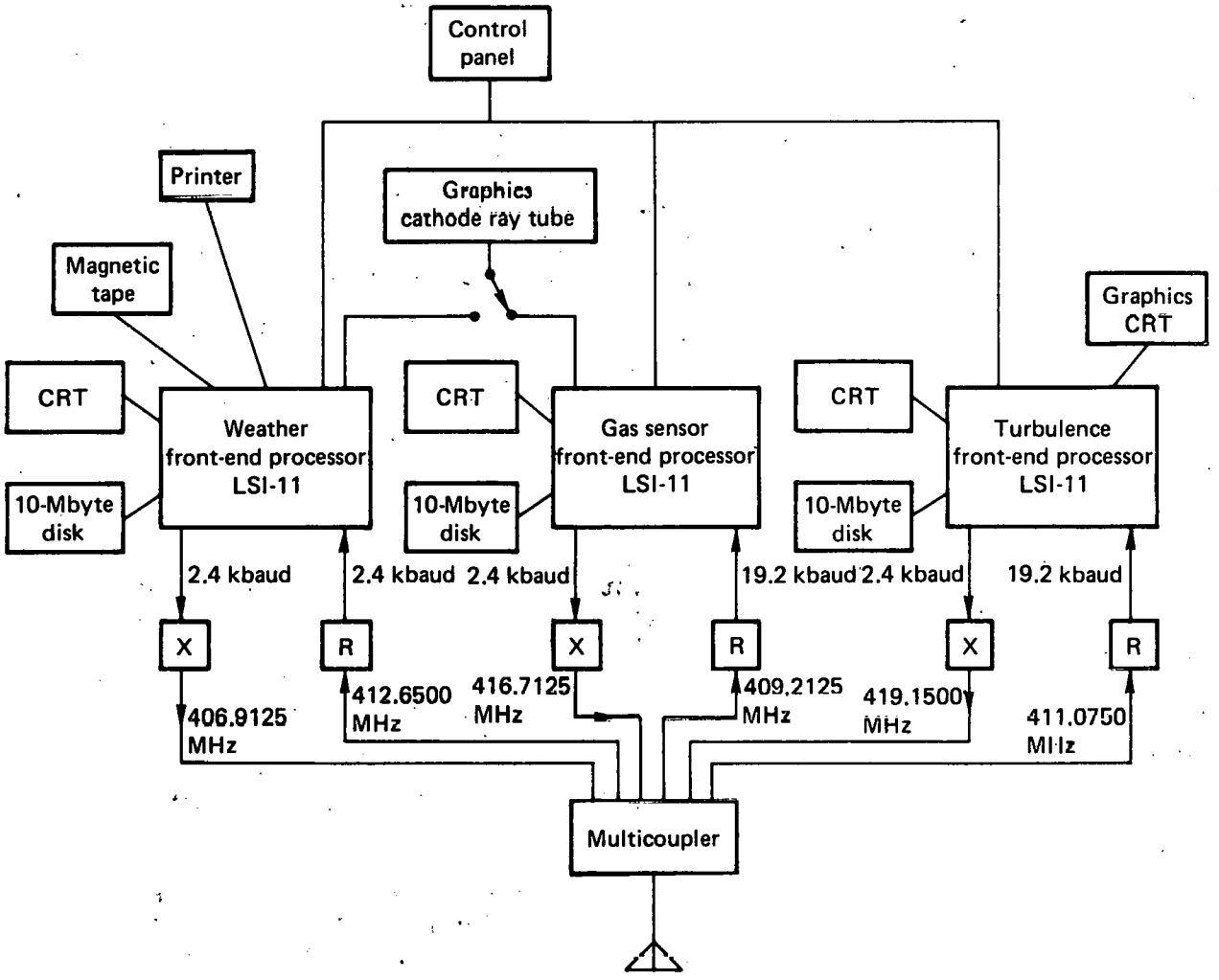

FIG. 6. Command control and data recording system block diagram.

to the 20 anemometer stations. During the experiment, each computer will accumulate data from its subsystem of instruments and store it on a disk. After the experiment, the data can be displayed, printed, checked, calibrated, compressed, and rearranged before being written on tape for analysis with the LLL computers. Since there will be such a large amount of data produced by these experiments it is important that it be in a form that is convenient for the data analyst to use.

The continual display of the wind field, both upwind and downwind of the spill pond, will allow us to more accurately predict when the wind direction is such that the gas cloud will pass over the instruments. Figure 7 shows a calculation of the gas cloud, averaged over time, from a 30-m^3/minute, 40-m^3 LNG spill into the wind field measured experimentally last year for Avocet 1 (LNG 18). The shape of the cloud shows the wind shift that occurred during the course of this test. We believe that by monitoring the upwind anemometers before the test, we can avoid major wind shifts during the test.

PROPOSED EXPERIMENTS

The experimental program will consist of several parts, or test series, each with different objectives. Each test series will involve a number of experiments. The first two series, which involve mostly dispersion, comprise a total of about 30 experiments, 20 of which can be performed at China Lake. The actual number of tests may be more or less than this depending on the weather conditions at the spill test facility. Some ideas on turbulence and pool spread and vaporization experiments, which might be performed later, are given in the last two sections.

Every effort will be made to get the anemometer and turbulence stations operational at least one week before the dispersion tests begin so that wind field and turbulence characteristics in the experimental area at China Lake can be studied. This will provide both operational experience and base line wind field information prior to the tests.

FAR FIELD DISPERSION

Probably the most important series of experiments will attempt to determine gas concentration contours within the gas cloud under varying spill rates, spill volumes, and wind and stability conditions. This will be done measuring concentration at various radial locations downwind. The instrument array shown in Figure 1 is basically designed

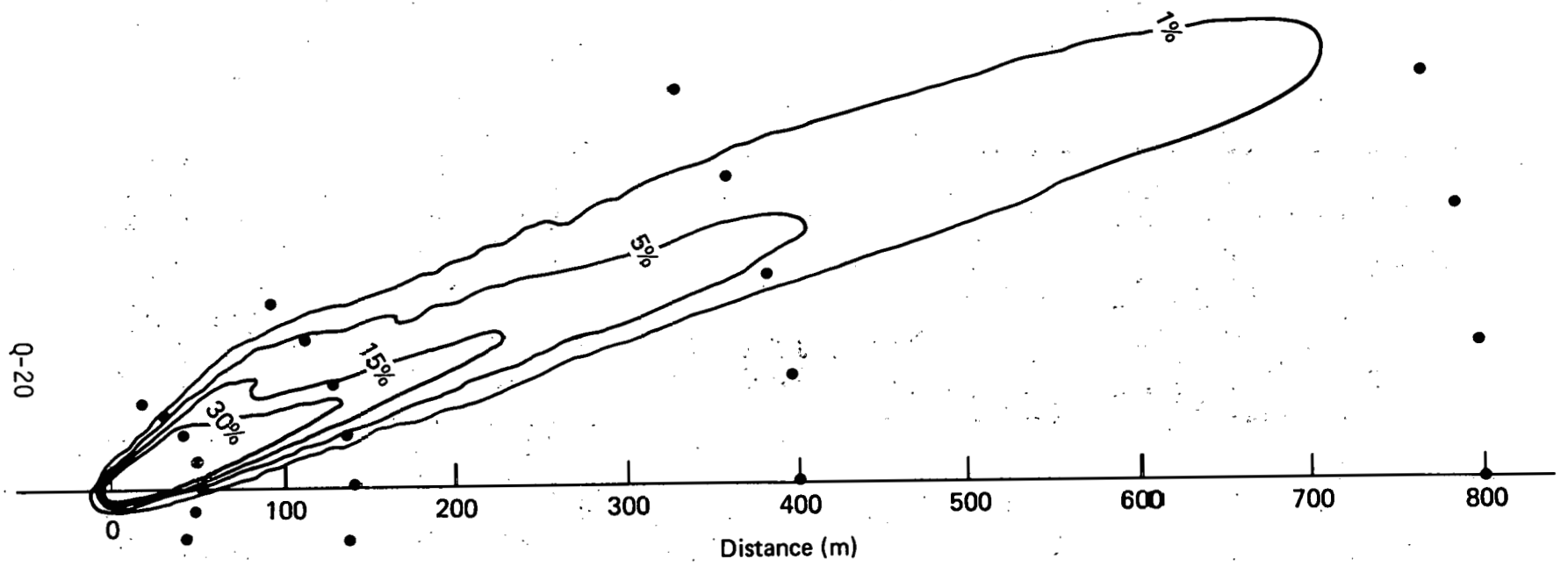

FIG. 7. Avocet-1 30 m^3/min time-average plume.

for this purpose. It will be important for these relatively small spills to measure concentrations at distances further downwind than the LFL concentration because they will help better determine the concentration gradient at the LFL and the significance of concentration fluctuations in this region. Since the concentration gradients in this region appear to be small, the comparison of experimental data, out to concentrations of about 2% with calculations will exercise the codes over large distances and may be effectively the same as comparing with LFL (5%) data from larger spills. This is valid as long as the gas concentrations are high enough to still have a significant effect on the atmosphere. Remote measurements using LIDAR would be very useful in this region of the cloud since a large area must be covered and fog will not be present.

Spill rate will be an important parameter in each of the test series and, according to calculations, has a particularly significant effect on concentration contours far downwind. Long spill tests, which of necessity will involve low spill rates, will be necessary so that data can be taken for a long enough period of time to make statistically significant comparisons with the normal atmosphere. We will need tests at spill rates of about 5, 15, and 30 m^3/minute, under varying weather conditions. Spills under very low wind conditions (1-2 m/s) are necessary, but probably not possible at China Lake. We will do tests under the lowest, steady wind conditions possible, however, and anticipate these to be about 3-5 m/s. In addition, we would like to perform tests under the more readily available higher wind conditions of 6-8 m/s. This forms a matrix of 9 experiments, which is shown graphically in Figure 8. That part of the matrix that can be performed at the NWC facility is shown unshaded in the figure.

We believe that several tests will be necessary in each of the different wind speed categories because of differences in other variables, such as atmospheric stability and humidity, which might occur during the tests. Some measure of repeatability would also be desirable. Whether various stability conditions can be obtained at a given wind speed and with the wind from only the prevailing southwesterly direction is uncertain. Stability is unlikely to be an independent variable, at least at the China Lake site.

SOURCE DEFINITION AND NEAR FIELD DISPERSION

Late in the 1980 test series, or in 1981, source definition experiments will consist of direct measurements of LNG pool spread and vaporization rate at the water surface. Because good techniques for making these measurements have not yet been developed and because of the complex terrain features within 100 m of the spill

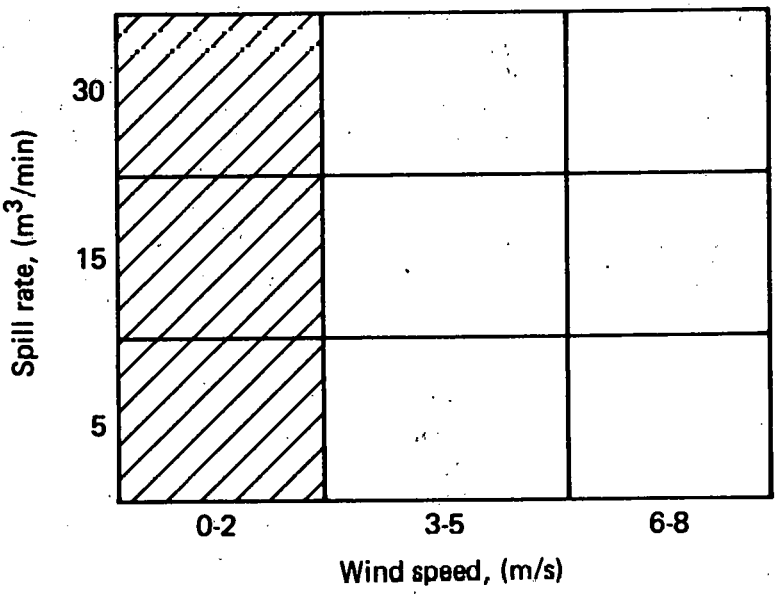

FIG. 8. The matrix of independent variables for the 40-m^3 spill tests. The shaded area defines those that probably cannot be performed at the NWC facility.

point at China Lake, we will initially try to characterize the vapor source by intensely instrumenting this area. This will allow us to assess the effect of the terrain over the first 100 m and determine an effective source as well as estimate source parameters such as boiloff rate, rate of vapor movement up the hill, and rate of air entrainment for the gas emerging from this area. These estimates can be made from the data only indirectly, through a series of computer model calculations. Figure 9 is a diagram of what the instrument array might look like for these experiments. It would be desirable to make both near and far field dispersion measurements on the same experiment. Consequently, the 10 gas sensor stations and three anemometer stations not shown in Figure 9 will be left in the far field configuration. This will allow some connection to be made between the two series of experiments. These tests can be considered complementary to the far field dispersion tests and as such should be performed for a matrix of test conditions similar to that shown in Figure 8.

TURBULENT MIXING

During 1980, six stations will be making fast response measurements that will be used to get information on turbulence. For the experiments described in the preceding sections, these stations will probably be scattered throughout the cloud. Later in the experimental series it may be desirable to make correlation studies of turbulence and gas mixing at various specific locations within the dispersing cloud. Since these measurements can probably not be done until FY-81, more fast response stations can be added to the array, making it possible to very densely instrument a small part of the cloud. The dense array of instruments could then be moved to other parts of the cloud in a series of experiments designed to investigate turbulent mixing as a function of downwind distance. It may also be desirable to arrange the fast response instruments in a row at a series of radial positions on a series of experiments. This would provide turbulence profiles through the cloud rather than simply point measurements.

POOL SPREAD AND VAPOR GENERATION

Measurements of maximum pool radius have been made for spill volumes up to 10 m^3. Measurements of the time dependence of the pool radius have not yet been made, nor have measurements of the time dependence of the vaporization rate. Pool size and vaporization rate are determined largely by spill rate; consequently, it will be necessary to do a series of experiments at different spill rates. Since these tests

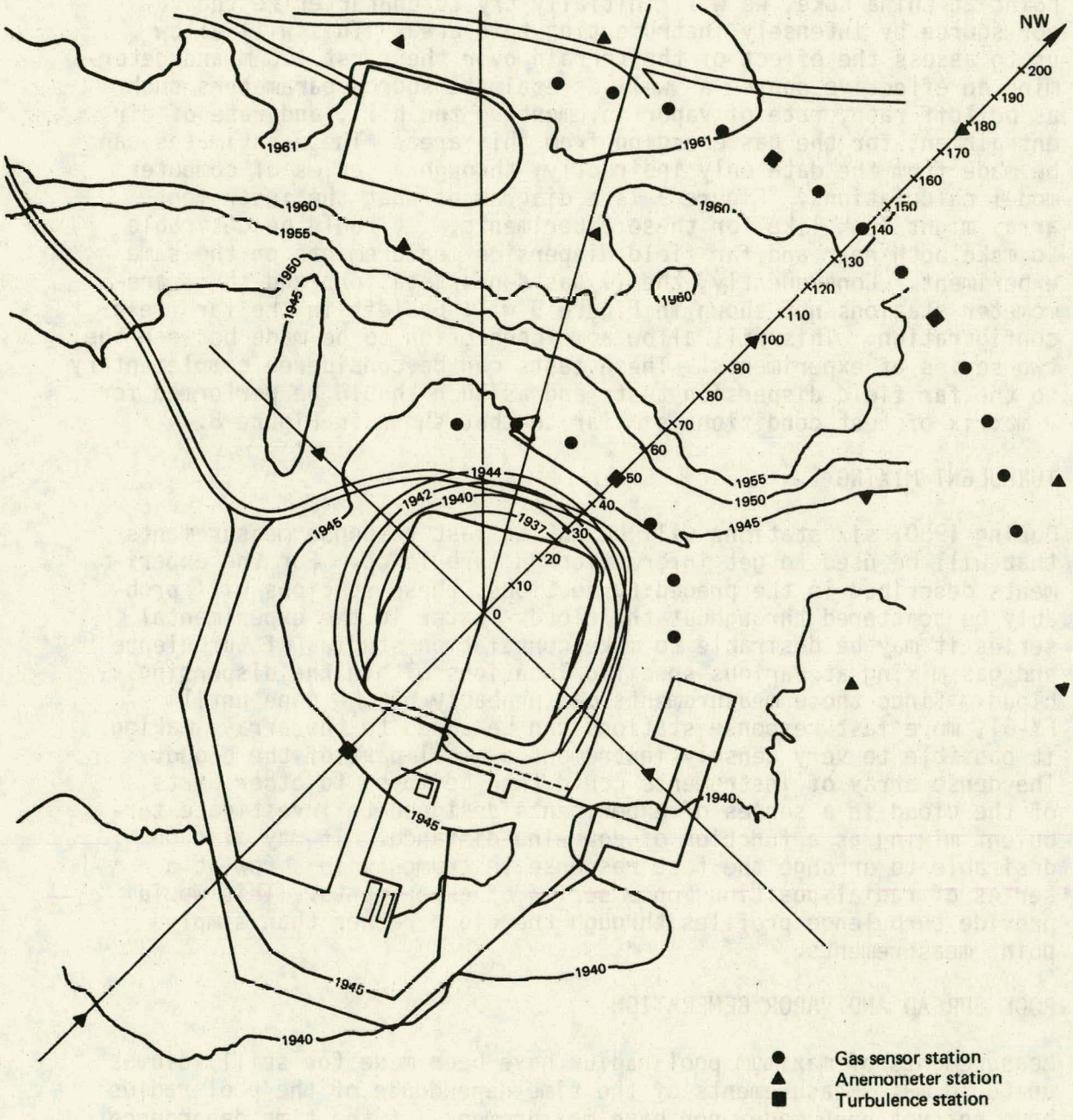

FIG. 9. Source definition and near field diagram array.

will involve instrumentation and techniques which may not yet be developed, specifics cannot yet be given. However, if the instrumentation and techniques are ready, these tests could be performed late in the 1980 series. Otherwise, they will be done in 1981.

LAND SPILLS

A series of experiments similar to that outlined for spills on water will also be performed for spills on land. These will occur after the water spills, and we should be able to take advantage of knowledge gained there to truncate the experimental matrix. Techniques will have been developed for making direct measurements of pool spread and vaporization, thus eliminating the need to do the near field dispersion and source definition experiments. The far field dispersion experiments will be most important for the land spills as well as the water spills and will probably require a similar matrix of experiments (see Figure 8). This implies spills at various rates into confined or unconfined areas under varying weather conditions.

EXPERIMENTAL PLAN SUMMARY

A summary of the measurements to be made and the instruments to be used, including their location, numbers, and performance characteristics, is given in subsection I below. Subsection II summarizes the experiments themselves including the test conditions, number of tests, and measurements to be made on each test.

I. Measurements:

A. Gas concentration:

Location:

- Three vertically (1, 3, 8 m) at each of 30 stations at varying radii out to 800 m or more (3 x 30 = 90 gas sensors).
- Infrared imaging from above and from the side.

Time response:

- Fast, 5-10 samples/second at five turbulence stations (3 x 5 = 15 fast sensors).
- Slow or averaged to 1 second at 25 stations (3 x 25 = 75 slow or averaged sensors).

Hydrocarbon species:

- Total Hydrocarbons - 15 IST stations (45 sensors), four MSA stations (12 sensors).
- Separated Hydrocarbons - 11 LLL-IR stations (33 sensors), (methane, ethane/propane)

  (11 JPL-IR sensors will be available in July).

B. Temperature:

Location:

- One thermocouple at each gas sensor and one betwen sensors at some stations (109 tc's).
- Two for net radiometer heat flux measurements and two for surface heat flux measurements at seven stations (4 x 7 = 28).

Time response:

- The nominal response time for the 10-mil thermocouples being used is about 0.5 seconds in a 5 m/s wind.
- Heat flux measurements will be slow.

C. Wind:

Location:

- Three anemometers vertically (1,3,8 m) at each of six turbulence stations (3 x 6 = 18 anomemeters).
- One (2 m) at each of 20 anemometer stations (20 anemometers).

Time response:

- Fast, propeller bivance (three-component) at turbulence stations.
- Slow, cup and vane (two-component) at anemometer stations.

D. Humidity:

Location:

- One measurement at each of seven stations.

Time response:

- Few seconds.

II. Experiments

A. Far field dispersion:

Number of tests	9-18 (6-12 at NWC in 1980).
Spill rate	5, 15, 30 m^3/min.
Spill volume	40 m^3.
Wind speed	0-2, 3-5, 6-8 m/s.
Measurements	Gas concentration, temperature, wind, humidity.

B. Source definition and near field dispersion:

Number of tests	9 (6 at NWC in 1980)
Spill rate	5, 15, 30 m^3
Spill Volume	40 m^3
Wind speed	0-2, 3-5, 6-8, m/s
Measurements	Gas concentration, temperature, wind, humidity.

C. Turbulent mixing:

- Six turbulence stations will make fast response measurements on the 1980 NWC experiments listed in II-A and II-B.
- Measurements: Wind speed and direction (three-component), gas concentration, and temperature at six turbulence stations.

D. Pool spread and vapor generation:

- Secondary determination, based on gas concentration measurements from the source definition and near field dispersion experiments listed in II-B, will be made initially.

- Primary measurements on the spill pond itself will be made either late in the 1980 test series or in 1981.

E. Land spills (1981):

- The test series will probably be similar to that listed for A, far field dispersion tests.

SCHEDULE

The schedule for the 1980 experiments is given in Table 2. The experiments are expected to begin in early May and continue through September at China Lake.

TABLE 2. SCHEDULE FOR 1980 DISPERSION EXPERIMENTS AT CHINA LAKE

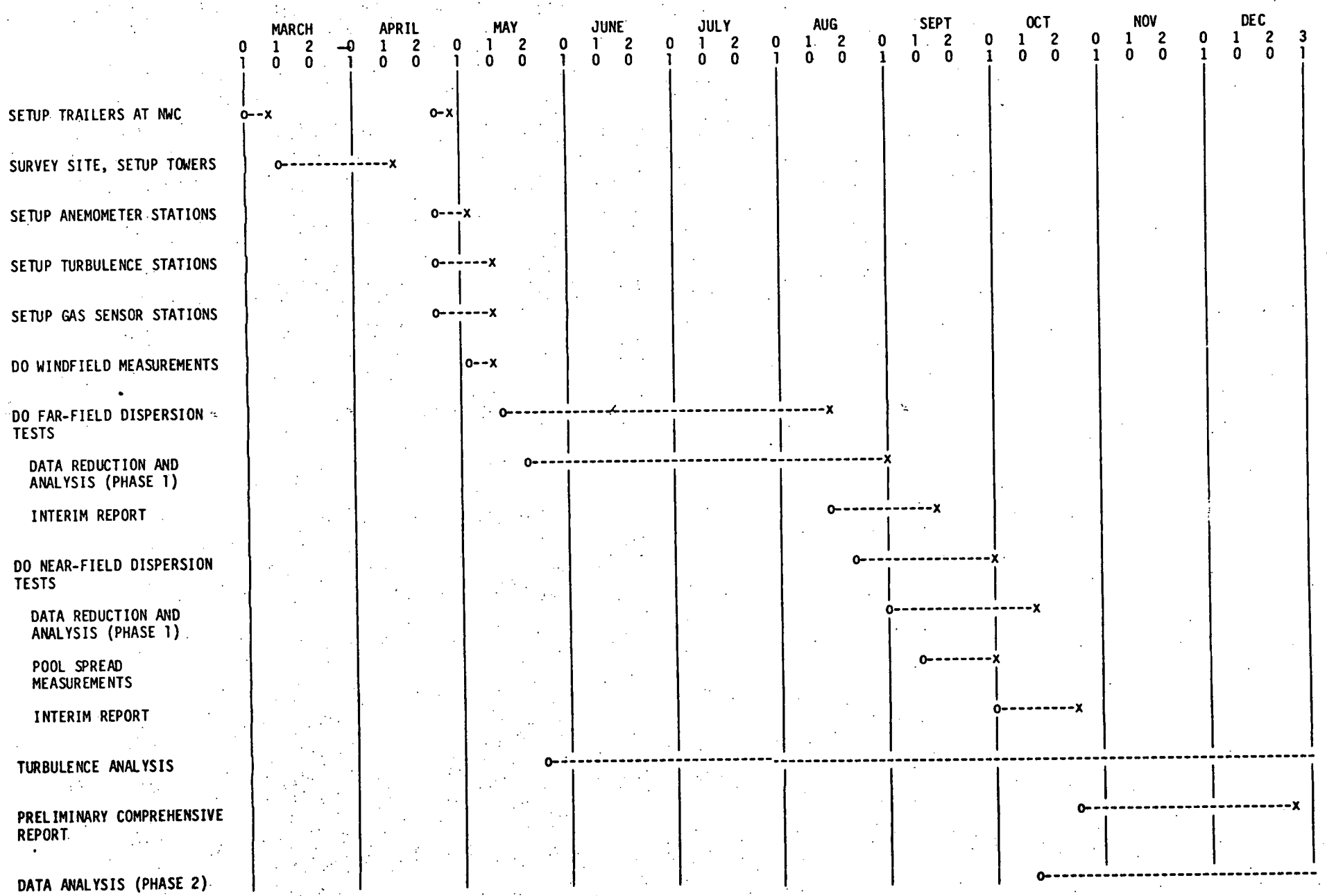

THIS PAGE

WAS INTENTIONALLY

LEFT BLANK

REPORT R

China Lake 40-m^3 LNG Spill Facility

C. D. Lind
J. C. Whitson

Prepared for the
Environmental and Safety Engineering Division
U.S. Department of Energy
under interagency agreement
DE-AI-01-79EV10072

Naval Weapons Center
China Lake, California 93555

THIS PAGE

WAS INTENTIONALLY

LEFT BLANK

REPORT R

TABLE OF CONTENTS

FIGURES

SUMMARY

This report describes the modified LNG spill facility at the Naval Weapons Center (NAVWPNCEN) China Lake, California and outlines the proposed spill tests to be conducted at this facility.

INTRODUCTION

Since 1973 the NAVWPNCEN has been investigating the fire and explosion hazards of liquified fuels.[1,2] As part of this program a facility was constructed capable of spilling up to 5.7 m^3 of liquified fuels on a water test basin and studying the combustion or dispersion of the vapor produced. Using this facility spills of liquified natural gas (LNG), liquified petroleum gas (LPG), and gasoline and liquid nitrogen (LN_2) have been performed.[3]

Additional spill tests involving much larger quantities are needed in order to defintely quantify the hazards associated with massive spills, as could occur during marine transport. The extrapolation of hazards from a 5.7 m^3 spill up to that resulting from a 25,000 m^3 spill (one compartment of a LNG carrier) cannot be accomplished with confidence; hence larger controlled spills are required. Ultimately spills of 1000 m^3 will be required to verify scaling laws derived form small scale experiments. Prior to this, however, intermediate size spills (40-100 m^3) are needed to help verify the scaling laws and provide design and safety criteria for a 1000 m^3 facility.

The original 5.7 m^3 facility is now being expanded so that it will be capable of safely handling up to 40 m^3 of LNG. This current expansion consists of: the minor enlargement of the existing water test basin to a larger, more circular basin; the installation of an additional cryogenic liquid storage tank capable of spilling up to 40 m^3 of LNG; appropriate cryogenic piping and valving to deliver the LNG to either the enlarged test basin or to a newly constructed diked dry test basin; and associated remote spill control and monitoring systems. Site expansion is expected to be completed by April 1980.

FACILITY DESCRIPTION

Figure 1 is a site plan showing the layout of the expanded facility as it will be upon completion. The 40 m^3 tank is located approximately 30 m south of the original 5.7 m^3 tank.

The 40 m^3 spill tank is a vacuum jacketed tank 10.7 m long by 3.5 m in diameter with a total water volume of 52 m^3; its design operating pressure is 2.4 bars. The liquid fuel exits the tank by means of a 20 cm diameter vertical stainless steel diptube upon pressurization of

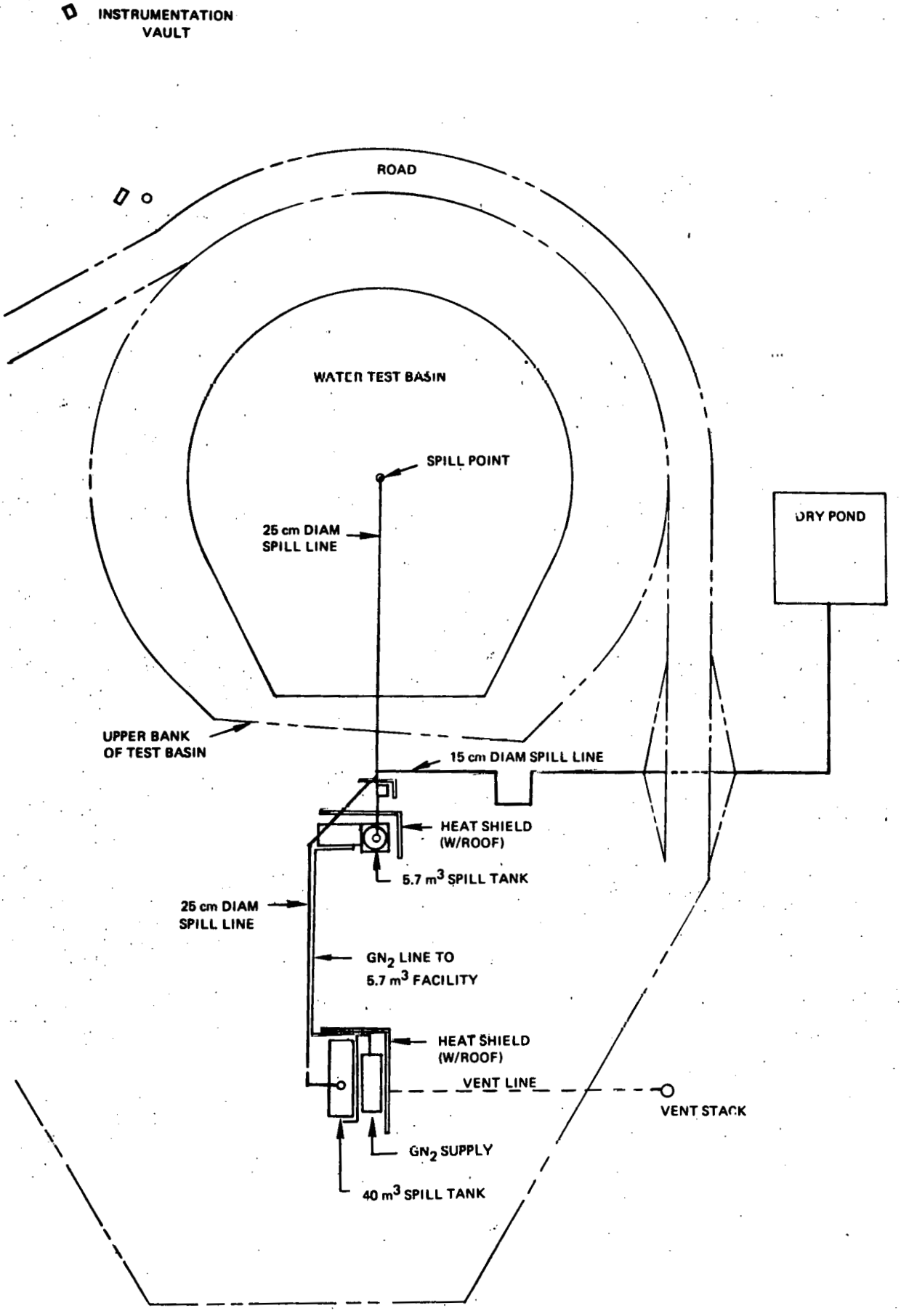

Figure 1.- Modified Site Plan

the tank with gaseous nitrogen (GN_2). A 25 cm diameter, insulated stainless steel spill line runs from the 40 m^3 tank to a junction north of the 5.7 m^3 tank. A 25 cm diameter line continues from this point to the center of the water test basin while a 15 cm diameter, insulated, stainless steel spill line extends from this point to the edge of the 15 m x 15 m x 0.15 m dry pond. Switchover from spills on the water test basin to the dry pond will be accomplished by use of spectacle blinds at the piping junction point. In this way it will then be possible to spill from either the 40 m^3 tank or the 5.7 m^3 tank on either the water test basin or the dry pond.

Large heat shield structures are used to provide thermal protection for both spill tanks while a smaller heat shield protects the cool-down and spill valves. The heat shields protecting the 40 m^3 tank also provides protection for the GN_2 supply trailer.

The tank is loaded from a loading point 15 m from the tank through a 10 cm diameter insulated stainless steel loading line. During loading the tank is vented by means of a 20 cm diameter vent line and 18 m high vent stack.

Pressurization of the tank prior to a spill is achieved through three stages of pressure reduction from approximately 138 bars at the GN_2 trailer down to the operating pressure of the tank, 2.4 bars. This pressurization is remotely controlled and monitored from the control van.

The control van is located 250 m northwest of the tank and also contains controls for the remote operation of the vent system and the cool-down and spill valves. In addition, remote monitoring of the tank liquid level, tank and spill line temperatures, tank internal pressure, nitrogen supply pressure and liquid flow rate is performed at the control van. Communication between the van and tank sites is by means of talk-back speakers.

A new instrumentation vault is located approximately 75 m northwest of the water test basin spill point. Underground instrumentation lines and coaxial cables run from this vault to the control van. Field emplaced instrumentation can then be connected to this vault with only a minimum of overground instrumentation line.

The water test basin has been enlarged from its previous 51 m x 51 m to a more circular shape with an average diameter of 58 m. The average depth remains at approximately 1 m. The slopes of all but the south bank have also been reduced to provide less turbulent wind flow over the water test basin.

Figures 2 through 5 are representative photographs taken during the

early stages of the site modification. Figure 2, taken from the northwest bank of the water test basin, shows the original 5.7 m^3 facility but without the original heat shield. Figure 3 shows the 40 m^3 vacuum jacketed spill tank being loaded for movement to the spill site. Figure 4 shows the heat shields being constructed at the cool-down and spill valves; the original 5.7 m^3 tank and the 40 m^3 tank. Figure 5 shows the water test basin drained prior to final enlargement; the spill line supports in place and the heat shield structures essentially complete.

DATA ACQUISITION SYSTEM

The system consists of two 126 channel multiplexers (EON Instrumentation, Inc., Model PCM-212-128 Encoder) a high speed analog tape recorder (Ampex Model FR 1200) and a telemetry processor (EMR Telemetry Model 708). Analog signals either $\pm$ 50 mv or $\pm$ 5 v are inputted to the multiplexers in the field. The multiplexers scan each input at a selectable rate of up to every 4 ms and perform an analog to digital conversion to produce 12 bit words. The data in the form of a digital stream is sent to the control room on a single coaxial cable where it is input to both the processor and the recorder. The processor decodes the input and displays any 32 signals on a CRT. The type of display and mathematical conversions are operator controllable. The processor has a hard copy output to preserve CRT display and 16 digital to analog converters for connection to strip chart recorders. The analog tape record can be replayed through the processor to obtain different channel output or display or can be computer processed to obtain more conventional formatted computer tape for computer processing.

OPERATIONAL PROCEDURE

In general the operational procedure for the 40 m^3 facility will be similar to that of the 5.7 m^3 facility. The tank is loaded from an over-the-road trailer and a sample is taken for later analysis. At this point all personnel are cleared from the spill site and subsequent steps are performed remotely. The remote vent valve is closed; the three stages of pressure regulation are set and the spill tank is pressurized. The cool-down valve is opened, cooling the spill line; the spill valve is then opened and the test conducted. A "heel" of approximately 1.2 m^3 remains in the tank after the test.

PLANNED TESTS (FISCAL YEAR 1980)

Prior to conducting spills of hazardous materials the pressurization-vent system will be checked out using gaseous nitrogen. Following this approximately three 5 m^3 of liquid nitrogen (LN_2) will be used to check out facility operation and the effect of splash plate versus no splash plate on the end of the spill line.

FIGURE 2
Original 5.7 m^3 Facility

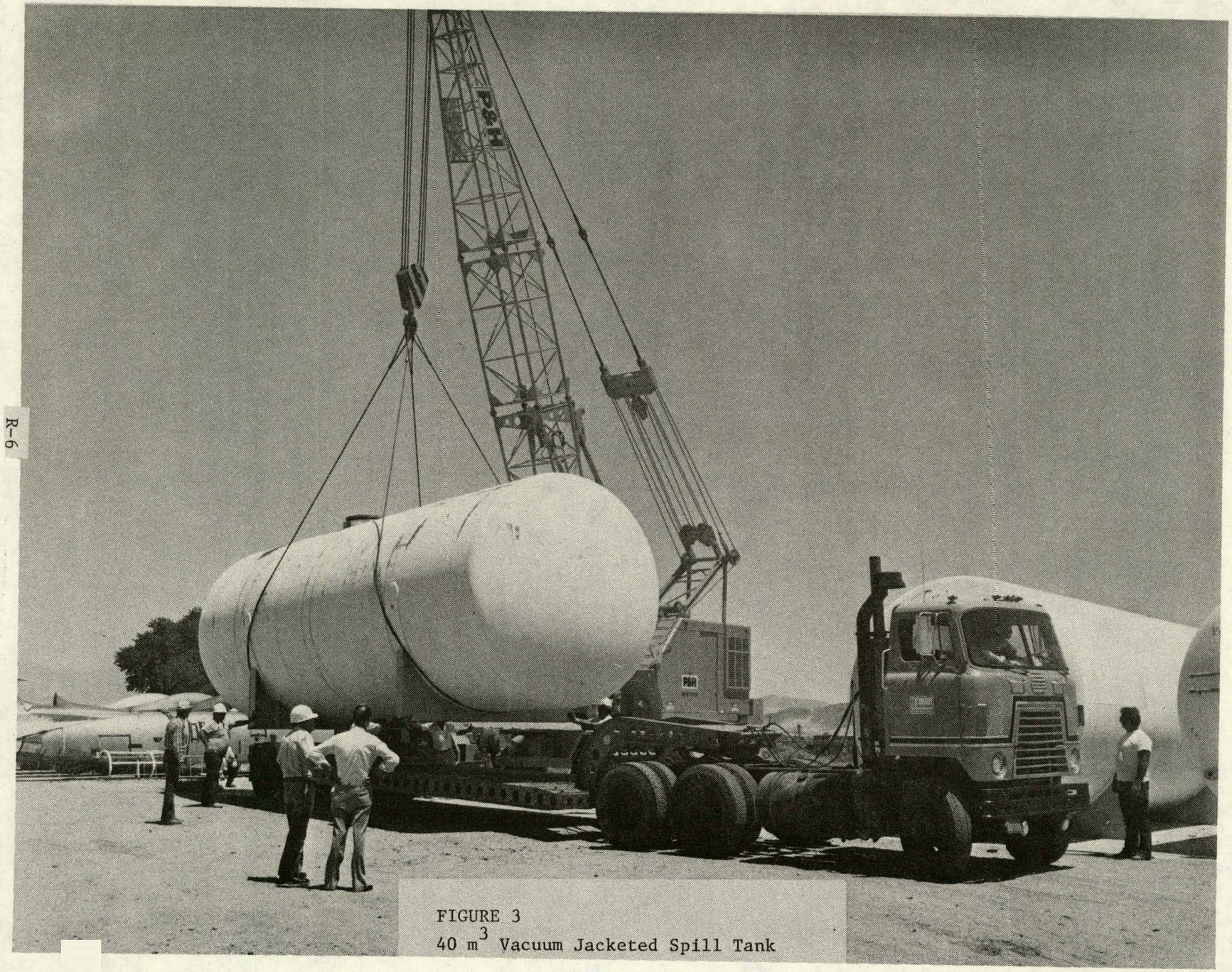

FIGURE 3
40 m^3 Vacuum Jacketed Spill Tank

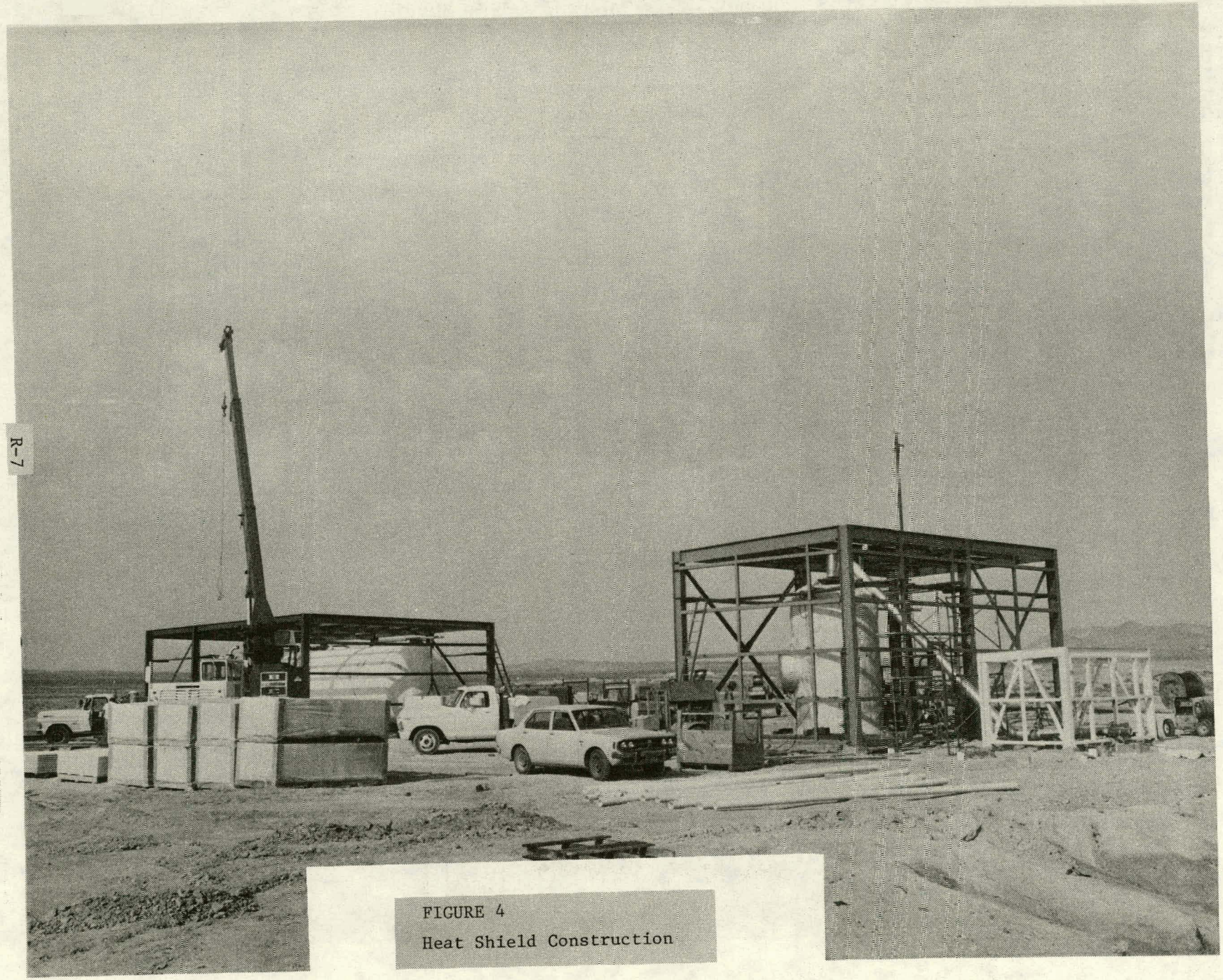

FIGURE 4
Heat Shield Construction

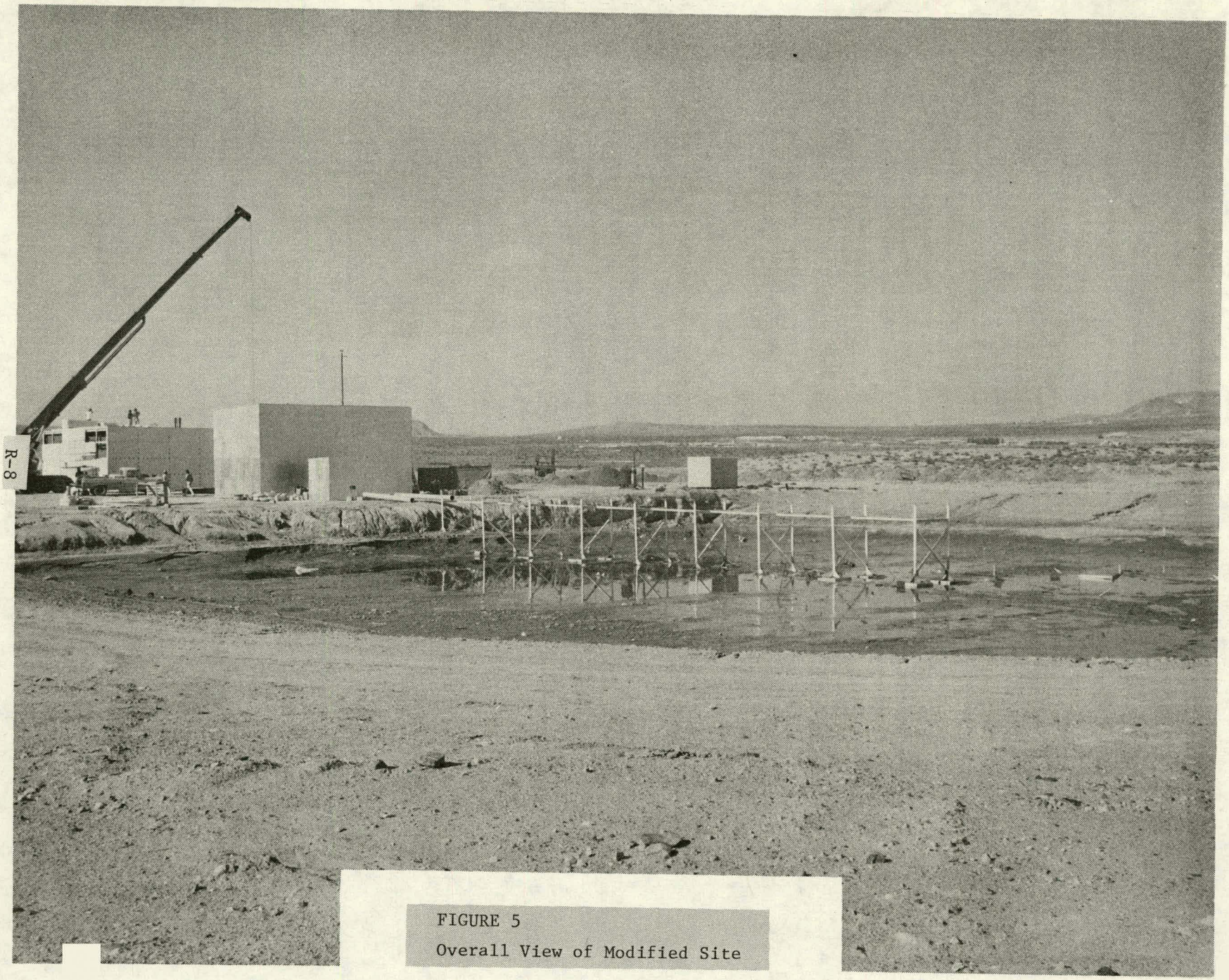

R-8

FIGURE 5
Overall View of Modified Site

Spills of LNG will consist of the following:

1. LNG Pool Fire - water spill

The object will be to check out the facility and instrumentation with "live" material and to make radiometric measurements. A total of four spills are planned; two 5 m^3, one 20 m^3 and one 40 m^3.

2. LNG Dispersion - water spill

The object is to determine dispersion characteristics under different atmospheric stability conditions. Twelve tests are planned, 6 - 20 m^3 and 6 - 40 m^3; detailed planning is being carried out by Lawrence Livermore Laboratory.

3. LNG Vapor Fires - water spill

The object is to determine premixed flame characteristics and make radiometric measurements. A total of 7 tests are planned; one 5 m^3, one 15 m^3, one 20 m^3 and four 40 m^3.

REFERENCES

1. C. D. Lind and J. C. Whitson, Explosion Hazards Associated with Spills of Large Quantities of Hazardous Materials, Phase I. (U.S. Coast Guard Report CG-D-30-75.), October 1974, ADA001242.

2. C. D. Lind and J. C. Whitson, Explosion Hazards Associated with Spills of Large Quantities of Hazardous Materials, Phase II. (U.S. Coast Guard Report CG-D-85-77.), November 1977, ADA047585.

3. C. D. Lind and J. C. Whitson, Liquified Gaseous Fuels Safety and Environmental Control Assessment Program: A Status Report, DOE/EV-0036, May 1979, Rept. L.

REPORT S

Technical Information for Environmental Analysis of 1000-m^3 LNG Spill Test Effects at Frenchman Flat, Nevada

W. C. O'Neal
W. J. Hogan

Prepared for the
Environmental and Safety Engineering
Division
U.S. Department of Energy
under Contract W-7405-ENG-48

Lawrence Livermore Laboratory
Livermore, California 94550

THIS PAGE

WAS INTENTIONALLY

LEFT BLANK

REPORT S

TABLE OF CONTENTS

FIGURES

TABLES

APPENDIX TABLES

SUMMARY

Lawrence Livermore Laboratory has analyzed the environmental effects of LNG spill tests at the proposed national LNG test site at Frenchman Flat, Nevada. The results of the analysis were then compared to activities and effects described in existing Environmental Impact Statements for Frenchman Flat. It was concluded that the proposed LNG spill tests would be covered by the existing EI Statements for Frenchman Flat.

Technical Information For Environmental Analysis Of 1000 m^3 LNG Spill Test Effects At Frenchman Flat, Nevada

Introduction

The Department of Energy (DOE) asked the Lawrence Livermore Laboratory (LLL) to evaluate each of 69 federally-owned facilities for possible use as a location for an LNG field test facility. As part of those evaluations we considered the adequacy of existing Environmental Impact Statements (EIS's). For the most likely candidate location, the Frenchman Flat basin, a detailed analysis of the possible environmental effects of the proposed tests was carried out. For the other eight final candidates a cursory examination of the potential environmental impact was done. The results of those analyses are described in Appendix A of this report.

Next, the results given in Appendix A were compared with the relevant EIS's for Frenchman Flat to determine whether they adequately accounted for impacts similar in nature and magnitude to those estimated for the LNG tests. Since the proposed tests would have an impact on the environments of both the Nevada Test Site (NTS) and the Nellis Air Force Range (NAFR), both EIS's were considered. However, since they are similar, this report will cite only the relevant portions of the NTS EIS.

Finally, the estimated environmental impact of doing the tests at Frenchman Flat was compared to that for each of the other eight final candidates. Based on the limited information available, a judgment was made about whether the estimated impact at Frenchman Flat was greater than, equal to, or less than that at each of the other final candidates.

The Adequacy of Existing EIS's

The Environmental Impact Statement for the Nevada Test Site describes in detail the environmental effects of the underground nuclear test program which is the principal activity at NTS. Activities other than nuclear testing are described in more general terms and treated by comparing their impact to that of nuclear testing.

The section of the EIS covering other activities begins:

> "The underground nuclear test program described above constitutes the primary effort at the Nevada Test Site. However, as has been the case in previous years, the experimental program will include a variety of nuclear and non-nuclear projects and experiments wherein the ERDA laboratories and ERDA contractors, as well as other government agencies and their contractors, take advantage of the facilities available, the climate, the remoteness, and the controlled access of the Nevada Test Site. Such projects and experiments are necessarily conducted on a basis not to interfere with the primary mission, and unless associated with one of the underground nuclear tests, are usually conducted in part of the test site remote from the areas used for underground nuclear testing. Those which are expected to take place are described here. It is expected that additional experiments similar to these, but not yet identified, will also take place".[1]

One category of experiments described involves the use of chemical explosives:

> "This category includes a wide variety of tests employing chemical explosives in one form or another, static or dynamic, inert testing or explosive testing."[2]

In assessing the impact of other NTS activities the EIS concludes:

> "As regards other activities at the NTS, for the most part, effects are registered immediately and those effects are very small in comparison with the effects of underground nuclear testing."[3]

The EIS notes that, to date, 27 square miles of habitat have been permanently removed from use by wildlife and vegetation due to the installation of roads, power lines, support facilities, etc. and that additional plant cover has been disturbed due to off-road vehicular traffic.

Each underground nuclear test disturbs up to 0.3 square miles of habitat due to the formation of subsidence craters. There have been several hundred underground tests at NTS to date and it is anticipated that they will continue at about 20 or so per year.

The largest LNG experiments (1000 m^3) could, in the worst case, burn or scorch vegetation over an area of up to four square miles. Only a few of these largest tests need be conducted and they would probably be done within the same scorched area. The portions of Frenchman Flat that have any vegetation at all are only sparsely covered and therefore, range fires are not likely. In any event, such tests will be carried out with appropriate firefighting equipment available. The burning and scorching of what little vegetation exists is not likely to destroy the root structures. Thus, the rate of recovery will be relatively fast.

The environmental analysis considered the dust and hydrocarbons airborne after each LNG test. We estimated that these emissions would most likely be within the standards imposed by the Clean Air Act when they left the NTS/Nellis outer boundary. If the smaller scale tests indicate guidelines may be exceeded, then proper variances will be obtained. Burning permits will be obtained for most burn tests.

Due to the above considerations, LLL feels that the LNG scale effects experiments can be carried out at Frenchman Flat at a minimal incremental environmental cost over that already paid for the nuclear test program. The Nevada Operations Office agrees with this conclusion in principle. They state:

> "It appears that the Environmental Impact Statement for the NTS adequately covers the proposed LNG experiments." (See Appendix B.)

and

> "We would expect, based on our dicussions with LLL staff to date, that the current EIS will suffice." (See Appendix C.)

NVOO is, however, asking that LLL perform environmental effects studies during the program to confirm their belief. Since LLL will be extensively monitoring the phenomena which occur in these tests anyway, such environmental studies should be only a small increment over our other efforts.

Since the larger tests in this area will sometimes involve the dispersal and burning of natural gas within the portion of Nellis AFR contained in the Frenchman Flat basin, we have considered whether such activities would be covered by their draft EIS.

The Nellis Air Force Range is used for underground nuclear tests (by DOE at Pahute Mesa) and gunnery and bombing practice over an area of many thousands of acres, as described in the Nellis Draft EIS. The effects of the activities are collapse craters, explosions, sonic booms, limited range fires from flares, tracers and bombs, pollutant emissions from aircraft, and fugitive dust from construction activities. Some of the effects damage vegetation and animal habitat areas.

The Nellis EIS is in the process of revision; however, the draft EIS contains many general statements about Nellis activities which are similar in nature to those cited from the NTS EIS. It, too, anticipates unspecified future tests whose impacts will be similar to those for the current activities. As with the NTS EIS, we estimate that the proposed LNG tests will cause effects similar to, but less extensive than, those incurred from the existing activities. Therefore, we feel that the proposed tests are within the scope of the Nellis Draft Environmental Impact Statement.

A Comparison of Frenchman Flat with Alternative Sites

Appendix A contains not only a detailed analysis of the potential environmental impact of doing the proposed LNG spill effects tests at Frenchman Flat in the NTS, but also a much briefer analysis for each of the eight final alternate sites. To fully assess the environmental impact at each of the alternate sites would require a much more thorough analysis than that presented in the Appendix. However, the readily available information proved to be sufficient to compare to first order the potential impacts at the alternate sites with that at Frenchman Flat.

Our judgments about the magnitude of the potential environmental impacts at each of the final candidate sites are contained in Table 1. In some cases readily apparent features of alternate sites allowed us to make definite judgments about the probable magnitude of certain impacts, e.g., fire. In other cases, e.g., endangered species, sufficient information was not available to us to make an absolute judgment. In these cases, fortunately, the detailed analysis of Frenchman Flat revealed a minimal impact. Therefore, we were able to conclude that it is unlikely that further investigation would reveal an alternative site with a smaller impact.

Table 1 led us to the conclusion that no reduction in the overall environmental impact could be made by choosing a site other than Frenchman Flat. The choice of Hunter Liggett, San Clemente Island, Eglin AFB, or Hanford Works would all be likely to result in an increased impact relative to Frenchman Flat. On the basis of limited information, White Sands MR, Hill AFR, Wendover AFR, or China Lake NWC all appeared to entail similar environmental impacts if the specific sites were chosen appropriately within those installations.

Since the environmental impacts of the remaining five sites was judged to be approximately equal, other factors (such as cost, logistics, etc.) were used to choose from among them.[4] On the basis of these other factors we recommend the selection of Frenchman Flat for the location of the proposed LNG spill effects tests.

TABLE 1. Comparison of Environmental Impact at NTS to the alternate sites. Impacts not shown below, e.g., smoke and air quality, are similar at all sites.

Site	Control of Hazards	Fire	Explosion	Endangered Species	Antiquities
Frenchman Flat, Nevada Test Site, NV	Easy	small	small	unlikely	unlikely
Hunter Liggett MR, CA	Moderate	large	medium	unknown	unknown
White Sands MR, NM	Easy	small	small	unknown	unknown
San Clemente Island, CA	Difficult	medium	medium	unknown	unknown
Eglin AFB, FL	Easy	large	medium	unknown	unknown
Hill AFR, Utah	Easy	small	small	unknown	unknown
Wendover AFR, Utah	Easy	small	small	unknown	unknown
Hanford Works, WA	Easy	small	medium	unknown	unknown
China Lake NWC, CA	Easy	small	small	unknown	unknown

REFERENCES

1. Final Environmental Impact Statement-Nevada Test Site, Nye County, Nevada, ERDA, September, 1977, p. 3-33.

2. IBID.

3. IBID, p. 5-2.

4. J. Cramer, W. Hogan, Evaluation of Sites for LNG Spill Tests, UCRL-52570, Lawrence Livermore Laboratory, September 1978.

APPENDIX A

ENVIRONMENTAL ANALYSIS FOR A PROPOSED TEMPORARY LNG SPILL TESTING FACILITY AT FRENCHMAN FLAT

INDEX

I. DESCRIPTION OF PROPOSED ACTION

The Lawrence Livermore Laboratory (LLL) has been asked by the Department of Energy (DOE) to participate in its liquefied energy fuels (LEF) safety research program. LLL's role will be to develop a set of computer models capable of describing the possible effects of accidental releases of LNG (Liquefied Natural Gas) to the environment and to collect sufficient experimental data that the models can be used to predict the phenomena of large ($\sim$150,000 m^3) spills based upon what can be learned from smaller experiments.

It is expected that the verification of the models will require an extensive experimental program. Tests will be run to study vapor generation and dispersion, pool fires, flame propagation in dispersed clouds, fireball formation, and rapid deflagration or detonation.

At the program's peak there may be 30 to 50 tests per year for a few years involving 10 to 1000 m^3 of LNG per test. Appropriate facilities and apparatus will be constructed at various locations in the Frenchman Flat basin to carry out and diagnose these tests. Because the DOE program is concerned with safety research for liquefied petroleum gas (LPG), liquefied hydrogen (LH_2) and liquefied ammonia (LNH_3) as well as for LNG, the facilities constructed will be designed to handle or to be easily converted to handle all four LEF's. However, the required research programs for all but LNG have not yet been defined sufficiently to permit an evaluation of their environmental impact. Therefore, this document will treat only the environmental impact of the LNG experiments. Many of the observations, however, will apply equally well to the other fuels.

At the spill site (see Figure 4) will be located:

(1) A pond of water 600 m in diameter and varying in depth from 0.6 to 3 m.

(2) A dry spill area for diked and undiked land spills.

(3) A cryogenic storage complex for about 1000 m^3 of LNG.

(4) Cryogenic pipelines connecting the above.

Around the spill site will be located an array of instrument stations. This array for any one test could consist of 50-60 towers, 18 m

or so tall, with a few reaching 60 m. These would be located in a fan shaped area predominantly on the downwind side of the spill site. Wind directions have not been selected yet, but should include winds blowing from the southwest, north, southeast and northwest (see Figure 4). An area in the center of the dry lake bed will be diked for dispersion tests over water.

Other remote instruments and weather stations will be placed at various locations throughout the Frenchman Flat basin. At the proposed flame propagation facility south of the spill point will be located a 100 m long 2-3 m diameter steel shock tube which ends in various structures built to study fireball formation, detonation and rapid deflagration.

For studies of vapor generation and dispersion, tests will involve spilling 10 to 1000 m^3 of LNG on water and soil and measuring the composition of the vapor as it disperses downwind. No ignition will be attempted in these tests. In addition to the in-situ and remote sensors, we may attempt to collect airborne samples with small, remote controlled aircraft.

In the pool fires various amounts of LNG up to 1000 m^3 will be spilled on water and soil and ignited immediately. The radiative output and other parameters of the resulting fire will be measured.

To study flame propagation, tests will first be run in the shock tube facility and in large plastic bags containing various gaseous mixtures. Then spills will be conducted in which the vapor is allowed to disperse outside the spill area before ignition is attempted. Flame propagation rates will be measured and conditions for fireball formation will be examined. Certain gas distributions may be artificially created for this portion of the study.

The studies of rapid deflagration and detonation will also begin at the flame propagation facility. Eventually, however, attempts will be made to allow a detonation to propagate from the tube into a partially confined or unconfined region of space. At first, this will be into a plastic bag filled with a controlled gas mixture but in later tests it will be determined if the confined detonation (or rapid deflagration) can be made to propagate into an unconfined cloud generated from a spill. Various kinds of initiators will be examined to determine which are more likely to lead to detonation.

II. DESCRIPTION OF EXISTING ENVIRONMENT

A. Location (see Figures 1, 2, 3, & 4)

Frenchman Flat, Nevada Test Site (NTS), is a typical desert alluvial basin with a dry lake bed (playa) in the center at 910 m elevation. It is located about 80 km NW of Las Vegas, Nevada. The nearest population center is Mercury, Nevada, (17 km south) a DOE support facility for NTS. The playa straddles the boundary of NTS and Nellis Air Force Range, a bombing and gunnery range. Three (3) km east of the NTS-Nellis boundary is the western boundary of the Desert National Wildlife Range (DNWR) which has been proposed as a wilderness area. Four (4) km north of the playa is a shallow burial storage site for low level radioactive waste. Six (6) km north of the playa is an occasionally used support location for DNA projects. Mercury Highway, the main north-south access road in NTS, is 6 km west of the playa center. In the past, the Frenchman Flat playa was used for atmospheric nuclear tests, and for non-nuclear explosives testing. It is currently used for non-nuclear explosive tests.

B. Adjacent Land Use

NTS is surrounded on the north, west and east by Nellis Air Force Range, which is used for bombing and gunnery practice in the bottom of the broad valleys between the mountain ranges. However, none of the portion of Frenchman Basin within the Nellis boundaries is so used except for occasional aircraft over flights. The area south and west of NTS contains the public highway, Route U.S. 95, the towns of Beatty (pop. 500, distance 75 km), Lathrop Wells (pop. 40, distance 46 km), and Indian Springs (pop. 1800, distance 30 km) from Frenchman Flat. The area has been used in the past for mining, farming and grazing, although it is essentially arid desert land.

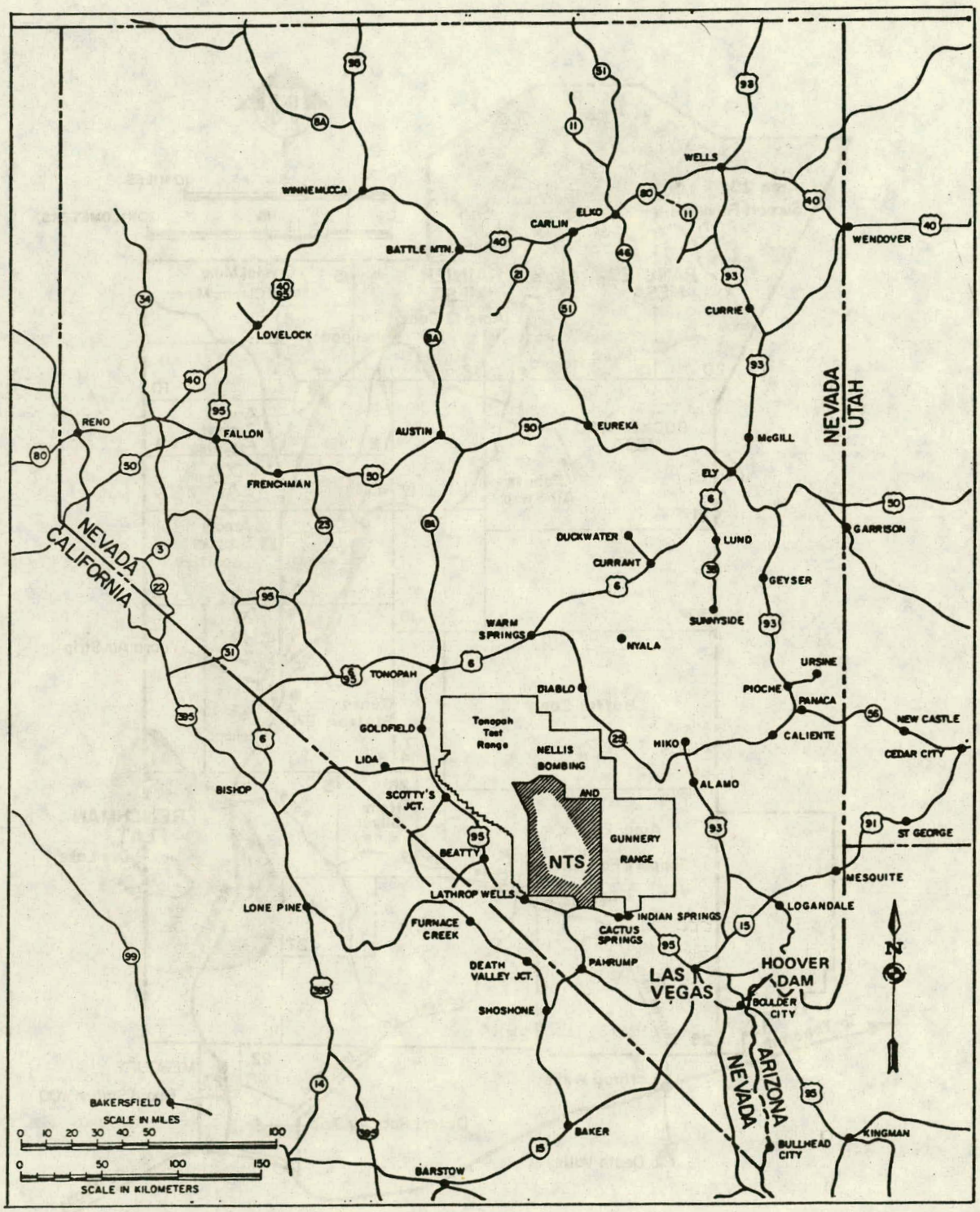

FIGURE 1 LOCATION MAP

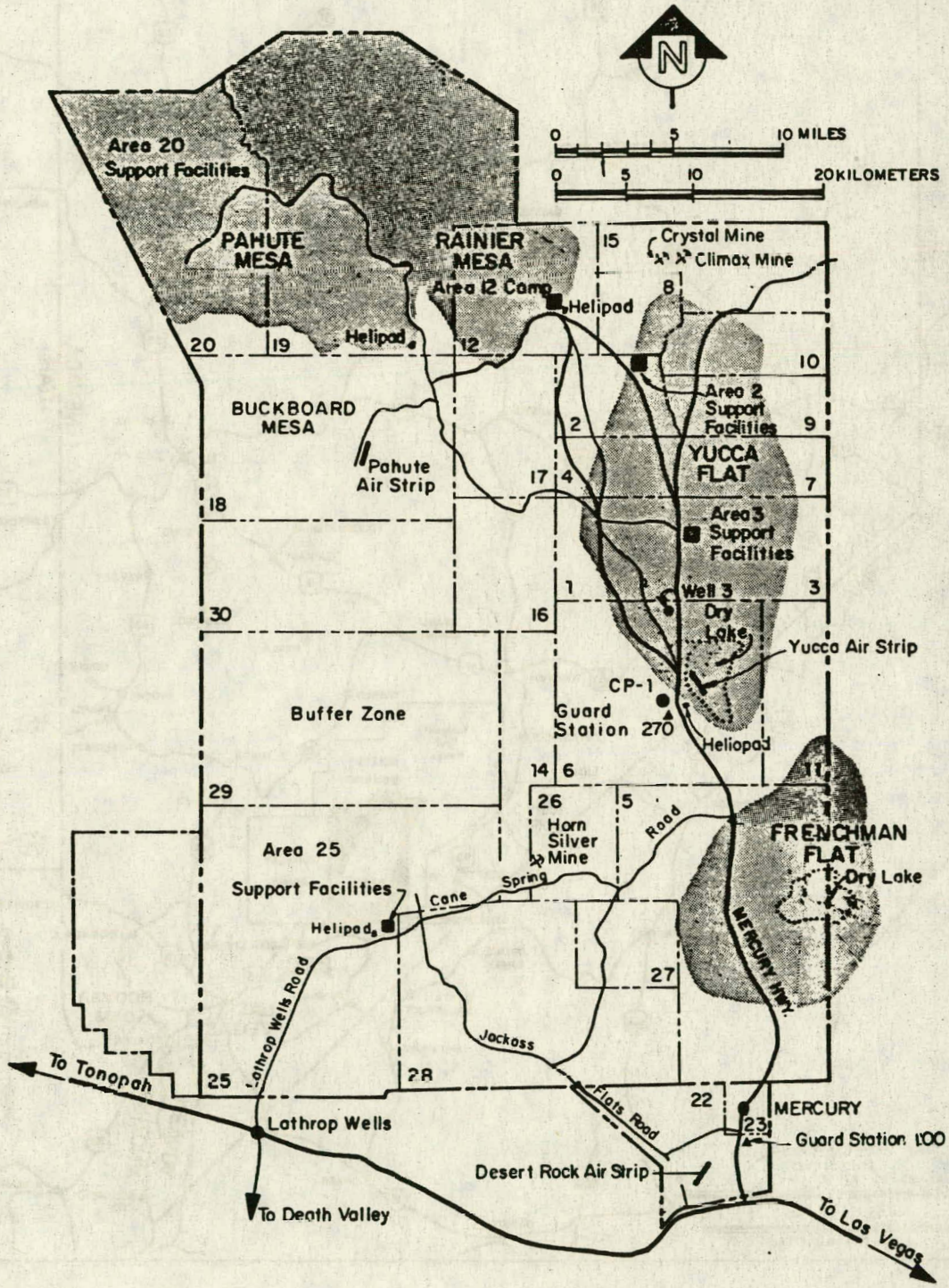

FIGURE 2 NEVADA TEST SITE

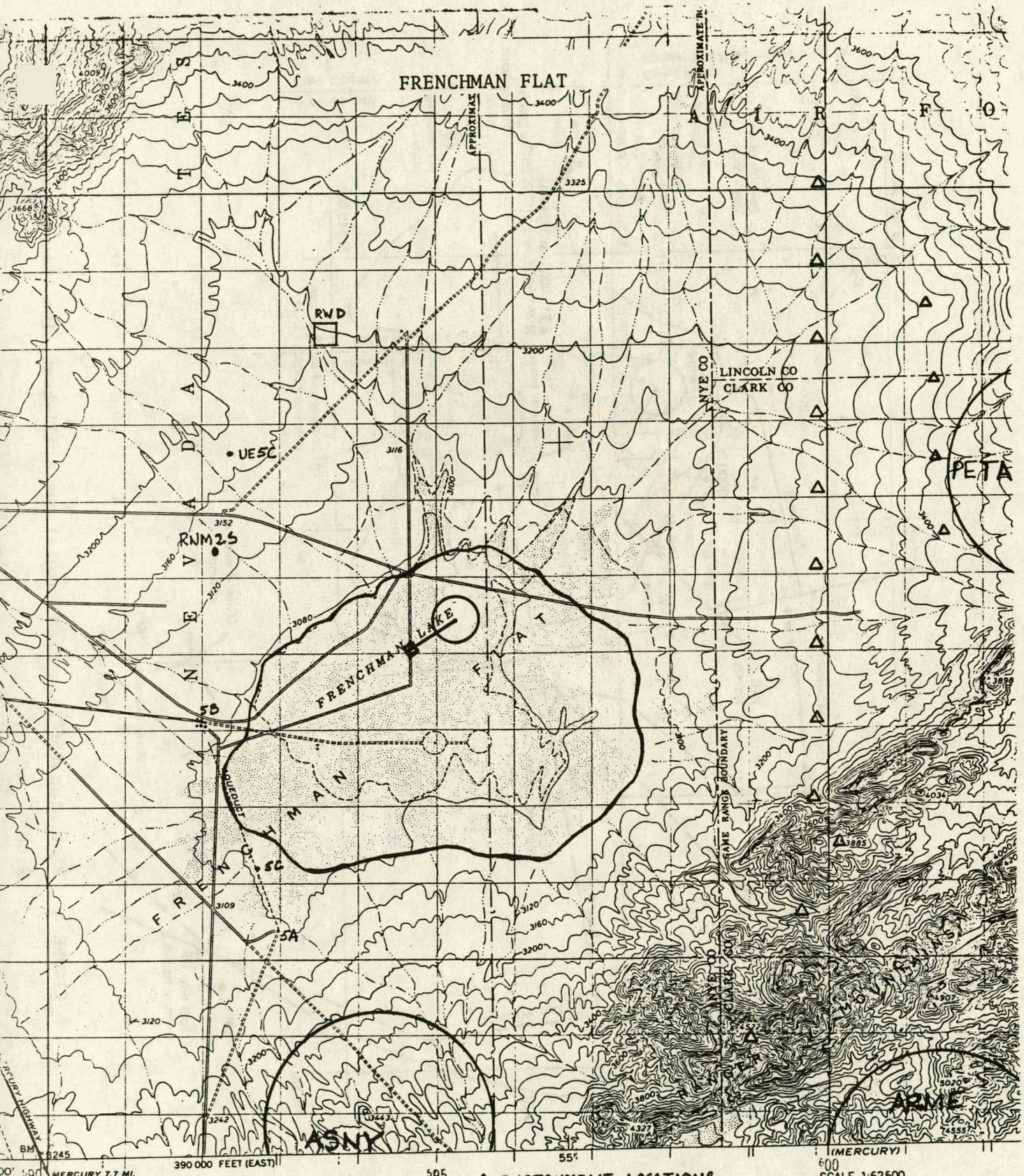

Δ INSTRUMENT LOCATIONS

SCALE 1:62500

apped by the Army Map Service
ublished for civil use by the Geological Survey
ontrol &GS and USCE
opogra. n aerial photographs by photogrammetric methods
erial photographs taken 1952. Field check 1952
olyconic projection. 1927 North American datum
0,000-foot grid based on Nevada coordinate system,
est and central zones
000-meter Universal Transverse Mercator grid ticks,

FIGURE 3

Mi 1 ½ 0 1 2

FT 3000 0 3000 6000 9000 12000 15000

KM 1 5 0 1 2 3 4

16°
TRUE NORTH
MAGNETIC NORTH

S-15

CONTOUR INTERVAL 40 FEET
DASHED LINES REPRESENT 20-FOOT CONTOURS
DATUM IS MEAN SEA LEVEL

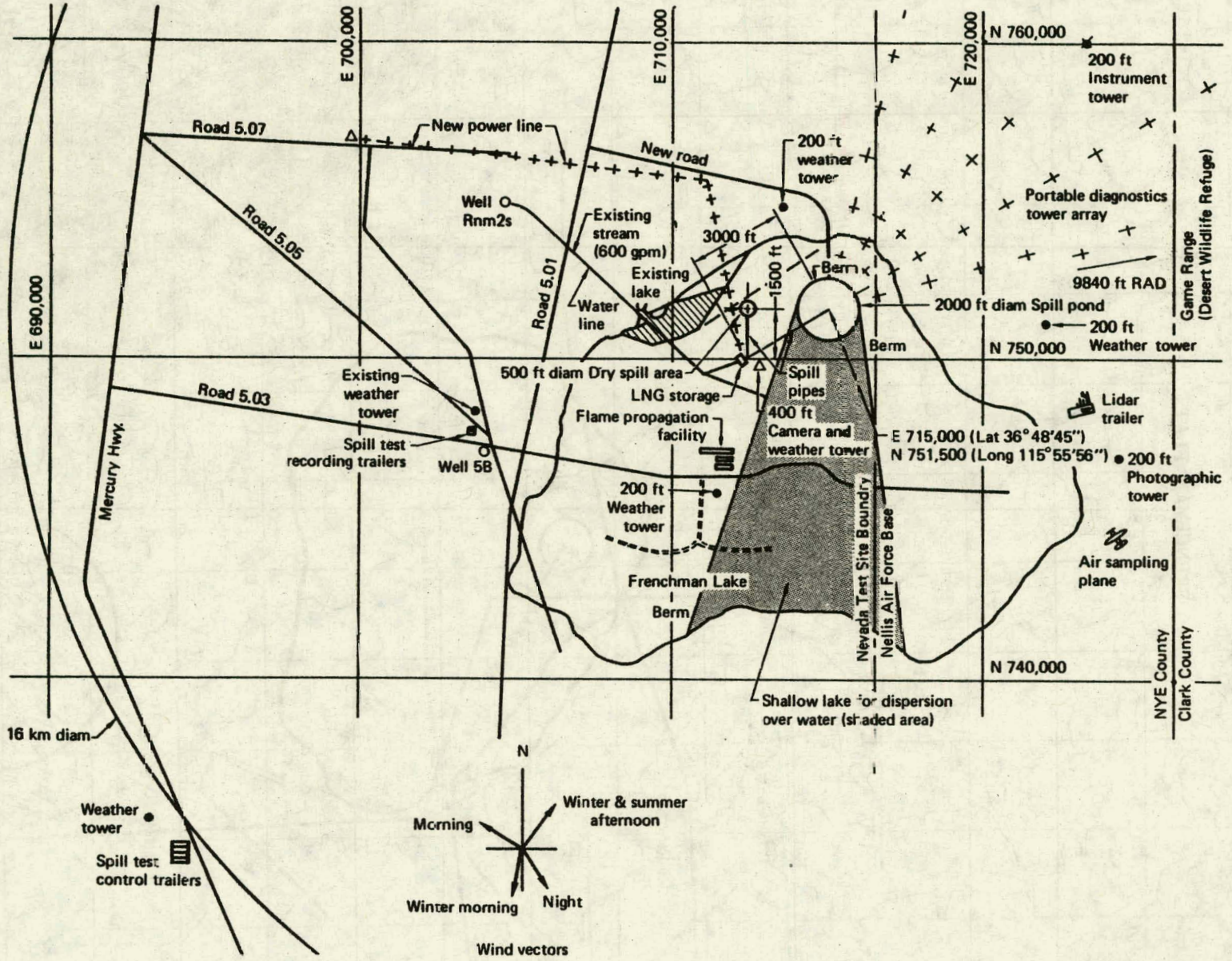

FIGURE 4 Plot plan for liquefied natural gas spill-test site, Nevada Test Site.

C. Climate

The climate of Frenchman Flat is affected by higher elevation west-to-east air flow over the Sierras from fall through spring, and south-to-north air flow from the Gulf of California in summer. Throughout the year the predominant local day-time wind direction is from the southwest. The Frenchman Basin exhibits a mountain-valley diurnal wind shift which flows up-slope during the day and down-slope at night. A temperature inversion accompanies the nighttime down-slope winds. Rainfall averages about 10 cm per year and occurs mainly in winter and summer. Temperature varies from an average low of -7°C in January to an average high 36°C in July. Relative humidity typically varies from 10% to 60%.

D. Air Quality

Other than radioactive air sampling, no air quality monitoring is done at Frenchman Flat. However, the general area of Clark County at times exceeds Federal air quality standards due to particulate pollution originating locally and in the Las Vegas metropolitan region. Very small amounts of low level radioactive particles from past atmospheric nuclear tests at Frenchman Flat are sometimes resuspended by high winds and dust devils. Occasional chemical explosive tests at Frenchman Flat produce hydrocarbon smoke and gases. The existing air pollution at Frenchman Flat, if any, does not exceed present air quality standards.

E. Geology & Topography

The present geology of Frenchman Basin consists of mountains made up of upthrusted and folded seabed sediments overlain by volcanic rocks surrounding a playa. The playa has been formed from weathering plus wind and water erosion of the mountains washing sands, gravels, silts, and clays down to a level flood plain. The thickness of the alluvial sediments is over 300 m. During winter and summer wet seasons, the relatively impervious lake bed soil supports many centimeters of mildly saline run-off water. There are several craters

northwest of the playa from underground nuclear detonations. There is a large shallow crater near the center of the playa from the "SMALL BOY" surface nuclear blast. The soil surrounding the SMALL BOY and other tests contains small amounts of radioactive particles. The playa contains many surface and underground ruins from past explosive tests. In the north end of the playa, a temporary lake has formed in a diked area. The lake is fed by water continuously pumped from a tritium migration test well, RNM2S, located northwest of the playa. Low tritium levels (625 pc/l) are present in the well water.

Four wells supplying potable water are located along the western end of the playa. The water is used for the Mercury water supply, construction and other purposes. The total flow capacity of all wells is about 1700 gpm.

F. Vegetation

The Frenchman Flat playa is largely barren with occasional saltbush and other plants in the wet areas. The alluvial fans and washes surrounding the playa are partially covered with low shrubs consisting of sagebrush, creosote bush, saltbush, grass, perennials, and annuals. There was an endangered species of milkvetch (Astragalus nyensis, ASNY) in an area about 4 km south of the playa center, an endangered species (Arctomecon merriamii, ARME) in the Desert National Wildlife Range (DNWR) 8 km SE of the playa, and a threatened species (Penstamon thurberi, PETA) 8 km ENE in the DNWR, as shown in Figure 3. The vegetation surrounding the playa has not been disturbed much since the atmospheric nuclear tests were concluded many years ago, although many unmarked unimproved roads crisscross the area and these see occasional use. (See Figure 3) Surveys and analyses made in 1979 and 1980 indicate that the above species are no longer considered threatened or endangered.

G. Animals

The diverse habitats of NTS are occupied by a wide variety of small animal species. In the Frenchman Basin and surrounding mountains, over a period of time there could be as many as 1000 species of insects, and over 200 species of reptiles,

birds, mammals, and fishes (goldfish at well 5B pond). None of these species is considered endangered or threatened. However, the Nevada Fish and Game Commission has prepared a list of "protected" species containing: Kit Fox, Spotted Bat, all Eagles, Falcons, Hawks and Owls, Osprey, Turkey Vulture, Belted King Fisher, White Pelican, White Faced Ibis, Common Nighthawk, Lesser Nighthawk, Roadrunner, and Desert Tortoise. Most of the protected species may occur permanently or transiently within the Frenchman Basin.

H. Archeological, Paleontological, & Historical Sites

The Frenchman Basin contains no reported archeological or historical artifacts, or remains. Archeological surveying is continuing at specific proposed locations for construction activities. There are some Lower Paleozoic fossils exposed in the eastern part of NTS, but none reported in the Frenchman Basin area. When new sites for construction are located, surveys for artifacts will be made prior to excavation and construction.

I. Seismicity & Ground Motion

Southern Nevada has generally moderate seismic activity. Frenchman Flat lies in the 1969 NOAA Seismic Risk Zone 2. There have been 23 seismic events within NTS during the 26 years from 1935-1961, all with magnitude less than Richter 4.5. From 1961 to 1973 there were 390 seismic events and aftershocks mostly from nuclear tests. There were 322 announced tests during this period.

The largest known earthquake near NTS was the Owens Valley (160 km west) earthquake of March 26, 1872, with estimated 8.3 Richter magnitude.

In the past there have been nuclear tests of about one megaton at NTS which produced ground motions leading to minor structural damage in structures within NTS. The present moratorium on yields in excess of 150 kiloton limits expected ground motions at Frenchman Flat to 0.14 g or less.

III. SAFETY

A. Description of LNG

The hazardous material to be tested is liquefied natural gas, whose properties are listed below:

State:	Liquid
Temperature:	-160°C at atmospheric pressure
Composition:	(varies with source) for the San Diego Gas & Electric LNG, Methane 92.2 Vol. % Ethane 5.3 Propane 1.1 Nitrogen 1.4
Specific Gravity:	0.452
Density:	3.8 lb/gal (0.452 gm/cm^3)
Flammability Limits:	5% to 15% NG/Air by Volume
Heating Value:	13,000 cal/gm, 1056 Btu/ft^3 gas, 23,176 Btu/lb Liquid
Expansion Ratio:	1 m^3 Liquid expands to 620 m^3 gas at STP

B. Handling Hazards

Natural gas is not toxic, but is an asphyxiate. LNG is a cryogenic fluid and will cause freeze burns if spilled on skin.

C. Storage

LNG will be delivered to NTS in 11,000 gal (42 m^3) LNG tank trucks which will unload the LNG into the storage tanks. The

storage tanks will be double wall construction with evacuated perlite in the annulus for insulation. The inner wall will be 304 stainless and the outer wall will be mild steel. All NTS, Federal and State codes will be adhered to in the design, construction and operation of the storage tank facility.

D. Test Procedures

To spill the LNG, the LNG tanks will be pressurized with nitrogen to force the LNG through the spill pipe into the spill basin. Proper materials, valves, fire protection systems and controls will be used to safely carry out tests.

Operating procedures in accord with NTS procedures will be written, approved and followed in the construction and operation of the LNG spill facility.

In some tests the NG vapor will be dissipated without ignition. In such cases the controlled zone will be large enough to assure that any gas leaving the zone is calculated to be in a non-flammable, safe condition.

In other tests the vapor will be ignited and burned. In these cases damaging thermal radiation will extend beyond the cloud itself. The controlled zone will account for this.

Experiments have shown that unconfined detonation of NG is very difficult to achieve and in fact has not yet been done. There will be careful control of the size, location and conditions under which experiments are done.

E. Hazards Control

1. Fire Control

During spill tests, there is some danger of spreading brush fires in the more heavily vegetated area; however, vegetation is sparse enough that it is not expected to

support a continuing fire. To control the fires, it may be necessary to clear fire break lines through the brush and to clear roadways for fire truck access. The cleared area will be minimized to avoid plant damage and blowing dust during heavy winds. Another option for fire control is chemical bombers.

2. Controlled Area

The potential maximum hazardous region for the proposed 1000 m^3 spill tests is bounded by a 16 km diameter hemisphere which includes part of the Mercury Highway. Within this volume air traffic will be restricted during some tests. Most tests will be done with the cloud moving in directions other than toward the Mercury Highway; therefore, it usually will not be necessary to close the highway. However, if a wind shift occurs during a test, Mercury Highway may be temporarily closed. The long range wind direction will be monitored with the NTS and Nellis weather station systems which will detect wind shifts up to one hour before test time. Extensive weather monitoring will be carried out within the basin by the program. All air and ground traffic and personnel will be controlled during each test to assure that no one unknowingly travels into the hazardous sector for any test. The exclusion zone for 80% of the tests will be much smaller than the 16 km diameter region. Any specific 1000 m^3 test will have a hazardous-to-people area of 8 km diameter as long as there are no major unexpected long term wind shifts. The 16 km circle represents the loci of 8 km circles for a wind in any direction.

If a wind shift occurs during a large test, it may be deemed advisable to evacuate downwind populated areas within the entire 16 km diameter controlled zone. Therefore an evacuation plan will be prepared for at least the 1000 m^3 tests, which will form one part of the overall safety procedure for the spill test program. The procedure will include actions to be taken if an accidental LNG spill or fire occurs in the facility itself, due to man or nature caused accidents such as operator error, tank failure, earthquakes, collisions or system failures.

IV. PROBABLE IMPACT OF PROPOSED ACTION

A. Construction Activities

There will be a considerable amount of construction and shallow excavation on the barren lake bed, with little damage to plants or animals. Up to 40 acres of land may be disturbed. Some dust will be generated, but in general it will not be radioactive since hot areas will be avoided for construction sites. In the surrounding vegetated areas, there will be some use of old jeep roads and some new roads constructed. Instrumentation stations will be placed at points accessible from these roads. No new roads or off-road traffic will be allowed in the Desert Wildlife Range east of Frenchman Flat. The work there will be limited to temporary placement of about 15 instrument stations placed next to existing roads or packed-in on foot or horseback. Each station will consist of a 3 m high, 10 cm diameter mast and base with instruments attached. The station locations are shown on Figure 3.

In the area between the NTS and the Nye County boundaries (see Figure 4) there will be an array of 40-50 steel instrument towers generally 18 m tall, with a few reaching 60 m in height. Some of the towers will be portable (mounted on trailers) and some will be the crank-up type on foundations. (Other portable apparatus, i.e., lidar vans and air sampling planes will also be deployed in this area.) Existing jeep roads will be used for access to the towers. When necessary, new jeep roads will be established.

There will be no impact on endangered or threatened plant species, because there are none in the affected area.

If artifacts are found during construction, actions to protect them will be taken. An environmental monitoring project will be instituted before major construction starts, and will continue throughout the program. The project will record the environmental effects of the program.

Water consumption for filling, and seepage and evaporation make-up for the spill pond will average about 300 gpm.

B. LNG Spill Tests

The effects on the environment from LNG spill testing results from (1) flameless vapor explosions, (2) freezing, (3) suffocation, (4) fires, and (5) chemical explosions and detonations.

1. Flameless Vapor Explosions

Flameless vapor explosions may occasionally occur during the spilling of LNG on water. The energy released is the fraction of the total thermodynamic energy in the liquid available during sudden vaporization of part of the liquid. The shock pressure for eardrum damage is about 5 psi. This is estimated to occur at 85 meters from the spill point for a 1000 m^3 instantaneous LNG spill, assuming 10% of the liquid would flash to vapor at supersonic velocity. Within 85 m, animals and plants may be damaged.

2. Freezing

The temperature of LNG liquid and undiluted vapor is -160°C. It will freeze and kill living cells on contact. During spills on water, there will be little impact on the biota, but spills on land will damage or kill insects and animals on or near the spill surface. Birds may be frightened away by the onrushing liquid and cloud. If the vapor temperature is below 0°C, some plant species may receive frost damage.

3. Suffocation

LNG vapor is not toxic, but if the concentration of oxygen is below 13%, suffocation may occur. Temporary lack of oxygen is not expected to harm vegetation. When the vapor cloud has dispersed to a concentration of 13% or more oxygen, no harm to biota will occur as long as the cloud is not ignited.

During LNG spilling, vaporization and dispersion, there may be some birds and small animals damaged from cold and asphyxiation. It is expected that none of these will be endangered or threatened species, but some may be State-of-Nevada "protected" species, if they happen to be in the area at the time, and are not frightened away by the commotion or the advancing visible

cloud. The injection of unburned hydrocarbons into the atmosphere is not considered a problem because the principle constituent, methane, is slow to oxidize, and would be only an intermittent contaminant. At the closest site boundary, 16 km distant, the natural gas concentration is calculated for a level terrain to be 0.05% for a 1000 m^3 spill. The Federal air quality standard for non-methane hydrocarbons (Clean Air Act 40 CFR Part 50.1) limits ambient air concentration to 0.24 ppm for any three hour period. The same conservative calculation suggests that a 1000 m^3 release (6% ethane and propane) at 16 km downwind may produce 1.8 ppm when spread over a three hour period. However, in reality there is a mountain range between the test site and the nearest boundary. It is expected that the dispersion of the gas will be accelerated due to the turbulence created by the mountains; therefore, the Clean Air Act limits are not likely to be exceeded. If, based on measurements from smaller spills, a spill is predicted to actually exceed 0.24 ppm, a variance will be obtained from the Nevada Environmental Commission. Measurements will be made to determine higher hydrocarbon concentrations at appropriate locations.

4. Fires

The LNG vapor will be ignited during the spill at the spill point for pool fire tests. The wood ignition distance realistically expected is about 500 m from the pool for a 1000 m^3 test, during calm wind conditions. The height of the flame will be over 800 m. When a dispersing vapor cloud is ignited some time after the LNG has evaporated, the realistically expected distance to wood ignition will be close to the above value for normal burn propagation. The hazardous distance from the spill point for plants and animals for dispersion plus burning tests is about 4 km from the spill point, including the dispersion distance. Beyond ~4 km, the cloud is not expected to be flammable. A fireball may develop from a vaporized cloud formed during conditions of very low wind speed or a calm. Much of the cloud is flammable and burns rapidly. The realistically expected distance to wood ignition for a 1000 m^3 spill is 1200 m. The fireball and hot gas ball may rise to a height of many km. The diameter of the fireball is calculated to be about 500 m.

The purpose of the test program is to accurately determine scaling relations so that the maximum hazardous distance from LNG spills and burns of various sizes can be predicted. Before 1000 m^3 tests are executed, smaller spills will be made which will allow more accurate predictions of the actual hazardous zone than the above estimates. Appropriate planning will then be done to protect designated areas from the hazards described.

When LNG clouds are ignited, within the burning cloud, and some distance from it, (i.e., within an area of 1200 m radius), animals and plants may be damaged. Since the cloud burn may be done over vegetated areas, range fires may be started, which could spread. Burn tests will not be done under conditions in which the danger of rapidly spreading range fire is high. However, fire fighting equipment and crews will be available to extinguish any spreading range fires.

There will be a smoke cloud after burn tests consisting of combustion products of the higher hydrocarbons. The cloud will be visible many kms from the burn site. Burning brush will also generate smoke which can persist some time after a test. When required, a burning permit will be obtained.

5. Explosions

There will be tests involving explosions and detonations in the shock tube facility and in dispersing LNG vapor clouds. The tests will start out small, and the effects will be measured. Sonic booms will be heard many km away, but will not damage plants or animals. Detonation tests using 1000 m^3 of LNG may not be done if tests at smaller sizes prove sufficient or if the hazards, as indicated by smaller tests, appear too high.

The air shock from the detonations would have no deleterious effect on any endangered or threatened plant species.

Effects from deliberate explosions, detonations in confined spaces, and tests of flame speed run-up to detonation in open spaces are estimated to be less than those from one kiloton of high explosives even for the largest tests. The shocks produced would damage eardrums (5 psi) at 500 m from the explosion. Animals within 1.5 km may be damaged by the shock or heat during the 1000 m^3 detonation tests.

A study has been made of the amount of relic radioactive dust from past nuclear tests which could be injected into the air and transported downwind in a 1000 m^3 LNG test[1] if a test were done over a contaminated area. A large amount of soil (up to 330 tons) could be lofted into the air and dispersed downwind. A fraction of the dust may contain very small amounts of radioactive debris from previous nuclear tests (95 m Ci/gm, max.). This may either fall out downwind of the explosion within the Frenchman Basin, or be dispersed in the upper winds.

The study results indicate that the air and ground dose rates would be within EPA standards.

The particulate air pollution allowed by the Clean Air Act 40 CFR 50.6 is 260 $\mu g/m^3/24$ hr, once per year. For a 1000 m^3 test, calculations based on Ref. 1 indicate that dust suspension could be 38 $\mu g/m^3/24$ hr. The radioactivity in the dust would be within allowable Federal guidelines. If such large tests are done often enough to exceed the guideline, a variance will be obtained from the Nevada Environmental Commission or the EPA.

V. ALTERNATIVES

Alternative 1 - No Project

If the project were not implemented, there would be no environmental impact. However, the project is urgently needed to provide

experimental data for verification and normalization of computer programs which predict the spill effects of LNG accidents. The information will be used to safely locate, design and regulate LNG receiving terminals and to regulate LNG shipping operations along the coasts of the United States.

Alternative 2 - Reduce the Scope of the Project

If the scope of the project were reduced, the environmental impact would be reduced. However, LNG spill tests of up to about 1000 m^3 are needed to verify the computer codes which will be used to calculate the safe transportation of LNG in tankers of up to 150,000 m^3 capacity and the subsequent storage of that LNG.

Alternative 3 - Locate the Project at a Different Site

LLL has extensively surveyed sites throughout the United States [1] and has recommended to the DOE that the Frenchman Flat site is the best considering safety, experimental and cost factors. The environmental impact at other sites evaluated is probably equal to or greater than that expected at Frenchman Flat. Relocation would result in program delays and subsequent delays in vitally needed regulatory information.

Preliminary Evaluation of Alternate Test Sites

We took as our list of potential sites for the LNG experimental facility an initial compilation of installations owned by the DOE and the military, as given in Ref. 4. Sixty-nine installations having areas greater than 64 km^2 are included. Table 1 lists these installations.

In view of the limited resources available for the site evaluation study, we used only information readily available at LLL. Our sources included atlases, government maps, published weather data, and other standard reference material. Since complete information was not available for most of these installations, we used negative factors or gross failure to meet one of our ten desired site characteristics, given in Table 2, as the basis for the initial screening. The three categories of desirable site characteristics where these deficiencies were most easily identified were Safety (No. 1), Minimal External Constraints (No. 2), and Low Costs (No. 8).

Table 1 shows the results of this cursory examination. It should be noted that if one strong reason was found for rejection of a site, we often did not examine that site further in relation to the other criteria. Therefore there may be other reasons besides those shown in the table for rejecting any particular site.

TABLE 1. Results of our initial screening of 69 DOE and military installations in the U.S. with areas greater than 64 km^2.

	Approximate Dimensions (km)	Why Judged Unacceptable
ALABAMA		
Fort Rucker	24x16	safety, cost
Redstone Arsenal	11x8	safety, cost
ALASKA		
Fort Greely	48x32	cost
Fort Wainwright	48x48	cost
Kodiak Naval Station	8x8	safety, cost
Yukon Command Training Site	112x48	cost
ARIZONA		
Fort Huachuca	32x16	safety
Luke Air Force Range	208x40	external constraints
Navaho Army Depot	16x16	safety
Wilcox Dry Lake Bombing Range	24x16	safety
Yuma Proving Ground	80x32	external constraints
ARKANSAS		
Fort Chaffee	32x16	safety
CALIFORNIA		
Camp Pendleton	32x16	safety, external constraints
Camp Roberts	24x16	safety
Edwards Air Force Base	56x24	external constraints
El Centro Naval Air Facility	80x32	cost
Fort Irwin	56x48	cost
Hunter Liggett Military Reservation	40x24	OK
China Lake Naval Weapons Center (North Range)	64x48	OK
China Lake Naval Weapons Center (South Range)	48x32	
National Parachute Test Range (Salton Sea)	24x16	safety, external constraints, cost
San Clemente Island	32x8	OK
Sierra Army Depot	32x16	safety, external constraints
Twentynine Palms Marine Corps Base	64x32	cost
Vandenberg Air Force Base	32x16	safety, external constraints
COLORADO		
Fort Carson	40x16	atmospheric conditions, cost
FLORIDA		
Eglin Air Force Base	80x32	OK
Tyndall Air Force Base	16x5	safety
GEORGIA		
Fort Benning	32x32	safety
Fort Gordon	32x16	safety
Fort Stewart	48x24	safety
HAWAII		
Kahoolawe Naval Reservation	16x8	safety, external constraints, cost
Pohakuloa Training Area	24x16	flat land, cost
IDAHO		
National Reactor Test Site (DOE)	48x40	external constraints
Saylor Creek Air Force Range	32x24	water supply
INDIANA		
Jefferson Proving Ground	32x16	safety

TABLE 1. (Continued)

	Approximate Dimensions (km)	Why Judged Unacceptable
KANSAS		
Fort Riley	32x32	cost
Smokey Hill Air Force Range	16x8	safety
KENTUCKY		
Fort Campbell	32x16	safety
Fort Knox	32x24	safety
LOUISIANA		
Fort Polk	32x8	safety
MISSOURI		
Fort Leonard Wood	24x24	safety
NEVADA		
Hawthorne Naval Depot	32x16	safety
Nellis Air Force Range	120x64	OK
Nevada Test Site (DOE)	64x48	
NEW MEXICO		
Fort Bliss Anti-Aircraft Range	40x32	safety
McGregor Range	64x32	external constraints, cost
Sandia Base (DOE)	8x8	safety
White Sands Missile Range & Holloman AFB	160x64	OK
NEW YORK		
Fort Drum	32x32	safety
NORTH CAROLINA		
Camp Lejeune Marine Corps Base	24x24	safety
Fort Bragg	32x24	safety
OKLAHOMA		
Camp Gruber	16x8	safety
Fort Sill	48x8	safety
OREGON		
Boardman Naval Bombing Range	24x16	safety
SOUTH CAROLINA		
Fort Jackson	24x16	safety
Savannah River Plant (DOE)	32x32	safety, external constraints
TEXAS		
Camp Bullis	24x16	safety
Fort Hood	32x32	cost
UTAH		
Dugway Proving Grounds	72x40	external constraints
Hill Air Force Range	64x32	OK
Wendover Air Force Range	64x32	OK
VIRGINIA		
Camp Hill	24x24	safety, external constraints
Camp Pickett	24x16	safety
Quantico Marine Corps Base	32x16	safety
WASHINGTON		
Fort Lewis	48x16	safety
Hanford Works (DOE)	56x40	OK
Yakima Firing Range	40x32	external constraints
WISCONSIN		
Camp McCoy	24x16	safety, atmospheric conditions

TABLE 2

REQUIRED SITE CHARACTERISTICS FOR
a 1000 m^3 LNG SPILL TEST SITE

1. Low safety hazards
2. Minimal external constraints
3. Acceptable surface winds
4. Flat land
5. Wide range of atmospheric conditions
6. Large body of water
7. Available water supply
8. Low costs
9. Rainfall
10. Variable topography

Over half of the installations were found unacceptable because of safety considerations. For the most part this judgment was based on the size and shape of the facility, the proximity of large population centers, and the existence of major highways adjacent to or through the test area. Approximately one-fourth of the installations had obvious external constraints such as conflict with the installation's prime mission, or lack of controlled visual or physical access or potential adverse environmental impact. One-third of the locations were judged to have unduly high operating costs because of remoteness, short testing season, or lack of identifiable support or facilities.

Many of the desert sites were similar to NTS in some respects, but were lacking in others. For example Dugway Proving Grounds remain contaminated and are therefore unsuitable. The Yuma Proving Grounds enclose a large wildlife area, the National Parachute Test Range at the Salton Sea contains a National Wildlife Refuge and is adjacent to a major recreational area.

The nine sites remaining after this initial screening were examined further with available information. Except for NTS and China Lake, none of the sites were visited. Each of the nine sites is described briefly below with the information available at this time.

1. Hunter Liggett Military Reservation

General: Army reservation in California, in the Central California coast range, approximately 150 miles SE of San Francisco. Encompasses a portion of San Antonio Reservoir. Varied topography.

Weather: Typical of California coastal valleys; some marine influence.

Topography: Varied, generally rugged, limited flat land.

Population: Sparse.

Vegetation: Mixed oakwoods, grassland.

Water: Adequate supply. Emcompasses a portion (1 mi by 5 mi) of San Antonio Reservoir.

Logistics: Travel distances from LLL are very reasonable.

Other: Vegetation may be excessive and would require clearing. If so, the site may be environmentally sensitive. San Antonio Reservoir is reported to be used by the public for recreational purposes; if this is so, controlled access could be a problem.

Environmental Impact:

Fire Potential

The heavy vegetation in Hunter Liggett results from the 60-90 cm of annual rainfall in the region. During 1000 m^3 vapor cloud burns, brushfires or forest fires would probably result unless the test area (200 square km) was cleared of most vegetation.

Explosions & Sonic Booms

During tests for the explosiveness of LNG vapor, tons of dirt and debris may be lofted from the ground surface, and sonic booms may be heard many km distant. Within parts of the 16 km diameter hazardous region, plants and animals will be damaged.

Endangered Species

An exact proposed location for a spill test area has not been specified and therefore no surveys have been made. However, there are endangered animal species in California which would have to be considered, i.e., the Light-footed Clapper-rail, various falcons, the Santa Barbara Sparrow, the San Joaquin Kit Fox, the Morrow Bay Kangaroo Rat and the Salt Marsh Harvest mouse. There are many endangered species of California plants which would also have to be considered.

Antiquities

The California Coast Ranges were extensively populated by Indians in the past. Any test area would have to be surveyed for artifacts, burial grounds and village sites before a test site was selected.

Contact: Jack Yamauchi.

2. White Sands Missile Range and Holloman Air Force Base

General: A huge area in south central New Mexico having dimensions approximately 160 by 64 km. White Sands National Monument, San Andres Wildlife Refuge, and Fort Bliss Range all lie within the southern third of the range. U.S. Highway 70 cuts across the southern corner. No other major highways are shown within the boundary. The San Andres mountain range runs the length of the site, leaving flat and desolate land on the east side.

Weather: Typical of high (4000 ft) southwest deserts. Would be expected to vary seasonally.

Topography: Extensive flat areas to the east of the San Andres mountains. Alkali flats and dry lake beds abound.

Population: Sparse. Most of the activities are located in the southern part of the range.

Vegetation: Anticipated to be sparse in the alkali flats areas. The higher regions have juniper and pinon.

Water: Scattered springs are shown in the higher regions. One lake is shown which could vary in size from 160 to 800 acres, could be alkaline.

Logistics: Oil and gas fields located approximately 150 miles to the east could be a potential source of LNG. Population centers are close enough to service the program.

Other: Range activities and restructions are unknown at this time.

Environmental Impact:

Fire Potential

A test site could probably be located in an alkalic flat area with sparse vegetation. There would be little brushfire danger and probably no need to clear the site of vegetation.

Explosions

Many tons of soil will be lofted during explosiveness testing. Sonic booms will travel many km. Because of the sparse vegetation and low animal population, little environmental damage will be incurred.

Endangered Species

There are endangered species of animals in New Mexico, i.e. the Masked Bobwhite and various falcons, which might be found in desert areas. A survey of a proposed test-site would be required for these and other endangered species of plants before a test-site could be selected.

Antiquities

The South Central region of New Mexico was populated in the past by Chiricahua Indians. Area surveys for artifacts would be required before site approval.

Contact: None.

3. San Clemente Island

General: Navy gunnery range off California, approximately 40 miles offshore of San Diego and Long Beach. Shoreline fairly rugged. Topography generally rugged. Highly isolated from public. The size is approximately 8 x 32 km.

Weather: Constant, predictable offshore winds can be expected. Some fog.

Topography: Rugged. Limited level land.

Population: Government only.

Vegetation: Grassland, coastal sagebrush.

Water: All around.

Logistics: Sea and air only. 40 miles offshore. Support of major or extended operations may be expensive.

Other: Principal attraction is its isolated marine location. There is little control over sea approaches.

Environmental Impact:

Fire Potential

The grassland and coastal sagebrush on the island present a fire hazard during vapor-cloud burn tests. Large areas would either be cleared before tests, or firebreaks cleared around the test area. Vapor cloud burning would be hazardous to the many species of shore and sea birds, and marine life common to California coastal islands.

Explosions

Environmental damage from explosions will be greater here than in desert sites due to higher populations of plants and animals.

Endangered Species

Some of the endangered species of plants and animals mentioned previously may occur on or near San Clemente Island. In addition, the Brown Pelican frequents the area. A survey, if not already done, would have to be made before selection of a test area.

Antiquities

In the past, Gabrielino Indians at times populated San Clemente Island. A survey for shell mounds, village sites and artifacts would be required before selection of a test area.

Contact: Mr. Jan Larson (Naval Air Station, San Diego, California).

4. Eglin Air Force Base

General: Air Force gunnery, bombing, and multipurpose installation in Florida on the Gulf coast, approximately 100 miles east of Mobile, Alabama. Encompasses 30 miles of shoreline of Gulf and along Choctawhatchee Bay. Generally wooded, low lying.

Weather: Mild weather with few extremes. Should be satisfactory for test purposes. Rainfall adequate to excessive. Some fog.

Topography: Low lying, gentle, some marshes, dunes.

Population: Large area of controlled access.

Vegetation: Mixed conifers, grasses.

Water: Along Gulf coast and bays. Plentiful water.

Logistics: Travel distance from LLL greater than most other sites.

Other: Recreational use of waterways may be difficult to control.

Environmental Impact:

Fire Potential

The vegetation at Eglin consists of Southern mixed forests inland and marsh and sand-dune vegetation on the coast. Depending on the test site selected, it would be necessary to clear a large area (200 sq. km) of pine and brush to prevent spreading forest or brush fires during vapor cloud burning tests. The abundant bird and animal life would be threatened by the cloud burns.

Explosions

Environmental damage from explosions will be greater here than in desert sites due to higher populations of plants and animals.

Endangered Species

The endangered species of animals which may occur at Eglin are: Aligator, Southern Bald Eagle, Brown Pelican, Cape Sable Sparrow, Dusky Seaside Sparrow, various woodpeckers, various darters, Key Deer, Florida Panther and Sea Cow. In addition, there are endangered species of plants to survey for before test-site selection.

Antiquities

The Indian nations which previously occupied the Eglin area are the Chatot, Tohome, Nanraba and Mobile. A detailed survey of the area for artifacts, burial grounds, etc., would be required before test-site selection.

Recreational Resources

If a shore-side location for a test site were selected, it could have an impact on use of waterways by fishermen, hunters, boaters and commercial traffic.

Contact: Mr. B. B. Toole.

5. Hill Air Force Range

General: Air Force bombing and gunnery range in Utah, immediately west of Great Salt Lake. Encompasses a 10-mile strip of shoreline and adjacent salt flats and wet lands. Desert, minimal vegetation. Varied topography.

Weather: Typical of most desert ranges, acceptable for most tests. Rainfall marginally adequate to accomplish tests for which precipitation is required. Detailed weather data not available.

Topography: Salt flats, wet lands, portion of Great Salt Lake.

Population: Sparse, large exclusion area.

Vegetation: Sparse.

Water: Adjoins Great Salt Lake. Water table shallow over much of site.

Logistics: Access from LLL and proximity of local supply centers is about average for the sites under consideration.

Environmental Impact:

Fire Potential

Due to the low rainfall of about 20 cm/year in the Hill AFB region, there is very sparse vegetation, and little fire hazard. Clearing of large areas would not be necessary.

Explosions

Because of the sparse vegetation, little environmental damage will be incurred from explosions.

Endangered Species

Various falcons and the Utah Prairie Dog may be found in Utah along with many endangered species of plants. Surveys would be required before test site selection.

Antiquities

The Shoshone Indian nation populated the area in the past. A survey for village sites, mounds, artifacts, etc., would be required prior to test site selection.

Contact: Mr. Arlo H. Stewart

6. Wendover Air Force Range

General: In Utah, south of Hill Air Force Range, and generally similar. Contains numerous intermittent small lakes.

Weather: Typical of most desert ranges, acceptable for most tests. Rainfall marginally adequate to accomplish tests for which precipitation is required. Detailed weather data not available.

Topography: Salt flats, intermittent lakes.

Population: Sparse, large exclusion area.

Vegetation: Sparse.

Water: Unknown. Water table reported shallow, site encompasses intermittent lakes.

Logistics: Access from LLL and proximity of local supply centers is about average for the sites under consideration.

Environmental Impact:

Fire Potential

Due to the low rainfall of about 20 cm/year in the Wendover AFR region, there is very sparse vegetation, and little fire hazard. Clearing of large areas would not be necessary.

Explosions

Because of the sparse vegetation, little environmental damage will be incurred from explosions.

Endangered Species

Various falcons and the Utah Prairie Dog may be found in Utah along with many endangered species of plants. Surveys would be required before test site selection.

Antiquities

The Shoshone Indian nation populated the area in the past. A survey for village sites, mounds, artifacts, etc., would be required prior to test site selection.

Contact: None.

7. Hanford Works

General: DOE site in south central Washington, approximately 70 miles east of Yakima. Encompasses 60 miles of Columbia River. Low desert vegetation, sagebrush. Varied topography.

Weather: Typical of high desert regions. Cold in the winter, but a large number of suitable test days should be available in the spring, summer, and fall seasons.

Topography: Varied.

Population: Sparse, large exclusion area.

Vegetation: Sparse.

Water: Columbia River traverses site.

Logistics: Travel time from LLL above average but not excessive. Information on local logistics not available.

Other: DOE installation.

Environmental Impact:

Fire Potential

The low precipitation of 20-30 cm/yr in central Washington produces sparse vegetation. Therefore, there would be little forest-fire hazard and probably no need to clear a large area of vegetation.

Explosions

Sonic booms may impact the Indian reservations during certain atmospheric conditions.

Endangered Species

Various falcons, Columbian White-tailed Deer, and endangered plant species may be found in Washington. Surveys would be required before site selection.

Antiquities

The Yakima and Umatilla Indian nations populated the area in the past and their present day reservations are nearby. A survey for Indian antiquities would be mandatory before site selection.

Contact: None.

8. China Lake Naval Weapons Center

General: Naval weapons development center in California, on the Mojave Desert, approximately 125 miles NE of Los Angeles. Desert, minimal vegetation. Varied topography. Includes two sites: a northern and a southern one.

Weather: Typical hot desert climate, windy at times, would permit a reasonable percentage of test days.

Topography: Mixed, with high mountains on north side of sites. Both the north and south sites are extensive.

Population: Large (4000) and generally centered at existing test facilities. Controlled population.

Vegetation: Mostly sparse, heavy brush in some areas.

Water: Water table is very high at certain locations, but in general water is rather scarce. Some existing wells.

Logistics: For transport of LNG this location is relatively good. Site requires a full day's travel from LLL, Livermore, on scheduled commercial airlines, but only about 1-1/2 hours on a chartered or LLL plane.

Other: The National Atlas shows the Naval Ordnance Test Station at China Lake is in two parts. The southern site is shown bordering Fort Irwin to the east.

Environmental Impact:

Fire Potential

The sparse vegetation in the high Mohave Desert does not present a fire hazard except in high wind situations when vapor cloud burn tests would not be conducted. There would be no need to clear large areas of vegetation.

Endangered Species

As previously mentioned, there are many endangered species of plants and animals in California. Surveys in proposed test site areas would be required before site selection.

Antiquities

The Kawaiisu Indian nation occupied the NWC area in the past. A survey for artifacts, burial sites, etc., would be required before site selection.

Contact: Mr. C. D. Lind.

VI. UNAVOIDABLE IMPACTS

The unavoidable effects on the atmosphere are occasional air pollution a little above Federal limits, occasional smoke clouds consisting primarily of carbon soot, and possible sonic booms. The unavoidable effects on flora and fauna will be damage to non-threatened and non-endangered species of plants and animals close to the test area from construction, freezing, asphyxiation, heat and shock waves. The magnitude of the damage is small because of the small populations in the relatively barren desert environment.

VII. RELATIONSHIP OF SHORT TERM USE TO LONG TERM PRODUCTIVITY

The temporary (5-10 yr) use of Frenchman Flat for the LNG tests will have no known effect on its subsequent use for other types of tests or for any other conceivable use. Even future agricultural or recreational productivity would not be affected by the LNG tests.

VIII. IRREVERSIBLE & IRRETREIVABLE COMMITMENTS OF RESOURCES

The construction of the temporary LNG spill facility will consume thousands of man-hours of human effort and many tons of steel, copper, nickel, concrete and other structural and electrical materials. Some of the equipment will be used for other purposes after the LNG Spill Program is completed. The spill tests will consume up to 20,000 m^3 of LNG, which otherwise would have been used for industrial or home heating. Thousands of cubic metres of liquid nitrogen will be used for cool-down and pressurization for the spill tests.

At the conclusion of the program the land at Frenchman Flat can be used for other activities.

IX. BALANCE OF BENEFITS

The goal of the LNG Spill Effects Program is to obtain information required to regulate the siting and operations of LNG shipping and terminals. Safe siting and operations will help protect citizens and property from LNG disasters. The spill tests will release burned and unburned hydrocarbons into a remote portion of the Nevada air periodically over a period of five or more years. For some of the large tests, the ambient air quality standards may be temporarily exceeded, but the knowledge gained will help protect lives and property in case of LNG ship and terminal accidents. Another benefit of timely information is the safe use of LNG which will substitute non-polluting natural gas for coal and oil.

GENERAL REFERENCES

1. Evaluation of Sites for LNG Spill Tests, UCRL-52570, APP. III, September 15, 1978.

2. Final Environmental Impact Statement, Nevada Test Site, September, 1977, ERDA-1551.

3. Draft Environmental Statement, Nellis Air Force Range, June, 1978.

4. An Approach to LNG Safety and Environmental Control Research, DOE/EV-0002, February, 1978.

5. Status of Endangered & Threatened Plant Species on Nevada Test Site, a Survey, EG&G 1183-2356, Pt. 2, May, 1978.

APPENDIX B APPROVAL MEMORANDUM

Department of Energy
Nevada Operations Office
P.O. Box 14100
Las Vegas, NV 89114

MAR 6 1978

Dr. Richard L. Wagner, Jr.
Associate Director for Nuclear Test
Lawrence Livermore Laboratory
P. O. Box 808
Livermore, CA 94550

Dear Dr. Wagner:

You have approval to consider the Nevada Test Site (NTS) as a location for your liquefied natural gas (LNG) spill facility as addressed in your letter of January 9, 1978. However, approval of this project will depend upon evaluation of your detailed proposals.

It appears that the Environmental Impact Statement for the NTS adequately covers the proposed LNG experiments. However, appropriate attention shall have to be given to NTSO-SOP Chapter 6003, "Preservation of Antiquities and Historic Sites," prior to committing an area for the LNG experiment facility. Also, it is suggested that you consider Jack Reed's (Sandia Laboratories) participation relative to blast and ducting effects.

Sincerely,

Mahlon E. Gates
Manager

cc: J. R. Gilpin, Dir., P&B
S. R. Elliott, Dir., OSH
E. M. Douthett, Dir., P&LS
B. C. Moore, Dir., NTSSO

APPENDIX C APPROVAL MEMORANDUM

Department of Energy
Nevada Operations Office
P.O. Box 14100
Las Vegas, NV 89114

August 2, 1978

Dr. R. L. Wagner
Test Director
University of California
Lawrence Livermore Laboratory
P. O. Box 808
Livermore, CA 94550

Dear Dr. Wagner:

APPROVAL TO CONDUCT LIQUID NATURAL GAS (LNG) SPILL EFFECTS TESTS AT THE NTS

A review of your proposal to conduct LNG Spill Effects Tests in the Frenchman Flat area of the NTS has been completed. Subject to the following conditions, approval of your request is hereby granted.

1. Environmental Aspects

The present final Environmental Impact Statement for the NTS addresses high explosive tests of a chemical nature. We would expect, based on our discussions with LLL staff to date, that the current EIS will suffice. Studies, however, of the effects of LNG on the environment during the smaller scaling experiments will be necessary in order to confirm this belief. It is understood that public perception of LNG tests could exert pressures toward the preparation of an additional assessment or statement for the larger tests. If it is not possible for you to perform these studies, funds should be provided to NV to perform them utilizing other contractors. We also request that you prepare operational procedures which will protect the endangered plant species in Frenchman Flat, and otherwise minimize adverse environmental effects.

As a part of standard operating procedures at the test site, NV will initiate an investigation of possible archaeological and historic cultural sites prior to any construction activities. If any such sites are found, NV will coordinate with the State of Nevada's Historic Preservation Officer as to their proper disposition.

2. Resuspension of Radioactive Particles

Due to the potential for resuspension and subsequent transport of radioactive material off the NTS during these tests, environmental monitoring will be required to document any release. A release would require dose computation offsite and effluent reports.

3. Safety Plans

A safety plan must be submitted and approved by NV prior to the commencement of testing. This plan should emphasize safety and health aspects in relation to facility and equipment sitings, LNG aerial and ground surface monitoring grids, safety equipment, and medical and fire fighting support.

4. Public Affairs Plan

NV will issue an LNG Public Affairs Plan which will be adhered to by all program participants.

5. Construction Operations

All construction operations for the LNG Spill Tests will be performed, according to present NTSSOP's (6001), by DOE contractors at the direction of NV (NTSS).

6. Coordination

Coordination for area use permits should be effected within the DOE Operations Coordination Center - CP-1, Nevada Test Site. Experiments will be coordinated and reviewed by NV on an individual basis.

7. Identification Badges

All visit requests and photographic permits should be submitted in writing, to the Director, Division of Safeguards and Security, and received by NV, seven days in advance of the visit.

8. Passes for Access and Egress of Equipment

All vehicles and equipment with a list of contents must be submitted to the Director, Property Management Division seven days in advance of delivery to arrange appropriate passes.

R. L. Wagner August 2, 1978

9. Transportation

The transportation of the Liquefied Natural Gas must be accomplished in accordance with the U. S. Department of Transportation and all other state and local government regulations. Additionally, the carrier used must have the authority to transport the substance.

10. Ability to Terminate the Program

NV will reserve the right to terminate the program at any time if it is judged that its continuation will detrimentally affect other NTS operations or facilities.

By copy of this letter, NV offices, agencies and contractors are to support the approved program. If you have any questions or require assistance in interpreting the aforementioned contingencies, please contact Wendy Arevalo, Plans and Budget Division - 598-3171.

Sincerely,

Mahlon E. Gates
Manager

PBD:WRA-1443

cc: L. Crooks, LLL, Mercury, NV
T. T. Scolman, LASL, Los Alamos, NM
J. W. LaComb, FC/DNA, Mercury, NV
H. Runnels, REECo, Mercury, NV
B. C. Moore, Dir., NTSSO
H. E. Viney, SL, Albuq., NM
H. F. Mueller, NOAA/WSNSO, Las Vegas, NV
C. J. Smits, Dir., CMD
T. H. Blankenship, Dir., S&SECD

Technical Report Documentation Page

1. Report No.	2. Government Accession No.	3. Recipient's Catalog No.
DOE/EV-0085 Vol 2 of 3	DOE/EV-0085 Vol 2 of 3	

4. Title and Subtitle

Liquefied Gaseous Fuels Safety and Environmental Control Assessment Program: Second Status Report

5. Report Date
October 1980

6. Performing Organization Code

8. Performing Organization Report No.

7. Author(s)

9. Performing Organization Name and Address

Pacific Northwest Laboratory
Post Office Box 999
Richland, Washington 99352

10. Work Unit No.

11. Contract or Grant No.

13. Type of Report and Period Covered

12. Sponsoring Agency Name and Address

U.S. Department of Energy
Environmental and Safety Engineering Division
Mail Room E-201 (EV-132)
Washington, D.C. 20545

14. Sponsoring Agency Code

15. Supplementary Notes

This report was prepared by Dr. John G. DeSteese and staff under the cognizance of Dr. John M. Cece and Dr. Henry F. Walter. Comments about this document may be directed to the latter at the address in box 12.

16. Abstract

The DOE Assistant Secretary for Environment has responsibility for identifying, characterizing, and ameliorating the environmental, health, and safety issues and public concerns associated with commercial operation of specific energy systems. The need for developing a safety and environmental control assessment of liquefied gaseous fuels was identified as a result of discussions with various Government, industry, and academic persons having expertise with respect to particular materials. A program to address relevant issues has evolved. (Full plan contained in DOE/EV-0036, May 1979)

The goal of the Program Plan is to gather, analyze, and disseminate technical information that will aid future decisions by industry, regulators, and the public relating to facility siting, system operations, and accident prevention. (This research complements related programs supported by other Government agencies and industry.) To accomplish the goal, three objectives have been identified: verified predictive capability; verified prevention methods; verified control methods.

Volume 1 of this document outlines the DOE Liquefied Gaseous Fuels Safety and Environmental Control Assessment Program, briefly summarizes the 25 technical reports, and includes annotated bibliographies for LNG and LPG. Volume 2 contains 19 research reports focused on LNG. Volume 3 contains 6 research reports on LPG, hydrogen, and anhydrous ammonia. These reports discuss key developments between January 1979 and April 1980.

Preceding documents reporting earlier information are DOE/EV-0036 (May 1979) and DOE/EV-0002 (February 1978).

17. Key Words		18. Distribution Statement
liquefied gaseous fuels		This document is available under catalog number DOE/EV-0085, Volume 2 of 3 from National Technical Information Service 5285 Port Royal Road Springfield, Virginia 22161
scale effects experiments		
vapor generation	flame propagation	
vapor dispersion	instrumentation	
flame propagation	release prevention	

19. Security Classif. (of this report)	20. Security Classif. (of this page)	21. No. of Pages	22. Price
Unclassified	Unclassified	624	Copy: $19.50 Fiche: $ 3.50

VOLUME 2 OF 3